ANATOLY ZAYATS
DAVID RICHARDS
EDITORS

NANO-OPTICS AND NEAR-FIELD OPTICAL MICROSCOPY

Nano-Optics and Near-Field Optical Microscopy

Artech House Series
Nanoscale Science and Engineering

Series Editors
Xiang Zhang and Kang L. Wang

Introduction to DNA Self-Assembled Computer Design, Christopher Dwyer and Alvin Lebeck

Design and Test of Digital Circuits by Quantum-Dot Cellular Automata, Fabrizio Lombardi and Jing Huang

Nano-Optics and Near-Field Optical Microscopy

Anatoly Zayats
David Richards

Editors

ARTECH
HOUSE
BOSTON | LONDON
artechhouse.com

Library of Congress Cataloging-in-Publication Data
A catalog record for this book is available from the U. S. Library of Congress.
British Library Cataloguing in Publication Data
A catalogue record for this book is available from the British Library.
ISBN-13: 978-1-59693-283-8

Cover design by Yekaterina Ratner

685 Canton Street
Norwood, MA 02062

10 9 8 7 6 5 4 3 2 1

Contents

Preface

Optical microscopy is ubiquitous throughout science and technology, with the flexibility, applicability, and range of optical contrast methods establishing it as an important tool in biology and materials science. However, conventional optical microscopy suffers from a natural and increasingly important limitation: It is fundamentally impossible to focus light on an area smaller than the size of the wavelength. This diffraction limit, recognized in the nineteenth century by Abbe, has provided a stimulus for the development of alternative techniques such as electron microscopy and atomic force microscopy. However, although such techniques have pushed spatial resolutions to the atomic level, in general, this has been with the loss of the advantages provided by optical microscopy—the interaction of light with matter renders unique information about the chemical, structural, and dynamic properties of matter through high-resolution spectroscopic contrast and ultrafast time resolution; it is noninvasive and nondestructive, and it allows the study of biological systems in their native environment.

Developments in nanoscience, biotechnology, and photonics now offer great challenges for the characterization and exploration of optical interactions on the nanoscale, with an ever-increasing need for optical imaging tools having the ability to resolve features with sizes in the range of 1 nanometer to 1 micron. These are the length scales relevant for biological cells and large biological molecules and complexes and for the rapidly developing class of materials known as nanostructures—artificial materials and molecular assemblies with submicrometer dimensions fabricated for an ever-increasing range of applications. Similarly, the development of new photonic and opto-electronic devices for optical communications technology requires techniques that can map the flow of light and capture localized optical fields on the nanometer scale. Conventional optical imaging is not possible at such nanometer length scales relevant for many of the technologies earmarked for significant growth in the coming decades (e.g., biotechnology and nanotechnology).

This book is concerned with a new approach, near-field microscopy, which has opened up optical processes on the nanoscale for direct inspection. The subsequent progress in near-field microscopy has led to the development of the new area of research of "nano-optics," which is concerned with the interaction of light and matter on the nanoscale, the manipulation of light in subwavelength dimensions, and nanolocal spectroscopy. Nano-optics addresses the key issues of optics on nanometer length scales, covering basic studies in physics, biology, and chemistry as well as making a significant impact on novel technologies such as nanomaterials, nanophotonics, and single-molecule devices. This multidisciplinary field has

blossomed dramatically in recent years with the development of exciting new nano-optical probes and the real promise of optical microscopy with true nanometer resolution.

In this book, leading researchers in the field from Europe and the United States provide an overview of different aspects of nano-optics. Throughout the book, there is a common thread of the use and development of the technique of scanning near-field microscopy (SNOM) to provide access to the study of optics at the nanoscale; also presented is the application of near-field microscopy to a number of materials and photonic systems. These include the visualization of light bending in photonic crystals and of plasmon fields in subwavelength dimension structures as well as nanoscale studies of light scattering, fluorescence, Raman scattering, and nonlinear optical processes that provide indispensable information on the properties of single molecules and functional materials on length scales down to 10 nm.

The book has been updated and extended from a theme issue of Philosophical Transactions of the Royal Society A published in 2004. The present volume is divided into four parts, each preceded by a brief introduction. Part I opens with a historical review of near-field optics, followed by a review of some fundamental aspects and applications of nano-optics, including photonic forces, fluorescence emission, and second-harmonic generation in the near-field. In the final chapter of Part I, a case study is presented of the conventional established implementation of SNOM. In Part II, the application of near-field microscopy is presented for the visualization of the optical fields in various photonic systems. Near-field microscopy offers the unique advantage here of allowing access to localized and confined fields through evanescent coupling. The burgeoning field of plasmonics, the study of the properties of surface plasmon polaritons on noble metal nanostructures, and their exploitation for a wide range of application is introduced in Part III. The following chapters address various aspects of the nano-optics of plasmonic systems, again with an emphasis on the use of near-field microscopy to probe localized and confined modes. Part IV discusses the development of so-called "apertureless" SNOM techniques. These techniques provide further insight into the near-field optical properties of metal and dielectric nanostructures and fluorescent molecules and nanoparticles and offer the promise of nanoscale optical imaging.

The book is intended for researchers and postgraduate students in the fields of optics, photonics, materials characterization, nanotechnology, and scanning probe microscopy. The text is useful for newcomers and scientists interested in applications of nano-optics and near-field microscopy, as well as for established researchers in this multidisciplinary area.

The editors would like to thank all of the contributing authors for making this book a reality, the Royal Society for its initial support of this project, and Ferhat Culfaz for his hard work in the final stages of bringing the manuscript to completion.

PART I

Nano-Optics and Near-Field Microscopy

Introduction

In *Philosophical Magazine*, E. H. Synge published a paper challenging the diffraction limitations of optical measurements. It was another 60 years before his proposed instrument was realized with the technique of scanning near-field optical microscopy (SNOM), which opened optical processes on the nanoscale for direct inspection. In Chapter 1, one of the founders of the field, Dieter Pohl, provides a review of the development of nano-optics, with an emphasis on the historical roots of the field up to the time it became an established branch of nanometer science and technology. The chapter concentrates on the decade 1984–1994 (in particular, on the principally new ideas that came up during that period), with a special focus on SNOM. Scientific development after 1994 is addressed in greater detail later in the book.

In the following three chapters of this introductory part of the book, a number of fundamental issues of nano-optics are addressed. In Chapter 2, Chaumet, Nieto-Vesperinas, and Rahmani review the recent advancements in near-field photonic forces. The authors discuss in detail the interaction of subwavelength particles with a substrate illuminated in total internal reflection and study the optical forces experienced by the particles. The influence of plasmonic excitations on the photonic forces experienced by metallic particles is addressed. (Plasmonic modes of metallic particles are considered in greater detail in Part III of this book.) The authors also explore the possibility of using a metallic tip to achieve the selective manipulation of nanoparticles (the use of metallic tips for near-field microscopy is considered in detail in Part IV of this book), and discuss the potential of photonic crystal structures for the generation of subwavelength optical traps.

In Chapter 3, Hecht reviews the use of single quantum systems (here mainly single fluorescent molecules) as local probes for nano-optical field distributions. The author begins by discussing the role of the absorption cross section for the spatial resolution attainable in such experiments and its behavior for different environmental conditions. It is shown that the spatial distribution of field components in a high-numerical aperture laser focus can be mapped with high precision using single fluorescent molecules embedded in a thin polymer film on glass. With this proof-of-principle experiment as a starting point, the possibility of mapping strongly confined and enhanced nano-optical fields close to material structures (e.g., sharp metal tips) is discussed. The mapping of the spatial distribution of the enhanced field at an etched gold tip using a single molecule is presented as an example. Energy transfer effects and quenching are identified as possible artifacts in this context. Finally, it is demonstrated that the local quenching at a sharp metal structure nevertheless can be exploited as a novel contrast mechanism for ultrahigh resolution optical microscopy with single-molecule sensitivity. The further development of "tip-enhanced" near-field fluorescence microscopy is discussed in greater detail in Part IV.

Near-field microscopy of second-harmonic generation combines the high surface sensitivity of nonlinear optical processes and the high spatial resolution of near-field optics. It enables investigations of nonlinear optical phenomena at the nanoscale and provides an opportunity to develop a highly sensitive optical technique for materials characterization.

In Chapter 4, Zayats and Smolyaninov provide an overview of near-field approaches for local studies of second-harmonic generation. Near-field second-harmonic generation at metal surfaces and nanostructures and related electromagnetic field enhancement and confinement effects are considered. The latter demonstrates the feasibility of achieving nanoscale light sources using second-harmonic generation. Applications of second-harmonic near-field microscopy for the characterization of magnetic and ferroelectric materials also are discussed. Nonlinear nano-optics can lead to the development of novel photonic devices on the subwavelength scale as well as new tools for imaging and local optical studies of materials and chemical and biological species.

Chapter 5 provides a case study of the application of the conventional, and commercially available, SNOM, in which an apertured probe is scanned in close proximity to the sample surface. An introduction to the implementation of this technique is provided before its application to a nanostructured functional material is considered. The example provided is the study of the photophysical and self-organization properties of thin films of blends of conjugated polymers, and the lateral nanoscale patterning of conjugated polymer structures. Such thin film plastic semiconductor nanostructures offer significant potential for use in optoelectronic devices. The authors consider the nature of the near-field optical distribution of the SNOM probe, which decays within the first ~100 nm of these semiconductor materials. While the topographic information obtained simultaneously with optical data in any SNOM experiment enables an easy comparison with the higher-resolution tapping-mode atomic force microscopy, the spectroscopic contrast provided by fluorescence SNOM gives an unambiguous chemical identification of the different phases in a conjugated polymer blend. This identification is further facilitated by the fact that the characteristic fluorescence decay lifetime also is a strong function of the local material composition. Fluorescence emission intensity, fluorescence decay lifetime, and photoconductivity SNOM indicate that intermixing of constituent polymers in a blend, or nanoscale phase separation, is responsible for the high efficiency of devices employing these materials as their active layer. A scheme also is demonstrated for nano-optical lithography with SNOM of conjugated polymer structures, which has been employed successfully for the fabrication of PPV [poly(*p*-phenylenevinylene)] nanostructures with 160 nm feature sizes.

CHAPTER 1

Optics at the Nanometer Scale

D. W. Pohl

1.1 The Age of Nanometer Science and Technology

In recent years, science and technology developed an unappeasable appetite for instruments that characterize material structures on the *nanometer scale* and/or that generate and manipulate structures of *nanometer size*. Even for such conventional areas as mechanical engineering, characterization, and structuring on the nanometer scale are topics of increasing relevance.

Nanostructures of interest typically measure less than 100 nm in more than one dimension. Examples of such tiny structures are readily found in biology (viruses, DNA), microelectronics (domain size in magnetic storage devices, transistor gates), and rheology (colloids). Extended thin films with thickness < 100 nm, however, would not be considered nanostructures according to the preceding definition.

The main parameters that specify a nanostructure are its shape and size, elemental and molecular composition, and dynamic properties. For characterization, microscopes with sub-100 nm resolution combined with high chemical specificity are required. Preferentially, such high-resolution microscopes should operate at ambient conditions or in a fluid environment. Furthermore, the ideal microscope would be fast enough to allow for dynamic observation on a fast time scale. The requirements imposed on instruments suitable for generation and manipulation of nanostructures are similarly severe.

This chapter outlines some contributions that optics can make to the field of nanometer science and technology. The chapter is organized as follows: Section 1.2 elaborates on the strengths and shortcomings of optics for the investigation of nanometer-scale structures in general. Section 1.3 concentrates on principles and applications of scanning near-field optical microscopy. Section 1.4 sketches the historical background of nano- and near-field optics. Finally, Section 1.5 is devoted to the development of nano-optics proper in the last two decades and its probable evolution.

1.2 The Role of Optics

1.2.1 Unsurpassed Chemical Specificity

The wealth of light/matter interactions allows for a variety of highly selective spectroscopic techniques. They provide information not only on the elemental composition of a sample but also on its chemical organization and structure.

Furthermore, optical techniques are unsurpassed with respect to power and dynamic response. The big problem of optics, however, is the difficulty to confine the electromagnetic energy to volumes sufficiently small for purposes of nanometer-scale characterization and modification.

1.2.2 Limitations

"Light cannot be confined to a linear dimensions much smaller than $\lambda/2$." This common wisdom known as the *diffraction limit* [1] may be considered a specialization of Heisenberg's uncertainty principle with respect to position (Δx) and momentum ($p_x = hk_x/2\pi$) of a photon:

$$\Delta x|\boldsymbol{p}_x| \approx h/2\pi$$

Here Δx and $\boldsymbol{p}_x$ refer to any of the three components of the position and the momentum vector, respectively. In medium i, the three components of the wavevector k_x have to satisfy

$$k_i{}^2 = k_x{}^2 + k_y{}^2 + k_z{}^2 \tag{1.1}$$

where $k_i = 2\pi/\lambda_i = n_i|k_0|$ with λ_i is the wavelength in medium i, n_i is the index of refraction, and $\boldsymbol{k}_0$ is the wavevector in vacuum.

1.2.2.1 Far-Field Optics (Classical Optics)

The problem of confinement is particularly severe in classical optics, which, by and large, utilizes *freely propagating* photons only. Free propagation is characterized by a k-vector whose three components are real; hence, none of them can be larger than k_i according to Equation 1.1. Therefore, the positional uncertainty of a photon Δx_{class} in a freely propagating beam of light (i.e., the minimum cross section) is

$$\Delta x_{class} \geq 1/|k_x| = \lambda_i/2\pi$$

For a focusing objective or for lithography applications, the smallest resolvable distance or the so-called *critical dimension*, respectively, is

$$\mathrm{CD} = k_1\lambda/\mathrm{NA}$$

λ and NA stand for wavelength and numerical aperture, respectively; k_1 (not to be confused with a wavevector) is the factor that depends on the intensity distribution of the light beam falling on the objective. For uniform illumination, $k_1 = 0.61$ (Rayleigh criterion); for an optimized ring-shaped illumination, k_1 can be as small as 0.36. With this and NA = 0.9, near-UV light (λ = 400 nm) can be focused down to CD $\approx$ 140 nm, a capability that is exploited in modern photolithography. With the same illumination, CD = 100 nm can be achieved with the best commercially available immersion objective (NA = 1.4). Thus, classical optics ends with respect to resolution right at the borderline of nanometer-size dimensions according to the preceding definition.

1.2.2.2 Near-Field Optics (NFO)

The diffraction limit becomes less of a deterrent if the concept of free wave propagation is abandoned and *evanescent waves* are used. Evanescent waves are characterized by amplitudes that decay rapidly into at least one direction in space. The respective component(s) (say, k_z) of the wavevector are imaginary (more general: complex). Hence, the residual component(s) k_x can be larger—in fact much larger—than $|\boldsymbol{k}_i|$ according to Equation 1.2, and Δx can be much smaller than $\lambda/2\pi \approx 100$ nm. *The use of evanescent waves is the key to optics on the nanometer scale.*

Strong evanescent waves are excited preferentially—although not exclusively—at the boundary of two different media. Due to their rapid decay, they are of importance only close to the interface. Therefore, these fields also are called *near-fields*. A characteristic feature of the near field is (besides $k_x > |\boldsymbol{k}_i|$) an energy density $\mathcal{E}$ that is larger than to be expected from the time-averaged flow of radiation through a volume element determined by the Poynting vector $\boldsymbol{S}$:

$$\mathcal{E} > (8\pi/c)\ |\boldsymbol{S}|$$

This is in contrast to the freely propagating wave where the equal sign holds. Well-known examples of near-fields are the exponentially decaying wave that is generated upon total internal reflection at a glass-air interface and the field around a radiating molecular dipole that decays with the third power of the distance next to the source (see [7]).

Even a Gaussian light beam—which might be considered the ideal free wave—contains evanescent components: Being its own Fourier transform, the lateral components of a Gaussian beam extend to infinity in k-space (i.e., beyond $k_x = |\boldsymbol{k}_i|$). In fact, any wave with a finite cross section must contain such nonpropagating components: The amplitude of these components is inversely proportional to the diameter of a light beam and hence exceedingly small in general. In the field distribution of a highly focused beam, however, they play a nonnegligible role. Conclusion: The only wave without evanescent components is the plane wave, an idealization that does not exist in nature.

1.2.3 Topics in Near-Field Optics

A main activity in NFO is *scanning near-field optical microscopy*, known as SNOM [3, 4] and NSOM [5, 6]. The use of two different names has historic reasons; it is of no relevance today. To make an end with this duplication (at least in this chapter) I will use a third acronym, NOM, unless reference is made to a specific experiment.

In NOM, advantage is taken of the strongly evanescent fields next to illuminated small apertures and scattering particles (see [7]). When implemented at the probe tip of a *scanning probe microscope* (SPM), they allow us to produce optical scan images with a lateral resolution of 10 to 50 nm, combined with the excellent chemical specificity of classical optical microscopes (COMs).

Besides NOM, a variety of further nano-optical topics evolved in recent years, such as single molecule microscopy and spectroscopy [8, 9], plasmon properties of metallic nanostructures [10–16] optical nanolithography [17, 18], optical

manipulation [19, 20], photonic crystals and bandgap structures [21], and optical antennas [22, 23]. As a common feature, all of these topics deal with structures whose critical parts are of nanometer size and that confine electromagnetic radiation on the nanometer scale.

1.3 Near-Field Optical Microscopy

1.3.1 Standard Design

In a standard NOM, the probe illuminates the sample and the light transmitted by the sample is recorded by a photodetector. The detector frequently is integrated into an (inverted) COM, which allows us to switch between conventional and near-field observation [24]. Light sources or optical detectors can be integrated into the probe, but most often they are mounted externally at *far-field* optical distances from the probe.

As usual in SPM, the probe is brought almost in contact with the sample to achieve high resolution. The distance is regulated in general by an auxiliary interfacial mechanism, originally based on scanning tunneling microscopy (STM) [3, 25], today mainly on frictional force (shear force, [26]). The frictional interaction is detected elegantly with the help of a watch quartz tuning fork to which the probe is attached [27]. Due to the small gap between the probe and the sample, the light from the probe illuminates a sample area that is approximately equal to its effective size D_{eff} (e.g., the aperture diameter).

1.3.2 NOM Probes

Two types of probes are mainly used: *apertured* or *A-probes* and *scattering* or *S-probes*. A- and S-probes are complementary to some extent, generating near-fields similar to that of a magnetic and electric dipole, respectively. Both require nanoscale structuring of the probe apex since they consist of *two* media—either the *metallic* screen with aperture or the metallic scattering particle, which have to be placed exactly at the apex of a *dielectric* tip. This is a technical challenge that has not yet been mastered satisfactorily. Progress in NOM and its application has been delayed considerably for this reason.

1.3.2.1 A-Probe

The most frequently used NOM probe consists of a tip made from a transparent material (glass, quartz) coated with an opaque metal film in such a way that a small opening is left at the very apex of the tip [3]. An alternative A-probe is the micropipette with metal-coated end face [5]. The most common design uses an optical fiber shaped at one end into a pointed, metal-coated tip with an aperture at its apex; it is illuminated by a focused laser beam at the other end [28]. The minimum size of the A-probe is limited by the finite transmissivity of the metallic screen, namely by the 1/e penetration depth for the electric field, about 20 nm for aluminum at visible wavelengths. The A-probe transmits very little light through the aperture. That is, it excites a weak evanescent wave only, but it provides perfect suppression of background radiation.

The main methods for aperture formation are plastic deformation [3, 29, 30], shadow evaporation [28], micromachining with lithographic techniques [31], erosion by a focused ion beam (FIB) (see, for instance, [32]), or an electrolytic process [33, 34].

Plastic deformation, the method originally used by Pohl, Denk, and Lanz in 1984 [3], had been abandoned after the first demonstration experiments because the apertures were found to be too unstable for operation with tunneling gap width control (then the only method available). Recently, the method was resumed with good success. It turned out that the stability is sufficient for shear-force distance regulation, which allows less intimate contact between probe and sample than does electron tunneling.

The simplest method of aperture formation is shadow evaporation where the very apex is left uncoated during metal evaporation. Size and shape of the resulting apertures, however, are difficult to control with this method. Therefore, shadow evaporation is well suited for exploratory experiments but insufficient for routine work.

Structuring by FIB is a very precise method—provided a FIB microscope is readily available for this purpose. Electrolytic structuring with the help of a *solid electrolyte* might be considered the poor person's alternative—but there is more to it; it allows us to integrate the opening process into the NOM microscope, rendering the process less prone to damage during manipulation. Furthermore, it is possible to refurbish a worn-out probe by reversal of the electrolytic process.

1.3.2.2 S-Probe

An alternative to the A-probe is the scattering probe, sometimes called an "aperture less" probe. While first demonstrated in combination with a surface-plasmon supporting metal film [35], the preferred implementation today is the (preferentially spherical) metal particle attached to a transparent probe tip [36]. Under appropriate illumination, the particle is surrounded by a strongly enhanced field over a distance that roughly equals the size of the particle. Near-field and radiation characteristics resemble that of an *electric* dipole. The field distribution allows for enhanced local interaction with a sample structure. Another type of S-probe exploits the scattering from a pointed metal (see, for instance, [37–39]) or dielectric tip [40–42]. Such a probe is easy to implement, but its properties are less well understood than those of the spherical scatterer. Numerical simulations indicate the possibility of strong field enhancement at the apex. The result of such simulations, however, depends to considerable extent on the assumptions made for the length of the (conical) tip.

The advantage of the S-probe compared to the A-probe is a higher near-field excitation for a given incident intensity and, at least in principle, no limitation with respect to the minimum effective size D_{eff} of the field confinement volume. The main disadvantage is the finite background illumination of the sample by the incident light field. If focused by classical means, the cross section is at least $\lambda/2$. This means that the enhancement has to exceed the background by at least a factor of $(\lambda / 2\, D_{\text{eff}})^2$. For coherent interaction, the factor refers to the electric field or to the electric energy density (i.e., the square of the field). An interesting alternative to classical illumination of the S-probe is the combination of aperture and scattering particle [43–45].

1.3.3 Image Formation

1.3.3.1 Real Space

The signal arriving at the detector after transmission through the sample depends on its optical properties, more specifically on its local complex dielectric constant $\varepsilon(\omega, x, y, z_S, z_P)$. The value of ε is a weighted average over a sample volume whose extension corresponds to the field distribution in the confinement zone. ω is the laser frequency; x, y are the lateral coordinates of the sample; and z_S, z_P are the position of sample surface and probe. The NOM-scan image represents, to a large extent, the variation of $\varepsilon(\omega)$ with x, y, but it also is influenced by variations in the probe-sample distance $z_P - z_S$.

1.3.3.2 Fourier Space

An intuitive understanding of NOM imaging can be derived by consideration of fields and sample structures in Fourier space. The highly confined field at the exit of an aperture, when decomposed into plane waves, has strong components with lateral k-vectors $k_x \gg |\boldsymbol{k}_i|$ (see Figure 1.1).

Small sample structures also have large-k Fourier components. The interaction of light with large k_x and small sample size allows for $\boldsymbol{k}$-vector combinations, the difference of which may be back on the light line and hence propagate toward the detector. The phase of these components depends on the relative position of probe and sample with respect to the size of the wavevectors involved. The relationship between the relevant $\boldsymbol{k}$-vectors and the aperture size leads to a resolving power comparable to the diameter of the aperture.

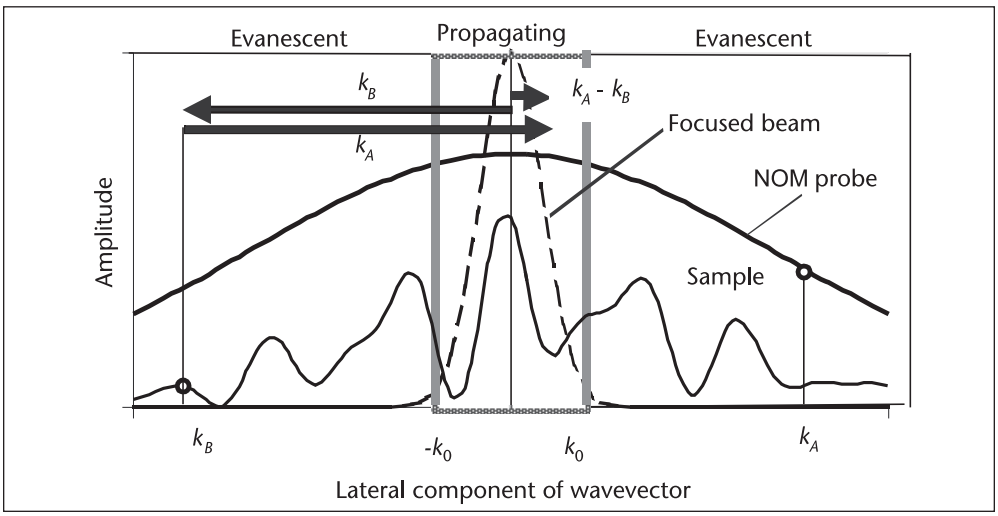

Figure 1.1 Fourier transform of the cross sections of a focused Gaussian beam (dashed line; note wings into the evanescent regime) and of the field behind the illuminated small aperture of a NOM probe (solid line) and of a sample surface with nanometer-sized dielectric structures. Evanescent wave vector component k_A of the aperture field combines with sample "wavevector" component k_B to form a difference wavevector $k_A - k_B < k_0$ that falls into the "allowed" range of the k-vector spectrum. The propagating wave with lateral wavevector $k_A - k_B$ carries the information on the structural component at k_B.

1.3.4 Modes of Operation

The NOM can be operated in different modes that are characterized by:

- Type of probe (aperture, scatterer, fluorescent particle, etc.);
- Path of probe during scanning: constant height (CHM), constant gap width (CGM), or constant signal intensity (CIM);
- Observation in transmission or reflection or an indirect mode (e.g., induction of electrical conductivity, heating);
- Contrast mechanism (absorption, phase, polarization, fluorescence, Raman scattering).

The previous list allows for many combinations. The most popular is aperture/CGM/transmission/absorption, but most of the other modes have been demonstrated as well. Operation in CGM is convenient but prone to *topographic* artifacts [46, 47]. For high-resolution imaging, it is recommended to record the image in CHM as well, which is immune against this artifact.

1.3.5 Image Interpretation/Computational Methods

Owing to the different principles underlying COM and NOM, images of the same object may differ in contrast and various aspects aside from the difference in resolution. For example, both phase and amplitude objects usually are visible in NOM images. Furthermore, the NOM image of an object depends on probe type, shape, and distance from the sample surface.

For this reason, image interpretation is an important part of NOM research. Most often, model situations must be computed numerically to understand the relationship between simple object structures and their images. This requires considerable computational effort since the interrogating electromagnetic field depends not only on the probe but also on sample structure. Hence, it is necessary to solve Maxwell's equations for complicated boundary conditions that, in addition, are different for every pixel of a scan image.

The task to solve Maxwell's equations under these circumstances bears great similarity to the problems encountered in *field theory*, in particular in antenna and radar technology. The computational methods developed for these purposes also can be readily used for NOM problems. Frequently used methods [48–55] are Green's function, multiple multipoles, finite elements, and finite-difference time-domain methods. As a common feature, all of them require considerable computational effort and none is clearly superior to the others. Thus, the choice between the different methods is a matter of individual expertise, but also of the type of problem to be solved.

1.3.6 Applications

As an optical method, NOM has the advantage of being operable under ambient conditions. Furthermore, NOM provides information on both optical and topographic properties of a sample surface in combination with an auxiliary SPM technique. Chemical and structural information can be obtained from detection of absorption, phase, fluorescence [56, 57], Raman scattering [58], short pulse dynamics, and polarization [59]. Two main areas of application potential are biology/medicine [28, 60, 61], and semiconductor research/microelectronics [62–64]; both deal with structures and structure definition in the 10 to 100 nm.

In addition to its use for characterization, NOM may be employed for optical manipulation [20] and local optical processing such as photolithography [18, 65] and heat treatment [66]. A further area of potential importance is NOM storage, which might allow us to extend, for example, compact disc technology to bit sizes in the sub-100 nm range.

1.4 Historical Background

1.4.1 NFO Before the Dawn of Nanometer Science and Technology

NFO had little interest in the earlier days of optics, although the idea of super-resolution optical microscopy can be found several times in the literature before 1984. However, a few other topics relating to NFO were studied quite carefully, namely:

- Rayleigh/Mie scattering by small particles;
- Particle plasmon polaritons;
- Förster transfer;
- Fluorescence quenching by a metallic mirror surfaces;
- Transmission of small apertures;
- Surface-enhanced Raman scattering.

These topics shall be briefly introduced in the following sections because they are relevant for NOM and the general understanding of NFO.

1.4.2 Antennas in Front of an Interface Between Two Media

The properties of a NOM probe resemble those of antennas in various aspects. The NOM probe actually may be considered an *optical antenna* whose radiation pattern is influenced by the structure of the sample similar to the influence that ground, buildings, and so forth, have on the radiation characteristic of a radio wave antenna.

The problem of the dipole antenna next to an extended body was encountered and studied in the early days of radio telecommunication around the turn of the nineteenth to twentieth century. The relevant wavelengths in those days were kilometers rather than submicrometers, but the problems were essentially the same as in NOM—namely how does the radiation characteristics of an antenna change upon variation of its environment; for instance, the approach to a medium with different dielectric properties? To answer that question, Maxwell's equations had to be solved—without the help of computers, of course.

Sommerfeld and coworkers studied the radiation from vertical [67] and horizontal dipole antennas next to grounds, as well as various details of the general solution. The discussion concentrated on the fields on Earth, the only situation of relevance in the early days. Intriguingly, they found a "ground wave" whose wavelength and amplitude depends on the properties of both media. The amplitude decreases normally to the direction of propagation and diverges for $\varepsilon = -1$. In optical terms, the "ground wave" was the then unknown surface *plasmon polariton* (SP) of a plane metal/dielectric interface [68]. The problem of the antenna opposite another medium was contemplated in the scientific literature over more than half a century [69] because of its great significance for telecommunications.

1.4.3 Molecule in Front of Another Medium

The fluorescence of a molecule in front of a metallic or dielectric surface follows the same laws as the radiation of the radio wave dipole above ground, except that the relevant frequencies are 10^6 to 10^9 times larger than before and the dielectric properties of matter are correspondingly different. Metals, in particular, may no longer be considered perfect conductors, but have finite complex dielectric constants with negative real parts.

Studies of this topic were stimulated by the discovery that monolayers of fluorescing molecules can be placed at well defined distances from a substrate, employing fatty acid salts as inert spacers in the nanometer range. Dramatic effects in fluorescent lifetime and intensity were observed with decreasing spacer thickness—in particular, a quenching of fluorescence for distances $< \lambda/2\pi$ [70]. This in turn triggered considerable theoretical efforts [71].

1.4.4 Fluorescence Resonant Energy Transfer (FRET)

A molecule is first pumped optically at its fluorescence excitation wavelength. The fluorescent energy can be absorbed by a second molecule if the latter resides within the near-field of the first. This makes itself felt in the fluorescence spectrum: It changes from that of the first to that of the second with decreasing distance. The Förster radius, defined as the distance where both fluorescence lines have the same intensity, typically is of the order of 3 to 10 nm. A typical NFO phenomenon, this is caused by the $1/r^6$ increase of electrical energy density of a dipole in its immediate proximity [72]. Therefore, FRET can be used to measure the distance between pairs of fluorescent labels. If one of the molecules was attached at the probe tip of a NOM, the position of molecules of the second type on a sample surface could be measured with very high precision [73, 74].

1.4.5 Rayleigh and Mie Scattering of Light

Any particle that is small compared to the wavelength can be treated approximately as an induced dipole, including the $1/r^6$ behavior of the electrical energy density in the near field. The highly confined field enhancement near such a submicroscopic particle is of immediate relevance here since it has the characteristics required for a NOM probe.

The (lowest order mode) scattered far field equals that of a dipole with moment

$$P = a^3 (\varepsilon_1 - \varepsilon_2) / (\varepsilon_1 + 2\varepsilon_2) \tag{1.2}$$

where a is the particle radius and $\varepsilon_{1,2}$ are the dielectric constants of the particle and the surrounding medium, respectively. For an inhomogeneous surrounding medium, ε_2 is a weighted average. If the particle is close to a sample surface, the effective ε_2 depends on its distance and local dielectric properties [75]. Moreover, higher-order scattering modes will be excited upon approach of a sample surface that breaks the spherical symmetry. This is the general background of NOM with S-probe in general.

The Rayleigh and Mie scattering theories can be readily extended to include plasmon effects in small particles (reviewed, for example, by [68, 76]). According

to Equation 1.2, the fields are strongly enhanced for $\varepsilon_1 + 2\varepsilon_2 \to 0$. Hence, it is not only the scattering efficiency that varies with the position of the scatterer but also its plasmon resonance frequency and damping.

1.4.6 Surface-Enhanced Raman Scattering (SERS)

In the mid 1970s, spectroscopists were surprised by the high intensity Raman scattering from adsorbates on rough surfaces of copper, silver, and gold [77]. (See also, for example, the review article of [78].) It turned out that huge field enhancement resulted from excitation of plasmons localized in small protrusions and crevices of the surface. The enhancement is a major cause for SERS but not sufficient to explain the experimental data completely [79].

1.4.7 Transmission of Small Apertures

The transmission of narrow apertures and slits in perfect metals was studied theoretically in context with shielding of electric devices against external electromagnetic radiation [80–82]. The analytical treatment by Bethe and Bouwkamp predicts a light flux transmitted through a small aperture proportional to the third power of its area; the electrical energy density next to the exit plane, however, varies with the square of the area only. This means that the energy density decays much faster with distance than for free wave propagation—a typical near-field phenomenon similar to that of an ideal dipole.

First experimental transmission studies of apertures with submicrometer diameters were reported by Lewis and his colleagues [83]. Recently, Tineke and his colleagues [84] reported on plasmon-mediated enhanced transmission through small apertures.

1.4.8 Early Proposals for Super-Resolution Optical Microscopy

Optical microscopists, by and large, were not aware of the potential of NFO for microscopy before (and even after) its experimental demonstration. Abbe's verdict was too convincing for the diffraction limit, restricting the resolution of a COM to approximately half a wavelength [i.e., 200 to 300 nm at best (Abbe 1874)]. In 1928, however, E. H. Synge [85] proposed to scan a tiny aperture above a sample to achieve higher resolution. Aside from the fact that he considered an aperture in a *flat* screen instead of a tip apex, his idea came very close to the schemes successfully used in present-day NOM.

However, little notice was taken of Synge's proposal, and a few years later he dismissed this valid scheme in favor of an invalid one [86]—namely to replace the *material* aperture (its screen) by the *immaterial* image of a point light source. The image, he suggested, would have the same size as the source if generated by an *ellipsoidal* mirror because of its 4π collection efficiency. This ignores the diffraction limit and hence is incorrect.

Another early predecessor of NOM was the demonstration of microwave NF imaging by Ash and Nichols [87]. They were able to resolve details as small as $\lambda/60$ in one dimension. A rudimentary far infrared NF microscope was reported by Massey [88]. A near-field microscope based on SERS was proposed by Wessel [89].

1.5 The "Age" of Nano-Optics

1.5.1 Start-up Phase (1984–1994)

The systematic exploration of optical near-fields for microscopy began in the early 1980s at the IBM Zurich Research Laboratory [90] and at Cornell University [91]. The first high-resolution single line scans of test objects, obtained in transmission with a so-called "optical stethoscope" were published in 1984 [3], followed soon by similar results obtained with a near-field scanning optical microscope (NSOM) [5]. First real scan images were published from 1985 to 1987, demonstrating a resolution of 20 to 50 nm [4, 6, 92]. The resolution in those early experiments is still among the best achieved with A-probes.

In the next round, based on an A-probe scheme developed by Fischer [93], NOM imaging *in reflection* was demonstrated [94]. The probe was flat, requiring a curved test sample for close approach. The resolution was comparable to that of transmission NOM. Reflection NOM also was demonstrated with probes that possessed a metallic protrusion instead of an aperture. The scattering intensity of this probe—which in fact was the first apertureless probe—went through a strong resonance upon approach. The resonance was attributed to plasmon excitation in the protrusion probe [35]. It was the first evidence for plasmon effects in NFO, which today is one of the most active branches in this field.

Another interesting form of NOM, called "scanning tunneling optical microscope" (STOM, [40]) or "photon scanning tunneling microscope" (PSTM [41, 42]) uses the pointed end of a *blank* optical fiber as a probe. The sample is transparent and illuminated so that total reflection occurs at the sample surface. The corresponding evanescent wave field outside the sample provides the interaction with the probe tip, in strict analogy to the tunneling electrons in STM. Fischer (1990) [37] devised a similar scheme employing a metal tip instead of glass fiber.

1.5.2 Consolidation and Generalization

NOM began to attract wider interest in the early nineties, marked by a first conference on this topic, the NATO Workshop on Near-Field Optics in Arc-et-Senans, France in 1992 [95]. The field was stimulated in particular by a series of exploratory NOM studies by E. Betzig and coworkers [65] at Bell Labs. Various modes of operation (e.g., fluorescence and polarization) were demonstrated with the help of a technically improved "NSOM," as well as different applications in biology and lithography. This work triggered further efforts in near-field microscopy.

At the same time, other forms of NFO began to raise more interest—in particular, the interaction of light with *single* (more precisely: singled out) molecules [56] including resonant energy transfer [96, 97] and Raman microscopy [58], trapping of particles by optical forces [20], localization and waveguiding in so-called photonic crystals, and plasmon excitation at nanometer-sized individual and coupled particles [11, 14, 16, 98–101] and *optical antennas* [22, 23].

With increasing numbers of experimental NOM data, the need for better theoretical understanding became obvious. Beginning around 1990, a number of theoretical groups began to work on the problems of field determination in a NOM environment [48, 49, 51, 54,102–105].

1.5.3 Outlook

A major trend in nano-/near-field optics is directed toward the development and manipulation of sophisticated probes, not only for microscopy but also as local sensors of their environment in general. The single molecule (the single quantum dot in particular) will continue to attract attention as ultimate probes. In NOM, main goals are higher resolution on the one hand and more practicable instruments on the other hand. To have an impact on other fields of science and technology, the NOM as an instrument must become more robust and simple than the instruments available today—a nano-engineering task that still waits for its realization.

Plasmon phenomena on the nanometer scale will be of considerable interest in view of their potential use in advanced integrated optical devices.

To summarize, it may be expected that NFO will continue to be under investigation, driven by the great potential of optical characterization, inspired by the variety of possible operating modes, and—last but not least—challenged by the great difficulties of the practical application.

References

[1] Abbe, E., "Beiträge zur Theorie des Mikroskops und der mikroskopischen Wahrnehmung," *Archiv f. Miroskop. Anat.*, Vol. 9, 1873, p. 413.

[2] Born, M., and E. Wolf, Principles of Optics, 6th edition, London: Pergamon Press, 1980.

[3] Pohl, D. W., W. Denk, and W. Lanz, "Optical Stethoscopy: Image Recording with Resolution $\lambda/20$," *Appl. Phys. Lett.*, Vol. 44, 1984, p. 651.

[4] Dürig, U., D. W. Pohl, and F. Rohner, "Near-Field Optical Scanning Microscopy," *J. Appl. Phys.*, Vol. 59, 1986, p. 3318.

[5] Harootunian, A. et al., "Super-Resolution Fluorescence Near-Field Scanning Optical Microscopy," *Appl. Phys. Lett.*, Vol. 49, 1986, p. 674.

[6] Betzig, E., M. Isaacson, and A. Lewis, "Collection Mode Near-Field Scanning Optical Microscopy," *Appl. Phys. Lett.*, Vol. 51, 1987, p. 2088.

[7] Pohl, D. W., "Scanning Near-Field Optical Microscopy (SNOM)," in *Advances in Optical and Electron Microscopy*, Vol. 12, 1991, p. 243.

[8] Basché, T. et al., *Single-Molecule Optical Detection, Imaging and Spectroscopy*, Weinheim, Germany: VCH Verlagsgesellschaft, 1997.

[9] Weiss, S., "Fluorescence Spectroscopy of Single Biomolecules," *Science*, Vol. 283, 2000, p. 1676.

[10] Warmack, R. J., and S. L. Humphrey, "Observation of Two Surface-Plasmon Modes on Gold Particles," *Phys. Rev. B*, Vol. 34, 1986, p. 2246.

[11] Bloemer, M. J. et al., "Optical Properties of Submicrometer-Size Silver Needles," *Phys. Rev. B*, Vol. 37, 1988, p. 8015.

[12] Marti, O. et al., "Near-Field Optical Measurement of the Surface Plasmon Field," *Opt. Comm.*, Vol. 96, 1993, p. 225.

[13] de Hollander, R. B. G., N. F. van Hulst, and R. P. H. Kooyman, "Near Field Plasmon and Force Microscopy," *Ultramicr.*, Vol. 57, 1995, p. 263.

[14] Bozhevolnyi, S., I. I. Smolyaninov, and A. V. Zayats, "Near Field Microscopy of Surface Plasmon Polaritons: Localization and Internal Interface Imaging," *Phys. Rev. B*, Vol. 51, 1995, p. 17916.

[15] Krenn, J. R. et al., "Investigation of Localized Surface Plasmons with the Photon Scanning Tunneling Microscope," *Appl. Phys. A*, Vol. 61, 1995, p. 541.

[16] Hecht, B. et al., "Local Excitation, Scattering, and Interference of Surface Plasmons," *Phys. Rev. Lett.*, Vol. 77, 1996, p. 1889.

[17] Fischer, U. Ch., and H. P. Zingsheim, "Submicroscopic Pattern Replication with Visible Light," *J. Vac. Sci. Tech.*, Vol. 19, 1981, p. 881.

[18] Naber, A., H. Kock, and H. Fuchs, "High Resolution Lithography with Near-Field Optical Microscopy," *Scanning*, Vol. 18, 1996, p. 567.

[19] Ito, H. et al., "Laser Spectroscopy of Atoms Guided by Evanescent Waves in Micron-Sized Hollow Optical Fibers," *Phys. Rev. Lett.*, 1996, p. 4500.

[20] Novotny, L., R. X. Bian, and X. S. Xie, "Theory of Nanometric Optical Tweezers," *Phys. Rev. Lett.*, Vol. 79, 1997, p. 645.

[21] Soukoulis, C. (ed.), 2001, *Photonic Crystals and Light Localization in the 21st Century: Proceedings of the NATO Advanced Study Institute*, Crete, Greece, June 18–30, 2000, The Netherlands: Kluwer Academic.

[22] Grober, R. D., R. J. Schoellkopf, and D. E. Prober, "Optical Antenna: Towards a Unity Efficiency Near-Field Optical Probe," *Appl. Phys. Lett.*, Vol. 70, 1997, p. 1354; Pohl, D. W., 2000, "Near Field Optics Seen as an Antenna Problem," in *Near-Field Optics: Principles and Applications/The Second Asia-Pacific Workshop on Near Field Optics*, Beijing, China, October 20–23, 1999 (M. Ohtsu and X. Zhu, eds.), Singapore: World Scientific, pp. 9–21.

[23] Mühlschlegel, P. et al., "Resonant Optical Antennas," Science, Vol. 308, 2005, p. 1607; Farahani, J. N., et al., "Single Quantum Dot Coupled to a Scanning Optical Antenna: A Tunable Superemitter," Phys. Rev. Lett., Vol. 95, 2005, Art. No. 017402.

[24] Hecht, B. et al., "Scanning Near Field Optical Microscopy with Aperture Probes: Fundamentals and Applications," *J. Chem. Phys.*, Vol. 112, 2000, p. 7761.

[25] Fischer, U. C., J. Koglin, and H. Fuchs, "The Tetrahedral Tip as a Probe for Scanning Near-Field Optical Microscopy at 30 nm Resolution," *J. Microsc.*, Vol. 176, 1994, p. 281.

[26] Betzig, E., Finn, P. L., and S. J. Weiner, "Combined Shear Force and Near-Field Scanning Optical Microscopy," *Appl. Phys. Lett.*, Vol. 60, 1992, p. 2484.

[27] Karrai, K., and R. D. Grober, "Piezo-Electric Tuning Fork Tip—Sample Distance Control for Near Field Optical Microscopes," *Ultramicr.*, Vol. 61, 1995, p.197.

[28] Betzig, E. et al., "Breaking the Diffraction Barrier: Optical Microscopy on a Nanometric Scale," *Science*, Vol. 251, 1991, p. 1468.

[29] Saiki, T., and K. Matsuda, "Near-Field Optical Fiber Probe Optimized for Illumination-Collection Hybrid Mode Operation," *Appl. Phys. Lett* ., Vol. 74, 1999, p. 2773.

[30] Naber, A. et al., "Enhanced Light Confinement in a Near-Field Optical Probe with Triangular Aperture," *Phys. Rev. Lett.*, Vol. 89, 2002, Art. No. 210801.

[31] Noell, W. et al., "Micromachined Aperture Probe Tip for Multifunctional Scanning Probe Microscopy," *Appl. Phys. Lett.*, Vol. 70, 1997, p. 1236.

[32] Veerman, J. A. et al., High Definition Aperture Probes for Near Field Optical Microscopy by Focused Ion Beam Milling," *Phys. Rev. B*, Vol. 72, 1998, p. 3115.

[33] Mullin, D. et al., "Use of Solid Electrolyte Erosion for Generating Nano-aperture Near-Field Collectors," *Appl. Phys. Lett.*, Vol. 71, 1997, p. 437.

[34] Bouhelier, A. et al., "Electrolytic Formation of Nanoapertures for Scanning Near-Field Optical Microscopy," *Phys. Rev. B*, Vol. 79, 2001, p. 683.

[35] Fischer, U. Ch., and D. W. Pohl, "Observation on Single-Particle Plasmons by Near-Field Optical Microscopy," *Phys. Rev. Lett.*, Vol. 62, 1989, p. 458.

[36] Kalkbrenner, T. et al., "A Single Gold Particle as a Probe for Apertureless SNOM," *J. Microsc.*, Vol. 202, 2001, p. 72.

[37] Fischer, U. Ch., "Resolution and Contrast Generation in Scanning Near-Field Optical Microscopy," in *Scanning Tunneling Microscopy and Related Methods* (R. J. Behm, N. Garcia, and H. Rohrer, eds.), *NATO ASI Series E: Applied Sciences*, Vol. 184, 1990, p. 475.

[38] Kawata, S., and Y. Inouye, "Scanning Probe Optical Microscopy Using a Metallic Probe Tip," *Ultramicr.*, Vol. 57, 1995, p. 313.

[39] Sánchez, E. J., L. Novotny, and X. S. Xie, "Near-Field Fluorescence Microscopy Based on Two-Photon Excitation with Metal Tips," *Phys. Rev. Lett.*, Vol. 82, 1999, p. 4014.

[40] Courjon, D., K. Sarayeddine, and M. Spajer, "Scanning Tunneling Optical Microscopy," *Opt. Comm.*, Vol. 71, 1989, p. 23.

[41] Reddick, R. C., R. J. Warmack, and T. L. Ferrell, "New Form of Scanning Optical Microscopy," *Phys. Rev. B*, Vol. 39, 1989, p. 767.

[42] de Fornel, F. et al., "An Evanescent Field Optical Microscope," *SPIE*, Vol. 1139, 1989, p. 77.

[43] Fischer, U. Ch., and M. Zapletal, "The Concept of a Coaxial Tip as a Probe for Scanning Near Field Optical Microscopy and Steps Towards a Realisation," *Ultramicr.*, Vol. 42–44, 1992, p. 393.

[44] Squalli, O. et al., "Improved Tip Performance for Scanning Near-Field Optical Microscopy by the Attachment of a Single Gold Nanoparticle," *Appl. Phys. Lett.*, Vol. 76, 2000, p. 2134.

[45] Frey, H.G. et al., "Enhancing the Resolution of Scanning Near-Field Optical Microscopy by a Metal Tip Grown on an Aperture Probe," *Appl. Phys. Lett.*, Vol. 81, 2002, p. 5030.

[46] Bozhevolnyi, S., "Topographical Artifacts and Optical Resolution in Near-Field Optical Microscopy," *J. Opt. Soc. Am. B*, Vol. 14, 1997, p. 2254.

[47] Hecht B. et al., "Facts and Artifacts in Near-Field Optical Microscopy," *J. Appl. Phys.*, Vol. 81, 1997, p. 2492.

[48] Dereux, A., and D. W. Pohl, "The 90° Prism as a Model SNOM Probe: Near-Field, Photon Tunneling and Far-Field Properties," in Near Field Optics (D. W. Pohl and D. Courjon, eds.), *NATO ASI Series E: Applied Sciences*, Vol. 242, 1993, p. 189.

[49] van Labeke, D., and D. Barchiesi, "Theoretical Problems in Scanning Near-Field Optical Microscopy," in *Near Field Optics* (D. W. Pohl and D. Courjon, eds.), *NATO ASI Series E: Applied Sciences*, Vol. 242, 1993, p.157.

[50] Girard, Ch. et al., "Importance of Confined Fields in Near-Field Optical Imaging of Subwavelength Objects," *Phys. Rev. B*, Vol. 50, 1994, p. 14467.

[51] Novotny, L., D. W. Pohl, and B. Hecht, "Scanning Near-Field Optical Probe with Ultrasmall Spot Size," *Opt. Lett.*, Vol. 20, 1995, p. 970.

[52] Carminati, R., and J. J. Greffet, "Reconstruction of the Dielectric Contrast Profile from Near-Field Data," Ultramicr., Vol. 61, 1995, p.11.

[53] Martin, O. J. F., Ch. Girard, and A. Dereux, "Dielectric vs. Topographic Contrast in Near-Field Microscopy," *J. Opt. Soc. Am. A*, Vol. 13, 1996, p.1801.

[54] Girard, Ch., and A. Dereux, "Near-Field Optical Theories," *Rep. Prog. Phys.*, Vol. 59, 1996, p. 657.

[55] Greffet, J. J., and R. Carminati., "Theory of Imaging in Near-Field Microsocopy," in *Optics at the Nanometer Scale* (M. Nieto-Vesperinas and N. Garcia, eds.), *NATO ASI Series E: Applied Sciences*, Vol. 319, 1996, p. 300.

[56] Moerner, W. E. et al., "Near-Field Optical Spectroscopy of Individual Molecules in Solids," *Phys. Rev. Lett.*, Vol. 73, 1994, p. 2764.

[57] Meixner, A. J. et al., "Super Resolution Imaging and Detection of Fluorescence from Single Molecules by Scanning Near-Field Optical Microscopy," *Opt. Engin*, Vol. 34, 1995, p. 2324.

[58] Deckert, V. et al., "Near-Field Surface-Enhanced Raman Spectroscopy of Dye Molecules Adsorbed on Silver Island Films," *Chem. Phys. Lett.*, Vol. 283, 1998, p. 381.

[59] Betzig, E., "Principles and Applications of Near-Field Scanning Optical Microscopy (NSOM)," in *Near Field Optics, NATO ASI Series E: Applied Sciences*, Vol. 242, 1993, p. 7.

[60] Hartmann, T. et al., "A Scanning Near-Field Optical Microscope (SNOM) for Biological Applications," in *Near Field Optics* (D. W. Pohl and D. Courjon, eds.), *NATO ASI Series E: Applied Sciences*, Vol. 242, 1993, p. 35.

[61] Muramatsu, H. et al., "Development of Near-Field Optic/Atomic-Force Microscope for Biological Materials in Aqueous Solutions," *Ultramicr.*, Vol. 61, 1995, p. 265.

[62] Goldberg, B. B. et al., "Near-Field Optical Studies of Semiconductor Heterostructures and Laser Diodes," *IEEE J. Sel. Topics in Quantum Electronics*, Vol. 1, 1995, p. 1073.

[63] Saiki, T. et al., "Spatially Resolved Photoluminescence Spectroscopy of Lateral P-N Junctions Prepared by Si-Doped GaAs Using a Photon Scanning Tunneling Microscope," *Appl. Phys. Lett.*, Vol. 67, 1995, p. 2191.

[64] Eah, S. K. et al., "Near-Field Photoluminescence of Si-Doped GaAs," *Opt. Rev.*, Vol. 3, 1996, p. 450.

[65] Betzig, E., and J. Trautman, "Near-Field Optics: Microscopy, Spectroscopy, and Surface Modification Beyond the Diffraction Limit," *Science*, Vol. 257, 1992, p. 189.

[66] Zeisel, D. et al., "Pulsed Laser Induced Desorption and Optical Imaging on a Nanometer Scale with Scanning Near-Field Microscopy Using Chemically Etched Fibers, *Appl. Phys. Lett.*, Vol. 69, 1996, p. 2941.

[67] Sommerfeld, A., "Über die Ausbreitung der Wellen in der drahtlosen Telegraphie," *Ann. d. Physik*, Volume IV, 1909, p. 665.

[68] Raether, H., "Surface Plasmons on Smooth and Rough Surfaces and on Gratings," in *Springer Tracts in Modern Physics*, Vol. 111, Berlin: Springer, 1988.

[69] Banos, A., *Dipole Radiation in the Presence of a Conducting Half Space*, Oxford: Pergamon Press, 1966.

[70] Drexhage, K. H., "Interaction of Light with Monomolecular Dye Lasers, in *Progress in Optics* (E. Wolf, ed.), Vol. 12, Amsterdam: North-Holland, 1974, pp. 161–232.

[71] Chance, R. R., A, Prock, and R. Silbey, "Molecular Fluorescence and Energy Transfer Near Interfaces," *Adv. Chem. Phys.*, Vol. 60, 1978, p. 1.

[72] Förster, Th., "Energiewanderung und Fluoreszens," *Die Naturwissenschaften*, Vol. 33, 1946, p. 166.

[73] Ozaki, H. et al., "Detection of DNA Bending in a DNA-PAP1 Protein Complex by Fluorescence Resonance Energy Transfer," *Biochem Biophys Res Commun.*, Vol. 231, 1997, p. 553.

[74] Hillisch, A., M. Lorenz, and S. Diekmann, "Recent Advances in FRET: Distance Determination in Protein-DNA Complexes," *Curr Opin Struct Biol.*, Vol. 2, 2001, p. 201.

[75] Ruppin, R., "Surface Modes and Optical Absorption of a Small Sphere above a Substrate, *Surf. Science*, Vol. 127, 1983, p. 108.

[76] Economou, E. N., and K. L. Ngai, "Surface Plasma Oscillations and Related Surface Effects," in *Advances in Chemical Physics* (I. Prigogine and S. A. Rice, eds.), Vol. 27, New York: John Wiley, 1974, p. 263.

[77] Fleischmann, M., P. J. Hendra, and A. J. McQuilan, "Raman Spectra of Pyridine Adsorbed at a Silver Electrode," *Chem. Phys. Lett.*, Vol. 26, 1974, p. 163.

[78] Chang, R. K., and B. L. Laube, "Surface-Enhanced Raman Scattering and Nonlinear Optics Applied to Electrochemistry," *Crit. Rev. Sol. State Mat. Sci.*, Vol. 12, 1984, p. 1.

[79] Otto, A., "Raman Scattering from Adsorbates on Silver," *Surf. Sci.*, Vol. 92, 1980, p. 145.

[80] Bethe, H. A., "Theory of Diffraction by Small Holes," *Phys. Rev.*, Vol. 66, 1944, p. 163.

[81] Bouwkamp, C. J., "On Bethe's Theory of Diffraction by Small Holes," *Philips Res. Rep.*, Vol. 5, 1950, p. 321.

[82] Leviatan, Y., "Study of Near-Zone Fields of a Small Aperture, *J. Appl. Phys.*, Vol. 60, 1986, p. 1577.

[83] Lewis, A. et al., "Development of a 500 Å Spatial Resolution Light Microscope," *Ultramicr.*, Vol. 13, 1984, p. 227.

[84] Tineke, T. et al., "Surface-Plasmon-Enhanced Transmission Through Hole Arrays in Cr Films," *J. Opt. Soc. Am. B*, Vol. 16, 1999, p. 1743.

[85] Synge, E. H., "A Suggested Model for Extending Microscopic Resolution into the Ultra-Microscopic Region," *Phil. Mag.*, Vol. 6, 1928, p. 356.

[86] Synge, E. H., "A Microscopic Method," *Phil. Mag.*, Vol. 7, 1931, p. 65.

[87] Ash, E. A., and G. Nicholls, "Super-Resolution Aperture Scanning Microscope," *Nature*, Vol. 237, 1972, p. 510.

[88] Massey, G. A., "Microscopy and Pattern Generation with Scanned Evanescent Waves," *Appl. Opt.*, Vol. 23, 1984, p. 658.

[89] Wessel, J., "Surface-Enhanced Optical Microscopy," *J. Opt. Soc. Am. B, Vol. 2*, 1985, p. 1538.

[90] Pohl, D. W., 1982, U.S. Patent 4604520.

[91] Lewis A. et al., "Scanning Optical Spectral Microscopy with 500 Å Spatial Resolution," *Biophys. J.*, Vol. 41, 1983, p. 405a.

[92] Pohl, D. W., W. Denk, and U. Dürig, "Optical Stethoscopy: Imaging with $\lambda/20$," *Proc. SPIE*, Vol. 565, 1985, p. 56.

[93] Fischer, U. Ch., "Optical Characteristics of 0.1 Ìm Circular Apertures in a Metal Film as Light Sources for Scanning Ultramicroscopy," *J. Vac. Sci. Tech.*, Vol. B3, 1985, p. 386.

[94] Fischer, U. Ch., U. T. Dürig, and D. W. Pohl, "Near-Field Optical Scanning Microscopy in Reflection," *Appl. Phys. Lett.*, Vol. 52, 1988, p. 249.

[95] Pohl, D. W., and D. Courjon (eds..), *Near Field Optics, NATO ASI Series E: Applied Sciences*, Vol. 242, 1993.

[96] Tan, W., and R. Kopelman, "Nanoscale Imaging and Sensing by Near-Field Optics," in *Fluorescence Imaging Spectroscopy and Microscopy,* Chemical Analysis Series Vol. 137 (X. Feng Wang and B. Herman, eds.), New York: John Wiley, 1993, p. 407.

[97] Vickery, S. A., and R. C. Dunn, "Scanning Near-Field Fluorescence Resonance Energy Transfer Microscopy," *Biophys. J.*, Vol. 76, 1999, p. 1812.

[98] Krenn, J. R. et al., "Squeezing the Optical Near-Field Zone by Plasmon Coupling of Metallic Nanoparticles," *Phys. Rev. Lett.*, Vol. 82, 1999, p. 2590.

[99] Bouhelier, A. et al., "Plasmon Optics of Structured Silver Films," *Phys. Rev. B*, Vol. 63, 2001, Art. No. 155404.

[100] Bozhevolnyi, S. I. et al., "Waveguiding in Surface Plasmon Polariton Band Gap Structures," *Phys. Rev. Lett.*, Vol. 86, 2001, p. 3008.

[101] Kawata S. (ed.), "Near Field Optics and Surface Plasmon Polaritons," in *Applied Physics*, Vol. 81, Berlin/Heidelberg: Springer Verlag, 2001.

[102] Vigoureux, J. M., J. M. Girard, and D. Courjon, "General Principles of Scanning Tunneling Optical Microscopy, *Opt. Lett.*, Vol. 14, 1989, p. 1039.

[103] Keller, O., S. Bozhevolnyi, and M. Xiao, "On the Resolution Limit of Near-Field Optical Microscopy," in *Near Field Optics* (D. W. Pohl and D. Courjon, eds.), *NATO ASI Series E: Applied Sciences*, Vol. 242, 1993, p. 229.

[104] Martin, O. J. F., A. Dereux, and C. Girard, "Iterative Scheme for Computing Exactly the Total Field Propagating in Dielectric Structures of Arbitrary Shape," *J. Opt. Soc. Am. A*, Vol. 11, 1994, p. 1073.

[105] Barchiesi D. et al., "Computing the Optical Near-Field Distribution Around Subwavelength Surface Structures: A Comparative Study of Different Methods," *Phys. Rev. E*, Vol. 54, 1996, p. 4285.

CHAPTER 2

Near-Field Photonic Forces

P. C. Chaumet, M. Nieto-Vesperinas, and A. Rahmani

2.1 Introduction

The ability to harness the mechanical effect of light on matter has spawned a new active research field at the crossing of many disciplines. In 1986, the *optical tweezer* was invented [1] as an outcome of extensive studies of the radiation pressure exerted by light on cells, particles, and atoms. Ever since, this technique has allowed the ability to nondestructively handle structures in a variety of configurations ranging from spectroscopy [2, 3], phase transitions in polymers [4], and light-assisted ordering of dielectric particles [5], to photonic force spectroscopy of cells [6] and biological molecules [7].

On a scale comparable to or smaller than the wavelength, strong photonic forces are the consequence of enhanced local fields. These concentrations of electromagnetic energy in subwavelength regions near tips, objects, or surfaces are linked to the important contribution of evanescent waves to the near-field of a scatterer. Therefore, a rigorous description of near-field photonic forces requires a careful analysis of the contribution of evanescent fields to photonic forces.

The light intensity enhancements in near-field regions near surfaces may give rise to enhanced gradient forces capable of trapping particles within nanometric scale regions [8–10]. Furthermore, evanescent waves can be used to control the position of a particle suspended over a surface and to estimate the colloidal interaction force between the particle and the surface [11–13]. The optical force created by standing evanescent waves also can be used to organize particles on a substrate [14].

This chapter presents a review of the main advances in basic studies aimed at understanding the action of optical forces in the near field. After a brief introduction to the theory of electromagnetic forces in Section 2.2, we present in Section 2.3 an illustration of the action of an evanescent wave on a dipolar particle. This example provides insight into the respective roles of the so-called *gradient* and *scattering plus absorption* force components. Then in Section 2.4, we address the effect of multiple scatterings of light on particles over flat substrates. This also will allow us to analyze the effect of the particle nature and size as well as distance to the substrate—a good understanding of these effects being essential for the design and interpretation of experiments. The role of near-field forces experienced by particles, used as probes for surface topography sensing, is addressed in Section 2.5. Here the role of plasmon-polariton resonances of metallic particles in the signal provided by force enhancements is discussed. Optical binding between illuminated particles is discussed in Section 2.6. In Section 2.7, we review studies of optical

manipulation of nanoparticles with apertureless probes and the application of photonic forces to SERS. In Section 2.8, we discuss the use of photonic crystal structures to foster new near-field trapping schemes. Finally, in Section 2.9, we present our conclusions.

2.2 Basic Theory of Forces Due to Electromagnetic Fields

2.2.1 Maxwell's Stress Tensor

The force **F** on a charge q, moving with velocity **v** in an external electromagnetic field in a medium that can be characterized by a permittivity ε and permeability μ, is $\mathbf{F} = q(\mathbf{E} + \frac{\mathbf{v}}{c} \times \mathbf{B})$ where **E** and **B** denote the electric field and the magnetic induction vectors, respectively. $\mathbf{B} = \mu\mathbf{H}$, **H** being the magnetic vector. In a system of charges, the total force equals the variation $d\mathbf{P}_{mec}/dt$ of the mechanical momentum of the system, and it is known [15, 16] that one has the conservation law

$$\frac{d\mathbf{P}_{mec}}{dt} + \frac{d\mathbf{P}_{field}}{dt} = \int_s \mathbf{T} \cdot \mathbf{n} ds \tag{2.1}$$

In Equation 2.1, S is any arbitrary closed surface that includes a volume V containing the system of charges; $\mathbf{P}_{field}$ is the total electromagnetic momentum given by Gordon [17]: $\mathbf{P}_{field} = \int_V \mathbf{S} dv/c^2$, c denoting the speed of light and $\mathbf{S} = \frac{c}{4\pi}(\mathbf{E} \times \mathbf{H})$ being the Poynting vector. **T** is Maxwell's stress tensor whose components are given by the following equation:

$$T_{ij} = \frac{1}{4\pi}\left[\varepsilon E_i E_j + \mu H_i H_j - \frac{1}{2}\delta_{ij}(\varepsilon E^2 + \mu H^2)\right], \ (i,j = 1,2,3) \tag{2.2}$$

In the common case of an electromagnetic field incident on a finite body, S and V are its surface and volume, respectively, or any surface and volume enclosing it. The electromagnetic vectors entering in Equations 2.1 and 2.2 correspond to the total field, namely incident and scattered fields.

Most experiments are conducted at optical frequencies and thus involve time-averaged electromagnetic fields. Let the electromagnetic fields be time-harmonic so that $\mathbf{E}(\mathbf{r},t) = \mathrm{Re}\left[\mathbf{E}(\mathbf{r})e^{-i\omega t}\right]$ and $\mathbf{H}(\mathbf{r},t) = \mathrm{Re}\left[\mathbf{H}(\mathbf{r})e^{-i\omega t}\right]$ (where Re denotes the real part). The definition of the time average is

$$\langle \cdot \rangle = \lim_{T\to\infty} \frac{1}{2T}\int_{-T}^{T} (\cdot) dt \tag{2.3}$$

Then the time average given in Equation 2.3, when applied to Eq. 2.1 yields the following average force:

$$\langle \mathbf{F} \rangle = \left\langle \frac{d\mathbf{P}_{mec}}{dt} \right\rangle = \int_S \langle \mathbf{T} \rangle \cdot \mathbf{n} ds \tag{2.4}$$

In Equation 2.4, $\left\langle \frac{d\mathbf{P}_{\text{field}}}{dt} \right\rangle = 0$ since $\langle \mathbf{S}(\mathbf{r},\mathbf{t}) \rangle = \frac{c}{8\pi}\text{Re}[\mathbf{E}(\mathbf{r}) \times \mathbf{B}(\mathbf{r})^*]$ [18, 19]. Also, the time-average of Maxwell's stress tensor is

$$\langle T_{ij} \rangle = \frac{1}{8\pi}[\text{Re}(E_i \varepsilon E_j^*) + Re(H_i \mu H_j^*) - \frac{1}{2}\delta_{ij}(\varepsilon|\mathbf{E}|^2 + \mu|\mathbf{H}|^2)] \tag{2.5}$$

with $i,j = 1,2,3$.

Therefore, modeling electromagnetic forces involves knowledge of the total field. Several procedures have been used to evaluate these fields in different configurations. The multiple multipole method has been used to find the force exerted by a near-infrared illuminated metal tip on a nanometric particle suspended in a liquid [8]. The coupled dipole method has been used to calculate the force on one or several particles due to an illuminated flat dielectric surface [20, 21], as well as to study the optical binding between the particles [22] (see also [23, 24]). The FDTD method also has been used to study these last two phenomena [25]. The integral method has been used to derive the force near a corrugated surface [26, 27] (see also [28, 29]).

2.3 The Dipole Approximation

Small particles with radius $a \ll \lambda$ respond to an external electromagnetic field with an induced dipole moment $\mathbf{P}$. Therefore, they experience a force [17]:

$$\mathbf{F} = (\mathbf{P} \cdot \nabla)\mathbf{E} + \frac{1}{c}\frac{\partial \mathbf{P}}{\partial t} \times \mathbf{B} \tag{2.6}$$

Let the external field be time-harmonic. By making use of the relations $\mathbf{P}(\mathbf{r},t) = \text{Re}[\mathbf{p}(\mathbf{r})e^{-i\omega t}]$, $\mathbf{B} = \frac{c}{i\omega}\nabla \times \mathbf{E}$, and $\mathbf{p} = \alpha\mathbf{E}$, α being the particle polarizability, one can write the time-averaged force on the particle as [19]

$$\langle F_j(\mathbf{r}) \rangle = \frac{1}{2}\text{Re}\left[\alpha \text{E}_\text{k} \frac{\partial E_\text{k}^*(\mathbf{r})}{\partial x_j}\right], \ (j,k = 1,2,3) \tag{2.7}$$

where * denotes the complex conjugate. The polarizability of the small particle, including the radiation-reaction term, is [30, 31]

$$\alpha = \frac{\alpha_0}{1 - \frac{2}{3}ik^3\alpha_0} \tag{2.8}$$

where α_0 is the static polarizability given by the Claussius-Mossotti equation, $\alpha_0 = a^3(\varepsilon - 1)/(\varepsilon + 1)$, and $\varepsilon = \varepsilon_2/\varepsilon_0$, the ratio between the particle permittivity ε_2 and that of the surrounding medium ε_0. The wave vector $k = \sqrt{\varepsilon_0}k_0$, with $k_0 = \omega/c$. For $ka \ll 1$, one can approximate α by $\alpha = \alpha_0 + \frac{2}{3}ik^3|\alpha_0|^2$.

For a wave propagating along $\mathbf{k}$, the electric-field vector can be written as follows:

$$\mathbf{E}(\mathbf{r}) = \mathbf{E}_0(\mathbf{r})e^{i\mathbf{k}\cdot\mathbf{r}} \tag{2.9}$$

Substituting Equation 2.9 into Equation 2.6, one obtains the force experienced by a dipolar particle as follows:

$$\langle \mathbf{F} \rangle = \frac{1}{4}\mathrm{Re}[\alpha]\nabla|\mathbf{E}_0|^2 + \frac{1}{2}\mathbf{k}\mathrm{Im}[\alpha]|\mathbf{E}_0|^2 - \frac{1}{2}\mathrm{Im}[\alpha]\mathrm{Im}[\mathbf{E}_0.\nabla\mathbf{E}_0^*] \tag{2.10}$$

In this case, Im denotes imaginary part. The first term is the gradient component of the force, whereas the second term represents the radiation pressure contribution to the scattering force. In the case of Rayleigh particle ($ka \ll 1$), by substituting the following approximation for α—$\alpha = \alpha_0 + \frac{2}{3}ik^3|\alpha_0|^2$—the second contribution also can be expressed as [32] $(|\mathbf{E}|^2/8\pi)C_{\mathrm{sca}}\mathbf{k}/k$, C_{sca} being the particle-scattering cross section, $C_{\mathrm{sca}} = (8/3)\pi k^4|\alpha_0|^2$. The last term is zero when the field has a single plane wave component, as in the next case.

2.4 Force on a Dipolar Particle Due to an Evanescent Wave

Let the small particle be immersed in the electromagnetic field of an evanescent wave whose electric vector is $\mathbf{E} = \mathbf{A}e^{-qz}e^{i\mathbf{K}\cdot\mathbf{R}}$, where $\mathbf{r} = (\mathbf{R},z)$ and $\mathbf{k} = (\mathbf{K},k_z)$, $\mathbf{K}$ and k_z satisfying $K^2 + k_z^2 = k^2$, $k^2 = \omega^2\varepsilon_0/c^2$, with $k_z = iq = i\sqrt{K^2 - k^2}$.

We assume that this field is created by total internal reflection (TIR) at a flat interface between two media of dielectric permittivity ratio $1/\varepsilon$. The incident wave, TE or TM polarized (i.e., with the electric vector perpendicular to or in the plane of incidence), impinges from the denser medium. Without any loss of generality, we can choose Oxz as the incidence plane so that $\mathbf{K} = (K,0)$. Let $t_\perp$ and $t_\parallel$ be the transmission coefficients for TE and TM polarizations, respectively. The electric vector is

$$\mathbf{E} = (0,1,0)t_\perp e^{iKx}e^{-qz} \tag{2.11}$$

for TE polarization and

$$\mathbf{E} = (-iq,0,K)\frac{t_\parallel}{k}e^{iKx}e^{-qz} \tag{2.12}$$

for TM polarization.

By introducing the preceding expressions (Eqs. 2.11 and 2.12) for the electric vector $\mathbf{E}$ into Equation 2.10, we readily obtain the average total force components. The scattering force is contained in the x,y-plane (i.e., the plane containing the propagation wave-vector of the evanescent wave), namely

$$\langle F_x \rangle = \frac{|t|^2}{2}K\mathrm{Im}[\alpha]e^{-2qz} \tag{2.13}$$

Whereas the gradient force component, which is directed along Oz, reads as follows:

$$\langle F_z \rangle = -\frac{|t|^2}{2}q\mathrm{Re}[\alpha]e^{-2qz} \tag{2.14}$$

In Equations 2.13 and 2.14, t stands for $t_\perp$ or $t_\parallel$ depending on whether the polarization is TE or TM, respectively.

For an absorbing particle, by using Equation 2.7 for α in Equations 2.13 and 2.14, one gets for the scattering and absorption force

$$\langle F_x \rangle = \frac{|t|^2}{2} K \frac{\mathrm{Im}[\alpha_0] + (2/3)k^3|\alpha_0|^2}{1 + (4/9)k^6|\alpha_0|^2} e^{-2qz} \tag{2.15}$$

and for the gradient force

$$\langle F_z \rangle = -\frac{|t|^2}{2} q \frac{\mathrm{Re}[\alpha_0]}{1 + (4/9)k^6|\alpha_0|^2} e^{-2qz} \tag{2.16}$$

It should be noted that except for $\mathrm{Re}[\varepsilon]$ between -2 and 1, $\mathrm{Re}[\alpha_0]$ is positive, thus making the gradient force directed toward the interface. On the other hand, since $\mathrm{Im}[\alpha_0]$ and $|\alpha_0|^2$ are always positive, the scattering force Equation 2.15 pushes the particle in the direction of propagation **K** of the evanescent wave. Of course, these forces increase with decreasing distance to the interface and are larger for TM polarization due to the orientation of the induced polarization in the particle.

In particular, if $ka \ll 1$, Equation 2.15 becomes

$$\langle F_x \rangle = \frac{|t|^2}{2} K e^{-2qz} \left[a^3 \mathrm{Im}\left(\frac{\varepsilon - 1}{\varepsilon + 2} \right) + \frac{2}{3} k^3 a^6 \left| \frac{\varepsilon - 1}{\varepsilon + 2} \right|^2 \right] \tag{2.17}$$

The first term of Equation 2.17 is the radiation pressure of the evanescent wave on the particle due to absorption, whereas the second term corresponds to scattering. This expression can be further condensed as

$$\langle F_x \rangle = \frac{|t|^2}{8\pi} \frac{K}{k} e^{-2qz} C_{ext} \tag{2.18}$$

The particle extinction cross section C_{ext} appearing in Eq. 2.18 is given by:

$$C_{ext} = 4\pi k a^3 \mathrm{Im}\left(\frac{\varepsilon - 1}{\varepsilon + 2} \right) + \frac{8\pi}{3} k^4 a^6 \left| \frac{\varepsilon - 1}{\varepsilon + 2} \right|^2 \tag{2.19}$$

2.5 Force on Particles upon Surfaces

Trapping dielectric particles and microorganisms was proved to be feasible through the action of gradient force components and is at the heart of the optical tweezers technique [1]. However, it is well established that the predominance of scattering and absorption components and their repulsive effect on metallic particles that have a large extinction coefficient [33] make the trapping of metallic particles more delicate. Later, gradient force trapping of subwavelength metallic particles was reported [34].

Kawata and Sugiura [35] reported the first experiments on forces due to evanescent waves created by TIR at a sapphire-water interface upon microspheres suspended close to the interface. Further experiments were done on a waveguide [36] or

through attachment of the sphere to an AFM cantilever [37]. These works aimed at estimating the magnitude of the force, although they did not conclusively establish its sign, which, as shown in the previous section and in what follows, depends on the particle polarizability. Further experiments on the trapping potentials for metallic particles in evanescent fields were conducted [38], confirming the aforementioned dependence on size and polarizability. We shall further analyze this topic next.

Since the contribution of evanescent waves to fields near surfaces is dominant, it is of interest to study the effect of these components on the force acting on a particle near a flat interface and the effect of multiple scattering on the electromagnetic field in which the particle is immersed. Concerning large particles, Mie's scattering theory [39] and ray optics [40] have been employed but they neglect the multiple interaction with the substrate. However, further calculations showed that multiple scattering is not at all negligible, and hence it can be neglected only in cases of dielectric particles whose size does not exceed a third of the wavelength and at a distance from the surface no smaller than the particle radius. Nevertheless, Arias-Gonzalez and Nieto-Vesperinas [41] showed that for metallic particles, this is true only for the scattering force component parallel to the surface. However, the oscillations as the distance varies, observable in the vertical component of the gradient force, also are present at larger distances even in the case of such smaller particles.

2.5.1 Dipolar Particles

The inset of Figure 2.1 shows the geometry used for Figures 2.1 and 2.4. Figure 2.1 shows the z component of the force normalized to the incident field computed at the position of the particle. The particle is a small dielectric sphere ($\varepsilon = 2.25$), its radius is $a = 10$ nm, and $\lambda = 632.8$ nm. The angle of incidence is larger than the critical angle θ_c. Assuming the sphere to be small, we used Equation 2.7 as well as a self-consistent method to compute the field and its derivative at the center of the sphere [9]. As the sphere gets closer to the substrate, the normalized force decays significantly. This is due to the interaction of the sphere with the evanescent field scattered by itself and reflected by the substrate at the sphere location. As this field decays when z increases, the interaction between the sphere and its field produces a negative gradient force. Notice that the decay of the force is stronger for TM polarization since in that case, the z component of the dipole associated with the sphere produces a stronger field than the component parallel to the substrate. When the sphere is far from the substrate, the normalized force becomes constant. This reflects the fact that the force

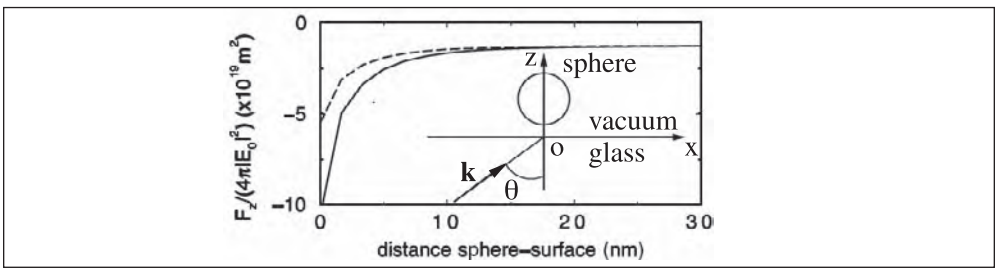

Figure 2.1 Normalized force in the z direction on a glass sphere with radius $a = 10$ nm, $\lambda = 632.8$ nm. The angle of incidence is $\theta = 42^\circ > \theta_c$. Solid line corresponds to TM polarization; dashed line, to TE polarization. The inset is the geometry of the configuration used. After Chaumet and Nieto-Vesperinas [9]. ©2002 American Physical Society.

decreases as e^{-2qz} with the distance z to the surface. (See also Equations 3.3 and 3.4.) It shows that the force depends only on the incident field and that there is no interaction between the sphere and the surface.

The dependence of the optical force on particles upon the wavelength, as discussed in Sections 3.2 and 3.3, can be applied to design a selective manipulation. The excitation of Mie resonances in spheres, like localized plasmons in metallic ones, enhance these forces [42]. Let us consider a particle of radius $a = 10$ nm made of silver or gold. Figure 2.2 shows the real and imaginary parts of the dielectric permittivity ε, of both materials versus λ when they are immersed in vacuum (thick curves) or in water (thin curves). As shown, the value of λ at which $\varepsilon = -2$ for a sphere (and that at which $\varepsilon = -1$ for a cylinder) corresponds to a relatively small value of the imaginary part of the permittivity for the case of silver, whereas for gold, it remains high around this value of λ. Immersing the particle in water produces the resonant condition at smaller $\mathrm{Im}(\varepsilon)$. Therefore, the eigenmode excitation is more efficient. The top figure shows the force versus wavelength, illuminated by a plane-propagating wave, on a gold cylinder in vacuum (thick curves) and in water (thin curves). The force on a cylinder is expressed in N/nm—namely as the magnitude per unit length. The calculation was performed with the partial-wave series for cylinders (plain curves), which is analogous to that of Mie for spheres, and by the dipole approximation (curves with symbols). The matching of both methods of calculation justifies the use of the dipole approximation for this particle size and material. The same applies to other similar metal particles (e.g., silver).

Figure 2.2 gives details of the relationship first between the gradient force and the real part of the dielectric permittivity and second between the scattering-plus absorption force and the imaginary part of this optical constant, addressed in Sections 3.2 and 3.3. A silver sphere in vacuum has been considered. Within the dipole approximation, two models of polarizability are plotted: the Clausius-Mossotti equation with the radiative reaction term of Draine (see Equation 2.8) and that of Dungey and Bohren [43]. First, evanescent wave illumination is created under TIR at a flat interface separating glass ($\sqrt{\varepsilon} = 1.51$) from vacuum. The angle of incidence is 50 degrees (critical angle: 41.47 degrees). The particle is placed at a distance of 20 nm from the plane. The interaction with the flat interface is considered negligible for this small particle at the distance used. Second, these magnitudes are plotted in Figure 2.3 when the illumination is done with a Gaussian beam of width 6000 nm at 0 degrees. The calculation has been performed at a displacement of 200 nm of the particle from the axis of the beam. Figure 2.3 illustrates how the gradient component of the force abruptly changes its sign at the resonant wavelength at which a localized surface plasmon is excited, thus becoming very small within a narrow interval of width governed by $\mathrm{Im}(\varepsilon)$ about this particular wavelength. Notice that, taking into account the relative position of the particle with respect to an incident evanescent wave or to an incident beam, considered here, an attractive force toward the higher-intensity region is negative in the former case and positive in the latter.

Using this dramatic dependence of the magnitude of the optical force on the wavelength through the shape, size and constitutive parameters of the particle, different metallic nano-objects placed on a dielectric substrate can be sorted by appropriately tuning the light frequency in or out of the plasmon resonance. Hence, two different trapping regimes may be identified depending on whether the illumination is performed in or out of the plasmon band so that the particles can be selectively guided or immobilized at the substrate interface [44]. Likewise, by tuning the

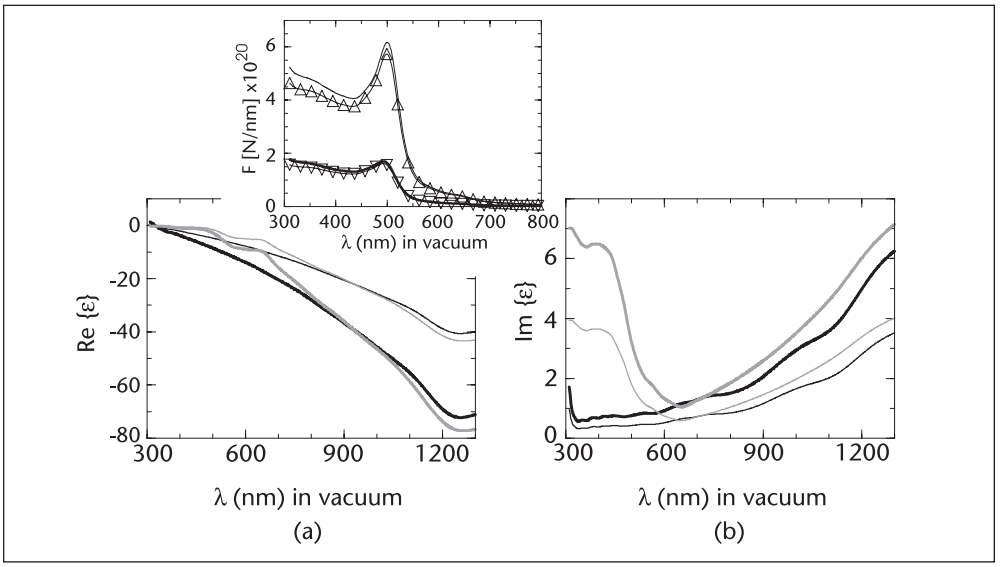

Figure 2.2 (a) Real and (b) imaginary parts of the dielectric permittivity for silver in vacuum (black thick curves) and in water (black thin curves) and gold in vacuum (gray thick curves) and in water (gray thin curves). The top figure shows the force on a gold cylinder (a =10 nm) in vacuum (thick curve) and in water (thin curve) exactly calculated by means of the partial-wave series. The same calculation is performed via the dipole approximation: a gold cylinder in vacuum (thin curve with inverted triangles) and in water (thin curve with up-pointing triangles). The illumination is done with a propagating plane wave. After Arias-Gonzalez and Nieto-Vesperinas [42]. ©2003 Optical Society of America.

wavelength, one can select short-range forces that tend to make the nanoparticles cluster, leading to intense and localized hot spots in the interstices of groups of particles. This effect has been observed in experiments of an enhanced Raman signal in trapped metal sphere ensembles [45–47] and in computer simulations [48].

2.5.2 Particles with Sizes on the Order of the Wavelength

For larger spheres, the object is represented as a set of dipoles. The self-consistent field at each dipole is computed and used in Equation 2.7 to obtain the force on each element of the discretization [20]. Far from the Rayleigh scattering regime (a = 100 nm), Figure 2.4(a) shows for a dielectric sphere that the two polarizations produce oscillations of the z component of the force with period $\lambda/2$. These oscillations are due to the interaction of the sphere with the incident field and the propagating waves scattered by the sphere and reflected by the surface. These propagating waves are negligible in the case of a sphere that is small compared to the wavelength. There also is a large difference in the magnitude of these oscillations depending on the polarization. This is a consequence of the different orientations with respect to the substrate of the set of dipoles forming the spheres.

Figure 2.4(b) shows the z component of the normalized force on a silver sphere with a = 100 nm, $\theta = 50^{\circ}$. Three wavelengths of illumination (λ = 255 nm, 300 nm, 340 nm) are considered. When the sphere is close to the substrate, we observe, as in the dielectric case, a decay of the force due to the interaction of the sphere with itself. Again, far from the surface, oscillations due to propagating waves appear. However, now the force is positive, except for TM polarization at λ = 300 nm.

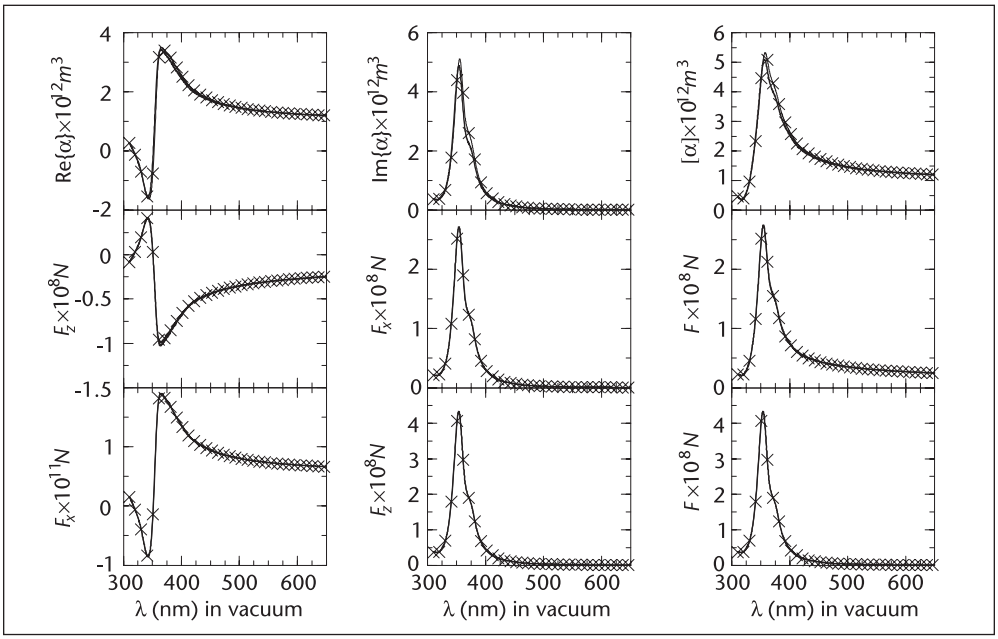

Figure 2.3 Dipole approximation. (From left to right) top: real part, imaginary part, and modulus of the polarizability for a silver sphere ($a = 10$ nm) in vacuum. Middle: vertical component, horizontal component, and modulus of the force on the same sphere (distance from plane: 20 nm) under evanescent plane-wave incidence (angle of incidence: 50 degrees). Bottom: horizontal component, vertical component, and modulus of the force on the same sphere under Gaussian beam illumination (width: 6000 nm at normal incidence) displaced a distance of 200 nm from the beam axis. Plain curves: Clausius-Mossotti polarizability with the radiative reaction term; curves with symbol: polarizability of Dungey and Bohren [43]. After Arias-Gonzalez and Nieto-Vesperinas [42]. ©2003 Optical Society of America.

We have seen in the previous section (see Equations 2.17 and 2.19) that for a dipolar particle, the z component of the force is due to the gradient force only, whereas the x component is proportional to the absorption and scattering cross sections. But for larger particles, the scattering and absorption forces acquire a positive z component due to multiple reflections inside the sphere. Since the absorption force is proportional to a^3, like the gradient force, both forces have the same order of magnitude. For $\lambda = 255$ nm or 340 nm, the real part of the polarizability is negative; hence, both the gradient and the absorption forces are positive. (See Equation 2.16.) For $\lambda = 300$ nm, the real part of the polarizability is positive; thus, there is a negative gradient force and a positive absorption force that entails different behaviors for the two polarizations. Assuming that the radiative part of the field in the normal direction is larger for TE polarization, the absorption force becomes larger than the gradient force. Conversely, for TM polarization, the gradient force remains larger than the absorption force, yielding a negative total force.

2.6 Forces and Surface Topography: Nanoparticle Resonances

Field intensity enhancements due to the excitation of morphology-dependent resonances in small particles [49] are well known for both isolated particles and arrays of particles [50]. Such metallic nanosystems have interesting optical properties. In

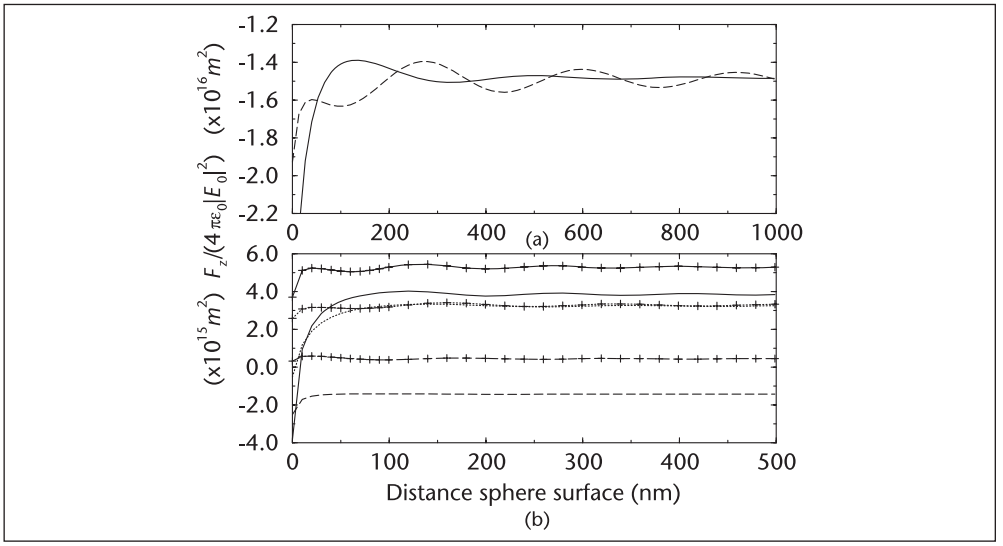

Figure 2.4 Normalized force in the z direction on a sphere with radius $a = 100$ nm. (a) Glass sphere with $\lambda = 632.8$ nm, $\theta = 42^\circ > \theta_c$. Solid line corresponds to TM polarization; dashed line, to TE polarization. (b) Silver sphere with $\theta = 50^\circ$ for the following wavelengths: $\lambda = 255$ nm (solid line), $\lambda = 300$ nm (dashed line), and $\lambda = 340$ nm (dotted line). Symbol +: TE polarization; no symbol: TM polarization. After Chaumet and Nieto-Vesperinas [20] and [21]. ©2000 American Physical Society.

particular, they can alter radiation pressure [51]; hence, they can play a role in near-field photonic forces. They also can be used to enhance the near-field optical signature of confined electromagnetic fields. Gu and Ke have demonstrated the use of a laser-trapped metallic particle as a new form of near-field probe [52, 53]. In their experiment, the photonic force is used to create a localized probe that will scatter the near-field. However, photonic forces also can be used directly to detect topographic variations.

Next, we discuss the use of particles in transducing surface topography into force signals. This constitutes a form of *near-field photonic force microscopy*.

Figure 2.5 illustrates the geometry for studying the near-field photonic force on a nanometric particle from a surface with defects: A cylinder (the 2-D version of a particle) immersed in water ($\varepsilon_0 = 1.7769$) varies its position over a water-glass interface ($\varepsilon_1 = 2.3104$). An incident Gaussian beam of half width at half-maximum w, either TE- or TM-polarized, is incident from the glass side at angle θ_0. We address the electromagnetic force on the nanocylinder illuminated under TIR so

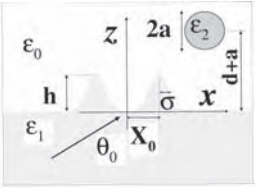

Figure 2.5 Geometry of the system.

that θ_0 is larger than the critical angle $\theta_c = 61.28^o$. Multiple interactions of the scattered wave between the object and the rough interface are considered. Silver cylinders of radius a at distance $d + a$ from the flat portion of the surface are addressed. The defects are two protrusions on the flat surface described by the height: $z = h[\exp(-(x - X_0)^2/\sigma^2) + \exp(-(x + X_0)^2/\sigma^2)]$. For this configuration, there is no depolarization in the scattering of either TE or TM waves. The field is rigorously calculated by a self-consistent method (e.g., the extinction theorem boundary condition [41]). The electromagnetic forces are then obtained from Maxwell's stress tensor, shown in Equation 2.5.

The near-field intensity distribution $|H/H_0|^2$ corresponding to the configuration of Figure 2.5 is shown in Figure 2.6 [27]. A silver cylinder of radius $a = 60$ nm varies its position at constant distance $d = 162.6$ nm above the interface. The system is illuminated by a TM-polarized Gaussian beam ($w = 4000$ nm) at $\theta_0 = 0^\circ$ and $\lambda = 387$ nm ($\varepsilon_2 = -3.22 + i0.70$). Figure 2.6(a) shows the aforementioned distribution when the particle is centered between the protrusions. A plasmon resonance is excited as manifested by the field intensity enhancement on the cylinder surface. At this resonant wavelength, the main Mie coefficient contributor is $n = 2$, which corresponds to the number of lobes ($2n$) along this surface [54]. Figure 2.6(b) shows the same situation but with $\theta_0 = 66^\circ$. The field intensities are markedly different from those of Figure 2.6(c), in which the wavelength has been changed to $\lambda = 316$ nm ($\varepsilon_2 = 0.78 + i1.07$) so that there is no particle resonance excitation at all. Figure 2.6(d) shows the same situation as in Figure 2.6(b) but at a different

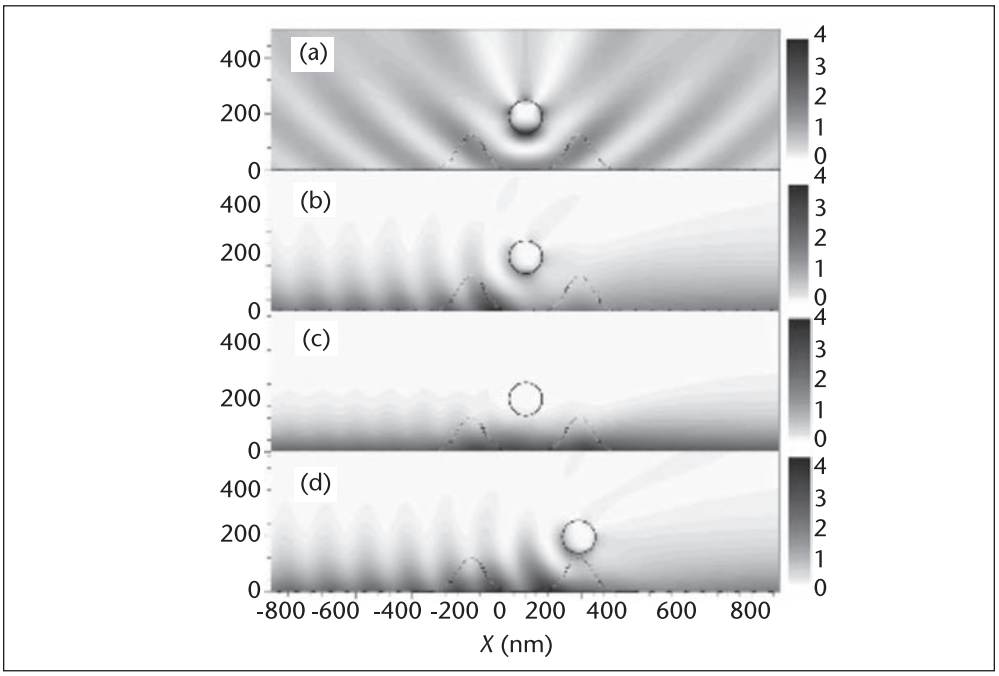

Figure 2.6 $|H/H_0|$; TM polarization from a silver cylinder with $a = 60$ nm immersed in water on a glass substrate with defect parameter $X_0 = 191.4$ nm, $h = 127.6$ nm, and $\sigma = 63.8$ nm at distance $d = 132.6$ nm. Gaussian beam incidence with $w = 4000$ nm. (a) $\lambda = 387$ nm (on resonance), $\theta_0 = 0^\circ$. (b) $\lambda = 387$ nm (on resonance), $\theta_0 = 66^\circ$. (c) $\lambda = 387$ nm (off resonance), $\theta_0 = 66^\circ$. (d) $\lambda = 316$ nm (on resonance), $\theta_0 = 66^\circ$. The cylinder is placed at (0,192.6) nm in (a), (b), and (c) and at (191.4, 192.6) nm in (d). After Arias-Gonzalez, Nieto-Vesperinas, and Lester [27].

x-position of the particle. Figures 2.6(b) and 2.6(d) show strong perturbations of the intensity map by the presence of the particle. This strong signal makes it possible for optical force microscopy at resonant conditions with such small metallic particles used as nanoprobes. One should also notice the interference pattern at the left side of the particle between the evanescent wave and the strongly reflected waves from the cylinder; in resonant conditions, it behaves as an efficient radiating antenna [55], due to its much larger scattering cross section on resonance. The fringe spacing is $\lambda/2$ (λ being the corresponding wavelength in water), and it is the same as that of the fringes below the particle in Figure 2.6(a).

The variation of the Cartesian components of the electromagnetic force are shown in Figure 2.7 [27] [F_x, Figures 2.7(a) and 2.7(b); F_z, Figures 2.7(c) and 2.7(d)] on displacing the particle at constant distance d above the interface at either plasmon resonance excitation ($\lambda = 387$ nm, solid lines) or off resonance ($\lambda = 316$ nm, broken lines). The incident beam power (per unit length) on resonance is 3.9320 W/m, and 3.9327 W/m at $\lambda = 316$ nm. Figures 2.7(a) and 2.7(c) show the force when $h = 127.6$ nm (protrusions) and $d = 132.6$ nm. On the other hand, Figures 2.7(b) and 2.7(d) display the force when $h = -127.6$ nm (grooves) and $d = 15$ nm. The illumination is done with a TM-polarized Gaussian beam of $w = 4000$ nm at $\theta_0 = 66^\circ$. These curves show that the force distributions resemble the surface topography on resonant conditions with a signal that is remarkably larger than off-resonance. This feature is especially manifested in the z component of the force in which the two protrusions are clearly distinguished from the rest of the interference ripples, as explained previously. Figure 2.7(c) also shows (thin lines) the scanning that conventional near-field microscopy would measure in this configuration, namely the normalized near-field intensity averaged on the cylinder cross section. These values are shown in arbitrary units; in fact, the curve corresponding to plasmon resonant conditions is

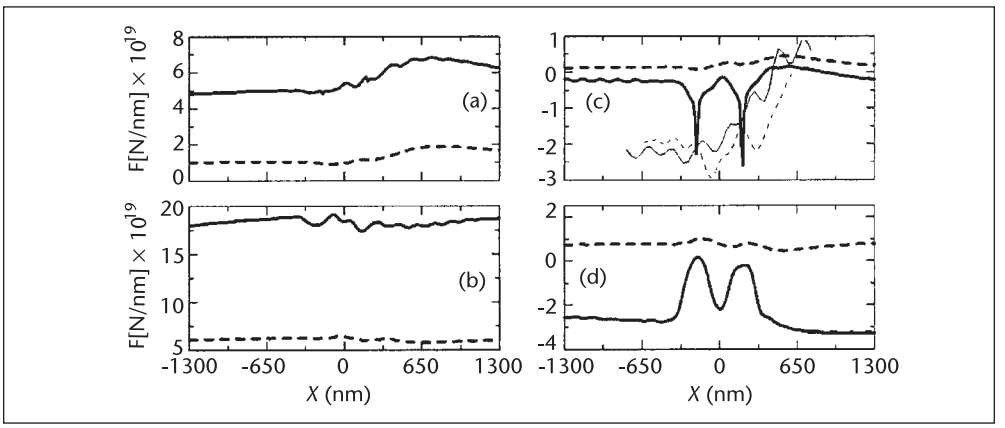

Figure 2.7 Force on a silver cylinder with $a = 60$ nm immersed in water and scanned at a constant distance on a glass surface with defect parameters $X_0 = 191.4$ nm and $\sigma = 63.8$ nm along Ox. The incident field is a TM-polarized Gaussian beam with $w = 4000$ nm and $\theta_0 = 66^\circ$. (a) Horizontal force, $h = 127.6$ nm, $d = 15$ nm. (b) Horizontal force, $h = -127.6$ nm, $d = 15$ nm. (c) Vertical force, $h = 127.6$ nm, $d = 132.6$ nm. (d) Vertical force, $h = -127.6$ nm, $d = 15$ nm. Solid curves: $\lambda = 387$ nm (on resonance); broken curves: $\lambda = 316$ nm (off resonance). Thin lines in (c) show $|H/H_0|^2$ (in arbitrary units) averaged on the perimeter of the cylinder cross section while it scans the surface. The actual magnitude of the intensity in the resonance case is almost 7 times larger than in the nonresonant one. After Arias-Gonzalez, Nieto-Vesperinas, and Lester [27]. ©2002 American Physical Society.

almost 7 times larger than that off resonance. The force distributions also show that resonance excitation enhances the contrast of the surface topography image. This also has been observed with other profiles, including surface-relief gratings. Figures 2.7(b) and 2.7(d) show some results for h inverted (namely the protrusion now being grooves); then the vertical component of the force distribution presents an inverted contrast. Notice in Figures 2.7(b) and 2.7(d) that the particle is closer to the surface, $d = 15$ nm, thus giving a higher image contrast. These results show that the positions and the sign of the defect height can be distinguished by optical force scanning.

In the case of larger particles, the multiple scattering with the surface increases; the presence of a resonance also enhances the intensity around the particle. However, this yields force signals with less resolution whose spatial distribution may present Goos-Hanchen shifts due to evanescent components, which in some cases may not follow so faithfully the surface topography [41].

2.7 Optical Binding

A few years ago Dufresne and his colleagues [56, 57] showed the possibility of creating nanocomposite materials with an array of optical tweezers generated by diffractive optics. More recently Eriksen, Mogensens, and Gluckstad [58] demonstrated the possibility of assembling microstructures with multiple-beam optical tweezers generated by the generalized phase-contrast method [59]; Metzger and his colleagues [60] determined the optical restoring force acting on the bound particles. Another way of creating microstructures is to use the interaction between the particles to achieve the assembling. The idea of optical binding was illustrated by Burns, Fournier, and Golovchenko [61] on particles immersed in water illuminated by an intense beam. They observed that the preferred relative separations between the particles related directly to the wavelength of illumination. This effect can be explained using Equation 2.7. We consider two spheres immersed in water under a plane wave illumination [see Figure 2.8(a)].

For dipolar spheres, the field at the position of the second sphere is the sum of the incident field and the field scattered by the first sphere:

$$\mathbf{E}(\mathbf{r}_2) = \mathbf{E}_0(\mathbf{r}_2) + \mathbf{S}(\mathbf{r}_2,\mathbf{r}_1)\alpha_1\mathbf{E}(\mathbf{r}_1) \tag{2.20}$$

where $\mathbf{S}(\mathbf{r}_2,\mathbf{r}_1)$ is free-space field-susceptibility tensor [15]. Using Equation 2.20 for the first and second sphere in Equation 2.7 and the fact that the incident wave is a plane wave in the z direction, the x component of the force for the second sphere can be written as

$$F_x(\mathbf{r}_2) = \frac{1}{2}\mathrm{Re}\left(\alpha_2 E_i(\mathbf{r}_2)\alpha_1^* E_i^*(\mathbf{r}_1)\frac{\partial}{\partial x}S_{ii}^*(\mathbf{r}_2,\mathbf{r}_1) \right) \tag{2.21}$$

where i stands for x if the polarization of the field is along the x-axis and y if the polarization of the field is along the y-axis. To get the force on the first sphere, the indices 1 and 2 must be exchanged. In the case of the experiments of Burns, Fournier, and Golovchenko [61], the particles were identical ($\alpha_1 = \alpha_2$); hence, the force in Eq. 2.21 becomes:

$$F_x(\mathbf{r}_2) = \frac{1}{2}|\alpha_1 E_i(\mathbf{r}_1)|^2\mathrm{Re}\left(\frac{\partial}{\partial \mathrm{x}}S_{ii}(\mathbf{r}_2,\mathbf{r}_1) \right) \tag{2.22}$$

Figures 2.8 shows the optical force in near-field [Figure 2.8(b)] and far-field regimes [Figure 2.8(c)]. To understand the behavior of the forces, we use Equation 2.22 with some approximations. In near-field (i.e., when the distance between the two spheres is small compared to the wavelength), we can make the nonretarded approximation ($k = 0$), which yields $\frac{\partial}{\partial x} S_{ii}(\mathbf{r}_2,\mathbf{r}_1) = -6(x_2 - x_1)/|x_2 - x_1|^5$ if $i = x$ and $\frac{\partial}{\partial x} S_{ii}(\mathbf{r}_2,\mathbf{r}_1) = 3(x_2 - x_1)/|x_2 - x_1|^5$ if $i = y$. Under the assumption that $\alpha_1 S_{ii}(\mathbf{r}_2,\mathbf{r}_1)$ is smaller than 1 (which assumes that the dipoles associated with the sphere are induced only by the incident field, which is perfectly valid for small glass spheres), we get the following:

$$F_x(\mathbf{r}_2) = -3|\alpha_1 E_{0_x}|^2/|x_2 - x_1|^4 \text{ for } i = x \tag{2.23}$$

$$F_x(\mathbf{r}_2) = (3/2)|\alpha_1 E_{0_y}|^2/|x_2 - x_1|^4 \text{ for } i = y \tag{2.24}$$

It appears clearly that according to the polarization of the incident field, the spheres either attract ($i = x$) or repel ($i = y$) each other. From Equations 2.23 and 2.24, it is easy to explain the repulsive and attractive forces. When the field is polarized along x, the field due to the first sphere at the location of the second sphere and the dipole associated with the second sphere are in phase. Owing to the gradient force, the second sphere is attracted by the higher-intensity field and goes toward the first sphere. When the polarization of the field is along the y-axis, the field due to the first sphere at the location of the second sphere and the dipole associated to the second sphere have opposite phases. Hence, the second sphere is attracted by the lower-intensity field and moves away from the first sphere.

The expression of the force in the far-field can be written by taking the limit for $|\mathbf{r}_2 - \mathbf{r}_1|$ large compared to the wavelength in Equation 22 and yields:

$$F_x(\mathbf{r}_2) = |\alpha_1 E_{0_x}|^2 \cos(k|x_2 - x_1|)/(x_2 - x_1)^2 \text{ for } i = x \tag{2.25}$$

$$F_x(\mathbf{r}_2) = -|\alpha_1 E_{0_y}|^2 \sin(k|x_2 - x_1|)/(x_2 - x_1)^2 \text{ for } i = y \tag{2.26}$$

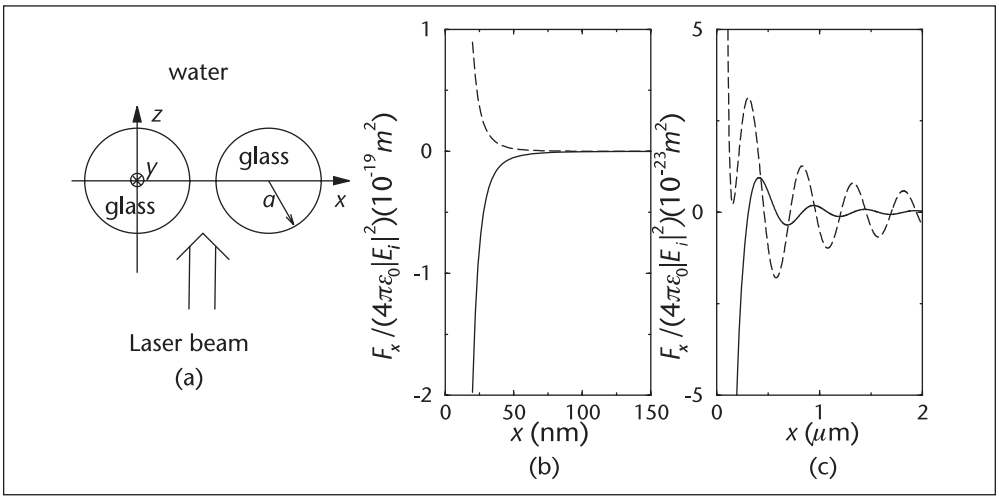

Figure 2.8 (a) Scheme of the geometry used to study the optical binding. Both spheres are in glass with $a = 10$ nm and $\lambda = 632.8$ nm in vacuum. (b, c) Solid (dashed) line obtained when the polarization of the field is along the x,y-axis. (b) Force in near field on the left sphere. (c) Force in far field on the left sphere. After Chaumet and Nieto-Vesperinas [22]. ©2001 American Physical Society.

The previous argument still applies; following the phase relation between the dipole associated to the sphere and the field scattered by the other sphere, the optical force is either attractive or repulsive as shown in Eqs. 2.25 and 2.26. This explains the oscillations observed in Figure 2.8(c). Notice that the oscillations for the two polarizations are shifted by $\lambda/4$ because they involve cosine and sine terms.

One also can compute the trapping potential normalized to k_bT (with $T = 290$K and k_b the Boltzmann's constant) for a large particle in water. The diameter of the particle is 200 nm [Figure 2.9(a)] and 400 nm [Figure 2.9(b)], the irradiance of the laser beam is $0.2\text{W}/\mu\text{m}^2$, and $\lambda = 632.8$ nm. The trapping potential needs to be larger than the Brownian motion. For instance, we want the potential wells to be deeper than $3k_bT$. The bars plotted in Figure 2.9 correspond to the $3k_bT$ limit. We see that when the size of the particle increases, the potential well becomes deeper. The trapping potential is deeper when the polarization is along the y-axis and it has a period of one wavelength. These results accurately reproduce the experiments of Burns, Fournier, and Golovchenko [61]. Notice that although they used a larger particle, the irradiance of the laser was weaker.

2.8 Optical Tweezers: Nanomanipulation with an Apertureless Probe

2.8.1 Manipulation of Lossless Particles

One of the most interesting applications of optical forces is the optical tweezers. They have proved useful not only for trapping particles but also for assembling objects ranging from microspheres to biological cells [56, 57, 59]. More recently, optical tweezers have been used to transport Bose-Einstein condensates over a large distance [62]. However, most of those manipulations involve objects whose size is on the order of one to several micrometers. It would be interesting to deal with neutral particles of a few nanometers.

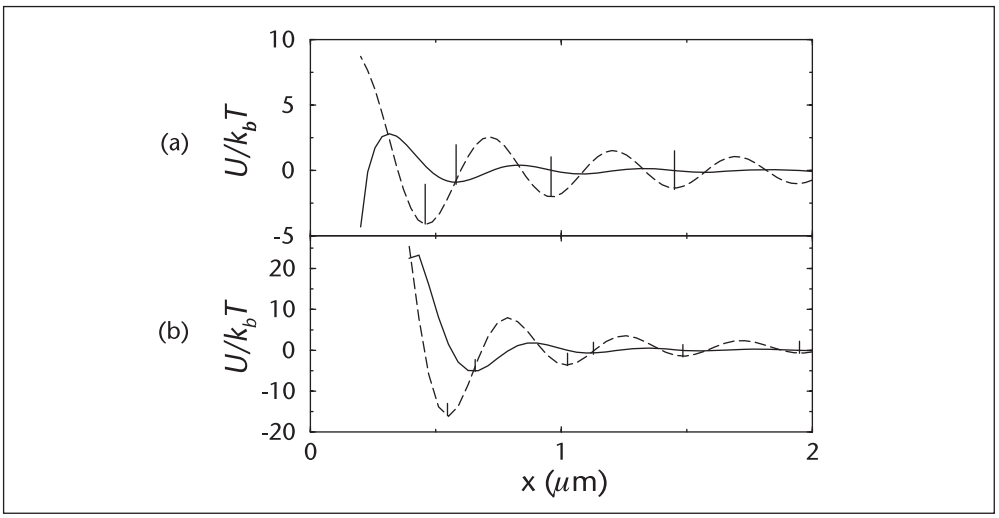

Figure 2.9 Potential of trapping normalized to k_bT for two identical glass spheres in water. Solid line for polarization following the x-axis and dashed line polarization following the y-axis. The height of the vertical bars correspond to a normalized potential equal to 3. (a) $a = 100$ nm; (b) $a = 200$ nm. After Chaumet and Nieto-Vesperinas [22]. ©2001 American Physical Society.

One solution consists of using a sharp metallic tip and the strong enhancement of the field at this metallic tip apex. Novotny, Bian, and Xie [8] used a gold tip in water illuminated by a monochromatic wave at $\lambda = 810$ nm; at this wavelength, the relative permittivity of gold is large and yields a strong enhancement of the field. The direction of the laser beam was perpendicular to the axis of the tip, and the field was polarized along the axis of the tip. Due to the strong discontinuity of the field at the tip apex, one gets an enhancement of the field of about 3000 localized at the tip apex. When a particle is in the region of the enhancement of the field, the optical force (here the gradient force) attracts the particle toward the tip apex. The particle can be moved by the tip; then the particle can be released by turning off the laser illumination.

The technique of Novotny, Bian, and Xie [8] requires one to find in water a particle of a few nanometers in size. A possibility would be to wait until a particle falls in the trap, but such an operating mode would not allow for a selective capture. Recently, we have proposed a method for selectively capturing particles [9, 10]. The idea of our nanomanipulation scheme is illustrated in Figure 2.10. A particle with relative permittivity $\varepsilon = 2.25$ and a radius $a = 10$ nm is either in air or vacuum above a dielectric substrate. The particle is illuminated by two evanescent waves created by TIR ($\theta = 43^\circ$) at the substrate/air interface. The two evanescent waves are counterpropagating (i.e., $\mathbf{k}_\parallel = -\mathbf{k}'_\parallel$) with the same polarization and a random phase relation; this is to ensure that the lateral force vanishes. The optical trap is created by the interaction of the incident waves with a tungsten probe with a radius of curvature at the apex $r = 10$ nm. The forces are computed for an irradiance of $0.05 W/\mu m^2$, which corresponds, for an Argon laser ($\lambda = 514.5$ nm) with a power of 5W, to a beam focused over an area of $100 W/\mu m^2$.

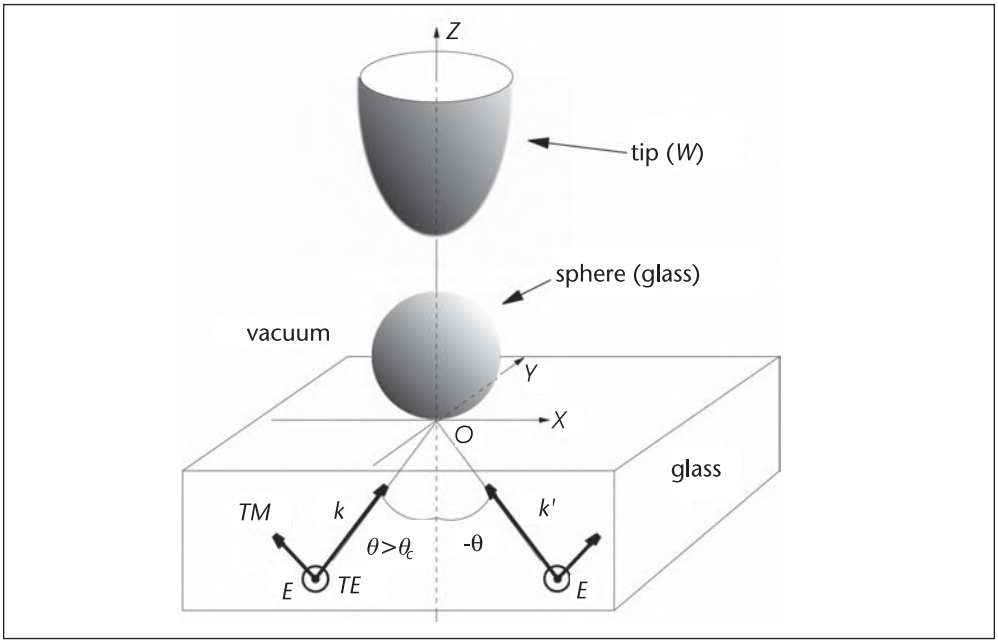

Figure 2.10 Schematic of the configuration. A dielectric sphere (radius 10 nm) on a flat dielectric substrate is illuminated under total internal reflection. A tungsten probe is used to create an optical trap. After Chaumet et al. [9]. ©2002 American Physical Society.

Figures 2.11(a) and 2.11(b) show the z component of the force experienced by the sphere versus the tip-substrate distance for TE and TM polarizations, respectively. As the tip gets closer to the sphere, one can see that the two polarizations yield different behaviors. First, when the tip is not present (far away from the substrate), one can see that the force is negative. This is due to the fact that the sphere is immersed in the evanescent incident field (which decays with the distance to the substrate); hence, the gradient force is negative. For TE polarization, the z component of the force becomes more negative when the distance between the tip and the sphere decreases. Assuming the sphere and the apex of the tip are two dipoles, it is easy to understand this effect. In TE polarization, we have two dipoles in first approximation parallel to the substrate; hence, they tend to repel each other as explained in the previous section. For TM polarization, the force becomes positive when the tip gets closer to the sphere. Due to the z component of the field, we obtain the effect described by Novotny, Bian, and Xie [8], (i.e., a large enhancement of the field at the tip apex). Hence, when the tip approaches the sphere, it experiences a positive gradient force that can counterbalance the negative force due to the incident field when the tip is close enough to the particle [inset of Figure 2.11(a)]. This leads to the trapping of the sphere at the tip apex. Then it is possible [Figure 2.11(c)] to lift the particle off the substrate in TM polarization. Note that the optical force decays slowly as the angle of illumination nears the critical value. (In TE polarization, the force is always negative.)

The procedure for selectively manipulating a nanometric sphere with an apertureless microscope is as follows: TE illumination is used while the tip scans the surface in tapping mode (or in constant-height mode if the area under investigation is small enough). Once an object has been selected, the tip is placed above the object and the polarization of the illumination is rotated to TM. The probe is brought down over the particle to capture it. Then the tip lifts the particle away from the substrate and moves it to a new position where it can be released by switching back to the TE polarization. This shows that the lack of trapping

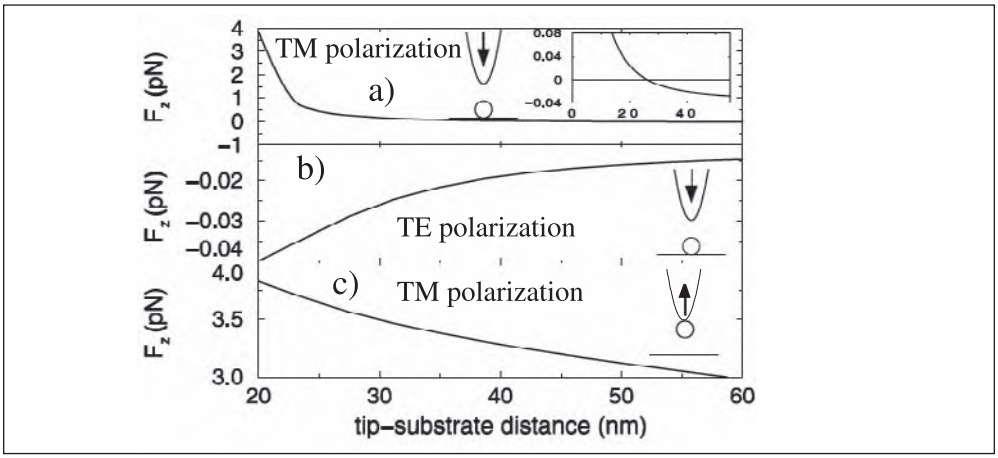

Figure 2.11 We have $a = 10$ nm, $\lambda = 514.5$ nm, and $\theta = 43^\circ$, and the arrow indicates the direction along which the tip is moved. z component of the force experienced by the sphere versus the distance between the tip and the substrate. (a, b) When the tip approaches the sphere. (a) TM polarization. The inset is an enhancement of (a) near the sign reversal. (b) TE polarization. (c) The tip lifts the sphere in TM polarization. After Chaumet et al. [9]. ©2002 American Physical Society.

capability of the tip under TE illumination is an important asset during the imaging/selection and the release of the particle phases of the manipulation.

2.8.2 Manipulation of Dielectric and Absorbing Particles

Figure 2.12 pertains to an absorbing particle with radius $a = 10$ nm and $\mathrm{Re}(\varepsilon) = 2.25$. We shall study the influence of the complex relative permittivity on the trapping and nanomanipulation process as the imaginary part of the relative permittivity increases. The trapping is performed with the same parameters that were used in Section 2.7.1, and the tip is in contact with the sphere. For both polarizations, the magnitude of the force that the sphere experiences is enhanced when the imaginary part of the relative permittivity increases. For a better understanding of this effect, let us write the real part of the polarizability α of a small sphere (compared to the wavelength of illumination):

$$\mathrm{Re}(\alpha) = a^3 \frac{(\varepsilon_r - 1)(\varepsilon_r + 2) + \varepsilon_i^2}{(\varepsilon_r + 2)^2 + \varepsilon_i^2} \tag{2.27}$$

with $\varepsilon = \varepsilon_r + i\varepsilon_i$. For our geometry, the z component of the optical force on the small sphere is due mainly to the gradient force that is proportional to the real part of the polarizability of the sphere (the first term of Equation 2.10). From Equation 2.27, it is obvious that when ε_i increases, the real part of the polarizability increases as does the gradient force; hence, the force becomes more positive for TM polarization and more negative for TE polarization. Note that as ε_i becomes very large, $\mathrm{Re}(\alpha)$ tends toward a finite limit. In conclusion, absorption helps manipulate the particle.

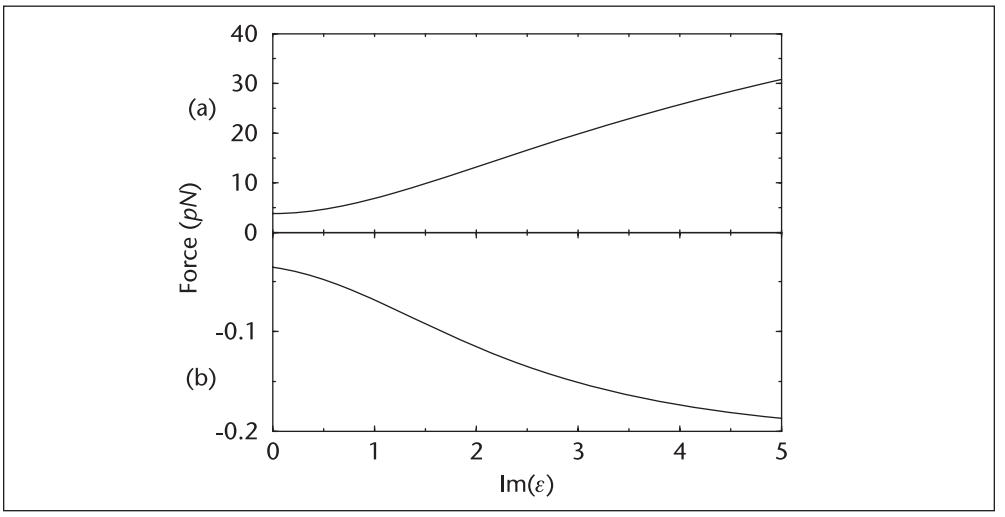

Figure 2.12 Influence of the absorption on the optical force. The particle trapped has $a = 10$ nm, $\lambda = 514.5$ nm, $\theta = 43^\circ$, and $\mathrm{Re}(\varepsilon) = 2.25$. (a) TM polarization. (b) TE polarization. After Chaumet et al. [65]. ©2005 American Physical Society.

2.8.3 Manipulation of Metallic Particles

Note that while the conventional optical tweezers technique can be used to trap Mie metallic particles [63], the previous scheme can be employed to manipulate metallic nanoparticles. Such particles of gold and silver possess unique qualities for creating localized enhancement of electromagnetic field. One of the most exciting uses of these enhanced electromagnetic near-fields is to amplify the weak Raman scattering by molecules for application in biophysics and biochemistry [64]. Surface enhanced Raman spectroscopy using metallic nanoparticles can greatly enhance the intrinsic Raman signature of a molecule and has the potential to achieve molecular identification at the single molecule level.

In this subsection, we study the optical force experienced by a sphere of gold, silver, or copper in the presence of a tip when the illumination is tuned to a plasmon resonance and when the illumination occurs outside any resonance. As is shown in Figure 2.13, the behaviors of the three spheres are similar and show that it is easier to manipulate the particle at the plasmon resonance. Notice that the resonance for the three metallic spheres occurs at different wavelengths, and more generally, the behavior of the force versus the wavelength is different. By using the dependence of the force on the spectral response of the sphere, it is possible to perform a material selective trapping. For example, at $\lambda = 325$ nm, the z component of the force on a silver sphere is close to zero, whereas it is around 12 pN for a sphere of gold. Hence, only the gold sphere would be trapped and manipulated at this wavelength. Notice that the resonance does not correspond exactly to the plasmon resonance of the

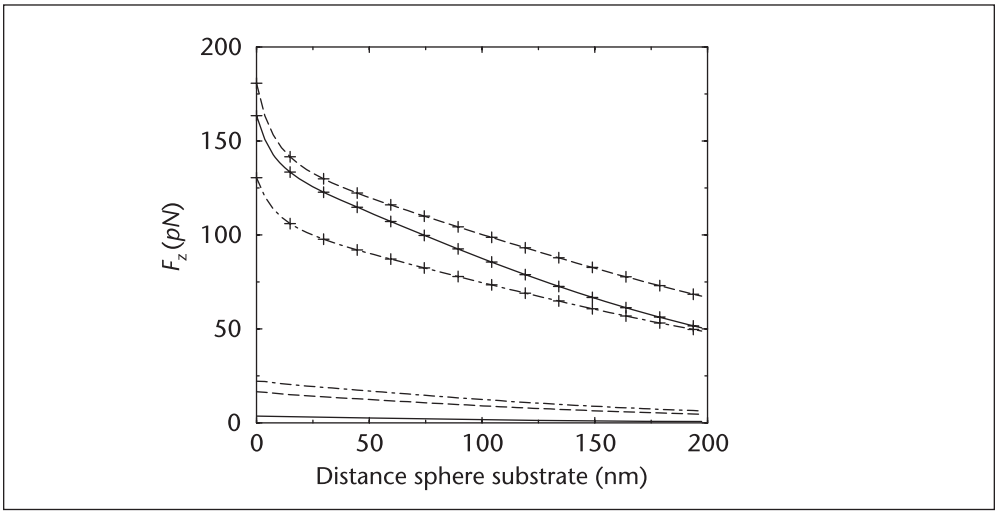

Figure 2.13 z component of the force when the sphere is manipulated (lifted) with the tip. The particle is made of silver (solid line), gold (dashed line), and copper (dot-dashed line). Curves with the + marker pertain to forces computed at the plasmon resonance wavelength ($\lambda_{au} = 640$ nm, $\lambda_{cu} = 605$ nm, $\lambda_{ag} = 480$ nm). Curves without a marker are computed away from the plasmon resonance ($\lambda_{au} = 400$ nm, $\lambda_{cu} = 400$ nm, $\lambda_{ag} = 300$ nm). After Chaumet et al. [65]. ©2002 American Physical Society.

sphere alone. This is due to the coupling between the trapped sphere and the tip, which causes a shift of the resonance compared to an isolated sphere. For more details on the optical manipulation of metallic particles, see Chaumet, Rahmani, and Nieto-Vesperinas [65].

Moreover, the strong coupling that we observe between the tip and the particle, which yields an enhancement of the electromagnetic field intensity between the metallic tip and the metallic sphere, can be used to achieve high SERS enhancement factors at the single molecule level. Indeed, we recently showed that by moving the tip from one particle to another, one can change the properties of the microcavity and therefore control the magnitude and spectrally tune the electromagnetic enhancement [66].

2.9 Nanomanipulation with a Photonic Crystal

In the previous section, the optical trap was achieved by first using a TIR configuration to generate an evanescent wave at the surface of the substrate. Next, a tapered metallic probe is used to "carve" an optical trapping potential in the evanescent wave by placing it in the near-field of the substrate. The combined effects of the evanescent wave and the probe are to create a localized, three-dimensional optical trap. Another recent approach consists of using a single optical element to create a patterned evanescent field directly: a photonic crystal (PhC) slab [67].

PhCs are periodic structures that possess photonic band gaps preventing the propagation of light at certain frequencies [68]. The wide interest in PhCs springs from the fact that their electromagnetic properties are related directly to their geometry. By tailoring the geometry of the PhC, one can impart certain characteristics to the electromagnetic field and, for instance, control the flow of light or modify the electromagnetic density of state. While controlling light through the *global* features of the PhC can be interesting, the most fascinating and promising applications of PhCs involve the use of "defects" (i.e., *local* alterations of the crystal structure). Such defects can produce states within the photonic band gap leading to electromagnetic confinement.

The potential for optical trapping of the PhC was noted by Toader, John, and Busch [69], who showed that the electromagnetic modes of an inverse opal PhC could be used to trap cold atoms using the gradient force. However, in the case of the opal structure, the 3-D trapping requires a 3-D PhC and assumes that the objects to be trapped can be infiltrated within the PhC structure. On the other hand, a PhC slab can be designed in such a way that nanoparticles can be trapped near its surface. The idea relies on the engineering of a defect mode within the PhC. A simple defect consisting of a missing hole in a triangular array of holes is shown in Figure 2.14(a). This defect creates a localized state (optical resonance) in the photonic band gap. [See Figure 2.14(b).] Notice that the microcavity created by simply removing one hole has a quality factor typically on the order of 100, which is several orders of magnitude smaller than for state-of-art PhCs, which have been reported.

The PhC is illuminated at the resonance wavelength λ by a plane wave along a direction perpendicular to the slab [from below on Figure 2.14(a)]. Consider a

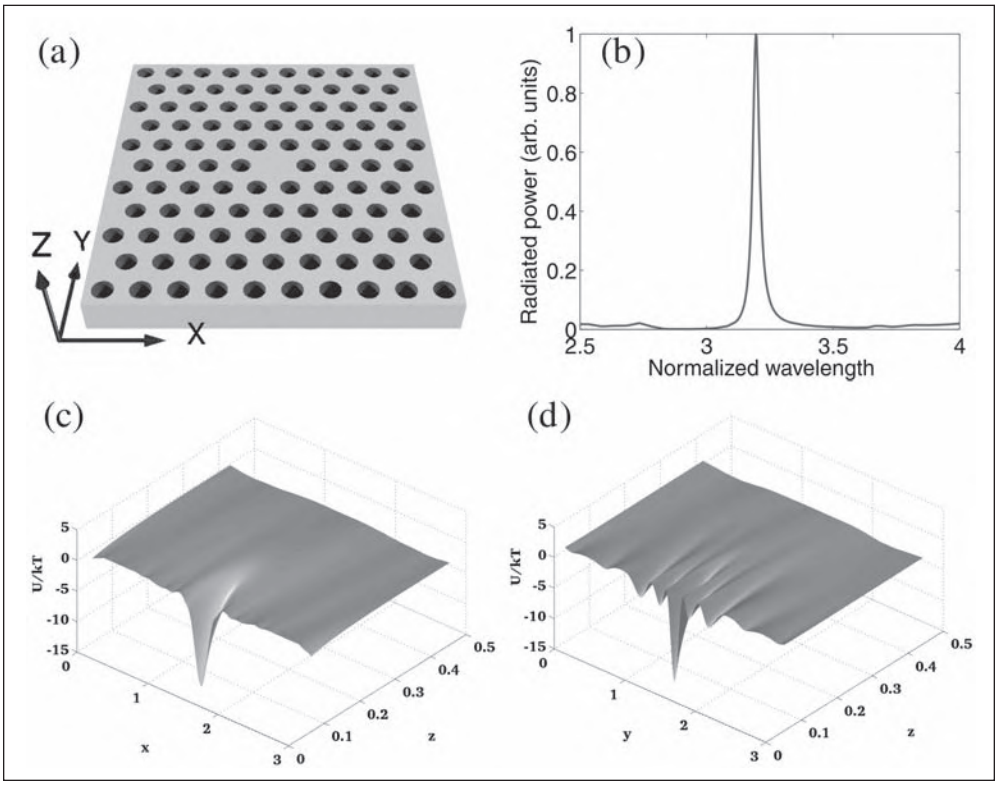

Figure 2.14 (a) A slab with refractive index 3.4 is immersed in a fluid with refractive index 1.33. The slab with thickness $t = 0.467a$ is perforated with a triangular lattice of holes with period a and hole radius $r = 0.333a$. A defect mode is introduced within the photonic band gap by omitting one hole in the crystal pattern. The optical cavity resulting from the missing hole supports a spatially and spectrally localized mode. (b) Cavity spectrum showing the resonance due to the defect mode. The wavelength is in units of a. (c) Optical trapping potential in the x,z plane for a nanoparticle (radius $0.49a$) above the cavity. (d) Optical trapping potential in the y,z plane. The potentials are normalized to k_bT, where T is the temperature of the fluid and k_b is Boltzmann's constant. After Rahmani and Chaumet [67]. ©2006 Optical Society of America.

spherical particle with relative permittivity 2.25 and radius $a = 0.04\lambda$. Given the size of the particle, we can use the dipole approximation to compute the optical force. Owing to the size of the particle, the weak optical contrast between the particle and the surrounding fluid, and the modest quality factor of the cavity mode, we neglect the influence of the particle on the optical response of the cavity (i.e., we treat the particle as a passive probe). We assume an irradiance of 10 $mW/\mu m^2$ and room temperature (300K). Figures 2.14(c) and 2.14(d) show the potential trap normalized to k_bT (k_b is the Boltzmann's constant) in planes x,y and y,z, respectively. The spatial minimum of the potential corresponds to the cavity H1. It is obvious from Figures 2.14(c) and 2.14(d) that the nanoparticle is trapped close to the PhC as the potential depth is larger that $10k_bT$. Hence, the nanoparticle is trapped in the near-field region above the H1 cavity. For more details about optical trapping with PhC, refer to Rahmani and Chaumet [67]. Note that more complex behavior can occur when the particle is able to perturb the cavity mode significantly. Barth and Benson [70], provide a good illustration of effects such as self-induced trapping.

2.10 Conclusion

Since the first realization that radiation pressure could be used to manipulate matter, the application of photonic forces has ranged from laser cooling and trapping of atoms and molecules to manipulation and assembly of small particles and biological systems. With the advent of NFO and nanophotonics, the ability to shape optical fields on the subwavelength scale has opened a new realm of application for photonic forces, a domain where evanescent modes of the electromagnetic fields prevail and where light can be confined to nanometric regions. This chapter reviews the basic conceptual and analytical tools needed to address the use of near-field photonic forces for trapping and manipulating small particles. Whereas the use of photonic forces in the near-field is still in its early stage, the properties of confined optical fields allied to the advances in far-field photonic forces offer an exciting prospect for the development of new applications in areas such as multiparticle assembling [57, 58, 60] and micromotors [71–73].

References

[1] Ashkin, A. et al., "Observation of a Single-Beam Gradient Force Optical Trap for Dielectric Particles," *Opt. Lett.*, Vol. 11, 1986, pp. 288–290.

[2] Sasaki, K. et al., "Pattern Formation and Flow Control of Fine Particles by Laser Scanning Micromanipulation," *Opt. Lett.*, Vol. 11, 1991, pp. 288–290.

[3] Misawa, H. et al., "Multibeam Laser Manipulation and Fixation of Microparticles," *Appl. Phys. Lett.*, Vol. 60, 1992, pp. 310–312.

[4] Hotta, J. et al., "Laser-Controlled Assembling of Repulsive Unimolecular Micelles in Aqueous Solution," *J. Phys. Chem. B*, Vol. 102, 1998, pp. 7687–7690.

[5] Burns, M. M., J.-M. Fournier, and J. A. Golovchenko, "Optical Matter: Crystallization and Binding in Intense Optical Fields," *Science*, Vol. 249, 1990, pp. 749–754.

[6] Pralle, A. et al., "Local Viscosity Probed by Photonic Force Microscopy," *Appl. Phys. A*, Vol. 66, 1998, pp. S71–S73.

[7] Smith, S. B., Y. Cui, and C. Bustamante, "Overstretching B-DNA: The Elastic Response of Individual Double-Stranded and Single-Stranded DNA Molecules," *Science*, Vol. 271, 1996, pp. 795–799.

[8] Novotny, L., R. X. Bian, and X. S. Xie, "Theory of Nanometric Optical Tweezers," *Phys. Rev. Lett.*, Vol. 79, 1997, pp. 645–648.

[9] Chaumet, P. C., A. Rahmani, and M. Nieto-Vesperinas, "Optical Trapping and Manipulation of Nano-object with an Apertureless Probe," *Phys. Rev. Lett.*, Vol. 88, 2002, Art. No. 123601.

[10] Chaumet, P. C., A. Rahmani, and M. Nieto-Vesperinas, "Selective Nanomanipulation Using Optical Forces," *Phys. Rev. B*, Vol. 66, 2002, Art. No. 195405.

[11] Sasaki, K., M. Tsukima, and H. Masuhara, "Three-Dimensional Potential Analysis of Radiation Pressure Exerted on a Single Microparticle," *Appl. Phys. Lett.*, Vol. 71, 1997, pp. 37–39.

[12] Clapp, A. R., A. G. Ruta, and R. B. Dickinson, "Three-Dimensional Optical Trapping and Evanescent Wave Light Scattering for Direct Measurement of Long Range Forces Between a Colloidal Particle and a Surface," *Rev. Sci. Instr.*, Vol. 70, 1999, pp. 2627–2636.

[13] Dogariu, A. C., and R. Rajagopalan, "Optical Traps as Force Transducers: The Effects of Focusing the Trapping Beam Through a Dielectric Interface," *Langmuir*, Vol. 16, 2000, pp. 2770–2778.

[14] Reece, P. J., V. Garcés-Chávez, and K. Dholakia, "Near-Field Optical Micromanipulation with Cavity Enhanced Evanescent Waves," *Appl. Phys. Lett.*, Vol. 88, 2006, Art. No. 221116.

[15] Jackson, J. D., *Classical Electrodynamics*, New York: John Wiley, 1975.
[16] Stratton, J. A., *Electromagnetic Theory*, New York: McGraw-Hill, 1941.
[17] Gordon, J. P., "Radiation Forces and Momenta in Dielectric Media," *Phys. Rev. A*, Vol. 8, 1973, pp. 14–21.
[18] Antoci, S., and L. Mihich, "Detecting Abraham's Force of Light by the Fresnel-Fizeau Effect," *Eur. Phys. J. D* , Vol. 3, 1998, pp. 205–210.
[19] Chaumet, P. C., and M. Nieto-Vesperinas, "Time-Averaged Total Force on a Dipolar Sphere in an Electromagnetic Field," *Opt. Lett.*, Vol. 25, 2000, pp. 1065–1067.
[20] Chaumet, P. C., and M. Nieto-Vesperinas, "Coupled Dipole Method Determination of the Electromagnetic Force on a Particle over a Flat Dielectric Substrate," *Phys. Rev. B*, Vol. 61, 2000, pp. 14119–14127.
[21] Chaumet, P. C., and M. Nieto-Vesperinas, "Electromagnetic Force on a Metallic Particle in the Presence of a Dielectric Surface," *Phys. Rev. B*, Vol. 62, 2000, pp. 11185–11191.
[22] Chaumet, P. C., and M. Nieto-Vesperinas, "Optical Binding of Particles with or without the Presence of a Flat Dielectric Surface," *Phys. Rev. B*, Vol. 64, 2001, Art. No. 035422.
[23] Chaumet, P. C., A. Sentenac, and A. Rahmani, "Coupled Dipole Method for Scatterers with Large Permittivity," *Phys. Rev. E*, Vol. 70, 2004, Art. No. 036606.
[24] Chaumet, P. C. et al., "Efficient Computation of Optical Forces with the Coupled Dipole Method," *Phys. Rev. E*, Vol. 72, 2005b, Art. No. 046708.
[25] Okamoto, K., and S. Kawata, "Radiation Force Exerted on Subwavelength Near a Nanoaperture," *Phys. Rev. Lett.*, Vol. 83, 1999, pp. 4534–4537.
[26] Lester, M., J. R. Arias-Gonzalez, and M. Nieto-Vesperinas, "Fundamentals and Model of Photonic-Force Microscopy," *Opt. Lett.*, Vol. 26, 2001, pp. 707–709.
[27] Arias-Gonzalez, J. R., M. Nieto-Vesperinas, and M. Lester, "Modeling Photonic Force Microscopy with Metallic Particles under Plasmon Eigenmode Excitation," *Phys. Rev. B*, Vol. 65, 2002, Art. No. 115402.
[28] Madrazo, R., and M. Nieto-Vesperinas, "Scattering of Electromagnetic Waves from a Cylinder in Front of a Conduction Plane," *J. Opt. Soc. A. A*, Vol. 12, 1995, pp. 1298–1309.
[29] Madrazo, R., and M. Nieto-Vesperinas, "Surface Structure and Polariton Interaction in the Scattering of Electromagnetic Waves from a Cylinder in Front of a Conductiong Grating: Theory for the Reflection Photon Scanning Tunneling Microsocpe," *J. Opt. Soc. A. A*, Vol. 13, 1996, pp. 785–795.
[30] Draine, B. T., "The Discrete Dipole Approximation and its Application to Interstellar Graphite Grains," *Astrophys. J.*, Vol. 333, 1988, pp. 848–872.
[31] Chaumet, P. C., "Comment on "Trapping Force, Force Constant, and Potential Depths for Dielectric Spheres in the Presence of Spherical Aberrations," *Appl. Opt.*, Vol. 43, 2004, pp. 1825–1826.
[32] Van de Hulst, H. C., *Light Scattering by Small Particles*, New York: Dover, 1981.
[33] Ashkin, A., and J. M. Dziedzic, "Stability of Optical Levitation by Radiation Pressure," *Appl. Phys. Lett.*, Vol. 24, 1974, pp. 586–588.
[34] Svoboda, K. et al., "Direct Observation of Kinesin Stepping by Optical Trapping Interferometry," *Nature*, Vol. 365, 1993, pp. 721–727.
[35] Kawata, S., and T. Sugiura, "Movement of Micrometer-Sized Particles in the Evanescent Field of a Laser-Beam," *Opt. Lett.*, Vol. 17, 1992, pp. 772–774.
[36] Kawata, S., and T. Tani, "Optically Driven Mie Particle in an Evanescent Field along a Channeled Waveguide," *Opt. Lett.*, Vol. 21, 1996, pp. 1768–1770.
[37] Vilfan, M., I. Musevic, and M. Copic, "AFM Observation of Force on a Dielectric Sphere in the Evanescent Field of Totally Reflected Light," *Europhys. Lett.*, Vol. 43, 1998, pp. 41–46.
[38] Sasaki, K. et al., "Analysis of Radiation Pressure Exerted on a Metallic Particle within an Evanescent Field," *Opt. Lett.*, Vol. 25, 2000, pp. 1385–1387.
[39] Almaas, E., and I. Brevick, "Radiation Forces on a Micrometer-Sized Sphere in an Evanescent Field," *J. Opt. Soc. Am. B*, Vol. 12, 1995, pp. 2429–2438.

[40] Walz, J. Y., "Ray Optics Calculation of the Radiation Forces Exerted on a Dielectric Sphere in an Evanescent Field," *Appl. Opt.*, Vol. 38, 1999, pp. 5319–5330.

[41] Arias-Gonzalez, J. R., and M. Nieto-Vesperinas, "Radiation Pressure over Dielectric and Metallic Nanocylinders on Surfaces: Polarization Dependence and Plasmon Resonance Conditions," *Opt. Lett.*, Vol. 27, 2002, pp. 2149–2151.

[42] Arias-Gonzalez, J. R., and M. Nieto-Vesperinas, "Optical Forces on Small Particles: Attractive and Repulsive Nature and Plasmon-Resonance Conditions," *J. Opt. Soc. Am. A*, Vol. 20, 2003, pp. 1201–1209.

[43] Dungey, C. E., and C. F. Bohren, "Light Scattering by Nonspherical Particles: A Refinement to the Coupled-Dipole Method," *J. Opt. Soc. Am. A*, Vol. 8, 1991, pp. 81–87.

[44] Zelenina, A. S. et al., "Tunable Optical Sorting and Manipulation of Nanoparticles via Plasmon Excitation," *Opt. Lett.*, Vol. 31, 2006, pp. 2054–2056.

[45] Svedberg, F. et al., "Creating Hot Nanoparticle Pairs for Surface-Enhanced Raman Spectroscopy through Optical Manipulation," *Nano Lett.*, Vol. 6, 2006, pp. 2639–2641.

[46] Svedberg, F., and M. Käll, "On the Importance of Optical Forces in Surface-Enhanced Raman Scattering (SERS)," *Faraday Discuss.*, Vol. 132, 2006, pp. 35–44.

[47] Zhang, Y. et al., "Optical Trapping and Light-Induced Agglomeration of Gold Nanoparticle Aggregates," *Phys. Rev. B*, Vol. 73, 2006, Art. No. 165405.

[48] Zelenina, A. S., R. Quidant, and M. Nieto-Vesperinas, "Enhanced Optical Forces between Coupled Resonant Metal Nanoparticles," *Opt. Lett.*, Vol. 32, 2007, pp. 1156–1158.

[49] Kreibig, U., and M. Vollmer, *Optical Properties of Metal Clusters*, Berlin: Springer-Verlag, 1995.

[50] Maier, S. A. et al., "Local Detection of Electromagnetic Energy Transport below the Diffraction Limit in Metal Nanoparticle Plasmon Waveguides," *Nature Materials*, Vol. 2, 2003, pp. 229–232.

[51] Ashkin, A., and J. M. Dziedzic, "Observation of Resonances in the Radiation Pressure on Dielectric Spheres," *Phys. Rev. Lett.*, Vol. 38, 1977, pp. 1351–1355.

[52] Gu, M., and P. Ke, "Image Enhancement in Near-Field Scanning Optical Microscopy with Laser-Trapped Metallic Particles," *Opt. Lett.*, Vol. 24, 1999, pp. 74–76.

[53] Gu, M., and P. Ke, "Depolarization of Evanescent Waves Scattered by Laser-Trapped Gold Particles: Effect of Particle Size," *J. Appl. Phys.*, Vol. 88, 2000, pp. 5415–5420.

[54] Barber, P. W., and R. K. Chang (eds.), *Optical Effects Associated with Small Particles*, Singapore: World Scientific, 1988.

[55] Krenn, J. R. et al., "Squeezing the Optical Near-Field Zone by Plasmon Coupling of Metallic Nanoparticles," *Phys. Rev. Lett.*, Vol. 82, 1999, pp. 2590–2593.

[56] Dufresne, E. R., and D. G. Grier, "Optical Tweezers Arrays and Optical Substrates Created with Diffractive Optics," *Rev. Sci. Instr.*, Vol. 69, 1998, pp. 1974–1977.

[57] Dufresne, E. R. et al., "Computer-Generated Holographic Optical Tweezer Arrays," *Rev. Sci. Inst.*, Vol. 72, 2001, pp. 1810–1816.

[58] Eriksen, R. L., P. C. Mogensens, and J. Gluckstad, "Multiple-Beam Optical Tweezers Generated by the Generalized Phase-Contrast Method," *Opt. Lett.*, Vol. 27, 2002, pp. 267–269.

[59] Macdonald, M. P. et al., "Creation and Manipulation of Three-Dimensional Optically Trapped Structures," *Science*, Vol. 296, 2002, pp. 1101–1103.

[60] Metzger, N. K. et al., "Measurement of the Restoring Forces Acting on Two Optically Bound Particles from Normal Mode Correlations," *Phys. Rev. Lett.*, Vol. 98, 2007, Art. No. 068102.

[61] Burns, M. M., J.-M. Fournier, and J. A. Golovchenko, "Optical Binding," *Phys. Rev. Lett.*, Vol. 63, 1989, pp. 1233–1236.

[62] Gustavson, T. L. et al., "Transport of Bose-Einstein Condensates with Optical Tweezers," *Phys. Rev. Lett.*, Vol. 88, 2002, Art. No. 020401.

[63] Gu, M., and D. Morrish, "Three-Dimensional Trapping of Mie Metallic Particles by the Use of Obstructed Laser Beams," *J. Appl. Phys.*, Vol. 91, 2002, pp. 1606–1612.

[64] Kneipp, K. et al., "Surface-Enhanced Raman Scattering and Biophysics," *J. Phys.: Condens. Matter*, Vol. 14, 2002, pp. R597–R624.

[65] Chaumet, P. C., A. Rahmani, and M. Nieto-Vesperinas, "Photonic Force Spectroscopy on Metallic and Absorbing Nanoparticles," *Phys. Rev. B*, Vol. 71, 2005, Art. No. 045425.

[66] Chaumet, P. C., A. Rahmani, and M. Nieto-Vesperinas, "Local-Field Enhancement in an Optical Force Metallic Nanotrap: Application to Single-Molecule Spectroscopy," *App. Opt.*, Vol. 45, 2006, pp. 5185–5190.

[67] Rahmani, A., and P. C. Chaumet, "Optical Trapping near a Photonic Crystal," *Opt. Express*, Vol. 14, 2006, pp. 6353–6358.

[68] Joannopoulos, J. D., R. Meade, and J. Winn, *Photonic Crystals*, Princeton: Princeton University Press, 1995.

[69] Toader, O., S. John, and K. Busch, "Optical Trapping, Field Enhancement and Laser Cooling in Photonic Crystals," *Opt. Express*, Vol. 8, 2001, pp. 217–222.

[70] Barth, M., and O. Benson, "Manipulation of Dielectric Particles Using Photonic Crystal Cavities," *Appl. Phys. Lett.*, Vol. 89, 2006, Art. No. 253114.

[71] Collett, W. L., C. A. Ventrice, and S. M. Mahajan, "Electromagnetic Wave Technique to Determine Radiation Torque on Micromachines Driven by Light," *Appl. Phys. Lett.*, Vol. 82, 2003, pp. 2730–2732.

[72] Sacconi, L. et al., "Three-Dimensional Magneto-Optic Trap for Micro-Object Manipulation," *Opt. Lett.*, Vol. 26, 2003, pp. 1359–1361.

[73] Chaumet, P. C., and C. Billaudeau, "Coupled Dipole Method to Compute Optical Torque: Application to a Micropropeller," *J. Appl. Phys.*, Vol. 101, 2007, Art. No. 023106.

CHAPTER 3

Nano-Optics with Single Quantum Systems

Bert Hecht

3.1 Introduction

Nano-optics is a branch of optics that describes the phenomena that occur when light interacts with pieces of nano-matter [1]—that is, pieces of matter that are very small by themselves or that exhibit features of subwavelength dimensions down to a few nanometers. Small particles, sharp tips, single molecules or atoms, and semiconductor quantum dots are just a few examples that fall into this category. A major finding of nano-optics is that under certain conditions in the vicinity of nanomatter, strongly enhanced and spatially confined optical fields can exist. The understanding and exploitation of such effects will have major impact on future optical technology because it will strongly influence such important fields as high-resolution optical microscopy, optical data storage, nonlinear optics, and optical communication.

The recent progress in nano-optics and nano-photonics is strongly based on the ever- improving understanding of how to tune the properties of nano-matter (i.e., its geometrical shape and material composition) and how to manipulate the incident light the right way as to achieve desired effects, such as extreme local field enhancement [2–5] or controlling of the flux of light at subwavelength dimensions [6–11]. Concomitantly, modern techniques for material processing on the nanometer scale, such as high-resolution focused-ion beam milling [12–16], become more widely available and novel; more complex (prototype) material structures can be created. A number of chapters in this book deal with the task of getting better control over nano-optical fields.

In this chapter, we discuss the interaction of single quantum systems (e.g., single fluorescent molecules) with confined light fields. This is important for several reasons: The interaction of light with single quantum systems, which can be modeled as quantum-mechanical few-level systems, can be accurately described theoretically. With respect to optics, single quantum systems, because they usually react as individual dipoles, represent the fundamental building blocks of nano matter. Thus, a single quantum system represents a precisely defined nano-optical model system whose behavior can be well predicted and compared to experiments. When the properties of a given quantum system are known, detailed knowledge of the exciting optical field can be obtained since it behaves like a nano-probe: Its fluorescence intensity depends on the square modulus of the electrical field strength along the direction of its absorption dipole moment. This allows us to measure with very

high precision the spatial distribution of specific field components in confined optical fields. It is obvious that the possibility to characterize nano-optical fields is a key requirement for further progress in the field of nano-optics.

Here we will elaborate on the conditions under which single quantum systems can be used to probe confined fields. We show that single fluorescent molecules can be exploited to perform precise metrology of confined fields, which is hardly possible otherwise. Also discussed are operation conditions for optimal performance as well as limits and pitfalls when mapping confined nano-optical fields bound to nano-matter using single quantum systems.

3.2 Interaction of Light with Single Two-Level Quantum Systems

We are interested in the amount of scattered light that is emitted by a single two-level quantum system as a function of the excitation intensity and the excitation frequency. The absorption cross section describes the geometrical area from which light is collected by the quantum system before it is reemitted in new directions or dissipated as heat.

We start out by considering the most fundamental system for studying the interaction of light with a single quantum system (i.e., the interaction of a single frequency laser field with a single two-level quantum system). If the spatial extension of the quantum system ($\sim$ 1 nm) is small compared to the length scale of the spatial intensity variations in the excitation laser field, the interaction of the laser field with the quantum system can be treated in the dipole approximation. A fully quantum mechanical solution of the problem then yields for the total scattering cross-section σ [17]

$$\sigma = \frac{3\lambda^2}{2\pi}\left[\frac{1}{\frac{1}{2}\left(\frac{\Omega}{\beta}\right)^2 + 1 + \left(\frac{\omega - \omega_0}{\beta}\right)^2}\right] \tag{3.1}$$

where Ω is the Rabi frequency. Ω describes the coupling strength of the two-level system with the laser field and is defined as $\Omega = -\mathbf{d}_{12}\cdot\mathbf{E}_0/\hbar$ with $\mathbf{d}_{12} = \langle 1|\hat{\mathbf{d}}|2\rangle$, where $\hat{\mathbf{d}}$ is the dipole operator of the system and $|1\rangle$ and $|2\rangle$ are the ground and the excited state of the two-level system, respectively. $\mathbf{E}_0$ is the exciting electric field vector. The other quantities appearing in Equation 3.1 are 2β, the decay rate of the excited state, and $\omega - \omega_0$, the detuning of the frequency of the excitation laser ω with respect to the resonance frequency of the two-level system ω_0.

For zero detuning and weak excitation, the scattering cross section of the two-level system approaches the limiting value of $3\lambda^2/2\pi$. This is a value along the order of $(\lambda/2)^2$, which is much larger than the size of any physical realization of a two-level system, like a molecule or an atom. The physical reason for this counterintuitive behavior is the following: For a pure two-level system that is pumped resonantly by a single frequency laser, the scattered light has a fixed phase relation to the excitation field and both can interfere in the vicinity of the two-level system. If both the incoming and the scattered fields are of comparable strength, the field dis-

tribution that would be present without the absorber is significantly altered in the vicinity of the two-level system. The interference results in a redirection of the energy flow toward the absorber, which can be studied by plotting the field lines of the Poynting vector around the absorber. This effect is well known and documented (e.g., in Figure 1 of [18] and Figure 7 of [19]).

A molecule or an atom excited as described previously would not be suitable as a local probe for nano-optical fields. However, the very large absorption cross section still could have interesting physical consequences such as a possible direct detection of single molecules or atoms by their absorption [20]. Experimental examples for two-level systems in this regime are, for example, single ions in traps [21] and molecules embedded in a matrix at cryogenic temperatures where all excitations such as phonons are frozen out [22, 23].

Looking at Equation 3.1, there are two ways of decreasing σ such that it becomes much smaller than the wavelength. The first possibility is to increase the excitation intensity. As is evident from Equation 3.1 and Figure 3.1(a), the absorption cross section falls off as $1/\Omega^2$ because of saturation of the transition. Here the scattered light no longer increases linearly with the excitation; it increases more slowly. The second possibility is to increase the detuning of the excitation laser. This also has the effect of increasing the relative magnitude of incident and scattered light since to achieve the same scattering, a higher excitation intensity must be employed. For a large detuning far out to the blue and when dealing with molecules, eventually one ends up pumping vibrational levels of the excited state (e.g., the first vibrational level of the molecule). This is sketched in Figure 3.2.

The vibrational levels dissipate the vibrational energy into the environment and therefore decay very rapidly ($\sim$ ps) to the vibrational ground state of the first excited state. The fluorescence that is emitted now, due to the interaction with the environment, has lost all memory about the excitation and can no longer interfere. This dephasing process reduces the size of the absorption cross section roughly to the physical size of the molecule and is present even at cryogenic temperatures. At

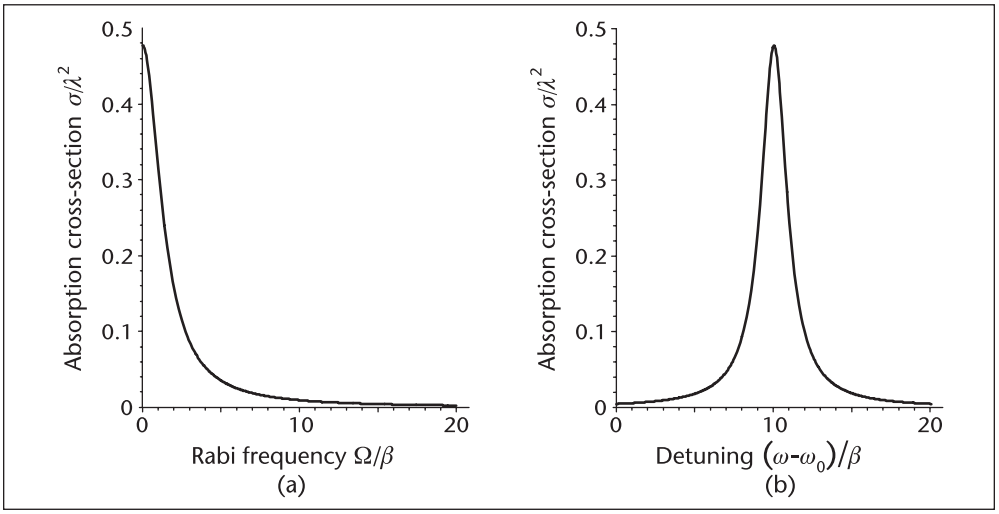

Figure 3.1 Absorption cross section of a two-level system as a function of (a) the Rabi frequency and (b) the detuning of the single-frequency excitation field. The peak absorption cross-section of $3\lambda^2/2\pi$ is reached at very weak excitation and zero detuning.

room temperature, collisions of a molecule with matrix phonons dominate all other dephasing processes. They destroy any coherence between excitation and emission, instantaneously reducing the absorption cross section again to roughly the physical size of the absorber. In conclusion, single quantum systems can be employed as probes for nano-optical fields with spatial variations on length scales well below the wavelength if under the experimental conditions chosen their absorption cross section is reduced well below its maximum value of $3\lambda^2/2\pi$. This is always the case when the coherence between excitation and scattered light is disturbed or their respective strength becomes unfavorable by any of the effects described previously. In particular, for single fluorescent molecules on surfaces or embedded in solid matrices at ambient condition, this condition is always fulfilled. For typical fluorescent dyes, the absorption cross section is of the order of 10^{-16} cm^2, which corresponds to (0.1 nm)^2.

3.3 Fluorescent Molecules at Ambient Conditions as Local Field Probes

Because of strong dephasing, single fluorescent molecules at ambient conditions can be described very well by a system of rate equations (see, for example, [24]) that relate the probabilities of finding the molecule in either of the states 1, 2, or 3 as defined in Figure 3.2. Here states 1 and 2 are the singlet ground and first excited state and 3 is the triplet state with population probabilities p_1, p_2, and p_3. The populations change with rates specified in Figure 3.2. In particular, $k_{21} = k_r + k_{nr}$ is the sum of the radiative and the nonradiative decay rate. Solving the respective system of rate equations for the three-level system under steady-state conditions leads to the following relations between the emission rate $R = k_r p_2$ and the excitation

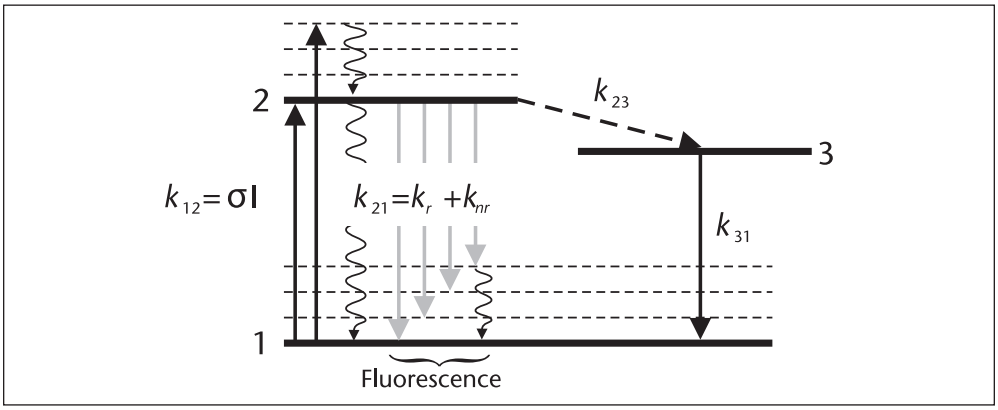

Figure 3.2 Jablonski diagram of the energy levels in a typical fluorescent molecule. Straight lines denote optical transitions, wavy lines denote nonradiative decay, and the dashed line denotes intersystem crossing. The excitation can be resonantly, pumping a zero-phonon transition, or nonresonantly, pumping higher vibrational states of the excited state. Red-shifted fluorescence occurs from the vibrational ground state of the excited state into vibrational levels of the ground state. A transition to a long-lived dark (triplet) state also is possible. Its presence strongly influences the photophysical parameters of the emission process. Labels: 1: ground state of the molecule; 2: singlet first excited state; 3: triplet first excited state; k_{12}: excitation rate; σ: absorption cross section; I: excitation intensity; k_{21}: total decay rate of the first excited singlet state; k_r: radiative decay rate; k_{nr}: nonradiative decay rate; k_{23}: intersystem crossing rate; k_{31}: triplet decay rate.

intensity that enters the equations via the relation $k_{12} = \sigma|E_d|^2$. Here $E_d = \mathbf{d}\cdot\mathbf{E}_0/|d|$ is the field component along the direction of the absorption dipole moment of the molecule. Finally,

$$R(E_d) = R_\infty \frac{\frac{|E_d|^2}{I_S}}{1 + \frac{|E_d|^2}{I_S}} \tag{3.2}$$

where R_∞ and I_S are defined by the photophysical parameters of the molecule as

$$I_S = \frac{(k_r + k_{nr} + k_{23})k_{31}}{\sigma(k_{23} + k_{31})}\hbar\omega \tag{3.3}$$

and

$$R_\infty = \frac{k_{31}k_r}{k_{23} + k_{31}} \tag{3.4}$$

Equation 3.2 describes a saturation behavior plotted in Figure 3.3. The saturation behavior is characterized by the two parameters R_∞ and I_S, where the former describes the emission rate at infinitely strong excitation and the latter is the intensity at which the emission rate equals $R_\infty/2$. Typical values for R_∞ and I_S for a single dye molecule at room temperature are $10^6 s^{-1}$ and 1 kW cm^{-2}, respectively.

For small excitation intensities (i.e., $|E_d|^2 \ll I_S$), a linear relation between the emission rate R and the absolute square of the excitation field component $|E_d|^2$ can be established as follows:

$$R = \frac{R_\infty}{I_S}|E_d|^2 = \sigma\frac{k_{21}}{k_{21} + k_{23}} \sim \sigma|E_d|^2 \tag{3.5}$$

The last step in Equation 3.5 is correct because the intersystem crossing rate k_{23} is small compared to the decay rate k_{21}. This equation relates the rate of emitted

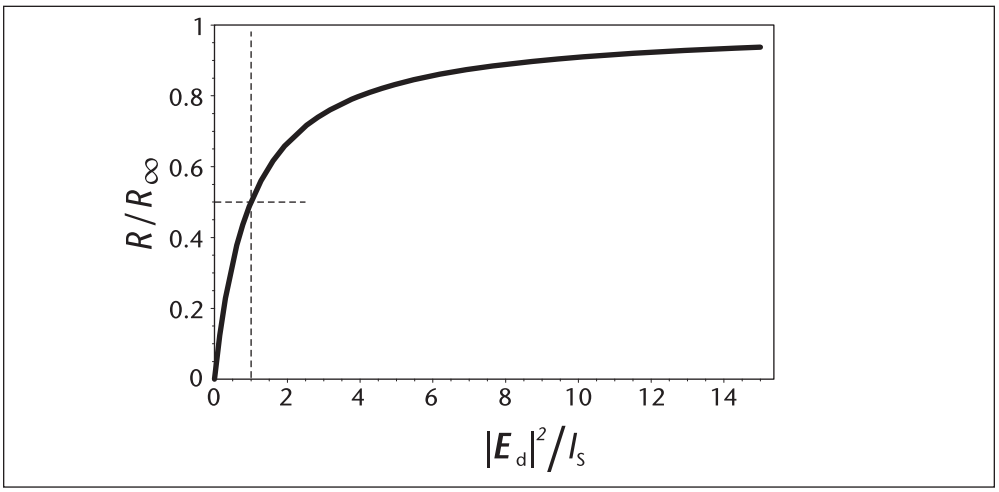

Figure 3.3 Saturation behavior of the emission rate of a single molecule as a function of the excitation intensity $|E_d|^2$.

photons with the absolute square of the field component along the absorption dipole moment of the fluorescent molecule and is at the core of field mapping with single quantum systems.

3.4 Mapping the Field Distribution in a Focused Laser Beam

Mapping confined optical fields is a rather difficult task. Ideally, for a full characterization, one would like to measure direction, amplitude, and phase of a given confined field distribution in three dimensions. Field amplitudes can be accessed by measuring the local intensity in a confined field. Usually, small scattering centers or fluorescent beads are employed for this purpose since their scattering is proportional to the local field intensity (see, for example, [25]). By using two foci of the same kind that are slightly offset, phase information also can be retrieved based on interferometric spatial autocorrelation [26]. NOMs also can be used to map confined fields, but with limited precision since the size of the optical probe disturbs the field to be measured [27]. Although useful, all of these methods are unable to measure the local electric field *direction*.

Building on what was discussed in the previous sections, here we will attempt to show that single fluorescent molecules immobilized in a polymer matrix at ambient conditions can map not only the local intensity of a focal field but also its direction. The possibility of mapping confined fields was first noted when distinct patterns appeared in images of single fluorescent molecules using aperture SNOM [28, 15] and confocal microscopy [29].

To fully demonstrate the power of this approach, we will apply it to a confined field that, unlike the fields in a subwavelength aperture, has field components of comparable magnitude in all three directions of a Cartesian coordinate system. This can be achieved by focusing a linearly polarized annular laser beam using a high numerical aperture (high-NA) microscope objective [30, 31].

Figure 3.4 illustrates how such a depolarization effect comes about in focusing with a high-numerical aperture microscope objective. It further shows how the specific spatial field patterns of the focal fields are produced by interference of the converging beams in the focal region. Figure 3.4(a) shows a side view of the focusing geometry. Beams at the outer rim of the lens become strongly deviated by refraction. This leads to a strong tilting of the electric fields for some of the incoming beams that introduces longitudinal field components. The latter are of opposite sign for the upper and the lower half of the lens and thus in the focal plane; on the y-axis, they cancel each other. Away from the y-axis, around the geometrical focus, however, significant z-oriented fields exist. Finally, this leads to the appearance of a double-lobed pattern. [See Figure 3.4(c), bottom.] Figure 3.4(b) illustrates how y-oriented fields are generated by high-NA focusing. It shows a view of the focusing geometry along the optical axis. Beams that start off the main axes at the outer rim of the lens contribute most strongly to such components due to the specific tilting of the electric field vectors upon refraction. Also, here it is evident that these field components must vanish on the x- and y-axis in the focal plane because of destructive interference. Finally, due to the nonzero y-oriented fields away from the geometrical focus, a four-lobed cloverleaf pattern appears. Usually, the y-patterns are weak compared to the x- and z-components, which are of comparable magnitude. However, if a

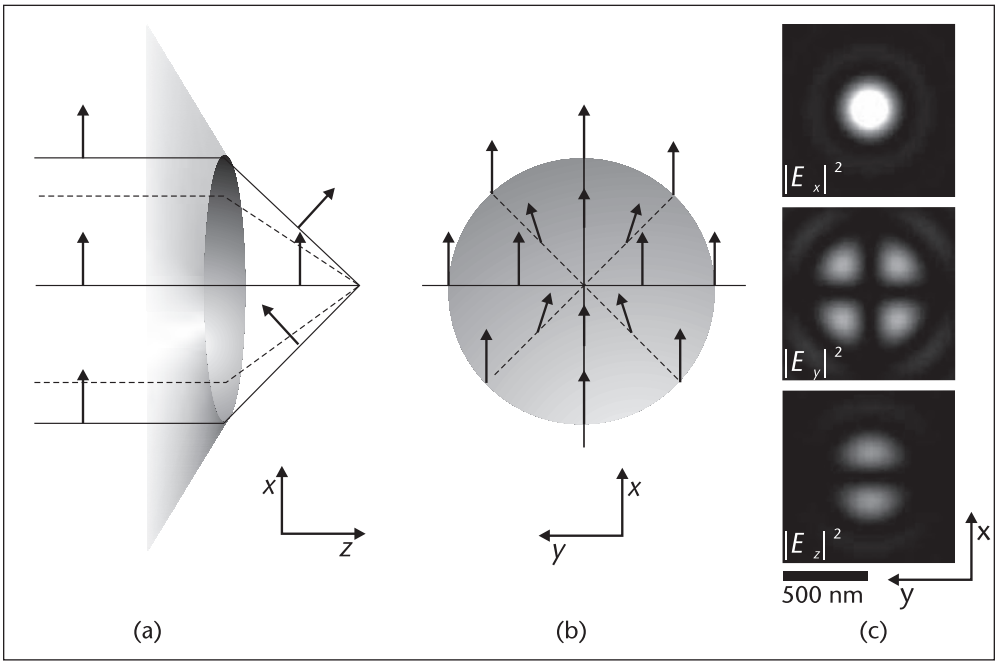

Figure 3.4 Focusing with high numerical aperture. (a) Side view of the focusing geometry for linear (*x*-)polarized incoming light. Rays at the outer rim are strongly deviated due to refraction. As a result, the electric field vector acquires a strong longitudinal field component. Longitudinal components from the upper and lower half-space cancel exactly in the geometrical focus and on the line $x = 0$ but not otherwise. This leads to a double-lobed spatial distribution of longitudinal fields around the focus as depicted in (c), bottom picture. (b) Front view of the focusing geometry for linear (*x*-)polarized incoming light showing that *y*-components are introduced by rays getting refracted at the diagonal positions. The *y*-components cancel on the lines $x = 0$ and $y = 0$. This results in a cloverleaf spatial pattern. (c) Spatial distributions of the field components present in a high numerical aperture focus.

plane interface between two dielectrics perpendicular to the optical axis is introduced that coincides with the focal plane, the *y*-patterns become more intense and are now comparable in strength to the *x*- and *z*-fields [31]. This is the field distribution of interest.

The experimental setup necessary to perform the field mapping is shown in Figure 3.5. It is essentially a scanning confocal optical microscope with a ring-shaped (annular) illumination beam [30, 31]. The diameter of the central beam block is chosen such that it is just below the critical angle of TIR. So most of the beams converging toward the focus will become totally internally reflected at the interface. The annular excitation beam is reflected into a high-NA microscope objective, which focuses the beam to a diffraction-limited spot on the sample. The sample is a 20 nm polymer film (PMMA) on glass that contains single fluorescent molecules (*,1'-dioctadecyl-3,3,3',3'- tetramethylindocarbocyanine*,DiI) in a low concentration such that single fluorescent molecules are spaced by more than a μm apart from one another. The refractive index of the film equals that of glass so that all of the molecules can be considered to sit very near to the dielectric-air interface. The orientation of absorption dipole moments in such a sample is random, so all possible field components can be probed. The excitation intensity is kept well below the saturation intensity of DiI. The fluorescence intensity is then proportional to the

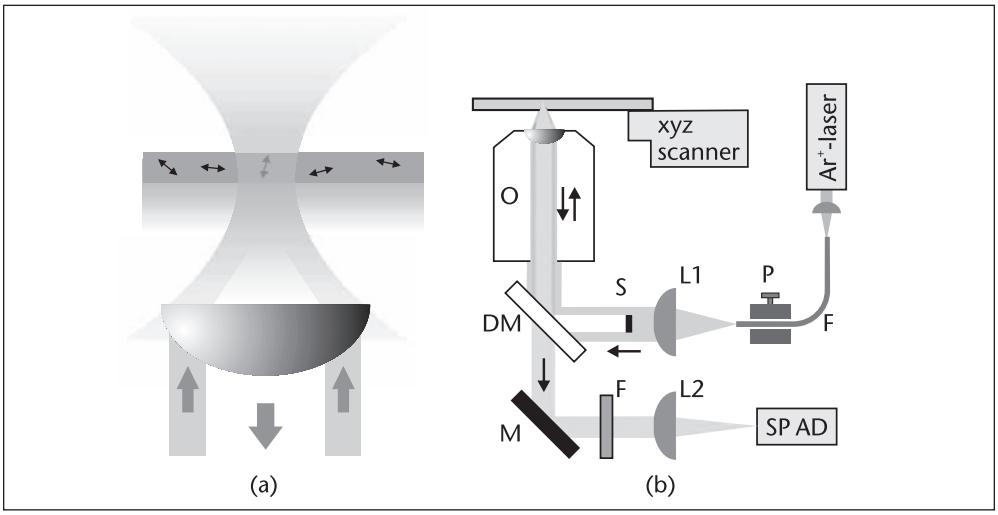

Figure 3.5 Scanning confocal optical microscopy with annular illumination focused to the polymer/air interface. (a) Detail of the sample showing randomly oriented molecules (double arrows) mapping the field distribution in the focus. (b) Overview of the setup. For details, see the text and [30, 31].

absolute square of the local field component along the absorption dipole of DiI. Note that in the setup of Figure 3.5(b), the confocal geometry is somewhat relaxed such that an area of about 1000 nm in diameter in the sample plane has a uniform collection efficiency; in other words, the active area of the detector demagnified back into the sample plane by geometrical optics has the size of roughly 1000 nm. This ensures that larger patterns can be mapped quantitatively. The spatial mapping of the focused field is done by raster-scanning the sample through the fixed focus and recording the fluorescence intensity at each pixel.

The result of such an experiment is shown in Figure 3.6. The left panel shows a typical single-molecule image obtained. Each molecule exhibits a specific pattern corresponding to the specific orientation of its absorption dipole. For better visibility of the patterns, the image has been median-filtered to suppress dark pixels due to triplet blinking. The right panel shows a set of calculated field patterns that should be observed for different discrete orientations of the molecular absorption dipole moment [30]. The strong resemblance between the calculated patterns and the measured data shows that the concept of a linear absorption dipole moment mapping the focal field is valid. It also shows that if the field distribution is well known, it is possible to obtain detailed insight into the orientation of individual molecules. However, we will not elaborate further on this issue, but rather refer the interested reader to the literature [31].

In the following discussion, we concentrate on the metrology issue. Figure 3.7 shows the direct comparison of measured and calculated fundamental field patterns without any fit parameters in a 1μm by 1μm square. Only a normalization factor was used to match the maximum fluorescence intensities in both theory and experiment. What is immediately evident is the exact fit of the positions of the respective maxima in each of the patterns. Also, the widths of the various peaks are extremely well matched. This demonstrates that, for the given conditions, the fields have been mapped by a single dipole that does not influence the field to be measured, as was discussed previously. Unfortunately, the field distributions analyzed

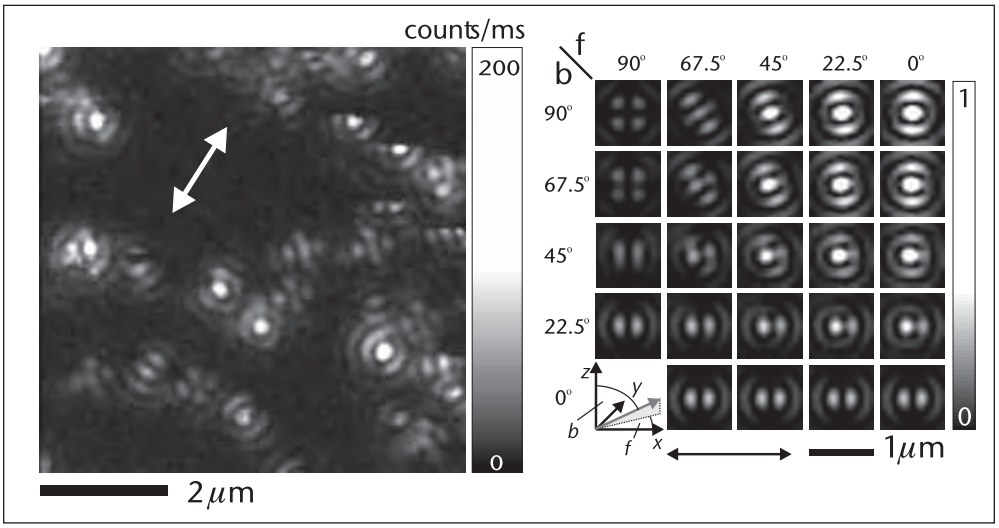

Figure 3.6 Experimental and theoretical field maps of an annular laser focus. Left panel: Scan image showing a variety of different patterns corresponding to dipoles of different orientations mapping different components of the same field distribution. Cut-off patterns appear due to photobleaching. Right panel: Simulation of patterns for the geometry of the experiment. Adapted from [30]. ©2000 American Physical Society.

here, because they are of far-field nature, have no features that would allow testing of the maximum resolution possible in this configuration. However, from the discussion, we can infer that the spatial resolution for field mapping should be limited only by the absorption cross section of the molecules used under the specific conditions of the experiment. As already mentioned, for ambient conditions and molecules embedded in a polymer, the absorption cross section becomes considerably smaller than 1 nm^2.

3.5 Mapping the Field Distribution at a Sharp Tip

It is obvious that the probing of optical *near-field* distributions would be a desirable extension of the methodology discussed previously. While mapping of the optical fields close to a subwavelength aperture has been done before [28, 15], the highly confined fields at a sharp metal tip have rarely been investigated in the context of single-molecule imaging, although other techniques have been applied to investigate the confinement of light at sharp tips [4, 5, 32–38]. Figure 3.8 shows a possible experimental setup for mapping the confined field at a tip with a single fluorescent molecule. It is very similar to the setup used for mapping the field distribution in the focused annular beam. Here a tip is illuminated by a focused laser beam of suitable mode profile through a glass slide that is coated with a 20 nm layer of PMMA. Again, the PMMA contains single fluorescent molecules in a suitable concentration as described previously. Mapping is performed by choosing a molecule as a probe by moving it to the focus and then scanning the tip with respect to this fixed molecule. While the tip is scanned, the fluorescence intensity of the molecule is recorded as a function of the tip position. When this is done, the field component along the absorption dipole of the molecule is mapped.

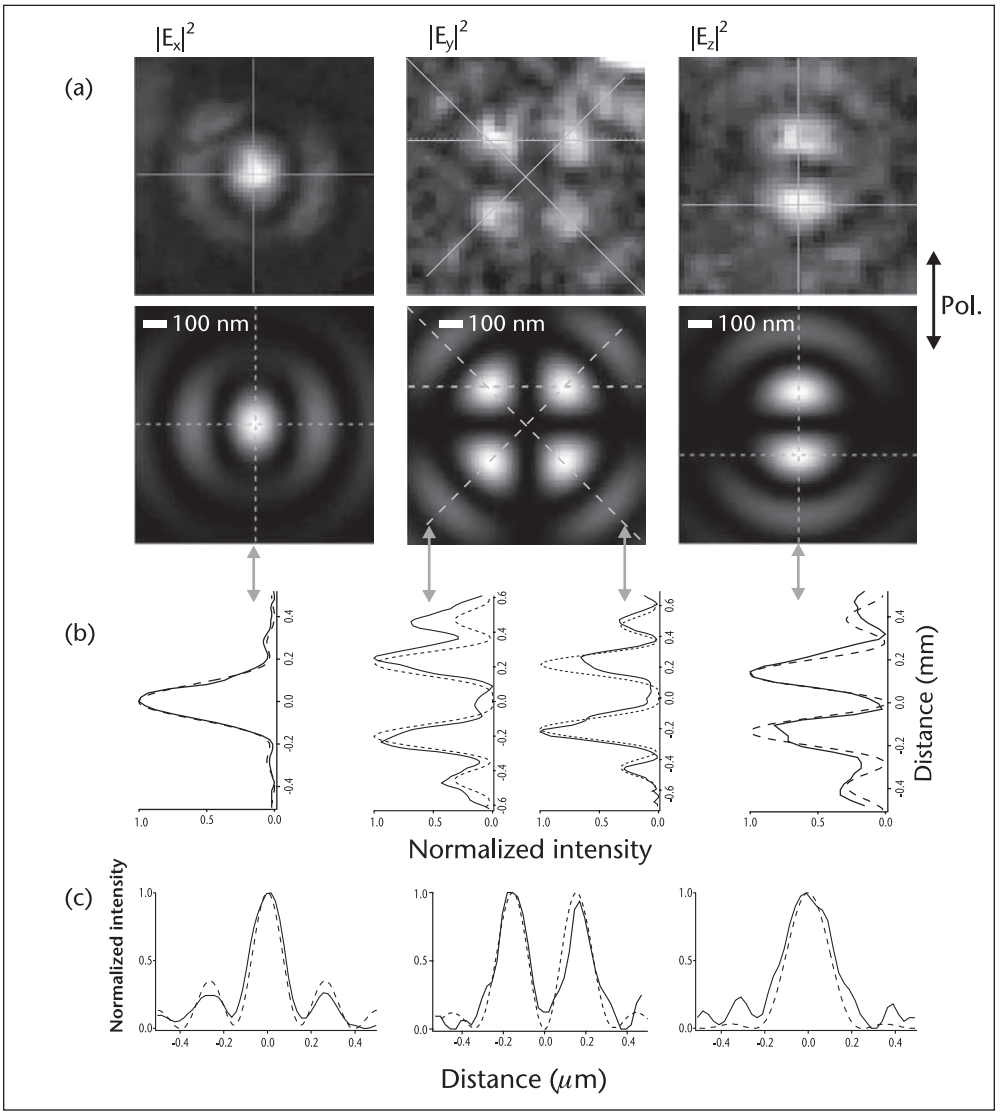

Figure 3.7 Metrology of confined fields. (a) Direct comparison of measured and calculated field patterns for the three fundamental absorption dipole orientations with respect to the interface and the incoming linear polarization. No fit parameters are used besides a normalization factor. Line cuts through (b) the measured and (c) the calculated patterns. The cuts are along the full and the dashed lines superimposed to the images. Adapted from [31]. ©2001 The Royal Microscopical Society.

In an ideal experiment, the orientation of the absorption dipole moment is characterized independently beforehand (e.g., by illuminating it with a focused annular beam). This allows us to determine the orientation by fitting theoretical patterns to measured ones (see, for example, [39]). This in turn would allow us to map specific field components of a strongly confined field. The latter experiment has not yet been performed. However, in a proof-of-principle study, it was shown that such experiments are feasible [40]. Figure 3.9 shows the respective results. Figure 3.9(a) shows a $10 \times 10\ \mu m^2$ confocal image of a thin PMMA film on a glass slide containing terrylene molecules. A bright molecule is chosen as the probe by moving it permanently into the far-field illumination focus by means of the sample scan stage. The

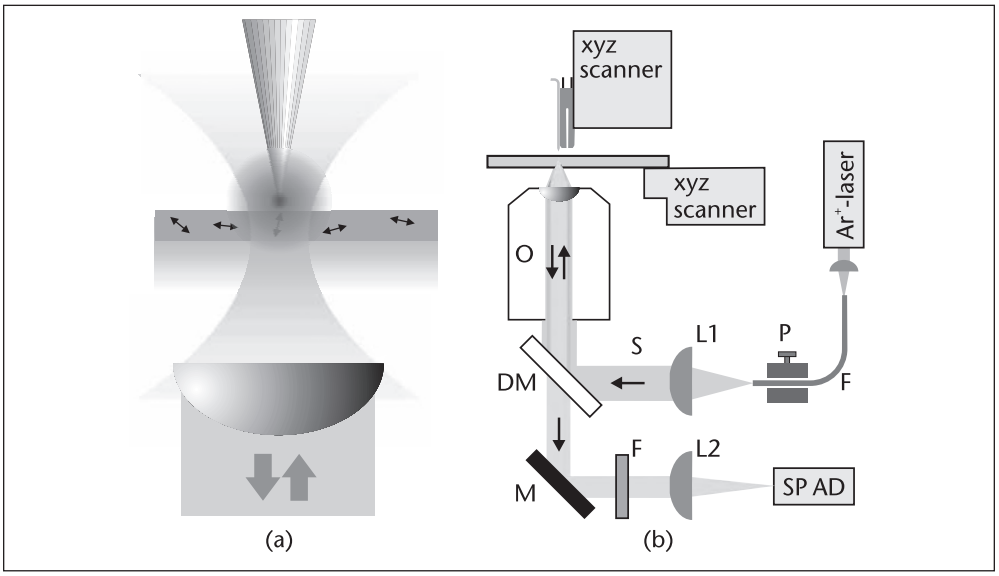

Figure 3.8 Mapping of nano-optical fields at a sharp tip. (a) Detailed view of the sample area. A probe molecule is illuminated continuously at a very low excitation rate such that its emission rate is just above the background. Then the tip is scanned over the molecule, and its fluorescence is recorded as a function of the tip position. (b) Overall setup similar to the one in Figure 3.5(b).

line cut in the inset of Figure 3.9(a) shows that the full width at half maximum (FWHM) of the fluorescence peak due to the molecule is about 480 nm. This relatively large size is due to the fact that a microscope objective with a numerical aperture of 0.9 was used.

The tip used in the present experiment is an etched gold tip made from a gold wire. After the molecule is found and positioned into the focus, the excitation intensity is lowered such that the fluorescence of the molecule is just barely visible. This has to be done since the local field at the tip is expected to be much enhanced with respect to the excitation field and the molecule would run into saturation otherwise. Figure 3.9(b) shows the fluorescence of the molecule chosen in (a) as a function of the tip position. The tip scan starts at the top left corner. The fluorescence stays at a very low level until the tip comes close to the molecule. A strong increase in the fluorescence of the molecule is observed as the tip is scanned over it. After the tip passes the molecule, the fluorescence decreases again and goes back to the original value. Figure 3.9(c) shows the image obtained in the subsequent tip scan. After a few lines, the molecule photobleaches, which is evident from the initial flickering and the final termination of the fluorescence. The remainder of the image consequently shows the effect of the tip alone. A faint background is visible that is presumably due to SERS from contaminants on the tip's surface. The difference of (b) and (c) is displayed in Figure 3.9(d). It represents the background-corrected spatial distribution of the enhanced field at the tip. Unfortunately, the orientation of the absorption dipole moment of the molecule is unknown in this experiment; consequently the mapped field component also is unknown. However, what is evident is the strong enhancement of the field beneath a gold tip. Figure 3.9(e) shows a line cut through (d) that was fitted by a Gaussian. The fit parameters yield the field enhancement factor and the width of the enhanced region. The fluorescence increases amounts to 5.7 ± 0.3, and the width is about 305 nm.

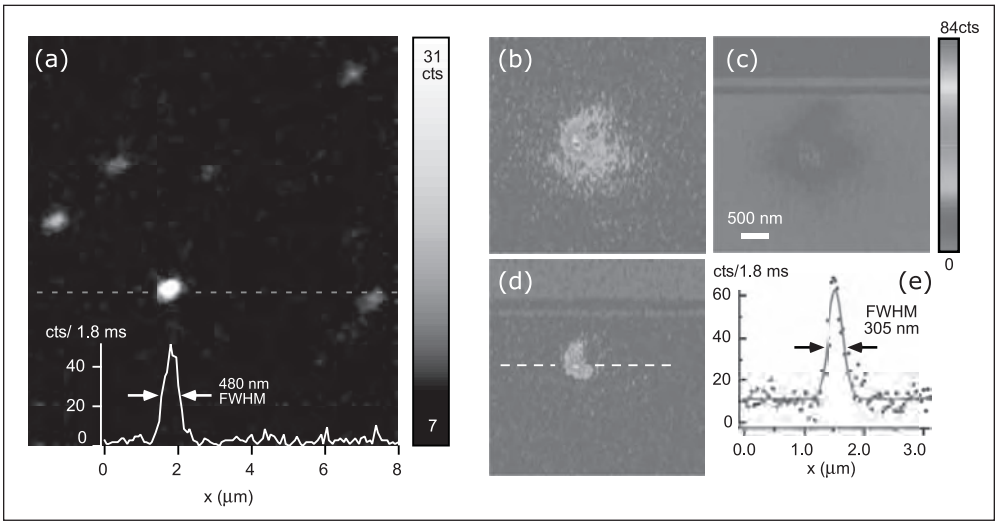

Figure 3.9 Mapping the field at a sharp gold tip. (a) Scanning confocal optical microscopy of the polymer film on glass containing the probe molecules (terrylene). Inset: Line cut through the probe molecule along the dotted line. (b) Fluorescence intensity of the probe molecule as a function of the tip position. Part (c) shows that the intensity is the same as (b) but that the molecule bleaches. The remaining signal is subtracted from (a) to generate the image in (d), which shows the true spatial distribution of the field component mapped by the probe molecule. (e) Gaussian fit to the line cut through (d) yielding the width and height of the peak over background. Adapted from [40]. ©2002 American Institute of Physics.

The intensity enhancement factor of 5.7 is clearly larger than 4. An intensity enhancement factor of 4 can be achieved at a plane perfect mirror simply by constructive interference. The width of the enhancement area is clearly smaller than the diffraction-limited spot size. [See Figure 3.9(a).] This indicates the near-field character of the observed phenomenon.

We will not go into detail about the reason for the enhancement observed. This is discussed at length in the original publication [40]. Briefly, it is believed that the enhanced fluorescence is due to localized plasmon fields, not to a nonresonant enhancement (lightning rod effect) at the tip apex. This is supported by observations. For gold-coated glass tips, a resonance at $h\nu = 2.11$ eV ($\lambda = 588$ nm), close to our wavelength, was reported [33]. When performing similar experiments with gold-coated atomic-force microscope tips at an excitation wavelength of $\lambda = 532$ nm, we observe no significant field enhancement. When Pt/Ir (90:10) tips instead of gold tips were used, no significant enhancement was observed. Considerable nonresonant enhancement occurs only at very sharp tips in the presence of excitation field components along the tip axis, which is not the case in the described experiment.

3.6 Energy Transfer and Quenching

In this section, we discuss an important effect that must be taken into account when optical fields are bound to material structures—that is, energy transfer and quenching effects.

It is a fundamental notion that nano-optical fields are bound to a material structure. The evanescent fields that are responsible for the spatial confinement can

exist only in a close symbiosis with collective electron excitations in metals or with driving propagating fields in a second half-space in the case of TIR. The presence of matter inevitably has an influence on the possibility of probing these nano-optical fields quantitatively since the field to be probed is interacting with and sustained by the nano matter and since the probe (and the field it emits into the far field toward a detector) feels the presence of nearby matter. The effect of nearby material structures on molecular fluorescence was studied theoretically and experimentally for stratified layered systems [41–43] and for spherical systems [44–47]. Phenomenologically, what happens is the following: (1) If a dissipative structure (i.e., an extended piece of metal with free electrons and associated ohmic losses) is brought within the near-field range of a probe molecule, the near field of the probe molecule induces motion of the electrons that quickly dissipate their gained energy (e.g., into heat). This opens up a new decay channel for the molecular-excited state with a nonradiative decay rate, k_{nr} (Figure 3.2) that allows deexcitation of the probe molecule without emission of a photon. For short distances, this nonradiative decay rate depends on the distance between the molecule and the extended metallic body as $1/r3$, where r is the distance, reflecting the decay of the dipolar near field. It follows that for short distances, the rate k_{nr} dominates the radiative decay rate k_{r} and few photons are emitted by the probe molecule while the excited state lifetime decreases dramatically. This effect is usually called quenching. (2) If a dielectric structure (e.g., a glass half-space [39, 48, 49]) or a suitable nanostructure (e.g., a metallic nanoparticle with a plasmon resonance, a dielectric sphere with a Mie resonance (whispering gallery mode) [50, 51], or a metal-coated tip [52]) is brought in close proximity to the probe molecule, the spectrum of electromagnetic modes available for accepting a fluorescence photon from the probe molecule is changed. In the case of strong coupling to one or few modes of a *resonant* nano or microstructure, this leads to an enhanced emission of the coupled system with a likely strongly modified far-field emission pattern. In other cases, the overall density of states is modulated, which leads to an enhanced or decreased lifetime of the excited state often coupled with a redirection of the emission [54]. Such effects can be observed for probe molecules on either side of a plane dielectric interface [39, 55, 56]. Since the fluorescence is collected in a constant solid angle, the collected fluorescence can increase or decrease in this case.

In the experiment described, we saw no direct evidence of quenching of the fluorescence by the metal tip; however, quenching may well be present. On the one hand, this could explain the small enhancement factor observed. On the other hand, the distance between the tip and an average molecule in the described experiment is rather large: It is the sum of the typical shear-force gap width of ~10 nm and the typical depth of a molecule in the polymer film of another ~10 nm. This is a rather large distance at which the quenching is less effective. In view of this argument, the enhancement factor measured must be viewed as a lower limit for the true value. In an ideal experiment, the fluorescence intensity in the full solid angle as well as the lifetime of the excited state should be measured for different distances to the material structure. Changes in the lifetime in this case could be translated into changes in k_{nr}, which can be correlated to the emission rate.

We can conclude that the stronger the field confinement, the more difficult it is to quantitatively probe the field by means of a small dipolar emitter due to the emitter's coupling to the nanomatter. The reason for this difficulty might be deeper

than one would expect from the discussion so far, which was built on a specific example of a probing scheme. In a famous paper [57] on the quantization of evanescent modes, commutation relations for the fields at different space-time points are derived that seem to exclude the sharp measurement of field amplitudes of evanescent fields at points with spacelike distances. This might be worth further investigation, but we do not go into further detail here.

In what follows, we show that the localized quenching process at a sharp metallized tip [58] may be used as a novel contrast mechanism to spatially resolve individual molecules by selective quenching [59, 60]. To observe and prove the presence of quenching, the average distance between the tip and the molecules must be reduced. This is done by applying contact mode atomic-force microscopy. Pulsed excitation (532 nm wavelength, 150 ps pulse width, 76 MHz rep. rate) is used to continuously probe the excited state lifetime of the molecules under investigation via time-correlated single-photon counting. Those two ingredients are the main new features of the experimental setup sketched in Figure 3.10 (left panel). Again, the fluorescent molecules are embedded in a thin polymer film on glass. The tip is now a $Si_3 N_4$ pyramid at the end of an AFM cantilever coated with a 20 nm layer of gold and operating in contact mode. Scanning electron microscopy images of the tip are displayed as insets Figure 3.10 (left panel). A wedgelike shape of the tip, which is clearly visible, is a well-known property of this type of probe. The length of the wedge is a little less than 200 nm. It is expected that the shape of the tip will somehow be reflected in quenching patterns observed.

The right panel of Figure 3.10 shows the result of a calculation that assumes that a system of stratified layers locally can well approximate the system under investigation. The lifetime of the excited state of a molecule just below the interface between air and polymer (glass) is plotted as a function of the width of the air gap between the polymer and the gold layer. For the two fundamental orientations of the molecular emission dipole moment, parallel and perpendicular to the interface,

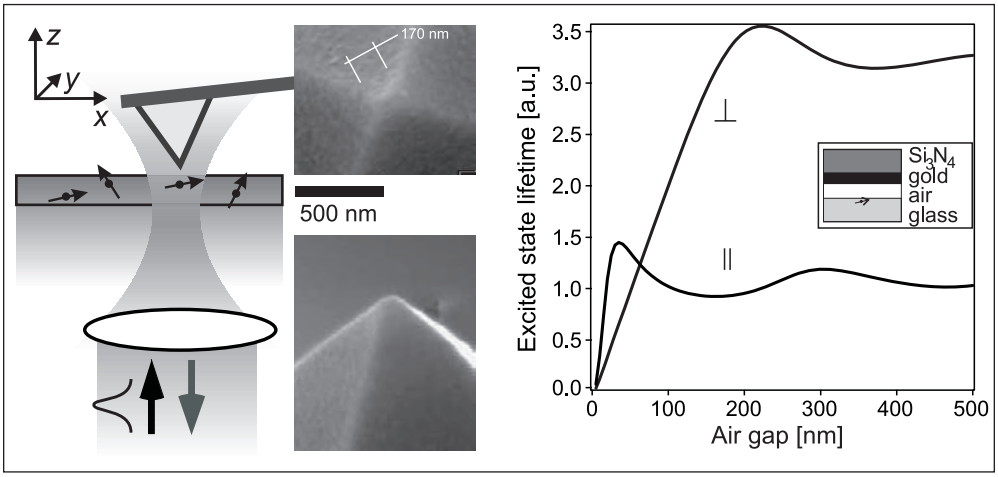

Figure 3.10 Experimental setup and theory for local quenching. Left panel: Contact-mode AFM in combination with a fixed pulsed laser beam. The inset shows scanning electron microcopy of the tips used. Clearly, the tip terminates in a wedge and not in a sharp tip as expected. Right panel: Theoretical prediction of the excited state lifetime of a molecule sitting right below the polymer/air interface as a function of the air gap width. Adapted from [53]. ©2002 American Institute of Physics.

a distinct behavior is observed. While for both orientations, a decay of the excited state lifetime with decreasing gap width is observed, this decay is more short-ranged for the molecule with the emission dipole parallel to the interface. Here a decay constant of less than 20 nm is observed, which clearly highlights the potential for ultra-high resolution optical microscopy of single molecules by selective quenching. It seems possible to resolve two molecules that are as close as ~20 nm by switching them off selectively by means of a sharp metallic tip. The power of this approach lies in the possibility of still obtaining the full spectral information (e.g., the emission spectrum) of the unperturbed molecule.

To provide a proof of principle, a quenching experiment was performed with samples that contained an isolated single molecule. Once a molecule is found in a confocal scan, it is kept fixed in the focus, and the AFM tip scan starts. Both the fluorescence intensity and the excited state lifetime of the molecule are recorded as a function of the tip position. The results shown in Figure 3.11 were obtained with the tip shown in Figure 3.10. The left panel shows behavior of the fluorescence intensity, while the right panel shows the excited state lifetime as a function of the tip position. While in the fluorescence intensity image the molecule starts to feel

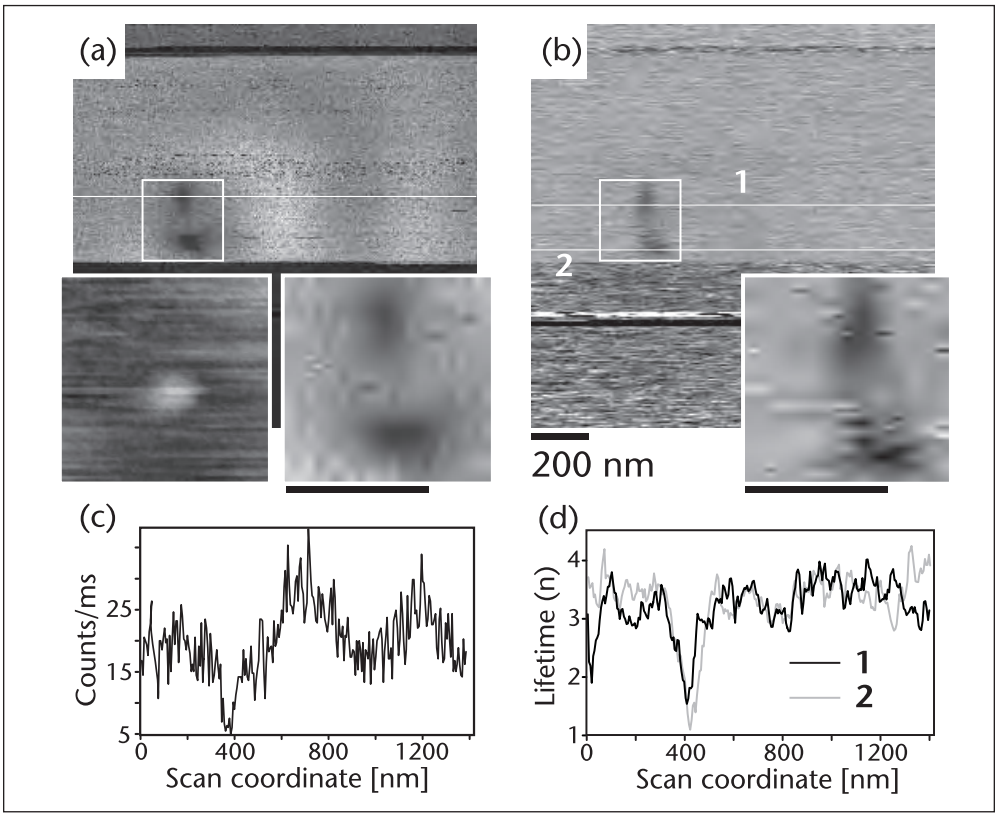

Figure 3.11 Local quenching of a single molecule by a metallized AFM tip. (a) Fluorescence intensity as a function of the tip position. Left inset: Topography at the position of the fluorescence dip. Right inset: Zoom of the region of the fluorescence dip marked by the white square. (b) Excited state lifetime as a function of the tip position. Inset: Zoom at the position of the lifetime dip marked by the white square. (c) Cut through (a) along the white line. (d) Cut through (b) along the white line. Adapted from [53]. ©2002 American Institute of Physics.

the presence of the tip, already at larger distances (which results in interference-like fringes), in the lifetime image, no such fringes are present. When the tip is in close proximity to the molecule, a strong local decrease in the fluorescence intensity is observed. Its shape resembles that of the wedge at the AFM tip apex; however, it is divided into two lobes. The separation can be explained through examination of the topographic image acquired simultaneously. It shows a contaminant particle just at the position of the separation. Its height is about 10 nm, which causes the tip to retract by this amount while it is scanning over the particle. According to the theory graph in Figure 3.10, this should be enough to remove the molecule completely from the quenching condition. Therefore, we conclude that the separation of the two lobes provides evidence of the strong distance dependence of the quenching effect predicted in Figure 3.10. At the same time, the lifetime of the molecular excited state shows a clear reduction at the same position where the decreased fluorescence occurs. The respective line cuts show that the lifetime image has a similar edge resolution to that of the fluorescence intensity image.

3.7 Conclusion

After all we have discussed, it is clear that there is a strong potential of single quantum systems, such as single fluorescent molecules, being used to study the properties of nano-optical fields. The theoretical resolution limit was found to be along the order of the physical size of the molecules under conditions where the absorption cross section is far from its peak value. We also have seen that it might not be so easy to exploit the potentially ultrahigh spatial resolution. This is because of the fact that optical fields with spatial variations on the nanometer scale can exist only in close proximity to some nanometer scale material structure that will strongly influence the emission of the probe molecule. This might be a deeper problem than it looks on first glance. It questions the principal possibility of measuring field strength in nano-optical fields. It is possible that nonzero field commutators at different spatial positions play a role in this context. Finally, we also have shown that if quenching effects occur, they are not at all detrimental, but they can be exploited as a contrast mechanism for high-resolution optical microscopy with single-molecule sensitivity by exploiting tip-induced local quenching effects.

Acknowledgments

The author would like to thank all of the people who contributed to the work described in this chapter (in alphabetic order): A. Kramer, M. Kreiter, M. Prummer, B. Sick, W. Trabesinger, and U. P. Wild. Stimulating discussion with H.-J. Eisler, T. Latychevskaia, Y. Lill, and D. W. Pohl is acknowledged. Financial support via a professorship of the Swiss National Science Foundation (SNSF); funding received from the National Competence Center for Research “Nanoscale Science”; and projects within the SNSF, the KTI/CTI of the Swiss Federal Office for Professional Education and Technology, and the Wolfermann-Nägeli foundation are gratefully acknowledged.

References

[1] Novotny, L., and B. Hecht. *Principles of Nano-Optics*, Cambridge: Cambridge University Press, 2006.

[2] Martin, O. J. F., and C. Girard, "Controlling and Tuning Strong Optical Field Gradients at a Local Probe Microscope Tip Apex," *Appl. Phys. Lett.*, Vol. 6, 1997, pp. 705–707.

[3] Sanchez, E., L. Novotny, and X. Xie, "Near-Field Microscopy Based on Two-Photon Excitation with Metal Tips," *Phys. Rev. Lett.*, Vol. 20, 1999, pp. 4014–4017.

[4] Stockle, R. et al., "Nanoscale Chemical Analysis by Tip-Enhanced Raman Spectroscopy," *Chem. Phys. Lett.*, Vol. 318, 2000, pp. 131–136.

[5] Hartschuh, A. et al., "High-Resolution Near-Field Raman Microscopy of Single-Walled Carbon Nanotubes," *Phys. Rev. Lett.*, Vol. 90, 2003, Art. No. 095503.

[6] Novotny, L., D. Pohl, and B. Hecht, "Scanning Near-Field Optical Probe with Ultrasmall Spot Size," *Opt. Lett.*, Vol. 9, 1995, pp. 970–972.

[7] Hecht, B. et al., "Local Excitation, Scattering, and Interference of Surface Plasmons," *Phys. Rev. Lett.*, Vol. 77, 1996, pp. 1889–1893.

[8] Ebbesen, T. et al., "Extraordinary Optical Transmission through Sub-wavelength Hole Arrays," *Nature*, Vol. 391, 1998, pp. 667–669.

[9] Krenn, J. et al., "Direct Observation of Localized Surface Plasmon Coupling," *Phys. Rev. B*, Vol. 7, 1999, pp. 5029–5033.

[10] Krenn, J. et al., "Squeezing the Optical Near-Field Zone by Plasmon Coupling of Metallic Nanoparticles," *Phys. Rev. Lett.*, Vol. 82, 1999, pp. 2590–2593.

[11] Bouhelier, A. et al., "Plasmon Optics of Structured Silver Films," *Phys. Rev. B*, Vol. 63, 2001, Art. No. 155404.

[12] Vasile, M. et al., "Scanning Probe Tips Formed by Focused Ion Beams," *Rev. Sci. Instrum.*, Vol. 9, 1999, pp. 2167–2171.

[13] Muranishi, M. et al., "Control of Aperture Size of Optical Probes for Scanning Near-Field Optical Microscopy Using Focused Ion Beam Technology," *Jap. J. of Appl. Phys.*, Vol. 2, 1997, pp. L942–L944.

[14] Lacoste, T. et al, "Contrast Enhancement Using Polarization-Modulation Scanning Near-Field Optical Microscopy (PM-SNOM)," *Ultramicroscopy*, Vol. 1–4, 1989, pp. 333–340.

[15] Veerman, J. et al., "Single Molecule Mapping of the Optical Field Distribution of Probes for Near-Field Microscopy," *J. Microsc.*, Vol. 2–3, 1999, pp. 477–482.

[16] Krogmeier, J., and R. Dunn, "Focused Ion Beam Modification of Atomic Force Microscopy Tips for Near-Field Scanning Optical Microscopy," *Appl. Phys. Lett.*, Vol. 27, 2001, pp. 4494–4496.

[17] Mandel, L., and E. Wolf, *Optical Coherence and Quantum Optics*, Cambridge: Cambridge University Press, 1995.

[18] Bohren, C., "Can a Particle Absorb More Than the Light Incident on It?" *Am. J. Phys.*, Vol. 4, 1983, p. 323.

[19] Paul, H., *Photonen, Eine Einführung in die Quanenoptik*, Stuttgart, Germany: Studienbücher, 1995.

[20] Plakhotnik, T., "Absorption and Coherent Emission of Single Molecules," *J. Lumin.*, Vol. 98, 2002, pp. 57–62.

[21] Guthöhrlein, G. et al., "A Single Ion as a Nanoscopic Probe of an Optical Field," *Nature*, Vol. 414, 2001, pp. 49–51.

[22] Moerner, W. E., and M. Orrit, M., "Illuminating Single Molecules in Condensed Matter," *Science*, Vol. 283, 1999, pp. 1670–1676.

[23] Michaelis, J. et al., "Optical Microscopy Using a Single-Molecule Light Source," *Nature*, Vol. 405, 2000, pp. 325–328.

[24] Loudon, R., *The Quantum Theory of Light*, Oxford: Oxford University Press, 1983.

[25] Bouhelier, A., M. Beversluis, and L. Novotny, "Near-Field Scattering of Longitudinal Fields," *Appl. Phys. Lett.*, Vol. 25, 2003, pp. 4596–4598.

[26] Muller, M. et al., "Method for Complex Focal Field Measurement of a High-Numerical-Aperture Lens Under CW and Pulsed Conditions," *Optics Commun.*, Vol. 1–3, 1997, pp. 16–20.

[27] Rhodes, S., K. Nugent, and A. Roberts, "Precision Measurement of the Electromagnetic Fields in the Focal Region of a High-Numerical-Aperture Lens Using a Tapered Fiber Probe," *J. Opt. Soc. Am. A*, Vol. 8, 2002, pp.1689–1693.

[28] Betzig, E., and R. Chichester, "Single Molecules Observed by Near-Field Scanning Optical Microscopy," *Science*, Vol. 262, 1993, pp. 1422–1425.

[29] Xie, X., and J. Trautman, "Optical Studies of Single Molecules at Room Temperature," *Annu. Rev. Phys. Chem.*, Vol. 49, 1998, pp. 441–480.

[30] Sick, B., B. Hecht, and L. Novotny, "Orientational Imaging of Single Molecules by Annular Illumination," *Phys. Rev. Lett.*, Vol. 21, 2000, pp. 4482–4485.

[31] Sick, B. et al., "Probing Confined Fields with Single Molecules and Vice Versa," *J. Microsc.*, Vol. 2, 2001, pp. 365–373.

[32] Zenhausern, F., Y. Martin, and H. Wickramasinghe, "Scanning Interferometric Apertureless Microscopy: Optical Imaging at 10 Angstrom Resolution," *Science*, Vol. 269, 1995, pp. 1083–1085.

[33] Ashino, M., and M. Ohtsu, "Fabrication and Evaluation of a Localized Plasmon Resonance Probe for Near-Field Optical Microscopy/Spectroscopy," *Appl. Phys. Lett.*, Vol. 11, 1998, pp. 1299–1301.

[34] Azoulay, J. et al., "Field Enhancement and Apertureless Near-Field Optical Spectroscopy of Single Molecules," *J. Microsc.*, Vol. 2/3, 1999, pp. 486–490.

[35] Hamann, H., A. Gallagher, and D. Nesbitt, "Near-Field Fluorescence Imaging by Localized Field Enhancement Near a Sharp Probe Tip," *Appl. Phys. Lett.*, Vol. 14, 2000, pp. 1953–1955.

[36] Hayazawa, N. et al., "Metallized Tip Amplification of Near-Field Raman Scattering," *Optics Commun.*, Vol. 1-4, 2000, pp. 333–336.

[37] Hayazawa, N. et al., "Near-Field Raman Scattering Enhanced by a Metallized Tip," *Chem. Phys. Lett.*, Vol. 335, 2001, pp. 369–374.

[38] Hillebrand, R., T. Taubner, and F. Keilmann, "Phonon-Enhanced Light-Matter Interaction at the Nanometer Scale," *Nature*, Vol. 418, 2002, pp. 159–162.

[39] Kreiter, M. et al., "Orientation Dependence of Fluorescence Lifetimes Near an Interface," *J. Chem. Phys.*, Vol. 920, 2002, pp. 9430–9433.

[40] Kramer, A. et al., "Optical Near-Field Enhancement at a Metal Tip Probed by a Single Fluorophore," *Appl. Phys. Lett.*, Vol. 9, 2002, pp. 1652–1654.

[41] Lukosz, W., and R. Kunz, "Light Emission by Magnetic and Electric Dipoles Close to a Plane Interface I. Total Radiated Power," *J. Opt. Soc. Am.*, Vol. 67, 1977, pp. 1607–1615.

[42] Lukosz, W., "Light Emission by Multipole Sources in Thin Layers. I. Radiation Patterns of Electric and Magnetic Dipoles," *J. Opt. Soc. Am.*, Vol. 71, 1981, pp. 744–754.

[43] Chance, R., A. Prock, and R. Silbey,. "Molecular Fluorescence and Energy Transfer Near Interfaces," *Adv. Chem. Phys.*, Vol. 60, 1978, pp. 1–65.

[44] Ruppin, R., "Decay of an Excited Molecule Near a Small Metal Sphere," *J. Chem. Phys.*, Vol. 4, 1982, pp. 1681–1684.

[45] Leung, P., and T. George, "Dynamical Analysis of Molecular Decay at Spherical Surfaces," *J. Chem. Phys.*, Vol. 11, 1987, pp. 6722–6724.

[46] Leung, P., "Decay of Molecules at Spherical Surfaces: Nonlocal Effects," *Phys. Rev. B*, Vol. 12, 1990, pp. 7622–7625.

[47] Dulkeith, E. et al., "Fluorescence Quenching of Dye Molecules Near Gold Nanoparticles: Radiative and Nonradiative Effects," *Phys. Rev. Lett.*, Vol. 89, 2002, Art. No. 203002.

[48] Lukosz, W., R. and Kunz, "Fluorescence Lifetime of Magnetic and Electric Dipoles Near a Dielectric Interface," *Optics Commun.*, Vol. 20, 1977, pp. 195–199.

[49] Macklin, J. J. et al., "Imaging and Time-Resolved Spectroscopy of Single Molecules at an Interface," *Science*, Vol. 272, 1996, pp. 255–258.

[50] Fan, X. et al., "Coupling Semiconductor Nanocrystals to a Fused-Silica Microsphere: A Quantum-Dot Microcavity with Extremely High Q Factors," *Opt. Lett.*, Vol., 21, 2000, pp. 1600–1602.

[51] Götzinger, S., O. Benson, and V. Sandoghdar, "Towards Controlled Coupling between a High-Q Whispering Gallery Mode and a Single Nanoparticle," *Appl. Phys. B*, Vol. 73, 2001, pp. 825–828.

[52] Gersen, H. et al., "Influencing the Angular Emission of a Single Molecule," *Phys. Rev. Lett.*, Vol. 85, 2000, pp. 5312–5315.

[53] Trabesinger, W. et al., "Continuous Realtime Measurement of Fluorescence Lifetimes," *Rev. Sci. Instrum.*, Vol. 73, 2002, pp. 3122–3124.

[54] Trabsinger, W. et al., "Single-Molecule Near-Field Optical Energy Transfer Microscopy with Dielectric Tips," *J. Microsc.*, Vol. 209, 2003, pp. 249–253.

[55] Drexhage, K., "Influence of a Dielectric Interface on Fluorescence Decay Time," *J. Lumin.*, Vol. 2, 1970, pp. 693–701.

[56] Novotny, L., "Allowed and Forbidden Light in Near-Field Optics. I. A Single Dipolar Light Source," *J. Opt. Soc. Am. A*, Vol. 1, 1997, pp. 91–104.

[57] Carniglia, C., and L. Mandel, "Quantization of Evanescent Electromagnetic Waves," *Phys. Rev. D*, Vol. 2, 1971, pp. 280–296.

[58] Yang, T., G. Lessard, and S. Quake, "An Apertureless Near-Field Microscope for Fluorescence Imaging," *Appl. Phys. Lett.*, Vol. 76, 2000, pp. 378–380.

[59] Novotny, L., "Single Molecule Fluorescence in Inhomogeneous Environments," *Appl. Phys. Lett.*, Vol. 25, 1996, pp. 3806–3808.

[60] Trautman, J., and W. Ambrose, "Near-Field Optical Imaging and Spectroscopy of Single Molecules," in *Single-Molecule Optical Detection, Imaging and Spectroscopy* (T. Basché, W. E. Moerner, M. Orrit, and U. P. Wild, eds.), Weinheim: VCH Verlagsgesellschaft, 1997.

CHAPTER 4

Near-Field Second-Harmonic Generation

Anatoly V. Zayats and Igor I. Smolyaninov

4.1 Introduction

When high-intensity light interacts with a medium, its electronic structure is strongly perturbed and the electromagnetic field is affected in a nonlinear manner. As a result, light with new frequencies can be generated through nonlinear optical processes [1]. The most pronounced and easily obtained nonlinear optical effect is the second-harmonic generation (SHG), which is a partial transformation of the incident optical field at frequency ω to the second-harmonic field at frequency 2ω. SHG is a useful tool for investigations of material properties and surface processes because of its intrinsic sensitivity to the structure and symmetry of materials and interfaces. In the electric dipole approximation, SHG is forbidden in materials with inversion symmetry, which made it an important technique for characterizing asymmetries of surfaces, interfaces, and thin films [2, 3]. SHG is extremely sensitive to surface structure down to the atomic scale, such as surface defects, structural inhomogeneities, and adsorbates. In many materials with poling structures such as ferroelectric and ferromagnetic materials and nonlinear optical polymers, the poling configuration can be related directly to the intensity of SHG, macroscopically or locally. In addition, systems in which inversion symmetry is broken by some applied external field (e.g., electric field) also may be investigated with SHG. In all of these cases, linear optical detection generally can't "see" the asymmetric or poled structures, but SHG can provide very high contrast.

The recent advances in SNOM have opened up the possibility of studying various optical phenomena with a resolution well below the diffraction limit [4]. Most of the initial efforts focused on the investigations of linear optical processes. However, theoretical analysis of the near-field effects in nonlinear optical spectroscopy in general and SHG in particular has been attracting interest for decades in relation to surface-enhanced nonlinear optical phenomena that occur in the near-field of surface features [5]. The possibility of studying nonlinear optical processes with SNOM and their specifics have been discussed theoretically [6, 7].

The first experimental observations of SHG using SNOM were achieved by Smolyaninov, Zayats, and Davis [8], followed by numerous applications of this technique for studies of metal surfaces and functional materials [9–13] in chemistry [14] and biology [15]. Further search for increased spatial resolution and nanoscopic light sources has led to the proposal and realization of apertureless second-harmonic SNOM employing the field enhancement effects at sharp probe tips [16, 17].

Near-field microscopy of SHG, which combines very high surface sensitivity of SHG with high spatial resolution provided by SNOM, has significant potential for probing the nonlinear optical response of a surface locally with subwavelength lateral resolution while simultaneously mapping the surface topography. The data obtained may allow comparison of experiment and theory in sufficient detail in order to study the essential features of SHG at surfaces and to provide better understanding of the underlying microscopic electrodynamics. The possibility of local observation of SHG from individual defects provided by SHG SNOM has resulted in significant breakthroughs in the comprehension of details of SHG at a microscopic level and hence local material properties. In addition to material characterization, investigations of SHG in the near field are of fundamental interest for understanding nonlinear optical processes on the nanoscale, the electromagnetic field confinement and enhancement, and quantum electrodynamic effects in nonlinear optical interactions. This can, in turn, lead to the realization of nonlinear optical devices on the nanometric scale.

In this chapter, we overview recent advances in this rapidly developing field of nonlinear nano-optics. In Section 4.2, various realizations of near-field second-harmonic microscopy are discussed. Section 4.3 is devoted to the studies of the near-field SHG at rough metal surfaces and related effects. The principles of apertureless SHG SNOM in various modes, such as tip-enhanced SHG and SHG from a probe tip, as well as feasibility of achieving nanoscopic light sources are considered in Section 4.4. Finally, in Section 4.5, the imaging of functional ferromagnetic and ferroelectric materials is described.

4.2 Near-Field Microscopy of SHG

Near-field SHG microscope can be exploited in both apertured and apertureless realizations [18]. We will consider these two techniques in turn.

4.2.1 Aperture-Based SHG SNOM

There are three possible experimental configurations for near-field second-harmonic measurements with an apertured probe (Figure 4.1): (1) the second-harmonic (SH) collection mode when the excitation is achieved by direct illumination of a sample and SH light is collected with a fiber tip, (2) the SH excitation mode when a surface is illuminated with fundamental light passing through a fiber tip and SH light is collected in the far field, and (3) the double-pass mode when SH excitation is achieved through a fiber tip and second-harmonic light is collected in the near-field with the same tip. In addition to subwavelength resolution, SHG SNOM provides additional parameters for local optical characterization such as the polarization of fundamental and SH light. Thus, the described techniques allow one to excite SHG locally at a specifically chosen surface area (excitation mode) or to detect local SHG before the SH contributions from individual surface features are averaged in the far-field zone (collection mode).

Collection mode SHG SNOM is most often used because SH generation requires high-intensity excitation light, which is achieved by a focused laser beam. In most experiments, femtosecond Ti:sapphire lasers are used, which provide high

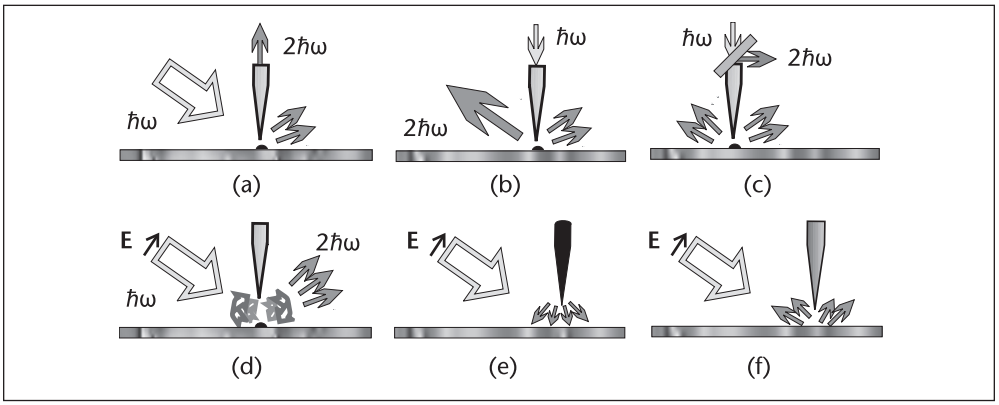

Figure 4.1 Schematics of near-field second-harmonic generation measurements in (a) SH collection, (b) SH excitation, and (c) double-pass mode. Schematics of an apertureless second-harmonic SNOM: (d) electromagnetic interaction between the tip and surface, (e) localized SH light source, and (f) surface SHG induced by a probe tip.

excitation power at a low pulse energy, thus effectively generating SHG but introducing low heating and sample damage. The SH signal collected by a fiber tip is usually filtered by an interference filter and detected by a gated photon counter. Shear-force distance regulation is conventionally used to keep a tip in a near-field proximity and at a constant distance from the surface, thus providing simultaneous topographic imaging.

In most SHG SNOM experiments, uncoated fiber tips are used. The biggest disadvantage of metal-coated fiber tips in nonlinear optical measurements is a strong perturbation introduced by the tip in the local electromagnetic field distribution and SH generation from the metal coating. Uncoated fiber tips introduce a much smaller perturbation since the dielectric constant of a fiber is much less than that of a metal. However, even for fiber (glass) tips, some degree of the electromagnetic field enhancement is associated with a tip apex [19]. This is crucial in near-field second-harmonic measurements for which the signal depends on the fourth power of the local excitation field. Due to the field enhancement, the surface area just below the tip dominates the detected SH signal. As a result, theoretically, the resolution of the SHG SNOM can be estimated to be as small as ~ 10 nm for 50 nm radius of a fiber tip apex [20]. In fact, more severe limitations on the resolution of a SHG SNOM are imposed by the small number of SH photons collected by the tip and the related shot noise and thermal drifts due to long signal acquisition times. The high repetition rate of pulsed Ti:sapphire lasers allows the image acquisition time to be kept in a reasonable range even at a low number of detected SH photons per pulse. The characteristic SH photon count rate in SNOM measurements is, on average, of the order of one SH photon count per 100–300 laser pulses. However, a long signal averaging time, which would help to register more photons, is not desirable due to possible drifts in the experimental apparatus. For that reason, the resolution of the SHG SNOM is in many cases limited by a low detected SH signal rather than the geometry of a probe tip and is determined by a trade-off in the choice of SH signal averaging time.

In the SHG measurements with uncoated fiber tips, the experimentally achievable spatial resolution is usually about 80–100 nm; however, it can be much higher

in some specific cases. The resolution and perturbation introduced by a fiber tip depends on the sharpness and size of the taper via the tip-induced field enhancement. It is possible to reduce the influence of the tip by choosing an appropriate tip apex shape. With less sharp tips, the influence of the tip-induced effects will be smaller and SHG will be directly related to the surface. Although the theoretical resolution in this case will be smaller than that for sharper tips due to a smaller electromagnetic field enhancement, the practical resolution will remain about the same (~100 nm) due to a better overall collection efficiency of such tips. Thus, the choice of the tip depends on the task at hand. For example, for studies of SHG from metal surfaces, perturbation introduced by a tip should be as small as possible. On the other hand, for local crystal analysis with SHG, the field enhancement at a probe tip that depends on the excitation light polarization can be advantageous. In the case of polarization measurements with uncoated fiber tips, SNOM resolution down to 40 nm was reported, which is related to the strong field enhancement in the vicinity of high refractive index materials [20].

4.2.2 Apertureless SHG SNOM

Another type of second-harmonic SNOM makes total use of the effect of the field enhancement at a metallic tip to achieve a local enhancement of nonlinear optical processes in the vicinity of the tip, similar to apertureless scanning near-field optical microscopy (ASNOM) schemes based on two-photon excited fluorescence [19, 21] and Raman scattering [22–24]. It provides much stronger light confinement and better spatial resolution than an aperture-based SHG SNOM [25]. This technique, however, poses the problem of image interpretation [26].

In SHG ASNOM, the excitation light illuminates the tip-surface junction and the scattered SH light is detected in the far field. [See Figures 4.1(d)–(f).] The signal related to nonlinear optical processes is determined by the superlinear dependencies on the intensity of the driving field (the fourth power of the local fundamental field in the case of SHG). This makes such techniques more sensitive to the field distribution over a surface than ASNOM based on linear optical processes. Not only the magnitude of the signal but also the spatial resolution of ASNOM is related to the field enhancement since it determines the effective surface area most strongly contributing to the measured signal. As discussed by Kawata, Xu, and Denk [19], in contrast to the scattering or conventional fluorescence, the light associated with nonlinear processes can be confined (falling faster than $1/r^3$ with a distance r from a tip apex) even without localized surface plasmon excitation.

An approach based on SHG is advantageous compared to other ASNOM schemes because there are almost no restrictions on tip and sample materials since all materials exhibit surface SHG. Only one tip or sample needs to posses strong SHG to provide second-harmonic ASNOM imaging. In different experimental realizations, the technique of apertureless second-harmonic SNOM allows one to probe the local second-harmonic field generated at the surface if the nonlinear susceptibility of the sample is higher than that of the probe tip (a nonlinear background-free analogue of ASNOM based on local scattering). In the opposite case, one can achieve a strongly confined second-harmonic light source at the tip apex with properties dependent on the topographic and dielectric properties of the surface under investigation. From an experimental point of view, an apertureless SHG SNOM

avoids some of the technical problems of both fluorescent and scattering-type ASNOMs: It maintains the advantages of a fluorescent ASNOM as the signal is spectrally isolated from the excitation light, while it is not affected by bleaching and aging problems and tip formation as, for example, metallic tips commonly used in STM or metal-coated cantilevers used in atomic force microscopy can be employed.

4.3 Near-Field SHG at Metal Surfaces

SHG from smooth and rough metal surfaces has been extensively studied in the far field. The studies of the SHG processes on smooth metal surfaces provide details of the electron dynamics in metals. SHG was used in the past to study interactions in correlated electron gas, Fermi surfaces in different metals, etc. The nonlinear polarization $\mathbf{P}(2\omega)$ induced by the excitation light $\mathbf{E}(\omega)$ is

$$P_i(2\omega) = \chi^{(2)}_{ijk} E_j(\omega) E_k(\omega) + \ldots \tag{4.1}$$

where $\chi^{(2)}_{ijk}$ is the second-order nonlinear susceptibility. Symmetry considerations show that this contribution is absent in centrosymmetric media. In this case, the only remaining source of nonlinearity is a surface where inversion symmetry is broken. This accounts for the unprecedented surface sensitivity of the SHG studies. Surface SGH observed in reflection obeys a set of selection rules. It can be excited with p-polarized light leading to p- or s-polarized SH light generated in the direction of the specularly reflected excitation light.

Real surfaces, however, possess various degrees of roughness. The consideration of roughness leads to several phenomena affecting SHG, such as relaxation of polarization selection rules and enhancement of the electromagnetic field at surface defects. Less obvious is the influence of weak and strong light localization effects on SHG from rough surfaces [27] that results in significant changes of the angular spectrum of SHG observed in the far-field region [28]. Even more pronounced changes should be expected in the near-field region close to the surface. Analyzing the near-field SHG measurements, one should consider the substantial influence of evanescent fundamental and second-harmonic fields. Phase-matching conditions and polarization selection rules are meaningless in the near-field of a rough surface. Both are defined with respect to the plane of incidence determined by the direction of propagation and the normal to the surface. There is no direction of propagation for an evanescent wave. A mean normal direction depends on the scale of observation, and a local normal does not coincide with the average normal to the sample surface.

To determine the contribution of near-field processes to the SH generation, the dependence of the second-harmonic signal on the tip-sample distance for s- and p-polarized excitation light was studied (see Figure 4.2). A strong decrease in the signal was observed at about 500 nm from the surface. This behavior is especially pronounced for s-polarized excitation. The initial drop in the signal is followed by a number of oscillations for both excitation polarizations: Each maximum for p-polarized excitation corresponds to a minimum for s-polarized excitation and vice versa. This behavior results from the electromagnetic interaction due to multiple reflections of fundamental and SH light between the glass tip and silver film surface. The phase shift between the distance dependencies can be explained by the π phase

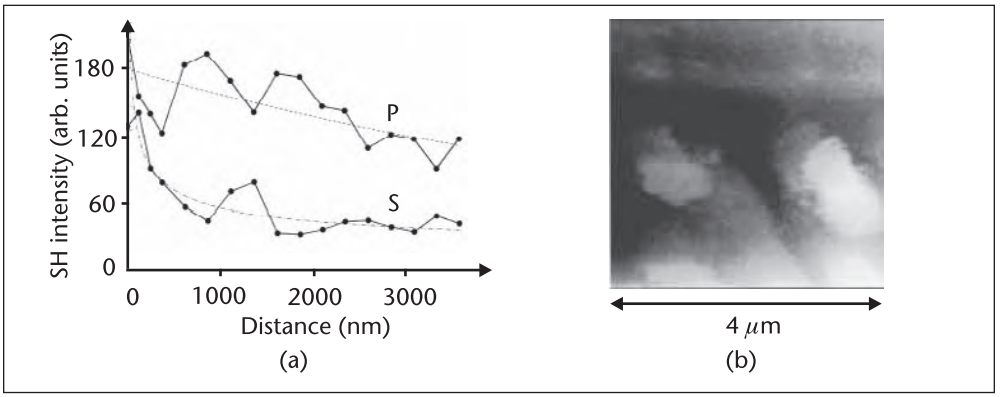

Figure 4.2 (a) Distance dependence of the SH intensity for s- and p-polarizations of the excitation light measured at the center of the surface region shown in (b). Dashed lines are power-law dependencies drawn as a guide to the eye.

shift between p- and s-polarized fundamental waves reflected between the tip and metal at angles larger than the Brewster angle. The ratio of the SH signals induced by p- and s-polarized light changes substantially in the near-field compared to the far-field region. This ratio falls from about 3 at a distance larger than 3 μm from the surface to approximately 1 near the surface. This substantial increase in the s-polarized light-induced evanescent SH field in the vicinity of a rough surface is a nontrivial near-field phenomenon; it is a consequence of relaxation of the polarization selection rules and phase matching conditions in the near field.

4.3.1 SHG Enhancement at Individual Surface Defects

In conventional experiments on surface SHG, one has the possibility of measuring only an intensity and an angular distribution of the SHG originated from the relatively large surface area (determined by the size of the illuminating spot) and, therefore, averaged over a large number of defects without exact knowledge of the surface morphology. Before the introduction of near-field optical techniques, the only experimental approach to SH characterization of rough surfaces was to change the distribution of defect sizes and shapes and then compare the measured tendencies of average SH enhancement with model predictions obtained for an average random defect ensemble. In an ideal experiment, one would like to know the exact size and shape of defects contributing to SHG. At the same time, the lateral distribution of the electromagnetic field over a surface is not uniform and depends on the surface defect structure. The local field intensity can vary by several orders of magnitude on a scale less than half a wavelength along the surface [29]. Therefore, in many cases, investigations of the averaged optical response do not result in an understanding of the underlying physics. The use of near-field measurements provides an opportunity to study SHG from specifically chosen defects before the SH contributions from individual defects are averaged in the far-field zone.

Studies of SHG generation from different types of individual surface defects have revealed that the main contrast mechanism for near-field SH imaging is topography variations. Such behavior is observed for different kinds of surface defects such as grooves, pits, and protrusions on a metal surface [8, 30–33]. In all

of these geometries, the enhancement of SH generation induced by s-polarized excitation occurs near the places on the surface where inhomogeneities are present. This effect has the same origin as the growth of the ratio of s- to p-polarized light-induced SH signals near the rough surface discussed in the previous section. The polarization of the excitation light is important for achieving a field enhancement. However, in the case of p-polarized excitation, the SHG related to surface inhomogeneities is observed in the background SHG due to the nonlinear processes in the electron gas close to a smooth surface.

Let us consider several examples of the SHG enhancement on individual surface defects. In the case of the surface shown in Figures 4.3(a) and 4.3(b), which is essentially flat with a narrow, deep groove, the SH image looks like a "negative" of the topographical image. The SH signal measured in the flat regions is much smaller than the signal measured near the groove. In the case of protrusions on a metal surface [Figures 4.3(d) and 4.3(e)], up to tenfold local enhancement of the SHG at defects with micrometer-size lateral dimensions has been observed, while average SHG enhancement was negligible (about 1.2 times).

In a general form, an enhancement of SHG excited and detected at a surface defect can be described as

$$I_{\mathrm{SH}} \sim |L(2\omega)L^2(\omega)|^2 \tag{4.2}$$

where $L(2\omega)$ and $L(\omega)$ are the field enhancement factors at fundamental and second-harmonic wavelengths, respectively [5]. The local field enhancement factor $L = L_{LR}L_{SP}$ takes into account the lightning rod effect (L_{LR}) due to the geometrical electromagnetic field enhancement at a highly curved surface and localized surface plasmon excitation (L_{SP}). For both enhancement mechanisms, the orientation of the light polarization with respect to a defect is important.

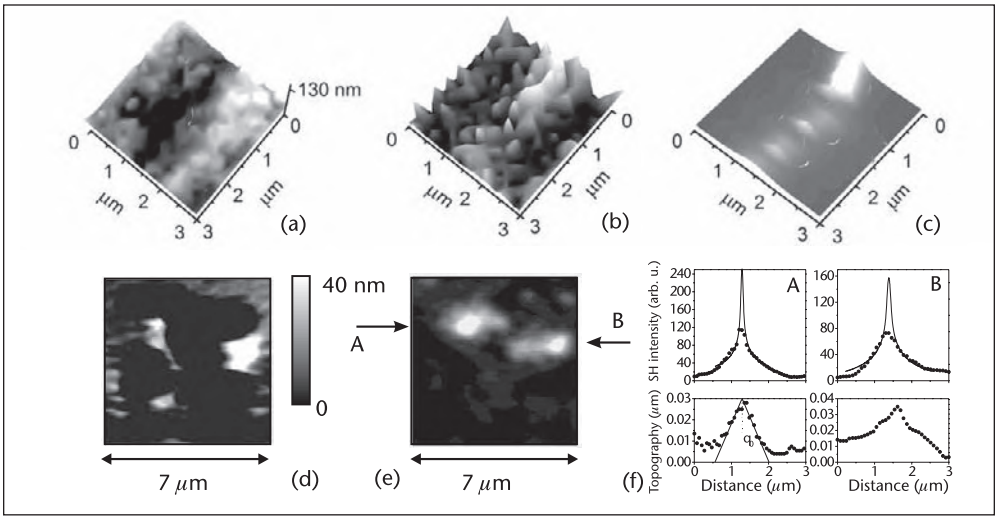

Figure 4.3 (a) Topography and (b) measured and (c) calculated SH images of the silver surface with the defect supporting localized surface plasmons. The fundamental wavelength is 1064 nm. (d) Topography and (e) SH image of a gold film in the case of the geometrical field enhancement on the surface defects. The fundamental wavelength is 790 nm. (f) Cross sections of topography and SH intensity related to the defects indicated by the arrows in (e). Symbols represent the experimental data; solid lines are the model calculations for the lightning rod effect.

For the defect in Figure 4.3(a), the main SHG enhancement effect is related to surface plasmons localized in the groove due to the variation in film thickness. For the parameters of the groove measured from the topographical image, the localized plasmon resonance is inferred to be close to the SH photon energy and the $L_{SP}(2\omega)$ term in Equation 4.2 dominates. The SH intensity distribution calculated in the model of the groove-related surface plasmon reproduces the experimentally observed image very well. [See Figures 4.3(b) and 4.3(c).]

The dipolar localized surface plasmons related to the protrusions on the gold surface in Figure 4.3(d) are estimated to be at about 0.9 eV, which is much lower than the energy of fundamental ($\hbar\omega \approx 1.57$ eV) and second-harmonic photons [33]. In this case, only the lightning rod effect, L_{LR}, is important. For estimation of this geometrical field enhancement, the surface defects can be considered as particles of a conical shape. The enhancement close to the apex of such particles can be estimated in the electrostatic model as follows:

$$E \sim E_z^{(0)} 1/r^{1-\nu} \tag{4.3}$$

Here $E_z^{(0)}$ is the component of the electric field parallel to the cone axis near the plane surface far from the defect; r is the distance to the cone apex; and ν is the first root of equation $P_\nu(cos(\theta_0)) = 0$, where P_ν and θ_0 are the Legendre function of the first kind and the cone opening angle, respectively. Depending on the cone angle, the parameter ν is in the range 0–1 for an ideal metal [34]. The corrections due to a finite dielectric constant of a material (which allow $\nu \geq -0.5$) as well as the influence of surroundings have been extensively discussed by Kawata, Xu, and Denk [19]. This model agrees fairly well with the experimentally measured SH intensity distributions [Figure 4.3(f)] for the parameters of the defects obtained from the topographic image. The finite resolution of the SNOM leads to averaging of the signal over the excitation area and therefore to subsequent reduction of the observed enhancement at a cone apex.

Dependence of the surface-enhanced SHG on the defect size was demonstrated for surface defects shaped in a form of cylindrical segments with adiabatically varying elevation [30]. The intensity of local SHG gradually increases with the local elevation of the defect. The size dependence of the near-field SHG signal calculated in a geometrical field enhancement model is in general agreement with the experimental data without any fitting parameters. The near-field studies of SHG from metallic gratings also has been performed. They show that in addition to the grating-related effects, imperfections (fine defect structure) of gratings play a significant role in SH generation. The influence of imperfections is very pronounced in the SHG images, showing the importance of the field enhancement at the surface defects of the grating [30, 31]. The contribution to SHG from the surface defects may dominate the SH intensity related to the periodic structure of a grating. This effect leads to the diffuse SH light generation from metallic gratings.

The SHG SNOM in the excitation mode was used to study the near-field optical response related to localized surface plasmon resonances and morphology of the metallic particles lithographically fabricated on a metal surface [35, 36]. These experiments also have evidenced the SHG processes specific to the near-field excitation where scattering efficiencies of the nanoparticles can be different from those in the far-field excitation.

4.3.2 SHG and Surface Polariton Localization on a Rough Surface

Generally, p-polarized light-induced near-field SH images are more complex due to the interplay between SHG processes related to surface inhomogeneities and surface plasmon polariton (SPP)-related effects. For example, in the case of a typical randomly rough surface (Figure 4.4) with a number of defects of various sizes, larger defects have different but uniform brightness in the SH image (e.g, on the right-hand side of the images). However, above the surface area with many small defects, the SH intensity distribution exhibits the presence of small bright spots not directly related to the defects (e.g., at the top of the images). The width of the spots is about 240 nm, which is about half a wavelength of the SH light. These spots have been identified as the result of SPP localization on randomly rough surfaces [8] similar to those observed in the linear SNOM images of rough metal films [37].

In fact, SHG at a rough surface and SPP excitation are closely related phenomena since every surface defect may act as a source of a surface wave. Localization effects in the SH generation from rough metal surfaces have been predicted by McGurn, Leskova, and Agranovich [27]. It has been shown that multiple scattering leading to light localization gives a considerable contribution to SHG. Both fundamental and second-harmonic SPP-related localization can contribute to the effect, giving rise to components of SH light propagating perpendicularly to the average sample surface and in the reverse direction to the fundamental wave propagation, respectively. This has been observed indirectly by measuring weak changes in the far-field angular distribution of the SH light [28]. The images observed in the near-field provide direct evidence of the SPP localization processes in SHG from randomly rough surfaces. Further SNOM studies have enabled identification of the spectral dependencies of this SPP localization phenomenon in SHG [38].

4.4 Apertureless Second-Harmonic SNOM

The effect of the SHG enhancement at the surface features discussed previously can be turned around and used to perform ASNOM based on local enhancement of SHG. Owing to the field enhancement at the extremity of a probe tip, the main source of SH light is situated at the surface area just under the tip if the surface nonlinearity is dominant, $\chi_s^{(2)} \gg \chi_t^{(2)}$, or at the apex of the tip if the tip nonlinear susceptibility is higher than that of the surface, $\chi_t^{(2)} \gg \chi_s^{(2)}$ [16, 17]. In these realizations, the SHG ASNOM

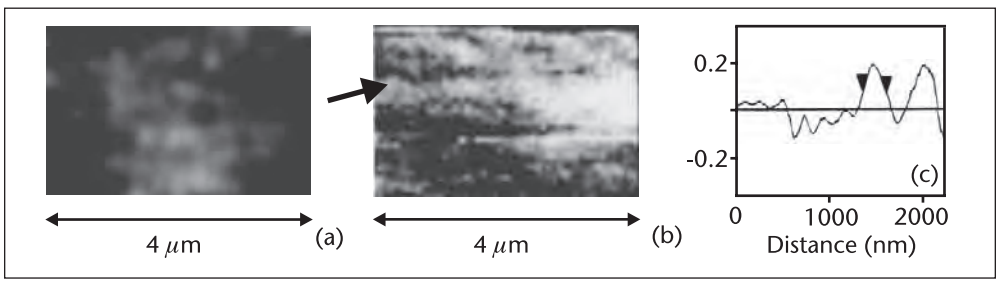

Figure 4.4 (a) Topography and (b) near-field SH intensity distribution above the arbitrary rough silver surface obtained with p-polarized excitation light. (c) The cross section of the SH image along the line indicated by the arrow.

technique is a nonlinear analogue of a linear scattering-type SNOM [39] or fluorescent-type ASNOM [40], respectively [see Figure 4.1(e) and 4.1(f)].

4.4.1 SHG in the Presence of a Probe Tip

If the near-field interaction between the surface inhomogeneities and the probe tip plays a dominant role and if the dimensions of the tip-surface junction are small compared to the distance to the observation point, we can neglect retardation effects and the SH intensity measured in the far field can be expressed as follows [16, 17]:

$$I(2\omega) \propto \left| \sum_i \chi_i^{(2)} \alpha_i^{eff}(2\omega)(\alpha_i^{eff}(\omega))^2 + \chi_t^{(2)} \alpha_t^{eff}(2\omega)(\alpha_t^{eff}(\omega))^2 \right|^2 E^4(\omega) \tag{4.4}$$

where $\chi_i^{(2)}$ and $\chi_t^{(2)}$ are the second-order nonlinear susceptibilities of the surface structure and the tip, respectively, and $\alpha^{eff}(\omega) = f(\alpha_t, \alpha_i, d_{ij}, \mathbf{E}(\omega)/E(\omega))$ is the linear effective polarizability that depends on the polarizabilities of the surface structure (α_i) and the tip (α_t) as well as their separations d_{ij} and the polarization of the fundamental light. This effective polarizability takes into account the field enhancement effects at the ω and/or 2ω frequencies related to the field concentration around highly curved surfaces (lightning rod effect) [34] as well as possible localized surface plasmon resonances if the incident electromagnetic field is in the resonance with the electron plasma oscillations in a metallic particle [41]. Although the tip as well as the sample may be made of SH-active material, for the sake of simplicity, we will assume that the SH signal discussed in the following considerations is generated by a layer of randomly oriented nonlinear molecules that cover the probe and/or the sample. Recently, the SH generation from the tip apex has been studied by Bouhelier et al. [42].

Instead of the effective polarizability α^{eff}, it is common to use the so-called field enhancement factor $L(\omega) = |E_{loc}/E_0| \sim \alpha^{eff}(\omega) = L_{LR}L_{SP}$, which shows the enhancement of the local electric field, E_{loc}, compared to the incident one, E_0. The field enhancement factor has a complex dependence on the dielectric properties of the surface and the probe tip, tip shape, surface topography, and their mutual geometrical configuration, leading to nontrivial object-image relations [26]. Such a complex behavior exists in any kind of ASNOM where the tip not only scatters (or produces) the near fields but also modifies the local surface polarizability due to the near-field electromagnetic interaction.

We will consider the second-harmonic intensity distribution around the apex of a perfectly conducting conical tip [16]. The corrections due to the finite dielectric constants of the tip and sample materials as well as the tip-sample interaction also can be taken into account [19]. The geometrical field enhancement, which is associated with the field concentration at the highly curved surfaces, is only weakly dependent on the excitation wavelength via the dielectric constant of the material as long as the electrostatic approximation is valid. However, one should take into account the contribution of the resonant field enhancement if the tip or the surface can support surface plasmon excitations. Due to the fundamental and second-harmonic field enhancement at the extremity of a probe tip, the main source of SH light is situated at the apex of the tip or at the surface region just underneath it. If a probe tip exhibits stronger second-order nonlinearity than a surface (or vice versa), the situation is simplified considerably. In the former case, the tip of ASNOM can

be considered as a strongly confined source of second-harmonic light (a nanoscale light source) whose properties (and, thus, radiation characteristics) depend on the surface structure underneath it. In the latter case, second-harmonic generation from the surface under investigation is modified by the probe tip.

4.4.1.1 SHG from a Probe Tip

When the nonlinear susceptibility of the tip is much higher than that of the surface, $\chi_i^{(2)} \ll \chi_t^{(2)}$, the signal of SHG ASNOM is determined by the second term in Equation 4.4:

$$I(2\omega) \propto |\chi_t^{(2)} \alpha_t^{eff}(2\omega)(\alpha_t^{eff}(\omega))^2|^2 E^4(\omega) \tag{4.5}$$

and the tip acts as a SH light source [see Figure 4.1(e)]. The field enhancement at the metallic conical tip dictates the spatial variation of the strength of the nonlinear response and, therefore, the attainable resolution. Takahashi and Zayats [43] studied the properties of near-field SHG from the probe tip apex under evanescent near-field fundamental illumination. Bouhelier et al. [42], Labardi et al. [44] and Neacsu et al. [45] investigated SHG from the probe tips under the far-field illumination. Detailed numerical modeling of the SH generation at the ASNOM tip and its polarization and distance dependencies was carried out by Laroche et al. [46].

Let us consider the confinement and polarization properties of the SHG light generated at the apex of a conical metal tip based on a simple electrostatic model of the SH field confinement [16, 17]. Figure 4.5(a) shows the SH as well as fundamental intensity distributions when the tip apex is assumed to have a radius of 10 nm. For the tip with an opening angle of 10°, the SH intensity decreases by 10^3 times at a distance of 100 nm from the apex. At the same time, the fundamental light intensity decreases by only 10 times. For a 60° tip, the field confinement is smaller: The SH and fundamental light intensities decrease at the 100 nm distance by 10 and 2 times, respectively. Thus, the SH field is much stronger confined to the probe tip than the fundamental field, thereby allowing the higher spatial resolution to be achieved in optical studies. Labardi et al. [44] experimentally imaged the fundamental scattering and SH radiation from metallized AFM tips and confirmed the predicted strong confinement of the SH light from the freestanding metallic tips. Bouhelier et al. [42] observed strong SHG confinement during the near-field interaction of the tip with the surface. In the latter case, depending on the polarization of the fundamental light, the SH field distributions around the tip has a complex structure since both transverse and longitudinal fields generated at the tip can be detected in this case.

The typical polarization dependencies of the scattering and SHG from a probe tip apex measured under the excitation in far and near field are presented in Figure 4.5(b). They reveal only two types of dependencies ($\cos^2\theta$ and $\cos^4\theta$) of the detected fundamental and SH intensities on the orientation of the fundamental light polarization with respect to the tip axis. Polarization contrast obtained with a second-harmonic signal significantly exceeds the polarization contrast of the linear scattering from the tip [43]. This is an important property for applications of light sources where polarization sensitivity is needed, such as magnetic and ferroelectric materials characterization.

Since the effective polarizability at both fundamental and second-harmonic frequencies $\alpha_t^{eff}(\omega)$ are sensitive to the variations of the topography and the dielectric

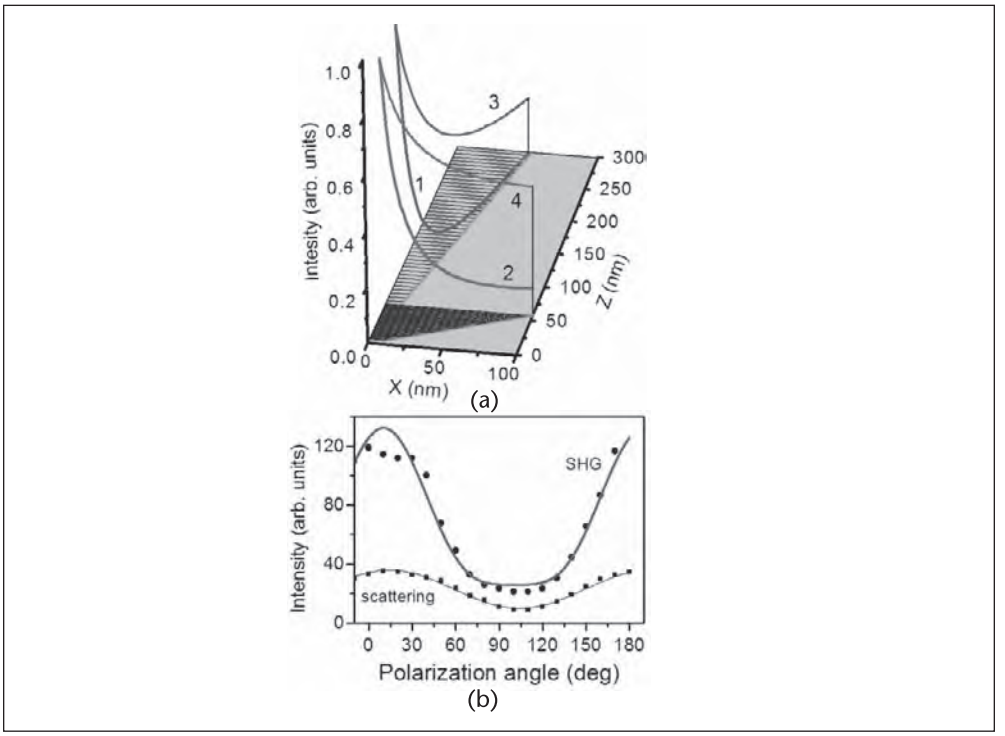

Figure 4.5 (a) Normalized spatial distribution of the SH (1, 2) and fundamental (3, 4) light intensities around a conical tip of 10° (1, 3) and 60° (2, 4) apex. (b) Polarization dependencies of (squares) scattering and (circles) second-harmonic generation from the tip apex in the near-field: (symbols) experiment; (solid lines) model fits. The polarization angle is measured with respect to the plane of incidence.

properties of the surface under the tip, the second-harmonic light generated at the tip is very sensitive to the properties of the surface and can be used to image and study the surface without the need of illuminating it. This can be advantageous for the studies of materials and objects that cannot withstand high intensities of the illuminating light.

Nano-Scale Light Sources via Local SHG

Electromagnetic field enhancement and light confinement are closely related phenomena. It is the confinement that leads to the strong field enhancement due to a small volume of the related electromagnetic modes. Various approaches to realization of local light nanosources (apart from apertured tips) rely on the electromagnetic field enhancement, linear and two-photon fluorescence, and SHG. The enhancement of the incident light field at a tip apex is one of the examples of a configuration leading to a strongly localized light source. However, it is achieved on a significant background of scattered light of the same wavelength. The confinement can be estimated from the localization size of surface plasmons at a tip apex. The nanoscopic volume of fluorescent material has initially been proposed as a localized light source followed by the implementation of a single molecule as a light source [40, 47]. Nonlinear optical processes enable even better light confinement, providing a light source with the electromagnetic field that drops faster than $1/r^3$ with a distance from a source [19, 21]. Nonlinear techniques make use of an enhancement of the electromagnetic field at a probe tip to achieve a local enhancement of the second-order nonlinear processes at or in the vicinity of the tip.

Light confinement effects and related nanoscopic light sources are important from a fundamental point of view and from potential applications. Nanolocal light sources and the ability to manipulate strongly localized electromagnetic fields are required for imaging and characterization of materials and devices on the nanoscale as well as for local optical and spectroscopic studies. They can be used for photolithographic fabrication of nanostructures as well as for optical and magneto-optical high-density data storage. Closely related to this is photochemistry and photobiology on the nanoscale. Using localized light sources, photochemical and photobiological transformations and photochemical reactions can be induced locally on the level of individual molecules. SHG-based nanoscopic sources provide a wide spectral tunability range and excellent polarization properties.

4.4.1.2 Tip-Enhanced Surface SHG

In the case when the tip nonlinearity is much lower than the sample nonlinearity, $\chi_i^{(2)} \gg \chi_i^{(2)}$, the first term in Equation 4.4 plays the dominant role:

$$I(2\omega) \propto \left| \sum_i \chi_i^{(2)} \alpha_i^{eff}(2\omega)(\alpha_i^{eff}(\omega))^2 \right|^2 E^4(\omega) \tag{4.6}$$

The SH light in this case is generated at the surface [Figure 4.1(f)], and the tip is used to modify and examine this SH field distribution (via modifications of α_i^{eff} due to the presence of the tip). This imaging mode is based on a principle similar to that of conventional scattering ASNOM or the tip-enhanced two-photon fluorescence or Raman scattering. The optical response of the surface is enhanced due to the local electromagnetic field modification by the tip. However, this enhancement may be stronger in the case of SHG than in some of the other techniques since both fundamental and SH field can be enhanced at the probe tip.

As shown in Figure 4.6, for different opening angles of a probe tip, the SH light generated at the surface covered with nonlinear molecules is confined under the tip for all of the tip parameters studied. As in the previous case, the tip provides

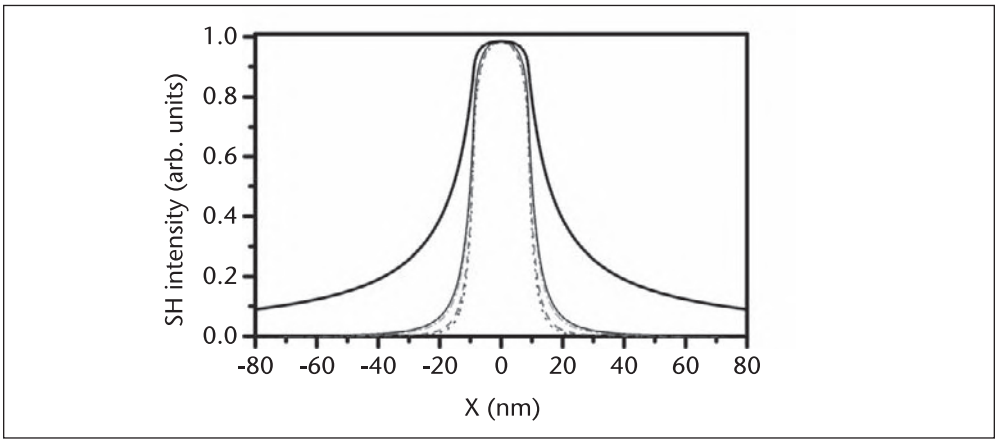

Figure 4.6 Surface SHG intensity variations in a presence of a conical metallic tip of a 10°, 20°, 45°, and 60° opening (dot, dash, dash-dot, and thin solid lines) placed 10 nm above the surface. Thick solid line shows the fundamental light intensity variation across the surface induced by the 60° tip.

stronger confinement of SH field compared to the fundamental field. Even for the tips with a 60° opening, the SH light is strongly confined, while the half-width of the fundamental light intensity distribution is already twice the size of the tip apex.

An increase of the separation between the tip and the surface influences the absolute value of the enhancement but has little effect on the relative spatial distributions of the light. This is in line with near-field SHG in a mesoscopic nonlinear pad, which has been shown to be much stronger confined than the fundamental light [48].

4.4.2 Self-Consistent SHG ASNOM Model

To understand the image formation mechanisms in apertureless SHG SNOM, the electromagnetic coupling between a surface and a probe tip at both fundamental and SH frequencies [Figure 4.1(d)] should be taken into account, similar to the calculations of SHG from randomly structured surfaces [16]. The local fields in the tip location over a surface should be self-consistently calculated, then used with appropriate second-order nonlinear susceptibilities of a tip and/or a surface. The local fundamental field is established due to the electromagnetic interaction between the tip and surface. SHG is driven by the fundamental local field at the surface and the tip and the coupling between them at second-harmonic frequency leads to the local second-harmonic field, which is responsible for the radiated SH light detected in ASNOM measurements.

The calculations based on this self-consistent model show that both fundamental and second-harmonic intensity distributions (Figure 4.7) for p-polarized excitation light reflect the surface structure. With an increase of the tip-surface distance, the fundamental light intensity (and the contrast of the images) drops significantly and respective images become broader. At the same time, the maximum SH intensity is observed at the scanning distance of about 7 nm from the surface when the excitation of second-harmonic surface plasmon related to the tip-defect system is achieved [17]. The SH images are subjected to much less widening than the linear images. This is directly related to the stronger confinement of the SHG mediated by a probe tip. The SH image contrast variations are about 4 times greater than those of the images obtained with the scattered fundamental light. In a real experiment, the contrast variation of the image in scattered light will be additionally affected by the background due to light scattering from the surface and tip shaft. Under excitation with s-polarized light, both SH and fundamental light images have complex structures related to an interplay between the components of the excitation and SH field parallel and perpendicular to the tip-defect axis during scanning.

4.4.3 Experimental Realization of SHG ASNOM

The first experimental realization of this apertureless technique has been achieved using a silver tip and a gold surface as a sample (see Figure 4.8). In these experiments, the second-order nonlinear susceptibilities of the tip and sample are of the same order of magnitude; therefore, the observed SH light is generated at both tip and surface. The lateral distribution of the second-harmonic intensity induced under the excitation with light having an electric field component parallel to the tip

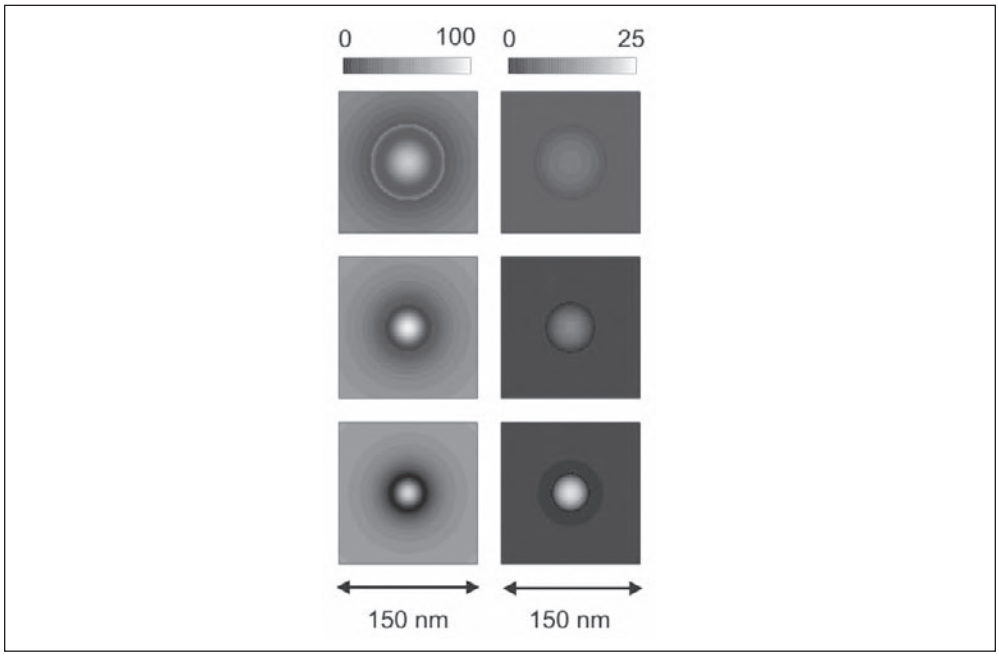

Figure 4.7 Near-field images of a 10 nm radius silver sphere calculated for (left) second-harmonic and (right) fundamental scattering SNOM measurements for the tip-surface distance of (from bottom to top) 1, 7, and 20 nm. The tip is modeled with a silver sphere of a 10 nm radius. The distances between spheres are measured from their surfaces. Excitation light ($\lambda = 740$ nm) is p-polarized with respect to a surface.

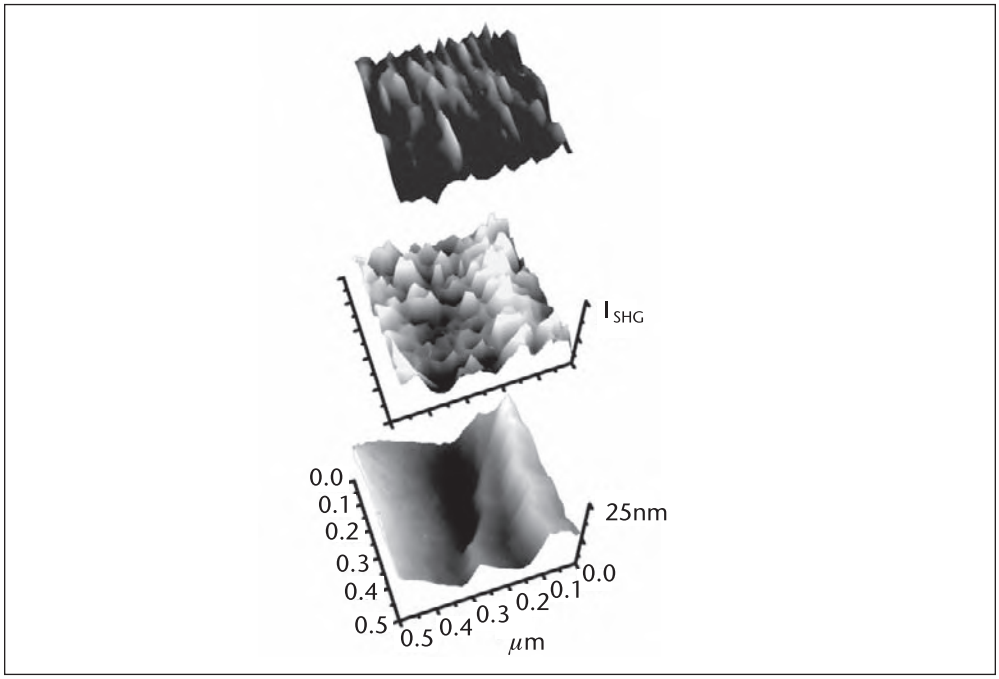

Figure 4.8 The images of a rough gold film surface obtained using an apertureless second-harmonic SNOM: (bottom) topography and SH light distribution measured with (middle) p-polarized and (top) s-polarized excitation light.

axis reveals complex behavior depending on the surface defect structure, but in general reflects the local topography. Lateral variation of the SH signal is related to the different degree of the electromagnetic field enhancement due to the interaction between the tip and surface defects. At the locations on the film surface where the defect structure is simple, the SH images show good correlation with the field enhancement at the individual defects (e.g., with the groove on the surface). In regions with complex surface structure, the SH image does not represent individual surface features, but rather the local field distribution in the system of interacting defects. Although localized surface plasmons have not been specially excited in these experiments, at a rough surface where features of all sizes and shapes are present, it is possible to find a defect (or ensemble of defects) and tip position for which localized plasmon can be excited at the tip-surface junction at the excitation or SH frequency [26]. They are the defects that dominate the recorded SH images. The field enhancement depends dramatically on the geometry, size, and mutual position of the tip and surface defects. Slight variations of the defect shape may result in significant variations of the enhancement and, as a result, the observed SH signal. By changing polarization of the excitation light or tip-surface distance, the interaction between the tip and surface (and, therefore, the resulting SH intensity) can be modified. The contrast in the SH images disappears under excitation with light having no electric field component parallel to the tip axis or when the tip is not in the near-field proximity to the surface [25]. An increase of the SH intensity with the tip approaching a surface is of the same order of magnitude as the one calculated for model systems [17].

Williame et al. [49] have recently conducted the experiments on the visualization of the field enhancement at rough metal surfaces using the apertureless SHG SNOM set-up with metallized AFM cantilevers. Their results are in agreement with the general trends observed and modeled previously, demonstrating much better resolution and higher sensitivity of the SHG measurements to the field variations across the surface compared to the fundamental light scattering.

4.5 Near-Field SHG Imaging of Functional Materials

SHG is a sensitive technique for the characterization and investigation of the symmetry properties of various important technological materials. It is known to be affected by crystal structure, magnetic and ferroelectric order, mechanical strain, etc. Far-field SH microscopy has already demonstrated its great potential in these fields [2, 3]. However, in many applications, spatial resolution below the diffraction limit of far-field optics is required. For example, better than 100 nm resolution is needed for characterization of thin ferroelectric films, which form the basis of a new thin film technology for data storage. The ultimate performance (density and speed of operation) of these devices depends on the spatiotemporal properties of individual ferroelectric domains. A better understanding of these properties requires experiments performed with nanometer spatial and subnanosecond temporal resolution. Near-field microscopy of SHG may be the technique of choice in such experiments. Its main advantages compared with other techniques are the possibility of spectral and time-resolved measurements in ambient conditions and in applied external electric and magnetic fields.

Linear optical techniques with subwavelength spatial resolutions providing magneto-optical contrast (i.e., the ability to discriminate between differently oriented magnetic domains) are based on various SNOM approaches with polarization resolution. These approaches rely on the magneto-optical Kerr or Faraday effects in reflection or transmission, respectively. Using linear apertured or apertureless SNOM, domain imaging has been achieved for polar (magnetization perpendicular to the surface) as well as in-plane magnetized materials and thin films [50]. Similarly, several optical techniques exist with which it is possible to image ferroelectric domain structures in the near-field using apertured and apertureless SNOM [51]. However, many linear optical techniques in this case are limited by the necessary application of electric fields perpendicular or parallel to the ferroelectric sample surface. In addition, ASNOM may require the implementation of interferometric signal analysis to recover the phase information on polarization direction variations.

Nonlinear optical techniques based on SHG are advantageous for functional materials imaging due to a much higher sensitivity to magnetization (or macroscopic polarization) variations in the magnetic (or ferroelectric) domain structures. High surface and interface sensitivity of SHG in combination with the high spatial resolution provided by SNOM has been validated as a powerful tool for imaging of magnetic and ferroelectric domains. The spatial resolution in the collection mode SHG SNOM, when the second-harmonic photons are collected with a SNOM tip, has typically been shown to be about 100 nm with uncoated fiber tips usually used in SHG measurements, reaching about 30 nm in the case of high-refractive index materials (such as piezo-electric films and crystals) with particular polarization properties [18, 20]. In the latter case, although the detection of the SH light is done with a bare fiber tip, the field enhancement effects are similar to those relevant to apertureless SHG SNOM discussed in Section 4.4.1.2. As was proposed by Smolyaninov et al. [20], the fiber tip can be partially coated with metal to provide additional field enhancement and scattering of the SH field into the fiber as well as to apply an external electric field to modify the ferroelectric domain structure under investigation.

SHG polarization analysis, which is, in many cases, essential for domain imaging, although in principle possible with an aperture-based SNOM, is not always feasible due to a weak SHG signal passing through the subwavelength aperture of a fiber tip. More importantly, due to the effects caused by depolarization at the tip apex and in the fiber, it is usually difficult to routinely achieve the polarization extinction better than 10 with apertured SNOM tips. As has been shown, a probe tip of ASNOM acts as an effective local polarizer due to polarization properties of the field enhancement; thus, polarization analysis of the detected light can be achieved efficiently in the apertureless configuration.

Thus, for magnetic and ferroelectric domain imaging, apertureless SHG SNOM has advantages in providing high sensitivity to domain orientation, stronger electromagnetic field enhancement—and, therefore, higher SH signal—better spatial resolution (stronger light confinement), as well as good polarization properties enabling polarization analysis of SH light in the near field. In addition, the apertureless configuration provides more flexibility in illumination/detection configurations needed to address various orientations of the domains and different components of the second-order susceptibility tensor that is needed for absolute determination of the domain orientation.

Applications of ASNOM to the observation of domain-orientation-dependent SHG has nontrivial consequences for imaging contrast mechanisms [25]. The presence of the tip significantly modifies both the local fundamental field and generated SH field. These effects are most important for metallic probe tips of ASNOM. However, even for uncoated fiber tips, the influence of the probe tip can be important. The fiber tip effects are, in many cases, negligible in linear SNOM measurements but cannot be neglected in SHG studies since the SH intensity is proportional to the fourth power of the local fundamental field. In addition, the mixing of the SHG signals from the tip and the sample also may be important [50, 51].

4.5.1 SHG Imaging of Magnetic Domains

Magnetization-induced SHG is a nonlinear version of the magneto-optical Kerr technique that has been shown to have a very large magneto-optical response [52]. SHG has been used successfully in far-field imaging of magnetic-domain structures and their dynamics. Magnetization-induced contrast depends on the polarization state of the excitation light and the orientation of the magnetization vector in the sample. In the dipole approximation, the nonlinear polarization $\mathbf{P}(2\omega)$ of a magnetic medium induced by the fundamental light $\mathbf{E}(\omega)$ is

$$P_i(2\omega) = \chi^{(2)}_{ijk} E_j(\omega) E_k(\omega) + \chi^{m}_{ijkl} E_j(\omega) E_k(\omega) M_l + \ldots \tag{4.7}$$

Here $\chi^{(2)}_{ijk}$ is the electric dipole contribution to the nonlinear susceptibility, χ^{m}_{ijkl} is the magnetization-induced term, and M_l is the magnetization of the medium. Thus, magnetization-induced contrast in SHG images depends on the form of χ^{m}_{ijkl} tensor. In the simplest case, if the magnetization has a component parallel to the surface and perpendicular to the electric field of the s-polarized excitation light, one can imagine that the motion of electrons near the surface becomes asymmetric because of the Lorentz force acting perpendicular to the surface. This gives rise to modification of SH generation. This SHG is insensitive to the sign of magnetization. The component of the electric field of the p-polarized excitation light parallel to the surface results in similar SHG. In this case, magnetization-induced SHG adds to the nonmagnetic contribution from the component of the electric field perpendicular to the surface. However, in the case of noncentrosymmetric materials, the contribution from the bulk of the magnetic material should be taken into account and the exact form of χ^{m}_{ijkl} tensor will be crucial for the contrast mechanism [53]. The bulk distribution of SHG also will be a factor limiting the resolution of SNOM via the probing depth, which defines the sample volume where SH light is generated and collected. The detailed analysis of the SHG SNOM contrast in magnetic domain imaging and the SNOM image formation mechanisms using near-field measurements of nonlinear magneto-optical effects with apertured probe as well as in apertureless mode has been performed by Dickson et al. [50].

Taking into account the preceding considerations, the s-polarized excitation light had been chosen for magnetic domain imaging. Magnetic domains on the [100] surface of a Ni single crystal had been studied. The images of SHG spatial distribution of a demagnetized sample reveal a number of bright and dark regions with characteristic rectangular shapes (see Figure 4.9). These features do not correlate with surface

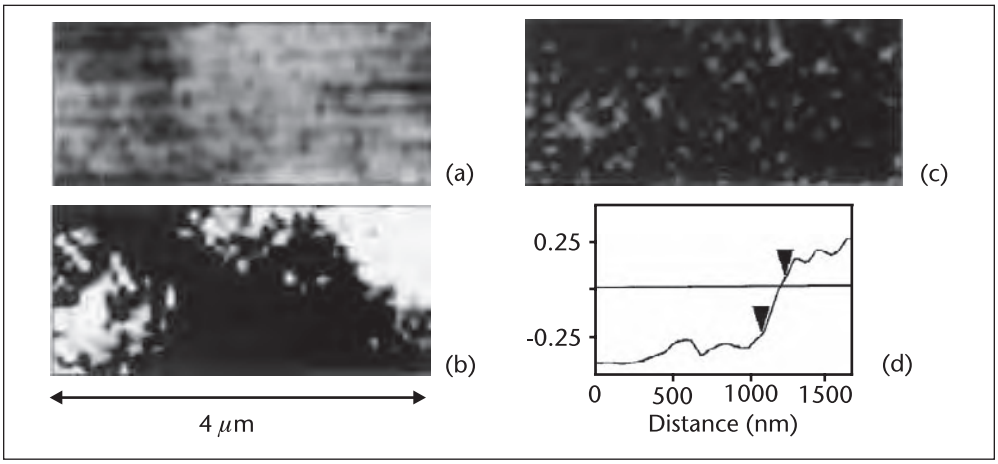

Figure 4.9 (a) Topography and (b, c) SH images of the Ni single crystal before (b) and after (c) magnetization. (d) The SH image cross section perpendicular to a domain wall.

topography, which is rather flat. The rectangular features have characteristic shapes of the domains of closure in Ni. The regions with uniform brightness are magnetic domains with different orientations of magnetization. The sizes of the domains observed are of the order of a few micrometers, which is the usual size of magnetic domains in Ni. After the sample was magnetized, the domain structure was erased [see Figure 4.9(c)]. Overall SH intensity also decreased in this case since the induced magnetization was perpendicular to the plane of incidence. The width of a transition region between the domains is about 150 nm. [See Figure 4.9(d).] This is close to the known thickness of a Bloch wall (magnetic-domain boundary) in nickel.

4.5.2 Local Poling Analysis of Ferroelectric Materials

Near-field SHG measurements provide a tool for nanometer scale crystal analysis that allows recovery of the local poling direction of individual ferroelectric domains since due to the symmetry considerations, the second-order susceptibility tensor $d_{ijk}^{(2\omega)}$ has the same form as the piezoelectric tensor [12, 20, 48, 51]. To understand the contrast of near-field SH images of ferroelectric materials, polarization properties of SH generation in the near field were studied using a poled single crystal of $BaTiO_3$. Phase-matched SHG is prohibited in the bulk of $BaTiO_3$ because of its strong dispersion. As a result, the measured SH signal originates at the surface, which makes the experimental situation look very similar to the case of a thin film. Near-field SH polarization dependencies measured in the SH collection mode with an uncoated fiber tip [Figure 4.10(a)] exhibit fourfold symmetry with respect to the fundamental light polarization rotation if the poling direction is in the plane of incidence of the fundamental light and parallel to the crystal surface (longitudinal configuration). The symmetry becomes twofold when the optical axis is perpendicular to the incidence plane (transverse configuration). If the poling direction is perpendicular to the crystal surface (polar configuration), the SH intensity is much weaker than in the previous cases and has twofold symmetry. Thus, the near-field SHG may be used reliably to recover the local poling direction of ferroelectric domains.

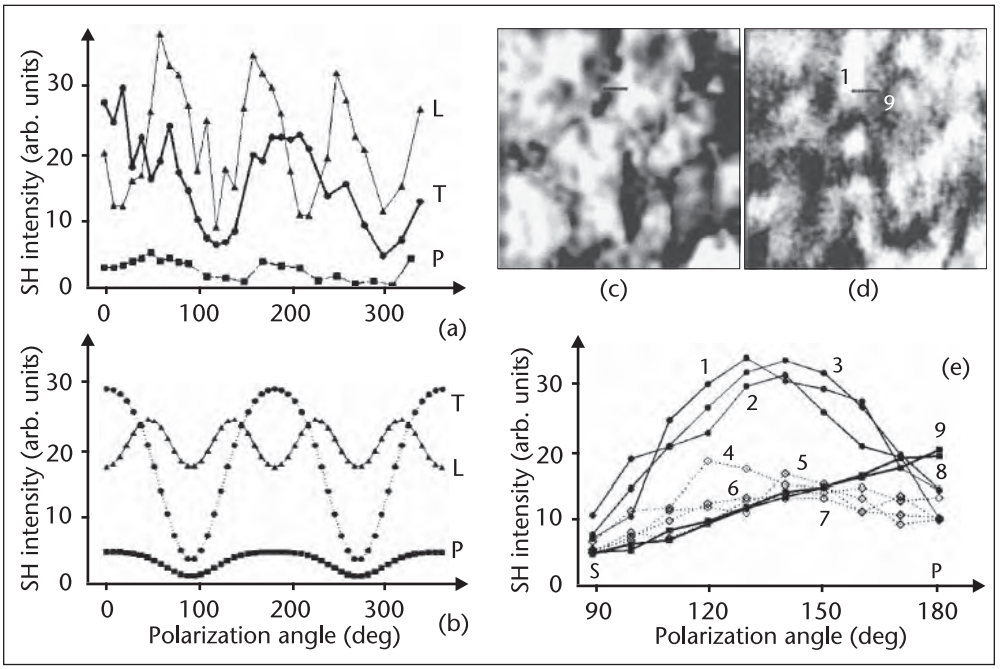

Figure 4.10 (a) Experimentally measured and (b) theoretical dependencies of the near-field SH intensity on the fundamental light polarization for polar (P), longitudinal (L), and transverse (T) poling directions of a $BaTiO_3$ crystal with respect to the incident fundamental light. Simultaneously measured (c) topography and (d) near-field SH image of a PZT film (size $3 \times 3\ \mu m^2$). Height variation within the topographical image is 75 nm. The SH image was obtained using p-polarized excitation light. (e) Near-field SH intensity dependencies on the polarization of the fundamental light taken at 9 points shown in the images (c, d): The points are numbered in succession from left to right along the line. The distance between the points is 45 nm.

As an example, we consider the transverse configuration with the ferroelectric domain orientation normal to the incidence plane of the fundamental light. Considering only nonzero components of the second-order nonlinear susceptibility tensor for $BaTiO_3$: $\chi^{(2)}_{yyz} = \chi^{(2)}_{xxz} = \chi^{(2)}_{yzy} = \chi^{(2)}_{xzx}$, $\chi^{(2)}_{zyy} = \chi^{(2)}_{zxx}$ and $\chi^{(2)}_{zzz}$, where z is the poling direction. The second-harmonic field components at the fiber tip location can be written according to Equation 4.1, taking into account the field enhancement effects described by Equations 4.2 and 4.3 as follows:

$$
\begin{aligned}
E_x(2\omega) &\sim \chi^{(2)}_{xzx} sin^2\psi cos\alpha \\
E_y(2\omega) &\sim (\gamma/\varepsilon_b)\chi^{(2)}_{xzx} sin^2\psi cos\alpha \\
E_z(2\omega) &\sim (\gamma^2/\varepsilon^2)\chi^{(2)}_{zxx} cos^2\psi sin^2\alpha + \chi^{(2)}_{zxx} cos^2\psi cos^2\alpha + \chi^{(2)}_{zzz} sin^2\psi
\end{aligned}
\tag{4.8}
$$

Here α is the angle of incidence, ψ is the polarization angle of the fundamental light defined with respect to the plane of incidence ($\psi = 0°$ correspond to p-polarized light), ε is the dielectric constant of ferroelectric material, and $\gamma = L_{LR}(\omega)$ is the enhancement factor related to a glass probe tip for the excitation field component parallel to the tip axis (E_y component). It can be very roughly estimated as $\gamma \sim n^2$, where n is the refractive index of a tip. The E_y component of the SHG field also can be enhanced at the tip apex. Numerical calculations of the

enhancement factors for different tip-surface pairs show that this approximation gives underestimated values of the enhancement [19]. In a simplified model, assuming that a SNOM tip collects only dipole radiation and the SH dipoles oriented in y direction do not radiate toward the tip, the SHG signal detected with SNOM will be $I_{SH} \sim E_z^2(2\omega) + E_x^2(2\omega)$. Similar calculations of the field at the tip apex can be performed for two other poling directions. According to this model, the polarization dependencies of the field $E(\omega)$ for the surface area around the tip should be approximately the same as for the field directly under the tip. Only the enhancement factor γ is different: γ changes from a maximum just under the tip apex to $\gamma = 1$ far from the tip. Thus, in the final result, one must replace the factors γ^4 and γ^2 by the average values $<\gamma^4>$ and $<\gamma^2>$ taken over the area around the tip from where the SH signal is collected. The best agreement with the experimentally measured symmetry properties of the near-field SH polarization dependencies was achieved with γ= 5–7 [see Figure 4.10(b)]. A much smaller value of the SH signal in the polar configuration is a consequence of the fact that I_{SH} only contains terms proportional to $<\gamma^2>$, while in the case of the longitudinal and transverse configurations, the SH signal is proportional to $<\gamma^4>$.

Local polarization measurements in different areas of thin $BaTiO_3$ and PZT ($PbZr_xTi_{1-x}O_3$) films show a close resemblance with the theoretical dependencies (see Figure 4.10). These materials have similar perovskite structure and belong to the same tetragonal symmetry class. The localized areas of the SH intensity variations in Figure 4.10(d) can be identified as regions with different poling directions. Point-by-point measurements of local SH polarization dependencies [Figure 4.10(e)] over the area which shows clear change in SH contrast have been performed by moving the tip in 45 nm steps (from left to right with respect to the image) as indicated in Figures 4.10(c) and 4.10(d). A full transition from fourfold symmetry (curves 1–3) to twofold symmetry (curves 8 and 9) has been observed with a narrow intermediate region (curves 4–7), which does not show any polarization dependence of SHG. High spatial resolution of the near-field SH measurements is evidenced by the observation of symmetry changes in the SH polarization dependencies in neighboring points. Such a high spatial resolution for uncoated fiber tips stems from the field enhancement effects at a glass tip apex, especially while imaging materials with high permittivity. A surface area just below the tip dominates the measured SHG signal similar to the case of ASNOM measurements with metallic tips discussed in Section 4.4. However, the enhancement and resolution depend on particular polarization properties of the sample under investigation (Equation 4.8).

It is possible, knowing the nonzero nonlinear susceptibility tensor components, to determine the local domain direction by comparing the near-field SH response obtained with different fundamental light polarizations and different angles of incidence. Such polarization dependencies are strongly influenced by the field enhancement effects [51]. Utilizing these polarization properties of the SHG and assuming that domains are related to grain structure of a polycrystalline PZT film, the SHG variations can be correlated directly to the topography of the film. This is illustrated in Figure 4.11. The SHG polarization difference image [Figure 4.11(d)] has been obtained by subtraction of the raw SH signal measured at different fundamental light polarizations. Grain/domain boundaries have been drawn as a visual guide. The area designated *A* shows almost no change in SHG as the fundamental light polarization is rotated from s to p. This may indicate a domain oriented in the

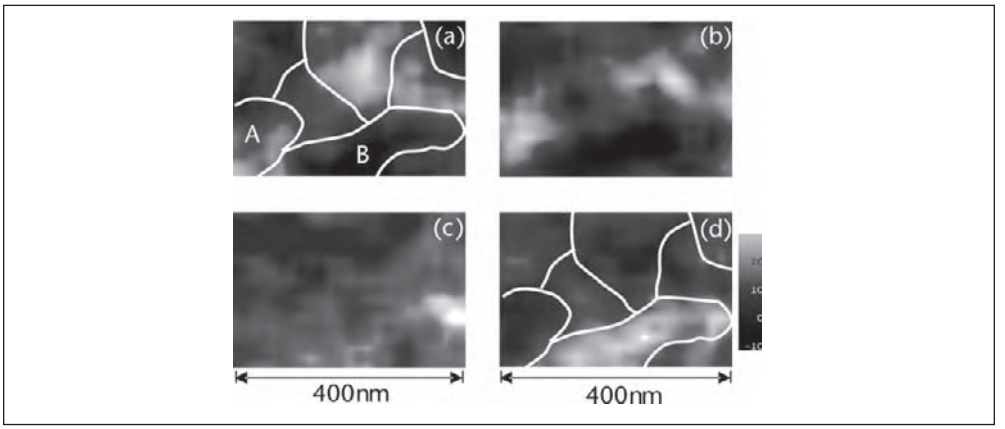

Figure 4.11 (a) Topography and (b, c) corresponding SHG SNOM images of the PZT film obtained with (b) p- and (c) s-polarized excitation light. The polarization-dependent change in the SH intensity is shown in (d). The grayscale variations in (d) from black to white correspond to an increase in the SH intensity with the fundamental light polarization rotated from s- to p- state. Possible grain boundaries have been traced on (a) and (d) to assist with visual interpretation.

longitudinal direction for a tip-surface combination exhibiting a small enhancement factor. The area marked *B* shows a strong increase in SHG for p-polarized fundamental light, indicating either transverse or polar orientation of the domain.

Thus, the advantages of the SHG SNOM imaging of magnetic and ferroelectric domain is that the SHG contrast related to domain orientation is similar to that in the far-field measurements but with different contributions from the susceptibility tensor components [51]. Nevertheless, in the ASNOM configurations with a tilted metallic tip exhibiting second-order nonlinearity comparable to that of the sample, the SH intensity contrast can be obtained for different domain orientations without the need for additional polarization analysis. The technique also provides better spatial resolution and stronger SHG signal due to the tip-induced field enhancement [25].

4.6 Conclusion

Since its recent development, near-field second-harmonic generation already has found numerous applications in imaging and local optical characterization of various materials and structures, including functional materials as well as chemical and biological species. Further extensions of the technique for third-harmonic generation and four-wave mixing on the nanoscale are already under development [14]. Nonlinear nano-optics in general and second-harmonic generation in particular have opened up fascinating opportunities in studies of the electromagnetic field enhancement effects and their applications for achieving nanoscale light sources. Implementation of novel nanofabrication technologies provide new opportunities for tailoring properties of nanostructures and probe tips to emphasize and target effects in nonlinear optics related to field enhancement and light localization. An understanding of nanoscale nonlinear processes might provide the possibility of developing nonlinear photonic devices on the subwavelength scales capable of operating at low light intensities.

Acknowledgments

We are indebted to all of our colleagues who contributed to the progress of the work reported in this chapter, among them C. C. Davis, W. Dickson, C. H. Lee, H. Liang, J. Mlynek, V. Sandoghdar, and S. Takahashi. The financial support from NSF, EPSRC, and The Royal Society is gratefully acknowledged.

References

[1] Shen, Y. R., *The Principles of Nonlinear Optics*, New York: Wiley, 1984.

[2] McGilp, J. F., "Optical Characterization of Semiconductor Surfaces and Interfaces," *Progr. Surf. Sci.*, Vol. 49, 1995, pp. 1–106.

[3] Yamada, S., and I. Y. S. Lee, "Recent Progress in Analytical SHG Spectroscopy," *Anal. Sci.*, Vol. 14, 1998, pp. 1045–1051.

[4] Richards, D., and A. V. Zayats (eds.), "Nano-optics and Near-Field Microscopy," *Phil. Trans. R. Soc. Lond.*, Ser. A, Vol. 362, 2004, pp. 699–919.

[5] Moskovits, M., "Surface-Enhanced Spectroscopy," *Rev. Mod. Phys.*, Vol. 57, 1985, pp. 783–826.

[6] Vigoureux, J. M., C. Girard, and F. Depasse, "Nonlinear Near Field Optics," *J. Mod. Opt.*, Vol. 41, 1994, pp. 49–58.

[7] Zhao, X., and R. Kopelman, "The Wave-Mixing Near Field Optics Amplifier: A Theoretical Feasibility Study for Non-linear NFO Experiments in Biology, Chemistry and Material Science," *Ultramicroscopy*, Vol. 61, 1995, pp. 69–80.

[8] Smolyaninov, I. I., A. V. Zayats, and C. C. Davis, "Near-Field Second-Harmonic Generation from a Rough Metal Surface," *Phys. Rev. B,* Vol. 56, 1997, pp. 9290–9293.

[9] Smolyaninov, I. I., A. V. Zayats, and C. C. Davis, "Near-Field Second-Harmonic Imaging of Ferromagnetic and Ferroelectric Materials," *Opt. Lett.*, Vol. 22, 1997, pp. 1592–1594.

[10] Bozhevolnyi, S. I., B. Vohnsen, and K. Pedersen, "Near-Field Optical Microscopy of Nonlinear Susceptibilities," *Opt. Commun.*, Vol. 150, 1998, pp. 49–55.

[11] Jakubchuk, D. et al., "Near-Field Probing of Nanoscale Nonlinear Optical Processes," *Opt. Lett.*, Vol. 24, 1999, pp. 1151–1153.

[12] Shen, Y. Z. et al., "Nanoscopic Study of Second-Harmonic Generation in Organic Crystals with Collection-Mode Near-Field Scanning Optical Microscopy," *Opt. Lett.*, Vol. 26, 2001, pp. 725–727.

[13] Labardi, M. et al., "Femtosecond Near-Field Optical Microscope for Nonlinear Nanospectroscopy," in *Plasmonics: Metallic Nanostructures and their Optical Properties* (M. I. Stockman, ed.), *Proc. SPIE*, Vol. 5927, 2005, pp. 210–216.

[14] Schaller, R. D. et al., "Nonlinear Chemical Imaging Nanomicroscopy: From Second and Third Harmonic Generation to Multiplex (Broad-Bandwidth) Sum Frequency Generation Near-Field Scanning Optical Microscopy," *J. Phys. Chem. B*, Vol. 106, 2002, pp. 5143–5154.

[15] Schaller, R. D. et al., "Near-Field Second Harmonic Imaging of Granular Membrane Structures in Natural Killer Cells," *J. Phys. Chem. B*, Vol. 104, 2000, pp. 5217–5220.

[16] Zayats, A. V., and V. Sandoghdar, "Apertureless Scanning Near-Field Second-Harmonic Microscopy," *Opt. Commun.*, Vol. 178, 2000, pp. 245–249.

[17] Zayats, A. V., and V. Sandoghdar, "Apertureless Near-Field Optical Microscopy via Local Second-Harmonic Generation," *J. Microsc.*, Vol. 202, 2001, pp. 94–100.

[18] Zayats, A. V., and I. I. Smolyaninov, "Near-field second-harmonic generation," *Phil. Trans. R. Soc. Lond., Ser. A*, Vol. 362, 2004, pp. 843–860.

[19] Kawata, Y., C. Xu, and W. Denk, "Feasibility of Molecular-Resolution Fluorescence Near-Field Microscopy Using Multi-photon Absorption and Field Enhancement Near a Sharp Tip," *J. Appl. Phys.*, Vol. 85, 1999, pp. 1294–1301.

[20] Smolyaninov, I. I. et al., "Local Crystal Analysis Using Near-Field Optical Second Harmonic Microscopy: Application to Thin Ferroelectric Films," *J. Appl. Phys.*, Vol. 89, 2001, pp. 206–211.

[21] Sanchez, E. J., L. Novotny, and X. S. Xie, "Near-Field Microscopy Based on Two-Photon Excitation with Metal Tips," *Phys. Rev. Lett.*, Vol. 82, 1999, pp. 4014–4017.

[22] Stöckle, R. M. et al., "Nanoscale Chemical Analysis by Tip-Enhanced Raman Spectroscopy," *Chem. Phys. Lett.*, Vol. 318, 2000, pp. 131–136.

[23] Hayazawa, N. et al., "Near-Field Raman Scattering Enhanced by a Metallized Tip," *Chem. Phys. Lett.*, Vol. 335, 2001, pp. 369–374.

[24] Hartschuh A. et al., "High-Resolution Near-Field Raman Microscopy of Single-Walled Carbon Nanotubes," *Phys. Rev. Lett.*, Vol. 90, 2003, Art. No. 095503.

[25] Zayats, A. V., "Apertureless Near-Field Microscopy Based on Second-Harmonic Generation," in *Advances in Nano-Optics and Nano-Photonics*, Volume 1: *Tip Enhancement* (S. Kawata and V. M. Shalaev, eds.), Amsterdam: Elsevier, 2006, pp. 237–275.

[26] Zayats, A. V., "Electromagnetic Field Enhancement in the Context of Apertureless Near-Field Microscopy," *Opt. Commun.*, Vol. 161, 1999, pp. 156–162.

[27] McGurn, A. R., T. A. Leskova, and V. M. Agranovich, "Weak-Localization Effects in the Generation of Second Harmonics of Light at a Randomly Rough Vacuum-Metal Grating," *Phys. Rev. B*, Vol. 44, 1991, pp. 11441–11456.

[28] O'Donnell, K. A., R. Torre, and C. S. West, "Observations of Second-Harmonic Generation from Randomly Rough Metal Surfaces," *Phys. Rev. B*, Vol. 55, 1997, pp. 7985–7992.

[29] Shalaev, V. M. *Nonlinear Optics of Random Media*, Berlin: Springer, 2000.

[30] Smolyaninov, I. I. et al., "Near-Field Imaging of Surface-Enhanced Second Harmonic Generation," *J. Microsc.*, Vol. 194, 1999, pp. 532–536.

[31] Zayats, A. V., I. I. Smolyaninov, and C. C. Davis, "Near-Field Microscopy of Second-Harmonic Generation," in *Novel Trends in Laser Spectroscopy and Optical Diagnostics* (A. Chikishev, V. N. Zadkov, and A. M. Zheltikov, eds.), *Proc. SPIE*, Vol. 3732, 1999, pp. 81–92.

[32] Zayats, A. V., I. I. Smolyaninov, and C. C. Davis, "Observation of Localized Plasmonic Excitations in Thin Metal Films with Near-Field Second-Harmonic Microscopy," *Opt. Commun.*, Vol. 169, 1999, pp. 93–96.

[33] Zayats, A. V. et al., "Second-Harmonic Generation from Individual Surface Defects under Local Excitation," *Phys. Rev. B*, Vol. 61, 2000, pp. 4545–4548.

[34] Landau, L. D., and E. M. Lifshits, *Electrodynamics of Continuous Media*, London: Pergamon, 1984.

[35] Zalevani-Rossi, M. et al., "Near-Field Second-Harmonic Generation in Single Gold Nanoparticles," *Appl. Phys. Lett.*, Vol. 92, 2008, Art. No. 093119.

[36] Celebrano, M. et al., "Mapping Local Field Enhancements at Nanostructured Metal Surfaces by Second-Harmonic Generation Induced in the Near Field," *J. Microsc.*, Vol. 229, 2008, pp. 233–239.

[37] Bozhevolnyi, S. I., I. I. Smolyaninov, and A. V. Zayats, "Near-Field Microscopy of Surface Plasmon Polaritons: Localization and Internal Interface Imaging," *Phys. Rev. B*, Vol. 51, 1995, pp. 17916–17924.

[38] Bozhevolnyi, S. I., J. Beermann, and V. Coello, "Direct Observation of Localized Second-Harmonic Enhancement in Random Metal Nanostructures," *Phys. Rev. Lett.*, Vol. 90, 2003, Art. No. 197403.

[39] Keilmann, F., and R. Hillenbrand, "Near-Field Microscopy by Elastic Light Scattering from a Tip," *Phil. Trans. R. Soc. Lond., Ser. A*, Vol. 362, 2004, pp. 787–805.

[40] Lewis, A., and K. Lieberman, "Near-Field Optical Imaging with a Non-Evanescently Excited High-Brightness Light-Source of Subwavelength Dimensions," *Nature*, Vol. 354, 1991, pp. 214–216.

[41] Zayats, A. V., I. I. Smolyaninov, and A. A. Maradudin, "Nano-Optics of Surface Plasmon Polaritons," *Phys. Rep.*, Vol. 405, 2005, pp. 131–314.

[42] Bouhelier, A. et al., "Near-Field Second-Harmonic Generation Induced by Local Field Enhancement," *Phys. Rev. Lett.*, Vol. 90, 2003, Art. No. 013903.

[43] Takahashi, S., and A. V. Zayats, "Near-Field Second-Harmonic Generation at a Metal Tip Apex," *Appl. Phys. Lett.*, Vol. 80, 2002, pp. 3479–3481.

[44] Labardi, M. et al., "Highly Efficient Second-Harmonic Nanosource for Near-Field Optics and Microscopy," *Opt. Lett.*, Vol. 29, 2004, pp. 62–64.

[45] Neacsu, C. C. et al., "Second-Harmonic Generation from Nanoscopic Metal Tips: Symmetry Selection Rules for Single Asymmetric Nanostructures," *Phys. Rev. B*, Vol. 71, 2005, Art. No. 201402.

[46] Laroche, T. et al., "Three-Dimensional Finite-Difference Time-Domain Study of Enhanced Second-Harmonic Generation at the End of a Apertureless Scanning Near-Field Optical Microscope Metal Tip," *J. Opt. Soc. Am. B*, Vol. 22, 2005, pp. 1045–1051.

[47] Michaelis, J. et al., "Optical Microscopy with a Single-Molecule Light Source," *Nature*, Vol. 405, 2000, pp. 325–328.

[48] Li, Z.-Y., B.-Y., Gu, and G.-Z. Yang, "Strong Localization of Near-Field Second-Harmonic Generation for Nonlinear Mesoscopic Surface Structures," *Phys. Rev. B*, Vol. 59, 1999, pp. 12622–12626.

[49] Williame, L. et al., "Linear and Non-Linear Near-Field Behavior on Random Metal Films and Surfaces, in *Plasmonic Nano-imaging and Nanofabrication* (S. Kawata, V. M. Shalaev, and D. P. Tsai, eds.), *Proc. SPIE*, Vol. 5928, 2005, pp. 1–8.

[50] Dickson, W. et al., "Near-Field Second-Harmonic Imaging of Magnetic Domains," *J. Appl. Phys.*, Vol. 97, 2005, Art. No. 033505.

[51] Dickson, W. et al., "Near-Field Second-Harmonic Imaging of Thin Ferroelectric Films," *Phys. Rev. B*, Vol. 72, 2005, Art. No. 094110.

[52] Kirilyuk, A., "Nonlinear Optics in Application to Magnetic Surfaces and Thin Films," *J. Phys. D*, Vol. 35, 2002, pp. R189–R207.

[53] Wegner, D. et al., "In-Plane Magnetization of Garnet Films Imaged by Proximal Probe Nonlinear Magneto-Optical Microscopy," *J. Appl. Phys.*, Vol. 88, 2000, pp. 2166–2168.

CHAPTER 5

Near-Field Microscopy and Lithography of Light-Emitting Polymers

Franco Cacialli, David Lidzey, and David Richards

5.1 Introduction

Conjugated polymers provide a class of film-processible semiconductor materials with significant potential for use in opto-electronic devices such as light-emitting diodes (LEDs) and photovoltaic cells [1, 2]. In particular, the advantages that conjugated polymers offer in terms of low-cost production and fabrication simplicity, stemming from their solution processibility, make them suitable for use in applications such as large area displays and solar cells. There is now considerable scope for the further development of these materials by the control of structure on a mesoscopic scale. The fabrication of conjugated polymer nanostructures through self-organization has been shown to be very effective for the improvement of the performance of conjugated polymer LEDs [3] and photodiodes [4], while lateral patterning on a range of length scales is required for multicolor displays [5], integrated electronics [6, 7], and the fabrication of smart photonic structures [8–10].

Depending on the length scale involved, these nanostructured systems can be investigated by means of different microscopies, such as atomic force microscopy (AFM) and transmission electron microscopy (TEM). For features with typical dimensions of a micron or larger, these systems can be investigated with optical probes in the far field. Indeed, the chemical specificity provided by optical techniques such as fluorescence and Raman microscopy usually makes them preferable to AFM, while TEM involves staining [4], which may be impossible or undesirable. Furthermore, optical probes provide information about the local optoelectronic properties, important for device optimization. However, in many conjugated polymer systems, the relevant length scales are below the classical Abbe diffraction limit, restricting the use of conventional far-field spectroscopies. This limit can be overcome through the use of near-field microscopy, which also provides topographic information to enable a correlation with the results of AFM. In this chapter, we will describe the use of SNOM for determining the structural composition and local optoelectronic properties of conjugated polymer nanostructures [11–15].

We also will demonstrate the use of SNOM as a photolithographic technique for the nanoscale patterning of polymer films [16].

5.2 Conjugated Polymer Blends

The ability to blend different semiconductors is a useful property of solution processible materials such as conjugated polymers. It allows the improvement of device performance by enabling the selection of the optimum material for each relevant process in device operation (charge transport, charge injection, and luminescence) as well as the fine-tuning of the overall device performance by control of the concentration. Furthermore, the generally low entropy of mixing polymers leads to phase separation on length scales ranging from a few nanometers to several microns [17, 18], which can be put to use for further device optimization.

For example, lateral phase separation within thin conjugated polymer films leads to systems with a high interfacial surface area, beneficial for the performance of photovoltaic devices when the differences in electron affinities and ionization potentials of the constituent polymers of the blend are such that efficient exciton ionization is enhanced at interfaces between the two materials [4, 19]. The absorption of light in a photovoltaic device leads to the creation of excitons, bound electron-hole pairs. Those excitons that diffuse to a polymer-polymer interface will participate in charge transfer to form unbound electrons and holes, with the electrons transferred to the material with the higher electron affinity and the holes to the material with the lower ionization potential. Furthermore, as the exciton diffusion length is of the order of ~10 nm in conjugated polymers, it is expected that a phase separation on a length scale comparable to or smaller than this will allow excitons created within a phase to diffuse easily to an interface to facilitate efficient charge transfer for the realization of highly efficient photovoltaic devices [4].

Within thin films of conjugated polymer blends, the length scales for phase separation can be varied from several microns to tens of nanometers by limiting the time allowed for solvent-enhanced self-organization through different processing routes [4,18]. Compositional gradients and fine nanoscale mixed-polymer phases are created in the final stages of film formation, when the majority of the solvent has evaporated and polymer mobilities are low. Understanding the nature of this phase separation and its impact on the optoelectronic properties of a conjugated polymer blend is highly desirable—for both a quantitative description of device operation and further performance improvement.

In this chapter, we will focus on blends of polyfluorene derivatives, which form a class of film-processible semiconductors providing a strong combination of desirable device properties—namely, color range, high efficiency, low operating voltage, and device lifetime [20]. These polymer blends have been fabricated by dissolving the constituent polymers separately in a solvent (such as chloroform or xylene), mixing the solutions together, and then either spin-coating films of ~100-nm thickness or drop-casting (under a solvent-saturated atmosphere) to create films of thickness 200–300 nm.

We will demonstrate how the spectroscopic contrast provided by fluorescence SNOM (either continuous wave (CW) or time-resolved) and scanning near-field photocurrent microscopy is able to reveal the composition of the different phases and provide

insight into the nanoscale optoelectronic properties of these materials. Moreover, the topographic information provided simultaneously with optical measurement in SNOM allows a direct comparison with the results of the higher-resolution technique of tapping-mode AFM so that the combined use of SNOM and AFM is able to provide a detailed picture of the phase separation properties of conjugated polymer blends.

5.3 Aperture SNOM

5.3.1 Application to Conjugated Polymers

We will describe in this chapter the application of the most conventional form of SNOM employing as a probe a subwavelength aperture, defined at the apex of a single mode optical fiber (see Figure 5.1). In particular, we will focus initially on fluorescence SNOM, in which light scattered from the sample is collected and spectrally analyzed as the tip scans over the sample, enabling the formation of a fluorescence image of the sample, thereby providing a chemical map of the system. This has been applied successfully to the study of a range of conjugated polymer systems, including aggregates in conjugated polymers [21], blends of luminescent derivatives of poly(*p*-phenylenevinylene) (PPV) [22], blends of conjugated polymers and inert matrices [11, 23, 24], binary blends of polyfluorene-derivative polymers [12, 13, 25], and ternary conjugated-saturated polymer blends [26]. We also will describe the use of the apertured SNOM probe as a nanoscale light source for the measurement of photocurrent in a conjugated polymer device [27] and for nano-optical lithography of thin film polymer nanostructures [16].

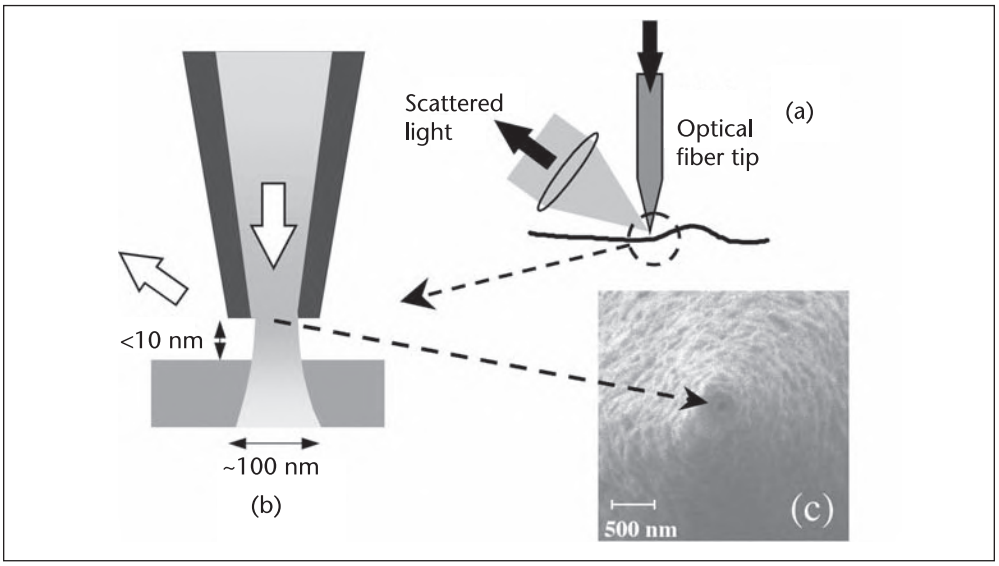

Figure 5.1 Schematic illustration of the SNOM measurements described here. (a) An optical fiber tip is raster-scanned across a sample surface, and fluorescence from the sample is collected in the far field with an objective lens. (b) Illumination is through an aperture of diameter < 100 nm defined at the end of the tip, which is held in close proximity to the sample surface. (c) End-on view of a SNOM tip. The black circle in the center is an aperture of < 100 nm diameter that has been drilled in the aluminum coating over the optical fiber tip using a focused beam of gallium ions.

5.3.2 Implementation

First, we will provide an overview of our implementation of this technique for the study of conjugated polymer systems. We have used two different optical fibers for the fabrication of the SNOM probes: a single-mode glass fiber for visible excitation (typically 365, 380, or 488 nm), and a fiber with a pure silica core and a fluorine-doped silica cladding, designed for single-mode transmission at 800 nm but able to provide high optical throughput in the near-ultraviolet (UV) (325 nm). For tips fabricated in-house, we have found that FIB processing provides the most reliable and reproducible route to the manufacture of suitable apertured SNOM probes. We have prepared these by etching the fibers in hydrofluoric (HF) acid using a self-termination process [28], then coating the entire probes with ~300 nm aluminum. Finally, ~300 nm of aluminum was FIB-sliced from the very apex of the probe, before FIB-drilling, head-on to the tip, an aperture in the tip of size 100 nm or less [29, 30]. This process produces durable probes with a well-defined aperture diameter, as illustrated in Figure 5.1(c), and a relatively high optical throughput. The ability to coat with a thick layer of aluminum precludes the occurrence of pin holes away from the aperture. However, this process does produce relatively blunt probes, limiting the topographic resolution they can attain and introducing the possibility of imaging artifacts [13, 31]. Further FIB processing can be used to sharpen the tips. We also have employed commercial probes supplied by Jasco, Inc. These gold-coated quartz probes are fabricated using a multistage etching process and offer very high light throughputs with good transmission in the UV.

The tip-surface distance was controlled with shear-force feedback, implemented by means of a quartz crystal tuning fork [32]. Images were taken by illuminating the samples in the near field through the fiber tip. The fluorescence was then collected in the far field using a microscope objective—either from the same side of the sample as the tip (see Figure 5.1) or in a "transmission" geometry for thin transparent samples involving the collection of light on the opposite side of the sample to the tip, which also allows the measurement of local absorption. Holographic notch filters or a high pass filter were used to reject light of the excitation wavelength, and the remaining fluorescence was selected with a band-pass filter. For CW measurements, light was detected using a photomultiplier or an avalanche photo diode. Alternately, it was spectrally dispersed and detected with a charge-coupled device (CCD). For time-resolved measurements, a pulsed laser was used as the excitation source (usually a frequency-doubled Ti:Sapphire mode-locked laser producing 100 fs pulses at 80 MHz). Light was then detected using a multichannel plate photomultiplier connected to a standard time-correlated single-photon counting system (TCSPC). This permitted us to record images of the temporal decay of luminescence with a temporal resolution of around 60 ps. In all measurements, topographic and optical information was recorded simultaneously; indeed, this is one of the key features that makes SNOM such a suitable technique for the characterization of conjugated polymer systems.

5.3.3 The Nature of the Near-Field Illumination

A consequence of the use of an optical probe is that, unlike other scanning probe microscopies such as STM and AFM, which are sensitive only to the first few atomic layers in the surface of a sample, SNOM can detect features below the sample surface. The decay length inside the sample of the evanescent near-field illumination from the SNOM aperture depends on the aperture diameter, the wavelength of light, and the complex refractive index of the material at that wavelength.

The form of the electric field distribution in the polymer layer may be determined in a straightforward manner by approximating the radiation emitted from a tapered metal-coated optical fiber tip to that produced by monochromatic light incident upon a subwavelength circular hole in a perfectly conducting metallic screen [33], as formulated by Bethe [34] and subsequently corrected by Bouwkamp [35]. Given the uncertainties in the nature of the SNOM probes, this simple approximation is sufficient to provide us with a useful basic description of the evanescent decay of emission from a near-field probe [36].

In Figure 5.2, we plot the integrated intensity per unit area as a function of depth below the surface of a polymer film; it is calculated using this model for illumination of 488 nm wavelength incident through an aperture of diameter 100 nm positioned 30 nm above the surface. We have considered the polyfluorene-derivative polymers poly(9,9-dioctylfluorene-co-benzothiadiazole) (F8BT) and poly(9,9-dioctylfluorene-co-bis-N,N'-(4-butylphenyl)- bis- N,N'- phenyl- 1,4-phenylenediamine) (PFB), the constituent conjugated polymers for the blends described later in this chapter that are particularly relevant to the fabrication of organic solar cells. The complex refractive indices, employed in the calculation, of the polymers at 488 nm were determined by variable angle ellipsometry [37]. Figure 5.2 presents the intensity decay for two mixtures of the polymers, representative of the different phases present in a blend film, one containing (by volume) equal parts of F8BT and PFB and the other 80% F8BT and 20% PFB [37]. It can be inferred that 90% of the absorption occurs in the top

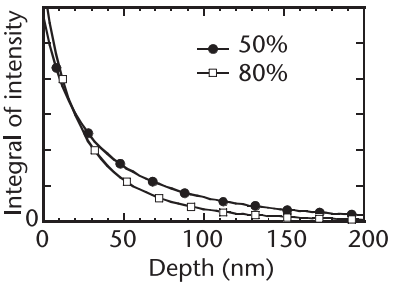

Figure 5.2 The variation, with depth below the polymer surface, of the illumination intensity integrated over the plane at that depth. Illumination at a wavelength of 488 nm is through a 100 nm diameter aperture, with the calculation performed using the Bethe-Bouwkamp model. The two curves are for different representative phases in blends of the conjugated polymers F8BT and PFB, containing 50% and 80% F8BT, respectively, by volume. ©2006 WILEY-VCH Verlag GmbH & Co. KGaA, Weinheim [27].

120 nm of the 50:50 phase and 88 nm of the 80:20 phase. At the same time, the FWHM of the electric (optical) field intensity, which characterizes the attainable resolution, increases from the aperture size of ~100 nm immediately inside the surface to ~170 nm at a depth of 100 nm.

5.4 CW and Time-Resolved Fluorescence SNOM of Polymer Blends

5.4.1 An Energy-Transfer Blend for Light Emitting Applications

An example of a fluorescence SNOM measurement of a blend suitable for application in a LED is presented in Figure 5.3. The blend is a binary system containing the green-emitting polyfluorene-based polymer F8BT in poly(9,9-dioctylfluorene), PFO, which is known to give efficiencies of up to 22 cd/A in light-emitting devices

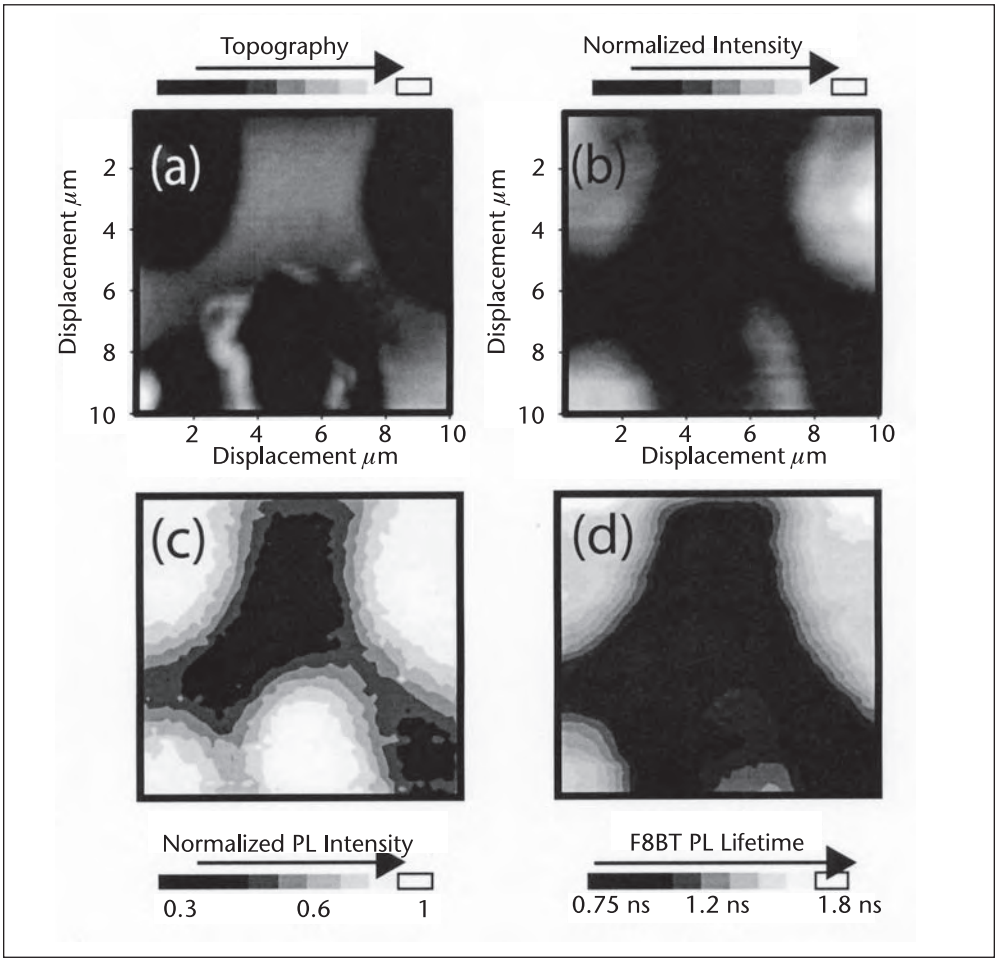

Figure 5.3 Results from a SNOM measurement of a thin polyfluorene blend film containing 50% F8BT and 50% PFO. (a) shows the surface topography, determined using the shear-force tip-height regulation mechanism. (b) shows the CW intensity of F8BT emission, determined using an APD detector. (c) shows the intensity of F8BT emission corresponding to the amplitude of the decay trace, recorded using the TCSPC detector system. (d) shows the fluorescence decay lifetime of F8BT emission recorded across the surface of the blend.

with suitable electrodes. In this system, the alignment of the highest occupied molecular orbital (HOMO) and lowest unoccupied molecular orbital (LUMO) levels is such that energy transfer of excitons from PFO to F8BT is energetically favorable. So in a blend with a high degree of intermixing between the two components for efficient energy transfer, no blue emission from the PFO should occur.

The blend studied contains 50% by weight F8BT and was prepared by spin-coating a xylene solution of the polyfluorenes onto a glass substrate. Tapping-mode AFM [38] revealed in similar films (composed of 25% F8BT by weight) a rich surface structure, suggestive of phase separation, with one phase forming circular regions 200–300 nm in diameter and protruding from the surface of the film. However, because of the lack of chemical specificity of the AFM probes, the compositions of the phases could not be identified. Phase-separated structure is evident in the shear-force topographic image presented in Figure 5.3(a), with a lower-lying phase known (on the basis of previous SNOM transmission measurements [23]) to be composed principally of PFO, which coexists within a higher-lying phase that is mainly F8BT.

The SNOM image presented in Figure 5.3(b) is of fluorescence excited at 380 nm using a pulsed laser source and then detected using a CW detector at wavelengths greater than 550 nm. At this excitation wavelength, light is principally absorbed by PFO; however, the emission detected corresponds mainly to emission from F8BT (whose emission peaks in the green at 530 nm). It can be seen that the F8BT emission is strongest from the lower-lying regions of the film, which are known to be composed predominately of PFO. This indicates that rapid energy transfer occurs from PFO to the F8BT, which is also locally present at a concentration thought to be between 5% and 10% by weight. Indeed, we estimate that in this film, more than 80% of all excitons initially created on PFO molecules undergo energy transfer via Förster transfer to F8BT. Note, however, that the strong variation in F8BT intensity between the PFO-rich phase (which emits strongly) and the higher-lying F8BT-rich phase (which emits weakly) occurs because light is only weakly absorbed by F8BT at 380 nm.

In Figures 5.3(c) and 5.3(d), we plot the fluorescence decay lifetime and emission amplitude of the F8BT emission recorded across the film, recorded using the TCSPC system. Here these images were recorded simultaneously with the images presented in Figures 5.3(a) and 5.3(b). Figure 5.3(c) shows that the decay lifetime of F8BT varies strongly across the film surface and takes its minimum value of 900 ps in the F8BT-rich phase. This lifetime increases by a factor of 1.8 times to between 1.5 and 1.8 ns in the PFO-rich phase. The observed fluorescence decay lifetime can be expressed as an effective decay rate, which is itself equal to the sum of all possible decay rates. If we assume that the radiative decay rate of F8BT is approximately the same in the PFO- and F8BT-rich phases, our measurements suggest that the density of nonradiative decay channels open to excitons on an F8BT molecule is significantly suppressed when it is located in the PFO-rich phase. We propose that this suppression of nonradiative decay results from the fact that F8BT molecules are "diluted" by the PFO matrix, which restricts intermolecular transfer to other F8BT molecules on which there might be a nonradiative defect. Note that back-transfer of excitons to PFO is energetically unfavorable due to the large difference in the energy gap of PFO and F8BT (~900 meV). Based on the fact that the photoluminescence (PL) quantum yield can be expressed using $\Phi_{F8BT} = \tau_{tot}/\tau_{rad}$ (where τ_{tot} and τ_{rad} are the observed decay lifetime and radiative decay lifetime of

F8BT, respectively), the variation in τ_{tot} suggests that Φ_{F8BT} is approximately 1.8 times greater in the PFO-rich phase than in the F8BT-rich phase.

This local variation of quantum yield can be detected in far-field measurements of the overall efficiency of PL emission recorded from the entire film. In particular, we find that the quantum yield of the blend has a maximum value of 70% at a relative F8BT concentration of 5%. At F8BT concentrations above 5%, this is reduced to an average value of 60% and only approaches the quantum yield of pure F8BT at relative F8BT concentrations greater than 60%. This suggests that when F8BT is trapped at a low concentration within PFO (less than 10%), the F8BT molecules approximate a homogeneous distribution within a PFO "matrix." This molecular distribution results in a series of isolated F8BT molecules between which exciton transfer to quenching sites is significantly limited, thus resulting in a maximum value of PL quantum yield. We note that the efficiency of an organic LED is directly dependent on the relative PL efficiency of the active emissive material within the device. Thus, our measurements suggest that maximum efficiency in PFO:F8BT LEDs will occur in devices containing a relatively low concentration of F8BT. This is indeed the case, with studies showing [39] that devices based on 5% F8BT: 95% PFO operate with optimal electroluminescence quantum efficiency.

5.4.2 A Charge-Transfer Blend for Photocells

We also have used fluorescence SNOM measurements to study the operation of conjugated-polymer blend materials used in a photovoltaic device. In such devices, excitons created after the absorption of light are rapidly dissociated by a charge transfer process between the different blend components. Time-resolved SNOM is a particularly useful technique to study such material systems, as the quenching of the exciton fluorescence is readily observable through a reduction in fluorescence decay lifetime. Thus, time-resolved SNOM can be used to directly image the local efficiency of exciton dissociation into both geminate and nongeminate polaron pairs—a key component of photovoltaic device operation.

The materials we have studied are a blend of F8BT and PFB. In these materials, the offsets between the HOMO and LUMO levels are aligned such that charge transfer of holes from the F8BT to the PFB is energetically favorable, whereas electrons remain in the F8BT. This, together with the hole-transporting properties of PFB, makes such blends particularly suitable for photovoltaic applications [17]. Figure 5.4(a) shows a topographic image of a typical phase-separated PFB:F8BT blend thin film. The film is composed of two main phases: a continuous higher-lying phase that AFM measurements have demonstrated to be predominantly F8BT-rich and a lower-lying phase that is PFB-rich. Figure 5.4(b) (recorded simultaneously with the topographic image) is a SNOM image showing the relative transmitted intensity of the laser at 440 nm. It is clear that the ratio of the transmitted light between the two phases is considerably smaller than the ratio of the attenuation coefficients of pure F8BT and PFB films at 440 nm. That results from the fact that neither of the phases is pure; instead, they are composed of an admixture of the two polymers. Indeed, quantitative X-ray mapping studies on a blend film of F8BT and a similar polyfluorene-based copolymer found that the lower-lying phase was around 90% pure [40].

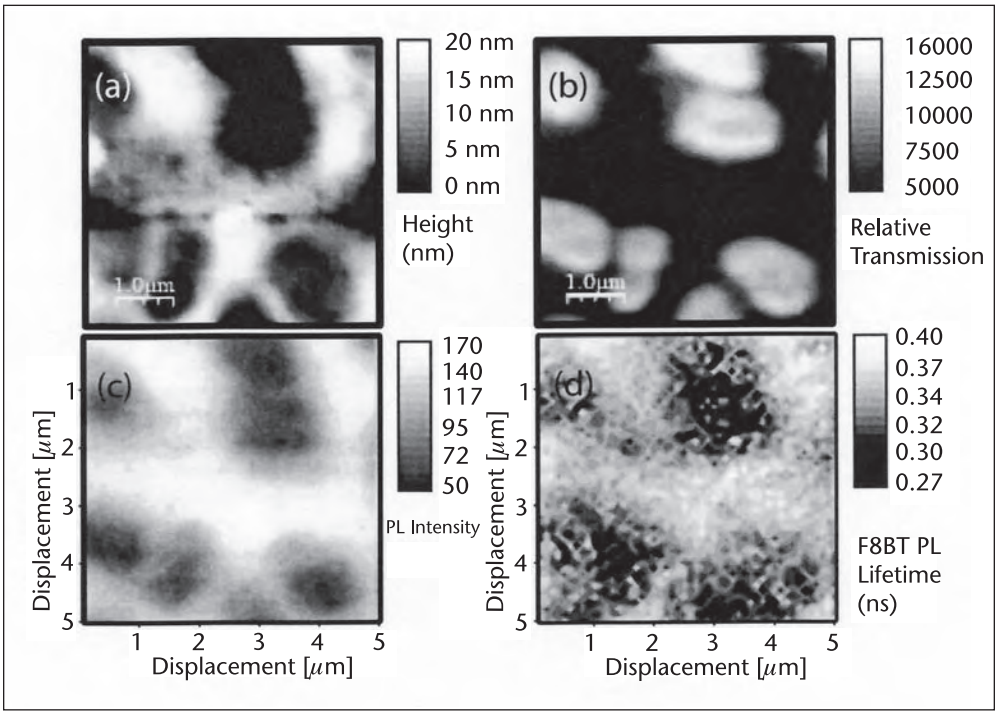

Figure 5.4 SNOM images of a conjugated polymer blend film containing 50% by weight F8BT and 50% by weight PFB. (a) shows film topography recorded using the shear-force tip-height regulation mechanism. (b) is the corresponding CW laser transmission image recorded at 440 nm to the topography image presented in (a). (c) and (d) show the amplitude and decay constant of the F8BT PL lifetime, respectively, detected at wavelengths greater than 550 nm (corresponding to F8BT emission). © 2008 American Institute of Physics [15].

We have used time-resolved SNOM to study the PL emission from the blend film at wavelengths greater than 530 nm. Figures 5.4(c) and 5.4(d) show the PL intensity and decay lifetime recorded following excitation into the F8BT component of the blend at 440 nm. It can be seen immediately that the higher-lying phase emits PL at wavelengths greater than 530 nm more strongly than does the lower-lying phase. This contrast is partially explained by the fact that the 440 nm laser light is preferentially absorbed by the higher-lying F8BT-rich phase; however, our time-resolved images suggest that the quenching efficiency of excitons on F8BT molecules in the two phases is different. Specifically, we find that the decay lifetime of F8BT in the higher-lying phase is 35% longer than that of the lower-lying phase (being 375 ps and 275 ps, respectively). The fluorescence decay lifetimes we measure are significantly shorter than that of pure F8BT films (which we measure as having a fluorescence decay lifetime of ~1.2 ns), confirming that luminescence is quenched by exciton dissociation resulting from charge transfer. We can use the PL decay lifetime maps shown in Figure 5.4(d) to estimate the PL quantum efficiency of F8BT in the F8BT-rich and PFB-rich phases. Here we assume that the intrinsic radiative decay lifetime of F8BT excitons is unchanged as a result of being mixed into a blend; however, its total decay lifetime reduces as a result of additional decay channels arising from exciton dissociation. Based on the fact that the PL quantum efficiency of the F8BT used here in a pure film is 41%, we estimate the PL quantum yield of PFB to be 13% and 9% in the F8BT-rich and PFB-rich phases, respectively.

The difference in PL quantum efficiency between the different phases indicates that exciton quenching on an F8BT molecule occurs more rapidly when the F8BT molecule is located in a PFB-rich phase. This may not be surprising, as the larger local density of PFB molecules surrounding an F8BT molecule located in a PFB-rich phase will increase the local density of molecular heterojunctions at which charge separation can occur, increasing the probability that an exciton will undergo dissociation. In contrast, an exciton sitting on an F8BT molecule that is located in an F8BT-rich phase will find less opportunity to undergo dissociation, thus resulting in a relatively greater photon yield and a longer decay lifetime. Critically, however, is the fact that the overall probability of exciton quenching in the different phases is relatively similar (to within 30%). Importantly, our measurements also suggest that the charge-generation efficiency should be relatively constant across each phase-separated domain. In the following section, we confirm this last conclusion by using SNOM to directly generate a local photocurrent across the different phases in an F8BT-PFB blend.

5.5 Photoconductivity SNOM

Given the suitability of blends of F8BT and PFB for photovoltaic applications, it also is valuable to learn more about the local properties of current generation in these systems. By using the apertured SNOM probe as a local light source, SNOM provides a means to map the photoconductivity of a polymer blend film with 100 nm resolution. Such near-field photoconductivity methods were first demonstrated by Buratto et al. [41] in the study of InGaAsP quantum-well lasers and later applied to stretch-oriented films of PPV [42].

The scheme we have employed for near-field photoconductivity microscopy is illustrated schematically in Figure 5.5. A planar thin-film device structure was used in which two electrodes formed a 150 μm gap on top of the polymer film of 200–300 nm thickness, spin-cast onto a quartz substrate. Because of the low number of charge carriers generated, we detected the current flowing through the channel between the electrodes using a lock-in detection scheme, where the exciting laser light intensity is modulated and the current is preamplified by an electrometer and recovered with a lock-in amplifier (see Figure 5.5). For these experiments, a potential difference of 400 V was applied across the electrodes, resulting in a field of ca. 12 kV cm^{-1} in the center between the electrodes, as determined from calculations of the electric-field distribution for the device. This low field strength is sufficient for photoconductivity measurements of conjugated-polymer blend systems. The external field is not required to split the excitons into a pair of uncorrelated charge carriers, which requires ca. 100 kV cm^{-1} [43, 44], but only to enable charge carriers to drift toward the electrodes, as the exciton dissociation is enabled by the polymer–polymer interface.

Near-field photocurrent microscopy allows the simultaneous measurement of topography, luminescence, and photocurrent. For measurements of a F8BT/PFB blend (see Section 5.4.2), we found that regions of a high luminescence count also coincide with areas of high photocurrent [27]. However, we should note that the interpretation of the near-field photocurrent images is more complicated than that of the fluorescence images because the electric field between the electrodes—and thus the near-field photoconductivity signal—may now be influenced significantly

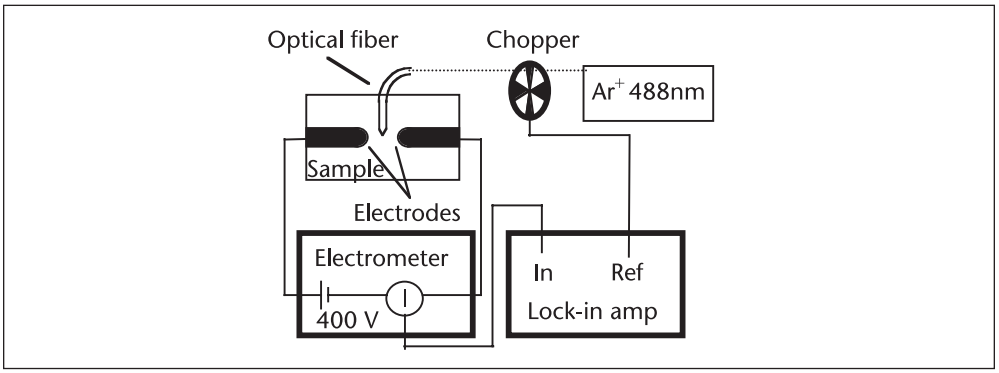

Figure 5.5 Schematic illustration of the experimental arrangement for scanning near-field photocurrent microscopy. The photocurrent response is measured by lock-in detection using a chopped laser beam. The sample is biased using the voltage source of an electrometer, which also performs a current-to-voltage conversion. ©2006 WILEY-VCH Verlag GmbH & Co. KGaA, Weinheim [27].

by the screening effect of the metallized fiber tip [42]. Indeed, a finite-element analysis of the distribution of the electric field distribution for the combined system (of device and SNOM probe) indicated a reduction of the applied DC electric field directly under the aperture to about half that with no tip present. Conversely, the field strength at the edges of the probe is enhanced. The effect of this tip screening diminishes with depth from the surface.

Significantly, we found in our measurements that the photocurrent is essentially constant within the individual blend phases and does not show an enhancement at their boundaries, as might be expected if these were the principal sites for interface-induced exciton dissociation. Indeed, it appears that the photocurrent generation efficiency is constant throughout the film, with near-field photocurrent contrast resulting only from changes in absorption efficiency. This is consistent with the phase separation process leading to domains richer in one of the components, rather than to pure domains, and to multiscale phase separation, as discussed in Section 5.4, with the micrometer-scale phase separation present in the blend not being the determining factor for photocurrent efficiency. However, although it may reasonably be inferred that the photocurrent efficiency is determined by the "nanoscopic" structuring of the polymer–polymer interfaces, the resolution afforded by our probes (100–150 nm) is not yet sufficient to resolve such fine phase separation in luminescence or photocurrent maps.

5.6 Near-Field Photolithography

SNOM also offers a route for patterning conjugated polymer nanostructures. The aim of patterning is, in general, the fabrication of well-defined features of the polymer films with minimum damage, with the resolution required for a specific application. To address the need for patterned polymer films, a number of techniques have been proposed in recent years for conjugated polymers (see, for example, Holdcroft [45] and references therein), including site-selective chemical vapor deposition on patterned precursors [46], micromolding in capillaries, screen or ink-jet printing, and holographic lithography [47]. Attempts to pattern conjugated polymers on submicron scales by scanning probe methods have relied on selectively

damaging exposed areas of the polymer, for example, with a STM [48] or with SNOM to induce local oxidation of soluble conjugated polymers [49, 50].

We will describe here an alternative scanning near-field optical lithographic (SNOL) approach based on the partial elimination of the labile groups in a soluble precursor [51] by exposure to a UV field and the subsequent removal of the unexposed material by dissolution in the precursor solvent [52], which has been employed successfully for the fabrication of PPV nanostructures with 160 nm feature sizes [16]. This patterning process is "direct" in the sense that it does not require a sacrificial photoresist and leads to polymer features surrounded by empty regions on the substrate. The precursor polymer in this process can be compared to a negative resist in classical optical lithography.

Thin films of the PPV "leaving-group" soluble precursor [51] poly(*p*-phenylene [1-(tetrahydrothiophen-1-io)ethylene chloride]) were spin-coated from a methanol solution on glass or silica substrates that were then exposed with UV illumination (325 nm) from an apertured SNOM probe. A shutter with a minimum exposure time of 6.5 ms was used to block the laser entering the SNOM optical fiber, allowing definition of arbitrary patterns as the tip was scanned over the sample. After this UV writing process, the nonexposed material was washed off in methanol and the patterned precursor was converted into the fully conjugated PPV by heating it at 220° C for 5 hours at less than 10^{-5} mbar. The PL efficiency of such PPV materials was found to be 25±3%, comparing well with the efficiency of less than 30% for nonpatterned PPV [53].

Tapping-mode AFM images of a two-dimensional periodic PPV structure with a 333 nm lattice constant patterned by SNOL and converted from the precursor are presented in Figure 5.6. During the conversion process, the height of the pattern was reduced from 45 nm to 32 nm, while the FWHMs of individual pillars shrunk to 200 nm. In the center of the pattern [Figure 5.6(a)], one column is missing intentionally to create a defect in the periodic structure, demonstrating the potential of this technique for the creation of arbitrary structures.

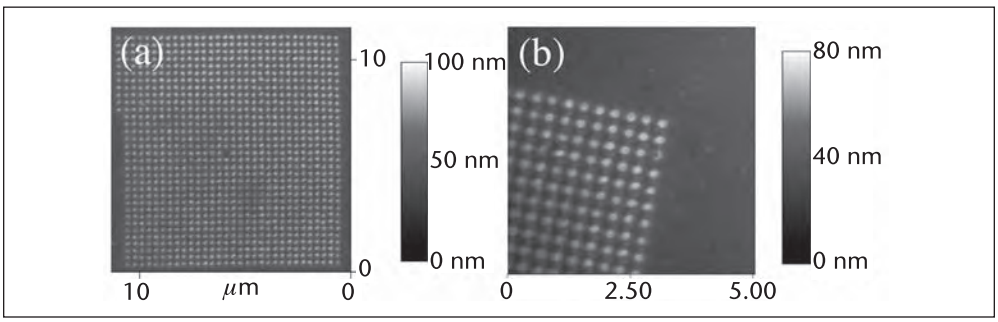

Figure 5.6 (a)Tapping-mode AFM image of a two-dimensional photonic structure with a 333 nm square lattice after thermal conversion. One pillar in the middle has been intentionally omitted to demonstrate that versatile structures can be fabricated. The pattern was written with the 325 nm line of a HeCd laser, and the power coupled into the fiber probe was less than 0.2 mW. (b) AFM image of a corner of the structure in (a). ©2003 American Institute of Physics [16].

5.7 Conclusions and Future Developments

Based on apertured probes, SNOM has been shown to be a valuable tool for the investigation of nanostructured thin films of conjugated polymer blends, providing access to the fluorescence and photoconductivity properties of these systems on 100 nm length scales—of the same order as those of the typical primary phase separation of these materials. Near-field fluorescence microscopy, in particular, is able to provide a chemical map of a blend through the spectroscopic contrast it affords, while the topographic information, obtained simultaneously with the optical data in any measurement, allows an easy comparison with the higher-resolution and more routine technique of atomic force microscopy. A SNOM probe also offers a promising route for the lateral patterning of conjugated polymer nanostructures, providing low damage and versatile processing.

Nevertheless, the 50–100 nm resolution limit provided by apertured probes still is not sufficient to probe these materials at the length scales of exciton diffusion (~ 10 nm), provide imaging at the molecular level (~1 nm), or define nanostructures with dimensions of ~10 nm or less. For those, we need to turn to some of the promising new "apertureless" nano-optics techniques discussed in the last section of this book. The development of such techniques should enable a detailed chemical analysis of the nanoscale phase separation in conjugated polymer blends, particularly through nano-Raman or infrared microscopy, and probe the photophysics of these systems on the length scales relevant to exciton diffusion and energy transfer.

Acknowledgments

The authors would like to acknowledge and thank R. Stevenson, R. G. Milner, R. Riehn, J. Chappell, and A. Cadby, who contributed to the work presented in this article, and thank the UK Engineering and Physical Sciences Research Council and Royal Society for financial support.

References

[1] Friend, R. H. et al., "Electroluminescence in Conjugated Polymers," *Nature*, Vol. 397, 1999, pp. 121–127.

[2] Cacialli, F., "Organic Semiconductors for the New Millennium," *Phil. Trans. R. Soc. Lond. A*, Vol. 358, 2000. pp. 173–192.

[3] Berggren, M. et al., "Light-Emitting-Diodes with Variable Colors from Polymer Blends," *Nature*, Vol. 372, 1994, pp. 444–446.

[4] Halls, J. J. M. et al., "Efficient Photodiodes from Interpenetrating Polymer Networks," *Nature*, Vol. 376, 1995, pp. 498–500.

[5] Kim, C., P. E. Burrows, and S. R. Forrest, "Micropatterning of Organic Electronic Devices by Cold-Welding," *Science,* Vol. 288, 2000, pp. 831–833.

[6] Garnier, F. et al., "All-Polymer Field-Effect Transistor Realized by Printing Techniques," *Science*, Vol. 265, 1994, pp. 1684–1686.

[7] Sirringhaus, H. et al., "High-Resolution Inkjet Printing of All-Polymer Transistor Circuits," *Science*, Vol. 290, 2000, pp. 2123–2126.

[8] Rogers, J. A., M. Meier, and A. Dodabalapur, "Using Printing and Molding Techniques to Produce Distributed Feedback and Bragg Reflector Resonators for Plastic Lasers," *Appl. Phys. Lett.*, Vol. 73, 1998, pp. 1766–1768.

[9] Riechel, S. et al. "A Nearly Diffraction Limited Surface Emitting Conjugated Polymer Laser Utilizing a Two-Dimensional Photonic Band Structure," *Appl. Phys. Lett.*, Vol. 77, 2000, pp. 2310–2312.

[10] Adawi, A.M. et al., "Spontaneous Emission Enhancement in Micropillar Cavities Containing a Fluorescent Molecular Dye," *Advanced Materials*, Vol. 18, 2006, pp. 742–747.

[11] Stevenson, R., M. Granström, and D. Richards, "Fluorescence Scanning Near-Field Optical Microscopy of Conjugated Polymer Blends," *Appl. Phys. Lett.*, Vol. 75, 1999, pp. 1574–1576.

[12] Stevenson, R. et al., "Fluorescence Scanning Near-Field Optical Microscopy of Polyfluorene Composite," *J. Microscopy*, Vol. 202, 2001, pp. 433–438.

[13] Stevenson, R. et al., "Ultraviolet-Visible Near-Field Microscopy of Phase-Separated Blends of Polyfluorene-Based Conjugated Semiconductors," *Appl. Phys. Lett.*, Vol. 79, 2001, pp. 833–835.

[14] Cadby, A. et al., "Imaging the Fluorescence Decay Lifetime of a Conjugated Polymer Blend by Using a Scanning Near-Field Optical Microscope," *Advanced Materials*, Vol. 19, 2007, pp. 107–111.

[15] Cadby, A. et al., "Mapping Exciton Quenching in Photovoltaic-Applicable Polymer-Blends Using Time-Resolved Scanning Near-Field Optical Microscopy," *Journal of Applied Physics*, Vol. 103, 2008, 093715.

[16] Riehn, R. et al., "Near-Field Optical Lithography of a Conjugated Polymer," *Appl. Phys. Lett.*, Vol. 82, 2003, pp. 526–528.

[17] Halls, J. J. M. et al., "Photodiodes Based on Polyfluorene Composites: Influence of Morphology," *Advanced Materials.*, Vol. 12, 2000, pp. 498–502.

[18] Arias, A. C. et al., "Microscale to Nanoscale Morphology Control of Polyfluorene Blends: A Combined Microscopic and Photovoltaic Investigation," *Macromolecule*, Vol. 34, 2001, pp. 6005–6013.

[19] Yu, G., and A. J. Heeger, "Charge Separation and Photovoltaic Conversion in Polymer Composites with Internal Donor-Acceptor Heterojunctions," *J. Appl.* Phys., Vol. 78, 1995, pp. 4510–4515.

[20] Bernius, M. T. et al., "Progress with Light-Emitting Polymers," *Advanced Materials.*, Vol. 12, 2000, pp. 1737–1750.

[21] Blatchford, J. W. et al., "Spatially and Temporarilly Resolved Emission from Aggregates in Conjugated Polymers," *Phys. Rev. B*, Vol. 54, 1996, pp. R3683–R3686.

[22] Webster, S. et al., "Application of Fluorescence Scanning Near-Field Optical Microscopy to the Study of Phase-Separated Conjugated Polymers," *Ultramicroscopy*, Vol. 71, 1998, pp. 275–279.

[23] Chappell, J. et al., "Correlating Structure with Fluorescence Emission in Phase-Separated Conjugated Polymer Blends," *Nature Materials*, Vol. 2, 2005, pp. 616–621.

[24] Cadby, A. et al., "Mapping the Fluorescence Decay Lifetime of a Conjugated Polymer in a Phase-Separated Blend Using a Scanning Near Field Optical Microscope," *Nano Letters*, Vol. 5, 2005, pp. 2232–2237.

[25] Milner, R. G. et al., "Phase Separation in Polyfluorene Blends Investigated with Complementary Scanning Probe Microscopies," *Mat. Sci. Technol.*, Vol. 18, 2002, pp. 759–762.

[26] Cadby, A. et al., "Suppression of Energy-Transfer between Conjugated Polymers in a Ternary Blend Identified Using Scanning Near-Field Optical Microscopy," *Advanced Materials*, Vol. 18, 2006, pp. 2713–2719.

[27] Riehn, R. et al., "Local Probing of Photocurrent and Photoluminescence in a Phase-Separated Conjugated-Polymer Blend by Means of Near-Field Excitation," *Advanced Functional Materials*, Vol. 16, 2006, pp. 469–476.

[28] Zeisel, D. et al., "Pulsed Laser-Induced Desorption and Optical Imaging on a Nanometer Scale with Scanning Near-Field Microscopy Using Chemically Etched Fiber Tips," *Appl. Phys. Lett.*, Vol. 68, 1996, pp. 2491–2493.

[29] Veerman, J. A. et al., "High Definition Aperture Probes for Near-Field Optical Microscopy Fabricated by Focused Ion Beam Milling," *Appl. Phys. Lett.*, Vol. 72, 1998, pp. 3115–3117.

[30] Muranishi, M. et al., "Control of the Aperture Size of Optical Probes for Scanning Near-Field Optical Microscopy Using Focused Ion Beam Technology," *Jpn. J. Appl. Phys.*, Vol. 36, 1997, pp. L942–L945.

[31] Hecht, B. et al., "Facts and Artifacts in Near-Field Optical Microscopy," *J.Appl. Phys.*, Vol. 81, 1997, pp. 2492–2498.

[32] Karrai, K., and R. D. Grober, "Piezoelectric Tip-Sample Distance Control for Near-Field Optical Microscopes," *Appl. Phys. Lett.*, Vol. 66, 1995, pp. 1842–1844.

[33] Stevenson, R., and D. Richards, "The Use of a Near-Field Probe for the Study of Semiconductor Heterostructures," *Semicond. Sci. and Technol.*, Vol. 13, 1998, pp. 882–886.

[34] Bethe, H. A., "Theory of Diffraction by Small Holes," *Phys. Rev.*, Vol. 66, 1944, pp. 163–182.

[35] Bouwkamp, C. J., "Diffraction Theory," *Rep. Phys.*, Vol. 27, 1954, pp. 35–101.

[36] Obermüller, C. et al., "Transmitted Radiation through a Subwavelength-Sized Tapered Optical-Fiber Tip," *Ultramicroscopy*, Vol. 61, 1995, pp. 171–177.

[37] Stevenson, R. et al., "Raman Microscopy Determination of Phase Composition in Polyfluorene Composites," *Appl. Phys. Lett.*, Vol. 79, 2001, pp. 2178–2180.

[38] Morgado, J. et al., "De-mixing of Polyfluorene Based Blends by Contact with Acetone: Electro- and Photo-Luminescence Probes," *Advanced Materials*, Vol. 13, 2001, pp. 810–814.

[39] Voigt, M. et al., "The Interplay between the Optical and Electronic Properties of Light-Emitting-Diode Applicable Conjugated Polymer Blends and Their Phase-Separated Morphology," *Organic Electronics*, Vol. 6, 2006, pp. 35–45.

[40] McNeill, C. R. et al., "Nanoscale Quantitative Chemical Mapping of Conjugated Polymer Blends," *Nano Letters*, Vol. 6, 2006, pp. 1202–1206.

[41] Buratto, S. K. et al., "Near-Field Photoconductivity—Application to Carrier Transport in InGaAsP Quantum-Well Lasers," *Appl. Phys. Lett.*, Vol. 65, 1994, pp. 2654–2656.

[42] De Aro, J. A., D. Moses, and S. K. Buratto, "Near-Field Photoconductivity of Stretch-Oriented Poly(para-phenylene vinylene), *App. Phys. Lett.*, Vol. 75, 1999, pp. 3814–3816.

[43] Deussen, M., M. Scheidler, and H. Bassler, "Electric-Field-Induced Photoluminescence Quenching in Thin-Film Light-Emitting-Diodes Based on Poly(phenyl-p-phenylene vinylene)," *Synthetic Metals*, Vol. 73, 1995, pp. 123–129.

[44] Vissenberg, M., and M. J. M. de Jong, "Theory of Exciton Migration and Field-Induced Dissociation in Conjugated Polymers," *Phys. Rev. Lett.*, Vol. 77, 1996, pp. 4820–4823.

[45] Holdcroft, S., "Patterning Pi-Conjugated Polymers," *Advanced Materials*, Vol. 13, 2001, pp. 1753–1765.

[46] Cacialli, F., and P. Bruschi, "Site-Selective Chemical-Vapor-Deposition of Submicron-Wide Conducting Polypyrrole Films—Morphological Investigations with the Scanning Electron and the Atomic-Force Microscope," *J. Appl. Phys.*, Vol. 80, 1996, pp. 70–75.

[47] Gigli, G. et al., "Holographic Nanopatterning of the Organic Semiconductor Poly (p-phenylene vinylene," *Appl. Phys. Lett.*, Vol. 73, 1998, pp. 3926–3928.

[48] Granström, M., "Micropatterned Luminescent Polymer Films," *Acta Polymerica*, Vol. 49, 1998, pp. 514–517.

[49] Wei, P. K. et al., "Surface Modification and Patterning of Conjugated Polymers with Near-Field Optical Microscopy," *Advanced Materials*, Vol. 8, 1996, pp. 573–575.

[50] De Aro, J. A. et al., "Nanoscale Oxidative Patterning and Manipulation of Conjugated Polymer Thin Films," *Synthetic Metals*, Vol. 102, 1999, pp. 865–868.

[51] Burroughes, J. H. et al., "Light-Emitting-Diodes Based on Conjugated Polymers," *Nature*, Vol. 347, 1990, pp. 539–541.

[52] Schmid, W. et al., "Photolithography with Poly-(p-phenylene vinylene) (PPV) Prepared by the Precursor Route," *Acta Polymerica*, Vol. 44, 1993, pp. 208–210.

[53] Morgado, J. et al., "Luminescence Properties of Poly(p-phenylene vinylene): Role of the Conversion Temperature on the Photoluminescence and Electroluminescence Efficiency," *J. Appl. Phys.*, Vol. 85, 1999, pp.1784–1791.

PART II

Nanophotonics

Introduction

Nanophotonics deals with the generation, guiding, manipulation, and conditioning of light in subwavelength scale devices. This is an important area with significant impact on telecommunications, information processing, the environment, and healthcare [1, 2]. Its main promise is in high-density, large-scale photonic integration, in analogy to electronic integrated chips, for applications in optical information processing, and for bio- and chemosensing. This includes purely photonic chips as well as hybrid electronic-photonic integrated circuitry where signals between the electronic components are transmitted in the form of photons. The recent progress in nanophotonics relies on our ability to fabricate subwavelength-size structures with sufficient precision and optical quality as well as on optical characterization tools capable of the required spatial resolution to monitor light behavior on subwavelength scales.

In addition to plasmonics, which is presented in Part III, one of the promising approaches in the development of nanophotonic applications is based on photonic crystals, artificial structures with periodic modulation of the refractive index, allowing the control of dispersion and propagation of light [3]. The best-known effects include transmission or rejection of light in a given wavelength range and waveguiding of light along straight and bent defects of a periodic photonic crystal structure. Due to difficulties in fabrication of three-dimensional photonic structures in the optical spectral range, two-dimensional photonic crystals are often considered. The utilization of photonic band-gap structures has already led to remarkable breakthroughs in optical integration, providing efficient interconnection between elements of photonic circuits and a relatively well-developed element base of passive components such as filters, waveguides, and nanocavities.

The application of scanning near-field microscopy for the monitoring and investigation of light propagation in photonic crystals are presented in the following two chapters. Volkov and colleagues consider the characterization of silicon-on-insulator photonic-crystal-waveguide (PhCW) structures at telecommunication wavelengths with a collection scanning near-field optical microscope. High-contrast and high-resolution SNOM images have allowed the visualization of Bloch harmonics of the PhCW; the precise determination of PhCW mode characteristics, including the dispersion of the propagation constant and bend loss; and the characterization of PhCW directional couplers. The capabilities and limitations of SNOM imaging for the characterization of PhCW structures also are discussed.

Chapter 7 is concerned with the SNOM imaging of temporal evolution of optical signal in photonic crystal structures. It describes how the dynamics of light propagation on a femtosecond time scale can be visualized with a near-field microscope; to that end, the near-field microscope has to be integrated in an interferometer. After discussion of the design considerations of such an interferometric near-field microscope, the measurements of the propagation of optical pulses through a photonic structure are presented. Time-resolved near-field experiments allow recovering of the phase and group velocity and show the significant influence of group velocity and higher-order dispersions on the pulse propagation in PhCW.

References

[1] Prasad, P., *Nanophotonics,* New York: John Wiley, 2004.
[2] Zheludev, N. I., M. Stockman, and A. V. Zayats (eds.), "Fundamental Aspects of Nanophotonics," *J. Opt. A: Pure Appl. Opt.*, Vol. 8, 2006, pp. S1–S295.
[3] Joannopoulos, J. D., S. G. Johnson, J. N. Winn, and R. D. Meade, *Photonic Crystals: Molding the Flow of Light*, Princeton: Princeton University Press, 2008.

CHAPTER 6

Near-Field Characterization of Planar Photonic-Crystal-Waveguide Structures

Valentyn S. Volkov and Sergey I. Bozhevolnyi

6.1 Introduction

Nanostructured media with sufficiently strong periodic modulation of the refractive index may exhibit, within a certain wavelength range, light reflection and inhibition of light propagation and are conventionally called photonic crystals (PhCs) [1, 2]. From the point of view of solid-state physics, the periodicity in a dielectric constant results in the photonic band gap (PBG) just like the periodicity in an electrostatic potential gives rise to the forbidden electronic energy band gap. Using the language of physical optics, the PBG effect in two and three dimensions can be viewed as an extension of Bragg reflection in one direction (e.g., occurring in lasers with distributed feedback), where it leads to a so-called stop gap, to Bragg diffraction of waves propagating in any direction. The PBG effect opens a way to control the flow of light on a wavelength scale by introducing various (e.g., line and point) defects in PhCs, thereby forming waveguides and cavities [2, 3]. Two-dimensional (2-D) PhCs combined with the structures exhibiting light confinement in the third dimension (e.g., planar slab wave guides) have been intensively investigated during the past few years with the purpose of realizing highly integrated photonic circuits [3–5]. Various configurations of photonic crystal waveguides (PhCWs) formed by line defects in 2-D PhCs have been experimentally studied, and many important issues have been clarified [5]. In this context, accurate and reliable characterization of PhCWs and the corresponding optical phenomena become of prime importance. It should be noted though that most of the characterization methods used until recently were of *indirect* nature. This has limited the amount of accessible information and may even have compromised the validity of the conclusions reached. Visualization of light propagation by imaging the PhCW surface with a camera [6] was one of the first characterization techniques used to investigate light propagation along PhCWs. This method relies on the presence of (accidental) surface defects that can scatter the radiation guided along a PhCW out of the surface plane toward the camera or is limited to imaging leaky modes above the so-called light line, resulting in a visible track along the PhCW whose average visibility is (roughly) proportional to the PhCW mode power. Light scattering out of the surface plane also has been facilitated with engineered defects—for example, with a trench etched close to the output of PhCW structures [7]. This technique seems to

be more reliable than the first one since the scattering efficiency is better controlled. Yet another approach to visualization of light propagation was based on intentional coupling to leaky modes that radiated from the PhCW top surface [8]. Imaging of the PhCW output edge with a camera [8] or a tapered fiber [9] was employed mainly to confirm that the light did go through a bent PhCW in question. The above-mentioned techniques have been of great help during early PhCW investigations but are qualitative by their nature and, thus, only of limited use. However, for high-quality PhCW structures, one can significantly improve the first method by detecting the light scattered by *air holes* of the PhCW structure, an approach that was recently shown to provide accurate loss characterization [10].

Quantitative input–output measurements of the power of light being transmitted by a sample containing a PhCW structure are not without problems either because the power level is determined not only by the PhCW transmission but also (and often mainly) by coupling light in and out of the sample and in and out of the PhCW structures. Relative measurements of the transmission spectra with and without a PhCW [11, 12] (or with and without a bend [13]) with subsequent normalization were considered generally to be reliable for loss measurements by calibrating away the aforementioned extrinsic effects. However, the transmission efficiency found in this way may exceed 100% [11–13], indicating that accurate characterization of low-loss PhCWs with this technique is somewhat problematic. Alternatively, one can make use of the Fabry-Perot resonance technique that was successfully applied for quantitative measurements of the propagation loss in straight PhCWs [14] and the modal reflection in bent PhCWs [15]. The Fabry-Perot interference method also was used to characterize the loss contributions of several consecutive waveguide elements [16] as well as to reveal extraordinarily large group velocity dispersion [17]. The latter was recently observed in time-domain experiments utilizing picosecond light pulses and autocorrelation detection [18]. As far as PhCW modal characteristics are concerned, conventional (far-field) imaging of the PhCW surface has been found suitable for mapping the dispersion diagram of the *leaky* (and thereby lossy) PhCW modes revealing Bloch wave components in the excited PhCW modes [19]. On the other hand, it is clear that a bound PhCW mode, which, for a given optical frequency, has a propagation constant larger than that in air (i.e., it is below the light line), *cannot* be observed with far-field imaging techniques because its field in air is *evanescent*. Its amplitude decays exponentially over a distance of the order of light wavelength. One way of accessing bound PhCW modes is to employ the evanescent field coupling between a tapered optical fiber and a PhCW [20].

Mapping of evanescent fields is one of the main applications of collection scanning near-field optical microscope (SNOM), whose fiber probe is used to pick up a tiny fraction of optical (e.g., evanescent) field near the sample surface and detect it as a function of scanning coordinates. Since the first demonstration of SNOM imaging of evanescent fields of waveguide modes [21], the SNOM has been used in a number of studies concerned with waveguide modes in integrated optical components [22, 23], including waveguide characterization at telecommunication wavelengths [24, 25]. Moreover, using heterodyne detection phase-sensitive SNOM [24, 25] in combination with the use of ultrafast pulses, the propagation of femtosecond laser pulses inside waveguides has been visualized and tracked (in both time and space), allowing for direct measurements of the

group and phase velocities [26]. Along with the progress in SNOM instrumentation, the understanding of image formation in the collection SNOM has been significantly improved. A naïve point of view that SNOM images represent maps of the electric (near-) field intensity has evolved into a more complicated picture based on the properly described image formation in the collection SNOM [27–29].

The use of SNOM techniques for investigations of complicated scattering phenomena occurring in PBG structures first started with studies of optical transmission through 2-D PhCs and the corresponding intensity distributions [30–32]. The SNOM imaging also has been applied to near-field probing of various PhC resonant structures [33–37] and the phenomenon of highly directional emission from subwavelength PhCWs [38]. As far as radiation guiding along PhCWs (by far a more complicated phenomenon than guiding along conventional photonic waveguides) is concerned, the potential of SNOM imaging to characterize PhCW modes has been explored only recently—first, with time-independent intensity measurements [39–42] and lately, with phase-sensitive and time-resolved visualization of pulse propagation [43–47].

Further material presented here is based on the results obtained at telecom wavelengths with the *amplitude* detection SNOM configuration. The chapter is organized as follows: in Section 6.2, the samples investigated and the experimental arrangement are described. A qualitative description of image formation in the collection SNOM is considered in Section 6.3 for the special case of SNOM imaging of PhCWs. Section 6.4 is devoted to the experimental results featuring the SNOM images of straight and bent PhCWs and their interpretation. Finally, we offer our conclusions in Section 6.5.

6.2 Sample Fabrication and SNOM Experimental Setup

All investigated samples were fabricated on silicon-on-insulator (SOI) wafers consisting of a perforated $SiO_2/Si/SiO_2$ trilayer film (cladding/core/buffer thickness c 0.1/0.3/1 μm) formed on a Si substrate [48]. Holes were arranged in triangular periodic arrays with different parameters, and single rows of missing holes defined the PhCWs along ΓK direction of the irreducible Brillouin zone of the lattice [2]. Electron-beam lithography was employed in the fabrication of these samples to produce hole patterns in a resist layer deposited on an SOI wafer. The patterned resist served as a mask in the process of reactive ion etching (RIE), resulting in the corresponding pattern of holes formed in the Si layer. After removal of the resist, the pattern was further transferred onto the SiO_2 layer by RIE, using the patterned Si layer as a mask. Finally, samples were thermally oxidized in order to grow a thin SiO_2 layer on top of the Si layer and on the inner walls of the air holes because the silica top cladding increases the vertical symmetry of the structures and smoothens out surface roughness of the structures [48]. Five different PhCW structures were fabricated and investigated: samples N1 and N2 having the same period of 428 nm but different hole diameters (namely, 325 and 350 nm correspondingly [49]) and sample N3 having the period $\Lambda \cong 410$ nm, hole diameter $\cong 200$ nm, and depth ~ 500 nm [39–41]. Samples N4 and N5 were similar to sample N1 having the same period $\Lambda \cong 428$ nm but different hole diameters: $\cong 200$ nm for sample N4 and $\cong 325$ nm for sample N5 [41, 50]. All samples contained a central PhC area

consisting of several PhC regions forming straight (samples N1 and N2) and bent (samples N3, N4, and N5) PhCWs of different lengths connected to tapered access ridge waveguides outside the PhC area (see Figure 6.1). Ridge waveguides, gradually tapered from a width of ~ 4 μm at the sample facet to ~ 1 μm at the PhC interface, were used to route the light into and out of the PhCWs. The design of PhCW structures was different for various samples. Thus, samples N1 and N2 contained straight PhCW regions of different lengths connected to tapered access ridge waveguides as shown in Figure 6.1(a). The PhC area for sample N3 consisted of five bent PhCWs of different lengths. Each waveguide had two straight sections connected by a 90° bend obtained by an adiabatic rotation (with the curvature radius of 7 μm) of the crystal lattice. Sample N4 contained double 60° bends (separated by 20Λ) sharp and smoothed by moving one or three holes from one side of the bend to the other one [Figure 6.1(c–e)] in a way similar to that used by Talneau et al. [15]. Finally, sample N5 contained PhCWs forming the PhCW directional coupler. Figure 6.1(f) shows a scanning electron micrograph

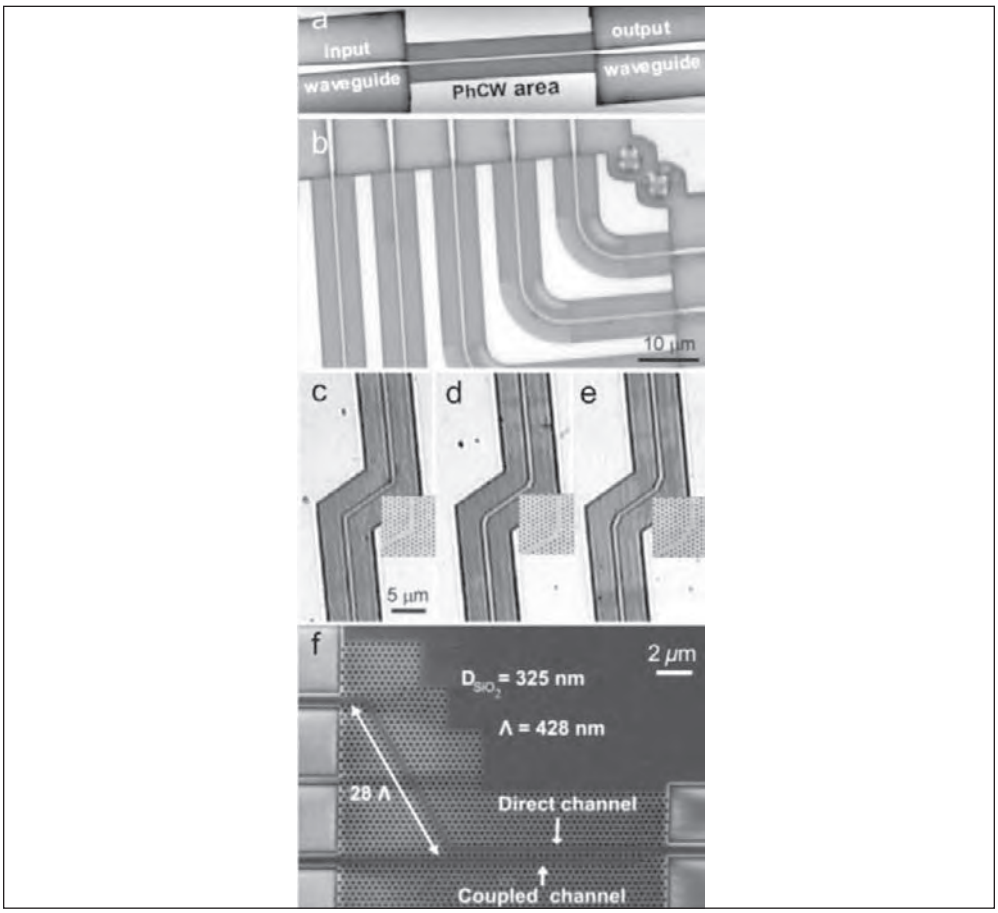

Figure 6.1 Optical microscope images showing top views of (a) the central part of sample N1, which contains straight PhCWs; (b) the central part of sample N3, which contains bent PhC waveguides; and double 60° (c) sharp and (d, e) smoothed bends of sample N4 with (d) one and (e) three holes being moved from one side of the corner to the other one. Insets show the scanning electron micrographs (SEMs) of the fabricated bends. (f) SEM of the directional coupler based on PhCs (sample N5).

(SEM) of the fabricated waveguide structure. The coupler has a coupling region with two PhCWs placed next to each other and separated by a single row of holes. The length of the region was 27Λ. Coupling of light is expected to take place from the "direct" channel to the "coupled" one. The longer intermediate PhCW in the fabricated coupler is needed to avoid coupling between two output ridge waveguides.

The experimental setup consisted of a collection SNOM with an uncoated fiber tip used as a probe and an arrangement for launching tunable (1500–1630 nm) TE/TM polarized (the electric field is perpendicular/parallel to the sample surface) radiation into the input ridge waveguide by positioning a tapered lensed polarization-maintaining single-mode fiber. The adjustment of the incoupling fiber [Figure 6.2(b)] with respect to the sample facet was accomplished when the light propagation along the sample surface was monitored with the help of a far-field microscopic arrangement [40]. These observations indicated the presence of propagation and bend loss visualized by scattered out-of-plane radiation field components. Following the fiber adjustment, the field distribution near the sample surface was probed with an

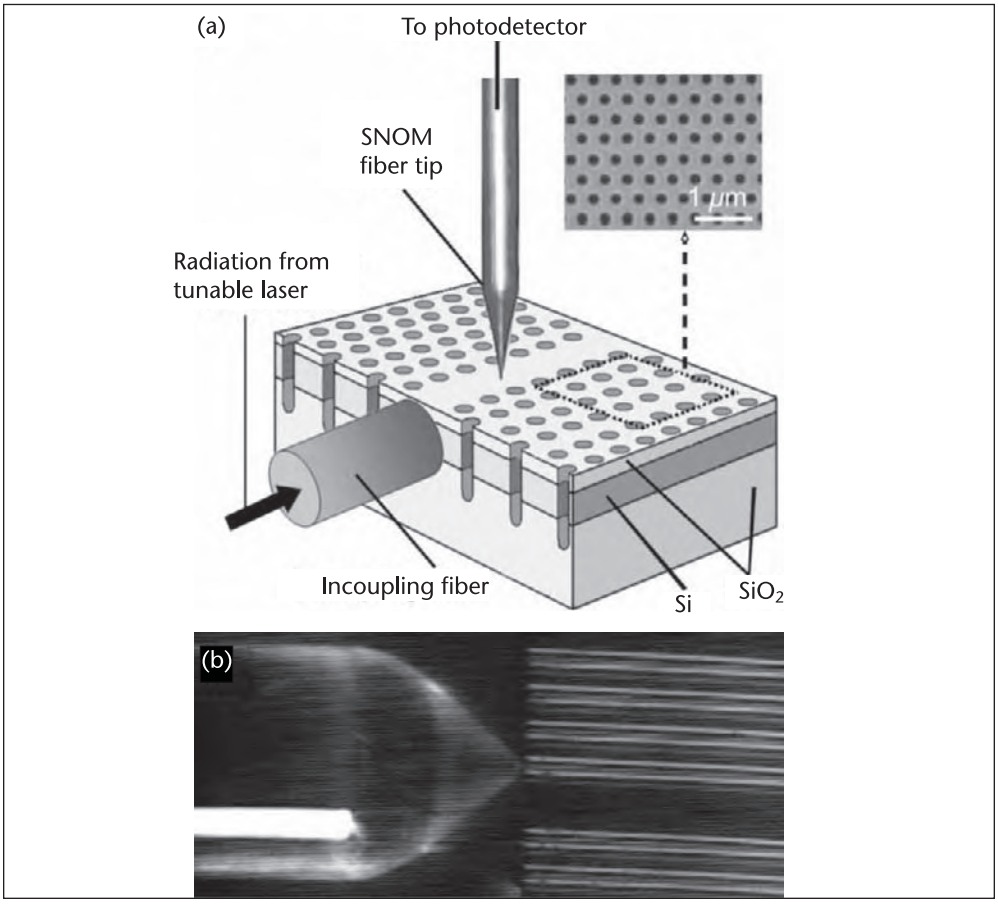

Figure 6.2 (a) Schematic layout of the experimental setup. (b) Optical microscope image showing a top view of the tapered incoupling fiber positioned against the access ridge waveguide.

uncoated sharp fiber tip of the SNOM apparatus [Figure 6.2(a)]. The tip was scanned along the sample surface at a constant distance of a few nanometers maintained by shear-force feedback. The near-field radiation scattered by the fiber tip was partially collected by the fiber itself and propagated in the form of the fiber modes toward the other end of the fiber, where it was detected by an InGaAs photoreceiver with the sensitivity of the order of femtowatts.

6.3 Near-Field Imaging of PhCWs: Qualitative Considerations

Typical topographical and near-field optical SNOM images obtained for the PhCW (sample N1) also featuring the access ridge waveguides are shown in Figure 6.3 [49]. On the topographical image [Figure 6.3(a)], one can easily recognize the PBG structure, but the pattern of holes that forms the PhCW followed by the input and output ridge waveguides is not clearly distinguishable, most probably because the scanning parameters were not optimized with respect to the topographical imaging. The near-field optical image [Figure 6.3(b)] exhibits several features also appearing on the images of other PhCWs and/or at other wavelengths. The light propagation along the input ridge waveguide and further in the PhCW and along the output ridge waveguide is clearly seen, as well as the light scattering at the junction between the PhCW and ridge waveguides. The light scattering at junctions results in scattered field components propagating (in air) away from the sample surface. These propagating components are detected with the SNOM fiber tip more efficiently than the evanescent field components [28] (e.g., associated with the PhCW and ridge waveguides modes), resulting in the image contrast distortion [40, 41]. Finally, the light propagating along the PhCW and ridge waveguides is well confined in the transverse direction, showing a somewhat irregular periodic pattern in the propagation direction [Figure 6.3(b)].

The periodic intensity pattern seen along the propagation direction can be related to the interference between fiber modes excited by the SNOM fiber tip interacting with *both* evanescent mode fields and weak optical fields forming a quasi-homogeneous background [40]. Note that in the detection process of a collection SNOM, a fiber probe picks up plane wave components of the detected field with the efficiency that decreases rapidly with the increase of the magnitude of the wave-vector projection on the surface plane [28]. All of these plane wave components contribute *linearly* (although differently) to the amplitude of the fiber

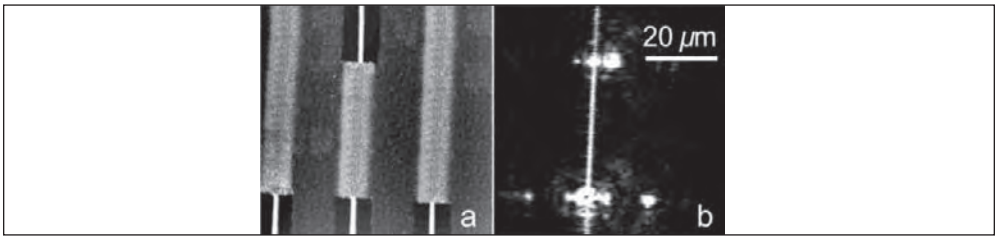

Figure 6.3 Grayscale (a) topographical and (b) near-field optical images ($66 \times 66\ \mu m^2$) obtained with a $40\ -\mu m\ -$long PhCW of sample N1 at the wavelength $\lambda \cong 1520$ nm for TM polarization. Taken from [49]. © 2005 American Physical Society.

mode(s) propagating toward a detector. Therefore, in the SNOM imaging of waveguide modes, especially those with large effective indices, even weak scattered optical fields caused by material inhomogeneities and fabrication defects can contribute to the detected signal. This contribution being coherent and most strong from the optical fields with small wave-vector projections results in an interference pattern superimposed on the image formed by a waveguide mode. Such an interference pattern is somewhat irregular due to different contributing plane wave components, exhibiting (on average) the interference fringes corresponding to the optical field with *zero* wave vector projection (propagating away from the surface)—that is, to the homogeneous coherent background.

In the case of the PhCW oriented along the x-axis, the field probed by the SNOM above the sample surface and along the PhCW can be approximated as follows [40]:

$$E_d(x,z) = B + \sum_m u_m^0 \exp\left[-z\sqrt{(\beta + mK)^2 - k_0^2}\right] \exp i(\beta + mK)x,$$
$$K = \frac{2\pi}{\Lambda},\ m = 0, \pm 1, \pm 2, \ldots \tag{6.1}$$

where the z-axis is perpendicular to the sample surface ($z = 0$) pointing to the air side, B represents a homogeneous background, $k_0 = 2\pi/\lambda$ is the wave number in air, u_m^0 is the amplitude of the main electric field component of the PhCW mode having the propagation constant $\beta \leq 0.5K$, Λ is the PhC lattice constant, and we assumed that all Bloch components are evanescent. Indeed, for the considered situation ($\Lambda \cong 428$ nm, $\lambda \cong 1500-1630$ nm), the PhCW mode propagation constant is expected to be in the range of 0.4–0.5K [51], implying that the propagation constants of all Bloch components are larger than the wave number in air.

Each of the field components described in Equation 6.1 contributes to the amplitude of the fiber mode amplitude, which is actually detected. However, the coupling efficiency decreases drastically with the increase of the wave vector surface projection $|\beta + mK|$ [28]. This dependency can be qualitatively explained by the circumstance that the effective detecting center of a SNOM probe fiber is situated at some distance inside the fiber [52] so that the evanescent fields are always probed at a nonzero distance from the surface. Keeping only the leading terms, the signal detected (along the PhCW) at the tip-surface distance z reads

$$S(x,z) \propto C(z) + 2h(0)Bh(\beta)u_0^0 \exp(-z/d_0)\cos(\beta x) + 2h(0)Bh(K-\beta)u_{-1}^0 \exp(-z/d_1)$$
$$\times \cos[(K-\beta)x] + 2h(\beta)u_0^0 h(K-\beta)u_{-1}^0 \exp(-z/d_2)\cos(Kx) \tag{6.2}$$

where $C(z)$ denotes the level of signal background whose distance dependence is due to the averaged intensity of the evanescent waves, $h(k)$ is the detection efficiency of the field component having the magnitude k of wave vector projection on the surface plane, and the penetration depths are given.

It is expected that $h(0) \gg h(\beta) > h(K-\beta)$ for the aforementioned reasons; therefore, the signal harmonics having spatial frequencies β and $K-\beta$ would dominate the spectrum (Equation 6.2). The preceding consideration can be generalized for the case of several PhCW modes. For example, for two modes having the propagation constants β_1 and β_2, the dominating signal harmonics would be those

with spatial frequencies β_1, β_2, $K - \beta_1$, and $K - \beta_2$. The occurrence of several PhCW modes might be caused by the excitation of different depth modes of the input ridge waveguide. One also can expect that some of the modes actually will be *index* guided modes that do not exhibit well-pronounced PBG properties.

6.4 Near-Field Characterization of PhCW Components

The preceding consideration has important implications to the interpretation of SNOM images and characterization of the PhCW structures. We make use of the corresponding implications in the following analysis of the SNOM images obtained with all samples.

6.4.1 PhCW Propagation Loss

Light propagation along the straight PhCWs of samples N1 and N2 and the associated loss were studied in great detail for both polarizations in the whole wavelength range available (1500–1630 nm) using the corresponding high-quality and high-resolution SNOM images obtained [49]. It is seen that the recorded field distributions are well confined (to the line of missing holes defining the PhCW), exhibiting wavelength-dependent variations along the propagation direction (see Figures 6.4 and 6.5). For TM polarization, efficient guiding along the PhCW was observed in the whole wavelength range (Figure 6.4) for both samples, a feature that suggests the absence of PBG and pure effective refractive index guiding of TM mode (similar to the conventional dielectric waveguiding). The signal cross sections (not shown here) turned out to be very close in shape to the Gaussian distributions, with the full width at half maximum (FWHM) increasing from ~760 nm to 788 nm with the increase of the light wavelength [49]. It should be noted though that the signal does not go to zero outside the PhCW, indicating the presence of a homogeneous background at the level of ~10% compared to the maximum signal. However, a high level of *signal* background (10%) does not mean that the scattered field, on average, is only 10 times smaller than the PhCW mode field. The scattered field is, in fact, considerably smaller than that because the detection efficiency of fields with low spatial frequencies is much higher than that of the evanescent PhCW mode [28]. At

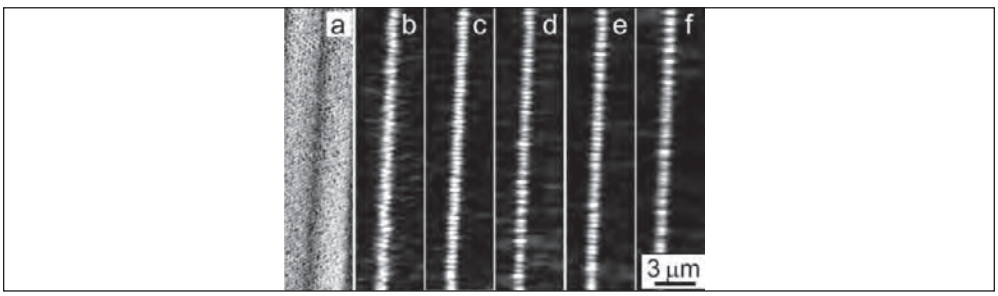

Figure 6.4 Grayscale (a) topographical and (b–f) near-field optical images ($5 \times 25\ \mu m^2$) obtained with a 40-μm-long PhCW (sample N1) at the wavelengths $\lambda \cong$ (b) 1500, (c) 1520, (d) 1550, (e) 1590, and (f) 1630 nm for TM polarization. The images are orientated in a way that the light propagates upwards. Taken from [49]. © 2005 American Physical Society.

the same time, for TE polarization, the efficient guiding was limited to the wavelengths shorter than 1522 or 1570 nm for the PhCW with a filling factor of 0.76 (sample N1) or 0.82 (sample N2), respectively. For longer wavelengths, we observed drastic and rapid deterioration of the waveguiding and PhCW mode confinement, ending up with the complete disappearance of the PhCW mode once the wavelength exceeded the cutoff value by merely 2 nm (see Figure 6.5). Such a critical wavelength dependence of the PhCW guiding for TE polarization can be considered as clear evidence of the well-defined PBG effect in the structure. It should be noted that the long-wavelength PBG edge was found shifting toward longer wavelengths with the increase of the filling factor, a circumstance that emphasizes the fact that the filling factor is an important design parameter for PhCWs.

Using the SNOM images obtained at different wavelengths (similar to those shown in Figures 6.4 and 6.5), one can directly determine the PhCW mode propagation loss and its dispersion. Variations in the detected signal along the PhCW axis, which can be used to determine the mode propagation constant (see the next subsection), made the precise evaluation of the propagation loss rather difficult. To circumvent this problem, we have determined the propagation loss by averaging over 11 profiles of the (~25 μm long) near-field distributions that were cut along the PhCW axis, finding the slopes of the best linear fits to the corresponding average cross sections. This procedure was carried out for different wavelengths, and the obtained results were recalculated as transmission through the 10-μm-long PhCW of sample N1 and the 40-μm-long PhCW of sample N2. The latter were compared with the transmission measurements conducted with the same samples using the conventional approach of measuring the transmission spectra for PhCWs of different lengths (see Figure 6.6). This (direct) comparison between the experimental transmission spectra and the data obtained from the corresponding SNOM images showed rather good correspondence in the wavelength ranges of mode guiding as seen from the SNOM images. At the same time, it became apparent that the conventional technique of characterization might turn out to be somewhat misleading as it does not provide clear evidence of the PhCW mode cutoff behavior, showing instead a gradual decrease in the transmission. One also can note that the transmission measurements tend to overestimate the propagation loss near the

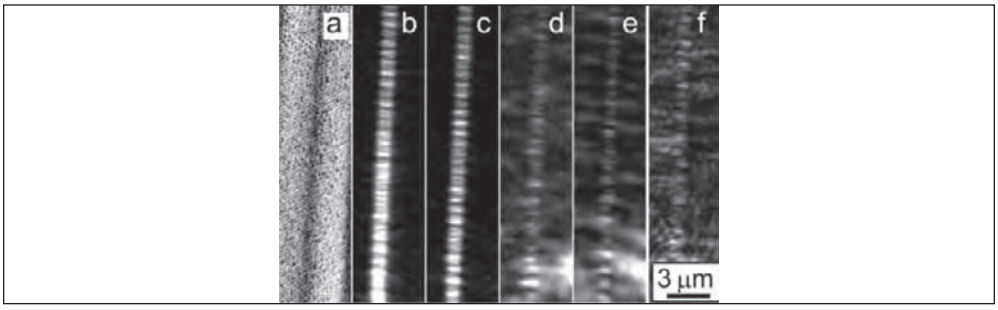

Figure 6.5 Grayscale (a) topographical and (b–f) near-field optical images ($5 \times 25\ \mu m^2$) obtained with a 40-μm-long PhCW (sample N1) at the wavelengths $\lambda \cong$ (b) 1500, (c) 1522, (d) 1524, (e) 1560, and (f) 1600 nm for TE polarization. The images are orientated in a way that the light propagates upwards. Taken from [49]. © 2005 American Physical Society.

PBG edge (Figure 6.6), probably because the coupling between the access ridge waveguides and the PhCWs becomes unstable due to a drastic increase in the FWHM of PhCW modes [53]. This means, in turn, that large propagation losses usually reported for the PhCW modes close to the PBG edges (these modes are interesting due to high dispersion and low group velocities) might be a result of overestimation. It should be kept in mind that the difference in spectral resolution of measurements performed using the tunable laser and a broadband light emitting diode (LED) also might have influenced the transmission curves obtained, for example, by smoothing the transmission curve measured with the LED.

6.4.2 PhCW Mode Dispersion

SNOM images obtained with a high resolution revealed that the intensity distributions along the PhCWs are quasi-periodic and wavelength-dependent (see Figures 6.4 and 6.5). We have related this remarkable feature (also found in the experiments on SNOM imaging of conventional waveguides [24]) to the interference between fiber modes excited by the SNOM fiber tip interacting with both PhCW mode evanescent fields and weak optical fields, forming a quasi-homogeneous background [40]. Dispersion of light propagation along the PhCW was studied in great details for sample N1 [49]. The typical spatial frequency spectrum of the optical signal variations along the PhCW measured at the wavelength of 1510 nm is shown in Figure 6.7(a) (for TE polarization), featuring several peaks that can be assigned (in agreement with arguments given in Section 6.3) to the spatial frequencies of two PhCW modes having the propagation constants β_1 and β_2. This fitting procedure was accomplished for both polarizations in the whole wavelength range available (1500–1630 nm). The lattice constant of 428 nm of this PhC was obtained from images made by a calibrated SEM and corroborated with SNOM topographical images. The PhCW mode propagation constants β_1

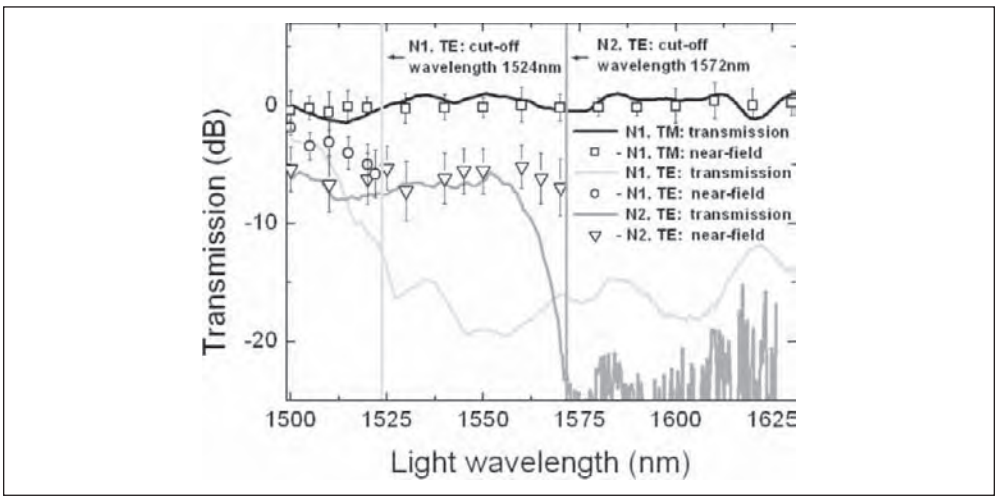

Figure 6.6 Transmission spectra measured with a 10-μm-long PhCW of sample N1 (black line corresponds to TM polarization; and light gray line, to TE polarization) and a 40-μm-long PhCW of sample N2 (gray line) plotted together with the results obtained from the averaged cross sections of SNOM images. Taken from [49]. © 2005 American Physical Society.

and β_2 were fitted to the experimental spectrum so that the frequencies $K - \beta_1$ and $K - \beta_2$ also would fit to the corresponding peaks as shown in Figure 6.7(a). One can further see that the spectrum structure, being well defined at low spatial frequencies, is more complicated around the frequency K of the lattice constant. Such a structure might be related to the PhCW modes reflected by the PhCW-ridge waveguide interface and the output edge of the sample and/or to the nonlinear response of the photoreceiver used for optical signal detection [40]. Considering current observations, we should remark that the mode with β_1 is most probably the main (true) PhCW mode, whereas the mode with β_2 is only index-guided and excited due to the multi-mode light propagation in the input ridge waveguide. The above fitting procedure was carried out (with sample N1) for other wavelengths in the spectrum range of 1500–1620 nm (for both polarizations), resulting in the dispersion curves measured with the SNOM [Figure 6.7(b)]. We can further identify the following reasons of uncertainty in the determination of mode propagation constants: the fact that the background contribution consists of many propagating field components with small but not zero wave vector projections on the surface plane and a finite length of the corresponding cross sections (~25 μm in this case).

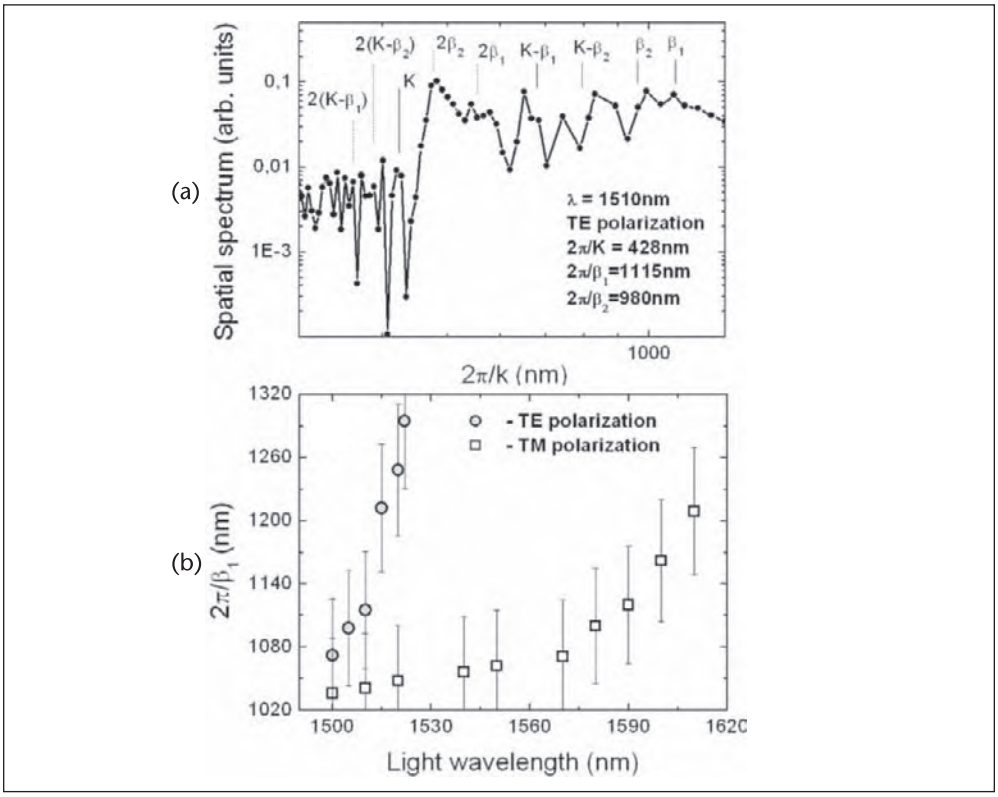

Figure 6.7 (a) Spatial frequency spectrum of the optical image obtained with the PhCW of sample N1 for TE polarization at the wavelength $\lambda \cong 1510$ nm. Positions of main peaks fitted to the experimental data are indicated with solid lines. Dotted lines indicate combination frequencies that may appear due to the backward propagating PhCW modes and/or nonlinear detection. (b) Wavelength dependence of the propagation constant of the main PhCW mode determined from the corresponding near-field optical images obtained for TM and TE polarizations Taken from [49]. © 2005 American Physical Society.

Nevertheless, the results obtained indicate that the propagation constant of the true PhCW varies faster with the light wavelength than that of free propagating (in air) radiation. For example, in the case of TE polarization, the ratio Λ/λ_{PCW} changed from 0.33 to 0.41 when the ratio Λ/λ varied from 0.28 to 0.29 [49]. Such dispersion is actually expected for the PhCW mode in SOI PBG structures [51].

Considering the wavelength dependence of the propagation constant determined from the corresponding spatial spectra, we calculated the phase and group velocities for TM- and TE-polarized PhCW modes in the wavelength range of 1500–1610 nm (see Figure 6.8). It is clearly seen that the group velocity rapidly decreases, reaching the values of ~ 0.11c at the light wavelength of 1610 nm for TM polarization [Figure 6.8(a)] and ~ 0.035c at the wavelength of 1522 nm for TE polarization [Figure 6.8(b)], as the wavelength increases toward the PBG edge. At the same time, the phase velocity does increase, although relatively slowly, so that the PhCW mode constant becomes closer to the light line in air for longer wavelengths. This behavior of the group velocity is in agreement with the recent results obtained with different techniques [18, 43]. Finally, the experimentally established large dispersion and significant reduction in the group velocity, which are directly related to the tight confinement and strong Bragg scattering in the PhCW, also were corroborated with the theoretical dispersion curves calculated with the three-dimensional (3-D) finite-difference time-domain (FDTD) method [49].

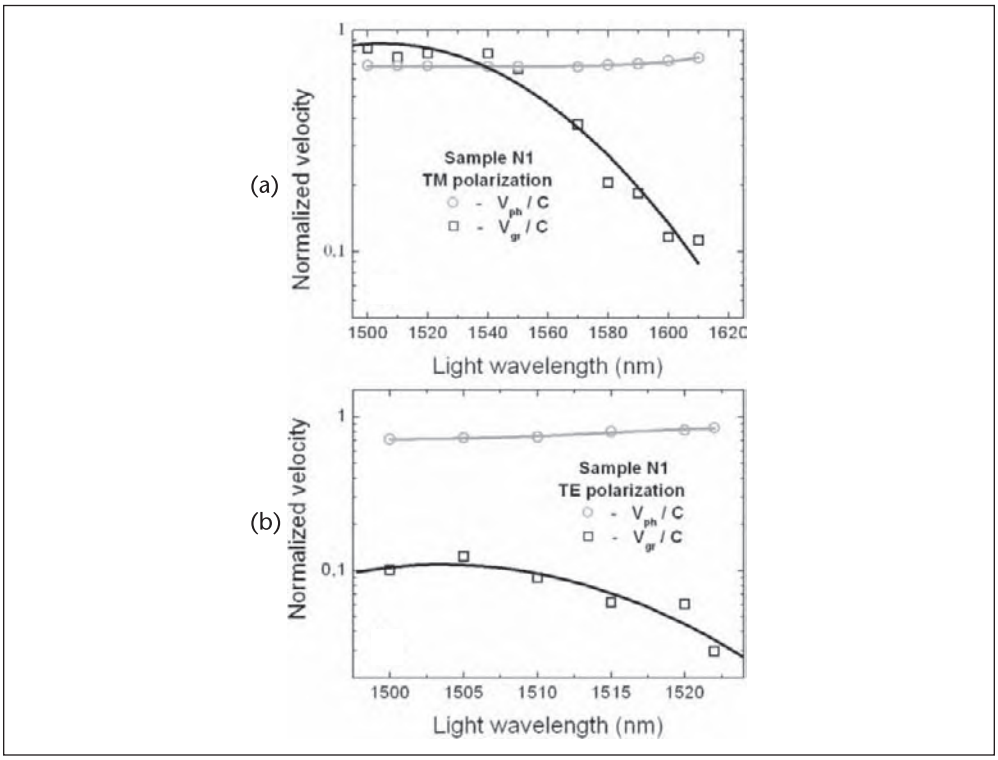

Figure 6.8 Group and phase velocities normalized to the speed of light in vacuum for the (a) TM-polarized and (b) TE-polarized PhCW mode of sample N1 as functions of the light wavelength. Solid lines (used to guide the eye) represent quadratic approximations by the least-square method. Taken from [49]. © 2005 American Physical Society.

6.4.3 Loss in Gradual PhCW Bends

Typical topographical and near-field optical SNOM images of the gradually bent PhCW (sample N3) also featuring the access ridge waveguide are shown in Figure 6.9 [40]. In the topographical image, one can recognize the pattern of holes that forms the PhCW following the output ridge waveguide and even distinguish individual holes, albeit only in the output PhCW region [Figure 6.9(a)]. The light propagation along the bent PhC waveguide and further on in the access ridge waveguide is clearly seen in the near-field optical image [Figure 6.9(b)], as well as the light scattering at the junction between the PhCW and the ridge waveguide. The radiation loss is visualized on the image appearing in the form of light scattering out of the bend in the forward direction that illuminates the edge of the neighboring PhC region. The variations of the detected signal along the PhCW axis [Figure 6.9(b)] made the precise evaluation of the propagation loss in straight parts of PhCWs rather difficult. Even for the longest PhCW (~50 μm), the propagation loss could, at best, be estimated as being within 10% and somewhat larger for longer wavelengths. These observations are in agreement with the transmission measurements conducted with a similar sample that resulted in the propagation loss of a few dB/mm at 1520 nm and increasing with the wavelength [48]. The bend loss could not have been determined from the transmission measurements because the coupling losses contribute to the measured overall transmission loss in the same manner. This circumstance makes the determination of bend loss with the help of SNOM especially important.

We have obtained SNOM images of the gradual bend of the longest PhCW at different wavelengths (Figure 6.10) and *directly* determined the bend loss by averaging the signal distributions (across the PhCW) over the PhCW length of ~ 5 μm before and after the bend. Here it is very important to remember that, contrary to the usual situation, the SNOM signal is proportional mainly to the PhCW mode *amplitude* [due to the presence of the background field (see Equation 6.2)], and not its intensity. The bend (power) loss was found to be increasing rapidly with the wavelength from the value of ~3 dB at the wavelength of 1520 nm to that of ~30 dB at 1570 nm. [See Figure 6.10(d).] Note that this range of the bend loss is considerably higher than that (1–6 dB) reported previously [40] mainly because of *correctly* taking into account the amplitude character of SNOM detection. Finally, it is worth mentioning that the determined bend loss is different not only for different

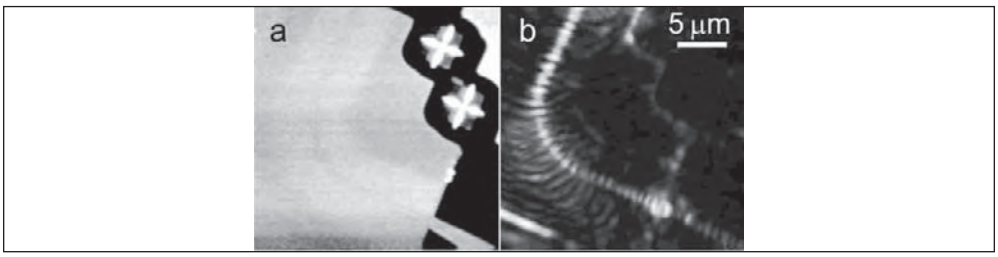

Figure 6.9 Grayscale (a) topographical and near-field optical images (22.5 $\times$22.5 μm^2) obtained with the shortest PhCW (sample N3) [Figure 6.1(b)] at the wavelength $\lambda \cong$1520 nm. One can distinguish the line of missing holes that defines the PhCW and clearly see the output ridge waveguide in the topographical image whose depth is 1.9 μm.

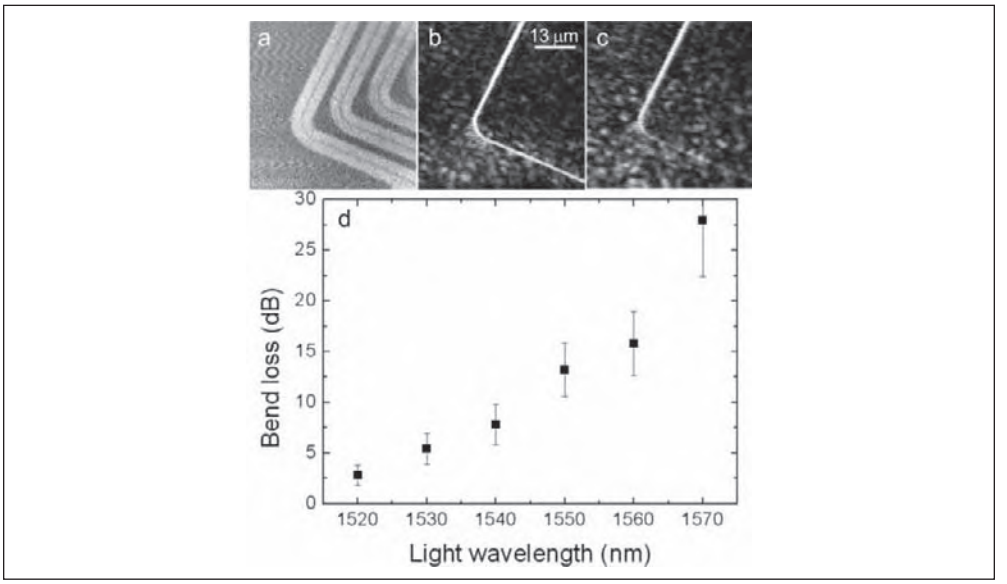

Figure 6.10 Grayscale (a) topographical and (b, c) near-field optical images (52.5 × 52.5 μm^2) obtained with the longest PhCW (sample N3) at the wavelength $\lambda \cong$ (b) 1520 and (c) 1570 nm. The depth of the topographical image is 0.51 μm. (d) Wavelength dependence of the bend loss measured for the longest PhCW (sample N3).

PhCWs but also for different adjustments of the fiber with respect to the *same* PhCW, especially with respect to the fiber displacement perpendicular to the surface plane [40].

6.4.4 Loss in Double 60° PhCW Bends

The SNOM investigations of sample N4 are in process, and their detailed account will be published elsewhere. Here we present preliminary results concerning the influence of moving holes from one side of the bend to the other on the bend loss. The topographical and near-field optical images obtained at the wavelength of 1530 nm with sample N4 containing double 60° bends sharp and smoothed by moving one or three holes [see SEM insets in Figure 6.1(c–e)] are shown in Figure 6.11. Talneau et al. reported the transmission measurements of a similar structure patterned into a GaInAsP slab on InP substrate, inferring that moving holes in the corner of a PhCW bend is very efficient in increasing the transmission [15]. Note that this conclusion was based on the interpretation of Fabry-Perot oscillations in the transmission spectra (i.e., was of *indirect* nature). In our case, the near-field images obtained demonstrate *directly* a significant increase in the transmission of radiation for smoothened bends [see Figure 6.11(d–f)]. In fact, radiation loss for the sharp double bend was so large that it was impossible to estimate its level with reasonable accuracy because of the very low signal level at the output PhCW (as compared to the background level enhanced due to strong radiation scattering at the bends). Noticing similar oscillations in the detected signal along the PhCWs, one conjectures that, also with this sample, the SNOM signal is (mainly) proportional to the PhCW mode amplitude. Averaging the signal distributions (across the PhCW) over the PhCW length of ~5 μm before and after the bend, the power loss of ~3 dB per bend was determined for the bends

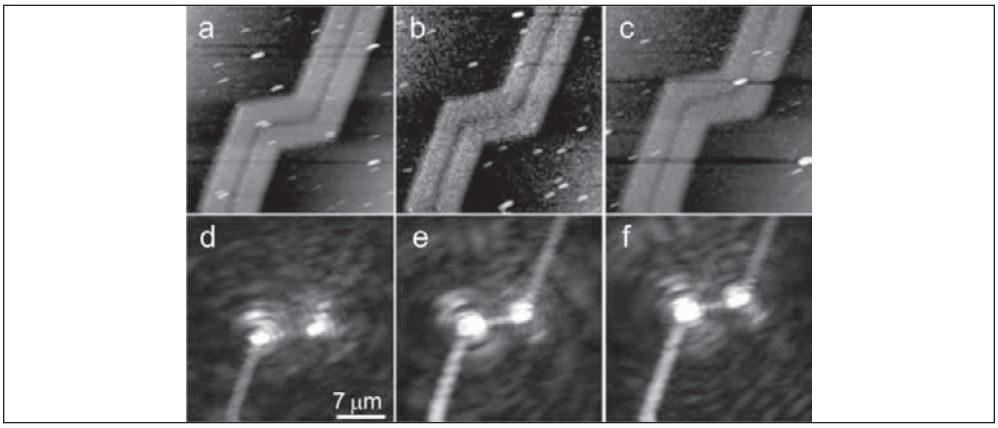

Figure 6.11 Grayscale (a–c) topographical and (d–f) near-field optical images obtained at the wavelength $\lambda \cong 1530$ nm with sample N4 containing double 60° (a, d) sharp and smoothed bends having (b, e) one and (c, f) three holes moved into the bend corner.

with both one and three holes being displaced. Finally, we should mention that even though this bend loss is the same for both configurations, the corresponding wavelength dependencies were found to be sufficiently different.

6.4.5 Directional Couplers (Sample N5)

SNOM also has been used to characterize more complicated PhCW structures such as diffraction grating couplers [54], Y-splitters [55], and directional couplers [50]. Ending a review of the results obtained with the SNOM detection, we consider in this subsection the characterization of a PhCW-based directional coupler with holes arranged in a triangular array. Until now, very little attention has been devoted to investigating the propagation of TM-polarized light in such PhCW structures since this arrangement provides PBG only for TE-polarized light; thus, the waveguides should not support leakage-free guidance [51]. In contrast with the naïve expectations, the low propagation and bend losses for TM-polarized light in different PhCW structures (exhibiting a band gap for TE-polarized light) have recently been experimentally demonstrated using the conventional technique for relative measurements of the transmission spectra [56]. Here we present the results of experimental investigations (by collecting SNOM) of TM-polarized light propagation in the PhCW coupler exhibiting PBG for TE-polarized light. The PhCW coupler was excited at different wavelengths (for TM-polarized light) and imaged with SNOM. The topographical and near-field optical images obtained for the directional coupler and output ridge waveguides in the broad wavelength range (1430–1630 nm) are shown in Figure 6.12. On the topographical image [Figure 6.12(a)], the input and output ridge waveguides connected to the PhCW coupler area are clearly shown. One also can recognize the PBG structure in the image, but the pattern of holes that forms the "direct" and "coupled" PhC channels following input and output ridge waveguides are not discernible because the scanning parameters were not optimized with respect

to the topographical imaging. On the near-field optical image [Figure 6.12(c)] obtained at the wavelength of 1430 nm inside the PhC area, one can observe light propagating along the input ridge waveguide and further in the "direct" PhCW, as well as strong light scattering from the PhC area originating at the junctions between the PhCW and ridge input/output waveguides. The features in light propagation (for the same wavelength) along the output ridge waveguide are more visible in the optical image exhibiting spatial periods down to 400 nm. [See Figure 6.12(d).] We found that the light intensity patterns (recorded for ridge waveguides and the directional coupler area) varied gradually with the increase of the light wavelength, redistributing the light power between the channels. Thus, we have observed the efficient coupling and light propagation into the "coupled" PhC channel at the wavelength close to 1505 nm [Figure 6.12(e)] together with the light guiding along both output ridge waveguides [Figure 6.12(f)]. Finally, the SNOM images shown in Figure 6.12(g, h) have been obtained with further increase of the light wavelength with almost all light being directed to the "coupled" channel at $\lambda \cong 1620$ nm. Note that at the same time, a bright spot in Figure 6.12(c) associated with the bend of the "direct" PhC channel is seen to gradually vanish for longer wavelengths, virtually disappearing at wavelengths close to 1620 nm [Figure 6.12(g)]. Such wavelength-dependent behavior, in our opinion, is originating from the efficient light coupling (from the bent "direct" PhC channel to the "coupled" one). Furthermore, the light scattering observed

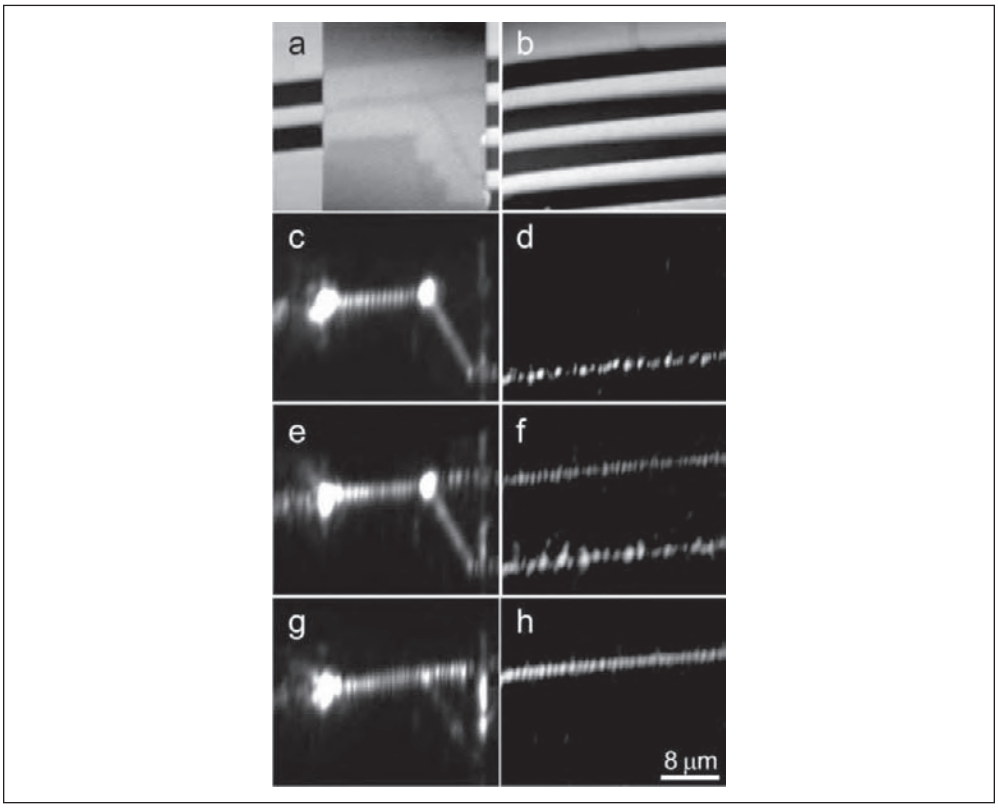

Figure 6.12 Grayscale (a, b) topographical and (c–h) near-field optical images ($30 \times 25\ \mu m^2$) taken at the wavelengths $\lambda \cong$ (c, d) 1430, (e, f) 1505 and (g, h) 1620 nm for TM-polarization. SNOM images are oriented in a way so that the light propagates rightward in the horizontal direction.

along the output edge of the PBG structure becomes more pronounced with the increase of the wavelength [see, for example, the bright elongated spot at the top of Figure 6.12(g)]. This observation can be accounted for by the index-guided TM mode leaking from the "direct" channel (in the bend region) and propagating further through the periodic structure in the forward direction. Such a process becomes more efficient for longer wavelengths due to the wavelength-dependent variations in the scattering strength of the periodic structure, which is known to decrease with increasing wavelength.

6.5 Conclusions

In this chapter, we considered usage of the collection SNOM for characterization of PhCW structures. The qualitative description of image formation in the collection SNOM was presented for the special case of SNOM imaging of PhCWs, with the (quasihomogenous) background field formed by PhCW mode scattering being taken into account. We imaged the propagation of light at telecommunication wavelengths along straight and bent regions of silicon-on-insulator PhCWs (with different filling factors) formed by removal of a single row of holes in the triangular lattice. High-quality SNOM images of PhCWs excited in the wavelength range of 1500–1630 nm was obtained and analyzed to determine the PhCW characteristics for TE and TM polarizations. Thus, we analyzed light intensity variations along straight PhCWs measured with the SNOM and related those variations to Bloch components of the PhCW mode. Using a phenomenological description of the SNOM imaging and assuming the presence of a quasi-homogeneous background field, we identified in spatial frequency spectra of the intensity variations of the corresponding Bloch harmonics and determined (for both polarizations) the dispersion of the PhCW mode propagation constant and, thereby, the mode group and phase velocities. The efficient guiding (for both samples) of the TM-polarized radiation was observed in the whole range of laser tunability. At the same time, for TE polarization, the efficient guiding was limited to the wavelengths shorter than 1552 or 1570 nm for the PhCW with a filling factor of 0.76 or 0.82, respectively. For longer wavelengths, we observed drastic and rapid deterioration of the wave-guiding and PhCW mode confinement once the wavelength exceeded the cutoff value by merely 2 nm. Such critical wavelength dependence of the PhCW guiding (for TE polarization) is, in our opinion, clear evidence of the well-defined PBG effect in the structure. Using averaged cross sections of the intensity distributions along the PhCW axis, the propagation loss was evaluated and found to agree with the corresponding transmission spectra.

Radiation loss for 90° gradual and 60° sharp PhCW bends was evaluated using averaged signal cross sections and taking into account the fact that the signal is proportional to the PhCW mode amplitude. We directly showed that the bend loss for 60° bends is significantly decreased for smoothed bends having one or three holes moved into the bend corner. Finally, we investigated the propagation of TM-polarized light at telecommunication wavelengths in a planar PhCW directional coupler. The directional coupler was found to be effective for the TM-polarized light in the wavelength range of 1500–1630 nm despite the fact that the PhC structure only exhibits photonic band gap for TE-polarized radiation.

The issues discussed in this work have implications to the SNOM characterization of any PhCW and to at least some types of conventional waveguide structures. The most important implication is related to the presence of a quasi-homogeneous coherent background formed by scattering of waveguide modes at imperfections and directional changes of waveguides. This background having a close to zero spatial frequency (in the surface plane) is detected more efficiently than the evanescent fields of waveguide modes [28]. The presence of such a background might be considered a drawback intrinsic for a particular configuration (of PhCW, access waveguide, coupling fiber, etc.) because it jeopardizes the accuracy of the determination of spatial frequencies. On the other hand, it increases the detected signal due to the mode field so that the signal becomes proportional to the field *amplitude* (not intensity). This feature is especially important when characterizing mode profiles and propagation (and bend) power loss. Finally, the measurements of the spectral modifications with the tip-surface distance are crucial for the interpretation of the signal variations along the PhCW measured with any SNOM technique.

We believe that the results presented in this work can help in designing further, more detailed and accurate SNOM investigations of PhCWs and, in general, PhC structures. The accurate PhCW characterization is particularly important since rigorous calculations of the properties of PhCW components are extremely difficult and time-consuming. The SNOM imaging can be used not only to quantitatively characterize properties of fabricated PhCWs (mode profiles and propagation constants including loss) and PhC structures (evaluation of loss and identification of loss channels), and thereby optimize their performance, but also to unveil many intriguing scattering phenomena occurring in PhCs.

Acknowledgments

The authors gratefully acknowledge the help of J. Arentoft, A. Boltasseva, P. I. Borel, L. H. Frandsen (COM, Technical University of Denmark), and M. Kristensen (University of Aarhus, Denmark) and of H. M. H. Chong (Glasgow University, UK) in fabrication and characterization of the samples used in this work. Useful discussions with T. Søndergaard (Aalborg University, Denmark) also are appreciated. This research is carried out in the framework of the national frame program "Planar Integrated Photonic Band Gap Elements (PIPE)" supported by the Danish Technical Research Council, contract No. 26-03-0158.

References

[1] Bykov, V. P., *Radiation of Atoms in a Resonant Environment*, Singapore: World Scientific, 1993.

[2] Joannopoulos, J. D., R. D. Meade, and J. N. Winn, *Photonic Crystals*, Princeton: Princeton University Press, 1995.

[3] Soukoulis, C. M. (ed.), *Photonic Crystals and Light Localization in the 21st Century, Dordrecht*, The Netherlands: Kluwer, 2001.

[4] Krauss, T. F., and R. M. De La Rue, "Photonic Crystals in the Optical Regime—Past, Present and Future," *Progress in Quantum Electronics*, Vol. 23, 1999, pp. 51–96.

[5] Busch, K. et al., *Photonic Crystals*, Berlin: Wiley-VCH, 2004.

[6] Baba, T., N. Fukaya, and J. Yonekura, "Observation of Light Propagation in Photonic Crystal Optical Waveguides with Bends," *Electronics Letters*, Vol. 35, 1999, pp. 654–655.

[7] Yamada, S. et al., "Observation of Light Propagation in Two-Dimensional Photonic Crystal-Based Bent Optical Waveguides," *Journal of Applied Physics*, Vol. 89, 2001, pp. 855–858.

[8] Lonãar, M. et al., "Waveguiding in Planar Photonic Crystals," *Applied Physics Letters*, Vol. 77, 2000, pp. 1937–1939.

[9] Tokushima, M. et al., "Lightwave Propagation Through a 120° Sharply Bent Single-Line-Defect Photonic Crystal Waveguide," *Applied Physics Letters*, Vol. 76, 2000, pp. 952–954.

[10] Lombardet, B. et al. "Propagation Loss Measurements and Fabry-Pérot Mode Analysis Using Out-of-Plane Light Scattering in Photonic Crystal Waveguides," *Applied Physics Letters*, Vol. 86, 2005, Art. No. 111111.

[11] Lin, S. Y. et al., "Demonstration of Highly Efficient Waveguiding in a Photonic Crystal Slab at the 1.5-μm Wavelength," *Optics Letters*, Vol. 25, 2000, pp. 1297–1299.

[12] Kawai, N. et al., "Confined Band Gap in an Air-Bridge Type of Two-Dimensional AlGaAs Photonic Crystal," *Physical Review Letters*, Vol. 86, 2001, pp. 2289–2292.

[13] Chow, E. et al., "Quantitative Analysis of Bending Efficiency in Photonic-Crystal Waveguide Bends at $\lambda = 1.55$ μm Wavelengths," *Optics Letters*, Vol. 26, 2001, pp. 286–288.

[14] Talneau, A., L. Le Gouezigou, and N. Bouadma, "Quantitative Measurement of Low Propagation Losses at 1.55 μm on Planar Photonic Crystal Waveguides," *Optics Letters*, Vol. 26, 2001, pp. 1259–1261.

[15] Talneau, A. et al., "Photonic-Crystal Ultrashort Bends with Improved Transmission and Low Reflection at 1.55 μm," *Applied Physics Letters*, Vol. 80, 2002, pp. 547–549.

[16] Märki, I. et al., "Characterization of Photonic Crystal Waveguides Based on Fabry-Pérot Interference," *Journal of Applied Physics*, Vol. 96, 2004, pp. 6966–6969.

[17] Notomi, M. et al., "Extremely Large Group-Velocity Dispersion of Line-Defect Waveguides in Photonic Crystal Slabs," *Physical Review Letters*, Vol. 87, 2001, Art. No. 253902.

[18] Asano, T. et al., "Time-Domain Measurement of Picosecond Light-Pulse Propagation in a Two-Dimensional Photonic Crystal-Slab Waveguide," *Applied Physics Letters*, Vol. 84, 2004, pp. 4690–4692.

[19] Lonãar, M. et al., "Experimental and Theoretical Confirmation of Bloch-Mode Light Propagation in Planar Photonic Crystal Waveguides," *Applied Physics Letters*, Vol. 80, 2002, pp. 1689–1691.

[20] Barclay, P. E. et al., "Probing the Dispersive and Spatial Properties of Photonic Crystal Waveguides via Highly Efficient Coupling from Fiber Tapers," *Applied Physics Letters*, Vol. 85, 2004, pp. 4–6.

[21] Tsai, D. P. et al., "Photon Scanning Tunneling Microscope Study of Optical Waveguides," *Applied Physics Letters*, Vol. 56, 1990, pp. 1515–1517.

[22] Choo, A. G. et al., "Near Field Measurements of Optical Channel Waveguides and Directional Couplers," *Applied Physics Letters*, Vol. 65, 1994, pp. 947–949.

[23] Balistreri, M. L. M. et al., "Visualization of Mode Transformation in a Planar Waveguide Splitter by Near-Field Optical Phase Imaging," *Applied Physics Letters*, Vol. 79, 2001, pp. 910–912.

[24] Campillo, A. L. et al., "Direct Measurement of the Guided Modes in LiNbO3 Waveguides," *Applied Physics Letters*, Vol. 80, 2002, pp. 2239–2241.

[25] Balistreri, M. L. M. et al., "Local Observations of Phase Singularities in Optical Fields in Waveguide Structures," *Physical Review Letters*, Vol. 85, 2000, pp. 294–297.

[26] Balistreri, M. L. M. et al., "Tracking Femtosecond Laser Pulses in Space and Time," *Science*, Vol. 294, 2001, pp. 1080–1082.

[27] Greffet, J.-J., and R. Carminati, "Image Formation in Near-Field Optics," *Progress in Surface Science*, Vol. 56, 1997, pp. 133–237.

[28] Bozhevolnyi, S. I., B. Vohnsen, and E. A. Bozhevolnaya, "Transfer Functions in Collection Scanning Near-Field Optical Microscopy," *Optics Communications*, Vol. 172, 1999, pp. 171–179.

[29] Bozhevolnyi, S. I., and B. Vohnsen, "Near-Field Imaging of Optical Phase and Its Singularities," *Optics Communications*, Vol. 212, 2002, pp. 217–223.

[30] McDaniel, E. B. et al., "Local Characterization of Transmission Properties of a Two-Dimensional Photonic Crystal," *Physical Review B*, Vol. 55, 1997, pp. 10878–10882.

[31] Phillips, P. L. et al., "Near-Field Optical Microscopy of Thin Photonic Crystal Films," *Journal of Applied Physics*, Vol. 85, 1999, pp. 6337–6342.

[32] Campillo, A. L. et al., "Mapping the Optical Intensity Distribution in Photonic Crystals Using a Near-Field Scanning Optical Microscope," *Journal of Applied Physics*, Vol. 89, 2001, pp. 2801–2807.

[33] Gérard, D. et al., "Near-Field Probing of Active Photonic-Crystal Structures," *Optics Letters*, Vol. 27, 2002, pp. 173–175.

[34] Okamoto, K. et al., "Near-Field Scanning Optical Microscopy of Photonic Crystal Nanocavities," *Applied Physics Letters*, Vol. 82, 2003, pp. 1676–1678.

[35] Kramper, P. et al., "Near-Field Visualization of Light Confinement in a Photonic Crystal Microresonator," *Optics Letters*, Vol. 29, 2004, pp. 174–176.

[36] Louvion, N. et al., "Local Observation and Spectroscopy of Optical Modes in an Active Photonic-Crystal Microcavity," *Physical Review Letters*, Vol. 94, 2005, Art. No. 113907.

[37] Cluzel, B. et al., "Subwavelength Imaging of Field Confinement in a Waveguide-Integrated Photonic Crystal Cavity," *Journal of Applied Physics*, Vol. 98, 2005, Art. No. 086109.

[38] Kramper, P. et al, "Highly Directional Emission from Photonic Crystal Waveguides of Subwavelength Width," *Physical Review Letters*, Vol. 92, 2004, Art. No. 113903.

[39] Bozhevolnyi, S. I. et al., "Direct Mapping of Light Propagation in Photonic Crystal Waveguides," *Optics Communications*, Vol. 212, 2002, pp. 51–55.

[40] Bozhevolnyi, S. I. et al., "Near-Field Imaging of Light Propagation in Photonic Crystal Waveguides: Explicit Role of Bloch Harmonics," *Physical Review B*, Vol. 66, 2002, Art. No. 235204.

[41] Bozhevolnyi, S. I., and V. S. Volkov, "Near-Field Characterization of Planar Photonic-Crystal-Waveguide Structures," *Philosophical Transactions of the Royal Society (London) A*, Vol. 362, 2004, pp. 757–769.

[42] Cluzel, B. et al., "Experimental Demonstration of Bloch Mode Parity Change in Photonic Crystal Waveguide," *Applied Physics Letters*, Vol. 85, 2004, pp. 2682–2684.

[43] Gersen, H. et al., "Real-Space Observation of Ultraslow Light in Photonic Crystal Waveguides," *Physical Review Letters*, Vol. 94, 2005, Art. No. 073903.

[44] Gersen, H. et al., "Direct Observation of Bloch Harmonics and Negative Phase Velocity in Photonic Crystal Waveguides," *Physical Review Letters*, Vol. 94, 2005, Art. No. 123901.

[45] Flück, E. et al., "Amplitude and Phase Evolution of Optical Fields Inside Periodic Photonic Structures," *Journal of Lightwave Technology*, Vol. 21, 2003, pp. 1384–1393.

[46] Flück, E. et al., "Near-Field Probing of Photonic Crystals," *Photonics and Nanostructures: Fundamentals and Applications*, Vol. 2, 2004, pp. 127–135.

[47] Engelen, R. J. P. et al., "Local Probing of Bloch Mode Dispersion in a Photonic Crystal Waveguide," *Optics Express*, Vol. 13, 2005, pp. 4457–4464.

[48] Arentoft, J. et al., "Low-Loss Silicon-on-Insulator Photonic Crystal Waveguides," *Electronics Letters*, Vol. 38, 2002, pp. 274–275.

[49] Volkov, V. S. et al., "Near-Field Characterization of Low-Loss Photonic Crystal Waveguides," *Physical Review B*, Vol. 72, 2005, Art. No. 035118.

[50] Volkov, V. S. et al., "Near-Field Probing of Photonic Crystal Directional Couplers," *Laser Physics Letters*, Vol. 3, 2006, pp. 288–293.

[51] Søndergaard, T., J. Arentoft, and M. Kristensen, "Theoretical Analysis of Finite-Height Semiconductor-on-Insulator-Based Planar Photonic-Crystal Waveguides," *Journal of Lightwave Technology*, Vol. 20, 2002, pp. 1619–1626.

[52] Nesci, A. et al., "Measuring Amplitude and Phase Distributions of Fields Generated by Gratings with Sub-wavelength Resolution," *Optics Communications*, Vol. 205, 2002, pp. 229–238.

[53] Volkov, V. S. et al., "Direct Observation of Surface Mode Excitation and Slow Light Coupling in Photonic Crystal Waveguides," *Nano Letters*, Vol. 7, 2007, pp. 2341–2345.

[54] Volkov, V. S., S. I. Bozhevolnyi, and D. Taillaert, "Near-Field Imaging of Light Diffraction Out of Slab Waveguides," *Laser Physics Letters*, Vol. 1, 2004, pp. 311–316.

[55] Volkov, V. S. et al., "Near-Field Characterization of Photonic Crystal Y-Splitters," *Physica Status Solidi (C)*, Vol. 2, 2005, pp. 4087–4092.

[56] Borel, P. I. et al., "Efficient Propagation of TM Polarized Light in Photonic Crystal Components Exhibiting Band Gaps for TE Polarized Light," *Optics Express*, Vol. 11, 2003, pp. 1757–1762.

CHAPTER 7

Tracking Light Pulses with Near-Field Microscopy

R. J. P. Engelen and L. Kuipers

7.1 Introduction

Many new optical structures have appeared in recent years that have intriguing properties due to nanoscale engineering. A few examples of such structures are metamaterials with a negative refractive index [1], SPP structures [2], and highly integrated optics such as PhC-based circuitry [3]. Near-field microscopy is an invaluable tool for investigating these structures, especially since intriguing effects often occur on length scales comparable to the diffraction limit or involve coupling phenomena on this length scale. With a near-field microscope, the intensity distribution of the light in or near a nanophotonic structure can readily be measured. Although such an investigation is useful to gain an understanding of the time-averaged propagation properties, it does not reveal the dynamics of the propagation of light. These dynamics play an important role in, for example, ultrafast optical circuitry, which is expected to improve the bandwidth of optical networks. In these structures, multiple optical components must be integrated into one device possibly not larger than a square millimeter. A local time-resolved near-field investigation is crucial for a detailed understanding of all of the dynamic processes involved in such a composite device. Also in nonlinear optics, time-resolved near-field investigations are highly beneficial. For example, self-phase modulation or soliton formation can be monitored while the light propagates. How pulses evolve while undergoing a nonlinear interaction with, for example, a nanostructure would be a fascinating topic for a time-resolved near-field investigation from both an academic and an engineering point of view. The relevant time scale in such a study is usually in the femtosecond domain. This poses a challenge in near-field microscopy, since most NOMs map a time-averaged optical field in a nanostructure. Time-resolved microscopy with such a system would be limited by the frame rate of the microscope; given the typical acquisition time of near-field microscopy, this would result in a time resolution of several minutes.

Time-resolved experimental investigations can be performed using high-speed electronics. Fast electronics may be able to record data up to the nanosecond regime. Specialized optical recording systems could possibly extend this range into the picosecond regime [4]. But it is impossible to record optical signals in the femtosecond range only with electronic means. The only option available on this timescale is to detect optical signals using other optical signals. The most common approach to obtaining femtosecond time-resolved data in near-field microscopy is to incorporate the scanning setup in an interferometer. In Section 7.2, the principles

of the heterodyne interferometer are discussed. The technique is applied in Section 7.3 to find the phase and group velocity of light propagating through a ridge waveguide. The effect that very strong dispersion has on the tracking of pulses with a near-field microscope is discussed in Section 7.4, both analytically and using a series of measurements on a PCW.

7.2 Heterodyne Interferometry

A practical approach to using a near-field microscope with an interferometer is to place the microscope including the sample in one branch of a Mach-Zehnder interferometer [5, 6]. In order to explain time-resolved near-field experiments, it is useful to review the principles of the interferometer. Therefore, the basic properties are introduced, including a discussion on the requirements on light sources in the interferometric setup.

7.2.1 Mach-Zehnder Interferometer

Figure 7.1 schematically depicts a Mach-Zehnder interferometer with a microscope integrated. The incoming light is split into two branches—the signal branch and the reference branch. The signal branch of the interferometer contains the photonic structure under investigation and the near-field microscope. In the reference branch, the light propagates through the air. A small portion of the light in the structure is picked up by the near-field probe and mixed with the light from the reference branch. When the light of the two branches is mixed at the second beam splitter, the detector registers an interference signal. The intensity I_D on the detector will therefore be

$$I_D(t) = \varepsilon_0 c\{|E_R(t)|^2 + |E_S(t)|^2 + 2|E_R^*(t)E_S(t)|\} \tag{7.1}$$

where ε_0 and c are the permittivity of free space and the speed of light in vacuum, respectively. E_R and E_S denote the electric field in the reference branch and signal branch, respectively. For monochromatic laser light, the amplitude $|E|$ is constant in time. Equation 7.1 can then be simplified to

$$I_D = \varepsilon_0 c\{|E_R|^2 + |E_S|^2 + 2|E_R||E_S|\cos(\Delta\phi)\} \tag{7.2}$$

In this equation, $\Delta\phi$ denotes the phase difference between the fields. There are three terms in Equation 7.2. The first two are the intensities of the light in the two branches and are not phase-sensitive. The last term, however, mixes the two fields and is called the interference term. This is an advantage of the interferometric approach: The intensity from the probe ($\varepsilon_0 c|E_S|^2$) is usually very weak, but in the interference term, the weak field from the signal branch is amplified by the strong field of the reference light. This allows the measurement of time-averaged intensities in the signals branch down to the femtoWatt regime.

If the near-field probe is moved to a different position on the surface of the sample, the optical path length of the signal branch changes. When the optical path from probe to mixing point remains the same (e.g., by using a fiber), only the path through the sample increases in length. Due to this change in length, the phase in

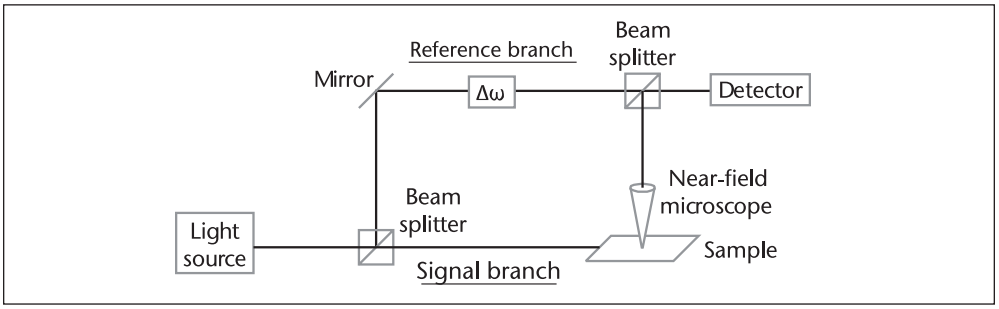

Figure 7.1 Schematic representation of a near-field setup incorporated into a Mach-Zehnder interferometer. The incoming light is split into two branches—denoted signal branch and reference branch. In the signal branch, the light is coupled into a photonic structure and picked up by a near-field probe. The signal light and the reference light are mixed interferometrically with the second beam splitter, and the interference between them is detected. In a heterodyne interferometer, the optical frequency of the light in the reference branch is shifted by $\Delta\omega$ so that the interference with the signal light yields a time-modulated interference signal on the detector.

the signal branch will change accordingly, leading to a change in $\Delta\phi$, which results in a change of the interference signal.

Our goal is to perform a time-resolved investigation of light in a photonic structure. Not surprisingly, this can be achieved with the same interferometric setup. When using Fourier-limited (see Section 7.2.3) laser pulses, the detector signal is

$$V_D(\tau) = \frac{C_D \varepsilon_0 c}{T} \int_0^T \mathrm{d}t \, \{|E_R(t)|^2 + |E_S(t+\tau)|^2 + 2|E_R(t)||E_S(t+\tau)|\cos(\Delta\phi(\tau))\} \quad (7.3)$$

with C_D the constant that describes the conversion of optical intensity to an electronic signal of the detector. Since the integration time of the detector T is usually much larger than the repetition rate of the laser, individual pulses are not detected. τ denotes the time difference in traversing the reference branch compared to the signal branch. The contribution of the interference term is maximal when the pulses in the signal and reference branches traverse the interferometer in the same time. Typically, to have a significant interference effect, the time difference τ must be, at most, in the order of the laser pulse duration ($\sim$ 100 fs).

In summary, if the position of the near-field probe on the surface of the sample is changed, the optical path length also changes. As discussed previously, the resulting interference signal will change due to differences in relative phase $\Delta\phi$. At larger τ, the interference term also changes since the temporal overlap of the pulses at the detector is changed.

7.2.2 Lock-in Detection

In most experimental setups, the frequency of the reference beam is intentionally slightly shifted with respect to the frequency of the incoming laser beam. In that case, the voltage of the detector for Fourier-limited pulses becomes

$$V_D(\tau) = C_D \varepsilon_0 c \langle|E_R|\rangle^2 + \langle|E_S|\rangle^2 + \frac{1}{T}\int_0^T \mathrm{d}t \, 2|E_R(t)||E_S(t+\tau)|\cos(\Delta\phi(\tau) + \Delta\omega t)\} \quad (7.4)$$

The frequency shift $\Delta\omega$ is usually in the kHz range, and its period is longer than the integration time T of the detector. The interference of two beams of light with a slightly different optical frequency results in a time-modulated detector signal with a frequency of $\Delta\omega$. The modulated signal can be readily detected with a lock-in amplifier (LIA). The output of the LIA contains only the interference term in Equation 7.4. The LIA has a double output. One output ($V_{LIA,\cos}$) contains the cosine of the phase difference, as follows:

$$V_{LIA,\cos}(\tau) = 2C_{LIA}C_D\varepsilon_0 c\cos(\Delta\phi(\tau))\frac{1}{T}\int_0^T \mathrm{d}t\,|E_S(t+\tau)\|E_R(t)| \tag{7.5}$$

The other output ($V_{LIA,\sin}$) is shifted by 90 degrees in phase and therefore gives the sine of the phase with the same amplitude as the cosine contribution:

$$V_{LIA,\sin}(\tau) = 2C_{LIA}C_D\varepsilon_0 c\sin(\Delta\phi(\tau))\frac{1}{T}\int_0^T \mathrm{d}t\,|E_S(t+\tau)\|E_R(t)| \tag{7.6}$$

The combination of the two signals gives the complex phase evolution by:

$$\begin{aligned} V_{complex}(\tau) &= V_{LIA,cos} + iV_{LIA,sin} \\ &= 2C_{LIA}C_D\varepsilon_0 c\,\mathrm{e}^{i\Delta\phi(\tau)}\frac{1}{T}\int_0^T \mathrm{d}t\,|E_S(t+\tau)\|E_R(t)| \end{aligned} \tag{7.7}$$

In this equation, the phase difference $\Delta\phi(\tau)$ depends on the difference in optical path length of the branches and therefore shows the same evolution as the actual phase inside the photonic structure $\phi(z)$ as a function of position z. The cross-correlation of the fields amplitudes (the integral) is closely related to the actual field amplitude $E_{sig}(t)$, as is discussed in Section 7.3.3. In fact, as a function of τ, the shape of the cross-correlate qualitatively has the same shape in time as the actual pulse in the signal branch at the position of the probe. The amplitude of the interference signal (closely related to the actual E-field amplitude) is simply $|V_{complex}|$ and the phase is $\arg(V_{complex})$.

7.2.3 Light Source Requirements

The preceding treatment assumes a source of pulsed laser light since the assumption relates more to the intuition. However, only the temporal coherence of the light source matters for the time-resolved imaging. As such, a noncoherent light source (e.g., a broadband LED or an incandescent lamp) also can be used instead of a pulsed laser system.

This can be understood by evaluating Equation 7.1 again.

$$I_D = \varepsilon_0 c\{|E_R|^2 + |E_S|^2 + 2|E_S^* E_R|\} \tag{7.8}$$

As explained in Section 7.2, a heterodyne interferometric experiment ensures that only the interference term is detected. So

$$V_{LIA}(\tau) = 2C_{LIA}C_D\varepsilon_0 c\frac{1}{T}\int_0^T \mathrm{d}t\,E_R^*(t)E_S(t+\tau) \tag{7.9}$$

This equation describes the output of the LIA and is proportional to the cross-correlate of the field in the signal branch and the reference branch. Assuming that a noncoherent light source with a constant amplitude is used, the interference will tend to zero when τ becomes much larger than the coherence time of the light source (e.g., when the optical path length of the two branches differs significantly). The cross-correlation between the reference and signal light can be rewritten as a multiplication in the spectral domain:

$$V_{LIA}(\tau) = 2C_{LIA}C_D\varepsilon_0 cF^{-1}\{E_R^*(\omega)E_S(\omega)\} \tag{7.10}$$

Here F^{-1} denotes the inverse Fourier transform, and $E_R(\omega)$ and $E_S(\omega)$ may be complex. Equation 7.10 shows that to obtain a signal on the LIA (V_{LIA}), there must be spectral overlap between the light in the reference branch and the signal branch. This can be described in greater detail by separating the amplitudes and arguments of the spectra:

$$V_{LIA}(\tau) = 2C_{LIA}C_D\varepsilon_0 c\, F^{-1}\{A_S(\omega)A_R(\omega)e^{i(\gamma_S(\omega)-\gamma_R(\omega))}\} \tag{7.11}$$

In this equation, the spectral amplitudes are given by $A_R(\omega)$ and $A_S(\omega)$ and are real. The arguments $\gamma_R(\omega)$ and $\gamma_S(\omega)$ determine the temporal shape of the light. When $\gamma = 0$, the light is so-called Fourier-transform-limited. That indicates that the light consists of pulses, which are maximally compressed in time: Their width in time is determined by the Fourier transform of the spectrum.

In Equation 7.11, the exponent contains the difference in accumulated dispersion $\gamma_S - \gamma_R$. The argument $\gamma_S - \gamma_R$ will be nonzero if the dispersion in the two branches is not balanced. Let's assume that the dispersion in the two branches is balanced so that the complex exponential in Equation 7.11 yields unity. The only contributions left to the cross-correlation result (V_{LIA}) come from the spectra of the reference and signal light. Given this result, it does not matter what type of source produces the spectra. A broadband LED can give exactly the same result in an interferometric measurement as a femtosecond pulsed laser source. For the interferometric experiment, it does not matter what source is used since the cross-correlation V_{LIA} depends only on the spectrum.

When light propagates through a medium, it acquires a dispersion of $\gamma(\omega) = zk(\omega)$, where z is the propagation length through the dispersive medium and $k(\omega)$ is the dispersion relation of the material. The dispersion relation can be expanded as a Taylor series around a central frequency ω_0:

$$k(\omega) = \beta_0 + \beta_1(\omega - \omega_0) + \frac{\beta_2}{2}(\omega - \omega_0)^2 + \frac{\beta_3}{6}(\omega - \omega_0)^3 + \ldots \tag{7.12}$$

The propagation constants β_n describe the propagation of the light through a medium, where β_0 is the inverse of the phase velocity ($1/v_\phi$) and β_1 is the inverse of the group velocity ($1/v_g$). The higher-order terms are commonly used in describing pulse dispersion in, for example, fibers. The terms β_2 and β_3 describe the group velocity dispersion (GVD) and third-order dispersion (TOD), respectively. In each branch of the interferometer, the preceding equation describes the propagation of light, given that the medium through which the beam propagates has a uniform dispersion relation. Balancing the dispersion in the branches can be achieved with various materials, with different dispersive properties and different lengths, as long as the

accumulated dispersion is equal. The most straightforward approach is to build a symmetric interferometer where the branches of the interferometer contain exactly the same components. This then leaves, in principle, the unknown dispersion of the sample as the only source of imbalance, which is the desired situation.

For simplicity, the use of laser pulses is assumed unless otherwise indicated. The pulsed laser is easy to relate to, while, in fact, the same results will be obtained if a nonpulsed light source is used, provided it has the same spectrum.

7.3 Application in Near-Field Microscopy

In the following section, the interferometric setup will be used in a near-field measurement in order to characterize a photonic structure. The individual elements of the near-field setup are discussed, as is a measurement of pulses in a ridge waveguide and how to recover the phase and group velocities with the pulse tracking near-field microscope.

7.3.1 Setup Considerations

A number of groups have demonstrated a heterodyne version of the interferometric near-field microscope [7–11]. The microscopes can be separated into two types: scattering-type microscopes [8, 11] and collection-type, fiber-probe microscopes [7, 9, 10]. Scattering-type microscopes uses a sharp point to scatter light from the structure in all directions, while in collection-type, fiber-probe microscopes, light tunnels from the structure into a subwavelength tapered fiber. In principle, both types can be used for time-resolved and phase-sensitive investigations. In the following, the second type will be described in greater detail. Most groups use a femtosecond laser system as a light source. This has the advantage of a well-collimated beam with high average power and a high spatial coherence. Figure 7.2 shows a typical setup.

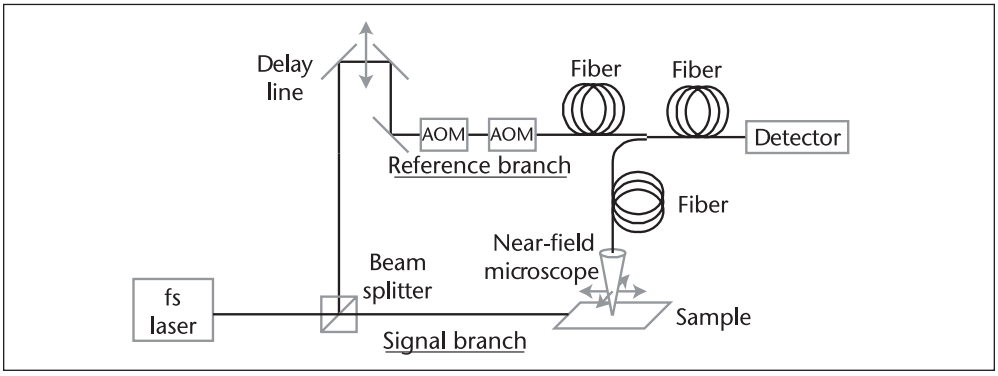

Figure 7.2 Schematic representation of a heterodyne near-field setup. The incoming femtosecond pulses are split into two branches by a beam splitter. In the signal branch, the light is coupled into a photonic structure and picked up by a fiber-optic near-field probe, which can be scanned over the surface of the sample. The light in the reference branch also is coupled into a fiber. The signal light and the reference light are recombined by a fiber coupler and transported by a fiber to the detector. The optical frequency of the light in the reference branch is shifted by two acousto-optic modulators (AOMs) in a crossed configuration. A delay line is included in the reference branch.

The frequency shifting in the reference branch, which is necessary for the heterodyne detection, is achieved by passing the laser beam through two crossed acousto-optic modulators (AOMs). In such a modulator, the incoming wave is Doppler-shifted by an ~ 80 MHz acoustic wave. Two AOMs are used in a crossed configuration to obtain an overall shift of the frequency of tens of kHz, which is the frequency difference in the two modulators. The interference of the original wave and the frequency shifted wave results in a time-modulated interference signal as described in Section 7.2.2. Note that the specific use of AOMs as described here may lead to some confusion. A traveling-wave AOM accomplishes a shift in the frequency of the light without inducing an extra time dependence of the optical amplitude, which a standing-wave modulator induces.

Using a tapered fiber probe is advantageous in that the distance from probe apex to mixing point does not change during scanning. Therefore, it also is convenient to use fiber optics in the rest of the optical setup. The dispersion in these fibers generally is not negligible. The same holds for the dispersion caused by the AOMs. This is not detrimental to the measurements, however, as long as the dispersion in the two branches is balanced, as discussed in Section 7.2.3. One method for balancing the dispersion is to use the same length of optical fiber in each branch and to distribute the two AOMs over the two interferometer branches.

7.3.2 Pulse Tracking in a Waveguide

In a near-field experiment, a probe is scanned over the surface of a sample. When the detection path after the near-field probe is purely fiber-optic, the optical path length, from probe apex to mixing point, does not change as the probe is scanned over the surface of the sample. However, the distance over which the light propagates in the sample until the light reaches the probe may change. As a result, the delay time τ between the two branches of the interferometer will change. At small changes of τ (e.g. equivalent to a few optical cycles), consecutive constructive and destructive interference can be observed at the detector. Note that the amplitude in the reference branch is, in general, much higher than in the signal branch. Therefore, the intensity of the interference will not reach zero. At larger changes of τ, of the order of the coherence time of a pulse, the effective temporal overlap of the signal pulse and the reference pulse becomes smaller. This results in a reduction of the interference amplitude.

In a near-field measurement, the delay time τ continuously changes when the probe is scanned. Therefore, a map of the interference will appear like a snapshot of the propagating pulse: The interference fringes resemble the (co-)sine of the phase of the E-field, and the interference envelope resembles the pulse envelope in space.

7.3.3 Determination of the Phase Velocity

A pulse tracking near-field measurement on a ridge waveguide as a model photonic structure is discussed next to demonstrate the working of the heterodyne interferometric setup. The waveguide under investigation is a 2.08 μm wide waveguide created by etching 3.5 nm deep in a 190 nm thick layer of Si_3N_4 on top of a SiO_2 layer. This waveguide can support two modes, one with the E-field oriented parallel to the slab and one with the E-field pointing out-of-plane. Each of the two modes has a different effective refractive index.

Since the phase of the light in the structure can be recovered with the interferometric near-field microscope and the optical frequency is known, the phase velocity can be measured in these waveguides. The signals $V_{LIA,cos}$ and $V_{LIA,sin}$ are depicted in Figures 7.3(a) and 7.3(b), respectively. The colorscale indicates the root-mean-square value of the heterodyne detector signal. Note that the interference signal is in the order of $\pm$ 1 mV, while the detector signal from only the reference light was 520 mV. The intensity in the reference branch is much higher than the intensity picked up in the signal branch. The intensities in each branch can be estimated using Equation 7.2. The power in the reference branch is found to be 0.1 μW, while the signal picked up by the near-field probe is approximately 0.1 pW; the intensity in the signal branch is 6 orders of magnitude lower than in the reference branch. The heterodyne detection scheme makes that the signal is amplified by the reference light and therefore can readily be detected.

In Figure 7.3, the waveguide is oriented along the z-direction and centered around $x = 5$ μm. A clear modulation pattern is present along z, which is strongest in the center of the waveguide and decreases away from $x = 5$ μm. The modulation is caused by the cosine term in Equation 7.5; the optical path length changes due to the scanning of the probe, resulting in consecutive constructive and destructive interference. The distance between two consecutive maxima is determined by $\Delta\phi$, the phase difference between the light in the reference branch and the signal branch. So when $\Delta\phi$ changes by 2π, the same signal is found, providing that the amplitude is constant. The optical path of the reference branch is constant, so the change in phase is due to

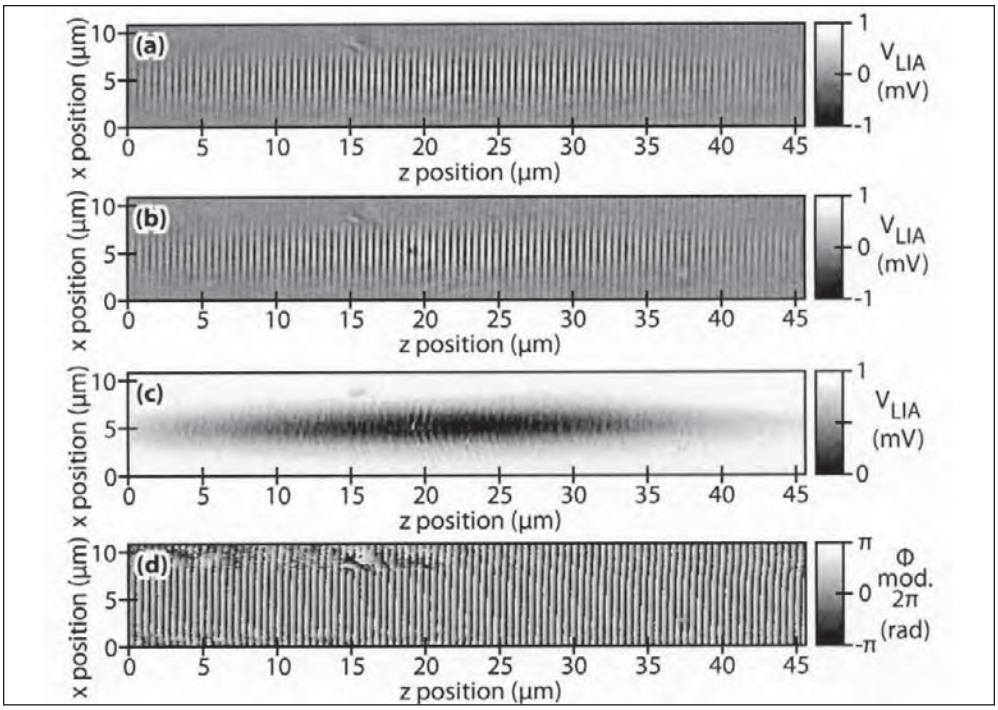

Figure 7.3 Results of a heterodyne near-field experiment on a femtosecond pulse in a ridge waveguide. (a) Signal from the lock-in amplifier representing the real part of the interference signal as in Equation 7.5. (b) Corresponding imaginary part of the interference signal as in Equation 7.6. (c) Amplitude of the interference calculated by evaluating the measurements in (a) and (b). (d) In a similar fashion, the phase, modulo 2π, also can be recovered.

the light in the signal branch only. A shift of 2π corresponds to a full cycle of the optical field in the structure; therefore, the distance between the two maxima is the same as the wavelength λ of the light in the waveguide.

The modulation pattern does not change away from the center of the waveguide in the direction perpendicular to the propagation (i.e., at larger or smaller x). This proves that the phase of the light in the waveguide does not change perpendicular to the propagation direction as is expected for a zero-th order propagating mode. The same holds for the second LIA output channel, proportional to the sine of $\Delta\phi$ (see Figure 7.3(b)). This appears to be the same image as in Figure 7.3(a), but the phase is shifted by $\pi/2$.

Now the real and imaginary part of $V_{complex}$ are recovered, as described in Equation 7.7. The amplitude of the interference can be calculated by taking the absolute value of $V_{complex}$. The amplitude of the interference is depicted in Figure 7.3(c). The highest amplitude is found in the center of the waveguide, along $x = 5\ \mu$m. The amplitude decays at larger and smaller x-positions. Note that the amplitude pattern is wider than the 2 μm wide waveguide. This is the result of weak confinement due to the small effective index difference between waveguide and the Si_3N_4 slab.

The interference amplitude decays significantly at small or large z-values, which gives the pattern shown in Figure 7.3(c) the appearance of a pulse in space. At small or large z-values, the time delay corresponding to the path length difference (τ) in the interferometer branches is larger than the coherence time of the light used. Therefore, the interference amplitude is lower at small and large z-values. (See Equation 7.7.) To what extent this pattern is an actual snapshot of a propagating pulse is discussed in Section 7.4.1.

In a similar fashion as the amplitude, the phase of the light can be extracted from the measurements by taking the argument of $V_{complex}$. The phase modulo 2π is shown in Figure 7.3(d). When a line is followed from left to right, the color changes gradually from white to black: The phase difference decreases. From $-\pi$, the phase jumps to π, which is represented by a color change from black to white.

Line traces of the measurement data are shown in Figures 7.4(a) and 7.4(b), showing the details of the amplitude ($|V_{LIA,complex}|$) and the real part of the lock-in signal ($\mathrm{Re}\{V_{LIA,complex}\} = V_{LIA,cos}$) along the line $x = 5.1\ \mu$m, respectively. The amplitude data show a near Gaussian shape. A slight modulation is visible on the amplitude data, which may be due to interference of the propagating light with light that is scattered out of the waveguide at imperfections or dust particles.

As mentioned before, the modulation of the $V_{LIA,cos}$ signal corresponds to the oscillations of the field inside the waveguide. So the distance between two consecutive maxima gives the wavelength of the light in the waveguide. To find the effective index of the light in the waveguide, the $V_{complex}$ signal is Fourier-transformed along the z-direction to recover the periodicity of the E-field oscillations. The result is depicted in Figure 7.4(c), in which the amplitude of the transformed data is given as a function of the wavevector k_z of the light (or $2\pi/\lambda$). A clear peak is present at $k_z = 13.3\ \mu\mathrm{m}^{-1}$, corresponding to a wavelength of 472 nm. Since the central wavelength of the laser pulses used is 810 nm in vacuum, the effective refractive index is 1.71, corresponding to a phase velocity (v_ϕ) of $1.75 \cdot 10^8$ m/s. The width of the peak in Figure 7.4(c) is determined by the spatial extent of the measured interference.

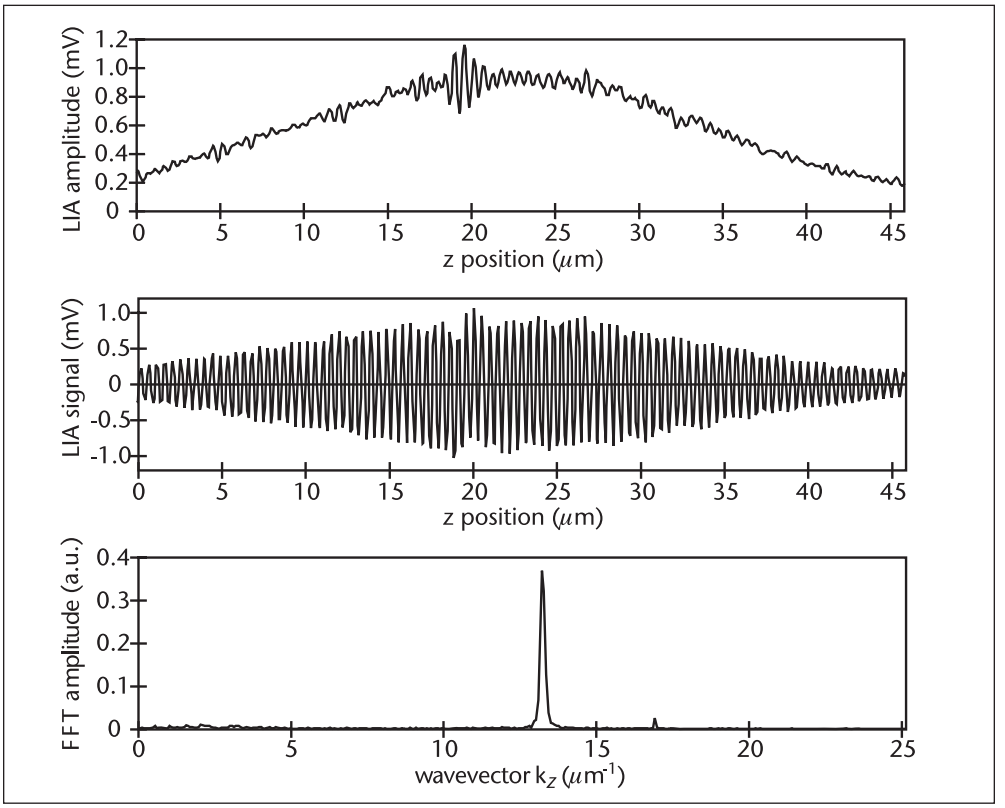

Figure 7.4 Details of the measurement shown in Figure 7.3. (a) Interference amplitude along $x = 5.1$ μm. (b) Real part of the complex measurement data showing the interference fringes due to scanning the probe over the waveguide. (c) Fourier transform of the complex measurement data showing the periodic components present in (b).

The preceding exercise for determining the wavevectors is a very useful tool for determining the optical properties of integrated optical structures. By repeating the process for different optical frequencies, the dispersion relation $k(\omega)$ is recovered. In periodically nanostructured materials (e.g.. PhCs), the relation between wavevector and frequency can become very complex [12]. This complexity can result in interesting optical properties, such as photonic bandgaps or slow-light propagation [13]. With a phase-sensitive near-field microscope, the fundamental properties of photonic structures can be recovered with unprecedented accuracy.

7.3.4 Determination of the Group Velocity

Other than the phase velocity, which is determined in the previous section, a second velocity of crucial importance is present in nanostructured devices: the group velocity. This velocity (v_g) describes how fast a wavepacket, such as a laser pulse, travels through a dispersive material. The group velocity is defined as follows:

$$v_g \equiv \frac{\mathrm{d}\omega}{\mathrm{d}k} \tag{7.13}$$

If the wavevector k is not linearly proportional to the optical frequency ω, the group velocity may be different from the phase velocity. This does not require nanostructuring of materials. The intrinsic dispersion of materials is already sufficient to cause a difference in phase and group velocity of 1% for quartz and 11% for silicon at a vacuum wavelength of 810 nm.

The interferometric near-field microscope allows tracking of pulses as they propagate through a photonic structure. This gives insight into the dynamic processes inside a photonic structure [14]. As a demonstration of the dynamics of pulses and how to track their propagation in a structure, the determination of the group velocity of a femtosecond pulse traveling through a simple model system is demonstrated: a conventional ridge waveguide.

In Figure 7.3, a measurement of a laser pulse in a ridge waveguide was presented. In fact, this measurement is one of a series of measurements. In the complete set of measurements, a series of scans over the surface of the waveguide is performed. Between successive measurements, the length of the reference branch was changed by moving the delay line in the setup (see Figure 7.2).

When the reference branch increases in length, the total length of the signal branch also must increase in order to achieve the maximum interference amplitude. The length of the signal branch can only become larger by changing the position of the near-field probe to a position further along the waveguide. As a result, each consecutive measurement for increasing lengths of the reference branch will result in a map of the interference amplitude, where the maximum of the interference envelope is at a different position in the waveguide.

A series of measurements, each with a different position of the delay line, is depicted in Figure 7.5. It appears to be a series of snapshots of the propagating pulse at different times. The delay time at which the measurement is started is defined as zero delay time. At delay time 192 fs, the interference amplitude is maximal close to $z = 5\ \mu$m: The optical path lengths of the reference branch and signal branch are equal at $z = 5\ \mu$m.

As the conversion of the reference branch length changes, a change in time delay is readily made; the changes in position can be tracked in time. In the waveguide, the pulse envelope moves with the speed of the group velocity. (Note that the phase moves with the phase velocity.) By evaluating the position of the maximum interference amplitude in the measurements, the group velocity can be found.

A Gaussian envelope is fitted to the interference amplitudes, and the center position of the envelope is determined. The center positions as a function of delay time are depicted in Figure 7.5(g). A linear dependence is found for the position of the pulse as a function of the delay time. The slope corresponds to $1.44 \cdot 10^8$ m/s, which is the group velocity of the pulse in the waveguide. The group index n_g is 2.08, which is considerably different from the effective index (for the phase) of 1.71.

The ridge waveguide has a fairly simple structure, which has a number of advantages for the analysis in this section. For example, the pulse retains it shape during propagation through the waveguide. Also, the pulse spectrum in the waveguide is the same as in the reference branch and remains that way. When that is not the case, care must be taken when drawing conclusions from the interferometric data. The challenges that arise if the dispersion in the structure is very large (and therefore deforms the pulse significantly) are addressed in the next section.

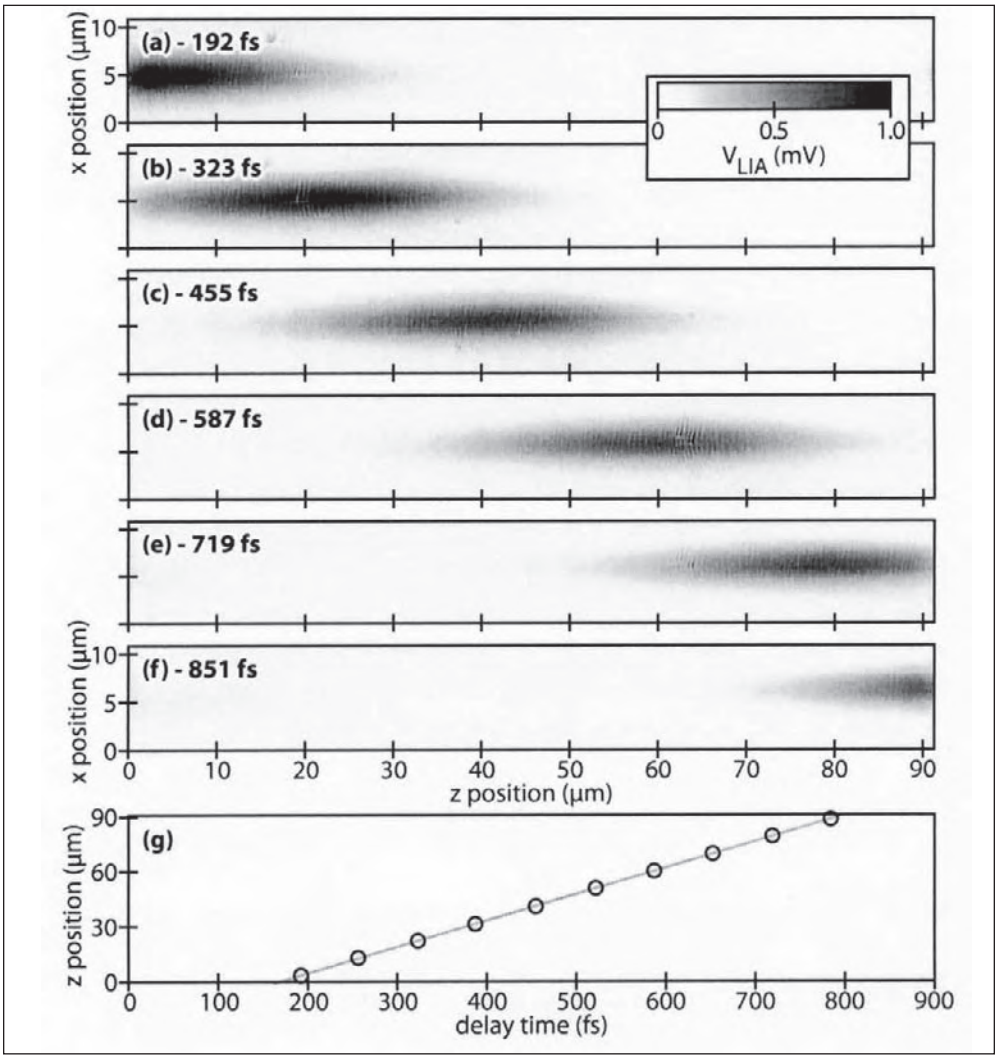

Figure 7.5 A series of pulse tracking measurements. (a–f) Amplitude of the lock-in signal of the same area ($91.6 \times 10.9\,\mu m^2$) of ridge waveguide. Between each measurement, the optical length of the optical delay line is increased by 19.8 μm, corresponding to a time delay of 132 fs. (g) Position of the center of the interference peak as a function of delay time. The gray line shows a fit to the measurements, corresponding to a group index of 2.08.

7.4 Pulse Tracking in Dispersive Media

In the previous section, the phase and group velocity were recovered. The propagation of light is governed by the dispersion relation $k(\omega)$, which can be expanded in a Taylor series as described in Equation 7.12. The first two terms of this expansion describe the phase velocity and group velocity. A strategy to find the first two values was described in the previous sections. To find the higher-order values, the analysis requires additional effort. This section starts with a description of the effect of GVD in near-field pulse-tracking experiments; subsequently, third and higher orders of dispersion are addressed.

7.4.1 The Influence of Group Velocity Dispersion

GVD causes a pulse to broaden in time as it propagates through a dispersive medium. This effect can be significant in any (solid) material; for example, in fiber-optic communication, pulses must be compressed after a few kilometers of propagation. Also, at a much smaller scale (within the scan area of a near-field microscope), this broadening may occur. The effect of GVD on interferometric near-field measurements still can be described analytically.

Assume that the pulse in the reference branch is Fourier transform-limited. The electric field of a Fourier-limited Gaussian pulse with a center frequency ω_0 is as follows:

$$E_{ref}(t) = A_{ref} e^{i(\omega_0 + \Delta\omega)t - t^2/\sigma^2} \tag{7.14}$$

The peak amplitude of the pulse in the reference branch is denoted by A_{ref}, and the width of the Gaussian pulse profile is determined by σ. The FWHM is related to σ by $FWHM = 2\sigma\sqrt{\ln 2}$. Since the frequency of the light in the reference branch is shifted, the $\Delta\omega$ appears again. The equivalent in the frequency domain is obtained via a Fourier transformation:

$$\widetilde{E}_{ref}(\omega) = \frac{A_{ref}\sigma}{\sqrt{2}} e^{-\frac{1}{4}(\omega - \omega_0 - \Delta\omega)^2\sigma^2} \tag{7.15}$$

The pulse in the signal branch is initially Gaussian, but after traveling through a portion of the photonic structure, it acquires some dispersion $k \cdot z$. Therefore, the electric field of the light is as follows:

$$\widetilde{E}_{sig}(\omega, z) = \frac{A_{sig}\sigma}{\sqrt{2}} e^{-\frac{1}{4}\sigma^2(\omega - \omega_0)^2} e^{ik(\omega)z} \tag{7.16}$$

Note that this is the E-field as a function of frequency, not time. To elucidate the effect of GVD only, the higher-order terms—β_3 and higher in the Taylor expansion of $k(\omega)$ (see Equation 7.12)—are taken to be negligible. By substituting the expansion for $k(\omega)$, Equation 7.16 becomes

$$\widetilde{E}_{sig}(\omega, z) = \frac{A_{sig}\sigma}{\sqrt{2}} e^{iz\beta_0 + iz\beta_1(\omega - \omega_0) + \left[\frac{1}{2}iz\beta_2 - \frac{1}{4}\sigma^2\right](\omega - \omega_0)^2} \tag{7.17}$$

At the detector, the interferometrically mixed signal from the reference branch and signal branch is detected. This signal is averaged for a characteristic time T. For the detected signal by the LIA, this yields the following cross-correlation of the fields:

$$V_{LIA,complex}(\tau, z) \propto \int_T dt\, E_{ref}(t + \tau) E_{sig}(t, z) \tag{7.18}$$

There are two ways to change the length of the branches: by moving the delay line in the reference branch (see Figure 7.2) or by changing the position of the probe. These two methods are described in the preceding equation by a change in τ or z, respectively. The detector signal is the convolution of the field in the reference

branch and the signal branch. The equivalent in the frequency domain is a multiplication of the fields:

$$V_{LIA,complex}(\tau,z) \propto F^{-1}\left[\widetilde{E}_{ref}(\omega)\widetilde{E}_{sig}(\omega,z)\right] \tag{7.19}$$

The following analysis will focus on the shape of the pulse envelope. Therefore, the phase of the interference signal will not be evaluated. As described in Equation 7.18, the amplitude of the complex measured signal from the LIA is proportional to the amplitude of the cross-correlated fields.

The two fields from the reference and signal branches in Equations 7.15 and 7.17 are multiplied to yield the following:

$$\widetilde{E}_{ref}(\omega)\widetilde{E}_{sig}(\omega,z) = \frac{A_{sig}A_{ref}\sigma^2}{2} e^{i\beta_0 z - \frac{1}{4}\sigma^2\Delta\omega^2 + (i\beta_1 z + \frac{1}{2}\sigma^2\Delta\omega)(\omega-\omega_0) + (\frac{1}{2}i\beta_2 z - \frac{1}{2}\sigma^2)(\omega-\omega_0)^2} \tag{7.20}$$

The signal of the LIA is found by taking the inverse Fourier transform of this equation:

$$V_{LIA,complex}(\tau,z) \propto \frac{A_{ref}A_{sig}\sigma^2}{2\sqrt{\sigma^2 - i\beta_2 z}} e^{-\frac{1}{4}\sigma^2\Delta\omega^2 + i\beta_0 z - i\omega_0\tau - \frac{(\tau - i\Delta\omega\sigma^2/2 - \beta_1 z)^2}{2\sigma^2 - 2i\beta_2 z}} \tag{7.21}$$

With the assumptions that $\Delta\omega \ll 1/\sigma \ll \omega_0$ and the timescale of τ is much larger than $\Delta\omega\sigma^2$, Equation 7.21 can be simplified to

$$V_{LIA,complex}(\tau,z) \propto \frac{A_{ref}A_{sig}\sigma^2}{2\sqrt{\sigma^2 - i\beta_2 z}} e^{i\beta_0 z - i\omega_0\tau - \frac{(\tau - \beta_1 z)^2}{2\sigma^2 - 2i\beta_2 z}} \tag{7.22}$$

In this equation, τ represents the delay time set by the delay stage in the reference branch and z is the propagation distance through the dispersive medium. Both variables change the phase of the measurement signal. The phase increases as the delay time increases, while the phase decreases as the distance z increases. The third term in Equation 7.21 also contains a complex value and describes the frequency chirp of the detected interferogram.

To determine the envelope of the interference, the absolute value of $V_{LIA,complex}(\tau,z)$ is calculated. Using Equation 7.21, this yields the following:

$$|V_{LIA,complex}(\tau,z)| \propto \frac{A_{sig}A_{ref}\sigma^2}{2\sqrt[9]{\sigma^4 + \beta_2^2 z^2}} \exp\left\{-\frac{\sigma^2(\tau-\beta_1 z)^2}{2\sigma^4 + 2\beta_2^2 z^2}\right\} \tag{7.23}$$

The term in the exponent contains $\tau - \beta_1 z$. This ensures that the movement of the interference envelope in space as a function of delay time has the same group velocity ($v_g \equiv 1/\beta_1$) as the actual propagating pulse in the photonic structure. This also allows a measurement of the group velocity, as demonstrated in Section 7.3.4.

Assuming that the propagation distance z through the photonic structure is small, the factor before the exponent reduces to $A_{sig}A_{ref}\sigma/2$. This implies that the signal level increases with an increase of the pulse width σ. This can be understood by realizing that the amplitudes A_{sig} and A_{ref} are the peak amplitudes. If the width increases, the energy in each pulse increases, as does the time-averaged intensity and signal level. On the other hand, if the pulse in the signal branch is broadened due to dispersion, the factor $\beta_2 z$ is no longer zero and the signal level goes down.

The term in the exponent describes the pulse shape. In the absence of dispersion, the term reduces to $\tau^2/(2\sigma^2)$. Compare this to Equation 7.14, which describes the field of a Gaussian pulse. The width of the interference envelope is always a factor of $\sqrt{2}$ broader than the actual width of the E-field. In fact, the width of a laser pulse is usually expressed as the width of the intensity of a pulse. In that case, the interference width is, in the absence of dispersion, twice as broad as the intensity width of the used laser pulses. In the case when dispersion is nonnegligible, $\beta_2 z$ is nonzero, the pulse broadens, as does the interference width.

In the experiments on the ridge waveguide as described in Section 7.3.2, femtosecond laser pulses were used with a FWHM of the intensity spectrum of 9 nm, which corresponds to a FWHM of the pulse intensity in a time of 107 fs. In a medium with a group index of 2.08 (from measurement), this results in a pulse width in a space of 15 μm. Using Equation 7.23, this results in an interference envelope that is twice as broad as the intensity width. The interference width in Figure 7.4(a) is 31 μm, which corresponds perfectly to the expected $2 \times 15 = 30$ μm when taking into account the small inaccuracy in the determination of the spectral width. Therefore, the GVD is expected to be low in the ridge waveguide.

7.4.2 The Influence of Higher-Order Dispersion

In the interferometric near-field setup, two methods are used to change the length of the interferometer branches: by the probe position z, which is changed by scanning the probe, and by the delay time τ by moving the delay line. These also are the two ways of performing a time-resolved near-field measurement: either scanning the probe (change z and keep τ fixed) or scanning the delay line at a fixed position z of the probe and thus changing τ. In the first option, the probe picks up light at various positions of z. The pulse probed at position z may be Fourier-limited, whereas a pulse picked up at a position further along the structure may be significantly dispersed. If the dispersion is very strong, the acquired dispersion at different positions will differ significantly. Therefore, the analysis of a pulse in a structure with strong dispersion becomes more complicated, especially when higher-order dispersion (β_3 or higher) plays a role.

If one is interested in the shape of the pulse or the change of pulse shape upon propagation, it is more suitable to scan the delay line. In this way, the temporal information of the pulse is recovered at a single position. Repeating the experiment at different positions can then reveal the changes in shape of a pulse upon propagation and makes the quantification of the dispersion more straightforward. This will be pursued in this chapter in dealing with a material with very strong dispersion: a PCW.

Figure 7.6(a) depicts a 2-D PhC structure. PhCs are periodic arrangements of dielectric materials with different refractive indices. The periodicity a must be in the order of the wavelength of light. Light propagating in such periodic media experiences a strong modulation of the dielectric constant and therefore behaves differently than in a bulk material [13]. One of the interesting properties is that some wavelengths of light cannot propagate through the material. This is also the case in the 2-D PhC in Figure 7.6(a). However, when a single row of holes is left unperforated in the hexagonal lattice of air holes, it can act as a waveguide.

In the PCW, propagating light is still strongly influenced by the periodic structure alongside the waveguide. The dispersion relation of the PCW is depicted in Figure 7.6(b) for a small range of optical frequencies. The polarization of this mode is

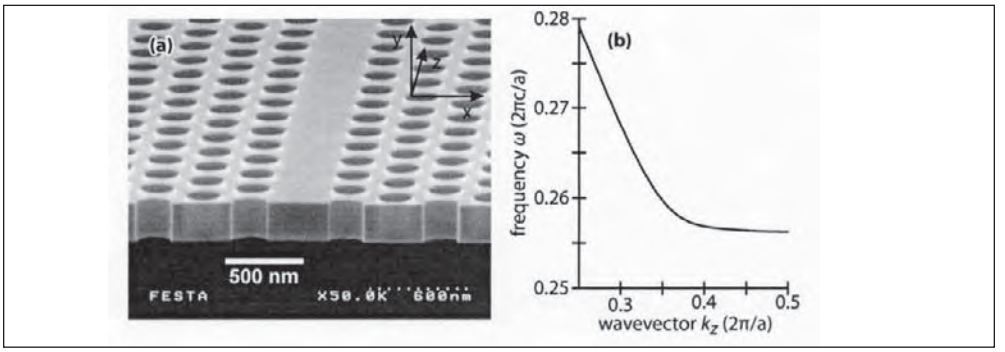

Figure 7.6 (a) SEM image of a PCW. The waveguide consists of one unperforated row of hole in a hexagonal lattice (period $a = 339$ nm) of air holes (radius 113 nm) in a 200 nm thick GaAs membrane. © Optical Society of America [16]. (b) Portion of the dispersion relation for light polarized in the plane of the membrane in the frequency range of 0.25–0.28 in normalized frequency units. The mode shown is confined to the waveguide and has an even symmetry of the electric field.

called TE (as opposed to TM) and has the E-field oriented in the plane of the membrane. One mode is plotted, indicating that only one propagation mode is allowed in the waveguide for this frequency range and polarization. As discussed in Section 7.3.4, the group velocity depends on the slope of the dispersion relation. In the figure, the slope of the curve is relatively steep at high optical frequencies. This steep slope corresponds to a relatively fast propagation mode: in this case $c/5$, with c being the speed of light in vacuum. As the frequency is lowered from 0.28 to 0.257, the group velocity gradually reduces to zero, since the slope of the dispersion relation flattens, until it is horizontal at $k_z = \pi/a$. When the slope is horizontal, the group velocity is zero.

A change of the group velocity must be accompanied by a nonzero GVD: The derivative of the dispersion relation changes; therefore the second-order derivative (GVD) must be nonzero. Since the change in the dispersion relation is very rapid, higher-order derivatives also may play a role. The third-order derivative, the TOD, causes an asymmetric broadening of a pulse as it propagates through the dispersive medium.

The strong dispersion of pulses through the PCW is investigated with the interferometric near-field microscope. To facilitate the analysis, the delay line is scanned; thus, insight is obtained of the pulse shape in time at a fixed position. The shape of the pulse will be investigated; therefore, only the envelope of the interference amplitude is of interest. For a comparison with theory, the absolute value of Equation 7.18 needs to be calculated.

Since the dispersion is very strong near the slow-light frequencies, higher-order dispersive terms also may play a role. Therefore, Equation 7.18 cannot easily be solved analytically. Assuming that the pulse in the reference branch is Fourier-limited, the resulting shape of the interferogram is a qualitative measure for the shape of the pulse in the structure because the interferogram is the field cross-correlate between the reference and signal branches with the reference pulse unchanged for every probe position.

A delay-line scan is performed at six different positions on the PCW, starting at 10 μm distance from the point where the light is coupled in via an objective. The procedure is repeated for five points, equidistantly spaced, with the last position at 116 μm from the start of the waveguide. The results for the optical frequency

of 0.2664 (in normalized units of $2\pi c/a$) are depicted in Figure 7.7(a). In these measurements, it is clear that the interference maximum for each measurement positions "A" up to "F" is at a different delay time. The time delay between two consecutive measurements at different positions is determined by the group velocity as long as the pulse shape does not change significantly from point to point. In this case, the group velocity is $c/5.3$.

The group velocity decreases at the lower optical frequency of 0.2635 and especially at 0.2603 (in normalized units). In Figure 7.7(b), the spacing between consecutive maxima has already increased due to a reduction of the group velocity down to $c/6.6$. Similarly, an even stronger reduction of the group velocity is found at the lowest optical frequency, where the v_g is reduced down to $c/9$.

In addition to a difference in group velocity, a broadening of the interferograms is observed. At $\omega = 0.2664$, the interferogram retains its initial shape, but as the pulses travel further along the waveguide, the interferogram is broadened from approximately 0.36 ps to 0.57 ps at position "F". This broadening is still moderate at this high frequency, but as the frequency is reduced to $\omega = 0.2603$, the pulses experience a much stronger broadening. At the same spatial position ("F"), the FWHM of the interferogram is 2.2 ps. Interestingly, as the pulse has propagated 116 μm, the shape of the pulse has become asymmetric for all frequencies. The largest asymmetry is found in the measurements at $\omega = 0.2603$.

Also, other modes can be recognized in Figure 7.7. Both air-guided light and a TM-polarized mode is detected at $\omega = 0.2664$. These modes are visible as smaller side lobes on the main pulse and can be discriminated by their group velocities.

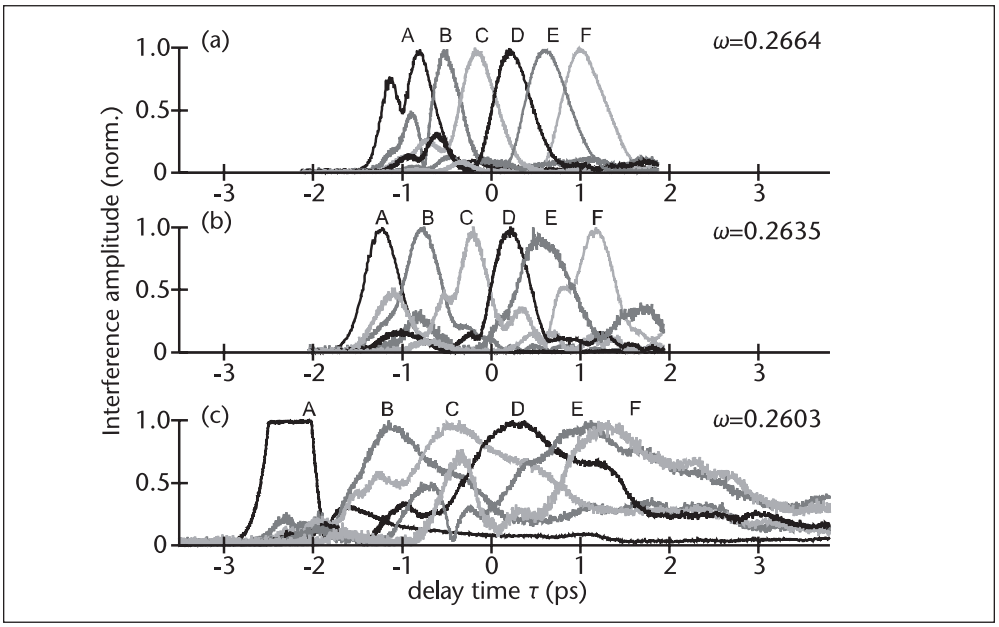

Figure 7.7 Cross-correlation functions of the pulses in reference branch and signal branch of the interferometric setup. At the normalized optical frequencies of 0.2664 (a), 0.2635 (b), and 0.2603 (c), interferograms are measured at six equidistantly spaced points on the waveguide between 10 μm (interferogram A) and 116 μm (interferogram F) from the membrane facet. The interference amplitudes are normalized with respect to their maximum. In the first curve in (c), the detection saturates because at this position, light from the coupling objective is picked up directly. © Optical Society of America [16].

Particularly in the measurement at position "A" at 10 μm from the facet, the air-guided light is relatively strong. This is not surprising since the light is coupled into the structure via an objective that focuses light onto the facet. Since a diffraction-limited spot at these wavelengths is larger in diameter ($\sim 3\ \mu$m) than the membrane thickness (200 nm), such coupling results in some light skimming over the surface of the PCW.

At $\omega = 0.2635$, a mode with the E-field polarized perpendicular to the membrane (TM) is very strong and causes a quasi-interference [15] with the dominant TE-polarized mode. At this frequency, the TM-polarized crystal mode travels at roughly the same group velocity as the TE defect mode. This causes the irregular pulse shapes in the interferograms in the measurement at $\omega = 0.2635$. For an unknown reason, the TM mode is particularly strong in the measurements at this frequency. In the other measurements, its influence is negligible.

To ensure that the effects observed in the measurements are due to higher-order dispersion, the experimental results are compared to simulations [16]. To this end, Equation 7.18 is solved numerically using the full dispersion relation $k(\omega)$ of Figure 7.6. The numerical result describes the interferogram at a specific point on the waveguide and thus could be compared directly to the measurements.

From the theoretical interferograms that fitted our experimental results at $\omega = 0.2603$, the magnitude of the dispersive terms is determined. The GVD is $\beta_2 = -1.1\ \text{ps}^2/\text{mm}$, and the TOD is $\beta_3 = 0.11\ \text{ps}^3/\text{mm}$. Those values are respectively 5 and 6 orders of magnitude higher than those found in fiber optics: Effects that play a role at many kilometers length scale in fibers now occur at tens of microns of propagation distances.

The interferograms obtained with the pulse-tracking near-field microscope are a qualitative representation of the shape of the pulse in the signal branch. The measured interferograms in this section are asymmetrically distorted. However, care must be taken when drawing conclusions from these measurements since the actual measured result is the cross-correlate of the light in the reference branch and the signal branch of the interferometer and may differ significantly from the actual optical field.

7.4.3 Slow-Pulse Propagation with Low Dispersion

The PCW that was studied in the previous section is a promising candidate for highly integrated photonic circuitry. Since some frequencies of light are not allowed to propagate in the crystal region of PhCs, waveguide bends can be very sharp [17], passive filters can be very small [3], and cavities can be fabricated with a low modal volume [18]. For some applications, the dispersive effects discussed in the previous sections are detrimental to the functioning of an actual PhC device. To that end, optical signals, which are a collection of pulses, must retain their shape and not broaden due to dispersion.

To that end, the material must have low dispersion so that the values of β_2, β_3, and higher terms are negligible. In addition, a low group velocity would be advantageous for enhanced light-matter interaction. In a device where nonlinear optical effects are exploited, a slow wave can increase the efficiency significantly [19], which may lead to low-power integrated nonlinear optics. The combination of slow light with low dispersion can be achieved with PCWs. In the literature, a number of

strategies are proposed, for example, by altering the hole radii alongside a PCW [20] or by changing the shape of the holes [21]. A third option, which will be investigated in greater detail, is to vary the width of the waveguide [12]. The pulse tracking near-field microscope will be used to investigate slow-light propagation with low dispersion.

Figures 7.8(a) and 7.8(b) present the PCW under investigation. The waveguide is wider than the one shown in Figure 7.6(a). In this case, the width is two rows of holes instead of one. The air holes with radius 118 nm are etched in a hexagonal lattice in a 240 nm thick Si layer on top of SiO_2. The corresponding dispersion relation for TE-polarized light is depicted in Figure 7.8(c). Multiple modes can be discerned in this figure, denoted A, B, and C. In addition, the magnitude of the wavevectors in bulk SiO_2 is depicted with the dashed gray line. This line is called the light line of SiO_2. All modes of the PCW with wavevectors left of this line can couple from the waveguide to the bulk SiO_2. This is a significant loss channel in PCWs. The modes with wavevectors right of the light line are bound to the waveguide and can propagate without radiative losses.

Based on that information, only two modes propagate with low losses through the waveguide: mode A with wavevectors between $|k_z| = 0.4$ and 0.5 (in units $2\pi/a$) and mode B in the same wavevector range. The curve of mode B shows close similarities with the mode in Figure 7.6(b). Therefore, it is a reasonable assumption that the dispersion also would be similar to the dispersion discussed in the previous section, where at a v_g of $c/9$, a very strong asymmetric distortion of the pulses is observed as they propagate through a W1 PCW. Mode A, however, has a more homogeneous slope left of the light line, indicated by the arrow in Figure 7.8(c). This suggests that the group velocity is low while the dispersion is small.

The propagation of pulses through this waveguide is investigated with the pulse tracking microscope. Femtosecond pulses are coupled into the waveguide

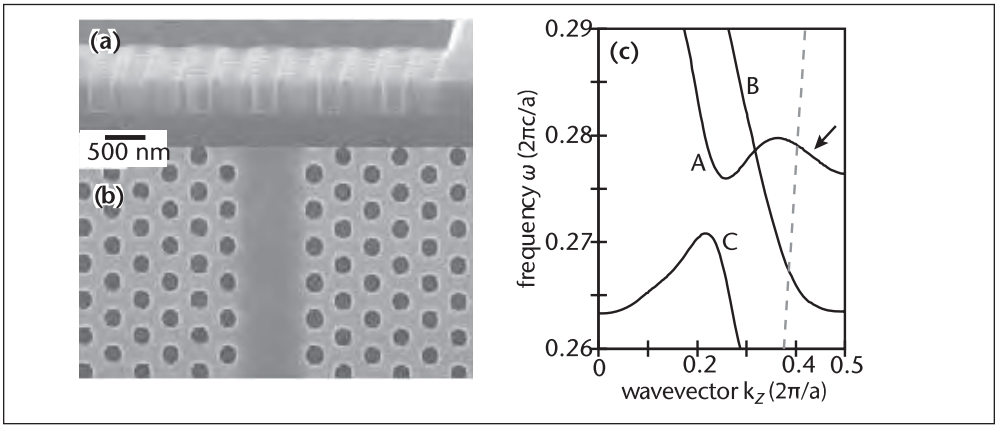

Figure 7.8 (a, b) SEM images of a PCW with a waveguide width of two rows of holes (W2). The crystal area is a hexagonal lattice (period $a = 420$ nm) of air holes (radius 118 nm) in a 240 nm thick Si layer on top of SiO_2. The images show a top view (a) and a side view (b). © Optical Society of America [12]. (c) Portion of the dispersion relation for light polarized in the plane of the top layer in the frequency range of 0.26–0.29 in normalized frequency units. Three waveguide modes are shown; all are confined to the waveguide, but they have different symmetries. Mode A and C have even in-plane symmetry, whereas B has odd symmetry. The light line of the SiO_2 is shown as the gray dashed line, indicating the wavevector of light in bulk SiO_2. The arrow indicates a slow mode with low dispersion.

with a central frequency of 0.278 with a spectral FWHM of 0.004, thus slightly exceeding the bandwidth of mode "A" left of the light line. The result of a series of pulse tracking experiments is shown in Figure 7.9. In Figure 7.9(a), several modes are already excited in the PCW. These are the modes already discussed (TE) and are possibly unwanted with the polarization along the direction of the pores (TM), although they have a much lower amplitude. In the consecutive images in Figures 7.9(b)–7.9(j) the propagation of the various modes is observed. Since some of the modes propagate with different group velocities or are excited at a slightly different time, they can be observed as individual pulses.

One mode resides in the waveguide for the longest period of time and exits the scanned area after approximately 16 ps. This mode is the slow mode with wavevectors in the range of $|k_z| = 0.4 \ldots 0.5$. An analysis of the group velocity, as performed in

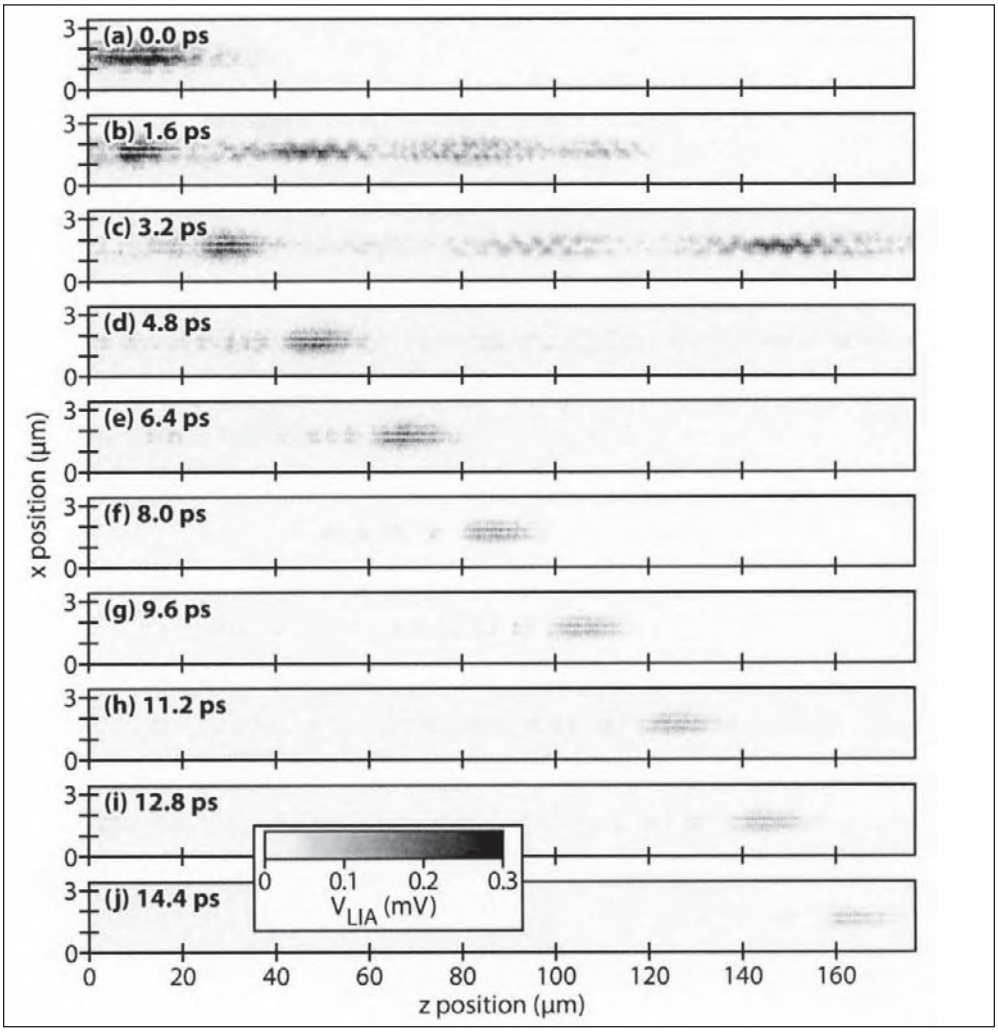

Figure 7.9 A series of pulse tracking measurements on a W2 PCW. (a–j) Amplitude of the lock-in signal of the same area ($176 \times 3.4\ \mu m^2$) of the waveguide. Several modes are excited in the waveguide at 0 ps. The modes can be resolved individually in (b) and (c) due to different group velocities. The group velocity of the slowest mode, which can be seen throughout (b) up to (j), is $c/25$.

Section 7.3.4, reveals that the group velocity of this slow mode is $c/25$. The velocity corresponds nicely to the slope of mode A at $\omega = 0.278$ in Figure 7.8.

The fact that the wave propagates at a low group velocity may not come as a surprise, given the knowledge from the dispersion relation. More interesting is the shape of the pulse as it propagates. In Figure 7.9, the pulse with the low group velocity does not appear to broaden. This is in contrast to the slow mode in Section 7.4.2 (see Figure 7.7) that broadens very rapidly within 106 μm of propagation even though it is faster than the slow mode in Figure 7.9 ($c/9$ vs. $c/25$). The slow pulse in Figure 7.9 retains its shape even after a propagation distance of 165 μm . Only the amplitude of the pulse decreases upon propagation, which is a known issue for slow light in PhCs [22, 23].

Upon close examination of Figure 7.9, one can see a pattern trailing the slow-light pulse. This trailing pattern is more easily seen in Figure 7.10. To obtain the curve in this figure, the measured V_{LIA} distribution is filtered to contain only the wavevectors in the range of $0.37 < |k_z| < 0.5$. This filtered data is subsequently averaged in the direction perpendicular to the waveguide to yield an average amplitude as a function of position z. Figure 7.10 shows the data corresponding to the delay time of 12.0 ps. In the figure, the maximum interference signal is found at 134 μm. At smaller distances, trailing fringes are clearly resolved.

The experimental results are compared to theory. For this, Equation 7.18 is solved numerically. Since the bandwidth of the used pulses is larger than the bandwidth of the slow mode, we changed the spectrum of $E_{sig}(\omega)$ with respect to the light in the reference branch. The dispersion relation used is the same as in Figure 7.8. Also, the decay of the light depends strongly on the group velocity. Therefore, a v_g-dependent loss is included in the calculations. The resulting interference amplitude as a function of distance is plotted in gray in Figure 7.10 and shows good agreement with the measurement data. The fringes on the trailing edge are caused by higher-order dispersion, of which TOD is most prominent. In addition, fringes are, in part, present due to the cutoff of the spectrum of the pulse due to the finite admitted bandwidth of the structure. However, the fact that the pulses still stay relatively compact makes the waveguide studied in this section promising for slow-light applications.

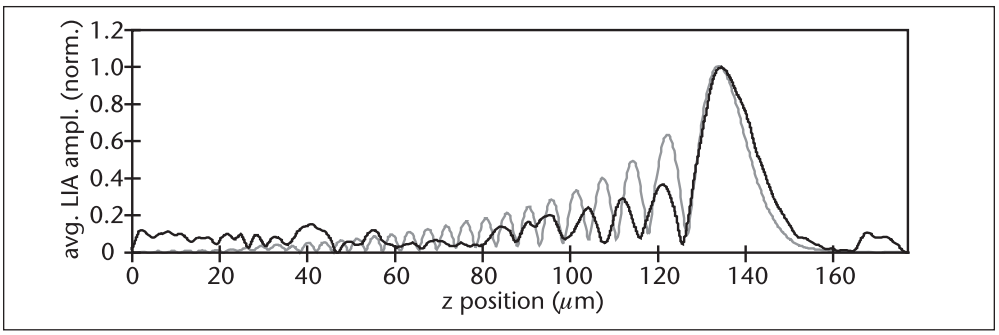

Figure 7.10 In black is shown the interference amplitude of the slow pulse measured at 12.0 ps delay time. (See Figure 7.9.) The data is filtered to show only the wavevectors in the range of $0.37 < |k_z| < 0.5$ (in units $2\pi/a$), corresponding to the slow mode [12]. The gray curve shows the corresponding result of a calculation using the dispersion relation shown in Figure 7.8(c). In the calculation, we included a cutoff of the spectrum and a group-velocity-dependent decay of the spectrum.

7.5 Conclusions

Phase-sensitive and time-resolved near-field investigations can be performed by integrating a near-field microscope into an interferometer. The heterodyne interferometer used in this chapter allows one to record optical field picked up by the near-field probe with average intensities down to the fW regime. For a time-resolved investigation, it is not necessary to use an ultrafast femtosecond laser system. Any light source with a bandwidth of several (tens of) nanometers is sufficient.

Time-resolved near-field investigations were performed using the interferometric near-field setup on three structures, a ridge waveguide and two PCWs. We demonstrated how to determine the phase velocity in the ridge waveguide and found a velocity of $1.75 \cdot 10^8$ m/s. We also measured the group velocity in the ridge waveguide using the time-resolved measurements and found a value of $1.44 \cdot 10^8$ m/s. Materials with a very strong dispersion can show pulse deformation within the size of the scan area. In that case, it still is possible to extract dispersive properties such as GVD and third-order dispersion. We found in a PCW at group velocities down to $c/9$ that the GVD and TOD have values of $\beta_2 = -1.1$ ps^2/mm and $\beta_3 = 0.11$ ps^3/mm, respectively. By altering the geometry of the PCW, the dispersive properties can be tuned. The near-field measurement of a pulse propagation through such a modified waveguide showed a propagating pulse with a group velocity of $c/25$, with a low dispersion.

Acknowledgments

This work is part of the research program of the Stichting voor Fundamenteel Onderzoek der Materie (FOM), which is financially supported by the Nederlandse Organisatie voor Wetenschappelijk Onderzoek (NWO). We thank Wico Hopman and René de Ridder for providing the ridge waveguide and Yoshimasa Sugimoto, Noaki Ikeda, and Kiyoshi Asakawa for providing the W1 PCW and the calculation of the dispersion relation. Thomas Krauss and Michael Settle are acknowledged for the W2 PCW and the SEM images thereof.

References

[1] Dolling, G. et al., "Simultaneous Negative Phase and Group Velocity of Light in a Metamaterial," *Science*, Volume 312, No. 5775, 2006, pp. 892–894.

[2] Bozhevolnyi, S. I. et al., "Channel Plasmon Subwavelength Waveguide Components Including Interferometers and Ring Resonators," *Nature*, Volume 440, No. 7083, 2006, pp. 508–511.

[3] Engelen, R. J. P. et al., "Ultrafast Evolution of Photonic Eigenstates in k-Space," *Nature Physics*, Volume 3, No. 6, 2007, 401–405.

[4] Altug, H., D. Englund, and J. Vučković, "Ultrafast Photonic Crystal Nanocavity Laser," *Nature Physics*, Volume 2, No. 7, 2006, pp. 484–488.

[5] Zehnder, L., "Ein Neuer Interferenzrefraktor," *Zeitschrift für Instrumentenkunde*, Volume 11, 1891, pp. 275–285.

[6] Mach, L., "Über Einen Interferenzrefraktor," *Zeitschrift für Instrumentenkunde*, Volume 12, 1892, pp. 89–93.

[7] Balistreri, M. L. M. et al., "Local Observations of Phase Singularities in Optical Fields in Waveguide Structures," *Physical Review Letters*, Volume 85, No. 2, 2000, pp. 294–297.

[8] Hillenbrand, R., and F. Keilmann, "Complex Optical Constants on a Subwavelength Scale," *Physical Review Letters*, Volume 85, No. 14, 2000, pp. 3029–3032.

[9] Nesci, A., R. Dändliker, and H. P. Herzig, "Quantitative Amplitude and Phase Measurement by Use of a Heterodyne Scanning Near-Field Optical Microscope," *Optics Letters*, Volume 26, No. 4, 2001, pp. 208–210.

[10] Nesci, A., and Y. Fainman, "Complex Amplitude of an Ultrashort Pulse with Femtosecond Resolution in a Waveguide Using a Coherent NSOM at 1550 nm," in *Wave Optics and Photonic Devices for Optical Information Processing II* (P. Ambs and F. R. Beyette, Jr., eds.), *Proceedings of SPIE*, Volume 5181, 2003, pp. 62–69.

[11] Gomez, L. et al., "Apertureless Scanning Near-Field Optical Microscopy: A Comparison between Homodyne and Heterodyne Approaches," *Journal of the Optical Society of America B*, Volume 23, No. 5, 2006, pp. 823–833.

[12] Settle, M. D. et al., "Flatband Slow Light in Photonic Crystals Featuring Spatial Pulse Compression and Terahertz Bandwidth," *Optics Express*, Volume 15, No. 1, 2007, pp. 219–226.

[13] Gersen, H. et al., "Real-Space Observation of Ultraslow Light in Photonic Crystal Waveguides," *Physical Review Letters*, Volume 94, No. 7, 2005, Art. No. 073903.

[14] Balistreri, M. L. M. et al., "Tracking Femtosecond Laser Pulses in Space and Time," *Science*, Volume 294, No. 5544, 2001, pp. 1080–1082.

[15] Balistreri, M. L. M. et al., "Quasi Interference of Perpendicularly Polarized Guided Modes Observed with a Photon Scanning Tunneling Microscope," *Optics Letters*, Volume 25, No. 9, 2000, pp. 637–639.

[16] Engelen, R. J. P. et al., "The Effect of Higher-Order Dispersion on Slow Light Propagation in Photonic Crystal Waveguides," *Optics Express*, Volume 14, No. 4, 2006, pp. 1658–1672.

[17] Chow, E. et al., "Quantitative Analysis of Bending Efficiency in Photonic-Crystal Waveguide Bends at $\lambda = 1.55$ μm Wavelengths," *Optics Letters*, Volume 26, No. 5, 2001, pp. 286–288.

[18] Akahane, Y. et al., "High-Q Photonic Nanocavity in a Two-Dimensional Photonic Crystal," *Nature*, Volume 425, No. 6961, 2003, pp. 944–947.

[19] Soljačić, M., and J. D. Joannopoulos, "Enhancement of Nonlinear Effects Using Photonic Crystals," *Nature Materials*, Volume 3, No. 4, 2004, pp. 211–219.

[20] Frandsen, L. H. et al., "Photonic Crystal Waveguides with Semi-slow Light and Tailored Dispersion Properties," *Optics Express*, Volume 14, No. 20, 2006, pp. 9444–9450.

[21] Saynatjoki, A. et al., "Dispersion Engineering of Photonic Crystal Waveguides with Ring-Shaped Holes," *Optics Express*, Volume 15, No. 13, 2007, pp. 8323–8328.

[22] Hughes, S. et al., "Extrinsic Optical Scattering Loss in Photonic Crystal Waveguides: Role of Fabrication Disorder and Photon Group Velocity," *Physical Review Letters*, Volume 94, No. 3, 2005, Art. No. 033903.

[23] Kuramochi, E. et al., "Disorder-Induced Scattering Loss of Line-Defect Waveguides in Photonic Crystal Slabs," *Physical Review B*, Volume 72, No. 16, 2005, Art. No. 161318.

PART III

Plasmonics

Introduction

The term *plasmonics* refers to the science and technology dealing with manipulation of electromagnetic signals by coherent coupling of photons to free electron oscillation at the interface between a conductor and a dielectric [1–5]. The coupling results in the formation of surface electromagnetic modes on the interface and the related free electron density charge waves [see Figure III.1(a)]. On a continuous interface, these are propagating surface electromagnetic modes called surface plasmon polaritons (SPPs). Solutions to Maxwell's equations at a planar metal-dielectric interface produce the dispersion relation of SPPs [(Figure III.1(b)]

$$k_{SPP}^2 = \left(\frac{\Omega}{c}\right)^2 \frac{\varepsilon_d \varepsilon_m}{\varepsilon_d + \varepsilon_m} \tag{III.1}$$

where Ω/c is the light wave vector in the adjacent dielectric and ε_d and ε_m are the permittivities of the dielectric and metal, respectively. The permittivity of the dielectric materials (ε_d) are positive, while the dielectric constant of the metal (ε_m) is negative; thus, the wave vector k_{SPP} is greater than the light wave vector $k_0 = 2\pi/\lambda$ in the adjacent dielectric. For this reason, the difference in the wave vectors, under the normal circumstances a surface polariton cannot be excited directly with light on a smooth metal interface and, reciprocally, surface polaritons propagating on a smooth surface cannot be transformed in light in the adjacent medium. The SPP field has a maximum on the interface and decays exponentially away from it [see Fig. III.1(c)]. The energy of the incident radiation is trapped at the metal-dielectric interface, and the enhanced electromagnetic fields are produced in the near-field.

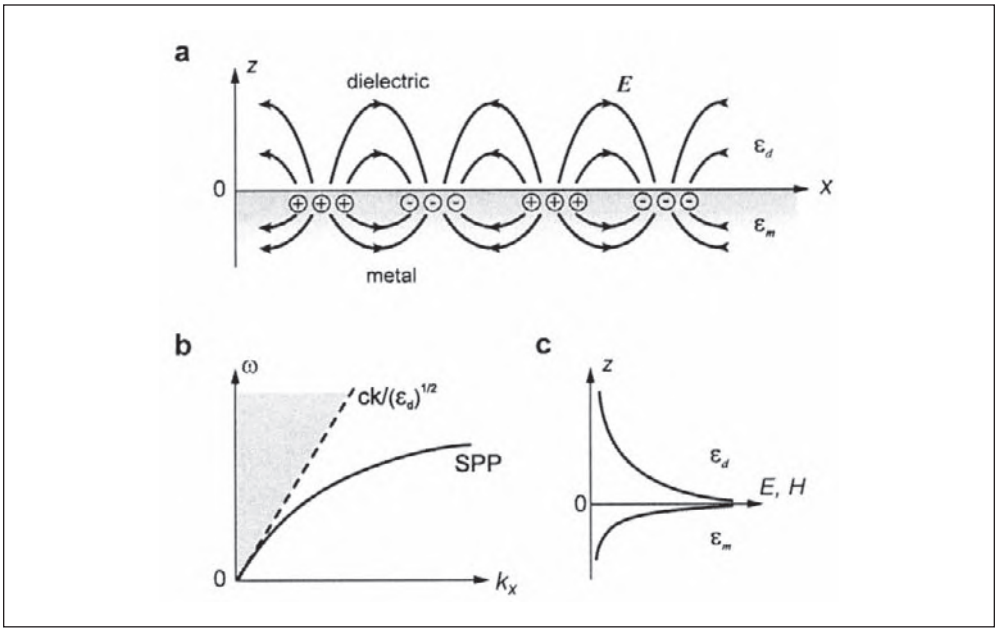

Figure III.1 (a) Illustration of surface plasmons represented by surface charge density fluctuations. (b) Dispersion relation of SPPs (solid line). The gray area denotes the light cone of propagating modes in the adjacent dielectric. (c) Illustration of the SPP electromagnetic field confinement to the metal/dielectric interface. © 2008. Odom & Gao.

In conventional (far-field) measurements, the SPP field cannot be observed before the scattering in light occurs (e.g., due to surface defects). With the development of scanning near-field optical microscopy, it becomes possible to study the surface polariton field directly in the near-field proximity to the surface where it exists. The implementation of SNOM has led to a breakthrough in surface polariton studies [2, 3]. The SPP scattering, interference, backscattering, and localization have been visualized and investigated directly on the surface. The idea of two-dimensional surface polariton optics has been proposed and realized experimentally, resulting in the development of optical elements for surface polaritons that allow SPP beams to be manipulated and directed on a surface similarly to optical beams in three dimensions. Various types of SPP waveguides that allow extreme subwavelength light guiding in the same circuitry as electric signals have been proposed [6–9]. Plasmonic crystals, a new class of two-dimensional photonic crystals based on SPP band-gap structures, have been studied in terms of light guiding and manipulation [10, 11] as well as for spectrally selective enhancement of reflection, transmission, and absorption of light [12, 13]. Most importantly, active photonic elements based on nonlinear surface polariton optics allowing control of the optical properties of the device with light are much easier to realize with SPPs due to the field enhancement effects [14, 15].

In addition to surface plasmons on a plane surface, in other geometries involving bound electron plasmas, such as metallic particles and voids of different topologies, localized surface plasma excitations exist (see Figure III.2). Such surface plasma excitations in bounded geometries are called localized surface plasmons (LSPs). They are characterized by discrete, complex frequencies that depend on the size and shape of the object to which the surface plasmon is confined and its dielectric constant. LSP resonances of subwavelength particles can be determined in a nonretarded (electrostatic) approximation by considering Mie scattering on a small metal particles [16]. In the case of a sphere, this gives the position of LSP resonances via

$$Re\varepsilon_m(\omega_{LSP})/\varepsilon_d + (l + 1)/l = 0 \tag{III.2}$$

where l is the angular momentum of the localized surface plasmon. For small spheres, only the dipole active excitation ($l = 1$) is important. LSPs can be resonantly excited with light of appropriate frequency (and polarization) irrespective of the excitation light wavevector. Therefore, LSPs also effectively decay via the emission of light. The strong confinement related to LSPs can produce an optical field that is enhanced by orders of magnitude over the incident field, leading to a wide range of applications. Perhaps the best known is surface-enhanced Raman scattering (SERS), which can now produce single molecule sensitivity [17, 18]. LSPs also have been shown to enhance the optical phenomena related to the adsorbed molecules, such as fluorescence and optical absorption [4, 5]. In addition, they are extremely sensitive to the geometry of the supporting structure, thus allowing an extensive tuning of the spectral properties and associated electromagnetic field distribution by appropriate structural design. Applications ranging from chemical sensing to surface enhanced spectroscopies and electromagnetic energy guiding take advantage of these unique properties [5, 19, 20]. LSPs are widely used in apertureless SNOM techniques to achieve the strong field confinement and thus the increased resolution compared to aperture-based SNOM as described in Part IV of this book.

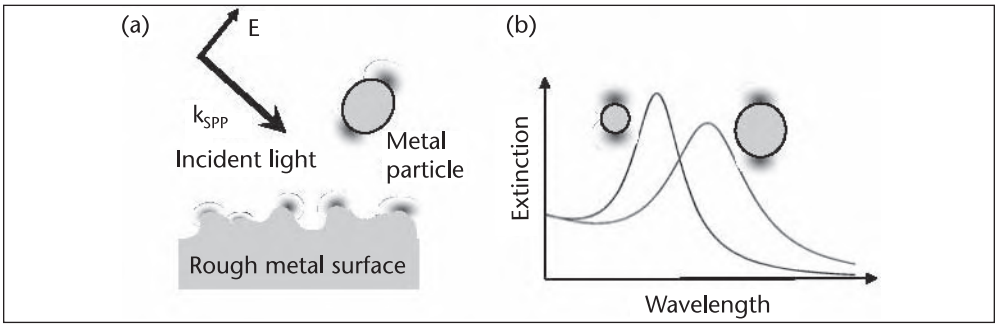

Figure III.2 (a) Illumination of a noble metal nanoparticle or nanostructured film at the wavelength of the localized surface plasmon resonance: Free electrons driven by the illuminating field create an oscillating dipole; this results in a confined evanescent field with significant enhancement in magnitude. (b) Schematics of the absorption spectra illustrate the strong dependence of the LSP resonance wavelength on shape and size of the nanoparticle. © 2008. Wurtz & Wiederrecht.

Despite many applications already underway, SPPs and LSPs on metal nanostructures produce a range of physical and chemical phenomena that impact an extraordinary breadth of basic science research and technological applications. Future applications include optical computing, high-bandwidth all-optical telecommunications routing, high-density optical data storage, ultrafast nonlinear optics, negative index metamaterials, and nanoscale sensors-on-a-chip to name only a few.

The three chapters in this section provide an overview of different aspects of nanoscale optical properties associated with surface plasmon excitations. First, near-field imaging and far-field spectroscopy of SPPs on metal films perforated with arrays of nanoholes are discussed. These hole arrays (having circular or anisotropic shapes) were patterned over large areas (> 10 cm^2) using a simple and innovative nanofabrication method called PEEL (Phase shifting photolithography, Etching, Electron beam deposition, and Lift-off). The microscale pitch of the nanohole arrays enabled direct visualization of SPPs in the near field and observation of high-order SPP Bloch modes in the far field. A theoretical model explaining the observed near-field behavior also is described.

Next, optics of randomly nanostructured metal films is discussed. These metal-dielectric films, also called semicontinuous films, are of great interest in nano-optics and nonlinear spectroscopy due to the significant enhancement of the electromagnetic field that may occur in random nanostructures. Compared to regular nanostructures, the random nature and cost-effective fabrication of semicontinuous films allow their wide use in biology and chemistry for sensing, imaging, and nonlinear spectroscopy, including SERS. The fabrication procedures, far-field and near-field imaging, and the theoretical description of the local electromagnetic field enhancement on semicontinuous metal-dielectric films are discussed, together with applications in fluorescence and second-harmonic generation spectroscopy.

The final chapter presents a review of the photo-physics of hybrid plasmonic systems consisting of molecular excitonic materials and nanostructures supporting plasmonic modes. Three main plasmonic systems, isolated metal nanoparticles, assemblies of strongly interacting nanorods, and extended thin metallic films, are considered. These geometries support localized or delocalized plasmonic modes, all of which are shown to coherently couple to molecular excitonic states. The unusual optical properties that result from strong coupling between the exciton

and surface plasmon are reviewed. The fabrication of hybrid plasmonic materials, their linear and nonlinear optical properties related to near-field coupling, ultrafast exciton dynamics, and ultimately its control through manipulation of the coupling strength are discussed.

References

[1] Raether, H., *Surface Plasmons on Smooth and Rough Surfaces and on Gratings*, Berlin: Springer Verlag, 1987.

[2] Zayats, A. V., I. I. Smolyaninov, and A. A. Maradudin, "Nano-Optics of Surface Plasmon Polaritons," *Phys. Rep.*, Vol. 408, 2005, pp. 131–314.

[3] Zayats A. V., and I. I. Smolyaninov, "Near-Field Photonics: Surface Plasmon Polaritons and Localized Surface Plasmons," *Journal of Optics A: Pure Applied Optics*, Vol. 5, 2003, pp. S16–S50.

[4] Barnes, W. L., A. Dereux, and T. W. Ebbesen, "Surface Plasmon Subwavelength Optics," *Nature*, Vol. 424, 2003, pp. 824–830.

[5] Maier, S. A., *Plasmonics: Fundamentals and Applications*, New York: Springer, 2007.

[6] Bozhevolnyi, S. et al., "Channel Plasmon Subwavelength Waveguide Components Including Interferometers and Ring Resonators," *Nature*, Vol. 440, 2006, pp. 508–511.

[7] Krenn, J., and J.-C. Weeber, "Surface Plasmon Polaritons in Metal Stripes and Wires," *Phil. Trans. R. Soc. Lond. A*, Vol. 362, 2004, pp. 739–756.

[8] Krasavin, A. V., and A. V. Zayats, "Passive Photonic Elements Based on Dielectric-Loaded Surface Plasmon Polariton Waveguides," *Appl. Phys. Lett.*, Vol. 90, 2007, Art. No. 211101.

[9] Conway, J. A., S. Sahni, and T. Szkopek, "Plasmonic Interconnects Versus Conventional Interconnects: A Comparison of Latency, Crosstalk and Energy Costs," *Opt. Express*, Vol. 15, 2007, pp. 4474–4484.

[10] Bozhevolnyi, S. I. et al., "Waveguiding in Surface Plasmon Polariton Band Gap Structures," *Phys. Rev. Lett.*, Vol. 86, 2001, pp. 3008–3011.

[11] Mikhailov, V. et al., "Dispersing Light with Surface Plasmon Polaritonic Crystals," *Phys. Rev. Lett.*, Vol. 99, 2007, Art. No. 083901.

[12] Genet, C., and T. W. Ebbesen, "Light in Tiny Holes," *Nature*, Vol. 445, 2007, pp. 39–46.

[13] Salomon, L. et al., "Near-Field Distribution of Optical Transmission of Periodic Subwavelength Holes in a Metal Film," *Phys. Rev. Lett.*, Vol. 86, 2001, pp. 1110–1113.

[14] Wurtz, G. A., R. Pollard, and A. V. Zayats, "Optical Bistability in Nonlinear Surface Plasmon Polaritonic Crystals," *Phys. Rev. Lett.*, Vol. 97, 2006, Art. No. 057402.

[15] Pacifici, D., H. J. Lezec, and H. A. Atwater, "All-Optical Modulation by Plasmonic Excitation of CdSe Quantum Dots," *Nature Phot.*, Vol. 1, 2007, pp. 402–406.

[16] Kreibig, U., and M. Vollmer, *Optical Properties of Metal Clusters*, Berlin: Springer, 1995.

[17] Moskovits, M., "Surface-Enhanced Spectroscopy," *Rev. Mod. Phys.*, Vol. 57, 1985, pp. 783–826.

[18] Nie, S., and S. R. Emory. "Probing Single Molecules and Single Nanoparticles by Surface-Enhanced Raman Scattering," *Science*, Vol. 275, 1997, pp. 1102–1106.

[19] Maier, S. A., and H. A. Atwater, "Plasmonics: Localization and Guiding of Electromagnetic Energy in Metal/Dielectric Structures," *J. Appl. Phys.*, Vol. 98, 2005, pp. 1–10.

[20] Haes, A. J. et al., "Localized Surface Plasmon Resonance Spectroscopy Near Molecular Resonances," *J. Am. Chem. Soc.*, Vol. 128, 2006, pp. 10905–10914.

CHAPTER 8

Near-Field Optical Characterization of Plasmonic Materials

Hanwei Gao and Teri W. Odom

8.1 Scanning Near-Field Optical Microscopy of Plasmonic Structures

NFO encompasses electromagnetic phenomena that can occur within subwavelength distances between a light source and an object. In the near-field, both propagating and evanescent waves are present and the effective collection of evanescent waves can eliminate the diffraction limitations of optical imaging [1]. Such ultrahigh resolution using visible light has widely impacted discoveries in physics [2, 3], chemistry [4–6], and biology [7]. Because of advances in imaging at nanometer length scales and nanofabrication methods, the generation and manipulation of surface plasmons (SPs)—collective electron oscillations at a metal-dielectric interface—have received significant attention. Compared to free space light, these trapped surface waves can propagate through subwavelength channels more efficiently and provide an alternative approach for miniaturizing optical devices such as waveguides [8–10], interferometers [11], demultiplexers [12], and plasmonic bandgap crystals [13]. Furthermore, the high electromagnetic field intensities at the metal surface from the evanescent nature of the SPs have been exploited in applications ranging from scanning plasmon microscopy [14] to surface-enhanced Raman spectroscopy [15] to plasmonic lithography [6].

This chapter will describe how SNOM and far-field spectroscopy can be used to visualize SPs on planar metal nanostructures and to reveal fundamental properties of how SPPs behave in nanohole arrays with microscale spacings.

8.1.1 Visualizing Surface Plasmon Polaritons on Metal Structures

Two SNOM configurations can characterize surface plasmon excitations. In the near field, the probe can deliver light to the sample (illumination mode) or collect light from the sample (collection mode). A variation of a collection mode SNOM is a PSTM, which is based on the Kretschmann configuration [16]. These different possibilities of delivering and collecting light through the SNOM tip offer distinct advantages for visualizing SPPs on metal structures. Illumination mode is favorable for probing the properties of metal nanoparticles [9, 17] because the tip acts like a local excitation source, while collection mode is ideal for imaging SPP waves on metal stripes (plasmonic waveguides) and other grating structures because of the evanescent nature of SPPs [18, 19].

One recent example using PSTM is the demonstration of an analogue of Young's double-slit experiment using SPPs [19]. The patterned, thin metal Au film consisted of three regions: (1) an area for the excitation of the SPPs, (2) two metal stripes used as plasmonic waveguides (playing the role of two slits), and (3) a region where SPP waves from the metal stripes could diffract and interfere [Figure 8.1(a)]. The SPP waves were launched in region 1 of the Au film by attenuated total reflection (via a prism with 780 nm light) and then guided by the two gold stripes. The near-field optical images indicated that the SPP waves diffracted from the two stripes and interfered with each other to produce a typical diffraction pattern [Figure 8.1(b)], which was similar to the calculated one based on conventional double-slit interference [Figure 8.1(c)].

8.1.2 Monitoring Effects of Localized Surface Plasmons on Metal Nanoparticles

Illumination-mode SNOM is well suited for monitoring surface plasmon coupling in chains of metal nanoparticles. When particles supporting localized surface plasmons

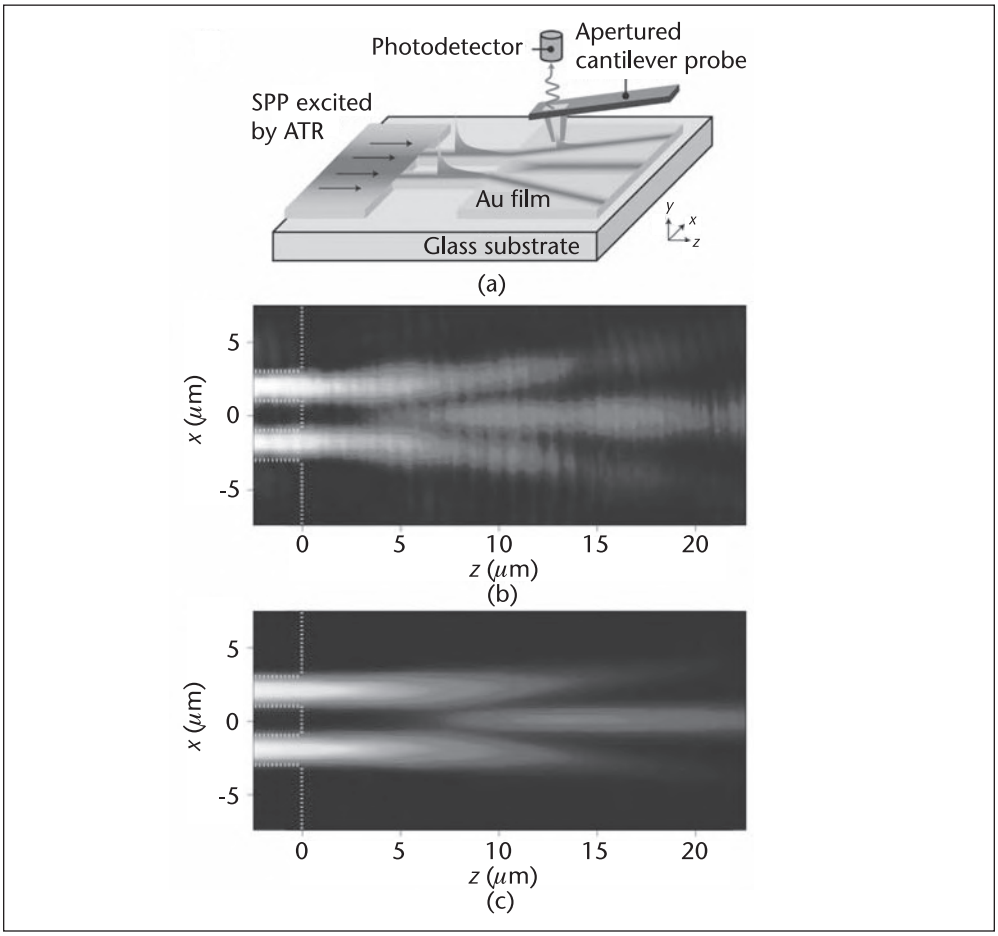

Figure 8.1 (a) Scheme of a PSTM for visualizing Young's double-slit experiment for SPPs. (b) Experimental near-field image demonstrating guided SPP propagation, diffraction, and interference. (c) Light intensity image predicted by numerical simulations of the equivalent dielectric structure. Figure reproduced with permission from [19], © (2007) Nature Publishing.

(LSPs) are patterned in a linear array and positioned very closely to each other (separations on the order of the particle size), the LSP from one particle can couple to the LSP of an adjacent one. Hence, electromagnetic energy can be transferred along the chain of nanoparticles [9]. Far-field microscopy cannot directly measure this energy transfer because even with a high numerical aperture lens (spot size several hundred nm), the light source cannot be focused onto a single nanoparticle without illuminating adjacent ones. Thus, illumination-mode SNOM offers significant advantages for testing energy transfer along a particle chain because a single nanoparticle can be locally excited.

To monitor the propagation of LSP-mediated energy transfer along Ag nanoparticles in a chain, fluorescent polystyrene spheres were deposited at different positions on and away from the chains and the emission was collected in the far-field [see Figure 8.2(a)]. Rod-shaped Ag particles with dimensions $90 \times 30 \times 30$ nm^3 and with an edge-to-edge spacing of 50 nm were patterned by e-beam lithography [Figure 8.2(b)] and excited using 570 nm light (corresponding to the maximum of the LSP resonance) delivered by a 100 nm aperture SNOM probe. Line scans of the SNOM optical images revealed that the fluorescence from spheres sitting on top of the Ag particle chains (WG) was significantly broader than the emission from isolated spheres (control) [see Figure 8.2(c)]. This broadening indicated that LSP-mediated electromagnetic energy transfer occurred along the nanoparticle chain. In addition, the propagation

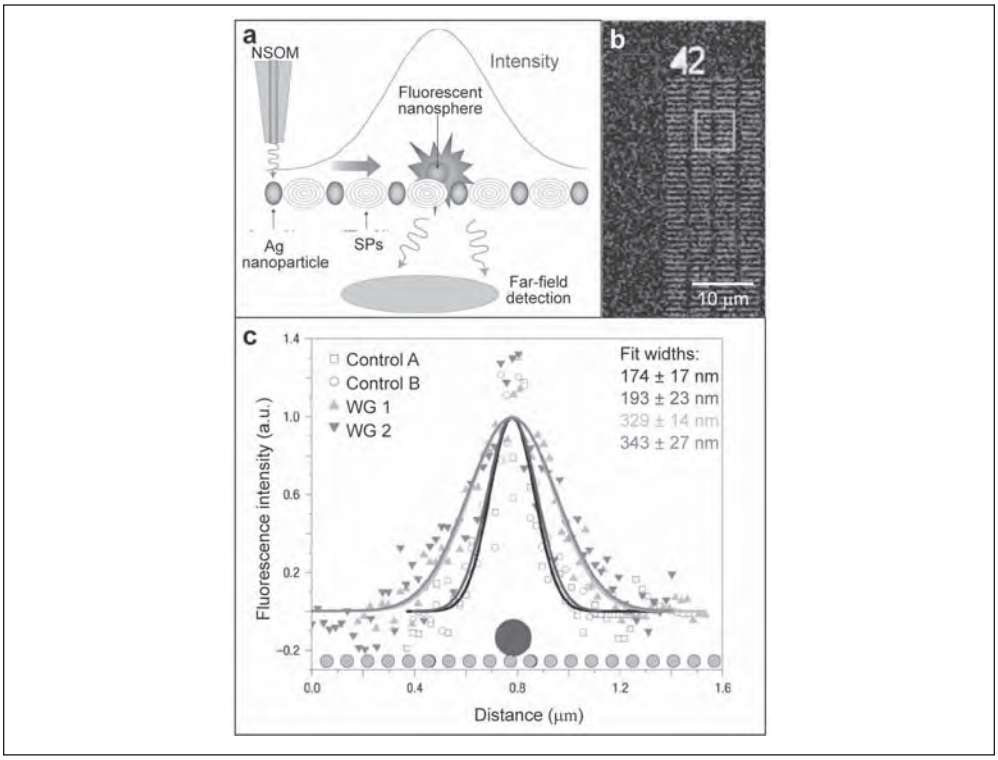

Figure 8.2 (a) Sketch of experimental setup for detecting energy transfer along a Ag particle waveguide. (b) SEM image of a 100 μm $\times$100 μm grid consisting of Ag plasmon waveguides. Inset: zoom-in SEM image of one nanoparticle chain. (c) Line scans of near-field fluorescent images along the plasmon waveguide direction. Figure reproduced with permission from [9], © (2003) Nature Publishing.

length (ca. 6 dB per 200 nm) was quantitatively measured by mapping the fluorescence from the polystyrene sphere along the length of the nanoparticle chain; this damping of the LSP propagation agreed with theoretical predictions.

8.2 Surface Plasmon Polaritons on Metal Films of Nanohole Arrays

8.2.1 Introduction

When light is incident on an opaque mask containing a single large hole, geometric optics provide a good description of the image on the screen behind the mask (the projection of the hole). [See Figure 8.3(a).] If the diameter of the hole decreases so that it is on the order of the wavelength, a pattern predicted by diffraction theory can be observed on the screen. [See Figure 8.3(b).] According to Huygens' Principle [20], this diffraction pattern is a result of the phase difference of the wave fronts originating from different positions of the hole. As the size of the hole in the mask decreases further, the diffraction pattern starts to vanish; eventually, the light diverges uniformly in the hemispherical space beyond the mask [see Figure 8.3(c)]. Bethe's theory on the optical transmission through a single subwavelength hole indicated that the transmission efficiency scaled as $(r/\lambda)^4$, where r is the radius of the hole [21]. Consequently, in classical optics, holes with subwavelength dimensions are considered semitransparent with low optical transmission. When a noble metal film is perforated with an array of subwavelength holes, however, the optical transmission through the hole array can be significantly higher than the sum of

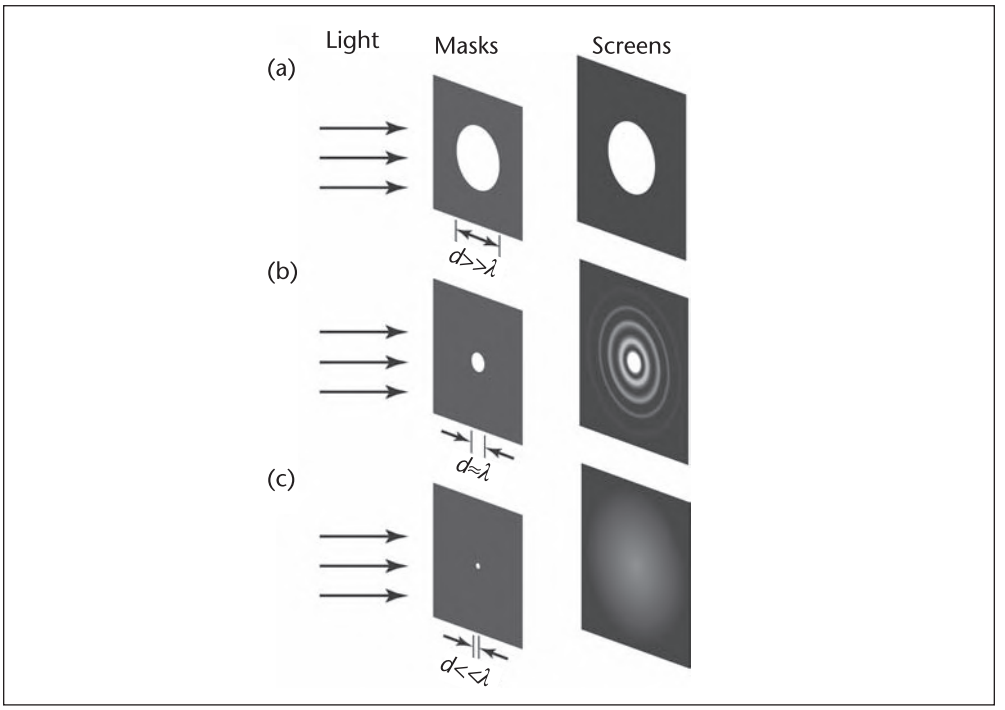

Figure 8.3 Far-field optical patterns projected on screens behind opaque masks perforated with holes with diameters (a) much larger, (b) on the order of, and (c) much smaller than the incident wavelength.

light transmitted through individual holes [22]. This so-called enhanced optical transmission (EOT) through subwavelength hole arrays, first reported in 1998, attracted significant attention and could be argued to have opened a novel direction in nanophotonics. The detailed mechanism behind the EOT stimulated debate for nearly a decade after the initial observation, with different proposed contributions including SPPs and composite diffracted evanescent waves [23].

The rest of this chapter will discuss how SNOM operated in collection and illumination modes, far-field spectroscopy, and theoretical models were combined to investigate EOT through arrays of nanoholes. Instead of studying subwavelength hole arrays, whose size *and* pitch are subwavelength in scale, we tested nanoscale holes patterned on a microscale pitch. Arrays of nanoholes separated by several microns in thin gold films enable the direct imaging of SPPs in the near field and high-order Bragg scattering or SPP-Bloch wave modes in the far-field.

8.2.2 Fabrication of Microscale Arrays of Nanoholes

Large-area metal films perforated with microscale arrays of nanoholes were fabricated using a nanofabrication procedure that we have developed called PEEL (a combination of **P**hase shifting photolithography, **E**tching, **E**lectron beam deposition, and **L**ift-off) [24] (see Figure 8.4). Unlike serial approaches to generating holes in films, such as FIB milling, PEEL is a parallel, high-throughput method that can produce very

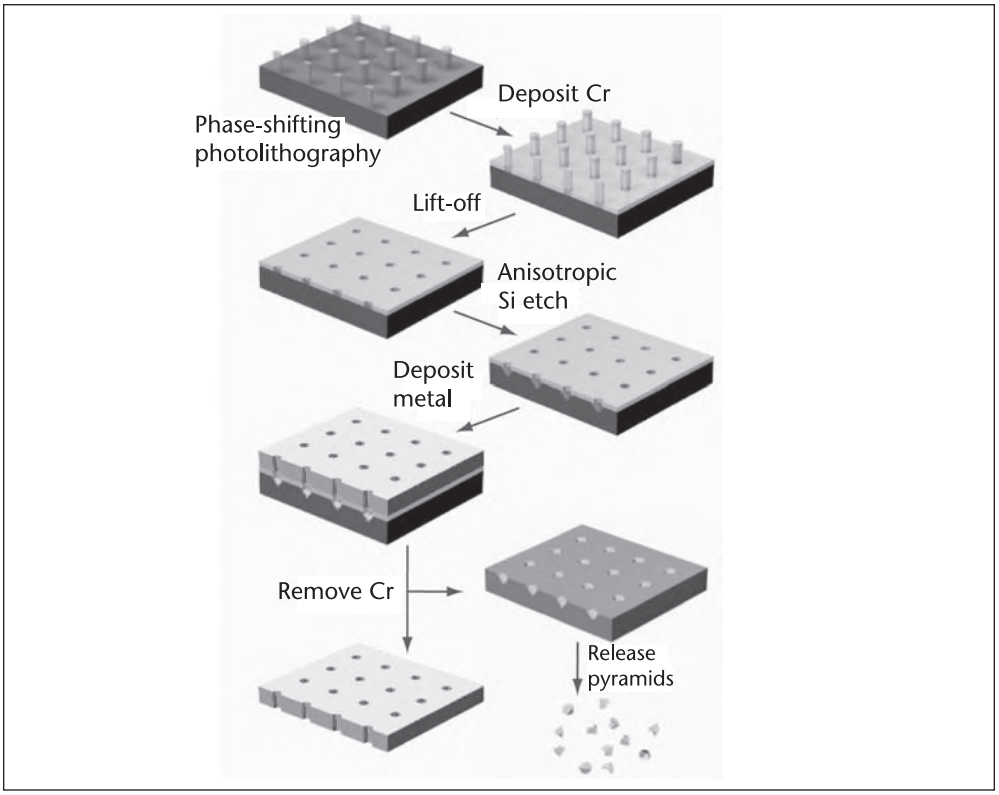

Figure 8.4 Scheme of the PEEL technique to simultaneously produce freestanding films of nanoholes and pyramidal nanoparticles.

uniform nanohole arrays over several square inches [see Figure 8.5(a)]. Here we outline only the primary procedural steps. First, posts in positive-tone photoresist are patterned on a Si (100) wafer using phase-shifting photolithography with a *h*-PDMS mask; a thin layer of Cr is then e-beam-deposited and lifted off to produce a Cr layer with holes. This Cr film acts as (1) a template for the hole patterns in the metal films and (2) a sacrificial layer to create freestanding films. The exposed Si is then anisotropically etched to form pyramidal pits beneath the Cr holes; e-beam evaporation is then used to deposit a single metal material or multiple materials of a desired thickness (t) (as thick as 500 nm) onto the patterned Cr film. After etching of the Cr layer, the perforated metal film is detached from the Si substrate and is freestanding. In the case where the diameter (d) of the posts is 250 nm and spacing between the posts (a) is 25 μm, freestanding films with 250 nm holes separated by 25 μm (i.e., nearly isolated nanoholes) are created [see Figure 6(b)]. We also can change the separation of the nanoholes by starting with photoresist posts with different spacings, such as a $\sim 2\ \mu$m. [See Figures 8.5(c) and 8.5(d).] Significantly, PEEL can transfer any photoresist pattern into metal or dielectric films with holes of the same geometric structure as the template. We demonstrated this flexibility by generating anisotropic nanoholes with elliptical or slitlike shapes [25] [see Figures 8.5(e) and 8.5(f)].

8.2.3 Illumination-Mode SNOM of Nanohole Arrays

8.2.3.1 Near-Field Optical Characterization

To investigate the optical properties of the microscale arrays of nanoholes, optically thick (t = 100 nm) Au films perforated with 2 μm spaced holes were analyzed using SNOM (Veeco Aurora III) in illumination mode [26]. A 633 nm laser or an 800 nm Ti/sapphire laser was coupled into an Al-coated tapered fiber probe and illuminated the

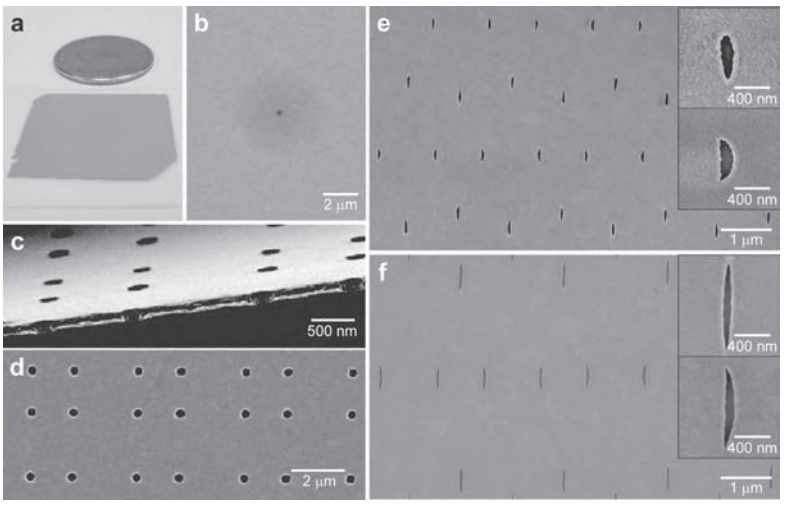

Figure 8.5 (a) Optical micrograph of a large-area, freestanding Au nanohole film on a glass substrate. (b) SEM image of an isolated (25 μm spaced array) hole in a Au film. (c,d) SEM images of circular nanohole arrays with $a \approx 2\ \mu$m (2 μm arrays) and (e) elliptical and (f) slitlike holes in Au films. Parts (a), (b), (e), and (f) reprinted with permission from ref. 25, copyright (2007) Wiley; parts (c) and (d) from [36], © (2005) ACS.

Au/air interface in the near-field region (~ 20 nm) from surface. The light transmitted through the glass substrate was collected in the far field with an avalanche photodiode. The tapered fiber probe had an 80 nm diameter aperture. Although far-field light intensity is collected, the optical image, which is constructed by plotting this light intensity as a function of the probe position, provides information about near-field phenomena. Under local illumination using λ_{ex} = 633 nm, the Au film exhibited enhanced transmission at the holes, which can be attributed to the LSPs of the holes coupling resonantly with the incident light (see Figure 8.6). Interestingly, fringes reminiscent of standing wave patterns were observed between adjacent holes, which indicated that the light from the SNOM tip was locally exciting SPP waves on the film surface.

8.2.3.2 Simulation of Near-Field Optical Images

To verify that the patterns were from SPPs, we carried out 3-D FDTD calculations to simulate the electromagnetic distribution in the near field [27]. The calculations focused on 100 nm thick Au films with four holes arranged in a square array (1.6 μm center to center) with air above and glass below. The SNOM tip also was included in the simulations. The incident wave was a fundamental HE_{11} mode of the SNOM fiber core that was launched from the upper part of the tip. We found that SPP waves were generated not only on the top Au/air interface but also on the bottom Au/glass interface because of the finite thickness of the metal film. The simulation revealed strong evanescent fields following the characteristics of SPPs at the Au/air interface. In addition, calculations showed that interference between the

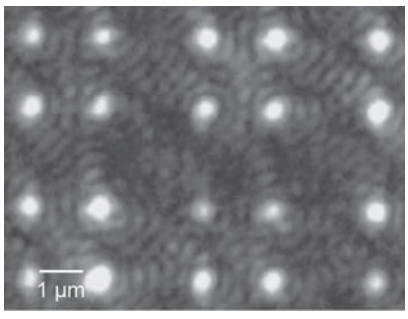

Figure 8.6 SNOM optical image of microscale arrays (spacing 1.6 × 2.4 μm) of nanoholes in a 100 nm thick Au film on glass. Figure reproduced with permission from [26], © (2005) ACS.

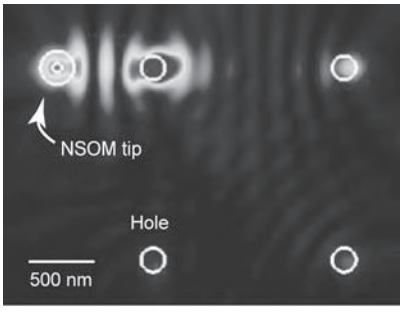

Figure 8.7 Calculated near-field SPP standing wave pattern at the Au/air interface for a specific SNOM tip position. Figure reproduced with permission from [26], © (2005) ACS.

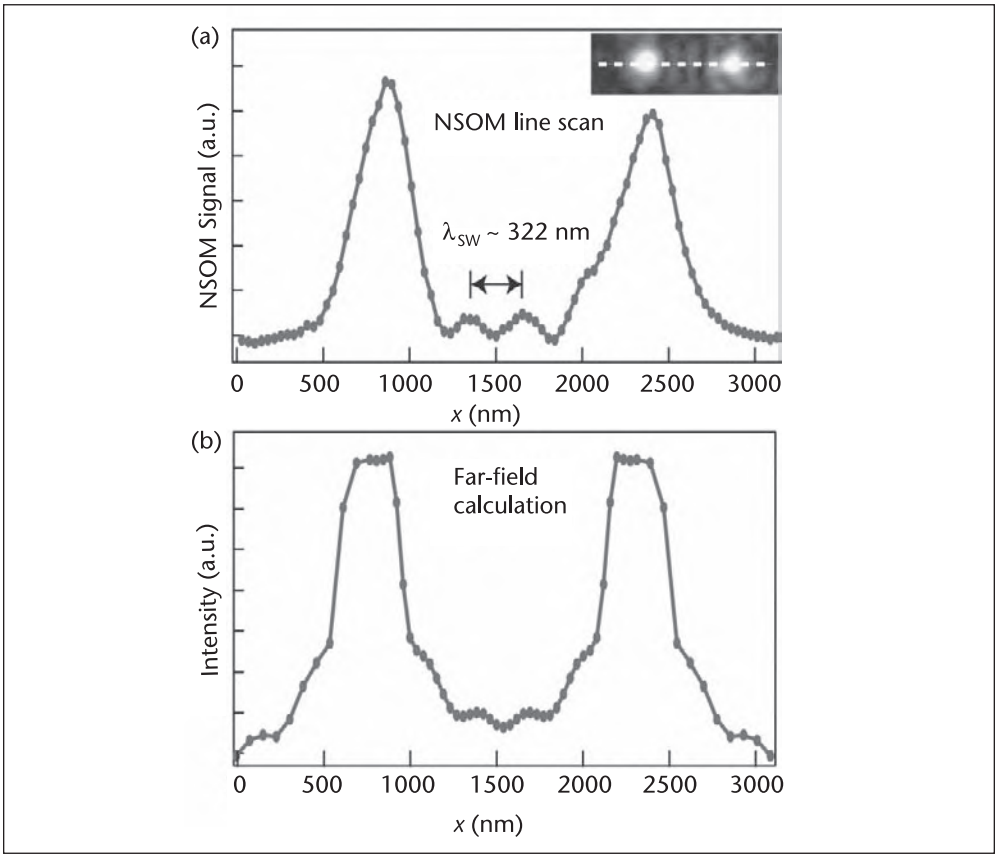

Figure 8.8 (a) Cross section of two neighboring holes from Figure 8.6. The fringes between the holes have a period of $\lambda_{sw} \sim 322$ nm. (b) Calculated far-field intensity from four holes (Figure 8.7) at different SNOM tip positions. The fringe spacing of $\lambda_{sw} \sim \lambda_{SPP}/2$ is present but is relatively small in amplitude compared to the transmission through the holes. Figure reproduced with permission from [36], © (2005) ACS.

SPP waves originating from the SNOM tip and the SPPs reflected by the holes appeared as standing waves between holes (see Figure 8.7).

By calculating the far-field amplitude at each SNOM tip location, we found that these standing wave patterns were most pronounced when the SNOM tip was located over a position of the SPP wave that corresponded to maximum intensity. The fringes produced by the standing wave in the near field should lead, in the far field, to intensity maxima with a period (λ_{sw}) that is approximately half the SPP wavelength ($\lambda_{SPP} = 603$ nm at $\lambda_{ex} = 633$ nm) [38] at the Au/air interface; indeed, fringes with $\lambda_{sw} \approx 322$ nm (roughly $\lambda_{SPP}/2$) were measured in the experiment (see Figure 8.8). The slight difference in the measured period of the fringes and the calculated $\lambda_{SPP}/2$ is not surprising because the fringe pattern follows a Bessel function versus position rather than a $\cos^2$ function. Thus, the first few peaks have a somewhat longer peak-to-peak distance. Note that each point of the theoretical result in Figure 8.8 represents a separate calculation with the SNOM tip at different positions.

A more quantitative understanding of the SNOM images required consideration of the near-field excitation of the hole as well as the SPP standing waves surrounding the hole. When SPP waves encounter a hole, they are partially reflected back to form

surface standing waves and partially scattered into far-field light. LSP resonances at the holes also are excited, and if the incident light is close to a LSP resonance ($\lambda_{ex} \approx \lambda_{LSP}$), far-field scattering is enhanced. This scenario describes what we observed in the 100 nm Au film on glass with 250 nm holes (Figure 8.6), where $\lambda_{LSP} \approx 630$ nm, which is close to $\lambda_{ex} = 633$ nm. As the film thickness decreases, light transmitted directly through the film will, in the far field, dominate over that coming from SPP scattering at the holes and the amplitude of the fringe pattern will decrease significantly or disappear, which is what we observed in 50 nm Au films using $\lambda_{ex} = 633$ nm [(see Figure 8.9(a)]. We could recover faint fringes in this 50 nm film using $\lambda_{ex} = 800$ nm because less light penetrates through the Au film at longer wavelengths. Moreover, we could observe how the orientation of the fringes changed at different polarizations [see Figures 8.9(b) and 8.9(c)].

8.2.3.3 Hole Arrays in Multilayered Films

To provide further evidence that the formation of the standing wave patterns was a result of the interference between the SPPs excited by the SNOM probe and the ones reflected by the holes, we prepared and analyzed films of nanohole arrays constructed from layers of different metals: Au and Ni. [See Figures 8.10(a) and 8.10(d).] We chose Ni because it exhibits a complex dielectric constant that is different from Au in the wavelength range of our experiment [28] and because it can function as an absorbing layer. A bimaterial film made of 50 nm Au and 50 nm Ni (Au/Ni; 50/50) was tested in the SNOM in two different configurations. In the first case, the film was placed on a glass substrate with the Ni side facing up. (The Au side was against the glass.) No fringe patterns were observed because no SPPs were excited in the Ni film. In the second case, the bilayer film was placed on the glass with the Au side facing up and standing wave patterns were observed between the holes.

We also investigated the effects of polarization on the Au/Ni films [see Figures 8.10(b) and 8.10(c)]. The directional dependence of the patterns clearly supports the fact that the fringe patterns can be attributed to SPP propagation combined with scattering from the holes. In addition, multilayer films (Au/Ni/Au) of a Ni core sandwiched between two layers of Au (40/20/40 nm) [Figure 8.10(d)] exhibited standing wave patterns with a period of $\lambda_{sw} \approx 320$ nm under $\lambda_{ex} = 633$ nm [Figure 8.10(e)], nearly identical to the Au-only case. Finally, we imaged a Au/Ni/Au film

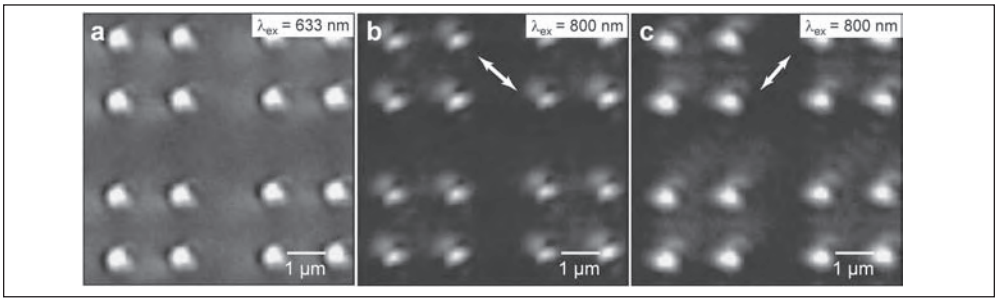

Figure 8.9 SNOM images of 50 nm Au films with 250 nm holes illuminated using (a) $\lambda_{ex} = 633$ nm and (b,c) $\lambda_{ex} = 800$ nm light. The use of longer wavelength light effectively increases the thickness of the film. The white arrows indicate the polarization direction (b) parallel and (c) perpendicular to the light from the tip. Figure reproduced with permission from [26], © (2005) ACS.

(40/70/40 nm) with λ_{ex} = 800 nm ($\lambda_{SPP} \approx$ 784 nm [29]) and observed fringes with an increased spacing of $\lambda_{sw} \approx$ 380 nm, which is also ca. $\lambda_{SPP}/2$ at this excitation wavelength [Figure 8.10(e)] and consistent with our theoretical model.

8.2.4 Collection Mode SNOM of Nanohole Arrays

Using illumination-mode SNOM, we found that SPPs could be generated at Au/air interfaces under localized excitation and that scattering of SPPs could occur at nanoholes in thin metal films. What was slightly complicated about this experiment, however, was that the excitation source (the light delivered by the SNOM probe) was scanned while the far-field light was collected. A more straightforward configuration for imaging the evanescent wave nature of SPs is when the SNOM tip functions as a near-field detector of the electromagnetic fields when the sample is illuminated uniformly from the far field. Therefore, SNOM in collection mode can easily visualize SPPs and provide direct evidence of SPP-assisted EOT through metallic nanohole arrays [30].

8.2.4.1 Near-Field Optical Characterization

Gold films with varying thicknesses (t = 50–180 nm) but with the same microscale spacings as those discussed in Section 8.2.3 (a = 2 μm, d = 250 nm) were investigated using collection mode SNOM. Note that this spacing a is smaller than the propagation length of SPPs (δ_{SPP}), ca. 10 μm [31]. We found that using a linearly polarized 633 nm HeNe laser as the far-field excitation source, Au films with different thicknesses (t = 125 nm and 75 nm) exhibited markedly different fringe periods

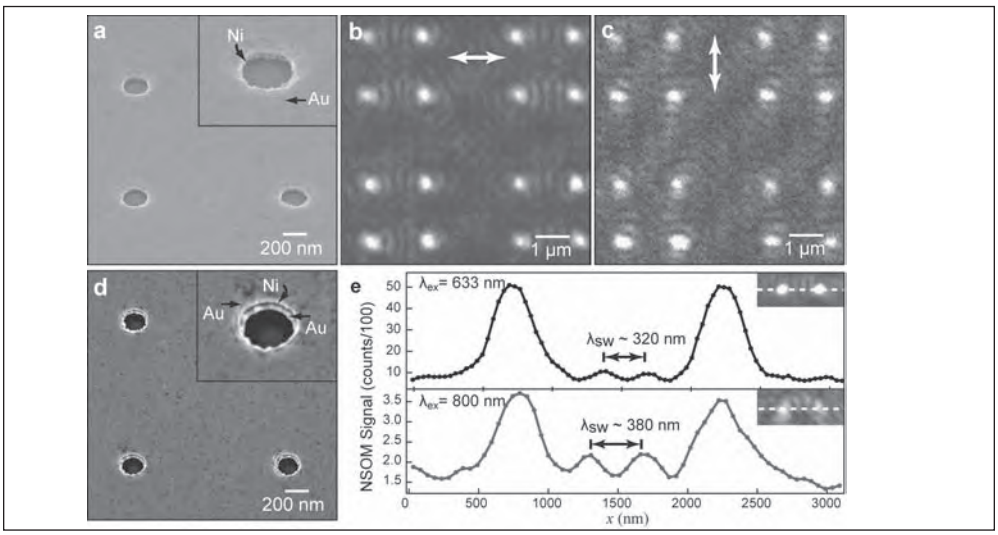

Figure 8.10 Structural and optical properties of bilayer and multilayer metal films. (a) SEM image of holes in a Au/Ni (50/50 nm) film. The tilt angle is 35°. SNOM images of Au/Ni film with polarization (b) parallel and (c) perpendicular to light from the tip. The arrows indicate the direction of polarization. (d) SEM image of 200 nm holes in a Au/Ni/Au (40/20/40 nm) film. The tilt angle is 25°. (e) SNOM cross section of two neighboring holes in a 40/70/40 nm film imaged under local λ_{ex} =633 nm and λ_{ex} =800 nm light. The period λ_{sw} of the SPP standing wave between the holes increases as the excitation wavelength increases. Figure reproduced with permission from [26], © (2005) ACS.

(λ_{sw}): $\lambda_{sw} \approx 300$ nm when $t = 125$ nm, and $\lambda_{sw} \approx 603$ nm when $t = 75$ nm. These periods are equal to or half of λ_{SPP} at the Au/air interface, which suggests a close relation between the fringes and the SPPs. To eliminate the interaction between SPPs from different holes, we also mapped the near-field optical images of 25 μm spaced holes with two thicknesses ($t = 50$ nm and 180 nm) [see Figures 8.11(c) and 8.11(d)]. Because δ_{SPP} is ca. 10 μm, nanoholes separated by 25 μm can be considered as isolated holes. Both film thicknesses exhibited fringes surrounding the holes, but interestingly, they showed $\lambda_{sw} = \lambda_{SPP}$. Furthermore, the direction of the fringes aligned with the polarization of the incident light, which is a characteristic of SPPs.

8.2.4.2 Modeling Surface Plasmon Interference

We can explain the dependence of the Au film thickness on the near-field optical images using a simple physical model based on interference between the SPPs launched by the holes and light transmitted through the film. An isolated hole at the top surface of a film (i.e., the surface closest to the SNOM probe) can act as a source of SPPs [32]; hence, the observed fringes can be attributed to interference between the SPPs launched by the hole and the light transmitted directly through the film [33]. The interference between SPPs and directly transmitted light (type I) could create fringes surrounding isolated holes with a period equal to λ_{SPP} [33]. In the case of 2 μm hole arrays, since $a \sim 2$ μm is less than δ_{SPP}, the interaction between the holes must be considered. Thus, the interference between SPPs launched from neighboring holes (type II) also can contribute to the formation of fringes in the near field for hole arrays and may produce standing waves of SPPs with a period of $\lambda_{SPP}/2$. Whether the fringes exhibit a period of λ_{SPP} or $\lambda_{SPP}/2$ depends on which type of interference is dominant. Compared with simulations based on FDTD methods that calculate electromagnetic field distributions, our model can provide an intuitive understanding of the mechanism behind the different interference patterns and how they relate to SPP-mediated EOT.

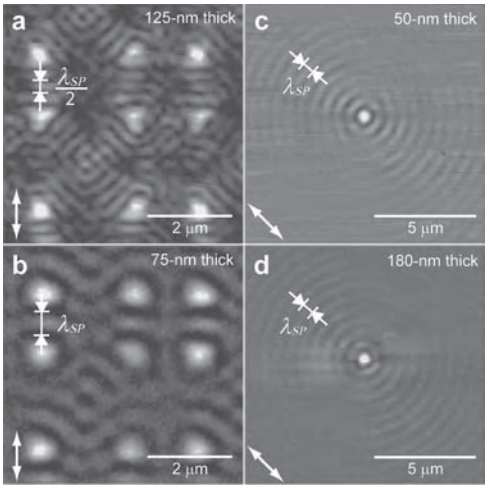

Figure 8.11 SNOM images of (a,b) isolated 250 nm holes and (c,d) microscale arrays of 250 nm holes in Au films of different thickness. Figure reproduced with permission from [30], © (2006) ACS.

Figure 8.12 depicts the one-dimensional (1-D) in-plane electric field of SPPs between adjacent holes and the directly transmitted light under incident excitation polarized along the x direction. The amplitude of the electric field in can be expressed as follows:

$$E_{SPP1}(x) = A_{SPP}e^{-x/\delta_{SPP}}\cos(k_{SPP}\cdot x)$$

$$E_{SPP2}(x) = A_{SPP}e^{-(a-x)/\delta_{SPP}}\cos(k_{SPP}\cdot(a-x))$$

$$E_l(x) = A_l$$

where A_{SPP} and A_l are the amplitudes of the SPPs and the directly transmitted light at the top surface, respectively, and k_{SPP} is the in-plane SPP wavevector (k_x). Because $a \sim 2\ \mu\text{m} \ll \delta_{SPP}$, the decay factors $e^{-x/\delta_{SPP}}$ and $e^{-(a-x)/\delta_{SPP}}$ do not change significantly from $x = 0$ to $x = a$ and can be neglected to simplify the expression. The total electric field is then reduced to the following

$$E_{tot}(x) = E_l(x) + E_{SPP1}(x) + E_{SPP2}(x) \tag{8.1}$$

$$E_{tot}(x) = A_l + 2A_{SPP}\cos(k_{SPP}a/2)\cos(k_{SPP}\cdot(2x-a)/2)$$

The total intensity between the holes is

$$I_{tot}(x) = |E_{tot}(x)|^2$$

$$I_{tot}(x) = I_1 + I_2 + I_3$$

$$= A_l^2 + 4A_lA_{SPP}\cos(k_{SPP}\cdot a/2)\cos(k_{SPP}\cdot(2x-a)/2)$$

$$+A_{SPP}^2\cos^2(k_{SPP}\cdot a/2)\cos^2(k_{SPP}\cdot(2x-a)/2)$$

The first term of I_{tot} (I_1) signifies the directly transmitted light through the film and does not depend on x. The second term (I_2) represents the interference between SPPs and the directly transmitted light. The third term (I_3) represents the interference between SPPs from neighboring holes. If the ratio A_l/A_{SPP} is large, I_2 tends to dominate I_{tot} and $\lambda_{sw} = \lambda_{SPP}$ [Figure 8.12(b)]; if the ratio A_l/A_{SPP} is small, I_3 will dominate I_{tot} and $\lambda_{sw} = \lambda_{SPP}/2$ [Figure 8.12(c)]. This straightforward derivation indicates that two types of interference can affect the overall near-field optical intensity and that λ_{sw} is determined primarily by the ratio A_l/A_{SPP}.

We performed collection mode SNOM measurements on Au nanohole arrays with increasing film thicknesses (t = 50, 75, 100, 108, 125, 150, and 180 nm) to test this model. SNOM images and optical line scans indeed verified the scenarios predicted by the interference model (see Figure 8.13). Hole array films with $t < 100$ nm exhibited $\lambda_{sw} = \lambda_{SPP}$, and those with $t > 108$ nm exhibited $\lambda_{sw} = \lambda_{SPP}/2$ (see Figure 8.14). In addition, the 2-D near-field distributions were simulated using $\delta_{SPP} = 10\ \mu$m, $k_{SPP} = 2\pi/\lambda_{SPP} = 0.0104\ \text{nm}^{-1}$, and the appropriate polarization angle. Figures 8.13(b) and 8.13(d) depict 2-D simulations for large and small A_l/A_{SPP} ratios, which are in excellent agreement with SNOM images of nanohole arrays in 100 nm thick films (large A_l/A_{SPP} ratio) and in 108 nm thick films (small A_l/A_{SPP} ratio) [see Figures 8.13(a) and 8.13(c)]. The correspondence between the experimental and theoretical images indicates that thinner films

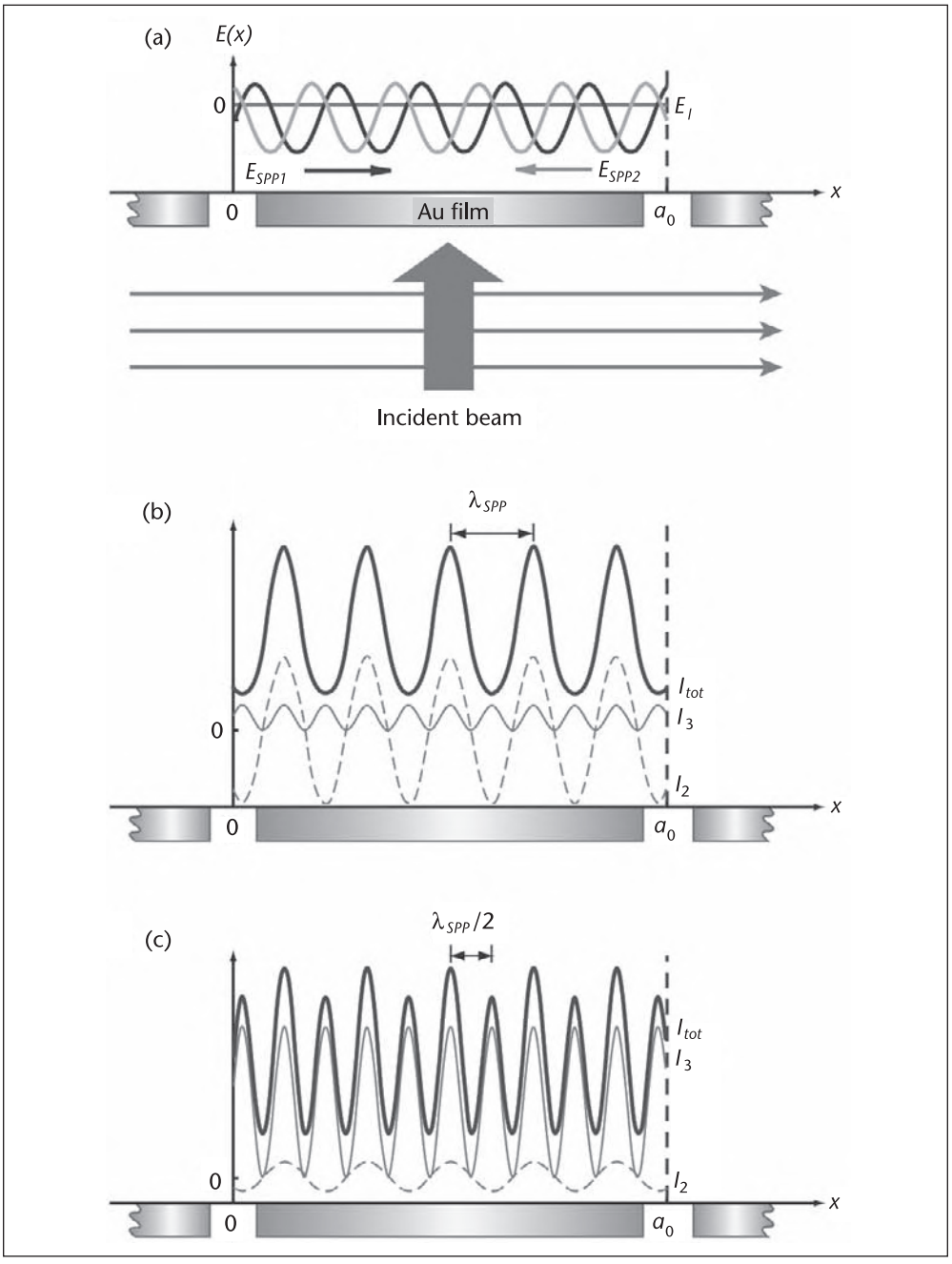

Figure 8.12 Scheme of the 1-D interference model. (a) In-plane electric fields of SPPs between adjacent holes and transmitted light under the incident light is polarized along the *x* direction. (b) Total intensity displaying $\lambda_{sw} = \lambda_{SPP}$, which is dominated by I_2 when the ratio A_I / A_{SPP} is large. (c) Total intensity showing $\lambda_{sw} = \lambda_{SPP}/2$, which is dominated by I_3 if the ratio A_I / A_{SPP} ratio is small. Figure reproduced with permission from [30], © (2006) ACS.

exhibit larger A_I/A_{SPP} ratios; that is, the thinner the film, the greater the amplitude of the directly transmitted light relative to the SPPs on the top surface. Depending on the competition between these two types of interference, λ_{sw} can be either λ_{SPP} or $\lambda_{SPP}/2$. To support the SPP interference model further, SNOM images of 50 nm

thick Au films were scanned with different linear polarization directions of the incident light. Figures 8.13(e)–8.13(h) showed that experimental images and calculated patterns also were in perfect agreement.

Because SPPs are supported only at the metal-dielectric interface, nonmetallic nanohole arrays should not exhibit similar fringes. SNOM measurements on a 90 nm Si film with a $a \sim 2\ \mu$m did not show any features (Figure 8.15), which demonstrated that the near-field optical fringes depend critically on the material properties and not only on the geometry of the array. These SNOM measurements, together with the physical model, provide direct evidence for SPPs when Au nanohole arrays were globally illuminated. Our systematic investigation of transmission through a series of metal films with different thicknesses revealed that SPPs can tunnel through subwavelength channels more efficiently than photons can; thus, the presence of SPPs improves the optical transmission efficiency through metal nanohole arrays.

8.2.4.3 Zeroth-Order Far-Field Spectroscopy

To characterize the optical properties of nanohole arrays completely, far-field spectroscopy was carried out to verify the relative transmission efficiency between SPPs and photons observed in the near-field studies and to relate SPPs to the EOT effect. Zeroth-order transmission measurements were carried out using an optical microscope coupled to a spectrometer and using illumination at normal incidence. In the transmission spectrum of an unpatterned 180 nm thick Au film (black curve in Figure 8.16), only the 500 nm peak (the interband transition of Au thin films) was observed, whose intensity can be considered as a measure of direct transmission through the film. Films with arrays of nanoholes, however, exhibited many distinct peaks (curve in Figure 8.16) because of high-order SPP Bragg coupling. When light illuminates a film perforated with arrays of nanoholes, photons can be converted into SPPs. Although the transmission of free-space light through a Au film or a single nanohole is inefficient, the electromagnetic energy of incident light can be transmitted through nanohole arrays in the

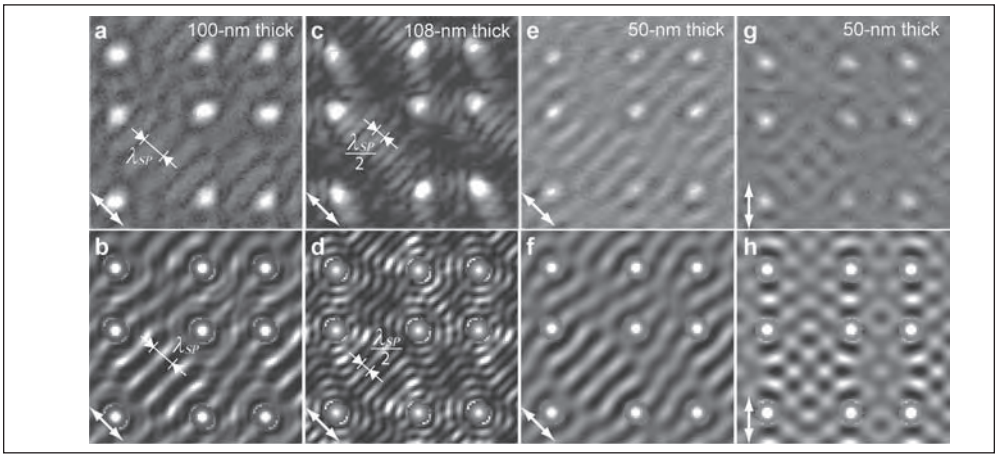

Figure 8.13 Experimental and simulated near-field images of nanohole arrays in gold films. (a–f) Near-field images of hole arrays with different film thickness and calculated images with different $A_{//}/A_{SPP}$ ratios. (g–h) Measured near-field and calculated images of hole arrays illuminated with light with a different polarization. Arrows indicate the polarization direction of the incident light. All images are 4.5 μm $\times$4.5 μm. Figure reproduced with permission from [30], © (2006) ACS.

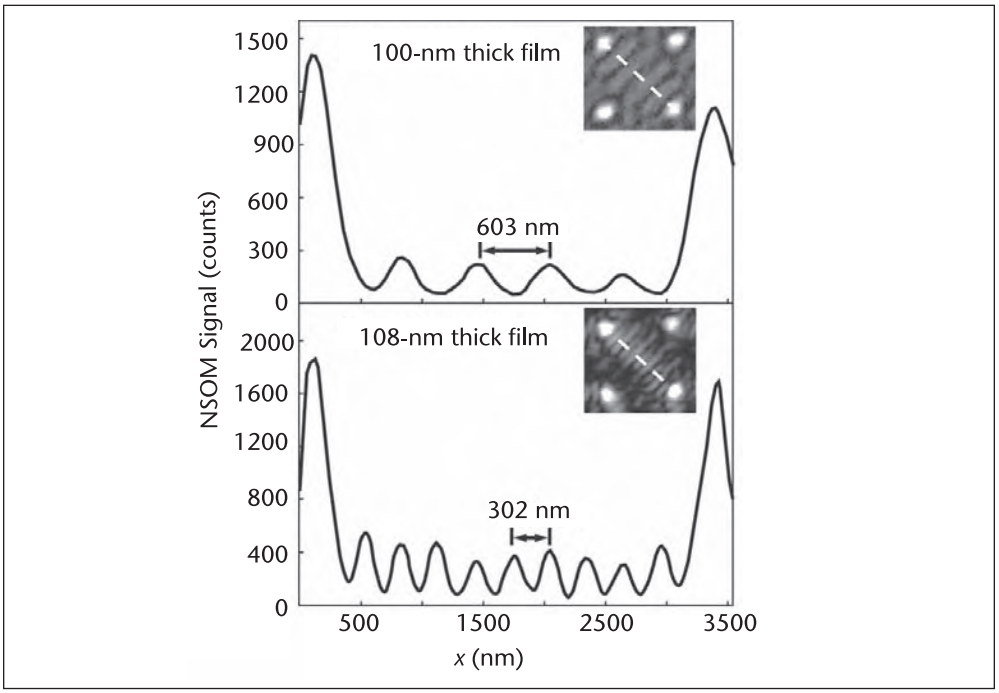

Figure 8.14 Line scans of SNOM images between nanoholes in a 2 μm spaced array. The fringe period $\lambda_{sw} = 603$ nm ($= \lambda_{SPP}/2$) for a 100-thick Au film, and $\lambda_{sw} = 302$ nm for a 108 nm thick Au film with $\lambda_{ex} = 633$ nm. Figure reproduced with permission from [30], © (2006) ACS.

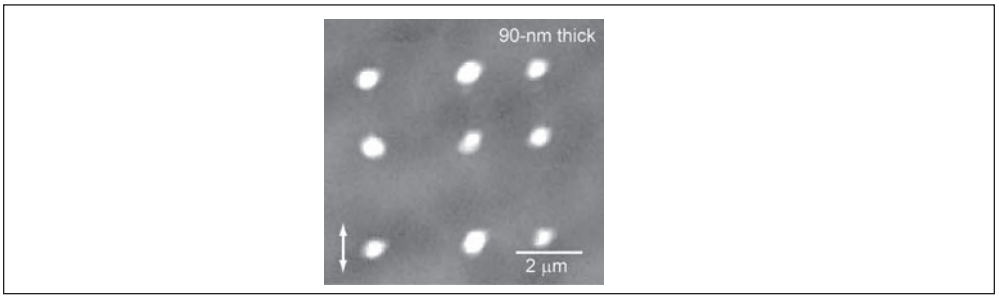

Figure 8.15 SNOM image of a 2 μm spaced nanohole arrays patterned in 90 nm thick Si film. Figure reproduced with permission from [30], © (2006) ACS.

form of SPPs. As described in Section 8.1, SPPs are trapped on a surface and are expected to propagate through subwavelength channels with much greater efficiency, which explains why SPPs may contribute to EOT. As anticipated, when the film thickness of the hole arrays decreased to 100 nm, the amplitude of the SPP peaks changed only slightly while the interband transition peak nearly doubled in intensity (curve in Figure 8.16). These far-field results are consistent with our analysis based on near-field measurements, which suggested that the thicker the film, the stronger the amplitude of the SPP peaks were relative to that of directly transmitted light. Comparison of the peak amplitudes in the spectra of the two different film thicknesses verifies that SPPs decay more slowly through the gold nanohole arrays than photons do.

With careful measurements, the SPP resonances observed in the far-field transmission spectra can be analyzed based on the theory of Bragg coupling. For example,

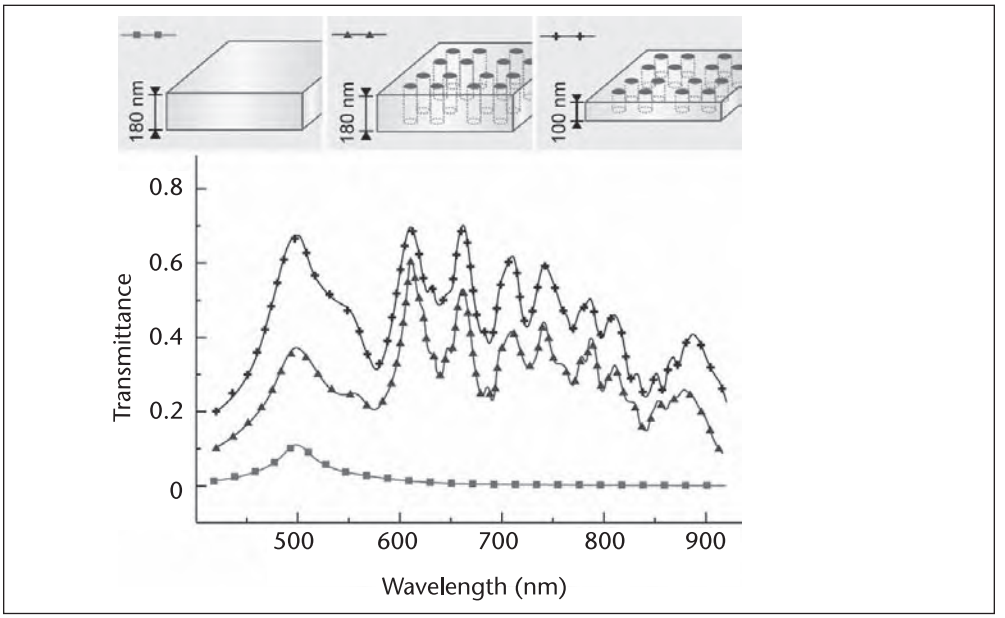

Figure 8.16 Transmittance of a solid Au film and nanohole arrays. 180 nm thick Au films exhibit only an intraband transition peak at 500 nm. Arrays of 250 nm holes ($a \approx 2\ \mu$m) in 180 nm films and 100 nm films exhibit SPP-Bloch wave peaks between 600 and 900 nm.

because a 1-D grating can add in-plane momentum of multiple $G = 2\pi/a_0$, the k_x of the incident light is modified when the light encounters a nanohole array:

$$k_x = k_{x0} + i\frac{2\pi}{a_0}$$

where $k_{x0} = 0$ for light incident in a normal direction, i is an integer, and a_0 is the lattice constant of the grating. Resonant coupling between incident light and SPPs, or SPP-Bloch waves (SPP-BWs), can occur when the in-plane momentum matches Equation 8.1. In the 2-D case of a square grating, where coupling can occur along both x and y directions, the SPP peaks can be expressed as follows:

$$\lambda_{SPP} = \ = \frac{a_0}{\sqrt{i^2 + j^2}} \sqrt{\frac{\varepsilon_{Au}(\omega)\varepsilon_d}{\varepsilon_{Au}(\omega) + \varepsilon_d}}$$

where i and j are integers corresponding to the mode order along the two lattice directions, $\varepsilon_{\mathrm{Au}}(\omega)$ is the frequency-dependent dielectric constant of Au, and ε_d is the dielectric constant of the surrounding dielectric material (air or glass). In the case of our microscale hole arrays where the lattice constant $a_0 = 4\ \mu$m (the unit-cell size, since the two sets of spacings a are 1.8 μm and 2.2 μm), the SPP-BWs are constrained by $17 \leq (i^2 + j^2) \leq 58$ at the Au/air interface and $40 \leq (i^2 + j^2) \leq 200$ at the Au/glass interface in the wavelength range of 550–950 nm. High-order SPP-Bragg coupling is expected with microscale arrays [see Figure 8.17(a)].

Angle-dependent transmission spectra of arrays of circular holes with $a_0 = 4\ \mu$m were acquired to confirm that these complex spectral features were indeed SPP-BWs. Transmission spectra were collected under different incident excitation angles ranging from 0° to 50° in 0.5° increments using p-polarized light.

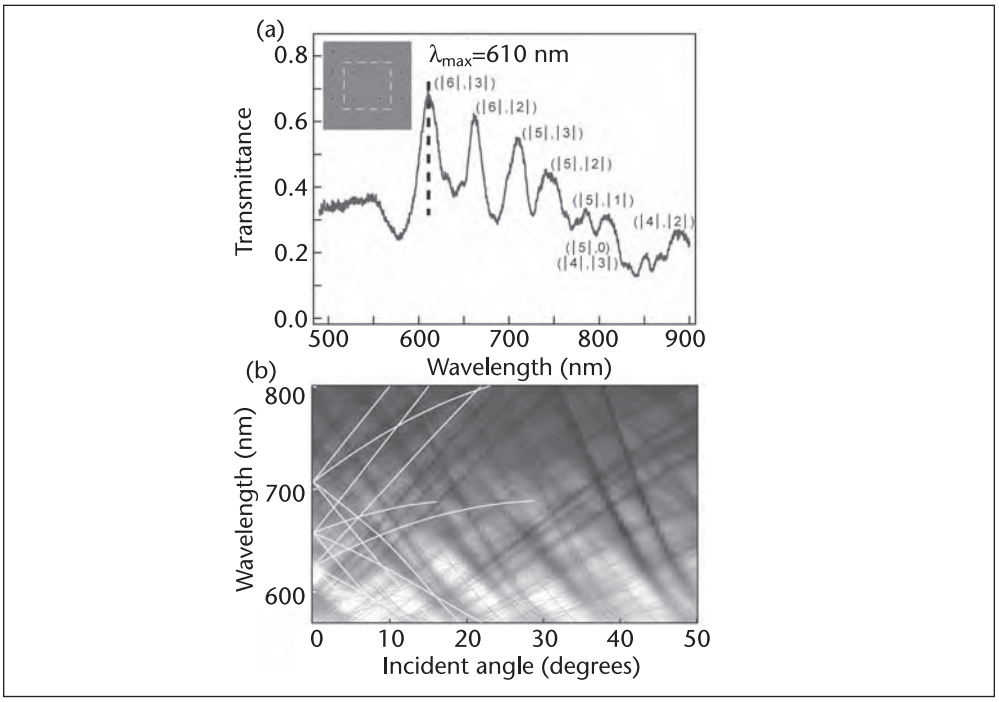

Figure 8.17 (a) Zero-order transmittance of arrays of 250 nm circular holes with $a_0 = 4$ μm under normal incidence illumination. Insets are SEM pictures of the hole array, and the white box depicts the unit cell. Representative SPP-Bloch wave modes are labeled as (|i|, |j|). (b) Dispersion diagram of hole arrays as a function of incident angle under p-polarized light. Calculated SPP dispersion curves at the air/Au interface are superimposed in gray. The curves corresponding to the modes indicated in (a) are in bold. Figure adapted with permission from [25], © (2007) Wiley.

Figure 8.17(b) depicts these compiled spectra in the form of a dispersion diagram. Superimposed on the dispersion diagram is the calculated dispersion curves of SPP-BWs on a 2-D square grating at the Au/air interface with $a_0 = 4$ μm using Equation 8.2. The trends in peak evolution as a function of angle are in good agreement with the theoretically predicted SP dispersion curves. Although more sophisticated theoretical approaches have been used to model the interaction between light and nanoholes or nanoslits [27, 34], Equation 8.2 with a microscale lattice spacing reproduces the major SPP peak trends reasonably well.

8.2.5 Near-Field and Far-Field Characterization of Anisotropic Nanohole Arrays

Near-field optical images also were obtained on 180 nm thick Au films of arrays of anisotropic, slitlike holes using collection mode SNOM. (See Figure 8.18.) Similar to the patterns that we observed on films of circular hole arrays, the fringes between the anisotropic holes indicated that SPP waves were launched by and reflected between holes. Unlike the arrays of circular holes, which exhibited polarization-dependent standing waves, the amplitude of the fringes between anisotropic nanoholes varied significantly with polarization [see Figures 8.18(b) and 8.18(c)]. The SNOM images suggest that SPPs can be generated more efficiently when the excitation light is polarized perpendicular to the long axis of the slits compared to when light is polarized parallel to the slits.

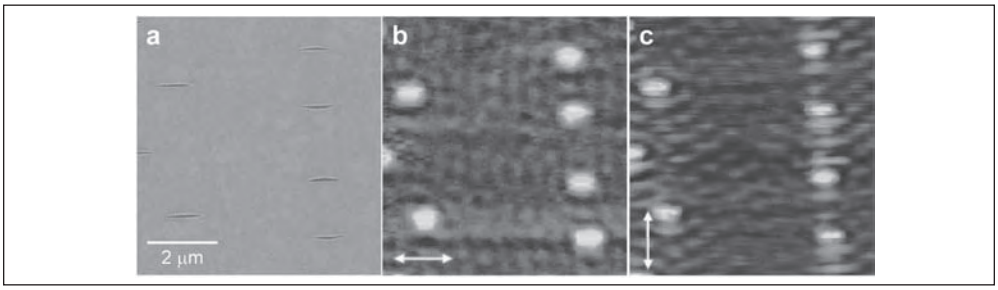

Figure 8.18 (a) SEM image of slitlike holes in 180 nm thick Au films. SNOM optical images with (b) horizontal polarization and (c) vertical polarization with respect to the long axis of the slitlike hole.

In addition, far-field transmission through 180 nm thick Au films of anisotropic nanohole arrays exhibited strong dependence upon the polarization direction of the incident light. Dramatic color changes tunable from green to red were observed as the polarization was rotated from $\theta = 0°$ to 90°, where θ is the angle between the long axis of the hole and the polarization direction of the incident light. To gain insight into this color change, single-hole spectroscopy was performed on elliptical and slitlike holes. Similar to how we analyzed the far-field spectra from circular hole arrays (Section 8.2.4.3), we first considered isolated, anisotropic holes where the SPPs contributions were eliminated from the optical transmission. Single, broad peaks at $\lambda_{max} = 750$ nm and 730 nm at $\theta = 90°$ in the spectra of isolated holes can be attributed to LSP resonances [see Figures 8.19(a) and 8.19(d)]. Note that the transmittance was significantly higher at $\theta = 90°$ compared to $\theta = 0°$: 21±3 times for elliptical holes and 50±4 times for slitlike holes.

These anisotropic holes spaced by several microns also exhibited complex spectral features in the far-field transmission when $\theta = 90°$ because of Bragg coupling of SPPs. The pronounced SPP peaks decreased when $\theta = 45°$ (were similar to those from unpolarized light excitation) and finally disappeared (or became very weak) when $\theta = 0°$. Interestingly, the subtle structural differences between the two hole shapes within these elliptical [Figures 8.19(b) and 8.19(c)] and slitlike [Figures 8.19(e) and 8.19(f)] hole arrays could be resolved by single-hole spectroscopy. Only LSPs contribute to the transmission in the case of isolated holes, while both LSPs and SPPs contribute in the microscale arrays of holes. Hence, we could determine the relative contributions of LSPs and SPPs on the polarization-dependent transmission by comparing the transmittance from an isolated hole to that of a single hole within a microscale array. The ratio of SPP versus LSP contributions to the transmittance can be calculated according to the following:

$$\frac{T_{SPP}}{T_{LSP}} = \frac{T_{array} - T_{isolated}}{T_{isolated}}$$

We found that the SPP contributions for anisotropic holes patterned at microscale spacings [Figures 8.5(e) and 8.5(f)] were 5–6 times greater than those from LSPs (at $\theta = 90°$).

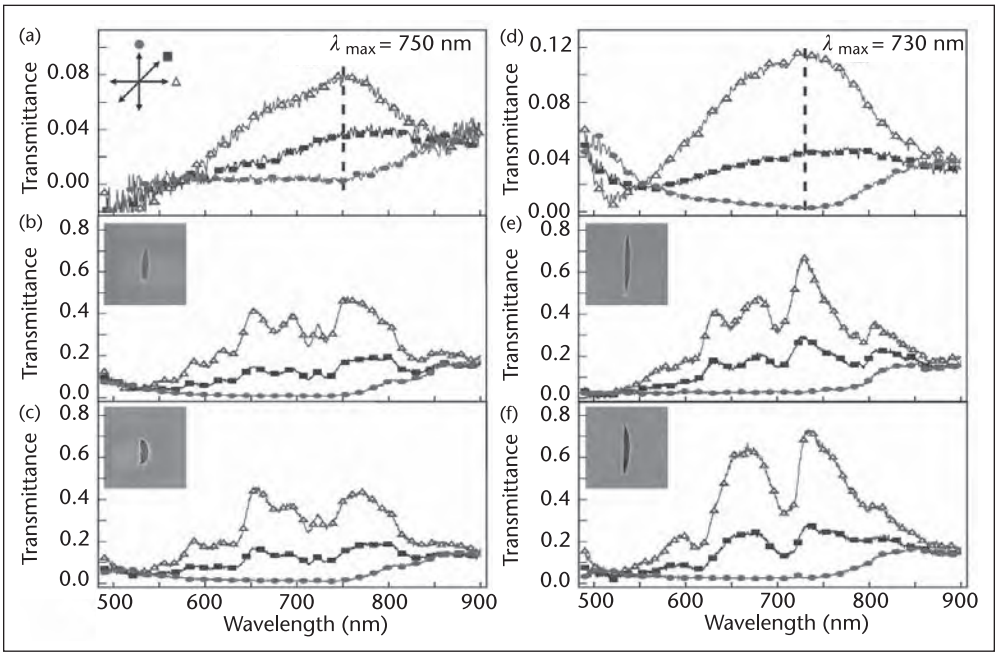

Figure 8.19 Polarization-dependent transmittance of anisotropic hole arrays. (Left) Transmittance of (a) an elliptical hole in a 25 μm array, (b) a symmetric elliptical hole in a 2 μm array, and (c) an asymmetric elliptical hole in a 2 μm array. (Right) Transmittance of (d) a slitlike hole in a 25 μm array, (e) a symmetric slitlike hole in a 2 μm array, and (f) an asymmetric slitlike hole in a 2 μm array. All polarized illumination is relative to the long axis of the hole (● = 0°, ■ = 45°, and △ = 90°). Figure adapted with permission from [25], © (2007) Wiley.

8.3 Future Directions and Outlook

SPs generated by subwavelength hole arrays exhibit fascinating optical properties. The EOT through nanoholes in metal films provides access to extremely small subwavelength light sources, which are crucial to the development of high-density integrated photonic circuits and optical storage devices. Furthermore, these periodic nanostructures allow the propagation of SPPs at certain frequencies (while forbidding others) and can behave as plasmonic band gap crystals. Line defects in these crystals can act as channels for plasmonic waveguides, and point defects can allow for plasmon-based lasers. These engineered structures are best investigated by near-field combined with far-field optical characterization. Importantly, near-field spectroscopy can offer new possibilities for mapping the localized electromagnetic fields in subwavelength hole arrays. Finally, because the resonant frequencies of SPPs excited in anisotropic nanohole arrays are tunable depending on the polarization and incident angle of the excitation source, these substrates are of intrinsic scientific interest and provide opportunities to develop electrically and mechanically controlled plasmonic devices.

Acknowledgments

This work was supported by the National Science Foundation, NASA, and the David and Lucile Packard Foundation. We thank Joel Henzie and Min Hyung Lee for their invaluable contributions in sample preparation and data analysis. We are very grateful to George C. Schatz, Stephen K. Gray, and Gilbert Chang for carrying out the FDTD calculations on the microscale arrays of nanoholes. T.W.O. is a DuPont Young Professor, a Cottrell Scholar of Research Corporation, and an Alfred P. Sloan Research Fellow.

References

[1] Novotny, L., and B. Hecht, *Principles of Nano-optics,* Cambridge: Cambridge University Press, 2006.

[2] Betzig, E., and J. K. Trautman, "Near-Field Optics: Microscopy, Spectroscopy, and Surface Modification Beyond the Diffraction Limit," *Science,* Vol. 257, 1992, pp. 189–195.

[3] Fang, N. et al., "Sub-Diffraction-Limited Optical Imaging with a Silver Superlens," *Science,* Vol. 308, 2005, pp. 534–537.

[4] Ambrose, W. P. et al., "Single Molecule Detection and Photochemistry on a Surface Using Near-Field Optical Excitation," *Phys. Rev. Lett.,* Vol. 72, 1994, pp. 160–163.

[5] Xie, X. S., and R. C. Dunn, "Probing Single Molecule Dynamics," *Science,* Vol. 265, 1994, pp. 361–364.

[6] Zinn, A. A, "Surface Plasmons Utilized to Achieve High-Density Nanolithography," *MRS Bulletin,* Vol. 29, 2004, pp. 606–607.

[7] Lewis, A. et al., "Near-Field Optics: From Subwavelength Illumination to Nanometric Shadowing," *Nature Biotech.,* Vol. 21, 2003, pp. 1378–1386.

[8] Maier, S. A. et al., "Experimental Demonstration of Fiber-Accessible Metal Nanoparticle Plasmon Waveguides for Planar Energy Guiding and Sensing," *Appl. Phys. Lett.,* Vol. 86, 2005, Art. No. 071103.

[9] Maier, S.A. et al., "Local Detection of Electromagnetic Energy Transport Below the Diffraction Limit in Metal Nanoparticle Plasmon Waveguides," *Nature Mater.,* Vol. 2, 2003, 229–232.

[10] Bozhevolnyi, S. I. et al., "Waveguiding in Surface Plasmon Polariton Band Gap Structures," *Phys. Rev. Lett.,* Vol. 86, 2001, pp. 3008–3011.

[11] Ditlbacher, H. et al., "Two-Dimensional Optics with Surface Plasmon Polaritons," *Appl. Phys. Lett.,* Vol. 81, 2002, pp. 1762–1764.

[12] Drezet, A. et al., "Plasmonic Crystal Demultiplexer and Multiports," *Nano Lett.,* Vol. 7, 2007, pp. 1697–1700.

[13] Kitson, S. C., W. L. Barnes, and J. R. Sambles, "A Full Photonic Band Gap for Surface Modes in the Visible," *Phys. Rev. Lett.,* Vol. 77, 1996, pp. 2670–2673.

[14] Specht, M. et al., "Scanning Plasmon Near-Field Microscope," *Phys. Rev. Lett.,* Vol. 68, 1992, pp. 476–479.

[15] Haynes, C. L., A. D. McFarland, and R. P. V. Duyne, "Surface-Enhanced Raman Spectroscopy," *Anal. Chem.,* Vol. 77, 2005, pp. 338A–346A.

[16] Kretschmann, E., and H. Reather, "Radiative Decay of Nonradiative Surface Plasmon Excited by Light," *Z. Naturf.,* Vol. 23A, 1968, pp. 2135–2136.

[17] Krenn, J. R. et al., "Squeezing the Optical Near-Field Zone by Plasmon Coupling of Metallic Nanoparticles," *Phys. Rev. Lett.,* Vol. 82, 1999, pp. 2590–2593.

[18] Weeber, J.-C. et al., "Surface Plasmon Routing along Right Angle Bent Metal Strips;" *Appl. Phys. Lett.,* Vol. 87, 2005, Art. No. 221101.

[19] Zia, R., and M. L. Brongersma, "Surface Plasmon Polariton Analogue to Young's Double-Slit Experiment," *Nature Nanotech.,* Vol. 2, 2006, pp. 426–429.

[20] Hecht, E. *Optics*, 4th ed., Reading, MA: Addison-Wesley, 2002.

[21] Bethe, H. A., "Theory of Diffraction by Small Holes," *Phys. Rev.,* Vol. 66, 1944, pp. 163–182.

[22] Ebbesen, T. W. et al., "Extraordinary Optical Transmission Through Sub-wavelength Hole Arrays," *Nature,* Vol. 391, 1998, pp. 667–669.

[23] Lezec, H. J., and T. Thio, "CDEW (Composite Diffracted Evanescent Waves): New Model for Enhanced Transmission of Subwavelength Apertures," *Opt. Express,* Vol. 12, 2004, p. 3629.

[24] Henzie, J. et al., "Large-Area Nanoscale Patterning: Chemistry Meets Fabrication," *Accts. Chem. Res.,* Vol. 39, 2006, pp. 249–257.

[25] Lee, M. H. et al., "Microscale Arrays of Nanoscale Holes," *Small,* Vol. 3, 2007, pp 2029– 2033.

[26] Kwak, E.-S., J. Henzie, and T. W. Odom, "Mesoscale Metallic Pyramids with Nanoscale Tips," *Nano Letters,* Vol. 5, 2005, pp. 1963–1967.

[27] Chang, S.-H., S. K. Gray, and G. C. Schatz, "Surface Plasmon Generation and Light Transmission by Isolated Nanoholes and Arrays of Nanoholes in Thin Metal Films," *Opt. Express,* Vol. 13, 2005, pp. 3150–3165..

[28] Ordal, M.A. et al., "Optical Properties of the Metals Al, Co, Cu, Au, Fe, Pb, Ni, Pd, Pt, Ag, Ti, and W in the Infrared and Far Infrared," *Appl. Opt.* Vol. 22, 1983, pp. 1099–1120.

[29] Quinten, M. et al., "Electromagnetic Energy Transport via Linear Chains of Silver Nanoparticles," *Opt. Lett.,* Vol. 23, 1998, pp. 1331–1333.

[30] Gao, H., J. Henzie, and T. W. Odom, "Direct Evidence for Surface Plasmon-Mediated Enhanced Light Transmission through Metallic Nanohole Arrays," *Nano Lett.,* Vol. 6, 2006, pp. 2104–2107.

[31] Lamprecht, B. et al., "Surface Plasmon Propagation in Microscale Metal Stripes," *Appl. Phys. Lett.,* Vol. 79, 2001, p. 51.

[32] Popov, E. et al., "Surface Plasmon Excitation on a Single Subwavelength Hole in a Metallic Sheet," *Appl. Opt.,* Vol. 44, 2005, p. 2332.

[33] Yin, L. et al., "Surface Plasmons at Single Nanoholes in Au Films," *Appl. Phys. Lett.,* Vol. 85, 2004, pp. 467–469.

[34] García-Vidal, F. J. et al., "Transmission of Light Through a Single Rectangular Hole in a Real Metal," *Phys. Rev. B,* Vol. 74, 2006, Art. No. 153411.

CHAPTER 9

High Enhancement and Near-Field Localization of Light on Semicontinuous Films

Samuel Grésillon, Emmanuel Fort, and Sandrine Leveque-Fort

9.1 Introduction

In the past decade, metallic devices at the nanometer scale have stimulated a broad range of interests in nanophotonics and near-field microscopy. For instance, sharp apertureless metal tips have been used to enhance the signal-to-noise ratio and the spatial resolution in a wide range of experiments: fluorescence [1–5], two-photon-excited fluorescence [6], infrared absorption [7], Raman scattering [8], and Coherent anti-Stokes Raman Scattering [9].

The unique properties of the metallic structures come from the excitation of modes associated with the collective oscillation of the conduction electrons at the surface of a metal [10]. These modes are called plasmon modes, and they give rise to specific optical properties [10, 11]. In the case of a nanostructured metallic thin film, plasmon modes are excited resonantly by the incident light, inducing significant local near-field enhancements.

Nanostructured metal-dielectric films naturally concentrate the evanescent field in nanometer-scale areas with unmatched field enhancements. The electromagnetic energy is accumulated in "hot spots," leading to local fields that can exceed the intensity of the applied field by four to five orders of magnitude [12]. Besides, in contrast to the use of sophisticated, designed nanostructures produced by electronic lithography, these random metallic films can be produced with simple inexpensive techniques making them potentially available for everyday applications such as biosensing [13].

Semicontinuous films are usually obtained by thermal evaporation or sputtering of metal onto a dielectric surface. During deposition, the thin film morphology evolves from isolated nanoparticles with diameters between 5 and 30 nm to percolated thin film (see Figure 9.1). When the metal filling factor increases and coalescence occurs, irregularly shaped self-similar clusters are formed on the substrate. The sizes of the structures diverge in the vicinity of the percolation threshold, where an infinite percolation cluster of a metal is eventually formed [14]. It is represented with the presence of a continuous conducting path between both sides of a sample [15]. At the percolation threshold, the metal-insulator transition occurs in the system. The structure of the film is self-affine, and all sizes of aggregates exist on the sample. In fact, the concept of scale invariance plays a crucial role in the description

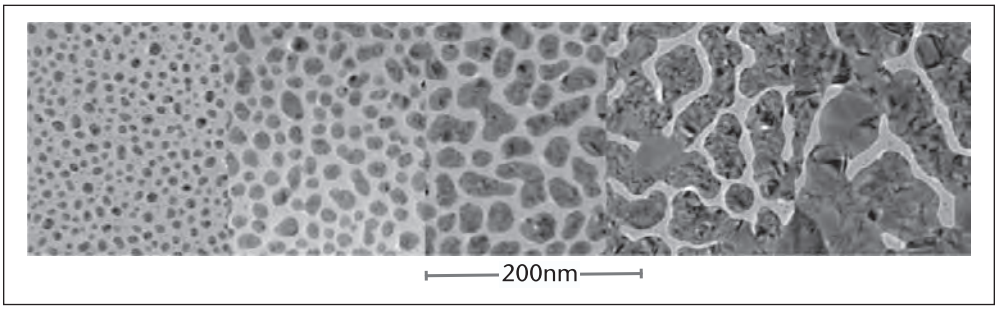

Figure 9.1 TEM images of silver-dielectric films with different nominal metal thicknesses (from left to right: 20 Å, 50 Å, 80 Å, 120 Å, and 160 Å). During deposition, the thin film morphology evolves from isolated nanoparticles with diameters between 5 and 30 nm to percolated thin film.

of various properties of percolation systems. Gefen and his colleagues have demonstrated that the scale invariance of percolating films can be described by a fractal formalism [16]. At higher surface coverage, the film is mostly metallic, with voids of irregular shapes. With further coverage, the film becomes uniform.

By changing the growth parameters during the thin film deposition, it is possible to control and tailor the characteristics of the nanostructured metallic film. The nominal film thickness associated with the percolation threshold can be tuned. Film morphologies are, for instance, highly dependant on substrate temperature, atomic flux, or surface preparation.

9.2 Enhancement of the Electromagnetic Field on Metal Film

9.2.1 Surface Plasmon Resonances

Enhancement of the EM field around metal films is due to localized or propagating modes associated with plasmonic effects. The structure of a semicontinuous metallic film is such that localized and propagating modes are present together and may couple. The peculiarity of semicontinuous films arise from the coupling between the two types of plasmon modes described earlier, LSP and SPP. As an example of possible applications, we describe shortly the coupling with fluorescent dyes and the fluorescence enhancement properties of plasmon resonances.

9.2.1.1 Polarizability of Metallic Particles

The general polarizability of a metal spherical particle [17] has the following expression:

$$\alpha(\omega) = \frac{4\pi r_p^3 \omega_{SP}^2}{\omega_{SP}^2 - \omega^2 - i\omega\gamma - i(2/3)k^3 r_p^3 \omega_{SP}^2} \tag{9.1}$$

where γ is the damping constant, ω_p is the plasma frequency of the free electrons, r_p is the particle radius, and k is the wavevector. The term $-i\omega\gamma$ accounts for damping by absorption, and the term $-i(2/3)k^3 r_p^3 \omega_{SP}^2$ accounts for radiative damping. Equation 9.1 is consistent with the law of energy conservation.

The effect of a metallic particle on the surroundings has been extensively studied in the case of metal-fluorescent coupling for both fundamental (cavity coupling [18], single atom emitters [19], etc.) and application issues [13, 20, 21]. It can be shown from the energy flow distribution of the entire system that one can separate the radiative and the nonradiative contributions in the fluorescence decay rate [22]. The variation of the different contributions to the decay rate strongly depends on the particle-fluorophore distance and on the dipole orientation of the fluorophore [23–25]. Recently, various groups have shown how silver particles can enhance the emission properties of rare-earth fluorophores [26–29].

In numerous systems, metallic particles are not isolated and not strictly spherical. The fact that metallic particles aggregate and form nonspherical shapes changes their absorption and scattering properties while maintaining their strong light interaction. With respect to their coupling with light, the main difference lies in the number and position of the resonance absorption peaks in the frequency range. When particles are very small compared to the wavelength, polarization and wavelength act together to control locally the intensity and the localization of the area where the light is concentrated. These concentrations of light, for which the word *hot spots* is often applied, are due to both geometrical and resonance (plasmon) effects. Itoh and collaborators show that coupling between the particles can further enhance fluorescence [29].

9.2.1.2 Coupling Between SPP and Light Emitters

Because of their dispersion curve, SPP modes always lie beyond the light line. As mentioned previously, this means that SPPs have a greater momentum (k_{SPP}) than free-space photons ($k = \omega/c$) of the same pulsation ω. Because of this momentum mismatch between SPP and incident plane-wave light, these modes cannot be coupled simply without providing the missing momentum. However, scattering by corrugation, roughness, or fluorophores can provide wavevectors large enough for resonant coupling. Fluorophores may decay nonradiatively through their near-field components via coupling to guided waves such as SPs and/or lossy waves. These decay channels depend on the fluorophore-metal distance and on the dipole orientation. Okamoto and his colleagues showed that the emission of light emitters based on InGaN quantum wells could be enhanced with use of rough metallic layers [30]. Roughness and imperfections by evaporated metal coatings can efficiently scatter SPPs into radiative modes. The measurements by Okamoto and his colleagues suggest that the size of the metal structures determines the SPP-photon coupling and light extraction. Biteen and her colleagues [31] studied the coupling between Si nanocrystals (nc-Si) and a highly roughened surface made of nanoporous gold thin film. They showed that this coupling can yield a fourfold enhancement in the fluorescence intensity at $\lambda = 780$ nm, which is related to the fourfold enhancement in radiative decay rate as a result of local-field effects.

9.3 Localization of Light on Semicontinuous Films

Since the sixties, it is known that the optical behavior of metal-dielectric films is very peculiar. Cohen's study observed that the transmission of thick metal-dielectric

films made of gold and silver in silica changed abruptly around the percolation threshold [32]. Later, Grannan, Garland, and Tanner showed on thick structures of silver in potassium that the transmission increases exponentially near the percolation [33], as predicted by Berman and Imry with an analytical model [34]. In the eighties, Yagil and Deutscher introduced a more elaborate theory to increase the domain of validity of the previous model [35]. Using renormalization of the real space and scaling laws based on the fractal dimension of the films, they reproduced the high absorption near the percolation threshold found by Gadenne [36, 37]. Today the optical effects of such structures is well understood on the macroscopical scale. However, there still is not a clear picture of what happens at the subwavelength scale.

9.3.1 Coupling Between Localized and Propagative Surface Plasmon Modes on Semicontinuous Metallic Films

The coupling of the localized modes of LSP with long-range interactions by means of the propagative modes of SPP occurs in semicontinuous metal films [10, 12, 38]. LSP allows strong confinement of light around metal particles. In a mix of metal particles of various sizes, LSP resonances occur at various photon energies depending on the wavelength and the polarization of the incident light. On the one hand, LSP resonances allow only very short range ($\leq$ 10 nm) coupling between the high-intensity EM fields. On the other hand, because of their propagative nature, SPPs can couple objects and resonances separated by large distances, up to several micrometers. In a simple picture of semicontinuous metal films, the propagation of SPPs enhances the resonant effect of LSP, which, in turn, gives rise to a higher intensity of the propagating SPP wave. In addition to the random nature of the LSP modes broadening the accessible launching angles for SPPs, the high number of existing metal shapes in the film increases the number of accessible resonance wavelengths and polarization. (See Figure 9.2.)

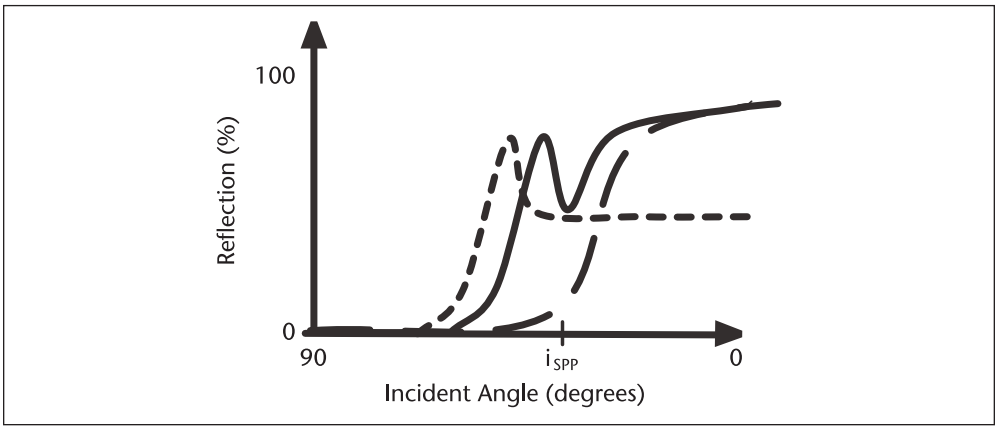

Figure 9.2 A schematic representation of the specular reflection of glass and thin metal films on glass with respect to the incident angle. For glass (long dashes), continuous metal film (continuous line) and semicontinuous metal film (short dashes). The curves have been horizontally shifted for comparison. The angle i_{SPP} is the incident angle at which coupling between light and SPP occurs. SPPs are then launched on the sample surface. The peak of the plasmon polariton resonance occurs at a precise angle i_{SPP} for continuous films. The plasmon peak is much broader for semicontinuous films [12].

The local EM field fluctuations on semicontinuous films are especially strong in the optical and infrared spectral ranges because of the localized plasmon oscillations. Quality factors of these plasmon resonances, proportional to the ratio between the absolute value of the dielectric constant and its imaginary part, can be very large [39]. In metal-dielectric films the dielectric constant ε_m for a metallic component is such that the real part, ε'_m, is negative and can be large in magnitude, whereas the imaginary part, ε''_m, is positive and relatively small. However, these schematic explanations do not allow a quantitative analysis of the near-field enhancement on the films.

9.3.1.1 Models for Near-Field Enhancement of the Electromagnetic Field on Semicontinuous Metal Films

Several theoretical considerations have been proposed to explain the near-field optical behavior of metal-dielectric films [40–42]. Among them, the analysis from Shalaev and coworkers [41, 43] takes into account the strong localization of the hot spots, whereas in some recent nonlinear experiments, enhancements are explained in terms of delocalized optical fields due to long-range interactions [42]. The two explanations are contradictory in some of their conclusions, and an overall agreement still has not been reached. For clarity and coherence with the following figures, we introduce Shalaev's analysis for the enhancement at the fundamental frequency.

The metal-insulator transition associated with the percolation threshold in semicontinuous thin films represents a geometrical phase transition. In second-order phase transitions, the fluctuations are scale-invariant and large. Yet in the case of percolation composite, the fluctuations are very different from a second-order phase transition, where the magnitudes of the fluctuations are of the order of unity and fluctuations exhibit long-range correlations. In metal-dielectric composites, the DC local electric field is concentrated in small areas so that the electric field maxima are separated by a distance of the order of the percolation correlation length. This later diverges when the metal concentration approaches the percolation threshold. The difference in fluctuations is even more important for the AC response. In the optical range, the local-field peaks are resonant; therefore, their magnitudes can be up to five orders higher than the applied field. At the same time, the distance between the peaks can be significantly different from the percolation length (see Figure 9.3).

In Shalaev's model, in order to study the interaction between a plane wave and a semicontinuous films, a Cartesian coordinate system is defined in which the film is in the x,y plane and the incident plane wave (with frequency $\omega = 2\pi c/\lambda$) is propagating normally to the surface of the film. In the Drude model, the dielectric function of the metal grains in the film can be written as $\varepsilon_m(\omega) = \varepsilon_b - 2(\omega_p/\omega)/(1 + i\omega_\tau/\omega)$, where $\varepsilon_b$is the interband contribution to ε_m, ω_p is the plasma frequency, and $\omega_\tau = 1/\tau$ is the relaxation rate ($\omega_\tau \ll \omega_p$). In the visible and infrared range, the losses in the grains are small and $\omega \gg \omega_\tau$. The real part of the dielectric function of the metal grain is larger in absolute value than the imaginary part, and the conductivity is almost purely imaginary.

It is possible to define a local conductivity that is metallic inside the grains and dielectric outside the grains. If the metal skin depth is larger than the grain size a_0,

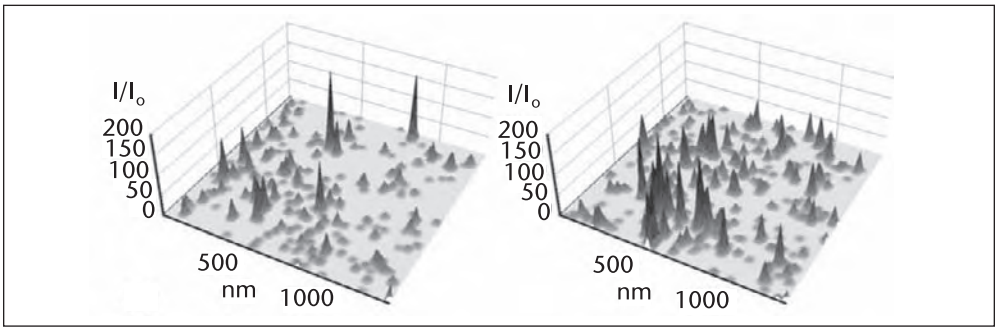

Figure 9.3 Theoretical SNOM images of localized optical excitations in percolation gold-glass film on the same spot for two different wavelengths, $\lambda = 720$ nm (left) and $\lambda = 790$ nm (right). From [44]. © 2001 by the American Physical Society.

the electric field can be considered homogeneous in the grains and the semicontinuous film is a 2-D object [43]. The quasi-static approximation is valid given the fact that the wavelength is larger than all of the characteristic sizes of the film (size of the grains, distance between the grains, etc.). With these hypotheses, it is possible to write the local electric field $\vec{E}(\vec{r})$ with the potential associated to the local fluctuation and the external field. From the current density with the current conservation law, it is possible to deduce the local field $\vec{E}(\vec{r})$ when the macroscopic field is known. Using renormalization, calculation of the effective conductivity and of the electric field distribution above a semicontinuous metal film is possible. It is worth noting that this theoretical description takes into account both SPPs, which are propagative, and LSPs, which are bound to geometrical discontinuities. This explains the success of this model with regard to the high enhancements at the fundamental frequency present on semicontinuous films.

It has been proposed that this random distribution of peaks (see Figure 9.3) is an analog to the localization of electrons and spins in random media [45]. Metallic grains are randomly distributed on the surface of the film, and the local field $\vec{E}(\vec{r})$ follows a random distribution. When the continuity equation for current density is discretized on a square lattice, it takes the form of Kirchhoff equations [46] whose matrix formulations are characterized by their Hamiltonian H. In case of short-range interactions, Anderson predicted localization of the eigenstates of H. This localization can be seen by giant fluctuations. Although these predictions were originally meant for electrons and spin, localization of light in 3-D random media was demonstrated [47, 48].

However, in Stockman, Faleev, and Bergman's view [42], Anderson's localized states are dark modes. They cannot be excited or coupled in the far field. The SP eigenmodes have both localized and delocalized states. The delocalization is attributed to long-range dipolar interactions. Therefore, in Stockman and his coworker's early findings, there is a considerable delocalization of the local fields at the fundamental frequency and hot spots should "spread out and overlap considerably" [49].

9.3.2 Nano-Optical Experiments on Semicontinuous Films

Near-field optical experiments do indeed show that the EM field is not homogenous on the surface of the films [50–53]. The EM field is strongly enhanced in a

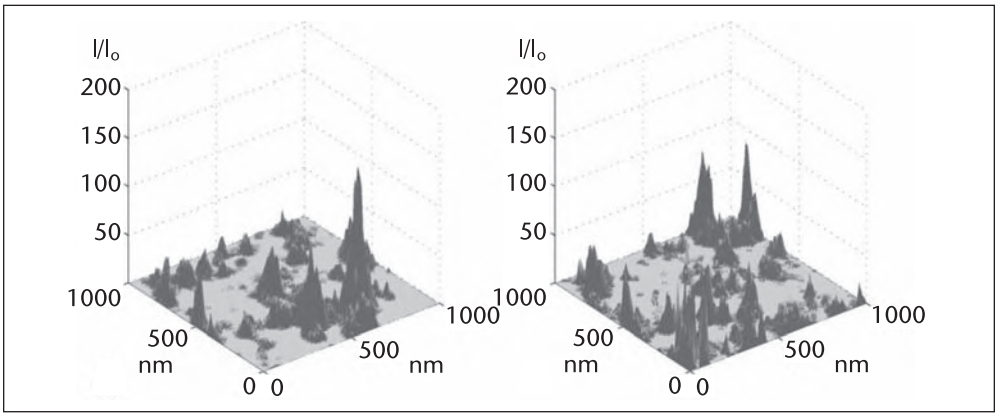

Figure 9.4 Experimental SNOM images of localized optical excitations in percolation gold-glass film on the same spot for two different wavelengths, $\lambda = 720$ nm (left) and $\lambda = 790$ nm (right). From [44]. © 2001 by the American Physical Society.

few randomly distributed positions. The sizes of the hot spots where the EM field is enhanced are much smaller than the incident wavelength. Typical sizes are close to the ones of the metallic grains, of the order of 10 nm. These results explain why on rough films, SERS [54] as well as enhanced PL [55–59] and SHG [60, 61] have been obtained.

The first experiments demonstrating localization of light have been carried out on rough gold films [51], aggregates [50, 62] and colloidal films [52] before demonstrations of the localization on semicontinuous films [44, 53].

The measured size of the hot spots where light is localized is indeed much smaller than the wavelength of light. In Figure 9.4, the effect of the change of wavelength predicted in [41, 43] is shown experimentally using an apertureless near-field microscope [63]. A slight change in the wavelength (Figure 9.4) or in the polarization properties of light (Figure 9.5) leads to a change of the position of the hot spots [44]. Near-field experiments have been performed on gold (images shown in Figures 9.4 and 9.5) and, more recently, on silver films [64]. These later measurements on silver show identical characteristics of the local enhancement properties. It reaches a factor of 2 to 4 times higher than gold for the same excitation wavelength, due to the higher quality factor of the plasmon resonance in silver.

Distances between enhanced peaks are on the order of the wavelength, in accordance with the prediction from Shalaev's analysis. However, in the SNOM images, the measured enhancement, of the order of 100, is smaller than the one calculated. In fact, hot spots are evanescent and the enhancement factor decreases sharply with the distance perpendicular to the sample surface. In the ASNOM used in these experiments, it is as if the near-field images were made at 20 nm from the sample surface, where enhancements are already two orders of magnitude smaller than the ones on the very surface of the film. The calculated and experimental SNOM images (Figures 9.3 and 9.4) are very similar, which confirms most of Shalaev's analysis. Unfortunately, the narrow wavelength range of these SNOM results is not sufficient to decide between the two theoretical explanations presented previously.

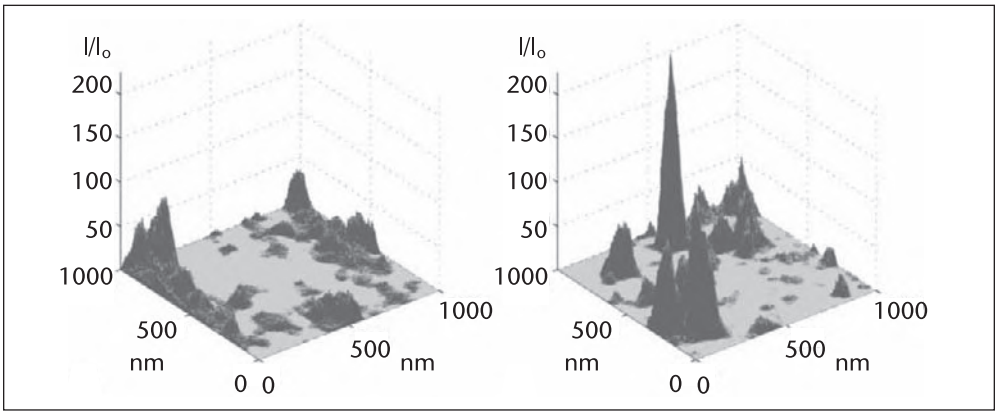

Figure 9.5 Experimental SNOM images of localized optical excitations in percolation gold-glass film on the same area for two perpendicular linear polarizations of light at $\lambda = 780$ nm. Directions of polarization are parallel and perpendicular to the axis of the images. From [44]. © 2001 by the American Physical Society.

9.3.3 Fluorescence Enhancements and Nonlinear Effects

Enhanced fluorescence on metal-dielectric films [13, 65, 66] is of particular importance. The fluorophores act as local sensors of the local EM field, allowing the evanescent field to be coupled to the propagating field and consequently to be detected in the far field. Since the fluorescence signal depends on the local field variations, the fluorescence map is related to the local field map. However, the diffraction-limited resolution of far-field microscopy does not permit the observation of the nanometric spatial variations of the hot spots. Thus, the measured fluorescence signal is an average over the whole fluorescent layer.

Far-field experiments were performed to study the global enhancement factor. In Figure 9.6, we show enhancement of the two-photon fluorescence signal measured in far-field epi-fluorescence microscopy for 0.01 monolayer of eosine deposited by thermal evaporation on various thicknesses of gold. The reference signal is taken on a bare glass substrate, and the laser wavelength is $\lambda = 833$ nm. The maximum enhancement is obtained at the percolation threshold of the gold thin film. This agrees with the hot-spot location for the origin of the signal, the hot spots being much stronger at the percolation threshold [41]. Hot spots, where enhanced fluorescence occurs, are situated primarily between the two metallic nanostructures (gap modes). To confirm this hypothesis, it was possible to show that the signal was due essentially to the fluorophores situated between the metallic islands (i.e., on the glass substrate). The fluorescence disappeared when the part of the fluorophores placed between the metallic structures was selectively removed (leaving intact the ones that were positioned on the metal as confirmed by SERS measurements). The relation between the fluorescence signal and the field enhancement is not linear since the presence of the metal alters the excitation and emission process. At very short fluorophore-metal distances, nonradiative energy transfers occur that quench the fluorescence signal.

Because of their strong nonlinear properties, metal-dielectric films also are especially important for no-linear optical applications [12, 49]. The local distribution of the electromagnetic field allows dramatic increases of nonlinear effects

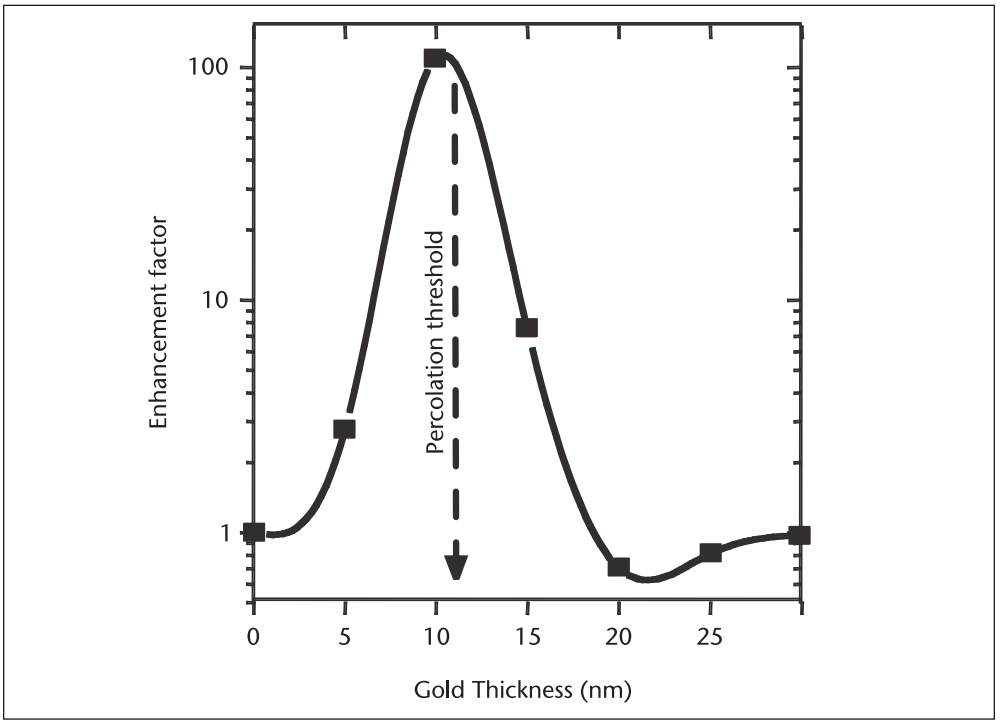

Figure 9.6 Enhancement of the two-photons fluorescence signal with respect to the metal coverage of eosine on gold-glass films measured in far-field epi-fluorescence microscopy. 0.01 monolayer of eosine is deposited by thermal evaporation on various thicknesses of gold. The reference signal is taken on bare glass substrate, and the laser wavelength is $\lambda = 833$ nm. The maximum enhancement is obtained at the percolation threshold of the gold thin film.

[61, 67–69]. Following Zyss's and Bozhevolnyi's papers [61, 68] on second-harmonic (SH) generation, Stockman found that the SH intensity maps show well-localized and isolated hot spots [49]. Contrary to his finding, at the fundamental frequency where hot spots are distributed and are coherent over a large scale and where fundamental hot spots overlap for different modes, SH eigenmodes can be Anderson-localized and show giant fluctuations in space. SH fields are not directly excited by the external field, but are generated in the near field. SH hot spots do not correlate necessarily with fundamental frequency hot spots. The absence of delocalization of SH eigenmodes is related to the fact that there should be a spatial coincidence of the SH and of the fundamental eigenmodes to excite SH.

9.4 Conclusion

With semicontinuous metal films, it is possible to obtain hot spots of the EM field on nanometer-size areas. This has been theoretically predicted by combining the local enhancement of LSPs and the propagating nature of SPP modes. However, it still is not very clear if the hot spots are subject to Anderson localization or to weak localization or if they are purely delocalized. The peculiar properties of semicontinuous metal films are now finding applications in numerous fields ranging from nonlinear spectroscopy to fluorescence coupling.

Acknowledgments

This work has been supported by the Région Ile-de-France in the framework of Sésame and C'Nano-IdF. C'Nano-IdF is the nanoscience competence center of Paris Region, supported by CNRS, CEA, MESR, and Région Ile-de-France.

References

[1] Hayazawa, N., Y. Inouye, and S. Kawata, "Evanescent Field Excitation and Measurement of Dye Fluorescence in a Metallic Probe Near-Field Scanning Optical Microscope," *Journal of Microscopy*, Vol. 194, Nos. 2–3, 1999, pp. 472–476.

[2] Azoulay, J. et al., "Field Enhancement and Apertureless Near-Field Optical Spectroscopy of Single Molecules," *Journal of Microscopy*, Volume, 194, Nos. 2–3, 1999, pp. 486–490.

[3] Hamann, H. F., A. Gallagher, and D. J. Nesbitt, "Near-Field Fluorescence Imaging by Localized Field Enhancement Near a Sharp Probe Tip," *Applied Physics Letters*, Vol. 76, No. 14, 2000, pp. 1953–1955.

[4] Yokota, H., K. Saito, and T. Yanagida, "Single Molecule Imaging of Fluorescently Labeled Proteins on Metal by Surface Plasmons in Aqueous Solution," *Physical Review Letters*, Vol. 80, No. 20, 1998, pp. 4606–4609.

[5] Stefani, F. D. et al., "Surface-Plasmon-Mediated Single-Molecule Fluorescence Through a Thin Metallic Film," *Physical Review Letters*, Vol. 94, No. 2, 2005, Art. No. 023005.

[6] Sanchez, E. J., L. Novotny, and X. S. Xie, "Near-Field Fluorescence Microscopy Based on Two-Photon Excitation with Metal Tips," *Physical Review Letters*, Vol. 82, No. 20, 1999, pp. 4014–4017.

[7] Knoll, B., and F. Keilmann, "Near-Field Probing of Vibrational Absorption for Chemical Microscopy," *Nature*, Vol. 399, 1999, pp. 134–137.

[8] Hartschuh, A. et al., "High-Resolution Near-Field Raman Microscopy of Single-Walled Carbon Nanotubes," *Phys. Rev. Lett.*, Vol. 90, No. 9, 2003, Art. No. 095503.

[9] Ichimura, T. et al., "Tip-Enhanced Coherent Anti-stokes Raman Scattering for Vibrational Nanoimaging," *Physical Review Letters*, Vol. 92, No. 22, 2004, Art. No. 220801.

[10] Zayats, A. V., and I. I. Smolyaninov, "Near-Field Photonics: Surface Plasmon Polaritons and Localized Surface Plasmons," *Journal of Optics A: Pure and Applied Optics*, Vol. 5, 2003, pp. S16–S50.

[11] Barnes, W. L., A. Dereux, and T. W. Ebbesen, "Surface Plasmon Subwavelength Optics, *Nature*, Vol. 424, 2003, pp. 824–830.

[12] Shalaev, V. M., *Nonlinear Optics of Random Media: Fractal Composites and Metal-Dielectric Films* (*Springer Tracts in Modern Physics)*, Berlin Heidelberg: Springer-Verlag, 2000.

[13] Fort, E., and S. Grésillon, "Surface Enhanced Fluorescence," *Journal of Physics D: Applied Physics*, Vol. 41, No. 1, 2008, Art. No. 013001.

[14] Voss, R. F., R. B. Laibowitz, and E. I. Allessandrini, "Fractal (Scaling) Clusters in Thin Gold Films Near the Percolation Threshold," *Physical Review Letters*, Vol. 49, No. 19, 1982, pp. 1441–1444.

[15] Gadenne, P., Y. Yagil, and G. Deutscher, "Transmittance and Reflectance In-Situ Measurements of Semicontinuous Gold Films During Deposition, *Journal of Applied Physics*, Vol. 66, No. 7, 1989, pp. 3019–3025.

[16] Gefen, Y. et al., "Solvable Fractal Family, and Its Possible Relation to the Backbone at Percolation," *Physical Review Letters*, Vol. 47, No. 25, 1981, pp. 1771–1774.

[17] Carminati, R. et al., "Radiative and Non-radiative Decay of a Single Molecule Close to a Metallic Nanoparticle," *Optics Communications*, Vol. 261, No. 2, 2006, pp. 368–375.

[18] Purcell, E. M., "Spontaneous Emission Probabilities at Radio Frequencies," *Physical Review*, Vol. 69, Nos. 11–12, 1946, p. 681.

[19] Haroche, S., and D. Kleppner, "Cavity Quantum Electrodynamics," *Physics Today*, Vol. 42, No. 1, 1989, pp. 24–30.

[20] Dubertret, B., M. Calame, and A. J. Libchader, "Single-Mismatch Detection Using Gold-Quenched Fluorescent Oligonucleotides," *Nature Biotechnology*, Vol. 19, 2001, pp. 365–370.

[21] Dulkeith, E. et al., "Fluorescence Quenching of Dye Molecules Near Gold Nanoparticles: Radiative and Nonradiative Effects," *Physical Review Letters*, Vol. 89, No. 20, 2002, Art. No. 203002.

[22] Das, P. C., and A. Puri, "Energy Flow and Fluorescence Near a Small Metal Particle," *Physical Review B*, Vol. 65, No. 15, 2002, Art. No. 155416.

[23] Thomas, M. et al., "Single-Molecule Spontaneous Emission Close to Absorbing Nanostructures," *Applied Physics Letters*, Vol. 85, No. 17, 2004, pp. 3863–3865.

[24] Anger, P., P. Bharadwaj, and L. Novotny, "Enhancement and Quenching of Single-Molecule Fluorescence," *Physical Review Letters*, Vol. 96, 2006, Art. No. 113002.

[25] Buchler, B. C. et al., "Measuring the Quantum Efficiency of the Optical Emission of Single Radiating Dipoles Using a Scanning Mirror," *Physical Review Letters*, Vol. 95, No. 6, 2005, Art. No. 063003.

[26] Hayakawa, T., S. T. Selvan, and M. Nogami, "Field Enhancement Effect of Small Ag Particles on the Fluorescence from Eu^{3+}-doped SiO_2 Glass," *Applied Physics Letters*, Vol. 74, No. 11, 1999, pp. 1513–1515.

[27] Strohhofer, C., and A. Polman, "Silver as a Sensitizer for Erbium," *Applied Physics Letters*, Vol. 81, No. 8, 2002, pp. 1414–1416.

[28] Naranjo, L. P. et al., "Enhancement of Pr^{3+} Luminescence in $PbO - GeO_2$ Glasses Containing Silver Nanoparticles," *Applied Physic Letters*, Vol. 87, 2004, Art. No. 241914.

[29] Itoh, T. et al., "Hyper-Rayleigh Scattering and Hyper-Raman Scattering of Dye-Adsorbed Silver Nanoparticles Induced by a Focused Continuous-Wave Near-Infrared Laser," *Applied Physic Letters*, Vol. 88, 2006, Art. No. 084102.

[30] Okamoto, K. et al., "Surface-Plasmon-Enhanced Light Emitters Based on InGaN Quantum Wells," *Nature Materials*, Vol. 3, No. 9, 2004, pp. 601–605.

[31] Biteen, J. S. et al., "Enhanced Radiative Emission Rate and Quantum Efficiency in Coupled Silicon Nanocrystal-Nanostructured Gold Emitters," *Nano Letters*, Vol. 5, No. 9, 2005, pp. 1768–1773.

[32] Cohen, R. W. et al., "Optical Properties of Granular Silver and Gold Films," *Physical Review B*, Vol. 8, No. 8, 1973, pp. 3689–3701.

[33] Grannan, D. M., J. C. Garland, and D. B. Tanner, "Critical Behavior of the Dielectric Constant of a Random Composite Near the Percolation Threshold," *Physical Review Letters*, Vol. 46, No. 5, 1981, pp. 375–378.

[34] Bergman, D. J., and Y. Imry, "Critical Behavior of the Complex Dielectric Constant Near the Percolation Threshold of a Heterogeneous Material," *Physical Review Letters*, Vol. 39, No. 19, 1977, pp. 1222–1225.

[35] Yagil, Y., and G. Deutscher, "Scaling and Renormalization in Transmittance of Thin Metal Films Near the Percolation Threshold," *Applied Physics Letters*, Vol. 52, No. 5, 1988, pp. 373–374.

[36] Gadenne, P. et al., "Scaling Theory for the Optical Properties of Semicontinuous Metal Films," *Physical Review B*, Vol. 43, No. 13, 1991, pp. 11342–11352.

[37] Gadenne, P. et al., "Optical Properties of Thin Semicontinuous Gold Films over a Wavelength Range of 2.5 to 500 μm," *Physical Review B*, Vol. 46, No. 4, 1992, pp. 2503–2511.

[38] Stockman, M. "Semiconductor Quantum Dots in Metal Nanostructures," *MAR05 Meeting of the American Physical Society*, Los Angeles, CA, 2005.

[39] Bohren, C. F., and D. R. Huffman, *Absorption and Scattering of Light by Small Particles*, 2nd edition, New York: John Wiley, 1998.

[40] Arya, K., Z. B. Su, and J. L. Birman, "Anderson Localization of Electromagnetic Waves in a Dielectric Medium of Randomly Distributed Metal Particles," *Physical Review Letters*, Vol. 57, No. 21, 1986, pp. 2725–2728.

[41] Shalaev, V. M., and A. K. Sarichev, "Nonlinear Optics of Random Metal-Dielectric Films," *Physical Review B*, Vol. 57, No. 20, 1998, pp. 13265–13288.

[42] Stockman, M. I., S. V. Faleev, and D. J. Bergman, "Localization Versus Delocalization of Surface Plasmons in Nanosystems: Can One State Have Both Characteristics?" *Phys. Rev. Lett.*, Vol. 87, No. 16, 2001, Art. No. 167401.

[43] Shalaev, V. M. et al., "Theory of Giant Raman Scattering from Semicontinuous Metal Films," *Physical Review B*, Vol. 55, No. 19, 1997, pp. 13234–13245.

[44] Ducourtieux, S. et al., "Near-Field Optical Studies of Semicontinuous Metal Films," *Physical Review B*, Vol. 64, 2001, Art. No. 165403.

[45] Anderson, P. W., "Absence of Diffusion in Certain Random Lattices," *Physical Review*, Vol. 109, No. 5, 1958, pp. 1492–1505.

[46] Bergman, D. J., and D. Stroud, "Physical Properties of Macroscopically Inhomogeneous Media," *Solid State Physics*, Vol. 46, 1992, pp. 147–269.

[47] Anderson, P. W., "The Question of Classical Localization: A Theory of White Paint," *Philosophical Magazine B*, Vol. 52, No. 3, 1985, pp. 505–509.

[48] Arya, K., Z. B. Su, and J. L. Birman, "Localization of the Surface Plasmon Polariton Caused by Random Roughness and Its Role in Surface-Enhanced Optical Phenomena," *Physical Review Letters*, Vol. 54, No. 14, 1985, pp. 1559–1562.

[49] Stockman, M. I. et al., "Enhanced Second-Harmonic Generation by Metal Surfaces with Nanoscale Roughness: Nanoscale Dephasing, Depolarization, and Correlations," *Physical Review Letters*, Vol. 92, No. 5, 2004, Art. No. 057402.

[50] Tsai, D. P. et al., "Photon Scanning Tunneling Microscopy Images of Optical Excitations of Fractal Metal Colloid Cluster," *Physical Review Letters*, Vol. 72, No. 26, 1994, pp. 4149–4152.

[51] Bozhelvolnyi, S. I. et al., "Direct Observation of Surface Polariton Localization Caused by Surface Roughness," *Optics Communications*, Vol. 117, 1995, pp. 417–423.

[52] Zhang, P. et al., "Mode Localization in Self-Affine Fractal Interfaces Observed by Near-Field Microscopy," *Physical Review B*, Vol. 57, No. 24, 1998, pp. 15513–15518.

[53] Grésillon, S. et al., "Experimental Observation of Localized Optical Excitations in Random Metal-Dielectric Films," *Physical Review Letters*, Vol. 82, No. 22, 1999, pp. 4520–4523.

[54] Weitz, D. A. et al., "Anomalous Low-Frequency Raman Scattering from Rough Metal Surfaces and the Origin of Surface-Enhanced Raman Scattering," *Physical Review Letters*, Vol. 45, No. 5, 1980, pp. 355–358.

[55] Lambe J., and S. L. McCarthy, "Light Emission from Electron Tunneling," *Physical Review Letters*, Vol. 37, No. 14, 1976, pp. 923–925.

[56] Boyd, G. T., Z. H. Yu, and Y. R. Shen, "Photoinduced Luminescence from the Noble Metals and Its Enhancement on Roughened Surfaces," *Physical Review B*, Vol. 33, No. 12, 1986, pp. 7923–7936.

[57] Downes, A., P. Guaino, and P. Dumas, "Color Mapping by Scanning Tunneling Microscopy: Chemical Analysis of Metal Surfaces," *Applied Physics Letters*, Vol. 80, No. 3, 2002, pp. 380–382.

[58] Drachev, V. P. et al., "Quantum Size Effect in Two-Photon Excited Luminescence from Silver Nanoparticles," *Physical Review B*, Vol. 69, No. 3, 2004, Art, No. 035318.

[59] Bouhelier, A. et al., "Surface Plasmon Characteristics of Tunable Nonlinear Photoluminescence in Single Gold Nanorods," *Physical Review Letters*, Vol. 95, 2005, Art. No. 267405.

[60] Boyd, G. T. et al., "Local-Field Enhancement on Rough Surfaces of Metals, Semi-metals, and Semiconductors with the use of Optical Second-Harmonic Generation," *Physical Review B*, Vol. 30, No. 2, 1984, pp. 519–526.

[61] Zyss, J. et al., "Local Second-Harmonic Generation Enhancement on Gold Nanostructures Probed by Two-Photon Microscopy," *Optics Letters*, Vol. 28, No. 9, 2003, pp. 713–715.

[62] Bozhelvolnyi, S. N. et al., "Direct Observation of Localized Dipolar Excitations on Rough Nanostructured Surfaces," *Physical Review B*, Vol. 58, No. 17, 1998, pp. 11441–11148.

[63] Grésillon, S. et al., "Nanometer Scale Apertureless Near-Field Microscopy," *Applied Surface Science*, Vol. 164, 2000, pp. 792–795.

[64] Kawata, S., V. M. Shalaev, and D. P. Sheng (eds). "Linear and Non-linear Near-Field Behavior on Random Metal Films and Surfaces," *Proceedings of SPIE*, San Diego, CA, 2005, p. 5928.

[65] Shimitzu, K. T. et al., "Surface-Enhanced Emission from Single Semiconductor Nanocrystals," *Physical Review Letters*, Vol. 89, No. 11, 2002, Art. No. 117401.

[66] Liu, H. et al., "Plasmon-Enhanced Molecular Fluorescence from an Organic Film in a Tunnel Junction," *Applied Physics Letters*, Vol. 88, No. 6, 2006, Art. No. 061901.

[67] Breit, M. et al., "Experimental Observation of Percolation-Enhanced Nonlinear Light Scattering from Semicontinuous Metal Films," *Physical Review B*, Vol. 64, 2001, Art. No. 125106.

[68] Bozhevolnyi, S. I., J. Beermann, and V. Coello, "Direct Observation of Localized Second-Harmonic Enhancement in Random Metal Nanostructures," *Physical Review Letters*, Vol. 90, No. 19, 2003, Art. No. 197403.

[69] Buil, S. et al., "Local Field Intensity Enhancements on Gold Semicontinuous Films Investigated with an Aperture Nearfield Optical Microscope in Collection Mode," *Journal of Applied Physics*, Vol. 100, No. 6, 2006, Art. No. 063530.

CHAPTER 10

Nano-Optics with Hybrid Plasmonic Nanoparticles

Gregory A. Wurtz and Gary P. Wiederrecht

10.1 Introduction

The fabrication of nanostructures and control of their interactions in integrated device architectures represent two of the great challenges that scientists face today. The last decade has witnessed increasing progress toward this aim primarily because of the development of fabrication and characterization tools suitable for nano-objects. One of the most promising routes toward a new generation of optical or optoelectronic applications is to make use of various SP modes [1–3]. Excitation of SPs produces a confined or evanescent electromagnetic field at the metal/dielectric interface with spatial extent much smaller than is typical in dielectric optical materials, thus the motivation to apply these materials to nanoscale optics [4–8]. Metal nanoparticles also have enormous optical extinction, making excitation and manipulation of the SPs possible at very low incident powers. For example, a noble metal nanoparticle that is 10 nm in diameter has an extinction coefficient in the range of $10^7\,M^{-1}cm^{-1}$, or about two orders of magnitude stronger than is typical for an organic laser dye.

A further step toward implementing nanoscale integrated optical circuitry needed to be taken by directing efforts toward designing active devices that demonstrate basic functionalities such as switching, lasing, energy storage, and conversion [2, 9, 10]. This can be achieved by coupling plasmonic modes with appropriately chosen active materials. The use of organic semiconductor materials such as J-aggregates are a focal point of this chapter. They are thought to offer great potential since they have the upper hand in low-cost manufacturing processes and possess attractive optical properties [11]. J-aggregates are characterized by a red-shifted and sharp absorption band relative to the monomer band, a result of exciton delocalization over the molecular building blocks of the aggregate [12–15]. The excitonic states have allegories to photosynthesis, which uses these states to collect, store, and guide energy to the reaction center for energy conversion and therefore can drive artificial devices on identical principles. The large oscillator strength and fast electronic response of J-aggregates are also of interest as photographic sensitizers, nonlinear optics related to superfluorescence, and solar photochemical energy conversion [14–25].

10.1.1 Hybrid Plasmonic Nanoparticles

Hybrid nanoparticles are composite objects comprising two or more interacting entities created to show enhanced optical behavior compared to the parent materials. While hybrid systems can sometimes refer simply to composites formed by combining organic and inorganic materials, here we will discern two major families of systems based exclusively on the nature of the interaction between the different components. One family of hybrid is defined as comprising coupled systems that support the eigenmodes of the isolated entities, essentially unperturbed by the coupling. The composing entities are then said to be *weakly coupled,* and the optical properties of the hybrid are merely a sum of the combined optical properties. This situation is encountered when metallic nanoparticles are embedded in a dispersionless organic matrix to enhance the nonlinear optical response of the system via the enhanced scattering cross section of the nanoparticles at the plasmon resonance [26]. Weak coupling also can be observed when plasmonic resonances overlap either the absorption or emission spectrum of an adjacent material. The aim in these configurations is to affect the dynamics of the hybrid by increasing the rate of radiative decay of the adjacent medium, for example [27–29]. Another example is recent work by A. Govorov and colleagues showing that the efficiency of chemical energy production of an excitonic photosynthetic system can be strongly enhanced in the presence of metal nanoparticles. In this case, it was shown that the calculated rate of production of excited electrons inside the reaction center is strongly increased due to the SP and fast electron-hole separation.

The second family of hybrids includes structures whose eigenmodes can only be described as resulting from the mixing of the eigenmodes supported by the constituting entities. In these situations, *strong coupling* occurs between the eigenmodes of the isolated structures and the optical properties associated with the hybrid system are unique relative to those of the constituents. This provides a powerful means to extensively tailor the optical properties of plasmonic systems in order to design their optical functionalities. For example, in their work on nanoshells, Nordlander and coworkers made an elegant analogy to molecular orbitals to describe the plasmonic modes supported by interacting concentric plasmonic shells [30]. In this description, the modes supported by each metallic shell contribute linearly to the formation of entangled, or hybrid, plasmonic modes in a manner similar to the formation of molecular orbitals on the basis of atomic orbitals. Such mixed plasmonic states stimulate increasing interest due to the dramatic changes they produce in the optical properties of the supporting systems. For example, the optical properties of linear arrays of closely spaced metallic nanoparticles are no longer governed by the dipolar response of individual nanoparticles. In fact, in this geometry, calculations have demonstrated the possibility of using near-field interactions between neighboring nanoparticles to create new polaritonic modes delocalized over the entirety of the array. This allows for electromagnetic energy to be transferred from nanoparticle to nanoparticle, effectively paving the way to ultra-integrated waveguide applications [31–34].

Other plasmonic systems showing original optical properties are based on strong coupling. They involve the mixing of smooth interface SPs [35], or localized and delocalized plasmonic modes [36], but also can include heterogeneous states

resulting from mixed plasmons and excitons modes [37–42]. Ultimately, the large polarizability and optical extinction of J-aggregates as well as their electrochemical activity and robustness makes coupling through linear or nonlinear processes to an inorganic substrate unusually strong. In particular, the narrow linewidth of the exciton band makes coherent interactions with low damping to other polarizable media a viable possibility. Some of the most polarizable inorganic templates in existence are metal nanoparticles that produce enhanced optical fields near their surfaces when interacting with visible electromagnetic radiation. Thus, metal nanoparticle/molecular J-aggregate heterostructures can produce unusually large and confined optical fields for exciting molecular excitons. This has been used to explore the exciton dynamics of J-aggregates near bulk metal surfaces [43]. Although coupling of the exciton to the plasmon of the metal generally leads only to ultrafast quenching of the exciton and its fluorescence [43], important exceptions do exist. For example, experiments on colloidal solutions of Ag nanoparticles covered with J-aggregates demonstrate the possibility of using the strong scattering cross section and associated enhanced field concentrations of SPs to generate stimulated emission of excitons of J-aggregates with very low excitation powers [44]. Their coupling with SPs appears, therefore, as a particularly attractive approach to creating low-powered optical devices performing chosen functionalities such as light sources, transistors, and sensors.

In addition, as mentioned earlier, the coupling of J-aggregates with plasmonic resonances presents genuine fundamental interest in the creation of mixed plasmon/exciton states [37–42]. These quasiparticles may be created if the energy of the excitonic mode is resonant with a plasmonic transition. Weak or strong coupling can then be achieved depending on whether the transitions probabilities associated to the system's eigenmodes are still governed by the Fermi Golden Rule. Therefore, tuning the coupling strength is of particular interest if one wants to tailor the absorption and emission characteristics of the molecular semiconductor. Strong coupling was observed in different systems, including microcavities where the quasiparticle comprises a cavity photon and a molecular exciton [45, 46], in plasmonic systems involving a SP and a waveguide photon [47], and more recently between a SP and an exciton [37, 39–41, 48]. Much of this development was sparked by the J-aggregation of cyanine dyes on the surface of noble metal nanoparticle colloids [49, 50].

10.1.2 Scope of the Review

The scope of this chapter centers firmly on nanostructures consisting of molecular excitonic materials interacting with the plasmonic metal nanoparticles. Particularly, the unusual optical properties that result from coherent coupling (strong coupling) between the exciton and plasmon are reviewed. Materials generation, ultrafast exciton dynamics, modulated extinction, nonlinearities, and ultimately control and manipulation of exciton dynamics through strong coupling are all reviewed here. This chapter does not attempt to review other outstanding research areas in plasmonics that also justifiably use the "hybrid" terminology. This includes, for example, the closely spaced metal nanoparticles described previously that interact through optical near-field dipole-dipole coupling to create collective plasmonic behavior delocalized over multiple nanoparticles [31, 33].

Another important plasmon hybridization model is that of the metallic shell structures, also described previously, where the plasmon on the inner surface and outer surface can "hybridize" in a conceptual manner much the same way that atomic orbitals can hybridize when forming a molecule [30, 51].

10.2 Materials

10.2.1 Colloidal Synthesis and J-Aggregate Deposition

The functionalization of colloidal metal nanoparticles with organic materials is well developed, encompassing many forms of chemical and physical interactions. Metal nanoparticle/dye hybrids can be covalently bound, such as lissamine bound to Au by a thioether group [52]. For J-aggregates (and the higher-energy H-aggregate cousin), the interaction is electrostatic, whereby the generally negative charge of molecular species that creates the aggregate is attracted to a positively charged aqueous metal nanoparticle colloid. Importantly, the electrostatic interaction allows for a degree of mobility that covalent binding does not offer, so that the molecules can stack in the "bricklike" structure that produces excitonic J-aggregates [11]. Kamat and coworkers conducted studies of cationic rhodamine 6G H-aggregate assemblies on negatively charged metal oxide and Au colloidal particle surfaces [53, 54]. Ag particles coated with rhodamine 6G also produced blue-shifted absorption bands, characteristic of H-aggregate formation [55]. Several research groups have studied J-aggregate hybrids with metal nanoparticles. Zhong and coworkers [56] have shown that positively charged indolenine cyanine dyes form J-aggregates with citrate Au-coated particles, and no J-aggregate formation takes place with negatively charged or neutral dyes, thus proving that an electrostatic interaction is a crucial factor in J-aggregate formation. These authors also have found that other molecular interactions contribute to J-aggregate formation, namely $\pi-\pi$ interactions of the adjacent dye molecules. Another study explored the nanoparticle size effects in J-aggregate formation of eosin on the surface of photochemically prepared Au particles [57].

J-aggregate formation between negatively charged thiacyanine (TC) dye and Au and Ag nanoparticles prepared by $NaBH_4$ reduction method was first studied by Kometani [49]. The dye originally used was 5,5'-dichloro-3,3'-disulfopropylthiacyanine sodium salt (TC, Hayashibara Biochemical Laboratories, Japan), shown in Figure 10.1(a). When formed on the nanoparticle, the exciton band was broadened and red-shifted by 10–20 nm from the 464 nm absorption band of TC J-aggregates in solution without nanoparticles. As illustrated in Figure 10.2(b), the morphology of the TC aggregate is such that the TC chromophore is adsorbed on the particle and the SO_3^- groups extend away from the nanoparticle to provide solubility [50]. Previous STM studies indicate that homogeneous coverage is obtained on nanoparticle surfaces [50].

10.2.2 Electrostatic Layer-by-Layer Deposition

Electrostatic layer-by-layer deposition is a very effective means for depositing molecules in high density and in an ordered fashion on thin metal films. It also enables tunable interactions by varying a number of parameters, such as the number of layers, the spacing between the resonant molecules and the metal film, and

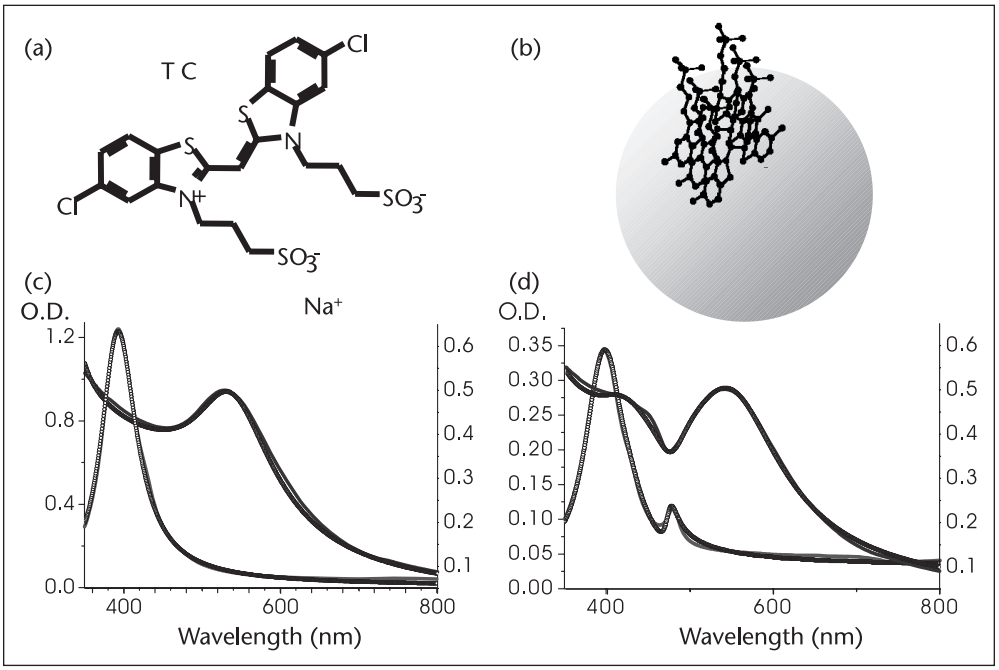

Figure 10.1 (a) The thiacyanine (TC) molecule, (b) the orientation of the J-aggregate on the nanoparticle, (c) the ground-state spectra of bare silver and gold nanoparticles, and (d) the ground-state spectra of TC J-aggregate coated silver and gold nanoparticles. In both cases, the silver spectra are represented by light gray solid lines, while the black solid lines relate to Au spectra. The calculated fits obtained from the core-shell model are plotted with the experimental data and represented by circular markers.

the interlayer spacings. The general premise, particularly with negatively charged molecular aggregates, is to place an inert but positively charged molecular layer on the bare metal substrate. This is followed by depositing a solution of the J-aggregate on the film, rinsing, and following with a solution of a positively charged molecular system (usually a polymer solution) onto the substrate. This can then be repeated to create a multilayer system of resonant molecules on an SPP-supporting metal film.

A specific methodology is given here for the SPP experiments reported in Section 10.3, using a Ag film and the J-aggregate forming meso-tetra (4-sulfonatophenyl) porphyrin (TSPP) [15, 58, 59]. First, a 50 nm thick Ag film is thermally deposited onto a 170 μm thick glass coverslip. A monolayer of cystamine ($C_4S_2N_2H_{12}$) is then deposited by placing a 10 mM solution onto the Ag film for 30 minutes, followed by copious rinsing with deionized water. Subsequently, the acidic 2 mM $TSPP^{2-}$ J-aggregate solution is placed onto the cystamine-coated Ag slide, which protonates the amine group of cystamine to produce a positively charged monolayer that attracts the negatively charged $TSPP^{2-}$ molecules. After 30 minutes, the slide is again rinsed with deionized water. This is followed by the deposition of poly(diallyldimethylammonium chloride) (PDDA) salt, in which the polymer is positively charged in solution. A 1 wt% solution is again placed on the film for 30 minutes, which subsequently creates a positively charged layer on top of the $TSPP^{2-}$ layer. For these studies, the $TSPP^{2-}$/PDDA deposition was repeated four additional times.

10.2.3 AAO Templating

Much of the J-aggregate hybrid nanoparticle work reviewed here uses anodic aluminum oxide (AAO) templating to create the coupled nanostructures. The anodization of aluminum (Al) represents a quick and efficient method for producing self-assembled nanostructures [60]. Due to the size of the pores as well as the flexibility in tuning the geometry of AAO template, theses materials represent a unique opportunity to create plasmonic structures with tunable resonances [48]. The literature gives plenty of examples where the optical properties of Ag, Au, Cu, and Au/Ag multilayers nanowires embedded in porous alumina have been studied [61, 62].

For the structures presented in this chapter, assemblies of Au nanorods (ANRs) are electrochemically grown in a substrate-supported, porous AAO template. The substrate is a multilayered structure comprising a 1 mm thick glass slide, a 10 nm thick Tantalum pentoxide (Ta_2O_5) base layer, and a 5 nm thick Au film acting as the working electrode for the electrochemical reaction. Both layers are grown using magnetron sputter deposition. Tantalum pentoxide was deposited by sputtering tantalum using a 20% oxygen/80% argon mixture. An Al film of up to 500 nm thick is then planar magnetron sputter-deposited onto the electrode. This Al film is subsequently anodized at constant voltage with a platinum counter-electrode in a 0.3 M sulfuric acid electrolyte at ~ 1°C to produce the porous alumina template [63].

The diameter, separation, and ordering of the Au rods in the assembly are determined by the geometry of the AAO template (i.e., the anodization conditions and postchemical etching processes). The rod diameter and spacing can vary from about 10 nanometers to a few hundred nanometers by altering the AAO growth conditions and postgrowth chemical etching processes. The length of the rods is chosen by controlling the electrodeposition time and can be varied from about 20 nm to the limiting value dictated by the thickness of the AAO template, typically a few hundred nanometers.

10.3 Strong Coupling and Modulated Ground States

10.3.1 Theoretical Background

In dealing with isolated spheroids, the ground-state extinction signature of metallic nanoparticles interacting with an excitonic shell can be described analytically using the Rayleigh-Gans theory. In this framework, the extinction cross section of an ellipsoid can be expressed in Equation 10.1 as follows:

$$\sigma_{Extinction_i} = \frac{1}{3}\sum_i \left(2\pi/\lambda Im\{\alpha_i\}\right) + \frac{1}{3}\sum_i \left(1/6\pi\left(2\pi/\lambda\right)^4 |\alpha_i|^2\right) \tag{10.1}$$

where λ is the vacuum wavelength of the illuminating electromagnetic radiation and α_i is the polarizability of the core-shell ellipsoid along axis i expressed in the electrostatic approximation for the dipolar term as [64]

$$\alpha_i = \frac{\upsilon((\varepsilon_{JAgg} - \varepsilon_d)[\varepsilon_{JAgg} + (\varepsilon_{metal} - \varepsilon_{JAgg})(L_i^{Au} - \rho L_i^{JAgg})] + \rho(\varepsilon_{metal} - \varepsilon_{JAgg}))}{[\varepsilon_{JAgg} + (\varepsilon_{metal} - \varepsilon_{JAgg})(L_i^{Au} - \rho L_i^{JAgg})][\varepsilon_d + (\varepsilon_{JAgg} - \varepsilon_d)L_i^{JAgg}] + \rho L_i^{JAgg}\varepsilon_{JAgg}(\varepsilon_{metal} - \varepsilon_{JAgg})} \tag{10.2}$$

In Equation 10.2, ν is the volume of the ellipsoid, ρ is the fraction of the total particle volume occupied by the inner ellipsoid, and L_i is a geometrical factor defined as $L_i = \frac{1-e^2}{e^2}\left(\frac{1}{2e}\ln\frac{1+e}{1-e} - 1\right)$ with $e^2 = 1 - \frac{b^2}{a^2}$ calculated for both the inner Au and outer J-aggregate ellipsoids of respective aspect ratio a/b.

The dielectric constant ε_d describes the optical response of the embedding medium, while the dielectric behavior of the metal (ε_{metal}) is described by a sum of the intraband transitions (electronic response of the free electrons in the conduction band) and interband transitions (electronic transitions between the *d* valence band and the *sp* conduction band). We utilized models for each of these transitions that have successfully reproduced optical properties of metallic nanoparticles [65, 66]. The intraband dielectric

$$\varepsilon_{intra} = \varepsilon_\infty - \frac{\omega_p^2}{\omega(\omega + i\gamma_{intra}(\omega))} \tag{10.3}$$

response is described by a Drude term (Equation 10.3) while the interband electronic response is modeled within the Random Phase Approximation (Equation 10.4):

$$\varepsilon_{inter} = K\int_{E_g}^{\infty} dx \frac{\sqrt{\hbar x - E_g}}{x}\left[1 - F(x,T)\right]\frac{\omega^2 - x^2 - \gamma_{inter}^2 - 2i\omega\gamma_{inter}}{(\omega^2 - x^2 - \gamma_{inter}^2)^2 + 4\omega^2\gamma_{inter}^2} \tag{10.4}$$

where ω_p is the bulk plasmon resonance frequency of the metal, γ_{intra} and γ_{inter} respectively characterize the plasmon and interband damping rates, E_g is the gap between a dispersionless *d* band and a parabolic *sp* band, and K is a constant reflecting the oscillator strength of the interband transitions [65]. K has been obtained by fitting the dielectric behavior of the bulk metal as tabulated in [67].

Finally, the exciton resonance has been modeled assuming a Lorentzian absorption lineshape (i.e., a homogeneously broadened absorption [68]) in a dielectric background ε_∞ with transition frequency ω_0, reduced oscillator strength f and linewidth γ_{agg} [69]. The dielectric response of the aggregate can then be expressed in Equation 10.5

$$\varepsilon_{Jagg} = \varepsilon_\infty + \frac{\omega_0^2.f}{\omega_0^2 - \omega^2 - i\omega\gamma} \tag{10.5}$$

The spectroscopic signature and dynamics of excitons when their resonances overlap the plasmon or interband transitions of metal nanoparticles leads to coherent polarization effects that can be described by considering the intensity transmitted in the far field expressed in Equation 10.6 as follows:

$$I \propto |\vec{P}_{exciton} + \vec{P}_{particle}|^2 \tag{10.6}$$

A schematic of this model system is illustrated in Figures 10.2(a) and 10.2(b). In the frequency range of interest, the calculations simply describe the interaction between two transition dipoles that are homogeneously broadened. The first is the

exciton absorption band of Lorentzian shape, and the second is the metallic core polarization, further developed as a sum of intraband and interband contributions. Equation 10.7 shows that the polarization ($\boldsymbol{P} = \alpha \boldsymbol{E}$) of the sample then produces a far-field scattering intensity written as

$$I \propto |\overrightarrow{P}_{exciton} + \overrightarrow{P}_{particle}|^2 = |\overrightarrow{P}_{exciton} + \overrightarrow{P}_{plasmon} + \sum_n \overrightarrow{P}^n_{d-sp}|^2 \tag{10.7}$$

where $\boldsymbol{P}_{plasmon}$ and $\boldsymbol{P}^n_{d-sp}$ represent the polarization of the free and the bound electron transition dipole moment, respectively. To quantify the polarization coupling in exciton-plasmon hybrids, we calculated the frequency-dependent scattering cross section of the hybrid system using Equation 10.1, obtained by conserving the dipolar term only from the Mie scattering development (Equation 10.2) [64].

10.3.2 Coherent Coupling Between a Dipolar Plasmon and a Molecular Exciton

Figure 10.1 illustrates the ground-state absorption spectra of bare (c) and TC-coated (d) Ag and Au nanoparticles. The ground-state spectra agree well with the results of Kometani et al., illustrating significant modulation of the nanoparticle extinction near the exciton resonance. Furthermore, the nanoparticles coated with TC show a sharp peak at λ= 481 nm on Ag nanoparticles but a pronounced decrease in the Au hybrid nanoparticles' extinction at λ = 474 nm. The modified extinction spectra point to constructive and destructive coherence effects between the nanoparticle electronic polarization and that of the exciton transition dipole. The best fits to the ground-state spectra is obtained by modeling $\sigma_{extinction}$ using Equations 10.1–10.5 setting $a = b$. (The particles are assumed spherical.) The calculations are shown along with the experimental data in Figures 10.1(c) and 10.1(d) and allow for an understanding of the different coherences in the two (Ag/TC, Au/TC) hybrid nanoparticles. For the amplitude and phase shown in Figures 10.2(c) and 10.2(d), we plotted Im($\sigma_{extinction}$) and Real($\sigma_{extinction}$) using the dielectric constant relative to Au and Ag. For the J-aggregate shell, we directly plotted Im(ε_{JAgg}) and Real(ε_{JAgg}). It is insightful to plot the optical response (amplitude and phase) of the metal core and molecular aggregate shell separately. These plots are illustrated in Figures 10.2(c) (Ag/TC) and 10.3(d) (Au/TC). The coherent coupling within the core-shell nanosystems is apparent from the phase plots associated with the respective contributors. In particular, one finds that for the Ag hybrid, the excitonic transition dipole is coherently coupled to the free electron-localized plasmon dipolar resonance of the metal core. This coupling manifests itself by a constructive interference of the respective transition dipole moments, leading to a net increase in the nanoparticles' extinction at 485 nm in Figure 10.2(c). Since the interband band edge for Ag lies at approximately 3.5 eV (350 nm), far from the exciton resonance situated at 2.6 eV (474 nm as obtained from the fits), the phase-sensitive coupling results solely from the interaction of the excitonic state with the free-electron plasmon resonance of the metal. The position of the respective peaks is then determined by the respective position and oscillator strengths of the two bands.

For Au nanoparticle hybrids, the exciton resonance is isoenergetic with interband transition dipoles from the metal core. (The interband band edge lies at 2.4 eV below the Fermi level.) As shown in Figure 10.2(d), this interband

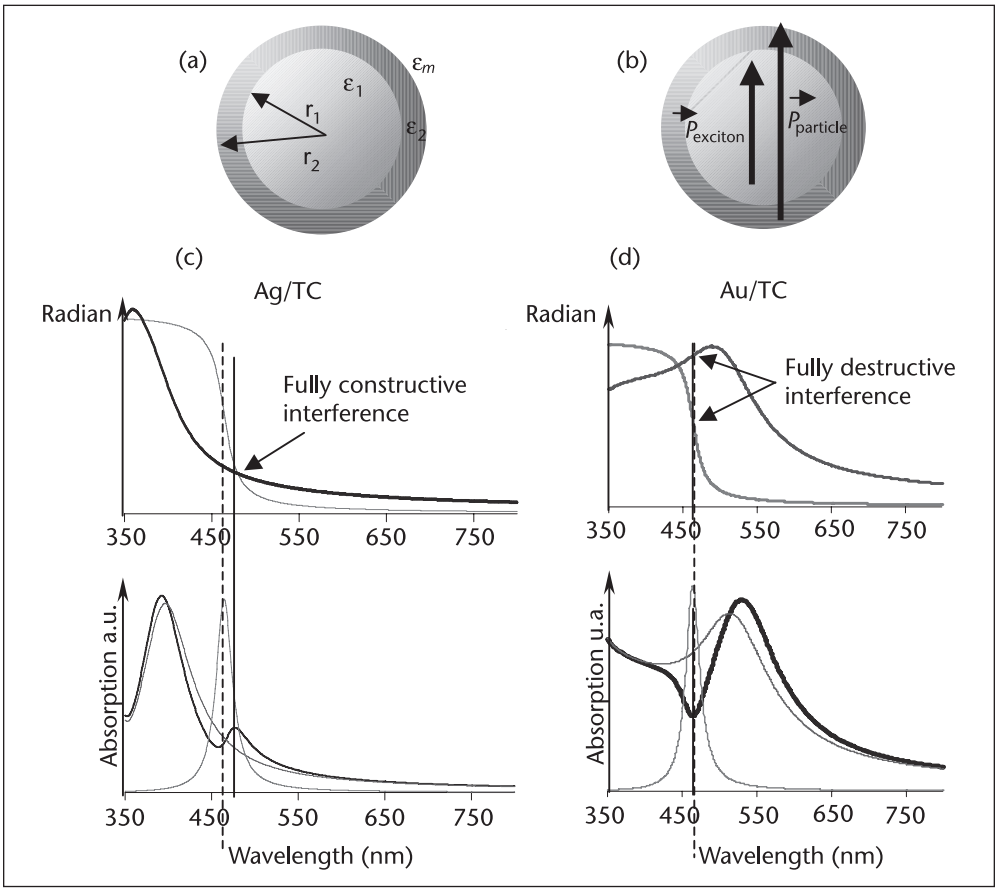

Figure 10.2 (a) The metal-aggregate core-shell model and associated optical dielectric constants. (b) The coherent coupling schematic of the electronic polarization in the metallic core with the excitonic polarization of the aggregate. (c) Phase and (d) amplitude of the core and shell contributions for Ag derived from the fits shown in Figure 10.1. (e) Phase and (f) amplitude of the core and shell contributions for Au using the fits shown in Figure 10.1. For (c) and (e), $Im(\alpha)$ was plotted while and for (d) and (f) $Arg(\alpha)$ was plotted for the metal core using the dielectric constant relative to Au and Ag. Here α represents the dipolar polarizability of the particles as expressed in Equation 10.2 for the core-shell system. For the J-aggregate shell, we directly plotted $Im(\varepsilon_2)$ and $Arg(\varepsilon_2)$. This contribution is shown by a gray solid line in (c) through (f). The contribution from the metal core is shown by a thin solid black line in (c) through (f), while the amplitude associated to the combined hybrid system is represented by a bold solid line in (d) and (f).

contribution at the exciton resonance produces an out-of-phase response between the excitonic and interband transition dipoles that results in a ground-state bleach at 2.6 eV (474 nm) showing very little sensitivity toward the position of the plasmon absorption; therefore, it is exclusively determined by the underlying exciton absorption frequency.

The transition dipole moment frequency of the adsorbed J-aggregate is estimated from the fits to be centered at 2.6 eV (λ_{JAgg} = 474 nm). The calculated exciton transition frequency is found to be identical for both hybrids, which indicates that similar intermolecular resonance energies ensure the aggregate's cohesion on Ag and Au. The intermolecular coupling strength can be estimated by the shift from ω_0, the monomer transition dipole frequency. The larger red shift indicates that a more robust aggregate is formed when on the surface of the nanoparticles than in

solution. In solution without nanoparticles, the J-aggregate exciton absorption is shifted by a value of 220 meV, while a shift by an additional 28% to 280 meV is observed for aggregates on nanoparticles. In a lower-limit estimate (nearest-neighbor approximation without taking into account the effects of disorder), a 10% increase in the resonant coupling energy of aggregates on metal nanoparticles results [70]. This increased stabilization is due to the interaction of the monomer with the particle's surface, as it is not observed in solution [70].

Another significant quantitative difference for the two hybrids lies in the exciton's bandwidth: γ_{agg} = 86 meV on Ag and γ_{agg} = 118 meV on Au. These compare to γ_{agg} in solution of 47 meV and the monomer linewidth of 250 meV. The bandwidth reflects the degree of localization of the excitonic state in the aggregate and is usually determined by disorder. Disorder includes a static contribution (i.e., site-to-site variations in the molecular transition dipole moments and variations in the intermolecular coupling energies) and a dynamic contribution from the thermal fluctuation of the molecules' nuclear coordinates [71]. Compared to the aggregate in solution, the exciton line broadening on the metal nanoparticles is likely due to the presence of the particle surface that introduces local field inhomogeneities.

10.3.3 Coherent Coupling Between a Delocalized Plasmon and a Molecular Exciton

When envisioning practical applications based on the optical properties of plasmonic quasiparticle systems, it is desirable to design structures for which some degree of control over the exciton-plasmon coupling strength is possible. Such a system is presented in Figure 10.3. The system consists of an assembly of ANRs surrounded by a dielectric shell of tubular geometry embedded in an alumina matrix. The rods are aligned in an anisotropic configuration with their long axis oriented perpendicularly to a transparent conducting substrate. The optical properties of the core-shell structure are determined by the strong coupling occurring within the assembly between the longitudinal (L) dipolar plasmon resonances of the rods. This resonant coupling can be tuned throughout the visible spectrum in the 550–900 nm range by varying the rod diameter, the aspect ratio, and the thickness of the dielectric shell. Conforming to a molecular description of the inter-rod coupling, adjusting these parameters is equivalent to modifying the energy level of the dipolar plasmonic orbitals (aspect ratio of the rods) and the spatial overlap between the orbitals (inter-rod distance). Therefore, the (ANR) geometry represents a unique means to control the positioning of the J-aggregate in the plasmonic structure as well as to control the mixing of the hybrid system's eigenstates, offering a unique possibility in the designing of molecular plasmonic nanodevices with tailored optoelectronic functionalities.

The extinction spectrum from an ANR in the AAO matrix is presented in Figure 10.3(b) as a function of angle of incidence. The spectra are dominated by two resonances whose angular dependency reflects the high degree of anisotropy in the system. The short axis of the nanorods leads to the appearance of a resonance around 500 nm that is associated to the excitation of the lowest order, i.e. dipolar, plasmon resonance of the rods. This transverse (T) resonance is addressed for electric fields polarized along the short axis and follows the behavior of a localized plasmonic mode [62]. The lower-energy resonance located around 750 nm is

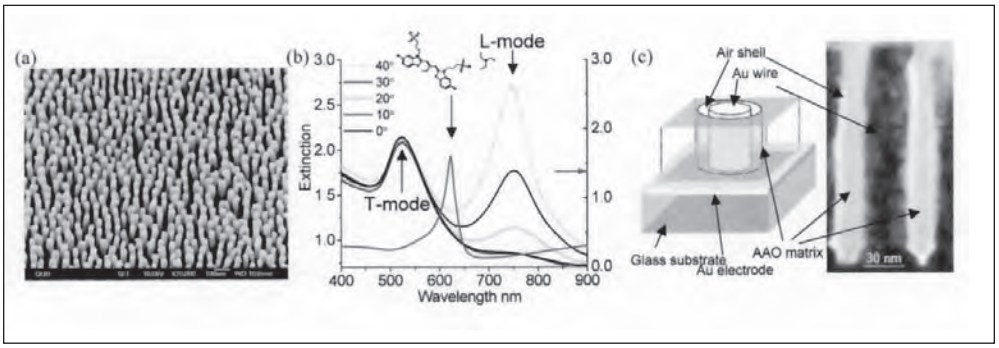

Figure 10.3 (a) SEM image of an assembly of Au nanorods (ANR) in air. (b) Associated extinction spectrum of the ANR embedded in the porous alumina template as a function of angle of incidence. The inset shows the molecular structure of the dye used to hybridize the ANR along with its extinction spectrum shown in a magenta line when J-aggregated on a 50 nm thick smooth Au film magnetron sputtered on a glass substrate. (c) TEM cross section of the ANR core-shell geometry along with a schematic illustration of the structure.

apparent only in the spectra for a component of the incident electric fields polarized along the long axis of the rods and is referred to as longitudinal (L) resonance. These resonances are regarded as eigenmodes of the structure. As mentioned earlier, the spectral position and the angular dependence of this mode are reminiscent of the nature of the coupling between the rods within the assembly. In fact, the L-mode observed in Figure 10.3(b) is a coupled resonance that is characteristic of the ANR's optical response as it results from the strong electromagnetic inter-rod coupling between the dipolar long-axis resonance supported by the nanorods when isolated. The latter resonance would appear around 2000 nm for an isolated rod of a similar aspect ratio and is located in the visible part of the spectrum in the ANR due to inter-rod dipolar coupling. The consequence of the L-mode interactive character is reflected in its associated delocalized field distribution shown in Figure 10.4(b) that is modified from the long-axis dipolar response of the isolated rods for which the field is concentrated at the rods' extremity [Figure 10.5(a)] to a maximum of the electric field in the inter-rod spacing [10]. A schematic energy diagram for the ANR's eigenmodes is shown in Figure 10.5(c). In this diagram, the effect of inter-rod coupling is reflected as a lowering in the L-mode potential energy, compared to the isolated L resonance, by a value C corresponding to the inter-rod coupling strength. In this example, C is evaluated to be around 1 eV.

Coupling of the excitonic state from the molecular aggregate to either or both of the plasmonic modes of the ANR then requires creating a shell around the rods in which to introduce the dye. A simple chemical etching reaction enables the creation of an air/vacuum shell of uniform and tunable thickness around the rods [48]. For the results presented here, shells of various thicknesses were created successively in the same ANR using a 75 mM aqueous solution of sodium hydroxide (NaOH). Etching reactions with 15 s time increments were carried out to create shell thicknesses of 2.5 nm, 3.8 nm, 5.6 nm, 7.7 nm, 8.9 nm, and 20 nm with a thickness distribution, measured by SEM, of 20%. The etching reaction was stopped by rinsing the ANR with purified water (18 $M\Omega$/cm). The sample was then dried with pressurized air before hybridization. The hybrid plasmonic/excitonic system is obtained by depositing a 25 μl droplet from a 5% (by weight) Benzothiazolium 5-chloro-2-(2-((5-chloro-3-(3-sulfopropyl)-2

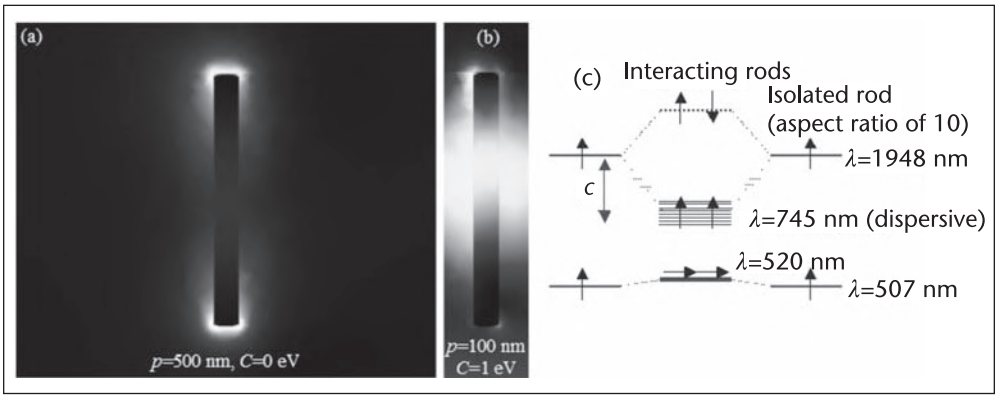

Figure 10.4 Calculated electric field distribution corresponding to the L-mode for an (a) isolated and (b) strongly interacting Au nanorod. The Au rods are 30 nm in diameter and 300 nm long. They are standing on a glass substrate, embedded in an alumina matrix (n = 1.6), and placed in a square array of period p. The superstrate is air. The illumination field is TM-polarized and is incident from the substrate side at an angle of 45 degrees in air. The inter-rod distance and inter-rod coupling strength are p = 500 nm C =0eV (chosen as the reference) and p =100 nm C =1eV in (a) and (b), respectively. A schematic energy diagram of the coupling mechanism is shown in (c).

(3H)-benzothiazolylidene)methyl)-1-butenyl)-3-(sulfopropyl), inner salt, compound N,N-diethylethanamine (1:1) dye (CAS RN 27268-50-4) methanol solution onto the core-shell structure. Upon methanol evaporation, the dye adsorbs onto the ANRs within the shell, where it spontaneously J-aggregates. Figures 10.5(a) and 10.5(b) show the extinction of the coupled system for shell thicknesses of 2.5 nm and 20 nm, respectively. The extinction of the J-aggregate when formed on a smooth Au film as well as the extinction of the bare ANR also are plotted in Figures 10.6(a) and 10.6(b) for comparison. Varying the shell thickness effectively tunes the plasmonic resonances of the ANR with no measurable effect on the excitonic transition energy located around the wavelength of 622 nm. In the following figure, the shell thickness is therefore used as a parameter to control the spectral overlap between the plasmonic modes of the ANR and the excitonic state of the J-aggregate.

From Figure 10.5(a), it can be deduced that when the overlap between the L-mode (λ_L = 737 nm) and the excitonic transition (λ_{JAgg} = 622 nm) is small, the spectral response of the extinction associated to the hybrid system ($\lambda_{hybrid+}$ = 745 nm, $\lambda_{hybrid-}$ = 622 nm) is determined essentially by the resonances of the isolated systems; that is, *weak coupling* is observed. Conversely, Figure 10.5(b) illustrates the regime where this overlap is strong (λ_L = 610 nm, λ_{JAgg} = 622 nm). The resonances of the hybrid system ($\lambda_{hybrid+}$ = 654 nm and =593 nm) then reflect the *hybridization* of the original resonances into mixed states with shared plasmon/exciton character; that is, *strong coupling* is observed. For clarity, these two coupling situations are schematically represented in Figures 10.5(c) and 10.5(d) by an energy diagram of the different states supported by the hybrid ANR. The labeling of these modes are further discussed in the following paragraphs.

The general behavior observed in Figures 10.5(a) and 10.5(b) can be understood following the procedure described previously and calculating the extinction cross section for an isolated ellipsoidal nanoparticle with a Au core surrounded by an excitonic shell and embedded in an homogeneous medium of dielectric constant ε_d.

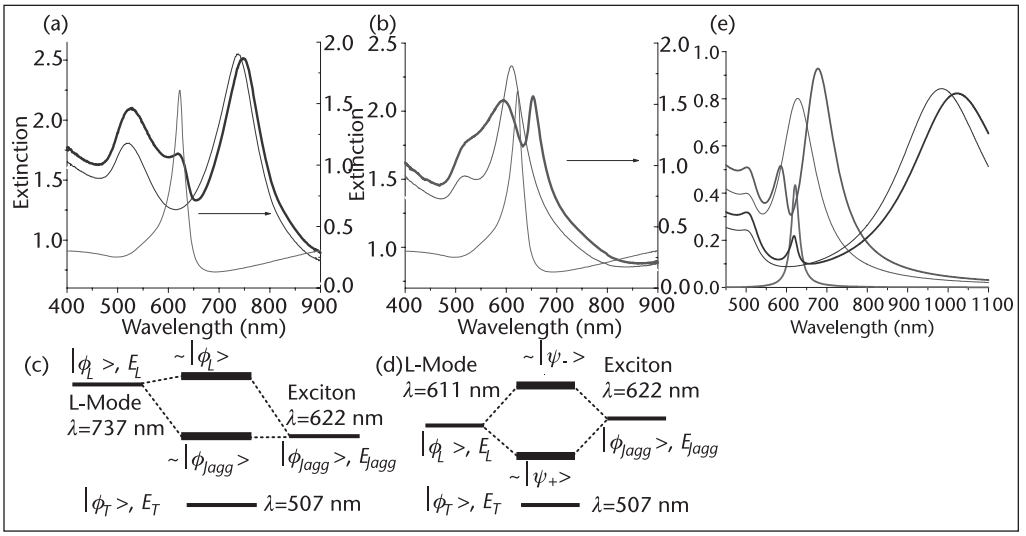

Figure 10.5 (a) Extinction spectrum of the hybrid ANR in the *weak plasmon-exciton coupling* regime along with the extinction of the isolated ANR and the extinction of the J-aggregate on a Au film. The shell thickness is 2.5 nm. (b) Extinction spectrum of the hybrid ANR in the *strong plasmon-exciton coupling* regime along with the extinction of the isolated ANR and the extinction of the J-aggregate on a Au film. The shell thickness is 20 nm. The spectra are taken for an angle of incidence of 40 degrees. (e) Extinction from a coated Au ellipsoid calculated in the dipolar limit and illustrating the general behavior observed experimentally in (a) and (b). The thin lines correspond to the isolated case, while thick lines describe the response of the hybrid system. A homogeneously broadened J-aggregate extinction is shown in magenta.

Here the dielectric constant ε_d of the embedding medium alumina is taken to be 2.56 while a polynomial fit of the data published in [72] is used to describe the dielectric constant of Au, ε_{Au}. The response of the shell was modeled by an excitonic resonance with a Lorentzian response in a dielectric background ε_∞. The anisotropy of the exciton's transition dipole moment was approximated by $\varepsilon_{JAgg//} = \varepsilon_\infty + \dfrac{\omega_0^2 . f}{\omega_0^2 - \omega^2 - i\omega\gamma}$ and $\varepsilon_{JAgg\perp} = \varepsilon_\infty$ for the contributions along and perpendicular to the aggregate's transition dipole moment, respectively. The high-frequency dielectric constant ε_∞ was extracted from ellipsometric measurement made on a thin J-aggregate film formed on a smooth Au surface, while the transition energy, reduced oscillator strength and damping of the excitonic state were determined by fitting the J-aggregate's absorption spectrum as measured on the smooth Au film in Figure 10.3(b). These parameters then take the respective values of $\varepsilon_\infty = 1.21$, $\hbar\omega_0 = 1.99$ eV ($\lambda = 622$ nm), $f = 0.054$, and $\hbar\gamma = 66$ meV. Figure 10.5(e) shows the calculated extinction cross section for core-shell ellipsoids with aspect ratios of 2.4 and 6 with a constant shell thickness of 2 nm. The thick lines correspond to the coupled plasmon/exciton system, while the thin lines describe the extinction of the Au ellipsoids but surrounded by an air shell. The extinction of the J-aggregate also is shown alongside by the magenta line spectrum. The aspect ratio of the ellipsoid was parameterized to modify the spectral overlap between the long-axis plasmonic resonance of the ellipsoid and the transition energy of the exciton and, therefore, the coupling strength between the two transition

dipole moments. In Figure 10.5(e), only the long-axis plasmonic mode was coupled to the excitonic transition, reflecting the experimental observations. In a situation where both T and L modes from the ellipsoid were to be coupled with the excitonic transition, four modes would be observed in the hybrid's extinction spectrum: two T modes as well as two L modes.

To gain better insight into the coupling mechanism, let us consider a 3-D physical system whose Hamiltonian is H_0. The eigenstates of H_0 are $|\phi_T>$, $|\phi_L>$, and $|\phi_{Jagg}>$ associated to the rods dipolar T plasmonic resonance; the ANR's L resonance; and the J-aggregate excitonic state. The corresponding eigenvalues are E_T, E_L, and E_{Jagg} satisfying $H_0|\phi_T> = E_T|\phi_T"$, $H_0|\phi_L> = E_L|\phi_L"$, and $H_0|\phi_{Jagg}" = E_{Jagg}|\phi_{Jagg}"$, with $<\phi_i|\phi_j>=\delta_{ij}$. Introducing coupling between these levels and searching for the eigenvalues of the coupled system in the $\{|\phi_T>, |\phi_L>, |\phi_{Jagg}>\}$ basis, we rewrite the Hamiltonian in the form of $H=H_0+V$, where V is a time-independent perturbation accounting for the coupling between the different eigenstates of the isolated system. Assuming that the J-aggregate's transition dipole moment is oriented along the long axis of the nanorods only ($V_{13} = V_{31} = 0$), the Hamiltonian takes the following simplified form, where V_{hybrid} couples $|\phi_L>$ and $|\phi_{Jagg}>$:

$$H = \begin{bmatrix} E_T+V_{11} & 0 & 0 \\ 0 & E_L+V_{22} & V_{hybrid} \\ 0 & V_{hybrid} & E_{JAgg}+V_{33} \end{bmatrix}$$

from which the eigenvalues are readily obtained:

$$E_T^{'} = E_T + V_{11}$$

$$E_{hybrid+} = \frac{1}{2}(E_L^{'} + E_{JAgg}^{'}) + \frac{1}{2}\sqrt{(E_L^{'} - E_{JAgg}^{'})^2 + 4V_{hybrid}^2} \tag{10.8}$$

$$E_{hybrid-} = \frac{1}{2}(E_L^{'} + E_{JAgg}^{'}) - \frac{1}{2}\sqrt{(E_L^{'} - E_{JAgg}^{'})^2 + 4V_{hybrid}^2} \tag{10.9}$$

where $E_L^{'} = E_L + V_{22}$ and $E_{JAgg}^{'} = E_{JAgg} + V_{33}$.

The eigenvector associated with $E_T^{'}$ is $|\psi_T> \sim |\phi_T>$, reflecting the fact that the J-aggregate's transition dipole moment and the T mode were taken to be perpendicular to each other in our expression of the coupling Hamiltonian V. In these conditions, no coupling between these two states is possible. Note that a similar result would be obtained in the weak coupling regime. This is not the case here since the excitonic response in the T direction would then be observed at a vacuum wavelength of 622 nm, adding a fourth resonance in the extinction of the hybrid structure. Consequently, for the T mode in the hybrid structure, the presence of the J-aggregate along the ANR results in a net change in the energy $E_T^{'}$ through a change in the dielectric constant in the shell, with an eigenvector that is essentially unchanged from its original dipolar form. Neglecting the core-shell geometry as

well as the presence of the substrate, an approximate expression for V_{11} can be found by assuming a lossless Drude-like dielectric response of the form $\varepsilon(\omega) = 1 - \omega_p^2/\omega^2$ for an Au ellipsoid embedded in an homogeneous medium of effective dielectric constant ε_{eff}:

$$V_{11} = \frac{\hbar\sqrt{\mathrm{L}}\omega_{\mathrm{p}}(\mathrm{L}-1)}{2\left[\varepsilon_{\mathrm{eff}}(1-\mathrm{L})+\mathrm{L}\right]^{3/2}}\Delta\varepsilon_{eff}$$

where ω_p is the bulk plasma frequency of Au, L is the geometric factor defined earlier, and $\Delta\varepsilon_{eff}$ reflects the change in dielectric constant induced by the introduction of the J-aggregate in the shell. V_{11} is an increasing function of the shell thickness through $\Delta\varepsilon_{eff}$ with an upper value of $V_{11}\sim-20$ meV measured for a complete removal of the AAO matrix ($\Delta\varepsilon_{eff}\sim\varepsilon_{air}-\varepsilon_{JAgg\perp}=-0.21$). The negative value of V_{11} reflects the increased index of refraction of the shell when introducing the dye. Similarly to V_{11}, V_{22} reflects the change in the L-mode position upon J-aggregation in the shell via the off-resonance high-frequency dielectric constant of the J-aggregate. However, V_{22} is more difficult to express analytically since the field associated to the L-mode within the ANR is no longer following the dipolar response of the isolated rod's long-axis resonance. An estimated value of V_{22} can be made by measuring the sensitivity of the L-mode as a function of shell thickness for an index of refraction in the shell $\sqrt{\varepsilon_{JAgg\perp}}$ of 1.1 [48]. This allows us to evaluate the variation ΔV_{22} of V_{22} over the shell thickness range considered in this study of about 65 meV, while V_{22} at 736 nm is about −20meV and ΔE_L is about 570 meV [48]. V_{33} is a measure of the variation of the intermolecular coupling J within the aggregate when it adsorbs on the ANRs with respect to a reference state measured in water: $E'_{JAgg} = E_{JAgg} + V_{33}$. The loss in potential energy of the HOMO upon J-aggregation determines the coupling energy J, which can then be defined from the transition energy ΔE_{JAgg} of the aggregate as $2J = \Delta E - \Delta E_{JAgg}$, where ΔE is the transition energy of the monomer and J is the positive coupling energy. To evaluate V_{33}, J-aggregation has been studied on a smooth Au film, a Borosilicate glass substrate, and porous AAO from the dye solution in Methanol. For all of those situations, the excitonic transition was observed at an identical wavelength of 622 nm, slightly blue-shifted from its value in water. This underlines that in the experimental configurations considered, it is the interfacial geometry that governs the aggregation energy rather than the material properties of the substrate itself. Comparing Figure 10.3(b) with Figures 10.5(a) and 10.5(b), it is deduced that J-aggregation in the shell around the rods leads to a intermolecular coupling energy similar to the one measured on planar interfaces, suggesting that the core-shell geometry does not strongly affect the value of J in the aggregate even for the smallest shell thicknesses studied (~ 2 nm). Consequently, the value of V_{33} is assumed to be shell-thickness-independent in the following calculations. Considering the absorption frequency of the J-aggregate in water (λ = 650 nm; i.e., $2J$ = 230 meV) and when adsorbed on ANRs (λ = 622 nm; i.e., $2J$ = 150 meV), we can deduce that $V_{33} = E'_{JAgg} - E_{Jagg} = \Delta E - 2J' - (\Delta E - 2J) = 80$ meV.

The eigenvectors $|\psi_+>$ and $|\psi_->$, associated to respectively $E_{hybrid+}$ and $E_{hybrid-}$, can be expressed as linear combinations of the L plasmonic orbital $|\phi_L>$ and the J-aggregate excitonic orbital $|\phi_{JAgg}>$ as follows:

$$|\psi_+\rangle = cos\frac{\alpha}{2}|\phi_L\rangle + sin\frac{\alpha}{2}|\phi_{JAgg}\rangle$$

and

$$|\psi_-\rangle = -sin\frac{\alpha}{2}|\phi_L\rangle + cos\frac{\alpha}{2}|\phi_{JAgg}\rangle$$

where

$$tan\,\alpha = \frac{V_{hybrid}}{\frac{1}{2}(E_L^{'} - E_{JAgg}^{'})}$$

The effect of the coupling matrix V on H_0 is to hybridize the L and excitonic states into two new eigenstates with a mixed plasmon-exciton character. It follows that if $|E_L^{'} - E_{JAgg}^{'}| \gg 2V_{hybrid}$, then $\alpha \sim 0$, $\cos\alpha/2 \sim 1$, and $\sin\alpha/2 \sim V_{hybrid}/|E_T^{'} - E_{JAgg}^{'}|$, from which, if we assume in this instance that $E_L^{'} > E_{JAgg}^{'}$, we deduce the wavefunctions of the system as follows:

$$|\psi_+\rangle = \phi_L\rangle + \frac{V_{hybrid}}{E_L^{'} - E_{JAgg}^{'}}|\phi_{JAgg}\rangle \sim |\phi_{JAgg}\rangle$$

$$\text{and } |\psi_-\rangle = -\frac{V_{hybrid}}{E_L^{'} - E_{JAgg}^{'}}|\phi_L\rangle + |\phi_{JAgg}\rangle \sim |\phi_{JAgg}\rangle$$

These hybrid orbitals then resemble the plasmonic and excitonic orbitals from the uncoupled system, in which case these orbitals represent a *weakly coupled* system as they retain their original character. This case is illustrated in Figures 10.5(a) and 10.5(c) for $E_{JAgg}^{'} > E_L^{'}$. Similarly, if we now consider the case for which $|E_L^{'} - E_{JAgg}^{'}| \ll 2V_{hybrid}$, then $\alpha \sim \pi/2$, $\cos(\alpha/2) = \sin(\alpha/2) \sim 1\sqrt{2}$, and

$$|\psi_\pm\rangle = \frac{1}{\sqrt{2}}\left[\,|\phi_L\rangle \pm |\phi_{JAgg}\rangle\,\right]$$

These functions are hybrid orbitals of the system of Figures 10.5(b) and 10.5(d) where the two original uncoupled orbitals overlap spectrally, in which case *strong coupling* is achieved.

The unique characteristic of the core-shell ANR geometry is to enable a continuous tuning of the plasmonic resonances by controlling the thickness of the shell created around the rods. Therefore, the spectral position of the L-mode can be scanned through most of the visible spectrum and across the excitonic resonance to modulate the mixing of these states. The result is shown in Figure 10.6(a) where the spectrum of the hybrid ANR is plotted for different positions of the L-mode in air. The occurrence of the strong coupling regime in the structure is evident since no resonances appear in the spectral range from 622–658 nm while the L-mode resonance was continuously tuned from 736–550 nm. The anti-crossing between the L-mode and the excitonic transition is illustrated in Figure 10.6(b). Deriving V_{hybrid} from Equations 10.8 and 10.9, we use Figure 10.6(a) to estimate the

coupling strength within the hybrid as a function of the overlap between the L-mode and the excitonic states as follows:

$$V_{hybrid} = \sqrt{\frac{(E_{hybrid+} - E_{hybrid-})^2 - (E_L - E'_{JAgg})^2}{4}} \tag{10.10}$$

where the assumption $E^{'} \sim E_L$ was made. The result is plotted in Figure 10.6(c) as a function of the original position of the L-mode. A similar relationship derived from an analytical theory for the optical properties of ellipsoidal plasmonic particles covered by anisotropic molecular layers is plotted in Figure 10.6(c) (top) for comparison [73]. These expressions lead to very similar values for V_{hybrid} as a function of the L-mode wavelength with a small overestimation of the coupling strength when using Equation 10.10. This overestimation reflects the effect V_{22} has on $E_L{'}$: the absolute value of V_{22} increases with shell thickness and is negligible at maximum coupling strength. This maximum is reached for an L-mode resonance in air located at 600 nm and corresponds to a Rabi splitting of 155 meV. This value is commensurate with the largest Rabi splitting observed in planar organic microcavities [74] and is similar to recent observations for a excitonic state mixed with a planar SPP [39].

The ability to control the coupling strength between a plasmon polariton and a molecular exciton both spatially and spectrally is a major step toward implementing active and passive plasmonic devices. Based on the hybrid nature of the coupled states, the nonlinear optical properties of such a nanostructured material should demonstrate extreme sensitivity over a large spectral range. That is, by addressing

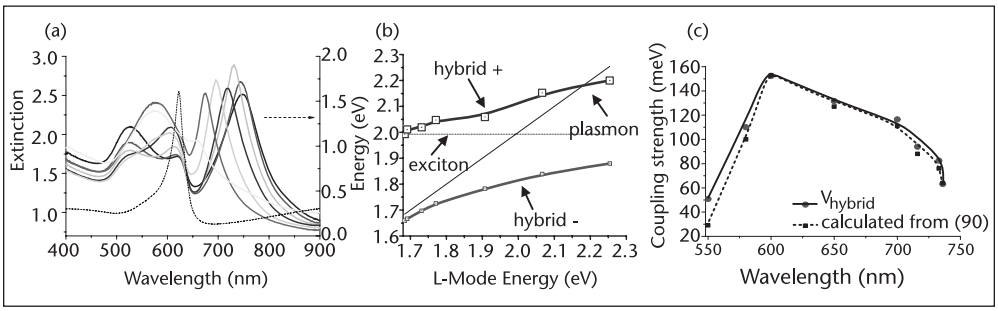

Figure 10.6 (a) Extinction from the hybrid ANR varying the coupling strength between the plasmonic L-mode and the molecular excitonic transition. The spectra are taken for an angle of incidence of 40 degrees. The plasmon-exciton coupling strength has been adjusted by tuning the spectral position of the L-mode from 736-550 nm by increasing the thickness of the shell around the Au rods. The L-mode resonance position in air for the hybrids was located at a wavelength (and corresponding shell thickness) of 736 nm (2.5 nm), 733 nm (3.8 nm), 716 nm (5.6 nm), 700 nm (7.7 nm), 650 nm (8.9 nm), 600 nm (20 nm), and 550 nm (no shell matrix completely removed), respectively. The black broken line shows the excitonic extinction on a 50 nm thick smooth Au film. (b) Energy diagram showing the anticrossing of the plasmonic (diagonal solid black line) and the excitonic (horizontal dotted black line). The energy branches of the hybrid system are plotted based on (a). The crossing of the high-energy branch and the plasmon line is due to V_{22} upon hybridization. (See text for details.) The size of the square markers represents the error bars. (c) Coupling strength calculated from Equation 10.2. The data are represented by circular dots, and the curve is a guide for the eye. For comparison, the black square dots are obtained using the formula for the coupling strength as derived in [10]. The dotted line is a guide for the eye.

one of the hybrid resonances, one would effectively affect both coupled resonances and therefore affect the extinction of the device from 550–700 nm. This could be achieved optically in a pump-probe configuration, for example, and possibly electrically by dynamically controlling the orientation/ordering of the molecular aggregate. Because of the coupled nature between plasmonic and excitonic states, future investigations on the emission properties of this hybrid structure should stimulate considerable interest as well [39]. Finally, we emphasize the practical interest of such a device, as the ANR's fabrication process is simple and scalable [63] while also demonstrating strong potential in the fabrication of nanodevices [75].

10.3.4 Ultrafast Dynamics of Mixed States

This section focuses primarily on the dynamics of mixed states obtained from the interaction between a localized plasmon and a molecular exciton as described in Section 10.3.2. Given the large differences in the exciton bandwidth for aggregates formed on isolated Ag or Au nanoparticles, it is reasonable to expect that exciton dynamics following photoexcitation of the metal nanoparticles will be strongly modified. We recently explored the exciton dynamics in the TC/Ag and TC/Au systems outlined previously via ultrafast pump-probe spectroscopy (Figure 10.1) [37, 76]. In these experiments, an ultrafast laser with a ~ 100 fs pulse width is used to optically excite the metallic core by using the 417 nm second harmonic of an amplified Ti:sapphire laser system described previously [77]. The excitation is not resonant with the J-aggregate exciton band. For Ag nanoparticles, this photon energy lies in the nanoparticle plasmon absorption band. For gold, 417 nm lies in the 5d-6sp interband transition region, but prior studies show that electron-electron scattering in Au nanoparticles produces an equilibration of conduction band electrons that occurs on a ~100 fs timescale [78]. This produces a transient bleach (TB) of the plasmon band that is faster than the time resolution of the apparatus. As a result, for both Ag and Au nanoparticles, excitation of the J-aggregate exciton is achieved via the evanescent field produced by the nanoparticle plasmon excitation [79]. DAS spectra were taken with variable optical delays at probe wavelengths of 450–750 nm.

A prominent aspect of the data is the large spectral differences for bare and coated nanoparticles. For example, the bare Au nanoparticles [Figure 10.7(a)] show spectra similar to that previously reported for uncoated nanoparticles, where an induced absorption on the low and high-energy side of the plasmon bleach is observed in the DAS. This is due largely to a simultaneous increase in the metallic core intraband damping constant (γ_{intra}) relative to the ground state, from 0.645 eV to 0.69 eV, and an increase in the interband damping (γ_{inter}) from 0.24 eV to 0.2856 eV. In contrast, the Au hybrid shows two distinctive transient signatures compared to the uncoated nanoparticles [see Figure 10.7(b)]. First, the hybrid's DAS spectrum shows a strong red-shift in the plasmon bleach (~ 20 nm) and the absence of any induced absorption on its low-energy wing [see Figure 10.7(b)]. Second, the blue side of the DAS is now composed of two peaks. The broad peak originates from increased interband scattering, whereas the most energetic positive feature is an excited-state absorption from the one-exciton to the two-exciton state [80]. For the Au core's contribution to the DAS taken at 2.7 ps in Figure 10.7(b), the data can be fit by an increase in γ_{inter} to 0.31 eV from the ground-state value of

0.245 eV and an increase of γ_{intra} from 0.65 eV in the ground state to 0.667 eV in the transient excited state. The fits also show that the red-shifted plasmon bleach is actually due to a blue shift of the plasmon absorption upon excitation to 9.25 eV from 9.20 eV in the ground state so that the lower-energy components of the plasmon band appear as a bleach in the DAS. The exciton lifetime is short, approximately 3 ps, as a result of resonant Förster energy transfer coupling of the excitonic states in the aggregates selectively to the interband transition dipoles in the Au core. These results can be compared to the coated Ag nanoparticle case, in which the resonant Förster energy transfer process is absent due to the interband transition shift into the UV spectral range and a SP near 400 nm, or far from resonance with the TC exciton. This represents a fundamental divergence from the Au hybrids transient response, resulting in an exciton lifetime of nearly 233 ps for the recovery of the one-exciton state, or far longer than the 3 ps electron-phonon coupling decay time of the Ag nanoparticle or the exciton lifetime on Au nanoparticles.

Referring to Figure 10.7(c), we propose the following interaction mechanism within the Ag/TC hybrid: The creation of the one-exciton state (path 1) is created by evanescent field excitation of the J-aggregates on the metal nanoparticles. This is followed by an efficient electron transfer from the one-exciton band to the conduction band of the metallic core (path 2). This scheme prevents any buildup in the exciton concentration that would lead to the often-observed blue-shifted induced absorption [18, 25, 80, 81]. Following the electron's fast relaxation to the Fermi level through electron-electron scattering (path 3), the long recovery time for this state is governed by the nonadiabatic back-transferred charge from the Fermi level of the particle to the ground state of the aggregate (path 4).

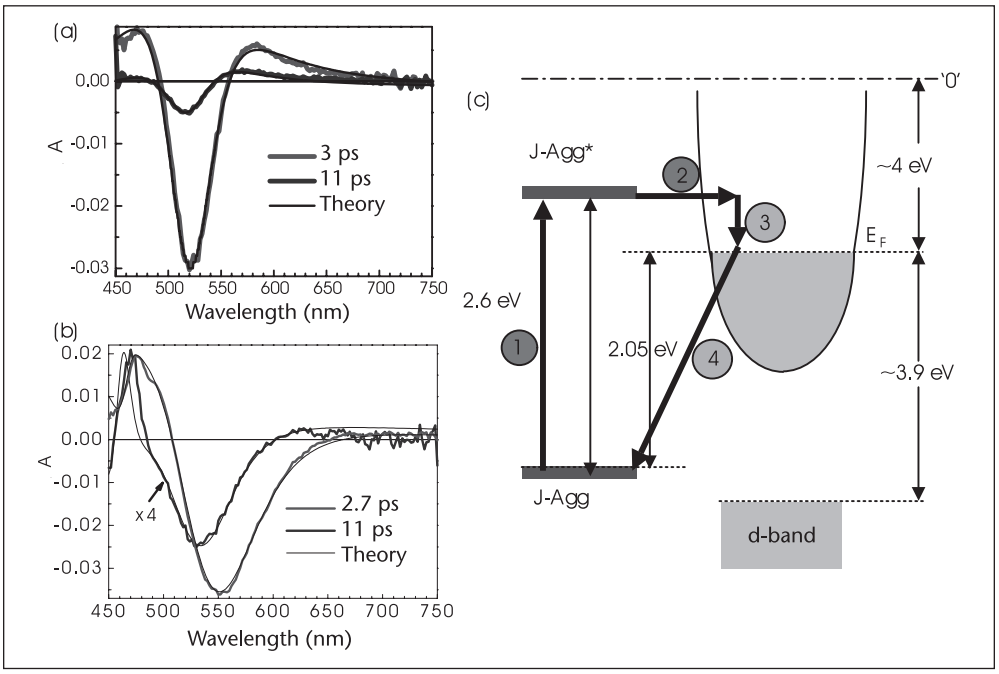

Figure 10.7 The transient absorption spectra for (a) bare and (b) TC-coated Au nanoparticles. (c) Schematic energy diagram for the Ag hybrid as obtained from electrochemical measurements performed on both TC J-aggregates and on Ag nanoparticles.

10.4 Ultrafast Control of Molecular Energy Redistribution Using Hybrid Plasmon-Exciton States

The manner in which a molecule redistributes energy is critically important for chemical reaction outcomes and the efficiency of organic molecular devices such as dye-based solar cells and organic light-emitting diodes (OLEDs). In most cases, energy redistribution following photoexcitation consists of competing pathways so that the device efficiency or reaction yield is fundamentally limited. As a result of these motivations, attaining control over molecular energy redistribution is an active area of research. This is technologically challenging because redistribution processes are usually initiated in the first few hundred femtoseconds following excitation. Therefore, most research efforts target ultrafast pulse shaping schemes to access vibrational states or electronic states within the coherence time of the particular excitation, otherwise known as coherent control.

Plasmonics (and specifically hybrid plasmonics) has recently been used to approach coherent control and energy redistribution from a new direction. It relies upon coupling molecular excited states to SPPs in metal films with nanoscale thickness. The idea is to create hybrid excited states due to coherent coupling between a chosen molecular state with that of a plasmon. A key factor is that the SPP in metal films of nanoscale thickness is easily tunable by changing the angle of incidence of the ultrafast laser beam that simultaneously probes the excited state of the molecule. [See Figure 10.8(a).] The initial test of this idea was recently reported, which used a porphyrin molecule that forms an aggregate with excitonic properties derived from two intramolecular excited states (Figure 10.1) [82]. The resulting two excitons (S_1, S_2) are highly polarizable and couple strongly to the plasmons in the metal. By optically exciting TSPP into the higher S_2 state with an ultrafast pump beam [Figure 10.8(a)], we can initiate or block energy transfer (internal conversion) to S_1 by overlapping the SPP produced by the probe with S_1 or S_2, respectively.

Plasmon gated molecular redistribution is analogous to an ultrafast molecular optical transistor where the plasmon is the gating signal, the S_1 state corresponds to the drain, and the S_2 state corresponds to the source [see Figure 10.8(b)]. The ultimate utility of this technique relies on its utility to work with a wide range of molecular systems, and studies are currently underway. If successful, this method will produce a wide range of new photochemical and photophysical device applications.

10.5 Near-Field Optical Response of Plasmon-Exciton Hybrid Nanoparticles

There are two motivations to characterizing the near-field optical (NFO) properties of hybrid nanostructures. First, because the interaction process between the plasmonic nanoparticle and the excitonic material is originating in the near-field region, the results obtained from the far-field measurements detailed earlier may enable us to draw only a partial picture of this interaction mechanism. Second, when envisioning assemblies of interacting nanostructures performing complex optical functions though near-field interactions, it becomes necessary to characterize the near-field scattering diagram of isolated and interacting nanostructures.

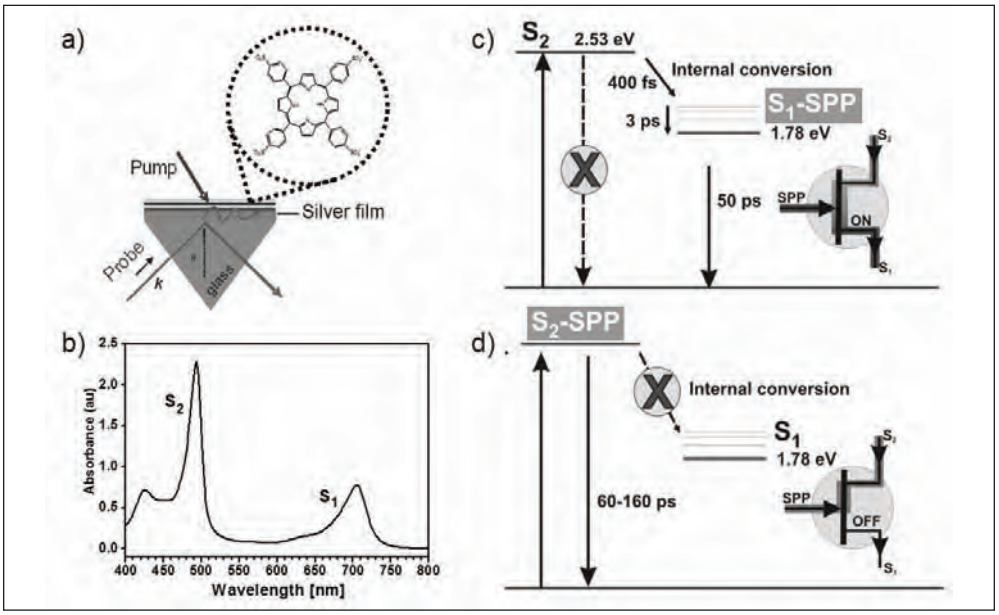

Figure 10.8 (a) The molecular structure of TSPP is shown, along with the ATR geometry of the optical experiments. (b) The ground-state absorption spectra for solutions of the TSPP J-aggregate are shown. Relaxation pathways also are shown when the SPP overlaps (c) the S_1 exciton or (d) the S_2 exciton. The process is analogous to an ultrafast all-optical transistor controlling the energy flow from S_2 to S_1 via SPP gating. The transistor is in its ON state for case (c) and OFF state for case (d).

In this section, we give a brief account of the NFO response of isolated Ag nanoparticles and their excitonic hybrids. The NFO response from the plasmon oscillation of a bare Ag nanoparticle is investigated first. For this purpose, the Ag nanoparticle is illuminated in TIR with a transverse magnetic (TM) polarized field at a wavelength of 415.4 nm [76]. Figure 10.9(a) presents the AFM for a 40 nm diameter particle supported by a glass substrate along with the corresponding NFO image in Figure 10.9(b). The NFO contrast corresponds to the component of the scattered field polarized parallel to the plane of incidence. Figure 10.9(b) features both strong spatial confinement and local enhancement that are characteristic for the particle resonant near-field response [83]. Expressing the NFO intensity as $I(r) = |E_i(r) + E_s(r)|^2 = |E_i(r)|^2 + 2Re\{E_i^*(r).E_s(r)\} + |E_s(r)|^2$, where E_i is the amplitude of the incident field, E_s is the amplitude of the scattered field, Re denotes the real part, and * denotes the complex conjugate, Figure 10.9(b) obtained at resonance—i.e., $|E_s(r)|^2 \gg |E_i(r)|^2$—is be dominated by the field scattered by the nanoparticle $I(r) \approx |E_s(r)|^2$.

We found dramatic changes to the condition in Figure 10.9(b) when characterizing the NFO response of the Ag/TC J-aggregate hybrid nanoparticle. In this illumination condition, the hybrid, while still excited within a resonance band (the higher-energy exciton-plasmon state), demonstrates a much weaker and more complicated near-field response that is more suitably described by $I(r) \approx |E_i(r)^2 + 2Re\{E_i^*(r).E_s(r)\}$, corresponding to an off-resonance excitation of the hybrid when $|E_s(r)|^2 \ll |E_i(r)|^2$. In

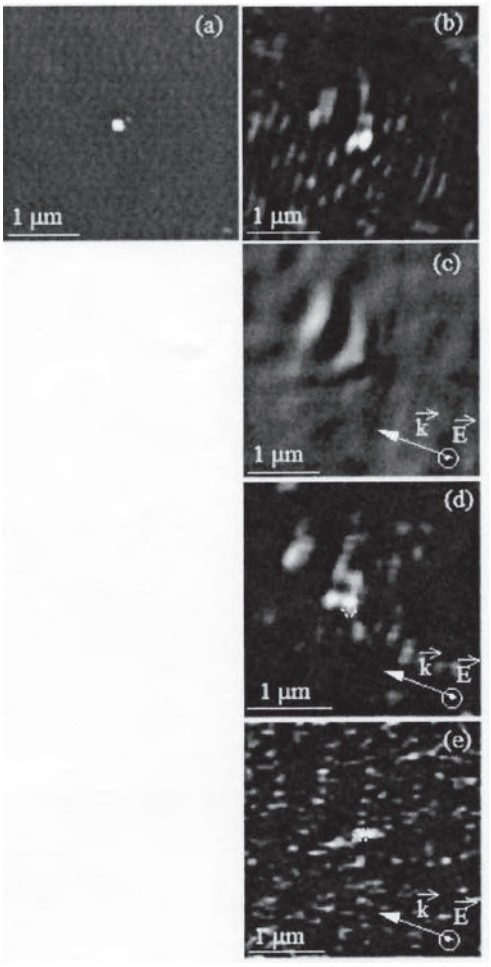

Figure 10.9 J-aggregate coated Ag particle supported by a glass substrate illuminated in TIR on a glass substrate. (a) corresponds to the AFM contrast of the 40 nm diameter bare Ag nanoparticle. (b)–(e) correspond to the near-field optical response of this particle for identical excitation but different detection conditions. The illumination wavelength is 415.4 nm, and both the incident and collected polarizations are TM. (b) corresponds to the NFO contrast of the bare Ag particle. (c) represents the NFO contrast for the Ag/TC hybrid and has been recorded in the same conditions as (b): The optical signal modulated at the probe vibration frequency *f* is shown. (d) represents the second harmonic (2*f*) contribution to the optical signal modulated by the probe. (e) represents the emission from the lower-energy hybrid state at a wavelength of ca. 480 nm. A white dotted outline in (d) and (e) indicates the location of the particle, as obtained from the corresponding AFM images not shown here.

fact, the NFO images of Figure 10.9(c)–(e), obtained under different detection conditions, support the far-field transient spectroscopy experiments showing that the J-aggregates absorb the field scattered by the particle plasmon oscillation; internal damping provides the subsequent relaxation pathway for the energy absorbed by the hybrid [76].

Recording the hybrid near-field response at the harmonics nf (n integer > 1) of the probe, vibration frequency f supports the occurrence of energy transfer between the Ag particle and its J-aggregate coating. Indeed, the hybrid shows very similar NFO contrasts up to the fourth harmonic ($4f$). Figure 10.9(d), obtained at $2f$, illustrates such a contrast. This image shows that a highly spatially confined field is present in the vicinity of the hybrid, and the existence of similar contrasts for higher harmonics underlines this confinement [84]. In fact, the appearance of nonlinearities in the hybrid's near-field modulation demonstrates the severe local nature of the interaction between the probe and the field scattered by the particle. This observation, along with the far-field results showing a quenching of the fluorescence, suggests that the hybrid is emitting light upon strong interaction with the probe; that is, the vicinity of the probe opens a radiative relaxation channel for the hybrid.

To gain more insight on these results, we collected the emission from the exciton-plasmon polariton expected around 480 nm for the lower-lying band. For this purpose, the resonant excitation of the hybrid is preserved at 415.4 nm while a band-pass filter centered at 450 nm is inserted in the collection system to collect the emission of interest, enabling only luminescence from the 480 nm state to be observed. Figure 10.9(e) represents the NFO contrast obtained under these conditions, where emission is observed only at the hybrid's location. As opposed to spontaneous emission for which light is usually detected at some distance from the emitting object [85], the spatial confinement of the source in Figure 10.9(d) supports the previously mentioned interpretation suggesting that the probe provides the radiative relaxation channel for the hybrid, leading to the emission of light by the lower mixed state. These measurements suggest that in a geometry in which such hybrid particles would be interacting, the luminescence from mixed states could be a channel for energy exchange in the near-field regime.

10.6 Conclusions

The field of hybrid nanoparticles promises to take nanoscale optics, photochemistry, and photophysics well beyond a simple scaling down of electromagnetic field volumes. Instead, they are part of a larger goal of developing hybrid structures with optical properties and functions that are qualitatively different from those found at larger- and smaller-length scales as a result of the creation of new, mixed optical states between different materials. We have shown that the tunable coupling between molecular excitonic J-aggregates and plasmonic nanostructures can impact a wide range of fields and is already being used to produce control of exciton dynamics and molecular energy redistribution. Much of this comes from the ease with which organic materials can be manipulated and functionalized in variable structures as compared to all inorganic devices. The extraordinary extinction and polarizability of molecular excitonic materials also leads to strong interactions that are increasingly being discovered. Ultimately, device applications in nonlinear optics, switching, optical limiting, and solar energy may well be realized.

Acknowledgments

GPW acknowledges support by the U. S. Department of Energy, Office of Science, Office of Basic Energy Sciences, under Contract No. DE-AC02-06CH11357. GW acknowledges support by the EPSRC (UK) and by the EU FP6 Network of Excellence Plasmo-Nano-Devices. GW also acknowledges *Invest Northern Ireland* for the provision of funding under Nanotec NI, facilitating the formation of the Centre for Nanostructured Media at the Queen's University of Belfast.

References

[1] Barnes, W. L., A. Dereux, and T. W. Ebbesen, "Surface Plasmon Subwavelength Optics," *Nature*, Vol. 424, 2003, pp. 824–830.

[2] Andrew, P., and W. L. Barnes, "Energy Transfer across a Metal Film Mediated by Surface Plasmon Polaritons," *Science*, Vol. 306, 2004, pp. 1002–1005

[3] Zayats, A.V., I. I. Smolyaninov, and A. A. Maradudin, "Nano-Optics of Surface Plasmon Polaritons," *Phys. Rep.*, Vol. 408, 2005, pp. 131–314.

[4] Kerker, M., "Founding Fathers of Light Scattering and Surface-Enhanced Raman Scattering," *Appl. Opt.*, Vol. 30, 1991, pp. 4699–4705.

[5] Faraday, M., "Experimental Relations of Gold (and Other Metals) to Light," *Philos. Trans. Royal Soc. London*, Vol. 147, 1857, pp. 145–181.

[6] Mie, G., "Beitrage Zur Optik Truber Medien, Special Kolloidaler Metallosungen," *Ann. Phys.*, Vol. 26, 1908, pp. 329–445.

[7] Liz-Marzan, L. M., "Nanometals Formation and Color," *Materials Today*, Vol. 7, 2004, pp. 26–31.

[8] Kreibig, U., and M. Vollmer, *Optical Properties of Metal Clusters*, Berlin: Springer, 1995.

[9] Seidel, J., S. Grafstrom, and L. Eng, "Stimulated Emission of Surface Plasmons at the Interface between a Silver Film and an Optically Pumped Dye Solution," *Phys. Rev. Lett.*, Vol. 94, 2005, Art. No. 177401.

[10] Wurtz, G. A. et al., "Guided plasmonic modes in nanorod assemblies: strong electromagnetic coupling regime." Opt. Express, Vol. 16, 2008, pp. 7460–7470.

[11] Kobayashi, T., *J-Aggregates*, Singapore: World Scientific, 1996.

[12] Jelley, E. E., "Spectral Absorption and Fluorescence of Dyes in the Molecular State," *Nature*, Vol. 138, 1936, pp. 1009–1010.

[13] Scheibe, G., "Uber Die Veranderlich-Keit Des Absorptionsspektrums Einiger Sensibilitisierungsfarbstoffe Und Deren Ursache," *Angew. Chem.*, Vol. 49, 1936, p. 563.

[14] Higgins, D. A., P. J. Reid, and P. F. Barbara, "Structure and Exciton Dynamics in J-Aggregates Studied by Polarization-Dependent Near-Field Scanning Optical Microscopy," *J. Phys. Chem.*, Vol. 100, 1996, pp. 1174–1180.

[15] Fukumoto, H., and Y. Yonezawa, "Layer-by-Layer Self-Assembly of Polyelectrolyte and Water Soluble Cyanine Dye," *Thin Solid Films*, Vols. 327–329, 1998, pp. 748–751.

[16] Eachus, R. S., A. P. Marchetti, and A. A. Muenter, "The Photophysics of Silver Halide Imaging Materials," *Annu. Rev. Phys. Chem.*, Vol. 50, 1999, pp. 117–144.

[17] Yamazaki, I. et al., "Sequential Excitation Energy Transport in Stacking Multilayers: Comparative Study between Photosynthetic Antenna and Langmuir-Blodgett Multilayers," *J. Phys. Chem.*, Vol. 92, 1988, pp. 5035-5044.

[18] Minoshima, K. et al., "Femtosecond Nonlinear Optical Dynamics of Excitons in J-Aggregates," *Chem. Phys. Lett.*, Vol. 218, 1994, pp. 67–72.

[19] Spano, F. C., and S. Mukamel, "Superradiance in Molecular Aggregates," *J. Chem. Phys.*, Vol. 91, 1989, pp. 683–700.

[20] Sanchez, E. J., L. Novotny, and X. S. Xie, "Near-Field Fluorescence Microscopy Based on Two-Photon Excitation with Metal Tips," *Phys. Rev. Lett.*, Vol. 82, 1999, pp. 4014–4017.

[21] Furuki, M. et al., "Fabrication and Femtosecond Optical Response of Langmuir-Blodgett Films with Two-Dimensional J-Aggregates," *J. Phys. Chem. B.*, Vol. 103, 1999, pp. 7607–7612.

[22] Misawa, K., and T. Kobayashi, "Ultrafast Exciton and Excited-Exciton Dynamics in J-Aggregates of Three-Level Porphyrin Molecules," *J. Chem. Phys.*, Vol. 110, 1999, pp. 5844–5850.

[23] Gagel, R., and R. Gadonas, "Evidence for Biexcitons and Dynamic Stark Effect in J-Aggregates from Femtosecond Spectroscopy," *Chem. Phys. Lett.*, Vol. 217, 1994, pp. 228–233.

[24] Fidder, H., J. Terpstra, and D. A. Wiersma, "Dynamics of Frenkel Excitons in Disordered Molecular Aggregates," *J. Chem. Phys.*, Vol. 94, 1991, pp. 6895-6907.

[25] Sundstrom, V. et al., "Annihilation of Singlet Excitons in J Aggregates of Pseudoisocyanine (Pic) Studied by Pico- and Subpicosecond Spectroscopy," *J. Chem. Phys.*, Vol. 89, 1988, pp. 2754–2762.

[26] Debrus, S. et al., "Z-Scan Determination of the Third-Order Optical Nonlinearity of Gold:Silica Nanocomposites," *J. Appl. Phys.*, Vol. 88, 2000, pp. 4469–4475.

[27] Gerber, S. et al., "Tailoring Light Emission Properties of Fluorophores by Coupling to Resonance-Tuned Metallic Nanostructures," *Phys. Rev. B*, Vol. 75, 2007, Art. No. 073404.

[28] Biteen, J. S. et al., "Plasmon-Enhanced Photoluminescence of Silicon Quantum Dots: Simulation and Experiment," *J. Phys. Chem.* C, Vol. 111, 2007, pp. 13372–13377.

[29] Dahmen, C., B. Schmidt, and G. von Plessen, "Radiation Damping in Metal Nanoparticle Pairs," *Nano Lett.*, Vol. 7, 2007, pp. 318–322.

[30] Prodan, E., C. et al., "A Hybridization Model for the Plasmon Response of Complex Nanostructures." Science, Vol. 302, 2003, pp. 419–422

[31] Krenn, J. R. et al., "Squeezing the Optical Near-Field Zone by Plasmon Coupling of Metallic Nanoparticles," *Phys. Rev. Lett.*, Vol. 82, 1999, pp. 2590–2592.

[32] Brongersma, M. L., J. W. Hartman, and H. A. Atwater, "Electromagnetic Energy Transfer and Switching in Nanoparticle Chain Arrays Below the Diffraction Limit," *Phys. Rev. B*, Vol. 62, 2000, pp. R16356–R16359.

[33] Maier, S. A. et al., "Local Detection of Electromagnetic Energy Transport Below the Diffraction Limit in Metal Nanoparticle Plasmon Waveguides." *Nat. Mat.*, Vol. 2, 2003, pp. 229-232.

[34] Citrin, D. S., "Plasmon-Polariton Transport in Metal-Nanoparticle Chains Embedded in a Gain Medium," *Opt. Lett.*, Vol. 31, 2006, pp. 98-100.

[35] Dionne, J. A. et al., "Planar Metal Plasmon Waveguides: Frequency-Dependent Dispersion, Propagation, Localization, and Loss Beyond the Free Electron Model," *Phys. Rev. B*, Vol. 72, 2005, Art. No. 075405.

[36] Kelf, T. A. et al., "Plasmonic Band Gaps and Trapped Plasmons on Nanostructured Metal Surfaces," *Phys. Rev. Lett.*, 2005, Art. No. 116802.

[37] Wiederrecht, G. P., G. A. Wurtz, and J. Hranisavljevic, "Coherent Coupling of Molecular Excitons to Electronic Polarizations of Noble Metal Nanoparticles," *Nano Letters*, Vol. 4, 2004, pp. 2121–2125.

[38] Cheng, M-T. et al., "Coherent Exciton-Plasmon Interaction in the Hybrid Semiconductor Quantum Dot and Metal Nanoparticle Complex," *Opt. Lett.*, Vol. 32, 2007, pp. 2125–2127.

[39] Bellessa, J. et al., "Strong Coupling between Surface Plasmons and Excitons in an Organic Semiconductor," *Phys. Rev. Lett.*, Vol. 93, 2004, Art. No. 036404.

[40] Dintinger, J. et al., "Strong Coupling between Surface Plasmon-Polaritons and Organic Molecules in Subwavelength Hole Arrays," *Phys. Rev. B*, Vol. 71, 2005, Art. No. 035424.

[41] Sugawara, Y. et al., "Strong Coupling between Localized Plasmons and Organic Excitons in Metal Nanovoids," *Phys. Rev. Lett.*, Vol. 97, 2006, Art. No. 266808.

[42] Wurtz, G. A. et al., "Molecular Plasmonics with Tunable Exciton-Plasmon Coupling Strength in J-Aggregate Hybridized Au Nanorod Assemblies," *Nano Lett.*, Vol. 7, 2007, pp. 1297–1303.

[43] Saito, K., "Quenching of Excited J Aggregates on Metals by Surface Plasmon Excitations," *J. Phys. Chem.* B, Vol. 103, 1999, pp. 6579–6583.

[44] Ozcelik, S., I. Ozcelik, and D. L. Akins, "Superradiant Lasing from J-Aggregated Molecules Adsorbed onto Colloidal Silver," *App. Phys. Lett.*, Vol. 73, 1998, pp. 1949–1951.

[45] Lidzey, D. G. et al., "Photon-Mediated Hybridization of Frenkel Excitons in Organic Semiconductor Microcavities," *Science*, Vol. 288, 2000, pp. 1620–1623.

[46] Hobson, P. A. et al., "Strong Exciton—Photon Coupling in a Low-Q All-Metal Mirror Microcavity," *Applied Physics Letters*, Vol. 81, 2002, pp. 3519–3521.

[47] Christ, A. et al., "Waveguide-Plasmon Polaritons: Strong Coupling of Photonic and Electronic Resonances in a Metallic Photonic Crystal Slab," *Phys. Rev. Lett.*, Vol. 91, 2003, Art. No. 183901.

[48] Evans, P. R. et al., "Plasmonic Core/Shell Nanorod Arrays: Sub-Attoliter Controlled Geometry and Tunable Optical Properties," *J. Phys. Chem.* C, Vol. 111, 2007, p. 12522–12527.

[49] Kometani, N. et al., "Preparation and Optical Absorption Spectra of Dye-Coated Au, Ag, and Au/Ag Colloidal Nanoparticles in Aqueous Solutions and in Alternate Assemblies," *Langmuir*, Vol. 17, 2001, pp. 578–580.

[50] Sato, T. et al., "Spectroscopic Properties of Noble Metal Nano-Particles Covered with J-Aggregates of Cyanine Dye," *Chem. Lett.*, Vol. 30, 2001, pp. 402–403

[51] Prodan, E. and P. Nordlander, "Plasmon Hybridization in Spherical Nanoparticles." *J. Chem. Phys.*, Vol. 120, 2004, pp. 5444–5454.

[52] Dulkeith, E. et al., "Fluorescence Quenching of Dye Molecules Near Gold Nanoparticles: Radiative and Nonradiative Effects," *Phys. Rev. Lett.*, Vol. 89, Art. No. 203002.

[53] Kamat, P. V., and N. Chandrasekharan, "Improving the Photoelectrochemical Performance of Nanostructured Tio2 Films by Adsorption of Gold Nanoparticles,"*J. Phys. Chem.* B, Vol. 104, 2000, pp. 10851–10857.

[54] Kamat, P. V. et al., "Dye-Capped Semiconductor Nanoclusters. Excited State and Photosensitization Aspects of Rhodamine 6g H-Aggregates Bound to Sio_2 and Sno_2colloids," *J. Phys. Chem.*, Vol. 100, 1996, pp. 11054–11061.

[55] Kerker, M. J., "The Optics of Colloidal Silver: Something Old and Something New," *Journal of Colloid Interface Science*, Vol. 105, 1985, pp. 297–314.

[56] Zhong, C.-J. et al., "Adsorption of Cyanine Dyes on Gold Nanoparticles and Formation of J-Aggregates in the Nanoparticle Assembly," *J. Phys. Chem. B*, Vol. 110, 2006, pp. 6673–6682.

[57] Ghosh, S. K. et al., "Dimerization of Eosin on Nanostructured Gold Surfaces: Size Regime Dependence of the Small Metallic Particle," *Chem. Phys. Lett.*, Vol. 412, 2005, pp. 5–11.

[58] Van Patten, P. G., A. P. Shreve, and R. J. Donohoe, "Structural and Photophysical Properties of a Water-Soluble Porphyrin Associated with Polycations in Solution and Electrostatically-Assemble Ultrathin Films," *J. Phys. Chem. B*, Vol. 104, 2000, pp. 5986–5992.

[59] Hammond, P. T., "Form and Function in Multilayer Assembly: New Applications at the Nanoscale," *Adv. Mater.*, Vol. 16, 2004, pp. 1271–1293.

[60] Martin, C. R., "Nanomaterials: A Membrane-Based Synthetic Approach," *Science*, Vol. 266, 1994, pp. 1961-1966.

[61] Zong, R.-L. et al., "Synthesis and Optical Properties of Silver Nanowire Arrays Embedded in Anodic Alumina Membrane," *J. Phys. Chem.* B, Vol. 108, 2004, pp. 16713–16716.

[62] Atkinson, R. et al., "Anisotropic Optical Properties of Arrays of Gold Nanorods Embedded in Alumina," *Phys. Rev. B*, Vol. 73, No. 23, 2006, Art. No. 235402.

[63] Evans, P. et al., "Growth and Properties of Gold and Nickel Nanorods in Thin Film Alumina," *Nanotechnology*, Vol. 17, 2006, pp. 5746–5753.

[64] Bohren, C. F., and D. R. Huffmann, *Absorption and Scattering of Light by Small Particles*, New-York: Wiley Science, 1983.

[65] Bigot, J.-Y. et al., "Electron Dynamics in Copper Metallic Nanoparticles Probed with Femtosecond Optical Pulses," *Phys. Rev. Lett.*, Vol. 75, 1995, pp. 4702–4705.

[66] Inouye, H. et al., "Ultrafast Dynamics of Nonequilibrium Electrons in a Gold Nanoparticle System," *Phys. Rev. B*, Vol. 57, 1998, pp. 11334–11340.
[67] Palik, E., *Handbook of Optical Constants of Solids*, Orlando: Academic Press, 1997.
[68] Gaizauskas, E., and K.-H. Feller, "Effects of Strong Excitation Induced Disorder on Pump–Probe Spectra of Molecular Aggregates," *J. of Lumin.*, Vol. 102, 2003, pp. 13–20.
[69] Pockrand, I., A. Brillante, and D. Mobius, "Nonradiative Decay of Excited Molecules Near a Metal Surface," *Chem. Phys. Lett.*, Vol. 68, 1980, pp. 499–504.
[70] Kirstein, S., and H. Mohwald, "Herringbone Structure in Two-Dimensional Single Crystals of Cyanine Dyes. II. Optical Properties," *J. Chem. Phys.*, Vol. 103, 1995, pp. 826–833.
[71] Nabetani, A. et al., "Optical Properties of Two-Dimensional Dye Aggregate," *J. Chem. Phys.*, Vol. 102, 1995, pp. 5109-5117.
[72] Johnson, P. B., and R. W. Christy, "Optical Constants of the Noble Metals," *Phys. Rev. B*, Vol. 6, 1972, pp. 4370–4379.
[73] Ambjörnsson, T. et al., "Resonant Coupling between Localized Plasmons and Anisotropic Molecular Coatings in Ellipsoidal Metal Nanoparticles," *Phys. Rev. B*, Vol. 73, 2006, Art. No. 085412.
[74] Agranovich, V. M., M. Litinskaia, and D. G. Lidzey, "Cavity Polaritons in Microcavities Containing Disordered Organic Semiconductors," *Phys. Rev. B*, Vol. 67, 2003, Art. No. 085311.
[75] Vlad, A. et al., "Controlled Growth of Single Nanowires within a Supported Alumina Template," *Nanotech.*, Vol. 17, 2006, pp. 4873–4876.
[76] Hranisavljevic, J. et al., "Photoinduced Charge Separation Reactions of J-Aggregates Coated on Silver Nanoparticles," *J. Am. Chem. Soc.*, Vol. 124, No. 17, 2002, pp. 4536–4537.
[77] Greenfield, S. R., and M. R. Wasielewski, "Optical Parametric Amplification of Femtosecond Pulses Tunable from the Blue to the Infrared with Microjoule Energies," *Appl. Opt.*, Vol. 34, 1995, pp. 2688–2691.
[78] Hodak, J. S., A. Henglein, and G. V. Hartland, "Photophysics of Nanometer Sized Metal Particles: Electron-Phonon Coupling and Coherent Excitation of Breathing Vibrational Modes," *J. Phys. Chem. B*, Vol. 104, 2000, pp. 9954–9965.
[79] Wurtz, G. A., J. Hranisavljevic, and G. P. Wiederrecht, "Photo-Initiated Energy Transfer in Nanostructured Complexes Observed by Near-Field Optical Microscopy," *J. Microsc.*, Vol. 210, 2003, pp. 340–343.
[80] Hamanaka, Y. et al., "Femtosecond Transient Absorption Study of Merocyanine J-Aggregates," *J. Lumin.*, Vols. 94, 2001, pp. 451–455.
[81] Vanburgel, M., D. A. Wiersma, and K. Duppen, "The Dynamics of One-Dimensional Excitons in Liquids," *J. Chem. Phys.*, Vol. 102, 1995, pp. 20–33.
[82] Wiederrecht, G. P., J. E. Hall, and A, Bouhelier, "Control of Molecular Energy Redistribution Pathways Via Surface Plasmon Gating," *Phys. Rev. Lett.*, Vol. 98, 2007, Art. No. 083001.
[83] Wurtz, G, A., N. M. Dimitrijevic, and G. P. Wiederrecht, "The Spatial Extension of the Field Scattered by Silver Nanoparticles Excited Near Resonance as Observed by Apertureless Near-Field Optical Microscopy," *J. Appl. Phys.*, Vol. 41, 2002, pp. L351–L354.
[84] Walford, J. N. et al., "Influence of Tip Modulation on Image Formation in Scanning Near-Field Optical Microscopy," *J. Appl. Phys.*, Vol. 89, 2001 pp. 5159–5169.
[85] Hamann, H. F. et al., "Molecular Fluorescence in the Vicinity of a Nanoscopic Probe," *J. of Chem. Phys.*, Vol. 114, 2001 pp. 8596–8609.

PART IV

Apertureless Near-Field Optical Microscopy

Introduction

For far-field optical microscopy with a typical wavelength $\lambda \sim 500$ nm, Abbe's diffraction limit forbids the recognition of sample features smaller than about 250 nm. As has been demonstrated in earlier chapters of this text, dramatic improvement of optical resolution beyond the diffraction limit became possible with the invention of near-field optical microscopy, which followed the invention of scanning probe techniques initially exploiting the tunneling of electrons (scanning tunneling microscopy, STM [1]), and forces (atomic force microscopy, AFM) [2]) that occur between a sharp scanning tip and a sample. Employing photons for tip sensing of a sample's optical properties was independently realized by two teams [3, 4]. In their original scanning near-field optical microscope (SNOM), the apertured-SNOM introduced in Part I of this book, the optical diffraction barrier is overcome by forcing light through a metallic aperture at the end of a probe that is maintained in close proximity to a surface, such that the surface is in the optical near-field of the aperture [5, 6]. In principle, the aperture diameter d could be made very small to achieve very high resolution. In practice, however, the common funnel-shaped geometry of a metallized, tapered glass fiber [7] causes the well-known waveguide cutoff effect [8]. Combined with low throughput of small apertures, this results in only a tiny fraction ($< 10^{-4}$ for a 100 nm aperture) of the light coupled into the fiber being emitted by the aperture [9, 10]. In the visible part of the spectrum, the low aperture-dependent throughput of the aperture probes limits the achievable resolution practically to about 50 nm [11].

In the following chapters, ultraresolution microscopy and lithography far beyond the classical Abbe diffraction limit of one-half wavelength, $\lambda/2$, and beyond a practical limit of aperture-based SNOM, approximately $\lambda/10$, are introduced. These "apertureless" scanning near-field optical microscopy (ASNOM) techniques circumvent this limit by replacing the small aperture with a sharp tip, such as an AFM probe, in the focus of a laser beam so that the microscope resolution is determined by the field confinement at the tip [12–14]. The nano-optical field in the vicinity of the tip apex can be strongly enhanced [29, 30] due to the resonant excitation of localized surface plasmons [15–17] or due to geometric considerations such as lightning rod [15, 18] and antenna effects [19, 20].

In general, two different ASNOM types can be distinguished. (1) Scattering type microscopy (s-SNOM) in which the nano-optical field at the tip apex polarizes a nearby sample. The subsequent emission into the far field at the same frequency of the incident light contains and reports information of this tip-sample interaction [21]. (2) Tip-enhanced microscopy [12] in which the tip-enhanced field can be used to locally excite various optical processes, giving rise to enhanced Raman scattering (tip-enhanced Raman scattering, TERS) [22–24], tip-enhanced harmonic generation [25], difference-frequency generation [26], and dye fluorescence [27–31], and has resulted in several reported measurements of spatial resolution down to 10 nm. Recently, apertureless near-field microscopy using single metal particles attached to dielectric tips has become an emerging technique [32–34]. Such tips are well defined and, compared to long, elongated tips, can be more easily modeled and understood.

The ASNOM discussed in Chapter 12 by Keilmann and Hillenbrand uses light scattering from a sharp tip (hence, s-SNOM) and has no wavelength-related resolution limit. Rather, its resolution equals approximately the radius a of the probing tip (for commercial tips, $a < 20$ nm) so that 10 nm is obtained in the visible corresponding to $\lambda/60$.

A resolution of $\lambda/500$ has been obtained in the midinfrared at $\lambda = 10\ \mu$m. The advantage with infrared, THz, and even microwave illumination is that specific excitations can be exploited to yield specific contrast. In the midinfrared, for example, the molecular vibrations offer a spectroscopic fingerprint to identify materials and chemical composition ("chemical recognition"); furthermore, the free-carrier dynamics offer the assessment of local conduction. Thus, the realization of a 10 nm resolving infrared microscope enables the power of infrared spectroscopy to benefit future nanoscience research. The s-SNOM can routinely acquire simultaneous amplitude and phase images to obtain information on refractive and absorptive properties. Plasmon- or phonon-resonant materials can be highlighted by their particularly high near-field signal level. Furthermore, the s-SNOM can map the characteristic optical eigenfields of small, optically resonant particles. The authors also describe theoretical modeling that explains and predicts s-SNOM contrast on the basis of the local dielectric function.

The limits of one-photon fluorescence as a contrast mechanism in nanoscale-resolution tip-enhanced optical microscopy are considered by Gerton and coworkers in Chapter 13. Specifically, the issue of how much tip-induced signal enhancement is needed to resolve single fluorescent molecules within densely packed ensembles is addressed. Modulation of the fluorescence signal induced by an oscillating tip and subsequent demodulation with a lock-in amplifier increases image contrast by nearly two orders of magnitude. Gerton and coworkers have developed a simple model of the signal modulation/demodulation scheme based on a variety of near-field measurements, which predicts that commercially available silicon tips should give sufficient contrast to resolve single fluorophores in the ensemble. Further, the use of time-resolved photon counting enables more powerful and sophisticated demodulation algorithms to be implemented, resulting in even larger gains in near-field contrast. Such a scheme enabled the authors to image the fluorescently labeled ends of short DNA oligomers with spatial resolution below 10 nm. This work is an important step toward the widespread application of tip-enhanced fluorescence microscopy to the nanoscale structural analysis of biomolecular systems.

Spectroscopic methods with high spatial resolution are essential for understanding the physical and chemical properties of nanoscale materials including quantum structures, biological proteins, and nanocomposite materials. In Chapter 14, Hartschuh and colleagues discuss how the enhanced electric fields near a sharp, laser-irradiated metal tip can be used for spatially confined measurement of various optical signals, enabling a detailed sample characterization far below the diffraction limit. Tip-enhanced fields also provide the sensitivity crucial for the detection of nanoscale volumes reaching down to 10^{-21} liters. Hartschuh and colleagues study the properties of the enhanced fields experimentally and demonstrate both photoluminescence and Raman imaging of carbon nanotubes with ~ 10 nm resolution. Nanoscale spectroscopy is used to visualize structural heterogeneities along single nanotubes, providing unprecedented insights into these structures.

Nanolithography and the fabrication of nanostructures are important branches of nanotechnology that may one day lead to many applications and research fields including ultrahigh-density storage, nanoelectronics, nanomechanics, and nanobiotechnology. Chapter 15 considers a recent approach of nanolithography based on the local optical interaction between photosensitive molecules and localized surface plasmons of metal nanostructures. Three selected examples characteristic of this domain of research are presented: tip-enhanced optical lithography, optical nanostructuring by in-plane plasmonic

structures, and the fabrication of new hybrid metal/polymer nanoparticles. The chapter highlights that this approach not only enables the fabrication of nanostructures with light but also opens the door to nano-photochemistry based on surface plasmon photonics.

There is one further approach to ASNOM that uses, instead of a metal or dielectric tip, a single molecule or fluorescent nanoparticle as a light source. In Chapter 16, Sekatskii introduces the method of fluorescence resonance energy transfer (FRET) SNOM in which a FRET pair is separated between a SNOM tip and a surface. The FRET-donor (or acceptor) fluorophore is located at the tip apex and is scanned in the vicinity of the sample containing the complementary fluorophore of the FRET pair, while the acceptor fluorescence (or donor fluorescence quenching) is detected. The spatial resolution for such an approach is governed not by the aperture size, but by the characteristic length scale for FRET (the Förster radius) and thus can attain values of 2–7 nm with the same (or higher) sensitivity of apertured-SNOM. The theoretical fundamentals of the method, its experimental realization, and connections with other types of near-field optical microscopy are discussed.

The book concludes with a brief overview in Chapter 17 of some recent work in this field—in particular, work concerned with the interaction between the localized surface plasmon of a metal tip and a nearby fluorophore and the development of nano-antennas for tuned resonance in the visible part of the spectrum. The chapter concludes with an overview of recent far-field approaches to nano-optical microscopy.

References

[1] Binnig, G., and H. Rohrer, "Scanning Tunneling Microscopy," *Helvetica Physica Acta,* Vol. 55, 1982, pp. 726–735.

[2] Binnig, G., C. F. Quate, and C. Gerber, "Atomic Force Microscopy," *Phys. Rev. Lett.* Vol. 56, 1986, pp. 930–933.

[3] Pohl, D. W., S. Denk, and M. Lanz, "Optical Stethoscopy: Image Recording with Resolution λ/20," *App. Phys. Lett.,* Vol. 44, 1984, pp. 651–653.

[4] Lewis, A. et al., "Development of a 500 Å Spatial Resolution Light Microscope," *Ultramicroscopy,* Vol. 13, 1984, pp. 227–232.

[5] Harootunian, A. et al., "Super-Resolution Fluorescence Near-Field Scanning Optical Microscopy," *Appl. Phys. Lett.,* Vol. 49, 1986, pp. 674–676.

[6] Betzig, E., and J. K. Trautman, "Near-Field Optics: Microscopy, Spectroscopy, and Surface Modification Beyond the Diffraction Limit," *Science*, Vol. 257, 1992, pp. 189–195.

[7] Betzig, E. et al., "Breaking the Diffraction Barrier: Optical Microscopy on a Nanometric Scale, *Science,* Vol. 251, 1991, pp. 1468–1470.

[8] Jackson, J. D., *Classical Electrodynamics*, New York: John Wiley, 1975.

[9] Novotny, L., and D. W. Pohl, "Light Propagation in Scanning Near-Field Optical Microscopy," *NATO Adv. Stud. Inst. E*, Vol. 184, 1995, pp. 21–33.

[10] Knoll, B., and F. Keilmann, "Electromagnetic Fields in the Cutoff Regime of Tapered Metallic Waveguides," *Opt. Comm.,* Vol. 162, 1999, pp. 177–181.

[11] Hecht, B. et al., "Scanning Near-Field Optical Microscopy with Aperture Probes: Fundamentals and Applications," *J. Chem. Phys.,* Vol. 112, 2000, pp. 7761–7774.

[12] Wessel, J., "Surface-Enhanced Optical Microscopy," *J. Opt. Soc. Am. B,* Vol. 2, 1985, pp. 1538–1540.

[13] Wickramasinghe, H. K., and C. C. Williams, "Apertureless Near Field Optical Microscope, U.S. Patent 4947034, 1990.

[14] Inouye, Y., and S. Kawata, "Near-Field Scanning Optical Microscope with a Metallic Probe Tip," *Opt. Lett.,* Vol. 19, 1994, pp. 159–161.
[15] Gersten, J., and A. Nitzan, "Electromagnetic Theory of Enhanced Raman Scattering by Molecules Adsorbed on Rough Surfaces," *J. Chem. Phys.,* Vol. 73, 1980, pp. 3023–3037.
[16] Martin, Y. C., H. F. Hamann, and H. K. Wickramasinghe, "Strength of the Electric Field in Apertureless Near-Field Optical Microscopy," *J. Appl. Phys.,* Vol., 89, 2001, pp. 5774–5778.
[17] Milner, R. G., and D. Richards, "The Role of Tip Plasmons in Near-Field Raman Microscopy," *J. Microscopy,* Vol. 202, 2001, pp. 66–71.
[18] Liao, P. F., and A. Wokaun, "Lightning Rod Effect in Surface Enhanced Raman Scattering," *J. Chem. Phys.,* Vol. 76, 1982, pp. 751–752.
[19] Farahani, J. N. et al., "Single Quantum Dot Coupled to a Scanning Optical Antenna: A Tunable Superemitter," *Phys. Rev. Lett.,* Vol. 95, 2005, Art. No. 017402.
[20] Taminiau, T. H. et al., "λ/4 Resonance of an Optical Monopole Antenna Probed by Single Molecule Fluorescence," *Nano Lett.,* Vol. 7, 2007, pp. 28–33.
[21] Knoll, B., and F. Keilmann, "Near-Field Probing of Vibrational Absorption for Chemical Microscopy," *Nature*, Vol. 399, 1999, p. 134–137.
[22] Stöckle, R. M. et al., "Nanoscale Chemical Analysis by Tip-Enhanced Raman Spectroscopy," *Chem. Phys. Lett.,* Vol. 318, 2000, pp. 131–136.
[23] Hayazawa, N. et al., "Near-Field Raman Imaging of Organic Molecules by an Apertureless Metallic Probe Scanning Optical Microscope," *J. Chem. Phys.,* Vol. 117, 2002, pp. 1296–1301.
[24] Hartschuh, A. et al., "High-Resolution Near-Field Raman Microscopy of Single-Walled Carbon Nanotubes," *Phys. Rev. Lett.,* Vol. 90, 2003, Art. No. 095503.
[25] Labardi, M. et al., "Highly Efficient Second-Harmonic Nanosource for Near-Field Optics and Microscopy," *Opt. Lett.,* Vol. 29, 2004, pp. 62–64.
[26] Lecaque, R. et al., "THz Near-Field Optical Imaging by a Local Source," *Opt. Comm.,* Vol. 262, 2006, pp. 125–127.
[27] Frey, H. G. et al., "Enhancing the Resolution of Scanning Near-Field Optical Microscopy by a Metal Tip Grown on an Aperture Probe," *App. Phys. Lett.,* Vol. 81, 2002, pp. 5030–5032.
[28] Hamann, H. F., A. Gallagher, and D. J. Nesbitt, "Near-Field Fluorescence Imaging by Localized Field Enhancement Near a Sharp Probe Tip," *App. Phys. Lett.,* Vol. 76, 2000, pp. 1953–1955.
[29] Gerton, J. M. et al., "Tip-Enhanced Fluorescence Microscopy at 10 nm Resolution," *Physical Review Letters,* Vol. 93, 2004, Art. No. 180801.
[30] Anger, P., P. Bharadwaj, and L. Novotny, "Enhancement and Quenching of Single-Molecule Fluorescence," *Phys. Chem. Lett.,* Vol. 96, 2006, Art. No. 113002.
[31] Kühn, S. et al., "Enhancement of Single-Molecule Fluorescence Using a Gold Nanoparticle as an Optical Antenna," *Phys. Chem. Lett.,* Vol. 97, 2006, Art. No. 17402.
[32] Kalkbrenner, T. et al., "A Single Gold Particle as a Probe for Apertureless Scanning Near-Field Optical Microscopy," *J. Microscopy,* Vol. 202, 2001, pp. 72–76.
[33] Kim, Z. H., and S. R. Leone, "High-Resolution Apertureless Near-Field Imaging Using Gold Nanosphere Probes," *J. Phys. Chem. B,* Vol. 110, 2006, pp. 19804–19809.
[34] Kalkbrenner, T. et al., "Optical Microscopy via Spectral Modifications of a Nanoantenna," *Phys. Chem. Lett.,* Vol. 95, 2005, Art. No. 200801.

CHAPTER 11

Near-Field Nanoscopy by Elastic Light Scattering from a Tip

Fritz Keilmann and Rainer Hillenbrand

11.1 Introduction

For more than a century, the classical light microscope has been serving science as a fruitful instrument. It is operated nearly exclusively with visible light illumination. As identified in the preceding introduction, a dramatic improvement of optical resolution has become possible through the invention of SNOM. However, the original version of an aperture SNOM that uses a submicrometric metallic aperture with diameter d meets a limit through the cutoff effect: light propagation becomes evanescent when the diameter is below the critical cutoff diameter, given by $d_c = 0.6\,\lambda/n$. The consequence is a drastic λ-dependent loss [1]. This limits the achievable resolution—depending on how small a signal power can be detected—practically to minimal apertures $d \approx \lambda/10$. For midinfrared illumination, therefore, the resolution of SNOM can be 1 μm at best, which is not a very interesting value for applications in the nanosciences.

Fortunately, an alternative SNOM principle exists with a much better resolution potential: use of a small scatterer instead of the small aperture [2–7]. It rests on the long-known fact that an illuminated particle [8] or a sharp tip [9] can exhibit enhanced optical fields in its neighborhood. Such tip-enhanced near fields are modified by the presence of a sample. As a consequence of this near-field interaction, the elastically scattered light observable in the far field carries information on the sample's local optical properties. This near-field scattering is the basis of what has been named s-SNOM: scattering-type scanning near-field optical microscope. This principle has early on been exploited in the microwave region, where the radiation is however confined in waveguides [10–13]. For higher frequencies, in practice, an AFM is used whose elongated metallized tip serves as a scatterer (see Figure 11.1). The radius of curvature a at its apex determines both the mechanical and the optical resolution. Note then that the optical resolution is *λ-independent*. Even bare Si tips provide, owing to their relatively high refractive index, a sufficient field enhancement to allow s-SNOM imaging [14–18].

This chapter is organized as follows. First, we introduce the principle of s-SNOM: its components and configurations. Then we consider theory, describing in detail a point-dipole model that can qualitatively explain the majority of all experimental findings. The following section gives experimental details, with an emphasis on how disturbing background scattering can be suppressed and how high-resolution amplitude and phase contrast is made possible by interferometric detection. The results are discussed for their significance of demonstrating the optical

contrast and resolution obtainable with s-SNOM. A special section is devoted to the resonant near-field interaction between tip and sample. It enables extremely high signal in s-SNOM images to arise from polariton excitation in samples (or tips) with negative dielectric constant. Going beyond probing a sample's local optical property, the s-SNOM also can be applied to analyze the patterns of the resonant optical eigenfields (i.e. near fields that may be directly excited by the illuminating beam near sharp or small sample structures). Finally, we mention application areas of s-SNOM in the nanosciences, such as the mapping of subsurface charge carriers in Si and the analysis of nanocomposite dielectrics. A special emphasis is placed on the infrared s-SNOM, owing to the unique values of infrared spectroscopy (e.g., for the chemical recognition and quality control of mixtures in chemical, pharmaceutical, petrochemical, and food industries; for the quantification of solid-state conductivity to characterize electronic devices; or for an understanding of exotic mechanisms provided by heavy, correlated Cooper-paired or spin-aligned electrons).

11.2 Principle of Scattering-Type Scanning Near-Field Optical Microscopy (s-SNOM)

A basic experimental setup is illustrated in Figure 11.1. Here an AFM is used as a base instrument (STM can be an alternative [19]) to scan a sample in close proximity of a cantilevered tip. This generates, first of all, a topographic image of the sample. The tip is illuminated by a focused visible or infrared beam so that the scattered light is recorded by a detector to give an optical image of the sample. It is the radius of curvature a of its apex that determines the mechanical and the optical transverse resolutions. In principle, input and output directions could be freely chosen. Backscattering, as shown in Figure 11.1, has the practical advantage that only one focusing objective must be adjusted.

Typically, the tip has a radius of curvature of $a \approx 20$ nm. The probing region is the gap between the tip apex and the sample, a space much smaller than the applied focus spot that typically has a diameter of λ. Due to the AFM tapping mode, this gap is sinusoidally varied between 0 and, for example, 40 nm. A strong modulation of the near-field scattering results—whereas advantageously, the

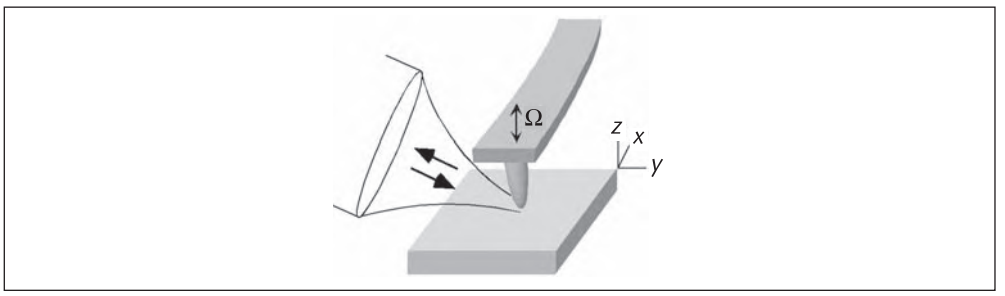

Figure 11.1 Principle of scattering-type SNOM. A focused light beam illuminates the tip region of an AFM where a sample is approached and scanned to produce a topographic image. By recording the scattered light, here in backward direction, an optical image is simultaneously generated. The tip oscillates at the cantilever's mechanical resonance frequency Ω (tapping mode) with the important consequence that the near-field optical signal becomes modulated at harmonics $n\Omega$, allowing an electronic filtering against otherwise overwhelming background scattering coming from the shaft and cantilever.

"background" scattering from portions of tip and sample outside the probing region is barely modulated—and therefore can be electronically eliminated from the detector signal.

An early implementation of s-SNOM [14] used a dielectric tip that has a principle limitation to the fraction of the illuminating power that can effectively couple to the probing gap. In contrast, highly conductive tip materials can greatly increase this fraction, as can be extrapolated from the effective functioning of metal antennas in radio and microwave engineering [1]. Antenna efficiencies have been experimentally analyzed up to the midinfrared region [20, 21], and one can hope that tailored tips [22] can, in the future, strongly increase the coupling of illuminating light into an enhanced probing near field and back out to a far-field detector.

For highly conductive metallic shafts, the antenna theory predicts that optical currents can be excited much stronger parallelly than perpendicularly to the shaft axis [1]. This antenna effect should make itself felt by forcing the probing near field to be fully *z*-polarized. We have tested this prediction in an experiment with an Au-coated tip illuminated by the midinfrared beam from a CO_2 laser, the polarization of which could be rotated while the light scattered to the detector did not pass through a polarizing element [23]. The result shown in Figure 11.2 illustrates clearly that the optical image loses contrast when the input polarization has no component along the shaft axis. This effect indicates that the shaft acts as an antenna—more precisely, that it can enhance the probing near field in *z*-direction.

Various mostly home-built s-SNOMs have been reported in the literature [6, 7, 14, 15, 19, 24–35]. We have built two AFM-based s-SNOMs to operate in tapping mode with visible [28] or midinfrared illumination [36]. Both use Pt-coated cantilevered tips available commercially (Nanosensors, www.nanosensors.com, or MikroMasch, www.spmtips.com). These instruments implement interferometric signal detection [30, 37, 38], which allows measuring both the amplitude and the phase of the near-field scattering interaction, especially enabling near-field phase contrast imaging [28, 34, 39–45]. We have realized three interferometer versions: a Michelson type with homodyne detection [36, 46], a Mach-Zehnder type with heterodyne detection [28, 47, 48], and a Michelson type with pseudo-heterodyne detection [49] as will be detailed in Figure 11.5.

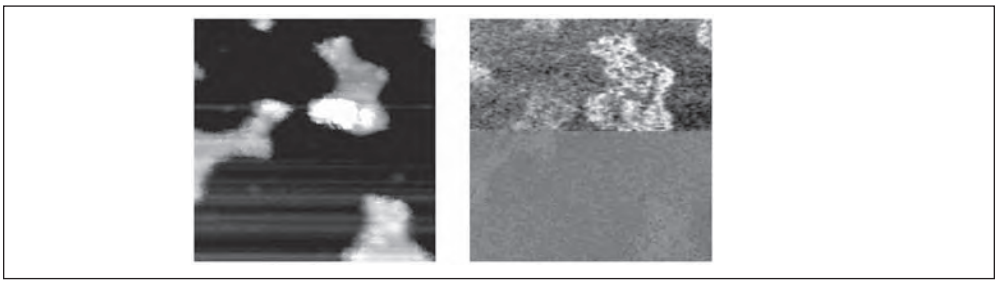

Figure 11.2 Topography (left) and infrared near-field image (right) of a test sample consisting of 20 nm high Au islands on Si (image area 1 μm^2). Halfway through the image scan, the polarization was flipped from z-y (upper part) to x (lower part) to investigate the antenna function of the tip shaft. © 1999 The Royal Microscopical Society [23].

11.3 Theory of Scattering-Type Scanning Near-Field Optical Microscopy

Two observables are of practical importance in s-SNOM—the *absolute* scattering efficiency, which determines the observable signal power, and the contrast or *relative* signal change, which results when probing different materials. A theoretical treatment of the scattering of a realistic, elongated tip is complicated [50] and has not been tried by us. The shaft's shape and length dominate the *absolute* scattering efficiency as can be expected from antenna theory. For qualitatively calculating the *relative* scattering when probing different materials, however, we have found a solution by simplifying the geometry [26, 28, 51, 52]. We assume that the near-field contrast (or generally, the way a sample influences the near-field between tip and sample) does not depend primarily on the existence of the tip's shaft. Rather, it suffices to approximate the elongated tip by the sphere that can be inscribed in its apex. (See Figure 11.3.)

Accordingly, we assume that the probe is a polarizable sphere with dielectric value ε_t, radius $a \ll \lambda$, and polarizability

$$\alpha = 4\pi a^3(\varepsilon_t - 1)/(\varepsilon_t + 2)$$

We further assume that the dipole induced in this sphere by an incident field E_i can point only in z-direction. This polarization direction is suggested by the antenna action of the tip's shaft leading to an enhanced near field. The sample, which fills the half-space $z < 0$ with dielectric value ε_s, is assumed to be polarizable only indirectly by the sphere's dipolar field (but not directly by the incident field) because the tip's enhanced near field exceeds the incident field. The configuration of a small sphere next to a flat sample has been theoretically treated before in the context of SERS [53, 54]. To simplify the calculation of the polarization induced in the sample, we replace the sphere by a point dipole of equal strength and direction located in the sphere's center. In the electrostatic limit (no retardation considered), the near field interaction between tip dipole and sample can be found by considering a "mirror" point dipole inside the sample whose direction is parallel to the tip dipole, with polarizability $\alpha\beta$ where

$$\beta = (\varepsilon_s - 1)/(\varepsilon_s + 1) \tag{11.1}$$

is the dielectric surface response function of the sample. The mirror's dipole field, decreasing with the third power of distance, interacts with the tip dipole.

Calculation of the near-field interaction between the tip and mirror dipoles yields the effective polarizabilities of both dipoles. Originally, these were added to obtain the combined effective polarizability [26]

$$\alpha_{eff} = \frac{\alpha(1+\beta)}{1 - \dfrac{\alpha\beta}{16\pi(a+z)^3}} \tag{11.2}$$

Since the scattered field $E_s \propto \alpha E_i$ from a point dipole generally is directly proportional to its polarizability α [56], Equation 11.2 is a centrally important result for s-SNOM, as it contains all that is necessary to predict relative contrasts observable

in s-SNOM. First, we note that ε, β and α are complex-valued quantities in general. Thus, the scattering

$$E_s \propto \alpha_{eff} E_i \tag{11.3}$$

from the coupled dipole system is, in general, also complex-valued, $\alpha_{eff} = se^{i\varphi}$, characterized by a relative amplitude s and a generally nonzero phase shift φ between the incident and the scattered light. The aim of measuring both of these quantities simultaneously motivated our development of interferometric detection.

Numerous s-SNOM studies [26, 34, 41, 42, 44–46, 57–60] have used Equation 11.2 to successfully predict and describe NFO contrasts of polymers, polar crystals, semiconductors, and metals. For comparison with experiment, relative contrast between two different materials was computed, and a good agreement was obtained in most cases. Note that the near-field contrast for a realistic tip has recently been simulated [18].

A reconsideration of the scattering experiment [61] led to formulating the scattering from the coupled dipoles slightly differently:

$$E_s = (1 + r)^2 \frac{\alpha}{1 - \dfrac{\alpha\beta}{16\pi(a + z)^3}} E_i \tag{11.4}$$

Here the factor $(1+\beta)$ in Equation 11.2 is replaced by one factor $(1+r)$, where r is the Fresnel reflection coefficient of the flat sample surface. This is because the electrostatic reflection coefficient β is not suitable for describing the far-field scattering as it can exceed unity, meaning that the mirror dipole would radiate stronger than the tip dipole, contradicting energy conservation. A further factor $(1+r)$ is introduced to

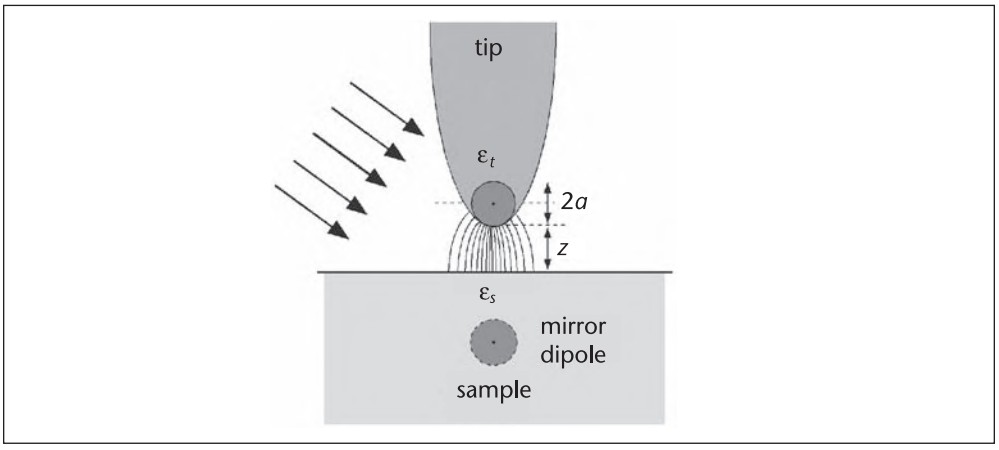

Figure 11.3 Modeling the near-field interaction in s-SNOM. The replacement of the probing tip by a point dipole allows one to predict how the scattered light depends on (i) the distance z between tip and sample and (ii) on the complex dielectric value ε_s of the sample. The former (i) is important for understanding how background scattering can be eliminated by harmonic signal demodulation. (See Section 11.4.) The latter (ii) represents the basis of s-SNOM's ability to display contrast between different sample materials and to understand this contrast in phase and amplitude. (See Section 11.6.) © 2004 Japanese Society of Microscopy [55].

account for the extra illumination of the probe via reflection at the sample surface, not taken into account in Equations 11.2 and 11.3, but already noted in [35, 62].

As a far-reaching consequence of the tip-dipole/mirror-dipole model, we note that the sample affects the s-SNOM signal mostly through its dielectric value ε_s taken at the wavelength of illumination. This provides the basis to view s-SNOM as a nanospectroscopic tool—to measure the local dielectric function for identifying nanosystems according to their known (far-field) optical and infrared dielectric spectra. We further observe that in Equations 11.2 and 11.4, the probing sphere also enters by its dielectric value ε_t, besides its radius and its distance z from the sample. Since both ε_t and z are constant during the imaging process, the optical image contrast essentially is determined by the sample's local dielectric value ε_s.

Before giving examples of material contrast, we discuss another consequence of Equation 11.2, the distance dependence $\alpha_{eff}(z)$, which as we shall see, is of prime importance for the practical, background-free performance of s-SNOM. As an example, we assume the sample to be Si with real dielectric value $\varepsilon_s = 15$ and the tip sphere to be Au, with radius $a = 10$ nm and dielectric value $\varepsilon_t = -10 + 2i$ (corresponding to $\lambda = 633$ nm).

As displayed in Figure 11.4, Equation 11.2 predicts a constant scattering at relatively large distance $z \gg 2a$. (Note that the neglect of retardation restricts the applicability of this modeling to $z \ll \lambda$) At a very small distance $z < \lambda$, however, both the scattering amplitude and the scattering phase increase sharply. Such a nonlinear rise occurs with any combination of dielectric values and can be taken as a signature of the near-field interaction. It is interesting that the z-range of near-field interaction is of the same order as the lateral width of the confined near field, both being of the order a, the sphere's radius [36]. A multipolar theory that includes retardation has recently given a similar result [63]. In the following section, we keep to the nonretarded dipolar approximation because it allows the simple solution Equation 11.2 from which direct conclusions of practical significance can be derived.

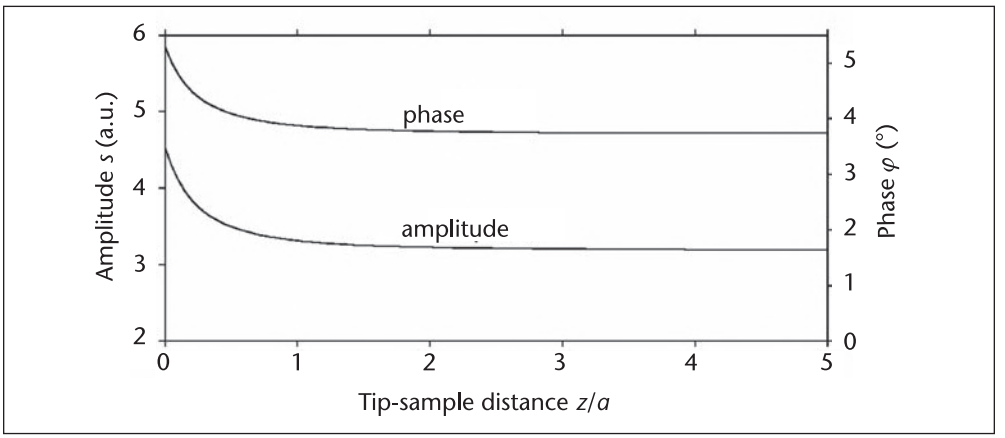

Figure 11.4 Calculated near-field scattering amplitude s and phase ϕ versus the distance z between the tip sphere and the sample. The signals' change is restricted to the range of the near-field interaction, $\Delta z \approx a$. The occurrence of a nonlinear approach characteristic is a necessary (and sufficient) condition for assuring, in a given experiment, that all tapping/illumination/detection parameters are correctly set for the recording of s-SNOM images.

11.4 Elimination of Background-Scattering Contributions from the Detector Signal

The nonlinear dependence $\alpha_{eff}(z)$ shown in Figure 11.4 is the basis of a signal processing technique essential to solving the experimental difficulty of how to deal with the massive, unwanted "background" scattering that generally dominates the detected signal. The focused laser beam illuminates a greater part of the tip shaft, which typically extends 10 μm from the cantilever, and the sample. Because there is no special attempt to match the incoming light to the largely unknown antenna property of the tip-sample configuration, only a small portion of the incident light can be assumed to reach the gap region and to contribute to the probing near field. Most of the intercepted light is scattered as unwanted background, without contributing to the near-field interaction. The early suggestion [12] of z-modulation and the electronic filtering of the detector signal at the tapping frequency Ω is generally not sufficient to suppress the background. Rather, a full elimination requires demodulating the detector signal at the second or higher harmonic of Ω [28, 47, 60, 64, 65]. The key is that the tapping motion, typically with an amplitude of $\Delta z \approx a \approx 20$ nm, modulates the near-field scattering much more strongly than the background scattering, inducing harmonics $n\Omega$ (where $n = 2,3$) by the nonlinear dependence $\alpha_{eff}(z)$ shown in Figure 11.4. A detailed analysis is given in [66, 67]. Before describing experimental details and results (Figures 11.6 and 11.7), we note that the successful elimination of background scattering by harmonic-demodulation processing has a price to be paid. The s-SNOM image no longer measures the near-field scattering $\alpha_{eff} = s \cdot e^{i\varphi}$ directly. Rather, it maps the complex quantity derived from it. To see this, consider the sinusoidal tapping motion between z and $z + 2\Delta z$ at frequency Ω which induces a time-periodic scattering $\alpha_{eff}(t)$. Because of the nonlinear dependence $\alpha_{eff}(z)$, the scattering signal is modulated at harmonics of Ω. In general, the time course can be described by a Fourier series with s_n and ϕ_n being Fourier coefficients. In the case of small modulation amplitude $\Delta z \ll a$, the Fourier coefficients are proportional to the n-th z-derivative of $\alpha_{eff}(z)$ [28, 47].

11.5 Experimental Realization of s-SNOM

We have introduced three operating versions of interferometric s-SNOM—heterodyne (a), homodyne (b), and pseudo-heterodyne (c)—as illustrated in Figure 11.5.

The heterodyne detection setup described in [28, 52] uses a HeNe laser beam of ≈ 1 mW power that is focused to the tip apex by an aspheric lens. Backscattered light is collected by the same lens and detected by a heterodyne interferometer. Here the reference beam is frequency-shifted by $\Delta = 80$ MHz. The detector measures the power $I = I_{ref} + I_s + 2\sqrt{I_{ref} I_s} \cos(\Delta t + \varphi)$ generated by the interference of the strong reference beam and the weak backscattered light from the probing tip. To measure both amplitude and phase, the detector signal is processed in a high-frequency LIA (Mod. 844 Stanford Research Systems) operating not at Δ but at the sum frequency $\Delta + n\Omega$ (where n designates the order of harmonic signal demodulation) [28, 47, 48]. This side-band filtering allows suppressing, in one

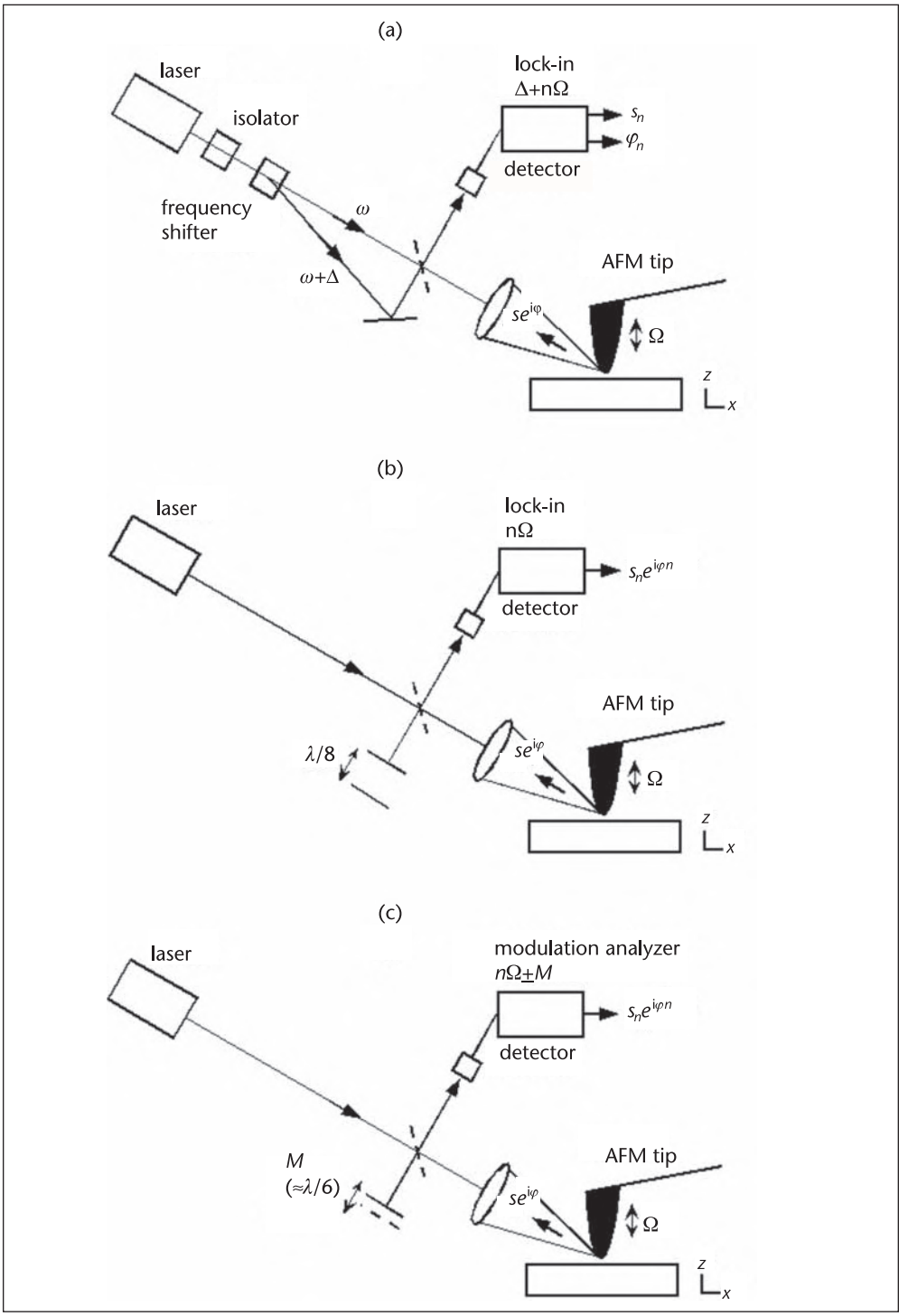

Figure 11.5 Sketches of optical layouts for interferometric s-SNOM. (a) Heterodyne system where the optical frequency in the reference arm of a Mach-Zehnder interferometer is offset by frequency Δ(80 MHz in [49]). (b) Homodyne system where the phase of the reference beam in a Michelson interferometer is alternated between $\psi = 0$ and 90° by mechanical mirror translation. (c) Pseudo-heterodyne system where the phase of the reference beam in a Michelson interferometer is modulated by $\Delta\psi = 151°_{pp}$ at frequency M by mechanical mirror translation.

instrument, any constant power as well as the tip's background scattering that beats with the reference to yield a modulation at Δ. Stated reversely, demodulation at $\Delta + n\Omega$ selects scattered light that is influenced by the mechanical modulation of the near-field interaction. The LIA produces two output signals simultaneously—one proportional to the amplitude; the other proportional to the phase of the detector modulation at frequency $\Delta + n\Omega$. This is very convenient because, at sufficiently large n, the amplitude output signal is directly proportional to sn and the output phase is directly proportional to φ_n measuring the pure near-field response. Because of interference with the reference beam, the near-field signal power level appears amplified by a factor twice the square root of the ratio between reference and near-field light powers, which can be a large factor in practice. This interferometric gain is a convenient byproduct of all of our schemes—(a), (b), and (c)—as it helps to optimize the signal/noise ratio [36].

Background reduction by harmonic demodulation becomes directly visible in approach curves such as that shown in Figure 11.6. At demodulation order n = 1, standing wave features dominate that extend far beyond the near-field interaction zone defined by $z < a$. These result from interference of different background contributions and may mask the expected near-field increase at $z < a$. (See Figure 11.4.) With increasing n, however, the near-field contribution becomes clearly visible and even steepens, whereas the standing wave features are suppressed and even lost in noise at $n = 3$. Note that the possibility of an artifact can arise because the tip periodically touches the sample. Therefore, the tapping motion can become nonsinusoidally distorted, which means that harmonics $n\Omega$ are excited in the mechanical motion. These mechanical harmonics cause direct modulations of the optical signal. This artifact effect has been studied and found to be dependent on the sample and the tapping characteristics—for example, on the tapping amplitude Δz and on whether the mechanical interaction is attractive or repulsive [68, 69]. We found that with small $\Delta z < 50$ nm and large setpoint $\Delta z/\Delta z_{free} > 0.9$, mechanical harmonics are negligibly small. A detailed analysis of this source of artifact can be found in [70]. To fully exclude an influence on the optical signal, a routine control is recommended for each s-SNOM image recording, namely to take an approach curve, such as that in Figure 11.6, at the beginning of an s-SNOM imaging session.

We demonstrated NFO mapping using higher harmonic demodulation by imaging a common test sample (see Figure 11.7). Its nanoscale structure is made by evaporating metal on a substrate that is covered by a monolayer of polystyrene (PS) microspheres. These are subsequently dissolved by dichloromethane and washed away [71]. Here we use a Si substrate with 20 nm high Au islands, as documented by the topographic image. Further, Figure 11.7 shows two optical near-field images taken at the fundamental and the third-harmonic demodulation orders, respectively. The former image (middle) displays—due to the influence of considerable background scattering—large patches that do not correspond to real sample structures. Furthermore, the islands appear in reversed, dark contrast. We explain the large patches by interference between various components of background-scattered light and the reversed contrast of the islands by a negative interference between the near-field-scattered light and the background-scattered light. The latter explanation can be experimentally tested by slight adjustments of the illuminating laser focus.

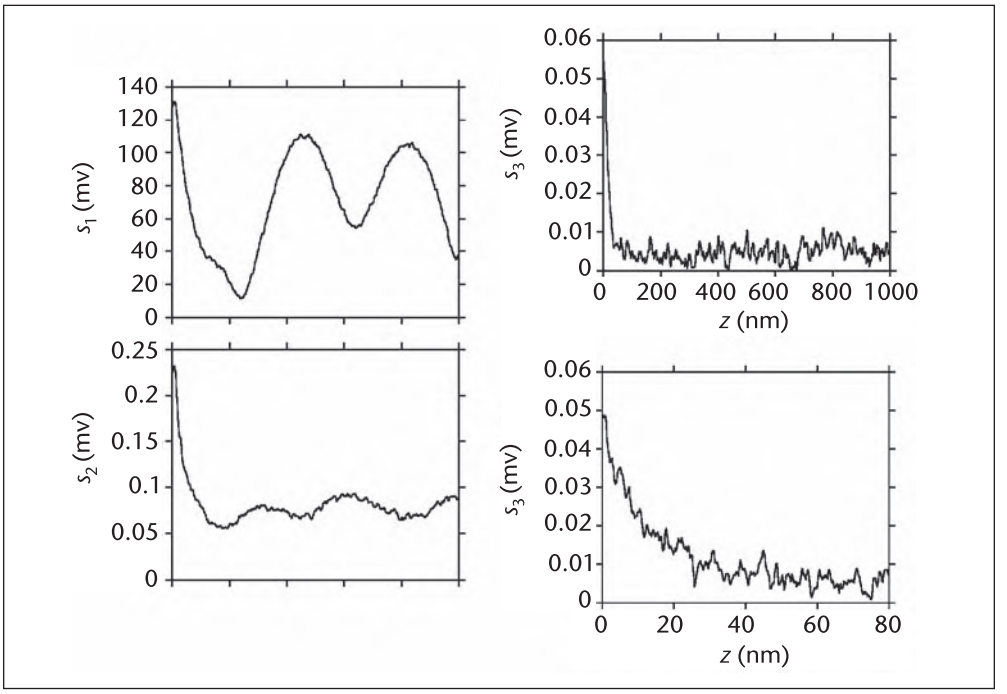

Figure 11.6 Comparison of experimental s-SNOM amplitude versus distance z between Pt tip and Si sample for $n = 1$-3 demodulation orders (tip radius $a \approx 20$ nm, tapping amplitude $\Delta z \approx 20$ nm, wavelength $\lambda = 633$ nm). The choice of a high n advantageously eliminates the background, steepens the near-field response, and sharpens the optical resolution. © 2002 American Institute of Physics [57].

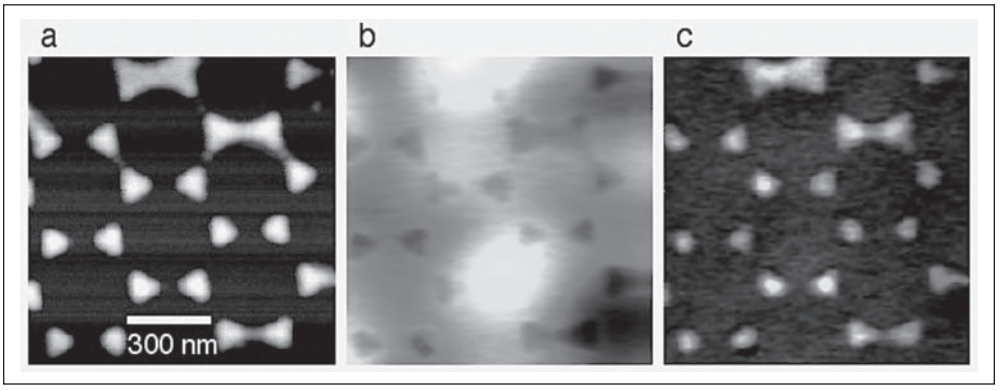

Figure 11.7 Experimental s-SNOM images of 20 nm high Au islands on Si. (a) Topography, (b) optical amplitude s_1 showing residual background scattering, and (c) optical amplitude s_3 showing pure near-field response. © 2001 The Royal Microscopical Society [47].

Indeed, small variations suffice to reverse the apparent near-field contrast, evidently by changing the background's phase [26, 60, 72]. However, the optical image taken at third-harmonic demodulation order (right) displays the Au islands with uniform brightness and in the positive contrast expected from calculations (Figure 11.8) independently of slight adjustments of the illuminating laser focus.

Both groups that pioneered the midinfrared s-SNOM used a CO_2 laser for tip illumination [25, 26]. We exploited the fact that this laser is step-tunable between

9.2 and 11.2 μm to demonstrate for the first time the principle possibility of near-field nanospectroscopy utilizing infrared vibrational [26, 46] or electronic [58] resonances.

The incident beam is attenuated (Lasnix 102, www.lasnix.com) to about 10 mW and focused to the tip apex by a Schwarzschild mirror objective with $NA = 0.55$ (Ealing, www.cohr.com). A focal spot with a diameter as small as 15 μm has been experimentally demonstrated [60]. The polarization is set to maximize the electric field component along the tip shaft in order to optimize the antenna coupling. Orthogonal polarization was experimentally shown to lead to loss of contrast (Figure 11.2) [23].

The mentioned early infrared s-SNOM work and that of other laboratories [31, 73–76] used simple direct detection of the scattered infrared light by a HgCdTe detector. While there is no external reference beam, we have observed that this detection is, nonetheless, of interferometric type [26, 51, 60]. The reason is the omnipresent background scattering that constitutes a reference beam that superimposes coherently with the near-field scattered light. Because there is no frequency offset, the detection system is, strictly speaking, a homodyne receiver. As mentioned previously, the phase of this interferometer can be adjusted by changing the focus of the incident beam [60]. Altogether the direct detection of scattered light is not an ideal method since it does not yield amplitude and phase.

Subsequently, our infrared s-SNOM was qualitatively improved [36] by introducing interferometric detection [Figure 11.5(b)] with an external reference beam, which is, of course, more controllable. This is achieved by splitting the incoming collimated CO_2 laser beam to generate a reference beam that is reflected from a piezoelectrically movable plane mirror. Thus, we form a Michelson interferometer that has the scattering tip at the end of the other side arm. The reference is much stronger than the background scattered light; therefore, we now have a homodyne receiver in which the reference phase can be conveniently set by moving the Michelson mirror. In practice, we continuously alternate between recordings using two mirror positions. The first position is obtained at the beginning of an experiment by maximizing the LIA detector signal (usually second- or third-harmonic demodulation). This position corresponds to positive interference between near-field scattered light and reference beam. The second position is obtained by moving a distance of $\lambda/8$, which changes the reference phase by $\varphi = 90°$. Simple computing yields an unambiguous pair of values, the amplitude and the phase of near-field scattering, for each pixel of the scanned image. Each scan line is repeated once, and the mirror position is switched after each scan. Typically, it takes 1 s to completely determine one 256 pixel line. With this method, the infrared s-SNOM produces simultaneous near-field phase-contrast images and near-field amplitude-contrast images.

Further improvement of background suppression has been achieved recently by introducing the pseudo-heterodyne detection technique [49]. [See Figure 11.5(c).] This results in complete elimination of background interference. It is based on a sinusoidal phase modulation at frequency M of the interferometer reference wave and sideband detection with a digital analyzer (now available as Neaspec PM-48, www.neaspec.com). Amplitude and phase of the scattered light are simultaneously measured in several demodulation orders. In contrast to the earlier established

heterodyne method [28], the pseudo-heterodyne scheme is more compact, needs no AOM, and can be operated in a significantly larger wavelength range spanning the entire near-UV to far-IR spectrum. The pseudo-heterodyne method provides reliable near-field imaging even in the case of weak contrasts, where both noninterferometric and homodyne interferometric detection methods fail [49].

11.6 Contrast and Resolution in s-SNOM Images

We recall from Equation 11.2 that the observable scattering $se^{i\varphi}$ (and consequently $s_n e^{i\varphi_n}$) depends on the dielectric values of both the tip and the sample. This means that the choice of tip material can influence what is seen in s-SNOM. For example, when an Au tip is used in the visible region, the s-SNOM amplitude and phase varies with frequency due to the strong variation of ε_t of Au, as we have calculated. (See Figure 11.2 of [28].) While such influences can, at least in principle, be accounted for (Equation 11.2), clearly a tip material that does not by itself show a strong dispersion within the studied spectral region should be preferable when measuring a sample's near-field spectrum. For a fixed-frequency application, on the other hand, the choice of a resonant tip material could greatly enhance the amplitude and/or phase sensitivity of the s-SNOM.

In the following paragraphs, we discuss how the dielectric value ε_s of the sample determines the near-field signal at contact, $z = 0$. We use Equation 11.2 to predict the relative contrast between various sample materials [36], thereby assuming a sinusoidal tapping motion between $0 \leq z \leq 40$ nm and taking full account of the harmonic signal demodulation in s-SNOM signal processing (here at 3Ω We assume the sphere material to be Pt for the practical reason that AFM tips coated with this metal are both durable and readily available. As shown in Figure 11.8, the theory predicts that typical low-refractive-index dielectrics such as PS produce a very weak near-field scattering s_3. It might, however, increase when such materials are absorbing. Much stronger near-field scattering is predicted for materials with large dielectric value Re (ε_s). Interestingly, this remains true independently of whether Re (ε_s) has a positive or negative sign and independently of whether the imaginary part is small or large. The highest s-SNOM amplitudes s_n are predicted for materials with negative Re (ε_s) ≈ -1 and very small Im (ε_s), which we call polariton-resonant materials as discussed next.

From the results in Figure 11.8, we predict that s-SNOM images will readily allow us to distinguish categorical material classes by amplitude contrast alone: polariton-resonant materials give exceptionally large signals; metals, large signals; semiconductors, medium signals; and low-index dielectrics, low signals [57]. Different metals will appear indistinguishable if probed with midinfrared illumination, but should appear with marked contrast difference when probed in the visible [77].

We have used a test sample composed of three different materials for determining the relative contrasts and the obtainable spatial resolution. (See Figure 11.9.) We have studied this sample in the visible and in the infrared s-SNOM, the aim being to compare the results obtained at widely different wavelengths [36].

The sample is prepared as in Figure 11.7 but without complete dissolution of the PS microspheres. Therefore, irregularly shaped PS remainders are found in many places. The topography alone does not suffice to distinguish between Au and

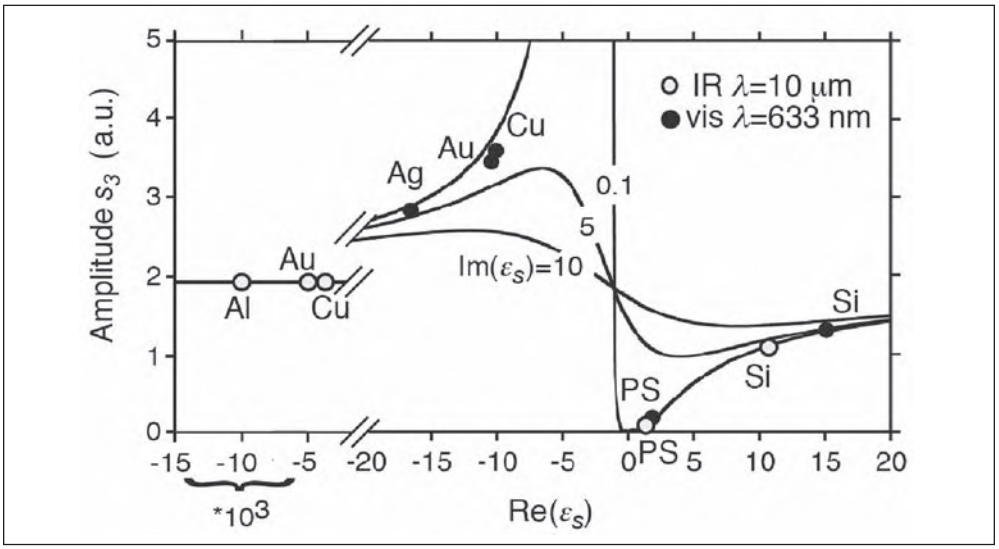

Figure 11.8 The basis for amplitude contrast: predicted s-SNOM amplitude s_3 of various sample materials at two different illumination wavelengths on a general graph where the abscissa is the real part of the sample's dielectric function and the imaginary part serves as a parameter (Pt tip with $a = 20$ nm, $\Delta z = 20$ nm). © 2003 The Royal Microscopical Society [36].

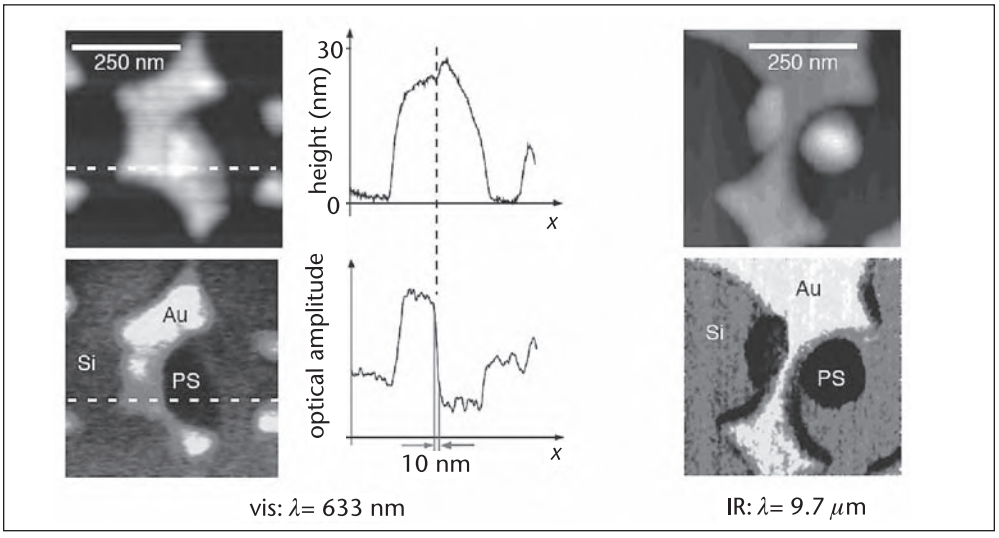

Figure 11.9 Experimental s-SNOM images obtained with a three-component test sample. Use of two different wavelengths (visible, left; mid-infrared, right) testifies (i) that resolution is independent of wavelength (10 nm from line trace through visible image, middle) and (ii) that image contrast is independent of wavelength, confirming predictions of the theoretical model. © 2002 American Institute of Physics [57].

PS, but the near-field images provide the needed extra information. In good agreement with our model calculation (Figure 11.8), the Au islands appear brighter than Si, which in turn appears brighter than PS. The near-field signal on PS is in the noise level for both wavelengths. When we compare the amplitude contrasts between Au and Si quantitatively, we find for $n = 3$ a ratio of about 3:1 at 633 nm and 1.7:1 at 10 μm wavelength (averaging over several images). These values agree nearly quantitatively with the predicted ratios of 2.5:1 and 1.8:1, respectively, so

the ability of s-SNOM to distinguish material classes is confirmed. In addition, this agreement can be taken as verification of the theoretical model.

Figure 11.10 shows further images from this test sample. Here we demonstrate the influence of the demodulation order n on the three-component image contrasts. Evidently there is no qualitative difference between the images obtained at $n = 3$ (middle) and $n = 4$ (right). This indicates a general robustness that we have often observed—of the s-SNOM image against changes of parameters of the background elimination procedure.

As to the spatial resolution, we observe in the visible near-field image (Figure 11.9 left) that the bright-to-dark transition between Au and PS materials occurs within 10 nm (see line scans). Since there is nearly no height step at this boundary, our measurement excludes the possibility of a height-induced artifact and proves that the NFO resolution is indeed 10 nm. The mid-infrared image (Figure 11.9 right) shows approximately the same resolution of roughly 20 nm, $\lambda/500$. Here the fact that the PS particles are somewhat higher makes an exact determination less stringent. These images can be taken as direct proof that the s-SNOM's resolution does not depend on the illuminating wavelength.

Artifacts in s-SNOM are briefly addressed here. Most common are topography-induced artifacts that have long been known already with the aperture SNOM [79]. They can arise because the optical signal changes with tip-sample distance (see Figure 11.6). Thus, any unintended distance change will induce a change of the optical signal. A specific manifestation of a topography-induced artifact is the edge-darkening artifact [32, 36]. It occurs when a sample feature has a steplike topography edge that hinders—only at the very edge—the tip from reaching the lower-lying surface. Therefore, the darkening effect is constrained to a stripe with lateral width equal to about the tip diameter a, following the topography step.

Another artifact mechanism is the error signal artifact [80–82]. It is related to the tip oscillation amplitude, which can become larger or smaller depending on the mean tip-sample distance. It represents a direct crosstalk from the error signal, which itself comes from insufficient slow feedback in the AFM regulation and can usually be avoided by using a sufficiently slow scan speed so that the error signal becomes negligible.

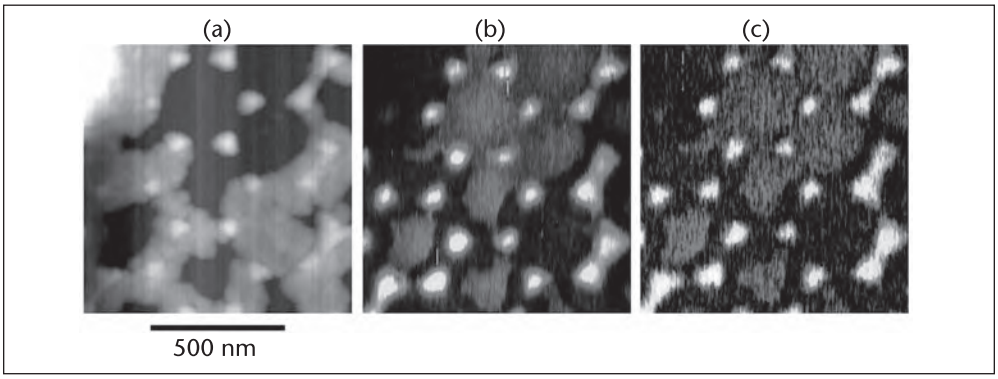

Figure 11.10 Experimental s-SNOM images obtained with a three-component test sample ($\lambda = 633$ nm). (a) Topography and (b,c) s-SNOM amplitude taken at $n = 3,4$ demodulation order, respectively. © 2005 The Korean Physical Society [78].

As a rule, the experimenter should suppress background scattering by suitably choosing the tapping amplitude, the setpoint, and the harmonic demodulation order. If suppression is incomplete, topography features often directly crosstalk into the scattering signal [82].

s-SNOM also is sensitive to the vertical composition below the sample surface [35] because the near-field at the probe tip extends into the sample surface [59]. This effect can be applied to NFO subsurface imaging, which was demonstrated with visible and IR s-SNOM and by tip-enhanced Raman microscopy [83]. IR s-SNOM images revealed Au nanostructures buried below polymer layers [84] and subsurface carriers in implanted semiconductor structures [58, 85].

Up to this point, we have described results obtained by near-field imaging of nanostructures larger than the tip radius. In this case, the NFO images can be considered as dielectric maps of the sample surface. The interpretation of the near-field contrast, however, becomes more complicated when nanoparticles smaller than the probe apex are mapped. Recently, it was observed that the near-field contrast in this case depends not only on the dielectric function of the particles but also on their size [43, 86, 87]. Even a size-dependent contrast reversal was reported [43]. In contrast to Figure 11.9, it has been observed that high refractive index particles smaller than the tip radius can appear much darker than the substrate, although the substrate has a smaller refractive index [43, 87]. In this case, the near-field coupling between the tip and the particle as well as between the tip and the substrate contribute to the signal amplitude s_n. When the probe follows the topography of a nanoparticle, the tip-substrate coupling decreases while a tip-particle coupling rises at the same time. The polarizability of small particles is often not strong enough to compensate the decreasing signal amplitude caused by the reduced tip-substrate coupling; the particle thus yields a reduced signal s_n relative to the substrate. On the other hand, strong tip-substrate coupling can be essential for probing very small particles. Although the particles appear darker than the substrate, the s-SNOM sensitivity (i.e., the absolute optical near-field contrast of the particles) is significantly improved as the tip-substrate coupling increases the local field enhancement at the tip apex [86].

11.7 Molecular Vibrational Near-Field Contrast

It was recognized early that infrared s-SNOM would have great value in analytical chemistry because it could enable the distinction and positive recognition of chemical species with nanoscale resolution [25, 88]. The basis for this are the "fingerprint" vibrational resonances, which, for a majority of chemical compounds, lie in the mid-infrared region between 3 and 30 μm wavelength. An early experiment at two different wavelengths already demonstrated, interestingly, that the spectral contrast provided by molecular vibration is rather high [26]. Further work with thin polymer films confirmed this result in theory and experiment (see Figure 11.11). This study allowed tracing out the near-field response of a vibrational resonance by step-tuning the CO laser over the wavelength region 5.6−6.3 μm, repeating the image recording of a given sample area many times but with different wavelengths, and extracting the near-field spectrum [59, 89].

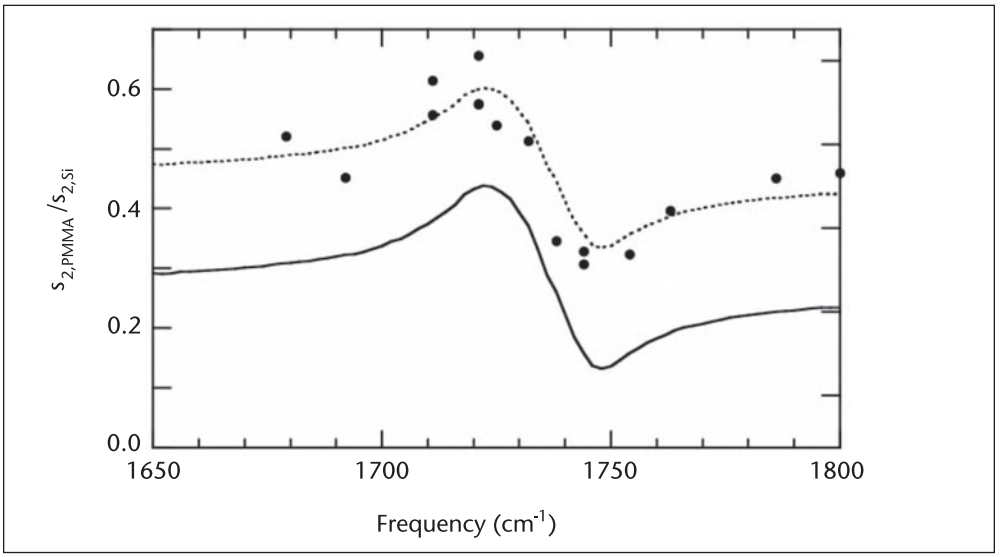

Figure 11.11 Spectroscopic s-SNOM amplitude contrast due to a molecular vibration [79]. The experimental points were taken with a 50-nm thick PMMA film partly covering a Si substrate. They clearly confirm the derivative-like lineshape that is predicted from the point-dipole/image-dipole model, as given for infinitely thick PMMA (full curve). The broken curve is offset by 0.18 as guide to the eye. The offset probably comes from the added near-field interaction between tip and high-index substrate ("see-through" effect). © 2004 American Institute of Physics [59].

The fact that the vibrational resonance does not exhibit a Lorentzian-like symmetric lineshape proves that the near-field interaction is not simply an absorption mechanism. Rather, we have a scattering response. Note the strong spectral modulation due to the resonance, which for the experimental points in Figure 11.11 amounts to $\pm 30\%$ in the scattering amplitude. This is much greater than the 4% resonance dip that would be expected in the transmitted spectrum of a 50-nm thick PMMA layer, according to its known absorption constant [59]. The enhancement of spectral modulation is advantageous for s-SNOM application since it enables a high sensitivity. This advantage can be expected to increase further, when future tips with reduced radius a would allow an improved spatial resolution. This is because the depth of probing—which is of the order of the tip radius a—would reduce as well. Thus, the near-field spectral signature would fully remain while the material's required thickness reduces to $\approx a$ (the probed volume $\approx a^3$). Plane-wave absorption would, in contrast, reduce with thickness [89].

The offset in Figure 11.11 was introduced to match the calculated curve with the experimental one. The offset is interpreted as a consequence of the finite film thickness. When the supporting substrate exhibits a relatively large, spectrally flat ε', as is the case with Si, its influence increases the scattering amplitude [86] without spectral distortion [59, 90]. As mentioned previously, the fact that the near field can extend through a thin film into a substrate opens the possibility for subsurface imaging of buried nanoscale objects [84].

A further confirmation of the predicted near-field signature due to vibrational resonance was conducted with even less sample material. As shown in Figure 11.12, a virus particle of only 18 nm diameter suffices to generate significant contrast. Both amplitude and phase contrasts of near-field scattering were evaluated with respect

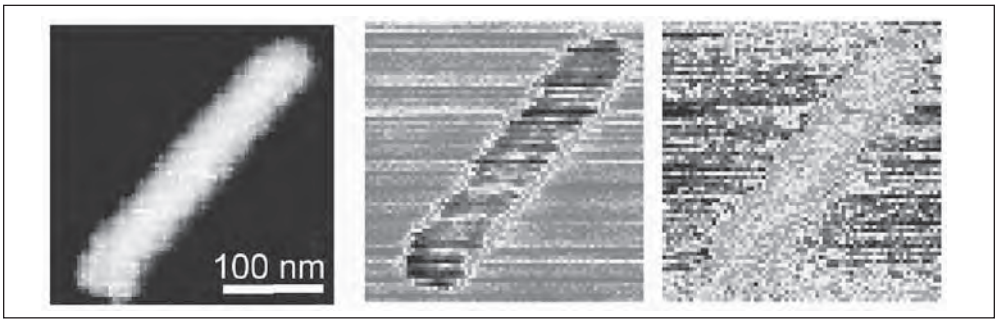

Figure 11.12 Single tobacco mosaic virus (18 nm diameter nominally) imaged in infrared-spectroscopic s-SNOM [42]. In topography (left), the virus appears broadened by convolution with the tip, which in this case has a radius of a $a \approx 30$ nm. The simultaneously acquired infrared ($\lambda = 5.96\ \mu$m) images (amplitude, middle; phase, right) show the same broadening. They reveal in the central region of the virus a distinct amplitude as well as phase contrast relative to the Si substrate. © 2006 American Chemical Society [42].

to Si and in fact showed for the first time that the phase signature of the vibrational near-field resonance has a symmetric Lorentzian-like shape, as predicted from the point-dipole model [42].

A further similar study of a test sample containing both TMV viruses and PMMA spherical beads in a crowded neighborhood testifies to the robustness of chemical recognition on the nanoscale offered by infrared-spectroscopic s-SNOM. The results shown in Figure 11.13 confirm the near-field spectral lineshapes of the virus of Figure 11.12, which was taken on a different substrate. Furthermore, they show that the near-field spectrum of PMMA beads matches that of PMMA film (see Figure 11.11). Since the lineshapes agree with calculations, the dipole model is confirmed to be sufficient for predicting and explaining near-field signatures due to molecular vibrations. The experimental signatures are not influenced by other materials that are close by. This enables local chemical recognition in a crowded environment [91].

11.8 Tip-Induced Polariton Resonance

We have discovered and demonstrated in two cases [46, 58] that the near-field-scattering amplitude in the probing of a polaritonic sample material can be enormously enhanced. With polaritonic material, we mean a material that interacts so strongly with light that its dielectric value becomes distinctly negative—in particular, Re $(\varepsilon_s) \approx -1$. This can occur by interaction with mobile charges (plasmon-polariton) or with a polar crystal lattice (phonon-polariton) or with interacting electron-hole pairs (exciton polariton). In all of these cases, at the frequency where Re $(\varepsilon_s) \approx -1$, the point-dipole model of near-field scattering (Equation 11.2) shows that because the dielectric surface response function β (Equation 11.1) becomes large, the scattering becomes large too. As Figure 11.8 already illustrates, the amplitude can become very high at this dielectric value, much higher than that of the noble metals, especially if the damping expressed by Im (ε_s) is small. This "tip-induced near-field resonance" is accompanied by strong phase changes, as first evaluated in the prediction Figure 11.3 of [58].

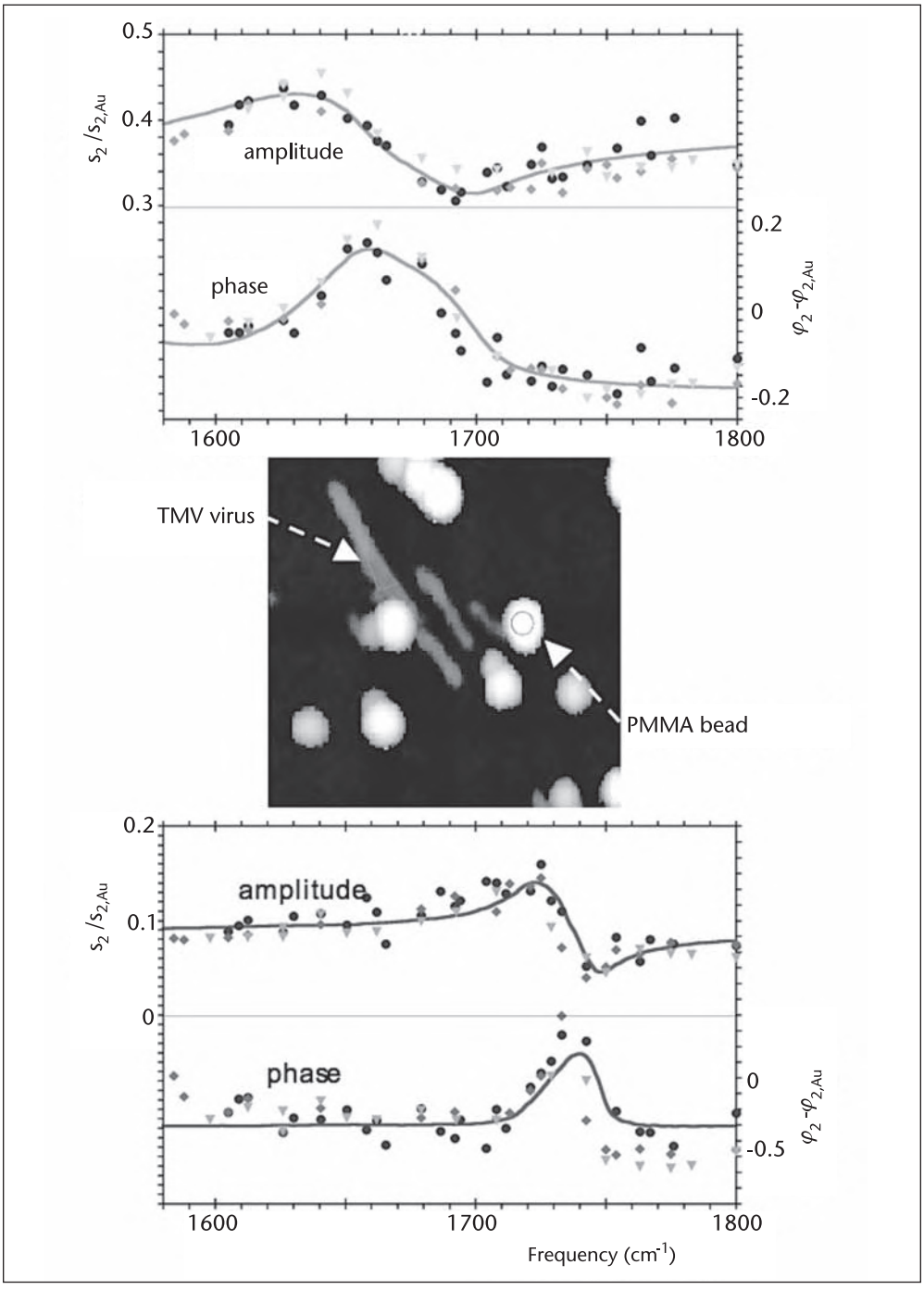

Figure 11.13 Spectroscopic s-SNOM imaging of TMV virus and polymer beads ($1\mu m \times 1\mu m$). The topography image (middle) reveals several TMV viruses and spherical PMMA beads on Au substrate. Consecutive imaging at numerous wavelengths allowed extraction of spectral data points from two particles (arrows). Curves represent model calculations with suitably chosen offsets. © 2006 American Chemical Society [42].

The tip-induced near-field resonance that was studied in great detail [41, 44, 46, 61, 92] is that of SiC caused by the phonon-polariton in the midinfrared (i.e., by the interaction of light with the fundamental lattice vibration). The s-SNOM equipped with a (nonresonant) metal tip is used to determine the resonance spectrum peaking at 10.6 μm wavelength. The response is determined relative to that of a 10 nm Au film partly covering the SiC crystal. At resonant illumination, the near-field amplitude of SiC exceeds that of Au by one order of magnitude (see Figure 11.14).

The resonance is exceptionally narrow (1% FWHM), more than an order of magnitude sharper than the far-field "Reststrahlen" reflectivity spectrum of SiC [46, 48]. This spectral narrowing promises a sensitive distinction of polar dielectrics. A given material can be highlighted to appear very bright in nanoscale composite structures by a suitable choice of the infrared frequency. Thus, near-field microscopy enables a much better material discrimination than is possible with the common diffraction-limited FTIR microscope, which has to deal with the spectrally wide far-field resonances. A specific application of the line narrowing is to discriminate not only between chemically different species but also between nanoscale crystalline subtypes or subphases of chemically homogeneous materials [46, 44, 93].

The sharp polaritonic near-field resonance is accompanied by a sizable phase response. A systematic study of the complex (amplitude and phase) contrast spectra showed that the underlying physical mechanism is indeed the coupling between tip and sample [92]. This coupling strength could be varied conveniently by changing the tip-sample separation, in practice by taking approach curves. As a result, the tuning of the near-field resonance by the approaching tip could be quantitatively determined and a qualitative agreement with the point-dipole model could be demonstrated.

With an improved experimental setup, the sharp phonon-polariton near-field resonance of SiC also has allowed a particular sensitive test of the point-dipole theory [67]. As it turned out, the spectral signature of the complex near-field contrast shows systematic differences between theory and experiment. This is probably due to the oversimplification of representing the metal tip with a point dipole. Accordingly, an improvement could be obtained by assuming the dipole to be extended such that one charge resides only in the tip's center of curvature while the other is distant on the tip shaft and does not participate in the near-field interaction. A suitable choice of parameters gave good quantitative agreement between theory and experiment [61].

In passing, we mention here the interesting new development of an s-SNOM that works without external illumination by scattering thermal equilibrium fields present at the sample surface, especially of polaritonic materials [94].

11.9 Nanoscale Coherent Imaging of Optical Eigenfield Patterns

In small metal particles, light can resonantly excite collective oscillation modes of conduction electrons. Such plasmon-resonant particles have long been known for their strong scattering and enhanced near-field close to the particle's surface

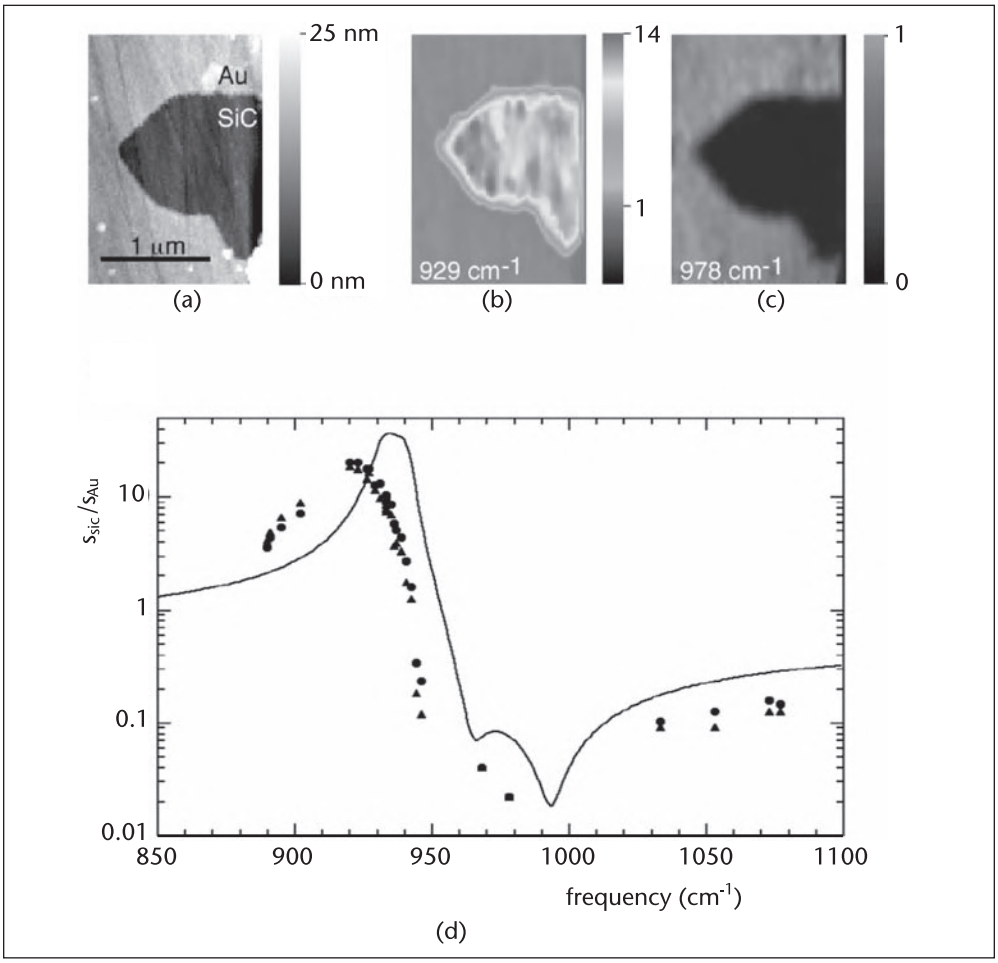

Figure 11.14 s-SNOM imaging of a partly Au-covered SiC sample. (a) Topography and (b,c) s-SNOM amplitude s_2 taken at two different midinfrared illumination frequencies that are on and off the tip-induced phonon-polariton near-field resonance, respectively. (d) Relative amplitude contrast of SiC in respect to Au versus laser wavelength; the curve represents the point-dipole model prediction. © 2002 Nature Publishing Group [46].

[95, 96]. Because of the enormous application potential of plasmon-resonant particles, such as in SERS for single-molecule detection [97] or guiding light in nanoscale dimensions [98], a method to study the near-field distributions is of utmost importance. In references [27] and [99] it has already been demonstrated that the particle's near-fields can be imaged by SNOM using fiber and scattering probes, respectively [100]. With our s-SNOM in the visible, we have shown that eigenfield patterns of plasmon-resonant particles can be mapped at nanoscale resolution as well as in their amplitude and phase distributions [39, 40].

The possibility of imaging the eigenfield E_p of a resonant particle rests on the fact that the particle can be excited directly by the illuminating field E_i [see Figure 11.15(a)]. We assume that this eigenfield acts as an additional illumination of the tip. Thus, the tip is excited by the sum of both fields, $E_{loc} = E_i + E_p$, and the measured field is $E_s \propto \alpha_{eff} E_{loc}$. After this model, a genuine mapping of the eigenfield pattern E_p is directly possible in the strong-enhancement limit $E_p \gg E_i$. We further assume that only

the z-oriented component of E_p is detectable, since other components couple only weakly to the shaft's antenna, which is, on the other hand, necessary for efficient emission. Near-field phase contrast in eigenfield imaging arises from an intrinsic phase shift between E_p and E_i [39].

We measured the eigenfield patterns of well-defined Au nanodiscs (91 nm diameter, 20 nm height) on glass, tailored to be in optical resonance with $\lambda = 633$ nm used to illuminate our s-SNOM. As illustrated in Figure 11.15(a), we expect antiphase optical fields near two pole regions due to the designed dipolar oscillation. To minimize a possible perturbation of E_p by the probing tip, we used a carbon nanotube tip [40]. We obtain good qualitative agreement between the measured amplitude and phase images [Figure 11.15(c)] taken at demodulation order $n = 2$ and with the exact electrodynamic field calculation (Figure 11.15), which does not include any influence of the tip on the particle's eigenfield. This demonstrates that the presence of the probing carbon nanotube bundle as well as the harmonic demodulation procedure does not perturb the eigenfield pattern significantly.

Using bare Si tips, we could furthermore observe [39] highly confined (< 10 nm) near fields in narrow gaps between resonant particles. (See Figure 11.16.) Such fields may be basic for colossally enhanced SERS [97, 101] to provide a mechanism for the observation of single molecules. Strong gap fields seem an ideal geometry for doing nonlinear spectroscopy of nanoscale objects and for other high-field physics experiments. They possibly could be mapped in nanometric resolution by s-SNOM equipped with a single-wall carbon nanotube probe tip.

The given formula $E_{loc} = E_i + E_p$ indicates that quite generally, neighboring objects on the sample can contribute to the illumination of the tip and thus modify the observed scattering contrast. Thus, the wanted mechanism of measuring localized near-field patterns can, at least in principle, turn into the unwanted effect of an s-SNOM artifact by close-by scattering objects. For further insight, consider an

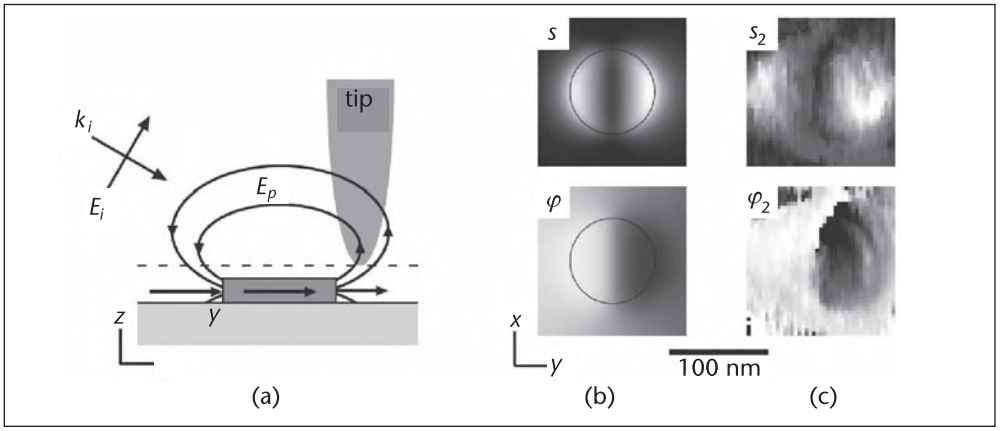

Figure 11.15 Dipolar surface-plasmon-polariton oscillation field pattern of an Au disk (91 diameter, 20-nm high) on glass induced at a wavelength of 633 nm. (a) Schematic side view of incident plane wave E_i and of the particle's eigenfield E_p. (b) Top view of near-field amplitude (upper row) and phase (lower row) for the fields z-component, which was obtained by exact electrodynamic calculation of the total field 10 nm above the disk as marked by the dashed line in (a). (c) Experimental s-SNOM amplitude E_2 and phase ϕ_2 images using a C nanotube tip as near-field scattering optical probe. © 2003 American Institute of Physics [40].

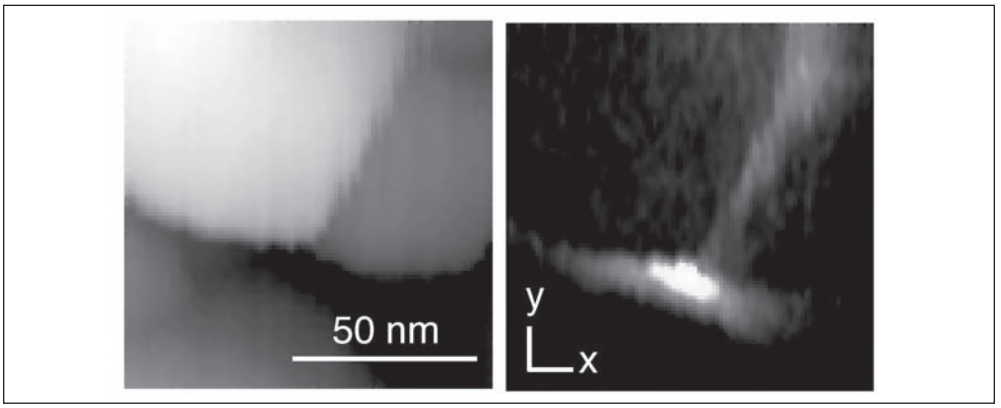

Figure 11.16 Surface-plasmon-polariton field pattern in a narrow space between Au particles on glass. Note the radiation at 633 nm wavelength becomes confined to a spot width of less than 10 nm (FWHM). © 2001 Springer-Verlag [39].

inhomogeneous or corrugated sample. Here a "particle" field E_p arises at the tip position through coherent superposition of many source eigenfields from individual inhomogeneities or topography features. These contributions might decay on a very short length scale (e.g., < 50 nm for small particles, as in Figure 11.15). Note such particle near fields give discernible contribution only when they are sufficiently strong (e.g., enhanced by optical resonance as shown in Figure 11.2 of [39]). Clearly, only objects within the illuminating laser focus can contribute to an s-SNOM artifact via close-by scattering objects. Therefore, a quantitative determination of the near-field contrast requires the sample to be homogeneous over the area illuminated by the laser beam focus. Yet at least in principle, even objects outside the illuminating laser focus might contribute an artifact: On a polaritonic sample material, the tip itself can be a source of outgoing propagating waves; and in this case, a suitably oriented distant reflector contributes an E_p field at the tip [102].

Interesting effects arise when localized "antenna" sources exist on a sample that launches propagating waves (in particular, propagating modes) bound to the surface, as is the case with surface plasmon-polaritons or surface phonon-polaritons. Their range can be many wavelengths. Clearly, their strength increases with the antenna efficiency by which the incoming field E_i scatters into the surface wave E_p. The surface phonon-polaritons emitted by line sources have been systematically studied by s-SNOM, and their complex spectral dispersion has been determined, including propagation direction, phase velocity, and attenuation [103]. Furthermore, local excitation, interference, and wavefront evolution have been mapped for the cases of surface plasmon- [104] and surface phonon-polaritons [105]. A particularly interesting application of s-SNOM is the mapping of surface-wave-mediated photonic effects such as image formation by a "superlens," as we have demonstrated with a SiC slab [106].

11.10 Applications of s-SNOM

From the given examples in Figures 11.9, 11.13, 11.15, and 11.16, it is clear that the s-SNOM has excellent capabilities. It should have a bright future for applications in the nanosciences. The presently achieved spatial resolution of 10 nm could

become even better if sharper tips become available, possibly by up to an order of magnitude. Various applications in nanophysics and nanotechnology can be foreseen that use, for example, the ability to discriminate between a metal, a semiconductor, and a low-refracting dielectric [57]. The s-SNOM, when used in the visible, should discriminate well between different metals (see Figure 11.8). The phase-sensitive mapping of nanoscale field distributions could be valuable in plasmon photonics to analyze the coherent control of plasmon-polariton excitation [107]. A special advantage over any other form of light microscopy is that the s-SNOM provides nanoscale information with midinfrared as well as far-infrared illumination. In fact, the antenna performance of the metal tip improves with the tip material's conductivity, which for metals in the infrared, improves monotonically with wavelength. Consequently, the s-SNOM can be predicted to function even better in the long-wavelength or THz spectral regions.

One major, unique ability of s-SNOM is the imaging of vibrational contrast, especially the midinfrared "fingerprint" spectra, which can identify any material's chemical composition. This application has been investigated by a number of research groups [25, 26, 31, 42, 59, 73–76]. Most of these studies used the restricted tuning range of the CO_2 laser, which, unfortunately, does not allow them to cover strong polymer or biopolymer resonances. The CO laser used in [42, 59] does cover such resonances, but is a rather bulky source requiring cryogenics. To fully exploit the chemical recognition application, other infrared coherent light sources must be introduced. These could be, for example, a series of fixed-wavelength or tunable quantum cascade lasers [108], as we have already tested [46], or optical parametric oscillators (OPOs) or free electron lasers or wide-band coherent THz or midinfrared radiation derived from femtosecond optical lasers [109–112]. As to the latter, we have recently succeeded to combine "coherent-comb" Fourier-transform infrared spectroscopy [111–113] covering the $8-12\ \mu$m region with s-SNOM, demonstrating near-field spectra in amplitude and phase contrast for every pixel while scanning [91, 114]. Unfortunately, the power of this broadband midinfrared beam is weaker by three orders of magnitude compared to monochromatic mid-infrared s-SNOM; therefore, this method remains unpractical until a stronger beam becomes available.

The ability to perform nanoscale-resolved microscopy in the infrared has further enormous application potential in solid state physics and material sciences. Midinfrared s-SNOM can be used for localized excitation on the nanoscale—in particular, of phononic resonances in polar crystals [44, 134]. As these resonances are highly specific for the chemical composition of the sample, s-SNOM enables the nondestructive characterization of nanocomposite materials and single nanoparticles [42, 86, 87]. The resonant excitation of lattice vibrations in polar crystals (optical phonons) via the infrared near fields at the tip apex also allows nanoscale mapping of structural properties such as local crystal quality, crystal damage, and growth defects [44, 115]. As an example, s-SNOM mapping of a FIB implanted SiC crystal demonstrated that phonon-polariton-resonant near-field interaction can be used to map the local crystal quality. (See Figure 11.17.) The ion-beam-induced crystal damage infers a strong phonon damping that is dramatically reducing the resonant near-field interaction. Thus, the amplitude signal s_2 at the resonance position 940 cm^{-1} is strongly reduced and the infrared image clearly reveals the implanted checkerboard pattern. The sharp resonance is extremely sensitive to even weak modifications of the lattice parameters, as we could demonstrate by distinguishing 4H and 6H SiC polytypes

having logitudinal phonon frequencies that differ by only 3 cm^{-1} [44]. We expect that phonon-polariton spectroscopy also could enable the mapping of local crystal orientation or nanoscale strain fields. Altogether these possibilities extend the capability of infrared s-SNOM from chemical to structural microscopy.

Another major, unique application of infrared s-SNOM stems from its ability to sense local conductivity. It was shown earlier that the presence of mobile carriers in Si can be probed by the infrared near field [58, 85]. Recently, we investigated microelectronic circuits of industrial relevance by monochromatic infrared s-SNOM. As shown in Figure 11.18, the different types of materials of these nanostructures are recognizable by characteristic amplitude and phase contrasts [45]. Also, close inspection of Figure 11.18 and comparison with electron microscopy images shows that the doped areas in Si exhibit distinct infrared contrasts originating from mobile charges. The analysis given in [45] demonstrates that the carrier density gradient extending from the contact into Si can be mapped and even quantitatively determined. As for a general application of s-SNOM mapping of carrier density, several probe frequencies distributed over the mid and far infrared are suggested in order to cover several orders of magnitude of carrier density (e.g., from 10^{16} to 10^{20} cm^{-3}). Far-infrared operation (THz frequencies) of an s-SNOM has been initiated by several groups [116–120] and has been realized recently [121]. THz s-SNOM can be expected to be developed to 10 nm resolution in the future.

The s-SNOM's general ability to determine complex local conductivity on a nanoscale may be of great value to condensed matter physics dealing with exotic conductivity phenomena. One example is correlated electron materials that have a tendency for spontaneous phase separation with nanoscale patterns [122]. Here mid-infrared s-SNOM has recently enabled the viewing and analyzing of nanoscale metallic puddles that form and grow when VO_2 crystals are heated through the insulator-metal Mott phase transition [123]. Long-wavelength infrared is the proper spectral range for mapping conduction phenomena such as Cooper pairs in superconductors, potential modulation in carbon nanotubes, and edge states in

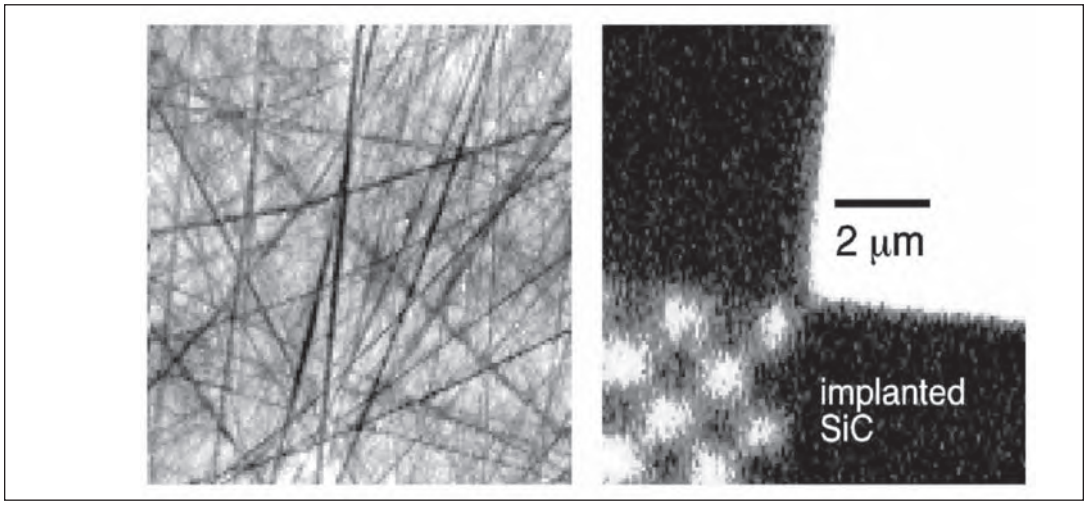

Figure 11.17 Analysis of crystal quality demonstrated by s-SNOM imaging of a focused-ion-beam implanted SiC crystal. While in topography (left), only the scratches from crystal polishing are seen; the infrared s_2 image (right) clearly reveals the ion-beam-damaged areas, which appear dark.

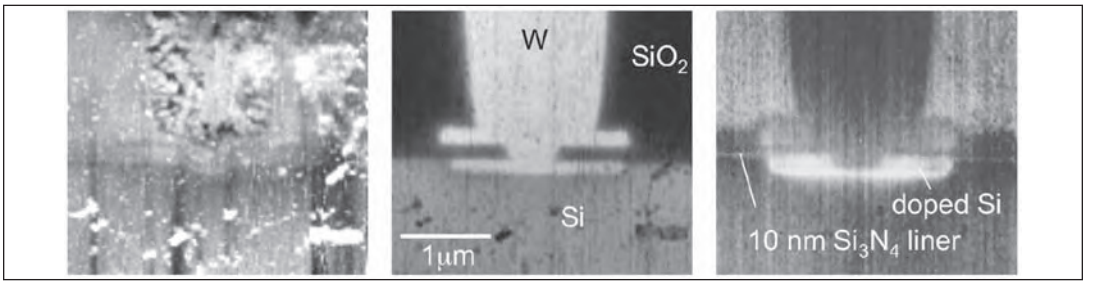

Figure 11.18 Nanometer-scale resolved s-SNOM images of a cross section of a MOS-transistor drain contact recorded at 10.8 μm wavelength. Interferometric infrared detection yields amplitude (middle) and phase (right) images with distinct material as well as doping contrasts simultaneously with topography (left) [45].

2-D electron systems [124] because its quantum energy matches that of Cooper pair breaking, plasmon-phonon coupling, and cyclotron resonance, all of which constitute well-established elementary solid state excitations not yet spectroscopically investigated on a nanoscale.

11.11 Outlook

The scattering SNOM has a proven potential to resolve nanostructures down to 10 nm detail. This is true irrespective of the wavelength of illumination, which can be chosen between visible and far infrared. s-SNOM enables numerous unique applications, among them the following:

- The chemical recognition by exploiting contrasts due to molecular resonance, important for chemical, pharmaceutical, petrochemical, and food industries
- The quantification of solid state conductivity such as for characterizing nano-electronic devices or for understanding exotic mechanisms provided by heavy, correlated, Cooper-paired, or spin-aligned electrons

Altogether s-SNOM can be regarded as a timely tool for solving characterization needs in the nanosciences and in nanotechnology.

Acknowledgments

It is a great pleasure to acknowledge the stimulating close cooperation with Bernhard Knoll, Thomas Taubner, Markus Brehm, Nenad Ocelic, Antonija Cvitcovic, Andy Huber, and Thomas Ganz.

References

[1] Jackson, J. D., *Classical Electrodynamics*, New York: John Wiley, 1975, p. 343.

[2] Synge, E. H., "Suggested Method for Extending Microscopic Resolution into the Ultra-microscopic Region," *Philosophical Magazine,* Vol. 6, 1928, pp. 356–362.

[3] O'Keefe, J. L., "Resolving Power of Visible Light," *Journal of the Optical Society of America,* Vol. 46, 1956, p. 359.

[4] Wessel, J., "Surface-Enhanced Optical Microscopy," *Journal of the Optical Society of America B,* Vol. 2, 1985, pp. 1538–1540.

[5] Wickramasinghe, H. K., and C. C. Williams, "Apertureless Near Field Optical Microscope," U.S. Patent 4,947,034, 1990.

[6] Specht, M. et al., "Scanning Plasmon Near-Field Microscopy," *Physical Review Letters,* Vol. 68, 1992, pp. 476–479.

[7] Inouye, Y., and S. Kawata, "Near-Field Scanning Optical Microscope with a Metallic Probe Tip," *Optics Letters,* Vol. 19, 1994, pp. 159–161.

[8] Mie, G., "Beiträge zur Optik trüber Medien, speziell kolloidaler Metallösungen," *Annalen der Physik,* Vol. 25, 1908, pp. 377–445.

[9] Daneu, V. et al., "Extension of Laser Harmonic-Frequency Mixing Techniques into the 9μ Region with an Infrared Metal-Metal Point-Contact Diode," *Applied Physics Letters,* Vol. 15, 1969, pp. 398–401.

[10] Fee, M., S. Chu, and T. W. Hänsch, "Scanning Electromagnetic Transmission Line Microscope with Sub-wavelength Resolution," *Optics Communications,* Vol. 69, 1989, pp. 219–224.

[11] Keilmann, F. et al., "Extreme Sub-wavelength Resolution with a Scanning Radio-Frequency Transmission Microscope," *Optics Communications,* Vol. 129, 1996, pp.15–18.

[12] Knoll, B. et al., "Contrast of Microwave Near-Field Microscopy," *Applied Physics Letters,* Vol. 70, 1997, pp. 2667–2669.

[13] Imtiaz, A. et al., "Nanometer-Scale Material Contrast Imaging with a Near-Field Microwave Microscope," *Applied Physics Letters,* Vol. 90, 2007, Art. No. 143106.

[14] Zenhausern, F., Y. Martin, and H. K. Wickramasinghe, "Scanning Interferometric Apertureless Microscopy: Optical Imaging at 10 Angstrom Resolution," *Science,* Vol. 269, 1995, pp. 1083–1085.

[15] Hamann, H. F., A. Gallagher, and D. J. Nesbitt, "Enhanced Sensitivity Near-Field Scanning Optical Microscopy at High Spatial Resolution," *Applied Physics Letters,* Vol. 73, 1998, pp. 1469–1471.

[16] Haefliger, D., J. M. Plitzko, and R. Hillenbrand, "Contrast and Scattering Efficiency of Scattering-Type Near-Field Optical Probes," *Applied Physics Letters,* Vol. 85, 2004, 4466–4468.

[17] Esteban, R., R. Vogelgesang, and K. Kern, "Simulation of Optical Near and Far Fields of Dielectric Apertureless Scanning Probes," *Nanotechnology,* Vol. 17, 2006, pp. 475–482.

[18] Esteban, R., R. Vogelgesang, and K. Kern, "Tip-Substrate Interaction in Optical Near-Field Microscopy," *Physical Review B,* Vol. 75, 2007, Art. No. 195410.

[19] Bragas, A. V., and O. E. Martinez, "Field Enhanced Scanning Optical Microscope," *Opt. Lett.,* Vol. 25, 2000, pp. 631–633.

[20] Wang, S., "Antenna Properties and Operation of Metal-Barrier-Metal Devices in the Infrared and Visible Regions," *Applied Physics Letters,* Vol. 28, 1976, pp. 303–305.

[21] Völcker, M., W. Krieger, and H. Walther, "Laser-Frequency Mixing in a Scanning Force Microscope and Its Application to Detect Local Conductivity," *Journal of Vacuum Science and Technology B,* Vol. 12, 1994, pp. 2129–2132.

[22] Krug, J. T., E. J. Sanchez, and X. S. Xie, "Design of Near-Field Optical Probes with Field Enhancement by Finite Difference Time Domain Electromagnetic Simulation," *Journal of Applied Physics,* Vol. 116, 2002, pp. 10895–10901.

[23] Knoll, B., and F. Keilmann, "Mid-Infrared Scanning Near-Field Optical Microscope Resolves 30 nm," *Journal of Microscopy,* Vol. 194, 1999, pp. 512–515.

[24] Hayazawa, N. et al., "Near-Field Raman Imaging of Organic Molecules by an Apertureless Metallic Probe Scanning Optical Microscope," *Journal of Chemical Physics,* Vol. 117, 2002, pp. 1296–1301.

[25] Lahrech, A. et al., "Infrared-Reflection-Mode Near-Field Microscopy Using an Apertureless Probe with a Resolution of λ/600," *Optics Letters,* Vol. 21, 1996, pp. 1315–1317.

[26] Knoll, B., and F. Keilmann, "Near-Field Probing of Vibrational Absorption for Chemical Microscopy," *Nature,* Vol. 399, 1999, pp. 134–137.

[27] Adam, P.-M. et al., "Localized Surface Plasmons on Nanometric Gold Particles Observed with an Apertureless Scanning Near-Field Optical Microscope," *Journal of Applied Physics,* Vol. 88, 2000, pp. 6919–6921.

[28] Hillenbrand, R., and F. Keilmann, "Complex Optical Constants on a Subwavelength Scale," *Physical Review Letters,* Vol. 85, 2000, pp. 3029–3032.

[29] Aigouy, L. et al., "Near-Field Optical Spectroscopy Using an Incoherent Light Source," *Applied Physics Letters,* Vol. 76, 2000, pp. 397–399.

[30] Sasaki, Y., and H. Sasaki, "Heterodyne Detection for the Extraction of the Probe-Scattering Signal in Scattering Type Scanning Near-Field Optical Microscope," *Japan Journal of Applied Physics,* Vol. 39, 2000, pp. L231–L323.

[31] Akhremitchev, B. B., S. Pollack, and G. C. Walker, "Apertureless Scanning Near-Field Infrared Microscopy of a Rough Polymeric Surface," *Langmuir,* Vol. 17, 2001, pp. 2774–2781.

[32] Bek, A., R. Vogelgesang, and K. Kern, "Apertureless Scanning Near Field Optical Microscope with Sub-10 nm Resolution," *Rev. Sci. Instr.,* Vol. 77, 2006, Art. No. 043703.

[33] Roy, D., S. H. Leong, and M. E. Welland, "Dielectric Contrast Imaging Using Apertureless Scanning Near-Field Optical Microscopy in the Reflection Mode," *Journal of the Korean Physical Society,* Vol. 47, 2005, pp. S140–S146.

[34] Kim, Z. H., B. Liu, and S. R. Leone, "Nanometer-Scale Optical Imaging of Epitaxially Grown GaN and InN Islands Using Apertureless Near-Field Microscopy," *Journal of Chemical Physics B,* Vol. 109, 2005, pp. 8503–8508.

[35] Raschke, M. B., and C. Lienau, "Apertureless Near-Field Optical Microscopy: Tip-Sample Coupling in Elastic Light Scattering," *Applied Physics Letters,* Vol. 83, 2003, pp. 5089–5091.

[36] Taubner, T., R. Hillenbrand, and F. Keilmann, "Performance of Visible and Mid-infrared Scattering-Type Near-Field Optical Microscopes," *Journal of Microscopy,* Vol. 210, 2003, pp. 311–314.

[37] Bridger, P. M., and T. C. McGill, "Observation of Nanometer-Scale Optical Property Discrimination by Use of a Near-Field Scanning Apertureless Microscope," *Optics Letters,* Vol. 24, 1999, pp. 1005–1007.

[38] Azoulay, J. et al., "Optical Contrast in Apertureless Microscopy," *Applied Optics,* Vol. 39, 2000, pp. 129–134.

[39] Hillenbrand, R., and F. Keilmann, "Optical Oscillation Modes of Plasmon Particles Observed in Direct Space by Phase-Contrast Near-Field Microscopy," *Applied Physics B,* Vol. 73, 2001, pp. 239–243.

[40] Hillenbrand, R. et al., "Coherent Imaging of Nanoscale Plasmon Patterns with a Carbon Nanotube Optical Probe," *Applied Physics Letters,* Vol. 83, 2003, pp. 368–370.

[41] Ocelic, N., and R. Hillenbrand, "Subwavelength-Scale Tailoring of Surface Phonon Polaritons by Focused Ion-Beam Implantation," *Nature Materials,* Vol. 3, 2004, pp. 606–609.

[42] Brehm, M. et al., "Infrared Spectroscopic Mapping of Single Nanoparticles and Viruses at Nanoscale Resolution," *Nanoletters,* Vol. 6, 2006, pp. 1307–1310.

[43] Kim, Z. H. et al., "Nanometer-Scale Dielectric Imaging of Semiconductor Nanoparticles: Size-Dependent Dipolar Coupling and Contrast Reversal," *Nanoletters,* Vol. 7, 2007, p. 225.

[44] Huber, A. et al., "Nanoscale Resolved Infrared Probing of Crystal Structure and of Plasmon-Phonon Coupling," *Nanoletters,* Vol. 6, 2006, pp. 774–778.

[45] Huber, A. J. et al., "Simultaneous Infrared Material Recognition and Conductivity Mapping by Nanoscale Near-Field Microscopy," *Advanced Materials,* Vol. 19, 2007, pp. 2209–2213.

[46] Hillenbrand, R., T. Taubner, and F. Keilmann, "Phonon-Enhanced Light-Matter Interaction at the Nanometre Scale," *Nature,* Vol. 418, 2002, pp. 159–162.

[47] Hillenbrand, R., B. Knoll, and F. Keilmann, "Pure Optical Contrast in Scattering-Type Scanning Near-Field Optical Microscopy," *Journal of Microscopy,* Vol. 202, 2001, pp. 77–83.

[48] Hillenbrand, R., "Nahfeldoptische Amplituden- und Phasenkontrastmikroskopie zur nanoskopischen Abbildung von Materialkontrast und optisch resonanten Partikeln," in *Fakultät für Physik*, Technische Universität München.

[49] Ocelic, N., A. Huber, and R. Hillenbrand, "Pseudo-heterodyne Detection for Background-Free Near-Field Spectroscopy," *Applied Physics Letters,* Vol. 89, 2006, Art. No. 101124.

[50] Porto, J. A., R. Carminati, and J. J. Greffet, "Theory of Electromagnetic Field Imaging and Spectroscopy in Scanning Near-Field Optical Microscopy," *Journal of Applied Physics,* Vol. 88, 2000, pp. 4845–4850.

[51] Knoll, B., *Abtastende Nahfeldmikroskopie mit Infrarot- und Mikrowellen*, Technische Universität München, 1999.

[52] Hillenbrand, R., F. Keilmann, and B. Knoll, "Optische Nahfeldmikroskopie," German Patent. p. DE 10035134, 2000.

[53] Ruppin, R. J., "Spherical and Cylindrical Surface Polaritons in Solids," in *Electromagnetic Surface Modes* (A.D. Boardman, ed.), New York: John Wiley, 1982, pp. 345–398.

[54] Aravind, P. K., and H. Metiu, "The Effects of the Interaction between Resonances in the Electromagnetic Response of a Sphere-Plane Structure; Applications to Surface Enhanced Spectroscopy," *Surface Science,* Vol. 124, 1983, pp. 506–528.

[55] Keilman, F., "Scattering-Type Near-Field Optical Microscopy," *Journal of Electron Microscopy,* Vol. 53, 2004, pp. 187–192.

[56] Bohren, C. F., and D. R. Huffmann, *Absorption and Scattering of Light by Small Particles*, New York: John Wiley, 1983.

[57] Hillenbrand, R., and F. Keilmann, "Material-Specific Mapping of Metal/Semiconductor/Dielectric Nanosystems at 10 nm Resolution by Back-Scattering Near-Field Optical Microscopy," *Applied Physics Letters,* Vol. 80, 2002, pp. 25–27.

[58] Knoll, B., and F. Keilmann, "Infrared Conductivity Mapping for Nanoelectronics," *Applied Physics Letters,* Vol. 77, 2000, pp. 3980–3982.

[59] Taubner, T., R. Hillenbrand, and F. Keilmann, "Nanoscale Polymer Recognition by Spectral Signature in Scattering Infrared Near-Field Microscopy," *Applied Physics Letters,* Vol. 85, 2004, pp. 5064–5066.

[60] Knoll, B., and F. Keilmann, "Enhanced Dielectric Contrast in Scattering-Type Scanning Near-Field Optical Microscopy," *Optics Communications,* Vol. 182, 2000, pp. 321–328.

[61] Cvitkovic, A., N. Ocelic, and R. Hillenbrand, "Analytical Model for Quantitative Prediction of Material Contrasts in Scattering-Type Near-Field Optical Microscopy," *Optics Express,* Vol. 15, 2007 p. 8550.

[62] Renger, J. et al., "Resonant Light Scattering by Near-Field-Induced Phonon Polaritons," *Physical Review B,* Vol. 71, 2005, Art. No. 075410.

[63] Porto, J. A. et al., "Resonance Shift Effects in Apertureless Scanning Near-Field Optical Microscopy," *Physical Review B,* Vol. 67, 2003, Art. No. 85409.

[64] Wurtz, G., R. Bachelot, and P. Royer, "A Reflection-Mode Apertureless Scanning Near-Field Optical Microscope Developed from a Commercial Scanning Probe Microscope," *Review of Scientific Instruments,* Vol. 69, 1998, pp. 1735–1743.

[65] Labardi, M., S. Patane, and M. Allegrini, "Artifact-Free Near-Field Optical Imaging by Apertureless Microscopy," *Applied Physics Letters,* Vol. 77, 2000, pp. 621–623.

[66] Gucciardi, P. G., G. Bachelier, and M. Allegrini, "Far-Field Background Suppression in Tip-Modulated Apertureless Near-Field Optical Microscopy," *Journal of Applied Physics,* Vol. 99, 2006, Art. No. 124309.

[67] Ocelic, N., "Quantitative Near-Field Phonon-Polariton Spectroscopy," Unpublished Ph.D. thesis, Technische Universität München, 2007.

[68] Hillenbrand, R., M. Stark, and R. Guckenberger, "Higher-Harmonics Generation in Tapping-Mode Atomic-Force Microscopy: Insights into the Tip-Sample Interaction," *Applied Physics Letters,* Vol. 76, 2000, pp. 3478–3480.

[69] Stark, M. et al., "Inverting Dynamic Force Microscopy: From Signals to Time-Resolved Interaction Forces," *Proceedings of the National Academy of Sciences,* Vol. 99, 2000, pp. 8473–8478.

[70] Bek, A., R. Vogelgesang, and K. Kern, "Optical Nonlinearity Versus Mechanical Anharmonicity Contrast in Dynamic Mode Apertureless Scanning Near-Field Optical Microscopy," *Applied Physics Letters,* Vol. 87, 2005, Art. No. 163115.

[71] Fischer, U. C., "Latex Projections Patterns," in *Procedures in Scanning Probe Microscopy* (R. J. Colton et al., eds.), New York: John Wiley, 1998, p. 10–11.

[72] Hudlet, S. et al., "Apertureless Near Field Optical Microscopy: A Contribution to the Understanding of the Signal Detected in the Presence of a Background Field," *Optics Communications,* Vol. 230, 2004, pp. 245–251.

[73] Akhremitchev, B. B. et al., "Monolayer-Sensitive Infrared Imaging of DNA Stripes Using Apertureless Near-Field Microscopy," *Langmuir,* Vol. 18, 2002, pp. 5325–5328.

[74] Raschke, M. B. et al., "Apertureless Near-Field Vibrational Imaging of Block-Copolymer Nanostructures with Ultrahigh Spatial Resolution," *Chem. Phys. Chem.,* Vol. 6, 2005, pp. 2197–2203.

[75] Samson, J. et al., "Setup of a Scanning Near Field Infrared Microscope (SNIM): Imaging of Sub-surface Nano-structures in Gallium-Doped Silicon," *Physical Chemistry Chemical Physics,* Vol. 8, 2006, pp. 753–758.

[76] Kopf, I. et al., "Chemical Imaging of Microstructured Self-Assembled Monolayers with Nanometer Resolution," *J. Phys. Chem. C,* Vol. 111, 2007, pp. 8166–8171.

[77] Koglin, J., U. C. Fischer, and H. Fuchs, "Material Contrast in Scanning Near-Field Optical Microscopy at 1–10 nm Resolution," *Physical Review B,* Vol. 55, 1997, pp. 7977–7984.

[78] Brehm, M. et al., "Consolidating Apertureless SNOM," *Journal of the Korean Physical Society*, Vol. 47, 2005, p. S80.

[79] Hecht, B. et al., "Facts and Artifacts in Near-Field Optical Microscopy," *Journal of Applied Physics,* Vol. 81, No. 6, 1997, pp. 2494–2498.

[80] Knoll, B., and F. Keilmann, "Scanning Microscopy by Mid-infrared Near-Field Scattering," *Applied Physics A,* Vol. 66, 1998, pp. 477–481.

[81] Billot, L. et al., "Error Artifact in Apertureless Scanning Near-Field Optical Microscopy," *Applied Physics Letters,* Vol. 89, 2006, Art. No. 23105.

[82] Gucciardi, P. G. et al., "Artifacts Identification in Apertureless Near-Field Optical Microscopy," *J. of Applied Physics,* Vol. 101, 2007, Art. No. 64303.

[83] Anderson, N. et al., "Sub-surface Raman Imaging with Nanoscale Resolution," *Nanoletters,* Vol. 6, 2006, pp. 744–749.

[84] Taubner, T., F. Keilmann, and R. Hillenbrand, "Nanoscale-Resolved Subsurface Imaging by Scattering-Type Near-Field Optical Microscopy," *Optics Express,* Vol. 13, 2005, pp. 8893–8899.

[85] Samson, J.-S. et al., "Set-up of a Scanning Near Field Infrared Microscope (SNIM): Imaging of Sub-surface Nano-structures in Gallium-Doped Silicon," *Phys. Chem. Chem. Phys.,* Vol. 8, p. 753.

[86] Cvitkovic, A. et al., "Infrared Imaging of Single Nanoparticles via Strong Field Enhancement in a Scanning Nanogap," *Physical Review Letters,* Vol. 97, 2006, Art. No. 060801.

[87] Cvitkovic, A., N. Ocelic, and R. Hillenbrand, "Material-Specific Infrared Recognition of Sub-10nm Particles by Substrate-Enhanced Scattering-Type Near-Field Microscopy," *Nanoletters,* Vol. 7, 2007, pp. 3177–3181.

[88] Keilmann, F., *Towards SNIM Scanning Near-Field Microscopy in the Infrared. Optics at the Nanometer Scale* (M. N.-V. N. Garcia, ed.), Dordrecht, The Netherlands: Kluwer, 1996, pp. 235–245.

[89] Taubner, T., "Infrarotspektroskopie im Nahfeld einer Tastspitze," Unpublished dissertation, *Technische Universität München,* 2004.

[90] Aizpurua, J. et al., "Substrate-Enhanced Infrared Near-Field Spectroscopy," *Optics Express,* Vol. 16, 2008, pp. 1529–1545.

[91] Brehm, M., "Infrarot-Mikrospektroskopie mit einem Nahfeldmikroskop," in *Fakultät für Physik*, Technische Universität München, 2006, p. 128.
[92] Taubner, T., F. Keilmann, and R. Hillenbrand, "Nanomechanical Resonance Tuning and Phase Effects in Optical Near-Field Interaction," *Nanoletters,* Vol. 4, 2004, pp. 1669–1672.
[93] Schneider, S. et al., "Impact of Optical in-Plane Anisotropy on Near-Field Phonon Polariton Spectroscopy," *Applied Physics Letters,* Vol. 90, 2007, Art. No. 143101.
[94] Wilde, Y. D. et al., "Thermal Radiation Scanning Tunneling Microscopy," *Nature,* Vol. 444, 2006, pp. 740–743.
[95] Kreibig, U., and M. Vollmer, *Optical Properties of Metal Clusters*, Berlin, Heidelberg: Springer-Verlag, 1995.
[96] Girard, C., A. Dereux, and O. J. F. Martin, "Theory of Near-Field Optics," in *Photons and Local Probes, Dordrecht, The Netherlands: Kluwer, 1995*.
[97] Kneipp, K. et al., "Single Molecule Detection Using Surface-Enhanced Raman Scattering (SERS)," *Physical Review Letters*, Vol. 78, 1997, pp. 1667–1670.
[98] Salerno, M. et al., "Plasmon Polaritons in Metal Nanostructures: The Optoelectronic Route to Nanotechnology," *Optoelectronics Review*, Vol. 10, 2002, pp. 217–224.
[99] Krenn, J. R. et al., "Squeezing the Optical Near-Field Zone by Plasmon Coupling of Metallic Nanoparticles," *Physical Review Letters*, Vol. 82, 1999, pp. 2590–2593.
[100] Wiederrecht, G. P., "Near-Field Optical Probing of Noble Metal Nanoparticles," *Eur. Phys. J. Appl. Phys.*, Vol. 28, 2004, pp. 3–18.
[101] Xu, H. et al., "Spectroscopy of Single Hemoglobin Molecules by Surface Enhanced Raman Scattering," *Physical Review Letters*, Vol. 83, 1999, pp. 4357–4360.
[102] Chang, Y. et al., "Fourier Analysis of Surface Plasmon Waves Launched from Single Nanohole and Nanohole Arrays: Unraveling Tip-Induced Effects," *Optics Express*, Vol. 16, 2008, pp. 740–747.
[103] Huber, A. et al., "Near-field imaging of mid-infrared surface phonon polariton propagation," *Applied Physics Letters*, Vol. 87, 2005, Art. No. 81103.
[104] Rindzevicius, T. et al., "Nanohole Plasmons in Optically Thin Gold Films," *J. Phys. Chem. C*, Vol. 111, 2007, pp. 1207–1212.
[105] Huber, A., N. Ocelic, and R. Hillenbrand, "Local Excitation and Interference of Surface Phonon Polaritons Studied by Near-Field Infrared Microscopy," *Journal of Microscopy*, Vol. 229, 2008, pp. 389–395.
[106] Taubner, T. et al., "Near-Field Microscopy Through a SiC Superlens," *Science*, Vol. 313, 2006, p. 1595.
[107] Hillenbrand, R., "Towards Phonon Photonics: Scattering-Type Near-Field Optical Microscopy Reveals Phonon-Enhanced Near-Field Interaction," *Ultramicroscopy*, Vol. 100, 2004, pp. 421–427.
[108] Faist, J. et al., "Quantum Cascade Laser," *Science*, Vol. 264, 1994, pp. 553–556.
[109] Auston, D. H., and K. P. Cheung, "Coherent Time-Domain Far-Infrared Spectroscopy," *Journal of the Optical Society of America B*, Vol. 2, 1985, pp. 606–612.
[110] Bonvalet, A. et al., "Generation of Ultrabroadband Femtosecond Pulses in the Mid-infrared by Optical Rectification of 15 fs Light Pulses at 100 MHz Repetition Rate," *Applied Physics Letters*, Vol. 67, 1995, pp. 2907–2909.
[111] Keilmann, F., C. Gohle, and R. Holzwarth, "Time-Domain Mid-infrared Frequency-Comb Spectrometer," *Optics Letters*, Vol. 29, 2004, pp. 1542–1544.
[112] Schliesser, A. et al., "Frequency-Comb Infrared Spectrometer for Rapid, Remote Chemical Sensing," *Optics Express*, Vol. 13, 2005, pp. 9029–9038.
[113] Schliesser, A., "Multiheterodyn-Spektroskopie mit Frequenzkämmen im mittleren Infrarot," in *Diplomarbeit*, Technische Universität München, 2005.
[114] Brehm, M., A. Schliesser, and F. Keilmann, "Spectroscopic Near-Field Microscopy Using Frequency Combs in the Mid-infrared," *Optics Express*, Vol. 14, 2006, pp. 11222–11233.
[115] Ocelic, N., and R. Hillenbrand, "Subwavelength-Scale Tailoring of Surface Phonon Polaritons by Focused Ion-Beam Implementation," *Nature Materials*, Vol. 3, 2004, pp. 606–609.

[116] van der Valk, N. C. J., and P. C. M. Planken, "Electro-Optic Detection of Subwavelength Terahertz Spot Sizes in the Near Field of a Metal Tip," *Applied Physics Letters*, Vol. 81, 2002, pp. 1558–1560.

[117] Chen, H. T., R. Kersting, and G. C. Cho, THz Imaging with Nanometer Resolution," *Applied Physics Letters*, Vol. 83, 2003, pp. 3009–3011.

[118] Planken, P. C. M., and N. C. J. van der Valk, "Spot-Size Reduction in Terahertz Apertureless Near-Field Imaging," *Optics Letters*, Vol. 29, 2004, pp. 2306–2308.

[119] Planken, P. C. M., C. E. W. M. Rijmenam, and R. N. Schouten, "Opto-electronic Pulsed THz Systems," *Semiconduct. Sci. Technol.*, Vol. 20, 2005, pp. 121–127.

[120] Buersgens, F. F., H. T. Chen, and R. Kersting, "Terahertz Microscopy of Charge Carriers in Semiconductors," *Applied Physics Letters*, Vol. 88, 2006, p. 112115.

[121] Ribbeck, H. G. V. et al., "Spectroscopic THz Near-Field Microscope," *Optics Express*, Vol. 16, 2008, pp. 3430–3438.

[122] Dordevic, S. V., and D. N. Basov, "Electrodynamics of Correlated Electron Matter," *Ann. Phys. (Leipzig)*, Vol. 15, 2006, pp. 545–570.

[123] Qazilbash, M. M. et al., "Mott Transition in VO2 Revealed by Infrared Spectroscopy and Nano-imaging," *Science*, Vol. 318, 2007, pp. 1750–1753.

[124] Merz, R. et al., "Nonequilibrium Edge-State Transport Resolved by Far-Infrared Microscopy," *Physical Review Letters*, Vol. 70, 1993, pp. 651–653.

CHAPTER 12

Single-Molecule Contrast in Tip-Enhanced Fluorescence Microscopy

Benjamin D. Mangum, Chun Mu, Ziyang Ma, and Jordan Gerton

12.1 Introduction

Biological cells fabricate and assemble molecular building blocks into diverse molecular networks with striking complexity and functionality. Such networks are critical components in the complicated machinery of the cell as they participate in a host of cellular functions including cell signaling and sensing, ion channel gating, endo- and exocytosis, viral infection, as well as many other processes. Precise structural measurements of these networks will yield information that can create the ability to optimize specific cellular functions, to engineer new functions, and to strengthen a cell's defense against disease. Further, these networks are prototypical nanosystems and should be studied in detail for insight into the rational design of synthetic molecular systems for a multitude of technological applications. To study biological systems in this context, it is crucial to observe their molecular machinery at work in a physiologically relevant environment. Doing so requires a number of conditions to be satisfied simultaneously: nanoscale resolution, single-molecule sensitivity, biochemical specificity, and the ability to measure in an aqueous environment. While electron microscopy, X-ray crystallography, and nuclear magnetic resonance spectroscopy can yield structural information with exquisite detail, they are not suited for in vitro studies of complex molecular networks due to limitations imposed by sample preparation or measurement procedures and their inability to identify individual molecules in a heterogeneous ensemble. Fluorescence microscopy/spectroscopy, on the other hand, meets all of the required benchmarks with the exception of resolution. With the continued development of nano-optical techniques, it may soon be possible to achieve nanoscale resolution imaging of viable biomolecular networks.

It has been shown that near-field optical microscopy/spectroscopy can be used to map the arrangement of molecules on a surface in air with nanoscale resolution, single-molecule sensitivity, and biochemical specificity; in principle, this can be done in an aqueous environment in vitro. However, a number of difficult technical challenges must be overcome before these accomplishments can be applied to the study of biomolecular networks and complexes. Of principle importance is the need to achieve sufficient near-field contrast to yield sensitivity to individual molecules within a dense, heterogeneous ensemble. It has been pointed out that first-order scattering processes such as one-photon fluorescence may not be well

suited for this purpose due to the linear dependence of the excitation rate on optical intensity, compared to higher-order scattering processes such as two-photon fluorescence or Raman scattering [1, 2]. In this chapter, we demonstrate both theoretically and experimentally that one-photon fluorescence can, in fact, be used to image dense samples with single-fluorophore sensitivity and nanoscale resolution within the context of tip-enhanced microscopy.

Fluorescence microscopy/spectroscopy is particularly powerful for studying biological systems because of its sensitivity to single molecules and the biochemical specificity afforded by modern conjugation methods. The major limitation of traditional optical microscopy is the limited resolution ($\sim$ 250 nm) imposed by classical light diffraction. Recently, a number of far-field microscopy techniques have been developed to exceed the conventional diffraction limit and even to obtain spatial resolution at the nanometer length scale [3]. These include 4-Pi microscopy, [4, 5], stimulated emission depletion (STED) microscopy [6], ground-state depletion microscopy (GSD) [7], saturated pattern excitation microscopy (SPEM) [8], reversible saturable optically linear fluorescent transitions (RESOLFT) microscopy [9], photoactivatable localization microscopy (PALM) [10, 11], and stochastic optical reconstruction microscopy (STORM) [12]. These techniques are a major step forward for nanoscale optical imaging of biological samples. But they also have some important limitations, including the need for specially designed and synthesized fluorophores, the need for large laser intensities (which can lead to sample damage), and very slow image acquisition speeds (which can prohibit the study of dynamic biological processes). Scanning near-field optical microscopy (SNOM) offers an alternative approach for high-resolution fluorescence imaging, and aperture-SNOM has been used to measure the nanoscale organization and orientation of biological molecules on surfaces and in membranes [13]. However, although 30 nm resolution is theoretically possible, resolution below 50 nm is seldom seen due to the severe cutoff in light transmission efficiency for small apertures [14].

In tip-enhanced fluorescence microscopy (TEFM), the enhanced field at the distal end of an Atomic Force Microscopy (AFM) probe causes a local increase in the one-photon fluorescence-excitation rate, and the resulting emission is then detected in the far field by a single-photon-sensitive avalanche photodiode (APD) (see Figure 12.1). In general, there is a competition between an increase in the detected fluorescence signal due to field enhancement and a decrease in signal caused by fluorescence quenching [15–17]. The enhancement should be proportional to the real part of the dielectric constant of the tip while the quenching should increase with the imaginary part. Thus, although metal tips should yield stronger field enhancement, they often produce a net decrease in fluorescence signal at short range [17]. Since both field enhancement and quenching are short-range effects ($<$20 nm), either can be used to obtain nanoscale resolution, although enhancement generally provides the larger contrast. Indeed, silicon AFM tips are observed to produce stronger near-field contrast compared to metal tips; thus, they are preferred for fluorescence studies of dense molecular systems. It should be noted that the reduction in fluorescence lifetime that accompanies quenching can be measured directly using pulsed lasers. Thus, tip-induced quenching can be used to study important nanoscale phenomena such as energy transfer and dissipation mechanisms, in both synthetic and biological systems.

The prospect of using TEFM to study biomolecular networks is greatly improved by the fact that AFM has already been used to characterize the topographical structure of protein complexes and networks embedded in biological membranes in vitro [18–21]. To minimize damage to soft samples, an AFM can be operated in tapping or intermittent contact mode: The cantilever probe is driven into rapid vertical oscillations, and the tip gently contacts the sample surface intermittently during each oscillation cycle. These fast vertical oscillations also can modulate the detected fluorescence, which leads to greatly improved contrast, as discussed in the next section. Although AFM provides nanoscale topographical resolution, it has no inherent sensitivity to the molecular-scale chemical composition of the sample. TEFM combines the attributes of tapping-mode AFM (nanoscale resolution, liquid compatibility) and fluorescence microscopy/spectroscopy (single-molecule sensitivity, chemical specificity) to yield a technique that holds much promise for structural studies of heterogeneous biomolecular networks.

In this chapter, we describe recent progress toward the goal of using TEFM for imaging biomolecular systems. In particular, we demonstrate that modulating the fluorescence using tapping-mode AFM greatly increases the near-field contrast. A theoretical and experimental analysis shows that appropriate modulation parameters and demodulation algorithms impart sufficient sensitivity for nanoscale imaging of high-density samples. Finally, we utilize optimized modulation/demodulation schemes to successfully resolve the fluorescently tagged ends of short (~13 nm) DNA oligomers in addition to individual quantum dots within high-density ensembles.

12.2 Contrast in Tip-Enhanced Fluorescence Microscopy

In scattering type (apertureless) SNOM (s-SNOM) a sharp tip, such as an AFM probe, is positioned into the focus of a laser beam. The primary advantage of s-SNOM is that it can achieve resolution that is limited principally by the tip sharpness to just a few nanometers [22]. On the other hand, s-SNOM techniques suffer from an increased background due to direct excitation by the laser; fluorophores located within the focal spot of the excitation laser add to the background signal while not contributing to the near-field signal. This high background is generally not an issue with aperture-SNOM since the light emerging from the aperture is already tightly confined to spot 50–100 nm across, effectively limiting the number of fluorophores that would be contributing to the background. Thus, to image dense samples such as biological systems with s-SNOM, it is very important to optimize the near-field contrast. This can be done by engineering the geometric and material properties of the tip to yield the largest field enhancement [23]. In particular, specific tip geometries that leverage antenna and lightning rod effects or that support plasmon resonances at the distal end can produce very large field enhancements and thus very high sensitivity for both imaging and sensing applications. In addition, metallic probes generally yield higher field enhancement than geometrically equivalent dielectric probes, but they also can cause fluorescence quenching at small tip-sample separations, thereby reducing contrast [17]. As discussed previously, we have found that silicon tips generally yield the best contrast in near-field fluorescence imaging.

Here we concentrate on the simple case of TEFM using standard, commercially available AFM tips and show that this situation can provide enough contrast to image high-density samples. A typical setup is shown in Figure 12.1: an AFM is situated atop an inverted microscope stage. The objective lens (1.4 NA) of the inverted microscope focuses an excitation laser onto a sample while the AFM probe is positioned into the center of the beam. To create both topographical and TEFM images, the sample is raster-scanned at a rate of 0.5–2.0 lines/s. As the sample scans, topographical images are generated one pixel at a time by continuously monitoring the average AFM-tip height. Simultaneously, photon counts generated within the time window corresponding to a given pixel can be summed to produce an image that displays the spatial distribution of the fluorescence emission intensity.

To generate strong enhancement, the optical field within the focus must be polarized parallel to the long axis of the tip (i.e., axial polarization). This polarization is obtained using either a laser-beam mask or a radial polarization generator (RPG). The beam mask produces an axially polarized evanescent field above the glass–air interface within a relatively tight focal spot (1.5 μm $\times$ 0.5 μm). This illumination scheme is similar to conventional total internal reflection fluorescence (TIRF) microscopy, except that the evanescent field is confined to a focal spot rather than a wide field. The RPG generates a radially polarized laser beam (TEM_{01*}) from a standard linearly polarized TEM_{00} mode. The requisite axially polarized field is created when the TEM_{01*} mode is focused tightly using a high numerical aperture objective [24, 25]. Furthermore, the TEM_{01*} mode produces a smaller focus spot, $\sim(250\ \text{nm})^2$, compared to focused-TIRF or a standard TEM_{00} mode. TEFM

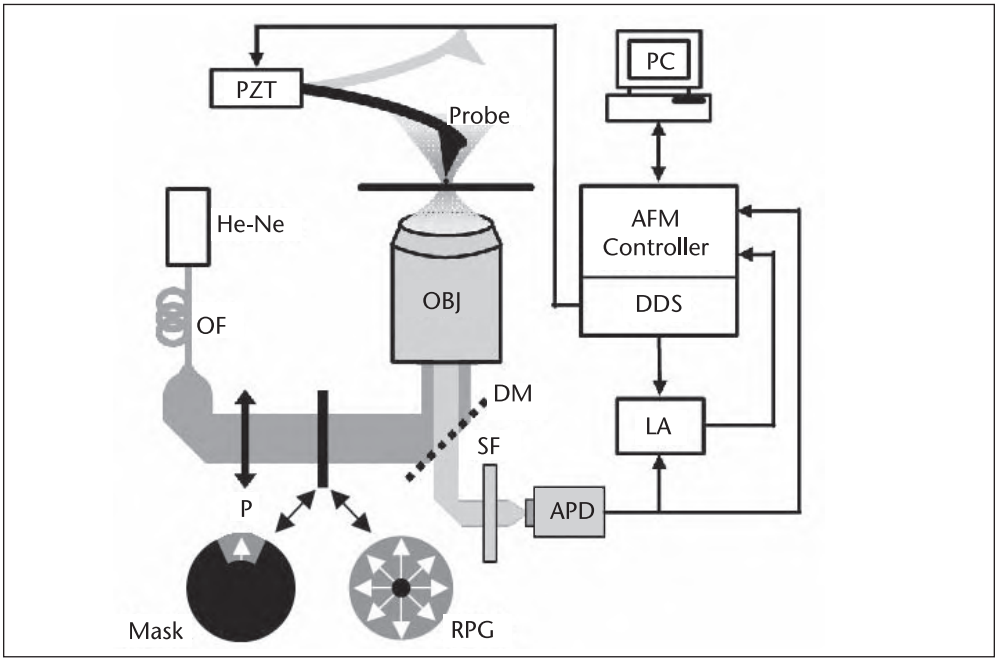

Figure 12.1 Experimental setup for TEFM. Labeled elements are as follows: He-Ne—helium-neon laser; OF—optical fiber; P—polarizer; Mask—laser-beam mask; RPG—radial polarization generator; DM—dichroic mirror; OBJ—microscope objective; Probe—AFM probe; PZT—piezoelectric transducer; SF—spectral filters; APD—avalanche photodiode; LA—lock-in amplifier; DDS—digital synthesizer; PC—personal computer. The arrows indicate the polarization of the laser beam.

typically requires very low optical powers (~200 nW) due to the tight laser focus, strong spectral rejection of nonfluorescent background signals, and high overall detection efficiencies (10%–20%).

In TEFM, the laser stimulates two distinct fluorescence signals: the far-field signal, S_{ff}, resulting from direct illumination of fluorophores within the laser focus, and the near-field signal, S_{nf}, resulting from the field enhancement at the tip apex. The resolution of S_{ff} is diffraction-limited, while S_{nf} has resolution given primarily by the sharpness of the tip [22]. Figure 12.2 shows a cartoon of an image composed of the superposition of S_{ff} and S_{nf} as well as a simulated profile through its center, where the peak signal ($S_{peak} = S_{ff} + S_{nf}$) has been identified. While it is not shown, we also assume some noise in the far-field signal. Within this context, contrast (C) and signal-to-noise ratio (SNR) are defined as:

$$C = \frac{S_{peak} - S_{ff}}{S_{ff}} = \frac{S_{nf}}{S_{ff}}$$
$$SNR = \frac{S_{peak} - S_{ff}}{\text{Noise in } S_{ff}} = \frac{S_{nf}}{\sigma_{ff}} \tag{12.1}$$

where σ_{ff} is the standard deviation (noise) in the far-field background. The near-field signal originates from a small area on the sample surface (a_{tip}) given by the near-field interaction zone, which is determined mostly by the tip sharpness, while the far-field background originates from a much larger area (A) given by the size of the laser focus.

The total fluorescence signal for a given pixel of the raster-scanned image, S_{peak}, is simply the sum of all photons collected during the pixel acquisition time (τ). The far-field signal S_{ff} is proportional to the number of fluorophores in the focal area of the excitation beam, N_{FA}, and to a dimensionless parameter k that characterizes the total efficiency of the system: $S_{ff} = k \cdot N_{FA}$. The probability of an illuminated fluorophore emitting a photon follows a Poisson distribution, $P_\gamma(n) = exp(-\gamma) \cdot \gamma^n/n!$, where $P_\gamma(n)$ is the probability of detecting n photocounts and $\gamma = S_{ff} = k \cdot N_{FA}$ is the expected average number of counts in the time interval τ. The standard deviation of such a distribution is given by $\sigma = \sqrt{\gamma} = \sqrt{k \cdot N_{FA}}$. The near-field signal, S_{nf}, is generated only when the tip is in close proximity to a fluorophore. In the limit of a

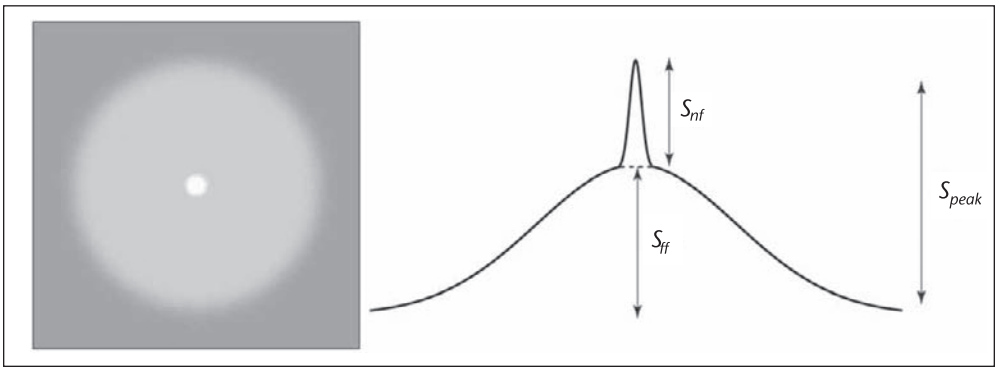

Figure 12.2 Cartoon of a fluorescent particle imaged by TEFM and the corresponding signal profile.

single fluorophore in the near-field zone, $S_{nf} = f \cdot k$, where f characterizes the enhancement in the fluorescence *signal* induced by the tip. f is a function of several parameters related primarily to the nature of the tip, such as its geometry and material properties. The value of f can adopt the range $-1 < f < \infty$, where $f = -1$ corresponds to complete quenching of a single fluorophore, $f = 0$ corresponds to no tip-induced effect (or no tip), and $f > 0$ corresponds to a tip-induced increase in the fluorescence signal. A value of $f = 1$ leads to $S_{peak} = k(N_{FA} + 1) = 2k$ if there is only one fluorophore in the focus area (i.e., $N_{FA} = 1$). In general, the peak signal from a single fluorophore is $S_{peak} = (f + 1)k$.

The overall system efficiency k is given by

$$k = I_0 \cdot \sigma_0 \cdot \tau \cdot Q \cdot CE \cdot \frac{\lambda}{hc}$$

where $I_0 = P_0/A$ is the intensity of the laser beam with power P_0 in a focal spot of area A, σ_0 is the absorption cross section of the fluorophore, τ is the pixel acquisition time, Q is the quantum yield of the fluorophore, CE is the collection efficiency of the detection system, and hc/λ is the energy of a photon with wavelength λ. Typical values for these parameters are shown in Table 12.1, where A is given for focused-TIRF illumination (1.5 μm × 0.5 μm) and σ_0 and Q are for CdSe quantum dots [26, 27].

The lower limit for detection of a near-field signal arises from the requirement that

$$SNR = \frac{S_{nf}}{\sigma_{ff}} = f\sqrt{\frac{k}{N_{FA}}} > 1 \tag{12.2}$$

Below this limit, the near-field signal is indistinguishable from stochastic fluctuations of the far-field background. On the other hand, to produce an image that can be interpreted visually dictates a more stringent requirement, namely that the contrast be larger than unity,

$$C = \frac{S_{nf}}{S_{ff}} = \frac{f}{N_{FA}} > 1 \tag{12.3}$$

In this model, it is straightforward to evaluate the minimum enhancement required for sensitivity to a single fluorophore within a dense ensemble. This is important for assessing the potential for applying TEFM to biological samples. A practical limit on density arises from the requirement that the average spacing between fluorophores be no smaller than the microscope resolution, which is given by the near-field interaction zone, a_{tip}. In this limit, $N_{FA} = A/a_{tip}$, where A is the area of the laser focus. Using a focused TIRF scheme, $A = 0.75\ \mu m^2$ and $a_{tip} = (10\ nm)^2$ suggests that an enhancement $f > 7{,}500$ is needed to achieve contrast greater than unity. Silicon tips are not capable of producing an enhancement factor this large, and metal tips have been predicted to yield enhancement factors of $f \sim 3{,}000$ [23]. Since employing a radially polarized laser beam yields a smaller focus spot, $A \approx (250\ nm)^2$ [25, 28],

Table 12.1 Typical Values for Parameters That Determine k

P_0 (nW)	A (μm^2)	σ_0 (nm^2)	τ (ms)	Q	CE	λ (nm)
100 – 200	0.75	0.2	0.75 – 3.2	0.5	0.2	543

the required enhancement predicted by Equation 12.3 is reduced to $f > 600$. This value is still out of range for silicon tips, which have demonstrated enhancement factors only as high as $f \sim 20$ [22].

At first glance, these predictions cast an unfavorable light on the possibility of using TEFM to image molecular-scale biological systems. In fact, a previous analysis based on an equivalent model suggested that only by employing higher-order scattering processes, such as two-photon fluorescence or Raman scattering, would it be possible to use tip-enhanced microscopy to investigate samples with high fluorophore densities [1, 2]. However, closer inspection reveals that this model is incomplete. In particular, it predicts that the contrast is independent of k, and thus intensity I_0. This is unphysical since it suggests that image contrast is still possible even in the absence of light, ($I_0 = 0$). Most importantly, this model neglects the possibility of improving contrast by employing appropriate data acquisition and analysis schemes. In particular, we show in the next section that modulating the fluorescence using tapping-mode AFM and then applying appropriate demodulation algorithms leads to the ability to image high-density samples, even with the modest values of f that can be obtained with silicon tips. Similar modulation/demodulation schemes are common in the context of electrical signal processing and are used extensively in NFO [22, 29–35].

12.3 Contrast with Fluorescence Modulation

To calculate the *SNR* and *C* for the case of an oscillating tip, Equations 12.2 and 12.3 must be modified to account for the fact that the tip only intermittently contacts the sample at a particular phase of its oscillation cycle. As shown in Figure 12.3, when the tip is at the highest position of its oscillation cycle, the fluorescence rate approaches the background scattering rate, which results in the far-field signal S_{ff}. At the bottom of its oscillation trajectory, the fluorescence rate is maximally modified by the presence of the tip, which results in the near-field signal S_{nf}. Note that S_{nf} can be positive or negative depending on whether the tip causes fluorescence enhancement or fluorescence quenching. Typically, silicon tips induce enhancement while metal-coated tips quench fluorescence, as shown in Figure 12.4. Thus, the peak signal, $S_{peak} = S_{ff} + S_{nf}$, can be larger or smaller than the background signal depending on the tip material and other experimental parameters.

Since the sample remains under direct laser illumination whether the tip is oscillating or not, the far-field signal for an oscillating tip is unchanged,

$$S_{ff}^{osc} = S_{ff} = k \cdot N_{FA} \tag{12.4}$$

However, since both enhancement and quenching decay very rapidly with distance from the tip apex, oscillating the tip induces a sharp modulation in the near-field signal as the tip alternately approaches and then retracts from the sample. One powerful method for measuring the spatial dependence of the modulated signal is to use time-correlated single photon counting (TCSPC) to permanently record the precise arrival time of each photon along with a time marker that corresponds to a particular constant phase in the probe-oscillation cycle. Each photon can then be assigned a phase value, θ_i, relative to the previous phase marker, and provided the oscillation amplitude is known, these can be correlated with the height of the tip above the sample, z [22, 29, 36]. Approach curves can be generated by freezing the

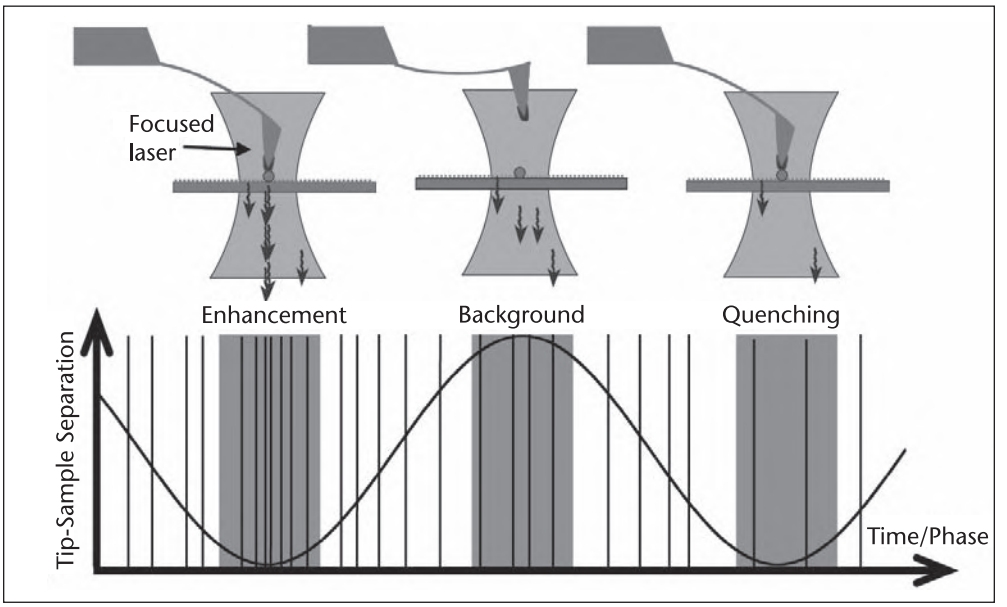

Figure 12.3 Schematic diagram of fluorescence modulation by an AFM probe oscillating in the laser focus. When the probe is up (middle), the tip has minimal influence on the fluorescence rate and the emitted photons (squiggly arrows) arrive at random intervals corresponding to the background scattering rate. When the probe is down, fluorescence is enhanced (left) leading to bunching of the photons or quenched (right) leading to antibunching. The sinusoidal curve (bottom) represents the oscillatory motion of a near-field probe and the way the emission of photons (indicated as vertical lines) corresponds to a given phase of the tip motion.

raster motion of the tip above an object of interest for some time and tabulating histograms of θ_i (Figure 12.4), or they can be extracted directly from particular regions of the raster images of a sample [29]. Since the photon timestamps and tip-oscillation phase markers are permanently recorded to a computer disk, the data can be analyzed off-line using arbitrary analysis algorithms designed to maximize contrast (see Section 12.4). In addition, it is straightforward to produce images corresponding to different ranges of tip-sample separation (i.e., tomography), which may be useful for imaging complex biological samples [22].

Each approach curve is a convolution of the tip-enhanced intensity distribution and the excitation probability distribution within the target. Thus, sharper tips and smaller objects generally yield sharper approach curves and, hence, better near-field resolution [22]. Figure 12.4 shows phase-delay histograms and their corresponding approach curves for quantum dots and fluorescent PS spheres. The enhancement approach curves are fit extremely well with a z^{-6} power-law decay, indicating that the tip-enhanced field is a dipole field [22, 29].

In phase space, the power-law spatial distribution can be approximated with a Gaussian distribution of phase angles, as shown by the solid-line fits in Figure 12.4. The center of the distribution is the preferred phase θ_p corresponding to tip-sample contact. After subtracting off the background, this distribution can be integrated to obtain the number of near-field photons collected. This integral is used to calculate the ratio γ of the number of photons collected in one oscillation cycle compared to the number that would have been collected had the tip been at the surface the entire time. γ accounts for the modulated fluorescence signal and is given by

$$\gamma = \frac{1}{2\pi}\int_{-\pi}^{\pi} e^{-(\theta_i-\theta_p)^2/2\theta_\sigma^2}\, d\theta_i \approx \frac{\theta_\sigma}{\sqrt{2\pi}} \tag{12.5}$$

where θ_σ is the standard deviation of the distribution, which can be obtained experimentally. Although the approach curve is independent of the oscillation amplitude, the width θ_σ is not since the amplitude establishes the portion of the approach curve that is sampled by the sinusoidal oscillations of the tip.

Since the tip spends only a portion of its oscillation cycle near the sample, the near-field signal is now a function of tip oscillation amplitude. When $\theta_\sigma \lesssim \pi/3$, the integral in Equation 12.5 is closely approximated by $\theta_\sigma/\sqrt{2\pi}$ (by extending the limits of integration from $-\pi \to \pi$ to $-\infty \to \infty$), and the modified near-field signal is then given by

$$S_{nf}^{osc} = S_{nf} \cdot \gamma \approx \frac{k \cdot f \cdot \theta_\sigma}{\sqrt{2\pi}} \tag{12.6}$$

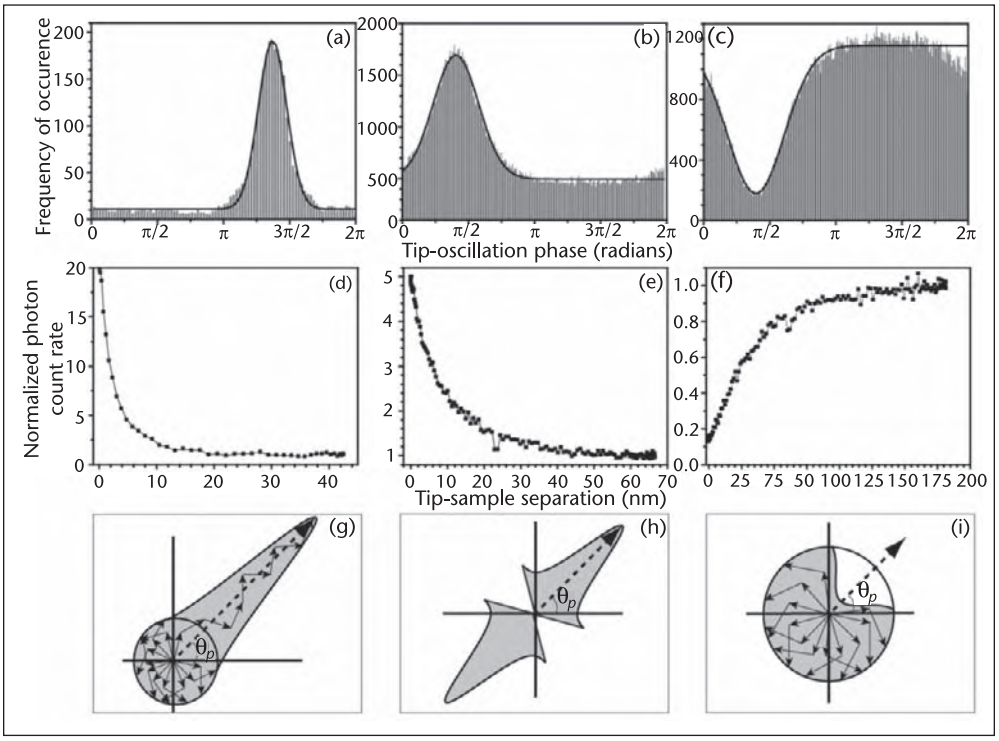

Figure 12.4 Photon phase-delay histograms (a–c) and corresponding approach curves (d–f) for an oscillating tip over a fluorescent particle. Panels (a) and (d) correspond to a silicon tip oscillating above a 5-nm diameter fluorescent quantum dot, panels (b) and (e) correspond to a silicon tip and a 20 nm diameter fluorescent polystyrene sphere, and panels (c) and (f) correspond to a Pt-Ir tip and a 20 nm diameter fluorescent polystyrene sphere. Solid lines in (a–c) are Gaussian fits to the phase histograms, as described in the text. Panels (g) and (i) schematically represent the phase-space addition of the near-field and far-field vector components of the photon signal during modulation by the tip, as described in the text. The far-field component can point in any direction and is represented by a circular envelope in phase space, while the near-field signal is biased (g) or antibiased (i) around the phase of tip-sample contact θ_p corresponding to enhancement and quenching, respectively. Panel (h) shows a Gaussian weighting function, which was used to enhance image contrast as described in the text.

Since γ is less than unity, $S_{nf}^{osc} \leq S_{nf}$. Using the definitions for the oscillating signals in Equations 12.4 and 12.6, both the contrast and *SNR* for images produced by an oscillating tip (tapping mode TEFM) can now be calculated as follows:

$$C_{sum}^{osc} = \frac{f \cdot \gamma}{N_{FA}}$$

$$SNR_{sum}^{osc} = f \cdot \gamma \sqrt{\frac{k}{N_{FA}}}$$

where the subscript "*sum*" indicates a direct sum of the photon signals. The contrast and *SNR* also have been reduced by a factor of γ compared to the nonoscillating scenario. Clearly, the advantage of modulation must lie in demodulating the fluorescence signal.

12.4 Improving Contrast via Demodulation

Various demodulation algorithms are widely used in many fields to recover small signals. Lock-in amplification is a particularly powerful technique that strongly suppresses background signals that fall outside a narrow frequency band and amplifies those background signals that are in phase with a (sinusoidal) reference signal. In TEFM, each detected fluorescence photon can be considered to be a unit vector with an angle θ_i equal to the instantaneous phase of the tip oscillation at the time of detection. In this picture, a lock-in amplifier (LA) can be treated as an instrument that simply performs a vector addition of the detected photons transmitted through its internal band-pass filter. This can be compared with the treatment developed previously where the scalar sum of the photons was computed. Once again, the fluorescence signal can be divided into near-field (**NF**) and far-field (**FF**) components, both of which are vector sums. The far-field component arises from an unbiased random walk in phase space, while the near-field component comes from a biased (enhancement) or antibiased (quenching) random walk about the particular oscillation phase corresponding to tip-sample contact, θ_p (see Figure 12.4). The sum of these two components will yield a resultant vector whose magnitude $|\mathbf{L}|$ is the lock-in signal. Large enhancement factors will increase **NF** and thus will lead to larger $|\mathbf{L}|$. Note that quenching generally yields a smaller lock-in signal than enhancement, and it will not be considered further in this section.

Since the far-field component **FF** results from an unbiased 2-D random walk with unit steps, its length is governed by the probability distribution

$$P(r) = \frac{2r}{N_{steps}} e^{-r^2/N_{steps}}$$

where r is the final end-to-end distance of the walk and N_{steps} is the number of steps in the walk [37]. This distribution has a mean μ_r and standard deviation σ_r given by

$$\mu_r = \sqrt{\frac{\pi N_{steps}}{4}}$$

$$\sigma_r = \frac{1}{2}\sqrt{N_{steps}(4 - \pi)}$$

In our case, N_{steps} is given by the number of detected far-field photons that are transmitted by the lock-in band-pass filter, $N_{steps} = \beta \cdot S_{ff}$, where $\beta < 1$. This gives

$$|\mathbf{FF}| = \sqrt{\frac{\pi}{4}\beta \cdot k \cdot N_{FA}}$$

$$\sigma_{|\mathbf{FF}|} = \frac{1}{2}\sqrt{\beta \cdot k \cdot N_{FA}(4 - \pi)} \approx \frac{1}{2}|\mathbf{FF}|$$

for the average length of the far-field component $|\mathbf{FF}|$ and its uncertainty $\sigma_{|\mathbf{FF}|}$.

The average magnitude of the near-field component $|\mathbf{NF}|$ can be estimated by projecting the unit vectors corresponding to each near-field photon onto the θ_p axis,

$$|NF| = \sum_i cos(\theta_i - \theta_p) = S_{nf}^{osc} \cdot \left\langle cos(\theta_i - \theta_p) \right\rangle \tag{12.7}$$

where the sum runs over all of the near-field photons, $i = 1 \rightarrow S_{nf}^{osc}$. For simplification, we define $\alpha = \left\langle \cos(\theta_i - \theta_p) \right\rangle$. Since the phase of each photon θ_i is Gaussian-distributed, the normalized expectation value is given by

$$\alpha = \frac{\int_{-\pi}^{\pi} \cos(\theta_i - \theta_p) e^{-(\theta_i - \theta_p)^2/2\theta_\sigma^2} d\theta_i}{\int_{-\pi}^{\pi} e^{-(\theta_i - \theta_p)^2/2\theta_\sigma^2} d\theta_i} \approx e^{-\theta_\sigma^2/2} \tag{12.8}$$

Note that α plays the same role in the vector sum that λ played in the scalar sum in Equation 12.6. With this definition for α, the average magnitude of the near-field component is given by

$$|\mathbf{NF}| = k \cdot f \cdot \gamma \cdot \alpha \approx k \cdot f \cdot \frac{\theta_\sigma}{\sqrt{2\pi}} \cdot e^{-\theta_\sigma^2/2}$$

When a LIA is used to demodulate the signal, an image is constructed one pixel at a time, where the value of each pixel is the magnitude of the lock-in vector,

$|\mathbf{L}| = |\mathbf{NF} + \mathbf{FF}|$. The near-field component **NF** points along θ_p, but the far-field component **FF** points in a random direction. Performing the vector addition of **NF** + **FF** and averaging over all directions for **FF**, the lock-in signal is given by

$$|\mathbf{L}| = \sqrt{|\mathbf{NF}|^2 + |\mathbf{FF}|^2} = \sqrt{(k \cdot f \cdot \gamma \cdot \alpha)^2 + \frac{\pi}{4} \cdot k \cdot N_{FA} \cdot \beta} \tag{12.9}$$

The contrast and *SNR* in the lock-in signal can now be readily found. When the position of the tip is far from a fluorophore, then **NF** = 0 and the lock-in signal is given simply by the background scattering, $|\mathbf{L}|_{bg} = |\mathbf{FF}|$. When the tip is directly over a fluorophore, the peak lock-in signal $|\mathbf{L}|_{peak}$ is given by Equation 12.9. Thus, the lock-in contrast C_{LI} and signal-to-noise ratio SNR_{LI} are equal to

$$C_{LI} = \frac{|\mathbf{L}|_{peak} - |\mathbf{L}|_{bg}}{|\mathbf{L}|_{bg}} = \left(\frac{4k(f \cdot \gamma \cdot \alpha)^2}{\pi \cdot N_{FA} \cdot \beta} + 1 \right)^{1/2} - 1$$

$$SNR_{LI} = \frac{|\mathbf{L}|_{peak} - |\mathbf{L}|_{bg}}{\sigma_{|\mathbf{FF}|}} \approx 2 \cdot C_{LI} \tag{12.10}$$

Requiring a contrast greater than unity in the lock-in image imposes the following constraint on the signal enhancement factor:

$$f > \frac{1}{\alpha \cdot \gamma} \sqrt{\frac{3\pi \cdot N_{FA} \cdot \beta}{4k}}$$

As before, we consider the case where there is only one fluorophore in the near-field zone $a_{tip} = (10\ \text{nm})^2$ and $N_{FA} = A/a_{tip} = 7{,}500$ fluorophores in the far-field focus of area $A = 0.75\ \mu\text{m}^2$ (focused-TIRF illumination). Using typical experimental values for $k = 10$ and $\beta = 0.15$ and optimized values for $\gamma = 0.4$ and $\alpha = 0.6$ (see Section 12.5) gives a required enhancement factor $f > 65$ to achieve a contrast greater than unity. Using radial polarization gives $N_{FA} = 600$ fluorophores within a much smaller focal area $A = (250\ \text{nm})^2$, which reduces the required enhancement to $f > 18$. These enhancement factors are very realistic for silicon tips and imply a strong feasibility for applying TEFM to dense biological samples.

Figure 12.5 shows an example of how the lock-in demodulation scheme can be used to improve the contrast and *SNR* for images of samples with high fluorophore density, in this case CdSe/ZnS quantum dots (4.0 nm × 9.4 nm). These images were obtained using a silicon tip oscillating with an optimized amplitude of ~30 nm peak to peak (see Section 12. 5) and focused-TIRF illumination. The visible quantum dot density for this image is $\sim 14\ \mu\text{m}^{-2}$, and there is clearly sufficient contrast to increase the density further. Measured approach curves indicate an enhancement factor of only $f \sim 4$ in this case because the size of the quantum dots relative to the tip leads to a somewhat small spatial overlap with the region of enhanced field, which dilutes the average enhancement factor. In addition, due to their elongation, these particular quantum dots most strongly absorb photons with polarization parallel to their long axis (C-axis), which should lie in the horizontal sample plane. Thus, they do not respond optimally to the tip-enhanced field whose polarization is predominantly vertical

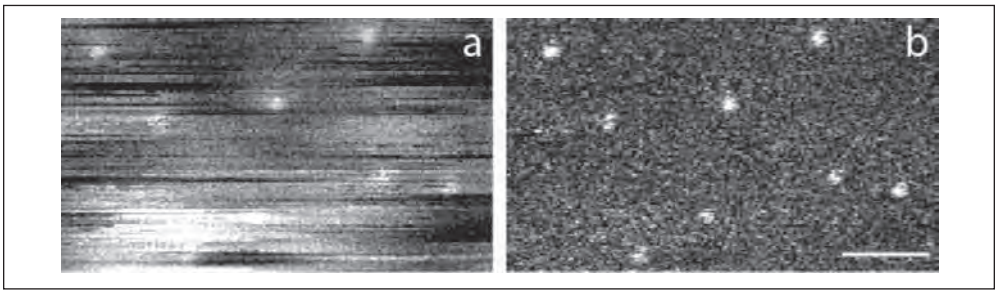

Figure 12.5 TEFM images of a high-density quantum dot sample. Panel (a) shows the scalar photon sum, while panel (b) shows the result of lock-in demodulation. The scale bar is 200 nm.

directly under the tip. It has been shown that spherical quantum dots and sharper tips can yield larger enhancement factors, up to $f \sim 20$ [22], as shown in Figure 12.4.

12.5 Optimizing Tip Oscillation Amplitude

The demodulated contrast and *SNR* given in Equation 12.10 are strongly influenced by the amplitude of oscillation of the AFM tip. When a very small amplitude is used, the oscillating near-field signal S_{nf}^{osc} given in Equation 12.6 is maximized ($\gamma \to 1$). But the near-field photon phases are spread nearly equally across the entire oscillation cycle ($\alpha \to 0$), so the average magnitude of the near-field component of the lock-in vector $|\mathbf{NF}|$ given in Equation 12.7 vanishes. On the other hand, very large amplitudes decrease the fraction of time that the tip spends in the near-field zone, so S_{nf}^{osc} becomes small ($\gamma \to 0$) but all of these photons tend to arrive at the phase corresponding to tip-sample contact giving a strong projection of **NF** onto θ_p ($\alpha \to 1$). Thus, to optimize the lock-in signal, the product $\gamma \cdot \alpha$ should be maximized. Using the approximations given in Equations 12.5 and 12.8, respectively, γ and α are function of θ_σ only. Thus, their product is maximized by requiring

$$\frac{d}{d\theta_\sigma}(\theta_\sigma \cdot e^{-\theta_\sigma^2/2}) = 0$$

The only physical solution to this equation is $\theta_\sigma^{opt} = 1$ radian. As defined in Equation 12.5, θ_σ is the standard deviation of the Gaussian distribution of photon phases about θ_p; thus, 68% of the near-field photons arrive in the range $[\theta_p - \theta_\sigma, \theta_p + \theta_\sigma]$. As the amplitude of oscillation becomes larger, the value of θ_σ becomes smaller and vice versa.

To relate θ_σ^{opt} to an optimal amplitude A_{opt}, we first define z_σ as the value of tip-sample separation z in an approach curve (Figure 12.4) such that the integrated area under the approach curve from $0 \to z_\sigma$ contains 68% of the near-field photons. The particular value of z_σ is measured experimentally and depends on the sharpness of the tip and the size and shape of the fluorescent object: Sharp tips and small objects (e.g., molecular fluorophores) result in the smallest values of z_σ. If the particular oscillation phase corresponding to tip-sample contact is set to $\theta_p = 0$, the equation of motion for the tip oscillation is given by

$$z = A(1 - \cos\theta) \tag{12.11}$$

where $\theta = \omega t$ and ω is the angular frequency of oscillation. Setting $z = z_\sigma$ and $\theta = \theta_\sigma^{opt} = 1$ gives

$$A_{opt} = \frac{z_\sigma}{1 - \cos(1)} \approx 2.1\, z_\sigma \tag{12.12}$$

Note that when the approximations made in Equations 12.5 and 12.8 are used, a value of $A_{opt} = 2.18\, z_\sigma$ is obtained compared to a value of $A_{opt} = 2.11\, z_\sigma$ when the integrals from Equations 12.5 and 12.8 are computed numerically. Thus, to obtain maximum contrast in the lock-in signal, the amplitude of oscillation should be adjusted to roughly double the measured value of z_σ.

Experimental values for the contrast and *SNR* as a function of the peak-to-peak oscillation amplitude of the tip are shown in Figure 12.6, along with the theoretical predictions developed previously. Isolated ($N_{FA} = 1$) CdSe/ZnS quantum dots (4.0 nm × 9.4 nm) were imaged with different amplitudes using many different tips from the same fabrication wafer. Each data point was computed from the measured values of S_{peak}, S_{bg}, and σ_{bg}, as defined in Equation 12.1 for ~15 different quantum dots [30]. The values of $f = 3.7 \pm 1.3$, $k = 11 \pm 5$, $\beta = 0.15 \pm 0.15$, and $z_\sigma = (7.5 \pm 2)$ nm were all obtained from a statistical analysis of image and approach curve data. Subsequently, θ_σ was computed using Equation 12.11 and the measured value $z_\sigma = (7.5 \pm 2)$ nm to obtain α and γ for each oscillation amplitude from Equations 12.5 and 12.8. Thus, the theoretical curves shown in Figure 12.6 contain no free parameters whatsoever. Nonetheless, the theoretical prediction for both the optimal oscillation amplitude and the entire amplitude dependence matches the data remarkably well. The optimal amplitude predicted by Equation 12.12 was doubled upon comparison to the data in Figure 12.6 to account for the fact that the data is measured as a function of peak-to-peak amplitude. After this conversion, the predicted peak-to-peak amplitude of 32±9 nm agrees with the experimental value of 32±4 nm.

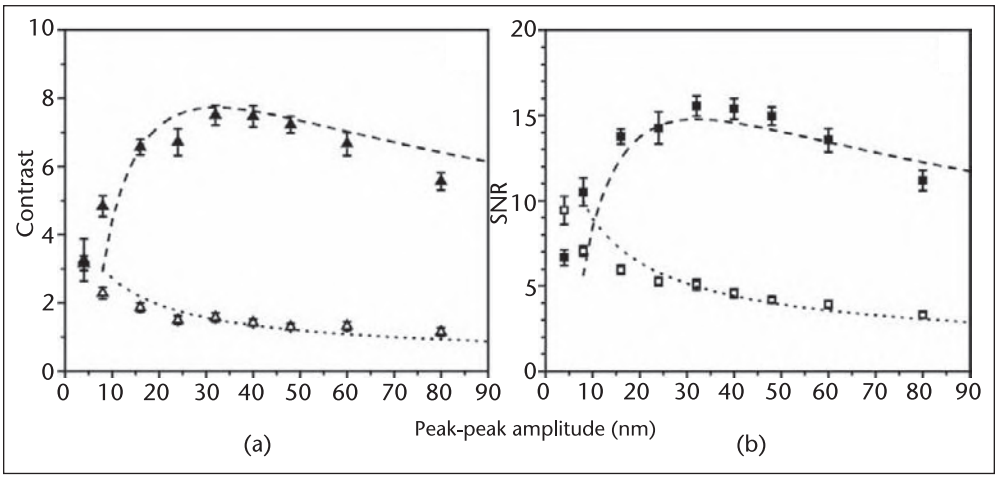

Figure 12.6 TEFM image contrast (a) and signal-to-noise ratio (b) for isolated quantum dots as a function of the tip oscillation amplitude. Data were obtained using BudgetSensors Multi-75 silicon tips. The data points correspond to the average value of ~15 measurements for the lock-in demodulation signal (closed symbols) and the scalar sum (open symbols), while the dashed and dotted lines are the corresponding theoretical predictions as described in the text.

12.6 TEFM Imaging of Single Molecules and DNA

As discussed previously, lock-in amplification is a powerful demodulation technique for increasing the contrast of TEFM images. The lock-in algorithm presented in Sections 12.4 and 12.5 can be implemented using a commercial LIA to analyze the data in real time; alternatively, TCSPC can be used to permanently record the arrival time of each signal photon and the lock-in algorithm can be applied off-line. The analysis developed previously is equally valid for either case, although off-line implementation should enable superior performance since there is no loss in signal fidelity caused by filtering, averaging, or amplification. TCSPC also imparts the flexibility needed to design and implement an arbitrary number of phase-sensitive analysis algorithms, which can be applied repeatedly to the same data set. Finally, as already discussed, TCSPC enables approach curves to be extracted directly from image data, eliminating the need for separate measurements and providing the means to perform near-field tomography [22, 29].

Ultimately, the power of TCSPC stems from its ability to correlate the arrival of each detected photon with the instantaneous oscillation phase of the AFM probe. With the phase of each detected photon in hand, it is possible to explore analysis algorithms that are even more sophisticated than lock-in amplification. In particular, Monte-Carlo simulations have indicated that significant gains in contrast can be achieved by applying a weighted phase filter whereby photons within a certain phase window centered around θ_p are selectively amplified according to a Gaussian weighting function before they are summed to produce the peak signal

$$S_{peak} = \sum_{\theta_i} e^{-[(\theta_i-\theta_p)/\theta_w]^2} N(\theta_i) \tag{12.13}$$

where $N(\theta_i)$ is the number of photons at θ_i, θ_w is the width of the phase weighting window, and the sum is over the range $\theta_p - \theta_w \rightarrow \theta_p + \theta_w$. Photons that fall outside the weighting window are simply eliminated before the sum is performed. The Gaussian weighting profile is extracted from approach-curve histograms, as shown in Figure 12.4, and θ_w can be optimized to reduce the bleed-through between the near-field and far-field signals. To offset the amplification of background photons, an identical weighting function is applied to the data centered around $\theta_p - \pi$

$$S_{ff} = \sum_{\theta_i} e^{-[(\theta_i-\theta_p+\pi)/\theta_w]^2} N(\theta_i) \tag{12.14}$$

where now the sum is over the range $\theta_p - \pi - \theta_w \rightarrow \theta_p - \pi + \theta_w$. To produce an image, the data corresponding to each pixel is first summed into "peak" and "far-field" bins (according to Equations 12.13 and 12.14). Then the background is smoothed by averaging S_{ff} for a given pixel with each of its four nearest neighbors yielding an average far-field signal $\bar{S}_{ff}$. On average, the background signal contributes equally to the peak and far-field bins; so the near-field signal for each pixel is given by $S_{nf} = S_{peak} - \bar{S}_{ff}$, and S_{nf} is set to zero whenever $(S_{peak} - \bar{S}_{ff}) < 0$. The image is then formed by plotting S_{nf} for each spatial pixel.

The near-field photons generated with an oscillating tip are naturally distributed according to a particular Gaussian profile. In a simple lock-in algorithm, the unit vectors corresponding to each near-field photon are summed to produce a

resultant vector that is biased toward θ_p. The phase-sensitive amplifier, on the other hand, preferentially amplifies those photons nearest to θ_p before a sum is performed. This additional degree of amplification leads to improved sensitivity to extremely small signals, such as those originating from single molecular fluorophores. Figure 12.7 compares TEFM images of isolated Cy3 fluorophores using the off-line phase-sensitive amplifier (middle column) and a scalar photon sum (left column). In this case, the filter width $\theta = \pi/3$ was chosen to optimize the image contrast [29].

Due to different orientations of the absorption dipole for each fluorophore, the images of single molecules can be elongated or symmetric. A total of 211 Cy3 molecules were imaged, and the measured image widths along the minor and major directions are tabulated in the histograms shown in Figures 12.7(c) and 12.7(f). The average FWHM for the minor and major directions are 6.8 and 9.6 nm, respectively, giving an average of 8.2 nm. The measured distribution of image widths suggests that the apparent width of any single fluorophore is not necessarily a robust indicator of spatial resolution. Nevertheless, the statistical averages obtained here do indicate very high resolution, close to one order of magnitude better than typical results of aperture-type near-field microscopy.

Numerical simulations of single-molecule fluorescence using an electrostatic dipole model for the tip-enhanced optical field were performed to understand the effect of absorption dipole orientation on the size and shape of single-molecule TEFM images [38–40]. In this model, the total optical field under the tip can be approximated by

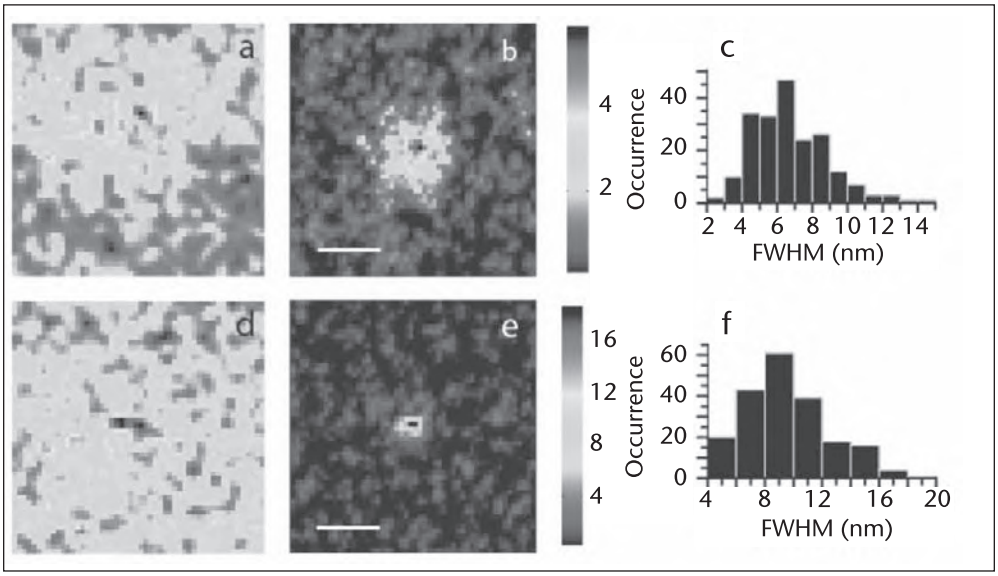

Figure 12.7 TEFM images of isolated Cy3 molecules. In panels (a) and (d), a sum of all of the detected photons was performed, while in panels (b) and (e), the Gaussian weighting function shown in Figure 12.4(h) was applied before performing the sum, as described in the text. Each figure was extracted from a 1×1 μm^2, 512×512 pixel image. The SNR for panels (b) and (e) is 16.2 and 25.5, respectively. Panels (c) and (f) show histograms of the FWHM of 211 analyzed images measured along the minor and major directions, respectively. Scale bars: 25 nm. Reprinted with permission from [29]. Copyright (2006) by the American Physical Society.

$$\vec{E}(\vec{r}) = E_0\left[z + \eta\left(\frac{3z}{r^4}\vec{r} - \frac{1}{r^3}\vec{z}\right)\right]$$

where E_0 is the field in the laser focus, η is an experimental value that characterizes the tip-induced field enhancement (note that f characterizes the fluorescence *signal* enhancement), and the coordinate origin corresponds to the tip center of curvature. Thus, the fluorescence intensity can be written as $[\vec{E}(\vec{r}) \cdot \vec{p}(\theta, \phi)]^2$, where $\vec{p}(\theta, \phi)$ is the single-molecule dipole moment oriented along the polar angle θ and azimuthal angle ϕ.

Figure 12.8 shows that the simulated images become more elongated as the dipole tilts away from the vertical tip axis. When $\vec{p}(\theta, \phi)$ is perpendicular to the tip axis ($|\theta - 90°| \leq 0.8°$), the images have two symmetric lobes, while when parallel to the tip axis ($\theta = 0°$ or $\theta = 180°$), the image has a symmetric rounded shape. The angle ϕ simply rotates the image in the horizontal plane. A careful analysis of experimental data for several isolated Cy3 molecules reveals asymmetric image patterns suggesting that orientational information can indeed be gleaned from TEFM images of single molecules [29]. A small sample of such images is shown in Figures 12.8(b)–(d).

In the past, the image widths of isolated fluorophores have been used as a measure of spatial resolution. When the size of the fluorophore is small (e.g., ~1 nm) and the sample surface is flat, this technique gives a reasonable approximation of the resolution (e.g., Figure 12.7). However, for more complicated situations, particularly those that might occur in dense biological samples, this method can lead to erroneous claims due to various topographical artifacts [14]. In any case, a better resolution indicator is provided by the classic Rayleigh criterion whereby the minimum resolvable distance between two point sources is measured. Since Cy3 molecules are smaller than one nanometer, they make excellent approximations of point sources, whereas quantum dots must be treated as extended objects since their

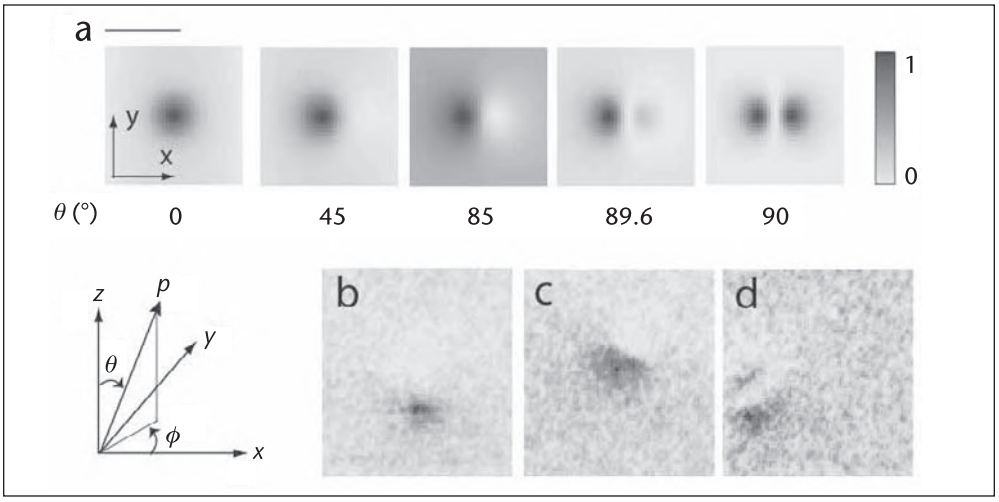

Figure 12.8 Dependence of the TEFM image pattern on the molecular dipole orientation. Panel (a) shows simulated images of an ideal dipole emitter imaged with a tip of radius 10 nm and a fluorescence enhancement factor of five. Panels (b–d) show experimental images (150 × 150 nm) demonstrating signal patterns similar to the simulations. Scale bar: 20 nm. Reprinted with permission from [29]. Copyright (2006) by the American Physical Society.

dimensions are comparable to those of the tip apex. Thus, a robust measure of resolution can be obtained by imaging pairs of Cy3 molecules whose separation can be precisely controlled.

To accomplish such a measurement, individual Cy3 molecules were attached to the 5′ end of 60-mers of single-stranded DNA (ssDNA). Complementary strands of ssDNA were prepared and annealed, yielding two Cy3 molecules linked by a 60 base-pair (bp) length of double-stranded DNA (dsDNA). The estimated fraction of doubly-labeled dsDNA was ~67%. The dsDNA chain is shorter than the DNA persistence length (~150 bp), so apart from any flexibility in the Cy3-DNA linker molecule, the Cy3 molecules are rigidly separated. A dilute solution of such Cy3 "dumbbells" was dried down onto mica-coated glass coverslips and subsequently imaged with TEFM

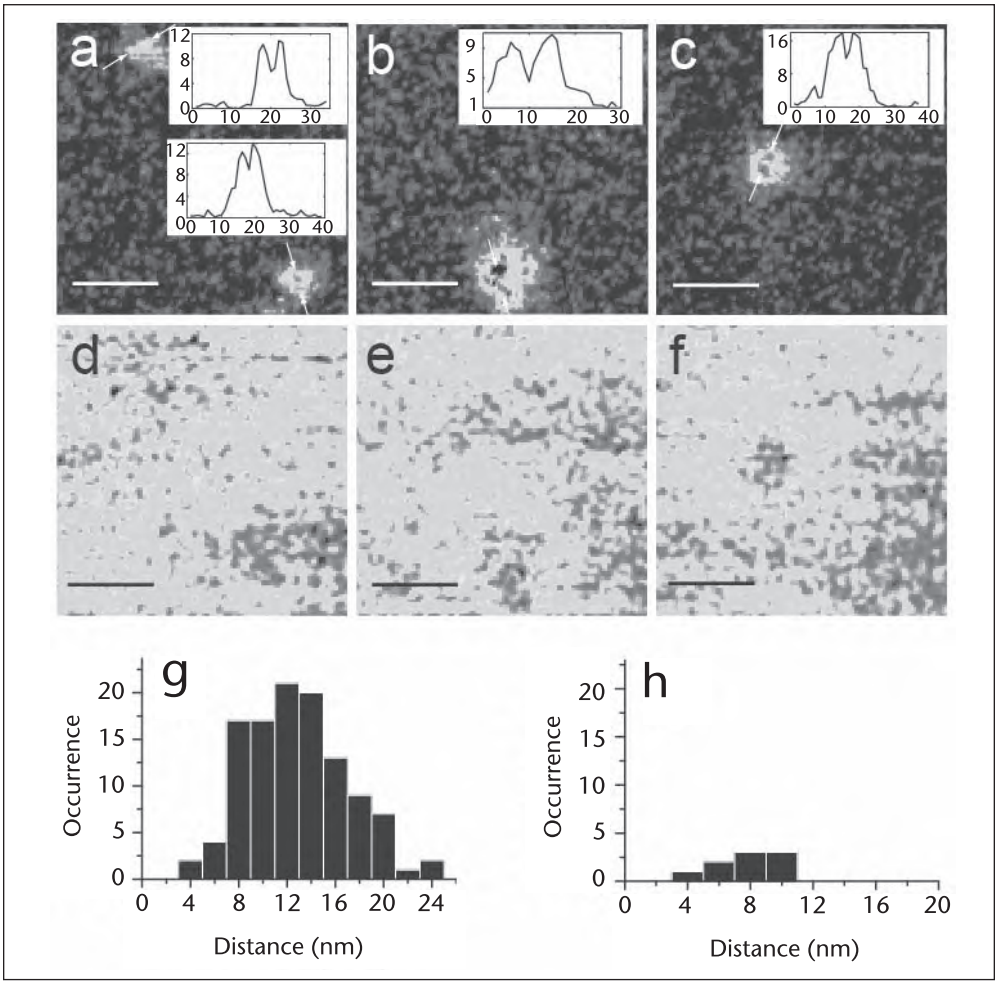

Figure 12.9 TEFM images of pairs of Cy3 fluorophores linked by short 60-mer lengths of double-stranded DNA. In panels (a–c), the Gaussian weighting function was applied to the fluorescence data, while in panels (d–f), a simple scalar sum was performed. The SNR is 12.4, 15.9, and 20.4 for panels (a), (b), and (c), respectively. The insets show the signal profiles along a line through the image centers (indicated by arrows), where the horizontal axis is in pixels (1 pixel = 1.95 nm). Panel (g) shows a histogram of measured separations between the two signal peaks corresponding to the Cy3 pairs. Panel (h) shows a histogram of measured separations between the two artifactual lobes in images of single Cy3 molecules. Scale bars: 50 nm. Reprinted with permission from [29]. Copyright (2006) by the American Physical Society.

using the weighted phase filter described previously. Figures 12.9(a)–(c) are the TEFM images of such molecule pairs using the weighted phase filter, and Figures 12.9(d)–(f) are the corresponding scalar sum images without the phase filter. Note that the contrast in the scalar sum images is insufficient to resolve the Cy3 dumbbells, while the filtered images clearly reveal double-peaked structures.

A total of 389 dsDNA oligonucleotides were imaged, 29% of which showed resolvable Cy3 dumbbells. Factors such as imperfect annealing, photobleaching, and worn tips can contribute to the failure to resolve the rest of the 67% of expected dumbbells. To verify that the double-lobed images resulted from dsDNA dumbbells rather than orientation effects (Figure 12.8), images of single Cy3 molecules were analyzed for the presence of double-lobed structures. Of the 211 molecules contributing to Figure 12.7, only 4% exhibited double-lobed artifacts [see Figure 12.9(h)]. Thus, the ends of the dsDNA dumbbells are resolvable when the phase-sensitive amplifier is used.

The histogram in Figure 12.9(g) shows the distribution of measured separations between the dumbbell ends. The mean of the distribution is 13.0 nm $\pm$ 0.4 nm, and the standard deviation of the distribution is 4.1 nm. Various factors can contribute to the width of the measured distribution, including the limited precision in determining the image centers, temporal drift of the sample caused by mechanical relaxation and thermal expansion, and the flexibility of the DNA-Cy3 polymer linker molecule (which is estimated to have a length of $\sim$0.6 nm). Simulations also show a systematic shift toward smaller image separations induced by coexcitation of both Cy3 molecules by the near field when the tip is positioned between them. This shift becomes more pronounced for larger tips since the degree of coexcitation then increases. The apparent width of the majority of single-molecule images indicates an upper bound for the tip radius of 15 nm. In this case, simulations show a 2.5 nm shift for two molecules separated by 15 nm. Therefore, the precision of our measurement of the DNA length has a statistical error of 3% and a systematic error up to 20%.

An unresolved paradox in X-ray diffraction studies of *A*-form DNA is that fibers of long DNA molecules with mixed sequences yield a consistent value of 2.6 Å/bp for the helical rise [41], but crystal structures of small oligonucleotides ($\sim$10 bp) reveal an average value of 2.83 Å/bp with a standard deviation of $\sim$0.36 Å/bp across different sequences [42]. The source of the discrepancy is as yet unresolved, although crystal artifacts, molecular weight effects, and incomplete sequence sampling may all play a role. The measurements described here allow an independent determination of the helical rise and do not suffer from artifacts due to crystal packing or small molecular weights. The result (2.17 Å/bp) agrees with the X-ray data of fibers within one sigma of our largest estimated experimental error and falls within the two-sigma limit of the sequence-dependent variation observed in crystal structure data [29].

12.7 Conclusions

Determining the structure of extended biomolecular networks and relating that structure to the physical mechanisms underlying various biological functions are very difficult and pressing problems in molecular-scale science. Current nanoscale structural analysis tools, including X-ray crystallography, electron microscopy, and AFM, have a number of limitations that prevent their application to extended networks

composed of heterogeneous mixtures of various biomolecules. Fluorescence microscopy, on the other hand, is a very powerful technique for analyzing heterogeneous molecular systems and when combined with the spatial resolution afforded by apertureless near-field microscopy, holds great promise as a future molecular-scale structural analysis tool.

Although the potential of apertureless fluorescence microscopy in structural biology has been recognized previously, a recurring criticism has been that first-order scattering processes cannot achieve the contrast needed to resolve individual molecules within a dense ensemble. In this work, we have explicitly addressed the issue and have shown theoretically and experimentally that it is in fact possible to achieve the needed contrast using carefully designed modulation/demodulation schemes. Two key issues discussed were the need to optimize various experimental parameters, such as the oscillation amplitude and material properties of the apertureless tip, and the benefits of using phase-sensitive demodulation techniques, such as lock-in amplification and single photon counting. Coupled with recent and future advances in scanning probe microscopy, such as imaging in water and fast-frame imaging speeds, it may ultimately be possible to combine optical resolution approaching that of electron microscopy with the ability to image biomolecules in physiological conditions.

References

[1] Novotny, L., "Near-Field Optical Characterization of Nanocomposite Materials," *J. Am. Ceram. Soc.,* Vol. 85, 2002, pp. 1057–1060.

[2] Novotny L., and B. Hecht, *Principles of Nano-Optics*, 1st ed., New York: Cambridge University Press, 2006.

[3] Hell, S. W., "Far-Field Optical Nanoscopy," *Science,* Vol. 316, 2007, pp. 1153–1158.

[4] Hell, S. W., and E. H. K. Stelzer, "Fundamental Improvement of Resolution with a 4Pi-Confocal Fluorescence Microscope Using Two-Photon Excitation," *Opt. Commun.,* Vol. 93, 1992, pp. 277–282.

[5] Gugel, H. et al., "Cooperative 4Pi Excitation and Detection Yields Sevenfold Sharper Optical Sections in Live-Cell Microscopy," *Biophys. J.,* Vol. 87, 2004, pp. 4146–4152.

[6] Klar, T. A. , E. Engel, and S. W. Hell, "Breaking Abbe's Diffraction Resolution Limit in Fluorescence Microscopy with Stimulated Emission Depletion Beams of Various Shapes," *Phys. Rev. E,* Vol. 64, 2001, Art. No. 066613.

[7] Hell, S. W., and M. Kroug, "Ground-State-Depletion Fluorescence Microscopy: A Concept for Breaking the Diffraction Resolution Limit," *Appl. Phys. B,* Vol. 60, 1995, pp. 495–497.

[8] Heintzmann, R., T. M. Jovin, and C. Cremer, "Saturated Patterned Excitation Microscopy—A Concept for Optical Resolution Improvement," *J. Opt. Soc. Am. A,* Vol. 19, 2002, pp. 1599–1609.

[9] Hofmann, M. et al., "Breaking the Diffraction Barrier in Fluorescence Microscopy at Low Light Intensities by Using Reversibly Photoswitchable Proteins," *Proc. Nat. Acad. Sci.,* Vol. 102, 2005, pp. 17565–17569.

[10] Betzig, E. et al., "Imaging Intracellular Fluorescent Proteins at Nanometer Resolution," *Science,* Vol. 313, 2006, pp. 1642–1645.

[11] Hess, S. T., T. P. K. Girirajan, and M. D. Masony, "Ultra-High Resolution Imaging by Fluorescence Photoactivation Localization Microscopy," *Biophys. J.,* Vol. 91, 2006, pp. 4258–4272.

[12] Rust, M. J., M. Bates, and X. Zhuang, "Sub-Diffraction-Limit Imaging by Stochastic Optical Reconstruction Microscopy (STORM)," *Nat. Methods,* Vol. 3, 2006, p. 793.

[13] Hollars, C. W., and R. C. Dunn, "Probing Single Molecule Orientations in Model Lipid Membranes with Near-Field Scanning Optical Microscopy," *J. Chem. Phys.,* Vol. 112, 2000, pp. 7822–7830.

[14] Hecht, B. et al., "Facts and Artifacts in Near-Field Optical Microscopy," *J. Appl. Phys.,* Vol. 81, 1997, pp. 2492–2498.

[15] Trabesinger, W. et a., "Single-Molecule Near-Field Optical Energy Transfer Microscopy," *Appl. Phys. Lett.,* Vol. 81, 2002, pp. 2118–2120.

[16] Hu, D. et al., "Correlated Topographic and Spectroscopic Imaging Beyond Diffraction Limit by Atomic Force Microscopy Metallic Tip-Enhanced Near-Field Fluorescence Lifetime Microscopy," *Rev. Sci. Inst.,* Vol. 74, 2003, pp. 3347–3355.

[17] Anger, P., P. Bharadwaj, and L. Novotny, "Enhancement and Quenching of Single-Molecule Fluorescence," *Phys. Rev. Lett.,* Vol. 96, 2006, Art. No. 113002.

[18] Goncalves, R. P. et al., "Two-Chamber AFM: Probing Membrane Proteins Separating Two Aqueous Compartments," *Nat. Meth.,* Vol. 3, 2006, pp. 1007–1012.

[19] Möller, C. et al., "Tapping-Mode Atomic Force Microscopy Produces Faithful High-Resolution Images of Protein Surfaces," *Biophys. J.,* Vol. 77, 1999, pp. 1150–1158.

[20] Schabert, F. A., C. Henn, and A. Engel, "Native *Escherichia coli* OmpF Porin Surfaces Probed by Atomic Force Microscopy," *Science,* Vol. 268, 1995, pp. 92–94.

[21] Scheuring S., and J. N. Sturgis, "Chromatic Adaptation of Photosynthetic Membranes," *Science,* Vol. 309, 2005, pp. 484-487.

[22] Gerton, J. M. et al., "Tip-Enhanced Fluorescence Microscopy at 10 Nanometer Resolution," *Phys. Rev. Lett.,* Vol. 93, 2004, Art. No. 180801.

[23] Novotny, L., R. X. Bian, and X. S. Xie, "Theory of Nanometric Optical Tweezers," *Phys. Rev. Lett.,* Vol. 79, 1997, pp. 645–648.

[24] Novotny, L. et al., "Longitudinal Field Modes Probed by Single Molecules," *Phys. Rev. Lett.,* Vol. 86, 2001, pp. 5251–5254.

[25] Dorn, R., S. Quabis, and G. Leuchs, "Sharper Focus for a Radially Polarized Light Beam," *Phys. Rev. Lett.,* Vol. 91, 2003, Art. No. 233901.

[26] Klimov, V. I., "Optical Nonlinearities and Ultrafast Carrier Dynamics in Semiconductor Nanocrystals," *J. Phys. Chem. B,* Vol. 104, 2000, pp. 6112–6123.

[27] Ebenstein, Y., T. Mokari, and U. Banin, "Fluorescence Quantum Yield of CdSe/ZnS Nanocrystals Investigated by Correlated Atomic-Force and Single-Particle Fluorescence Microscopy," *Appl. Phys. Lett.,* Vol. 80, 2002, pp. 4033–4035.

[28] Quabis, A. et al., "Focusing Light to a Tighter Spot," *Opt. Commun.,* Vol. 179, 2000, pp. 1–7.

[29] Ma, Z. et al., "Fluorescence Near-Field Microscopy of DNA at Sub-10 nm Resolution," *Phys. Rev. Lett.,* Vol. 97, 2006, Art. No. 260801.

[30] Xie, C. et al., "Tip-Enhanced Fluorescence Microscopy of High-Density Samples," *Appl. Phys. Lett.,* Vol. 89, 2006, Art. No. 143117.

[31] Knoll, B., and F. Keilmann, "Enhanced Dielectric Contrast in Scattering-Type Scanning Near-Field Optical Microscopy," *Opt. Commun.,* Vol. 182, 2000, pp. 321–328.

[32] Hillenbrand, R., B. Knoll, and F. Keilmann, "Pure Optical Contrast in Scattering-Type Scanning Near-Field Microscopy," *Journal of Microscopy,* Vol. 202, 2000, pp. 77–83.

[33] Gucciardi, P. G., G. Bachelier, and M. Allegrini, "Far-Field Background Suppression in Tip-Modulated Apertureless Near-Field Optical Microscopy," *J. Appl. Phys.,* Vol. 99, 2006, Art. No. 124309.

[34] Keilmann F., and R. Hillenbrand, "Near-Field Microscopy by Elastic Light Scattering from a Tip," *Phil. Trans. R. Soc. A,* Vol. 362, 2004, pp. 787–805.

[35] Lo, Y. L., and C. H. Chuang, "Analytical Analysis of Modulated Signal in Apertureless Scanning Near-Field Optical Microscopy," *Opt. Express,* Vol. 15, 2007, pp. 15782–15796.

[36] Ebenstein, Y. et al., "Interaction of Scanning Probes with Semiconductor Nanocrystals; Physical Mechanism and Basis for Near-Field Optical Imaging," *J. Phys. Chem. A,* Vol. 110, 2006, pp. 8297–8303.

[37] Strutt, J. W., "On the Resultant of a Large Number of Vibrations of the Same Pitch and of Arbitrary Phase," *Philosophical Magazine,* Vol. X, 1880, pp. 73–78.

[38] Zenhausern, F., Y. Martin, and H. K. Wickramasinghe, "Scanning Interferometric Apertureless Microscopy: Optical Imaging at 10 Angstrom Resolution," *Science,* Vol. 269, 1995, pp. 1083–1085.

[39] Knoll, B., and F. Keilmann, "Near-Field Probing of Vibrational Absorption for Chemical Microscopy," *Nature,* vol. 399, 1999, pp. 134–137.

[40] Bouhelier, A. et al., "Near-Field Second-Harmonic Generation Induced by Local Field Enhancement," *Phys. Rev. Lett.,* Vol. 90, 2003, Art. No. 013903.

[41] Zimmerman, S. B., "The Three-Dimensional Structure of DNA," *Annu. Rev. Biochem.,* Vol. 51, 1982, pp. 395–427.

[42] X.-J. Lu and W. K. Olson, "3DNA: A Software Package for the Analysis, Rebuilding and Visualization of Three-Dimensional Nucleic Acid Structures," *Nucl. Acids Res.,* Vol. 31, 2003, pp. 5108–5121.

CHAPTER 13

Tip-Enhanced Optical Microscopy

Huihong Qian, Neil Anderson, Carsten Georgi, Lukas Novotny, and Achim Hartschuh

13.1 Introduction

The general aim of scanning near-field microscopy (SNOM) is to extend the spatial optical resolution beyond the diffraction limit [1, 2]. In this chapter, we discuss the use of tip-enhanced microscopy [3] in which locally enhanced fields at laser-illuminated metal structures are used to increase the spectroscopic response of the system studied within a small sample volume [4–9]. The versatility of the technique allows the study of a variety of spectroscopic signals, including local fluorescence or Raman spectra, as well as time-resolved measurements such as fluorescence transients.

The second section of this chapter contains a brief theoretical description of electric field enhancement at a metal tip. Using this information, the experimental requirements and expected properties of the fields are discussed. In the third section, the general experimental setup is introduced. In the following two sections, applications of tip-enhanced spectroscopy to nanotubes are demonstrated.

13.2 Field-Enhancement at a Metal Tip

Field enhancement near nanoscale metal structures plays a central role for optical phenomena such as surface-enhanced Raman scattering (SERS), second harmonic generation (SHG), and near-field microscopy. The enhancement originates from a combination of the electrostatic lightning rod effect, which is due to the geometric singularity of sharply pointed structures, and localized surface plasmon (LSP) resonances that depend sensitively on the excitation wavelength. The incident light drives the free electrons in the metal along the direction of polarization. While the charge density is zero inside the metal at any instant of time, charges accumulate on the surface of the metal. When the incident polarization is perpendicular to the tip axis, diametrically opposed points on the tip surface have opposite charges. As a consequence, the foremost end of the tip remains uncharged and no field enhancement is achieved. On the other hand, when the incident polarization is parallel to the tip axis, the induced surface charge density is almost rotationally symmetric and has the highest amplitude at the end of the tip [10–12].

The calculated field distribution $\left[|E_{local}(\mathbf{r},\omega)|^2\right]$ within a plane parallel to the tip axis near a sharp gold tip located above a glass substrate and irradiated by an on-axis focused HG_{10} laser mode is presented in Figure 13.1(a). The figure demonstrates that the enhanced field is confined to the tip apex (diameter 20 nm) in all three dimensions. Thus, the illuminated tip represents a nanoscale optical probe. The

maximum enhancement of the electric field intensity $M = |E_{local}(\mathbf{r},\omega)|^2/|E_{in}(\mathbf{r},\omega)|^2$ calculated for a solid gold tip with a diameter of 10 nm at an excitation wavelength of 830 nm is around 250.

To establish a strong field enhancement at the tip, the electric field of the exciting laser beam needs to be polarized along the tip axis. The influence of tip shape and material on the field enhancement has been discussed in a series of publications with the aim to find the optimum tip [12–14].

Since Raman scattering and photoluminescence (PL) are distinct optical processes involving different electronic states of the sample material with different degree of coherence, the enhancement effects for both signals are expected to vary. A brief discussion of the enhancement mechanisms is given at the beginning of Sections 13.4 and 5.

13.3 Experimental Setup

The experimental setup is based on an inverted optical microscope with an *x,y* scan stage for raster-scanning a transparent sample [see Figure 13.1(b)]. As the light source in the Raman scattering and PL experiments presented in the following, we used a HeNe laser operating at 633 nm. The laser beam is reflected by a dichroic beam splitter and focused by a high numerical aperture (NA) objective (1.4 NA) on the sample surface. A sharp gold or silver tip is positioned in the focus of the beam and maintained above the sample surface at a distance of ≈ 2 nm by means of a sensitive shear-force feedback mechanism [15]. The optical signal is collected with the same objective, transmitted by the beam splitter, and filtered by a long or band pass filter to remove the fundamental laser light. The signal is detected by a combination of a spectrograph and a cooled CCD or by a single-photon counting APD after spectral selection by a narrow band pass filter. A NFO image is established by raster-scanning the sample and simultaneously recording

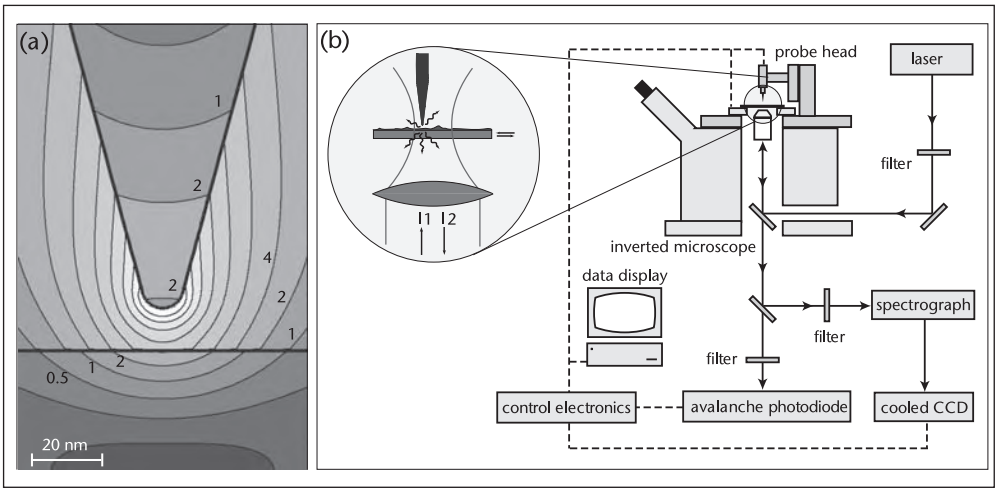

Figure 13.1 (a) Calculated field distribution $\left[|E_{local}(\mathbf{r},\omega)|^2\right]$ near a gold tip located above a glass substrate and irradiated by an on-axis focused HG_{10} laser mode. The contour lines scale by a factor of 2. (b) Schematic of the experimental setup. A sharp metal tip is scanned through a tightly focused laser beam. The optical signal is detected either by an APD or by a combination of a spectrograph and a CCD.

the optical signal. Sharp gold and silver tips are produced by electrochemical etching followed by FIB milling in the case of silver. SEM images of the tips are taken before and after scanning to ensure well-defined tip shapes.

To establish a strong field enhancement at the tip, the electric field of the exciting laser beam needs to be polarized along the tip axis (Section 13.2). To achieve this condition in our on-axis illumination scheme, we displace the tip from the center of the beam in the direction of polarization into one of the two L field lobes characteristic for strongly focused Gaussian beams or we use higher-order laser modes such as the HG_{10} mode or the radially polarized mode [10, 16] with strong L fields in the center of the focus.

13.4 Tip-Enhanced Raman Scattering

13.4.1 Introduction

Raman scattering probes the unique vibrational spectrum of the sample and directly reflects its chemical composition and molecular structure. A main drawback of Raman scattering is the extremely low scattering cross section that is typically 14 orders of magnitude smaller than the cross section of fluorescence in the case of organic molecules. SERS, induced by nanometer-sized metal structures, has been shown to provide enormous enhancement factors of up to 10^{15}, allowing for Raman spectroscopy even on the single molecule level [17]. The strongest contribution to SERS is of electromagnetic origin caused by the enhancement of the local field E^L with respect to the incident field E^0. For the present studies, we do not expect significant contributions from chemical effects based on charge-transfer processes between scatterer and metal or overlapping electron wave functions due to the large tip-sample separation of more than 1 nm.

The electromagnetic enhancement factor M_i is defined as the ratio between the measured Raman cross section in the presence and in the absence of the metal surface for each scatterer *i*. The integrated photon flux Φ_{Raman} is a linear function of the intensity of the incident laser light I at frequency ω_I and results from the sum of the Raman scattering cross sections σ_R^i of all scatterers within the detection volume.

$$\Phi_{Raman} = \frac{I_I}{\hbar\omega_I} \sum_{i=1}^{N} \sigma_R^i M_R^i \tag{13.1}$$

The electromagnetic enhancement M_i is caused by enhancement of both the incident field E^0 at ω_I and the scattered field E^0 at $\omega_I - \omega_\nu$ and can be expressed as the product with the total local electric field E^L

$$M_R = \left[\frac{E^L(\omega_I)}{E^0(\omega_I)}\right]^2 \left[\frac{E^L(\omega_I - \omega_\nu)}{E^0(\omega_I - \omega_\nu)}\right]^2 \approx \left[\frac{E^L(\omega_I)}{E^0(\omega_I)}\right]^4 \tag{13.2}$$

where we used $\omega_\nu \ll \omega_I$.

Enhancement factors are reported reaching up to 12 orders of magnitude for particular multiple particle configurations involving interstitial sites between particles or outside sharp surface protrusions [18]. For a single spherical particle, M_R is supposed to be much lower, in the range of 100 to 1000. Near-field Raman scattering induced by a laser-irradiated metal tip has been experimentally demonstrated by several groups [5, 7, 19–22].

13.4.2 Spatial Resolution, Field Localization, and Signal Enhancement

In this section, we present near-field Raman imaging and spectroscopy on single-walled carbon nanotubes (SWNTs). The major features of the method are demonstrated: high spatial resolution resulting from field localization and signal enhancement.

SWNTs are highly elongated, tubular graphitic molecules that have been the focus of intense interest due to a variety of potential technological applications. The unique properties of SWNTs arise from their particular 1-D structure that is directly linked to the characteristic Raman bands. Raman scattering of SWNTs has been studied intensively in the literature (e.g., [23, 24]), and Raman enhancements of up to 10^{12} have been reported for nanotubes in contact with fractal silver colloidal clusters [25].

In Figure 13.2(a), a near-field Raman image of SWNTs on glass is shown with the simultaneously acquired topography image of the same sample area in Figure 13.2(b). Raman images were acquired by detecting the intensity of the G band around 1600 cm^{-1} after laser excitation at 633 nm using a radially polarized laser mode while raster-scanning the sample. The spatial resolution can be determined from the width of the signals presented as line scans in Figures 13.2(c) and 13.2(d) to be about 20 nm. The sharpest images observed so far feature an optical resolution of 10 nm, limited by the tip diameter [21]. In general, the measured optical width is smaller than the topographic width by about a factor of 1.3 [21, 26]. While the topographic image of nanometers-sized objects will reproduce the tip shape, the fourth-order dependence of the Raman signal on the field enhancement will render steeper traces. (See Equation 13.2). The height of the observed SWNT is approximately 1 nm, as can be seen in Figure 13.2(d).

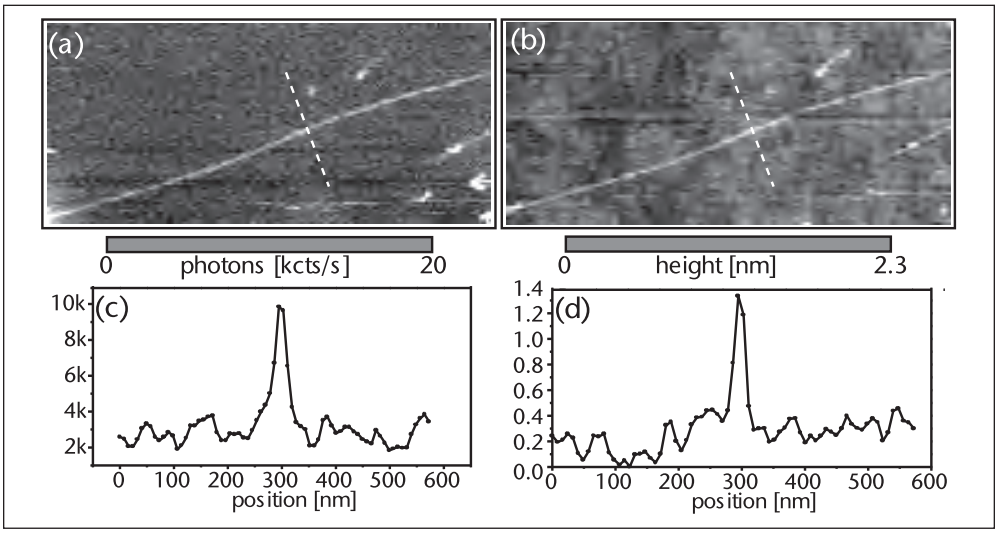

Figure 13.2 Simultaneous near-field Raman image (a) and topographic image (b) of SWNTs on glass. Scan area $2 \times 1\ \mu m^2$. The Raman image is acquired by detecting the intensity of the G band upon laser excitation at 633 nm. The dark regions in the topography image are caused by steps within the glass. (c) Cross section taken along the indicated dashed line in the Raman image. (d) Cross section taken along the indicated dashed line in the topographic image. The height of the individual nanotube is $\approx$ 1.0 nm. Vertical units are photon counts per second for (c) and nanometer for (d).

Raman spectra detected on top of a SWNT in the presence of the tip and without the tip are presented in Figure 13.3(a). The signal enhancement induced by the tip can be estimated by comparison of the integrated intensities of the observed Raman band. In the present example, the intensity of the G band of the SWNT between 1500 and 1650 cm^{-1} is approximately 12000 (background-subtracted). In absence of the tip, the signal is much weaker ($\leq$ 100). From Figure 13.3(a), it is clear that without the enhancement provided by the tip, the detection of the SWNT would have been impossible.

For an evaluation of the enhancement factor, the different areas probed by near-field and far-field components must be taken into account. The length of the SWNT (width $w \approx 1$ nm) is larger than the diameter of the focus ($f = 300$ nm), resulting in a probed area of approximately $f^*w = 1$ nm * 300 nm = 300 nm^2. A much smaller area is probed in the near-field [i.e., an area defined by the width of the near-field spot (15 nm) and the nanotube diameter ($\approx$ 1 nm)]. Normalizing the measured signals in Figure 13.3(a) with the ratio of the detected areas yields an enhancement factor of $M_R \approx 2400$. Since M scales approximately with the fourth power of the field enhancement, the locally enhanced field is roughly 7 times stronger than the incident field.

The optical resolution apparent in Figure 13.2 shows that the enhanced fields are laterally confined to the size of the metal tip. To demonstrate the confinement of the enhanced fields in the L direction, the tip is positioned above a nanotube and the Raman intensity is recorded as a function of tip-sample distance d [see Figure 13.3(b)]. According to Equation 13.2, the signal strength is expected to scale with the fourth power of the enhanced field. If we approximate the enhanced field by the field of a single dipole oriented along the tip axis, a distance dependence of d^{-12} is expected.

13.4.3 Mapping Molecular Junctions in Single-Walled Carbon Nanotubes

Determining whether a carbon nanotube is conducting or nonconducting is crucial when considering their suitability for electronic or photonic device applications.

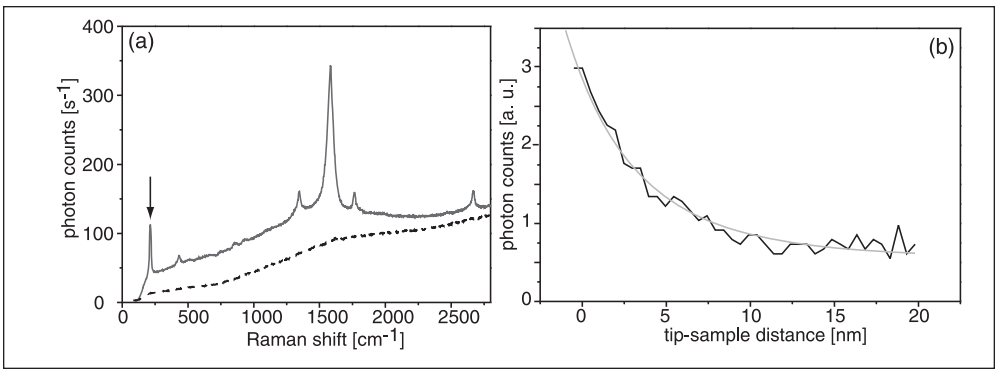

Figure 13.3 Tip-enhanced Raman spectra of SWNTs. (a) Spectra detected with tip on top of a SWNT (solid line) and with tip retracted by 2 μm (dashed line). The Raman signal of the radial breathing mode (RBM) is marked. Both spectra are on top of a broad background that is caused by scattering from the coverglass and the immersion oil (also detected in absence of SWNTs). (b) Dependence of the Raman scattering strength of the G band on the L separation between a single SWNT and the tip for small distances of less than 20 nm. The solid line is a model curve using a d^{-12} dependency.

Recent advances in our understanding of carbon nanotubes foresee potential application for specific types of nanotube configurations as nanoscale diodes and rectifiers [27–29]. Such configurations are known as intramolecular junctions (IMJs). An IMJ is formed through structural defects such as the formation of heptagon-pentagon pairs that facilitate the transition from one chirality, specified by the index pair (n,m), to a different chirality (n',m') [30]. Consequently, such a defect can give rise to metal-metal, metal-semiconducting, or semiconducting-semiconducting transitions. The electronic properties of IMJs have been studied previously from an experimental and theoretical perspective [27, 31, 32]. In this section, we reveal the utility of near-field Raman spectroscopy to probe molecular junction at the single nanotube level [33].

The Raman modes important in determining and studying the presence of IMJs in carbon nanotubes are, namely, the radial breathing mode (RBM), the defect-induced D band, and the tangential stretching G band. The ability to measure the Raman shift of a resonant RBM phonon (ν_{RBM})directly allows one to determine the diameter d_t and structure (n,m) of the carbon nanotube using the following relations [23]:

$$\nu_{RBM} = \frac{A}{d_t} \tag{13.3}$$

$$d_t = \frac{\sqrt{3}a_0}{\pi}\sqrt{n^2 + m^2 + 2nm}$$

where $A = 248\ \text{cm}^{-1}$, a_0 is the lattice constant of graphite ($a_0 \simeq 0.144$ nm), and (n,m) define the number of steps along the graphene basis vectors. A determination of whether a carbon nanotube is semiconducting or metallic based on detecting resonant RBM phonons can be supported by analyzing the frequency and lineshape of the G band. Semiconducting carbon nanotubes have a characteristic two-peak structure, where the lower frequency component is associated with vibrations along the circumferential direction and the higher frequency component is attributed to vibrations along the nanotube axis [34]. The G band in metallic SWNTs exhibits a Breit-Wigner-Fano feature on the low-energy side of a single Lorentzian peak.

Defects in carbon nanotubes, such as changes in the carbon-carbon bonding and sidewall vacancies, are characterized by the presence of a vibrational line centered around 1300 cm^{-1} [35]. For a change in structure to occur, a transformation in the carbon-carbon bonding in the nanotube sidewall must take place. Such structural changes can be caused by the formation of a pentagon-heptagon defect [36]. Therefore, localized disorder-induced (D-band) Raman scattering also should be observed at the junction region. We define an IMJ as a structural change in the nanotube sidewall that gives rise to a local perturbation of phonon modes. The spatial extent over which a phonon is affected depends on the nature of the phonon mode and the nature of the defect.

Figures 13.4(a) and 13.4(b) show the near-field Raman and topographic (AFM) images of a spatially isolated SWNT resting on a transparent glass substrate. The image contrast in (a) is provided by spectrally integrating over the G band. Shown in Figure 13.4(c) are a series of near-field Raman spectra acquired from a spatially isolated SWNT. The local Raman spectrum was acquired by positioning the gold

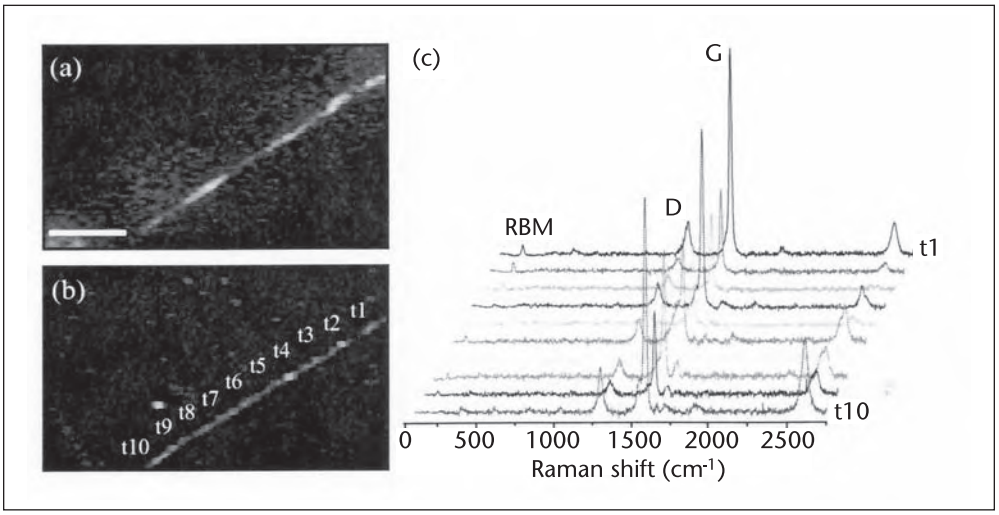

Figure 13.4 Near-field Raman imaging and spectroscopy. Near-field Raman image (G band) (a) and topographic (AFM) (b) images of a spatially isolated SWNT. Series of near-field Raman spectra acquired from a spatially isolated SWNT. The spectra are listed as t1-t10, corresponding to the location along the SWNT where the local Raman spectrum was measured, as shown in (b). The scale bar in (a) denotes 200 nm.

tip directly above the carbon nanotube at the locations indicated. Over the upper portion of the nanotube, a RBM frequency of $\nu^{sc}_{RBM} \sim 251\ \mathrm{cm}^{-1}$ was measured. Using Equation 13.3, the nanotube diameter was determined to be 0.99 nm and can be assigned to a semiconducting SWNT with diameter $d^{sc}_t \sim 0.94$ nm and structure $(n,m) = (10,3)$; $E_{ii} = 1.98$ eV [35]. Over the lower portion of the same SWNT, a RBM frequency of $\nu^{m}_{RBM} \simeq 192\ \mathrm{cm}^{-1}$ was detected. Using Equations 13.3, the nanotube diameter was calculated to be 1.30 nm and can be assigned to a metallic SWNT with diameter $d^{m}_t \simeq 1.25$ nm and structure $(n,m) = (12,6)$ with $E_{ii} = 1.93$ eV or $(n,m) = (13,4)$ with $E_{ii} = 1.94$ eV [35]. (The error associated with the experimentally determined phonon frequencies is $\sim 3\ \mathrm{cm}^{-1}$). These assignments are based on the requirement that the RBM frequencies be resonant or near-resonant with the excitation energy of $E_{laser} = 1.96$ eV [35].

Figure 13.5(a) reveals in detail the spectral evolution from the RBM phonon characteristic of a semiconducting nanotube [$\nu^{sc}_{RBM} = 251\ \mathrm{cm}^{-1}$; $(n,m) = (10,3)$] into a RBM phonon characteristic of a metallic nanotube $\nu^{m}_{RBM} \sim 191\ \mathrm{cm}^{-1}$; $(n,m) = (12,6)$ or $(13,4)$]. As the gold tip was positioned along the SWNT, the intensity of the RBM phonon along the semiconducting portion I^{sc}_{RBM} decreases, then disappears. On the basis of the measured resonant RBM phonon frequencies, we determine, in that we can spatially locate a node in the RBM intensity, that the IMJ affects the RBM phonons of the SWNT on a length scale of ~ 100 nm. That is, the length of the transition region is greater than the spatial resolution ($Res. = 40$ nm) of the present experiment (i.e., $L_{trans} > Res.$). After the junction, a second RBM phonon at 191 cm^{-1}, resonant with the excitation source, is detected, revealing that this portion of the SWNT is metallic. Once again, the Raman intensity I^{sc}_{RBM} decreases along the SWNT and disappears completely at the nanotube end (t10), indicating that a significant structural change has occurred that no longer supports a RBM phonon in resonance with our excitation source.

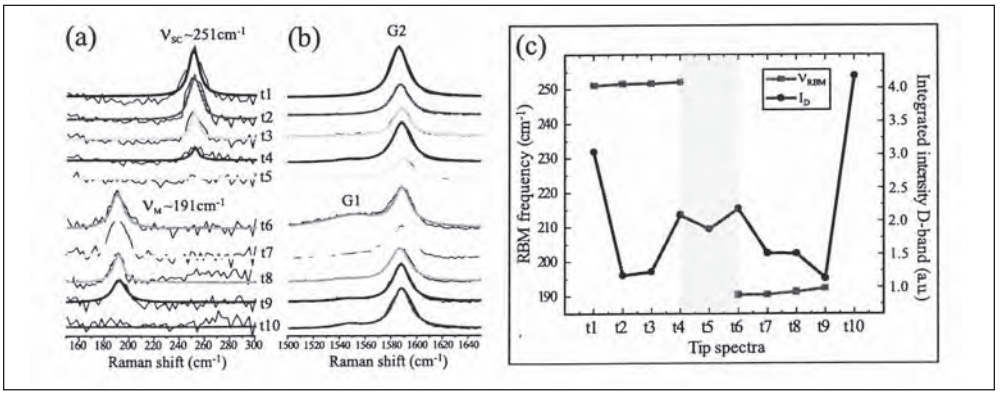

Figure 13.5 Probing a molecular junction using near-field Raman spectroscopy. By placing the gold tip directly above the SWNT, a change in RBM phonon frequency (a) and G-band lineshape (b) can be mapped along the nanotube. The resultant shift in RBM phonon frequency and G-band lineshape reveal that a structural change from semiconducting to metallic SWNT has occurred. Defect-induced (D-band) Raman scattering localized at the intramolecular junction is revealed by plotting the RBM frequency and integrated D-band Raman intensity as a function of position along the carbon nanotube (c). The plot reveals a direct correlation between increased D-band scattering and the spatial location of the transition region L_{trans}, defined by the absence of a resonant RBM phonon.

In addition to changes from a semiconducting to a metallic structure based on resonant RBM frequencies, a change in the frequency and lineshape of the G band is observed. The evolution of the G-band lineshape along the nanotube is shown in Figure 13.5(b). Over the upper portion of the nanotube, a single Lorentzian is observed, indicating that this portion of the nanotube is semiconducting. At the transition region (t5), a low-energy peak ($G1 \sim 1550$ cm^{-1}) appears, indicative of a metallic nanotube, and is present along the lower section (t6-t10). The presentation of G-band spectra clearly reveals the transition from a lineshape characteristic of a semiconducting to metallic structure and supports the existence of an IMJ based on changes in the measured resonant RBM frequencies.

Within our spectral detection window 700–1000 nm, no PL localized to the semiconducting portion of the SWNT was observed. The study of the near-field PL properties of carbon nanotubes is addressed in the following section.

It is known that the arrangement of carbon atoms in the nanotube sidewall must deviate from the typical hexagonal structure for IMJs to form in SWNTs. One possible arrangement is the formation of a pentagon-heptagon defect [36]. Therefore, in addition to detecting a structural change based upon measuring variations in resonant RBM frequencies and G-band lineshape, increased defect-induced (D-band) Raman scattering, localized to the transition region (L_{trans}), also should be detected. To reveal the change in D-band scattering that occurs over the spatial extent of the junction region L_{trans}, Figure 13.5(c) presents a plot displaying the variation in integrated Raman intensity of the defect-induced Raman peak and RBM phonon frequency as a function of position along the SWNT shown in (a) and (b). (The integrated D-band intensity was calculated with an accuracy of $r^2 \simeq 0.96$.). Figure 13.5(c) clearly reveals a pronounced increase in D-band scattering over the region (L_{trans}) [indicated by the dashed box in Figure 13.5(b)] bridging the semiconducting and metallic portions of the SWNT. That is, $L_{trans} \sim L_D$ (i.e. $L_D \sim 100$ nm).

In summary, a molecular junction that was imaged based on mapping two resonant RBM phonon frequencies along spatially isolated SWNTs has been

demonstrated using near-field Raman spectroscopy. The use of carbon nanotubes as a model system highlights the intrinsic strength of near-field-based techniques to probe the chemical composition of nanostructures. In the following section, near-field studies of the luminescent states in carbon nanotubes reveal new insights into the excitonic character of 1-D materials.

13.5 Tip-Enhanced Photoluminescence

13.5.1 Introduction

In general, tip-enhanced NFO spectroscopy makes use of the strongly enhanced electric field components close to a sharp metal tip under laser illumination. However, the resulting enhancement for Raman scattering and PL is expected to be different. For Raman scattering, the electromagnetic enhancement of the signal is caused by enhancement of both the incident field E_0 and the scattered field as described by Equation 13.2. On the other hand, the PL intensity depends on the excitation rate and the quantum yield η denoting the fraction of transitions from excited state to ground state that give rise to an emitted photon. The quantum yield is expressed in terms of the radiative rate k_r and the nonradiative rate k_{nr} through $\eta = k_r/(k_r + k_{nr})$. Accordingly, the PL enhancement due to the presence of the metal tip can be written as follows:

$$M_{PL} \approx (E_{local}/E_0)^2(\eta_{local}/\eta_0) \tag{13.4}$$

Here we have assumed that the system is excited far from saturation and we have ignored any vectorial field projections on the transition dipole axis. In terms of the Raman enhancement, the PL enhancement can be written as follows:

$$M_{PL} \approx (M_R)^{1/2}(\eta_{local}/\eta_0) \tag{13.5}$$

Because of the small separation between emitter and metal tip (about 1–2 nm) nonradiative transfer of energy from the electronically excited molecule to the metal followed by nonradiative dissipation has to be taken into account. This process represents an additional nonradiative relaxation pathway and reduces the number of detected fluorescence photons. While the theory of energy transfer between molecules and flat metal interfaces is well understood in the framework of phenomenological classical theory [40, 41], nanometer-sized objects are more difficult to describe.

Tip-induced radiative rate enhancement and quenching has been studied in literature theoretically [42–44]. Experiments on model systems formed by single molecules and spherical metal particles revealed a complex distance-dependent interplay between competing enhancement and quenching processes [45–47]. Small cone angles in tip-shaped metal structure are expected to reduce energy dissipation as compared to spherical particles [44].

13.5.2 Near-Field Photoluminescence Imaging

Semiconducting SWNTs are photoluminescent quasi-1-D systems with great promise for applications in photonics, optoelectronics, and nanoelectronics. PL measurements on single nanotubes using confocal microscopy revealed variations of

emission energies and excited state decay times from nanotube to nanotube [48, 49], indicating a significant role of defects and environmental perturbations. Similarly, these localized perturbations can be expected to limit the spatial extent of delocalized excitonic states along a nanotube and thus reduce the nanotube luminescence efficiency that is reported to be very low—around 10^{-3} to 10^{-4} [50, 51]. Near-field is ideally suited for visualizing and studying local fluctuations along single nanotubes [52].

The sample studied in our near-field PL experiments were made by spin-coating chirality-enriched, DNA-wrapped CoMoCAT SWNTs on a freshly cleaved thin layer of mica glued on a glass cover slide [39]. The mica layer was positively charged by Mg^{2+} ions to increase the surface adhesion of the negatively charged DNA site of the hybrid. The observed topographic height of the nanotubes is typically around 2 nm as predicted for single DNA-wrapped nanotubes [53].

As the excitation source, we used a HeNe laser operating at 633 nm that was focused on the sample by a 1.4 NA immersion oil objective after attenuation to 5 μW. Figure 13.6(a) shows the PL image of two nanotubes obtained by the light being detected by an APD after the spectral filtering using a 860 nm long pass filter. The PL signals are extended along the entire nanotubes, although with varying intensity. The image features very high spatial resolution of 10 nm given by FWHM [see in the cross section (b) taken along the dashed line in (a)].

The localized and very intense PL of the nanotube on the right indicates the presence of highly localized excited states. Localization could result from luminescent trap states formed by lower-lying excited states related to charged defects or local environmental perturbations. This also would explain the weak PL points observed along the left nanotube. An IMJ as studied in Section 13.4.3 also can turn a luminescent nanotube into a nonluminescent one [21, 38].

Figure 13.7 shows simultaneously obtained topography (a) and near-field PL images (b, c) of DNA-wrapped nanotubes from a sample area of 380 * 380 nm^2 upon laser excitation at 633 nm using 5 μW. The height observed in the cross section in Figure 13.7(d) taken along the dashed line in Figure 13.7(a) shows that both structures are single DNA-wrapped nanotubes. The nonuniform height along the

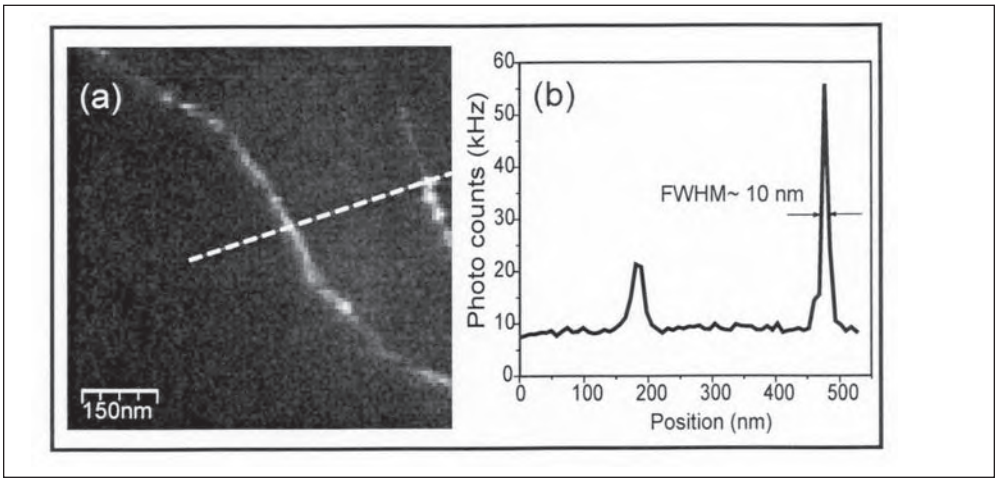

Figure 13.6 Near-field PL (a) image of DNA-wrapped single-walled carbon nanotubes on mica and cross section (b) taken along the dashed like in (a). The FWHM shows a spatial resolution of $\approx$ 10 nm.

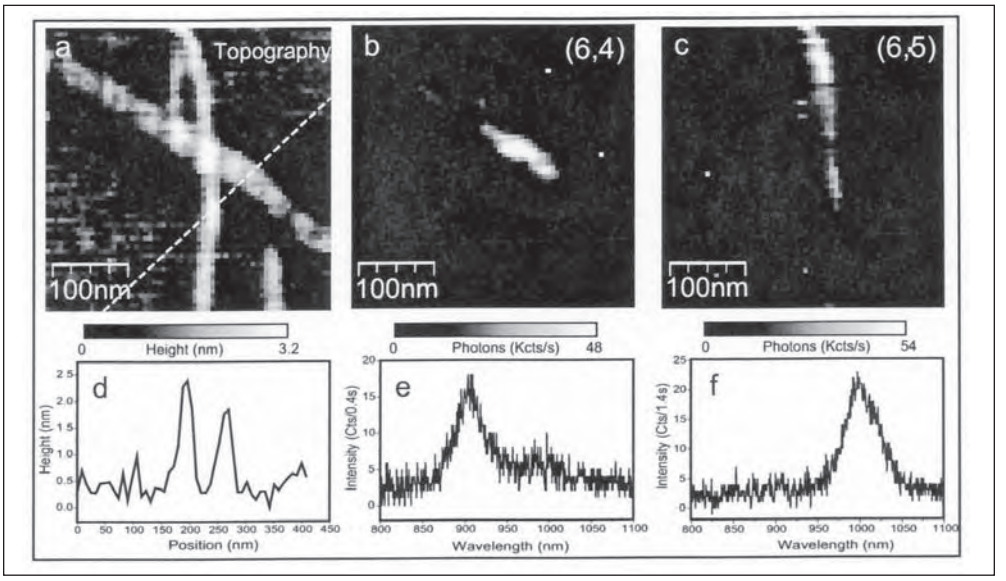

Figure 13.7 Simultaneously detected topography of DNA-wrapped SWNTs (a), near-field PL images from (6,4) nanotubes detected in the range from 875–930 nm (b), and (6,5) detected from 970–1025 nm (c). The scan area is 380 * 380 nm^2. (b) and (c) are obtained by measuring spectrum at each pixel and represent the integrated intensity within selected spectral windows. The acquisition time per spectrum is 400 ms. Cross section (d) taken along the dashed line in (a) shows the height of DNA-wrapped nanotubes. (e) and (f) are spectra from one of the pixels in image (b) and (c), showing the emission signals of nanotubes with different chiralities.

nanotube will be caused by segmented DNA wrapping. Figures 13.7(b) and 13.7(c) are 64 * 64 pixel PL images derived from spectra taken at each pixel. The nanotubes are optically separated and identified by integrating the emission intensity within selected spectral windows. Figure 13.7(b) displays the integrated intensity from 875 nm to 930 nm, corresponding to the PL of (6,4) nanotube, as shown in the spectrum in Figure 13.7(e). Figure 13.7(c) displays the integrated intensity from 970 nm to 1025 nm, corresponding to the PL of (6,5) nanotube, as shown in the spectrum in Figure 13.7(f). The red shift compared to the 873 nm emission energy from (6,4) nanotube and 975 nm from (6,5) nm [37] is induced by the increase of dielectric constant ε from the DNA wrapping. The lower right nanotube in the topography, which does not appear in both PL images, can be either a metallic nanotube or a nanotube luminescent at energy lower than 1050 nm beyond our detector range.

In both presented measurements, no near-field Raman signal was observed because of nonresonant excitation and the very lower excitation power. Simultaneous near-field Raman and PL imaging is possible, as has been shown in our previous work. Typically, the observed signal enhancement is weaker in the case of Raman scattering. We quantified the enhancement of PL and Raman signals from the same nanotubes in [52]. Equations 13.4 and 13.5 indicate that $M_{PL} > M_R$ is possible only if $(\eta_{local}/\eta_0) \geq 1$. Because the quantum yield cannot be larger than unity, $M_{PL} > M_R$ requires an unperturbed (intrinsic, in the absence of the tip) quantum yield that is very small (i.e., $\eta_0 \leq 1$as in the case of nanotubes). Since the nonradiative rate k_{nr} is not expected to be decreased by the tip, an increased quantum yield requires the enhancement of the radiative rate k_r in the presence of the metal

tip [42]. In general, tip-enhanced fluorescence microscopy (TEFM) is best suited to study weak emitters [54].

13.6 Outlook

The spatial resolution achieved in tip-enhanced near-field microscopy and spectroscopy is generally superior to aperture-based techniques. The field confinement is defined by the sharpness of the tip, and the field distribution is reasonably well approximated by the field of a dipole oriented in the direction of tip axis and located in the center of the tip apex. It is likely that the tip enhancement technique will provide resolutions better than 10 nm, a length scale comparable to biological proteins and semiconductor quantum structures. To become a routine technique, the field enhancement needs to be improved using favorable tip materials and geometries. In analogy to antenna theory, a finite tip size (e.g., $\lambda/2$) is expected to provide much higher enhancement. It is also desirable to reduce the far-field interaction area with the sample surface and to combine, for example, an aperture near-field probe with a finite-sized metal tip [55]. To clarify the trade-off between enhancement and quenching, dedicated experiments on single molecules are necessary. These studies require the simultaneous measurements of fluorescence yield and lifetime and the investigation of orientational and polarization properties [56]. Applied to Raman scattering, the tip-enhancement technique has great potential for clarifying open questions in SERS.

Acknowledgments

The authors want to acknowledge Mark Hersam for sample support and Nicolai Hartmann for help with sample preparation. This work was funded by the National Science Foundation (grant CHE-0454704), the U.S. Department of Energy (grant DE-FG02-05ER46207), the Deutsche Forschungsgemeinschaft (DFG-HA4405/3-1), and the Nanosystems Initiative Munich (NIM). N.A. acknowledges financial support from the Horton Fellowship, Laboratory of Laser Energetics, University of Rochester.

References

[1] Pohl, D. W., W. Denk, and M. Lanz., "Optical Stethoscopy: Image Recording with Resolution $\lambda/20$," *Appl. Phys. Lett.*, Vol. 44, 1984, pp. 651–653.

[2] Lewis, A. et al., "Development of a 500 Å Resolution Light Microscope," *Ultramicroscopy*, Vol. 13, 1984, pp. 227–231.

[3] Wessel, J., "Surface-Enhanced Optical Microscopy," *J. Opt. Soc. Am. B*, Vol. 2, 1985, pp. 1538–1541.

[4] Sánchez, E. J., L. Novotny, and X. S. Xie, "Near-Field Fluorescence Microscopy Based on Two-Photon Excitation with Metal Tips," *Phys. Rev. Lett.*, Vol. 82, 1999, pp. 4014–4017.

[5] Stöckle, R. M. et al., "Nanoscale Chemical Analysis by Tip-Enhanced Raman Spectroscopy," *Chem. Phys. Lett.*, Vol. 318, 2000, pp. 131–136.

[6] Hayazawa, N. et al., "Near-Field Raman Scattering Enhanced by a Metallized Tip," *Chem. Phys. Lett.*, Vol. 335, 2001, pp. 369–374.

[7] Hartschuh, A. et al., "High-Resolution Near-Field Raman Microscopy of Single-Walled Carbon Nanotubes," *Phys. Rev. Lett.*, Vol. 90, 2003, Art. No. 095503.

[8] Hartschuh, A. et al., "Tip-Enhanced Optical Spectroscopy," *Phil. Trans. R. Soc. Lond. A*, Vol. 362, 2004, pp. 807–819.

[9] Kawata, S., and V. M. Shalaev, eds., "Tip Enhancement," in *Advances in Nano-Optics and Nano-Photonics,* Amsterdam: Elsevier, 2007.

[10] Novotny, L., E. J. Sánchez, and X. S. Xie, "Near-Field Optical Imaging Using Metal Tips by Higher-Order Hermite-Gaussian Beams," *Ultramicroscopy*, Vol. 71, 1998, pp. 21–29.

[11] Larsen, R. E., and H. Metiu, "Resolution and Polarization in Apertureless Near-Field Microscopy," *J. Chem. Phys.*, Vol. 114, 2001, pp. 6851–6860.

[12] Martin, Y. C., H. F. Hamann, and H. K. Wickramasinghe, "Strength of the Electric Field in Apertureless Near-Field Optical Microscopy," *J. Appl. Phys.*, Vol. 89, 2001, pp. 5774–5778.

[13] Krug, J. T. I., E. J. Sánchez, and X. S. Xie, "Design of Near-Field Probes with Optimal Field Enhancement by Finite Difference Time Domain Electromagnetic Simulation," *J. Chem. Phys.*, Vol. 116, 2002, pp. 10895–10901.

[14] Novotny, L., "Effective Wavelength Scaling for Optical Antennas," *Phys. Rev. Lett.*, Vol. 98, 2007, Art. No. 266802.

[15] Karrai, K., and R. D. Grober, "Piezoelectric Tip-Sample Distance Control for Near Field Optical Microscopes," *Appl. Phys. Lett.*, Vol. 66, 1995, pp. 1842–1844.

[16] Quabis, S. et al., "Focusing Light to a Tighter Spot," *Opt. Comm.*, Vol. 179, 2000, pp. 1–7.

[17] Nie, S., and S. R. Emory, "Probing Single Molecules and Single Nanoparticles by Surface-Enhanced Raman Scattering," *Science*, Vol. 275, 1997, pp. 1102–1106.

[18] Xu, H. et al., "Electromagnetic Contributions to Single-Molecule Sensitivity in Surface-Enhanced Raman Scattering," *Phys. Rev. E*, Vol. 62, 2000, pp. 4318–4324.

[19] Nieman, L. T., G. M. Krampert, and R. E. Martinez, "An Apertureless Near-Field Scanning Optical Microscope and Its Application to Surface-Enhanced Raman Spectroscopy and Multiphoton Fluorescence Imaging," *Rev. Sci. Instrum.*, Vol. 72, 2001, pp. 1691–1699.

[20] Hayazawa N. et al., "Near-Field Raman Imaging of Organic Molecules by an Apertureless Metallic Probe Scanning Optical Microscope," *J. Chem. Phys.*, Vol. 117, 2002, p. 1296.

[21] Anderson, N., A. Hartschuh, and L. Novotny, "Nanoscale Vibrational Analysis of Single-Walled Carbon Nanotubes," *J. Am. Chem. Soc.*, Vol. 127, 2005, pp. 2533–2537.

[22] Pettinger, B. et al., "Tip-Enhanced Raman Spectroscopy (TERS) of Malachite Green Isothiocyanate at Au(111): Bleaching Behavior Under the Influence of High Electromagnetic Fields," *J. Raman Spectrosc.*, Vol. 36, 2005, pp. 541–550.

[23] Jorio, A. et al., "Structural (n,m) Determination of Isolated Single-Wall Carbon Nanotubes by Resonant Raman Scattering," *Phys. Rev. Lett.*, Vol. 86, 2001, pp. 1118–1121.

[24] Duesberg, G. S. et al., "Polarized Raman Spectroscopy on Isolated Single-Wall Carbon Nanotubes," *Phys. Rev. Lett.*, Vol. 85, 2000, pp. 5436–5439.

[25] Kneipp, K. et al., "Surface-Enhanced and Normal Stokes and Anti-Stokes Raman Scattering of Single-Walled Carbon Nanotubes," *Phys. Rev. Lett.*, Vol. 84, 2000, pp. 3470–3473.

[26] Bouhelier, A. et al., "Near-Field Second-Harmonic Generation Induced by Local Field Enhancement," *Phys. Rev. Lett.*, Vol. 90, 2003, Art. No. 013903.

[27] Yao, Z. et al., "Carbon Nanotube Intramolecular Junctions," *Nature*, Vol. 402, 1999, pp. 273–276.

[28] McEuen, P., "Nanotechnology Carbon-Based Electronics," *Nature*, Vol. 393, 1998, pp. 15–17.

[29] Baughman, R. H., A. A. Zakhidov, and W. A. de Heer, "Carbon Nanotubes-The Route Toward Applications," *Science*, Vol. 297, 2002, pp. 787–792.

[30] Iijima, S., T. Ichihashi, and Y. Ando, "Pentagons, Heptagons and Negative Curvature in Graphite Microtubule Growth," *Nature*, Vol. 356, 1992, pp. 776–778.

[31] Chico, L. et al., "Pure Carbon Nanoscale Devices: Nanotube Heterojunctions," *Phys. Rev. Lett.*, Vol. 76, 1996, pp. 971–974.

[32] Li, Y., U. Ravaioli, and S. V. Rotkin, "Metal-Semiconductor Transition and Fermi Velocity Renormalization in Metallic Carbon Nanotubes," *Phys. Rev. B.*, Vol. 73, 2006, Art. No. 035415.

[33] Anderson, N., A. Hartschuh, and L. Novotny, "Chirality Changes in Carbon Nanotubes Studied with Near-Field Raman Spectroscopy," *Nano Lett.*, Vol. 7, 2007, pp. 577–582.
[34] Dresselhaus, M. S. et al., "Raman Spectroscopy on Isolated Single Wall Carbon Nanotubes," *Carbon*, Vol. 40, 2002, pp. 2043–2061.
[35] Maultszch, J. et al., "Radial Breathing Mode of Single-Walled Carbon Nanotubes: Optical Transition Energies and Chiral-Index Assignment," *Phys. Rev. B.*, Vol. 72, 2005, Art. No. 205438.
[36] Saito, R., G. Dresselhaus, and M. S. Dresselhaus, "Tunneling Conductance of Connected Carbon Nanotubes," *Phys. Rev. B.*, Vol. 53, 1996, pp. 2044–2050.
[37] Bachilo, S. M. et al., "Structure-Assigned Optical Spectra of Single-Walled Carbon Nanotubes," *Science*, Vol. 298, 2002, pp. 2361–2366.
[38] Doorn, S. K. et al., "Raman Spectral Imaging of a Carbon Nanotube Intramolecular Junction," *Phys. Rev. Lett.*, Vol. 94, 2005, Art. No. 016802.
[39] Arnold, M. S., S. I. Stupp, and M. C. Hersam, "Enrichment of Single-Walled Carbon Nanotubes by Diameter in Density Gradients," *Nano Lett.*, Vol. 5, 2005, pp. 713–718.
[40] Chance, R. R., A. Prock, and R. Silbey, "Lifetime of an Emitting Molecule Near a Partially Reflecting Surface," *J. Chem. Phys.*, Vol. 60, 1974, pp. 2744–2748.
[41] Barnes, W. L., "Fluorescence Near Interfaces: The Role of Photonic Mode Density," *J. Mod. Opt.*, Vol. 45, 1998, pp. 661–699.
[42] Issa, N. A., and R. Guckenberger, "Fluorescence Near Metal Tips: The Roles of Energy Transfer and Surface Plasmon Polaritons, *Opt. Express,*, Vol. 15, 2007, pp. 12131–12144.
[43] Thomas, M. et al., "Single-Molecule Spontaneous Emission Close to Absorbing Nanostructures," *Appl. Phys. Lett.*, Vol. 85, 2004, pp. 3863–3865.
[44] Rogobete, L. et al., "Design of Plasmonic Nanoantennae for Enhancing Spontaneous Emission," *Optics Letters*, Vol. 32, 2007, pp. 1623–1625.
[45] Anger, P., P. Bharadwaj, and L. Novotny, "Enhancement and Quenching of Single Molecule Fluorescence," *Phys. Rev. Lett.*, Vol. 96, 2006, Art. No. 113002.
[46] Kühn, S. et al., "Enhancement of Single Molecule Fluorescence Using a Gold Nanoparticle as an Optical Nano-antenna," *Phys. Rev. Lett.*, Vol. 97, 2006, Art. No. 017402.
[47] Bharadwaj, P., P. Anger, and L. Novotny, "Nanoplasmonic Enhancement of Single Molecule Fluorescence," *Nanotechnology*, Vol. 18. 2007, Art. No. 044017.
[48] Hartschuh, A. et al., "Simultaneous Fluorescence and Raman Scattering from Single Carbon Nanotubes," *Science*, Vol. 301, 2003, pp. 1354–1356.
[49] Hagen, A. et al., "Exponential Decay Lifetimes of Excitons in Individual Single-Walled Carbon Nanotubes," *Phys. Rev. Lett.*, Vol. 95, 2005, Art. No. 197401.
[50] Wang, F. et al., "Time-Resolved Fluorescence of Carbon Nanotubes and Its Implication for Radiative Lifetimes," *Phys. Rev. Lett.*, Vol. 92, 2004, Art. No. 177401.
[51] O'Connell, M. J. et al., "Band Gap Fluorescence from Individual Single-Walled Carbon Nanotubes," *Science*, Vol. 297, 2002, pp. 593–596.
[52] Hartschuh, A. et al., "Nanoscale Optical Imaging of Excitons in Single-Walled Carbon Nanotubes," *Nano Lett.*, Vol. 5, 2005, pp. 2310–2313.
[53] Jin, H. et al., "Divalent Ion and Thermally Induced DNA Conformational Polymorphism on Single-walled Carbon Nanotubes," *Macromolecules*, Vol. 40, 2007, pp. 6731–6739.
[54] Aslan, K. et al., "Metal-Enhanced Fluorescence: An Emerging Tool in Biotechnology," *Anal. Biotechnol.*, Vol. 16, 2005, pp. 55–62.
[55] Frey, H. G. et al., "Enhancing the Resolution of Scanning Near-Field Optical Microscopy by a Metal Tip Grown on an Aperture Probe," *Appl. Phys. Lett.*, Vol. 81, 2002, pp. 530–532.
[56] Novotny, L., "Single Molecule Fluorescence in Inhomogeneous Environments," *Appl. Phys. Lett*, Vol. 69, 1996, pp. 3806–3808.

CHAPTER 14

Near-Field Optical Molecular Structuring and Manipulation Based on the Use of Localized Surface Plasmons

R. Bachelot, J. Plain, G. Lérondel, P. Royer, A. Vial, C. Hubert, O. Soppera, H. Ibn El Ahrach, G. P. Wiederrecht, and S. K. Gray

14.1 Introduction

Nanolithography and the nanostructuring of materials are important branches of nanotechnology that may one day lead to many applications and research fields including ultrahigh density storage, nanoelectronics, nanomechanics, and nanobiotechnology [1]. The current techniques of nanolithography are various and numerous. Most of them involve far-field illumination of the material to be modified. They are diffraction-limited, and the spatial resolution is theoretically not better than $\lambda/2n$, where λ is the wavelength of the source used and n is the refractive index of the medium. Among these techniques, let us cite X-ray and electron beam lithographies allowing for resolution better than 15 nm. Lithography using light is particularly appreciated for several reasons, including cost and simplicity. Presently, mask far-field optical lithography is the most widely used technique for pattern mass production in various fields such as microelectronics and micro-optics [2]. This technology is optimized and easy to implement compared with X-ray or ion-beam lithography. The photopolymers used are various and well known and have been optimized for several applications. However, the main limit of the optical lithography is its diffraction-limited spatial resolution. This is why the used wavelength was decreased step-by-step over the past 30 years (436, 365, 254, 248, 193, 157 nm). The current trend is to develop and use new small wavelength "extreme UV" sources (EUV, $\lambda = 13.5$ nm) that would enable a resolution better than 50 nm in the near future. However, this approach requires expensive development of new technologies: new sources, new optics, and new photopolymers. Another approach consists of increasing the refraction index: Immersion photolithography (using liquid) and solid immersion lens lithography (using a scanning microlens) allowed resolution to be improved by a factor of 2, mainly limited by refractive index of the available materials. The better resolution permitted by immersion UV lithography is presently about 65 nm. Current trends in optical lithography can be found in [3].

Near-field optical lithography (NFOL) is an alternative and elegant method of improving resolution. NFOL relies on the use of spatially confined evanescent fields as optical sources. Such sources are associated with high lateral k vectors and low effective wavelengths and are not diffraction-limited. The control, use, and study of such electromagnetic waves constitute the Near-field Optics (NFO) that has aroused considerable interest and efforts over the two last decades [4]. The advent of this science has opened a new field and appreciation for the control and manipulation of light at the nanoscale. Confined near fields are used extensively for optical microscopy and spectroscopy at the nanometer scale. Different chapters of the present book deal with these applications. Near fields have been used as local optical sources for high-resolution optical lithography too. A general survey of the literature on NFOL can be found elsewhere [5, 6]. In this chapter, we would like to focus our attention on the use of localized surface plasmons (LSP) supported by metal nanostructures (MNSs) for high-resolution optical lithography. We will call this approach surface plasmon optical lithography (SPOL). The principle of this approach relies on the local optical interaction between MNS and photosensitive molecules. A recent review paper proposed an overview of the explored optical interaction between MNSs and photosensitive materials [7]. In particular, the paper highlighted that this domain not only allows for production of nanostructures using light but also opens the door to nanophotochemistry based on surface plasmon photonics.

This chapter focuses on recent progress in SPOL through selected examples that are characteristic of this domain of research. The chapter is divided into the following three sections. In Section 14.2, we present an overview of the first results of tip-enhanced optical lithography on azobenzene-containing photopolymers. Section 14.3 presents more recent results of optical nanostructuring by in-plane MNS. In Section 14.4, we analyze very recent results on nanophotopolymerization by LSPs of Ag nanoparticles. Finally, we will conclude and evoke some promising routes.

14.2 Tip-Enhanced Optical Lithography on Azobenzene-Containing Polymers

The enhanced nano-optical field at the apex of a metal tip has been demonstrated to be powerful for SPOL on several materials including gold thin films [8], hydrogen passivated semiconductor surfaces [9], and polymer photoresists [10]. In particular, we have used metal tips to induce photo-isomerization of azobenzene dye molecules grafted to a polymer matrix. This specific material allows one, at the nanometer scale, to study the optical lightning rod effect and to perform SPOL. The photochemistry of this photopolymer is illustrated in Figure 14.1. Figure 14.1(a) shows an azobenzene group grafted to a polymer matrix of polymethylmethacrylate (PMMA). The absorption band of the azo dye is centered in the visible. (See the absorption spectrum in the inset.) The absorption peak is typically situated around $\lambda = 500$ nm. This is why the dye is usually named DR1 (Dispersed Red One). Figure 14.1(b) shows the process of isomerization schematically. The stable state of the azobenzene molecule presented on the left side is the transisomeric configuration. The absorption in the visible range of a photon induces the transition to the cis-isomer. This state is metastable, and the reverse transition to the trans state takes

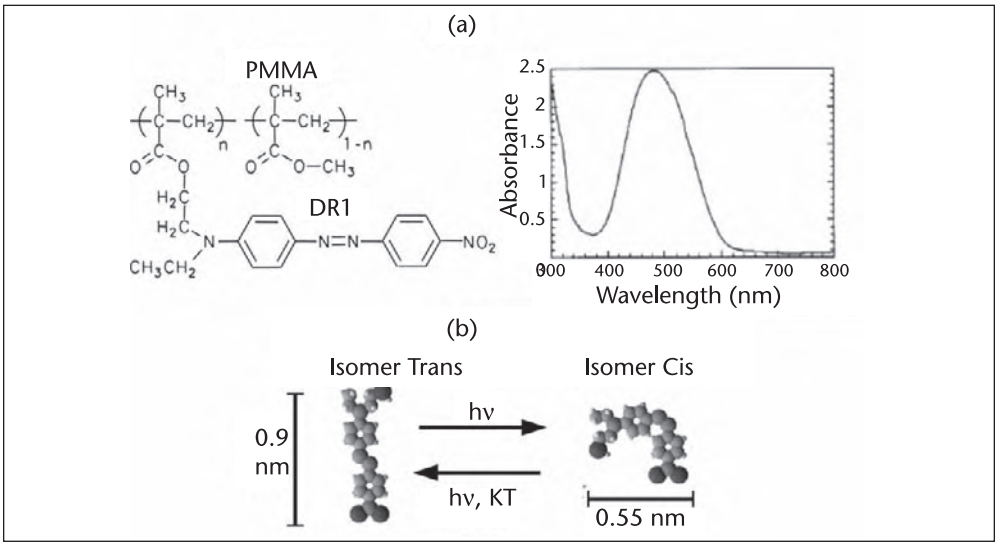

Figure 14.1 Photochemistry of the PMMA-DR1. (a) Structure. (b) Photoizomerization. Inset: Absorption spectrum of DR1.

place through thermal activation or optical absorption. Therefore, a molecule absorbing a photon undergoes a complete trans-cis-trans isomerization cycle. Provided there is a nonzero component of the light polarization vector along the intensity gradient, this transition induces a motion of the molecule and a related deformation of the matrix to which the molecule is grafted. The polarization selectivity lies in the fact that the azobenzene moieties in their trans state are strongly anisotropic and preferentially absorb the light polarized along their main axis. The required illumination conditions for observing matter migration are actually intensity-gradient and are a nonzero component of the polarization vector along the intensity gradient. As a consequence, the polymer is self-developing, and after illumination, its surface presents a topography related to the incident intensity distribution. Details on this material can be found in a recent comprehensive review paper by Natansohn and Rochon [11].

The deformation properties of azo-containing polymers under illumination were first used in the near field to perform NFOL and to map the electromagnetic field emitted by a metallized or uncoated probe for scanning near-field optical microscopy (SNOM) [6]. Here we describe SPOL on PMMA-DR1. PMMA-DR1 was illuminated with the presence of a metallized AFM tip at its surface. After illumination, the optically induced topography was characterized in situ by AFM using the same tip. This approach enabled a parametric analysis leading to valuable information on tip-field enhancement (TFE) [5, 12]. In particular, TFE was evaluated as a function of the illumination condition (e.g., state of polarization and angle of incidence) and the tip's features (e.g., radius of curvature and material). As a significant example, Figure 14.2 shows the influence of the illumination geometry. Figure 14.2(a) shows the AFM image obtained after illumination of p-polarization reflection mode of a metal-coated Si tip in interaction with the PMMA-DR1 surface. The center of the image corresponds to the tip position during the exposure.

The figure exhibits two different fabricated patterns: a far-field-type fringe system, which corresponds to diffraction by the tip cone, and a central nanometric dot due to the local enhancement of the electromagnetic field below the metallic tip. The far-field contrast (the fringes) vanishes when the tip is illuminated by TIR [Figure 14.2(b)], providing valuable information about the suitable way of illuminating a metal tip for SPOL. The height of the central near-field spot is very sensitive to the incident angle of polarization (Figure 14.3), confirming that the intensity of the local tip field is enhanced gradually from s-polarization to p-polarization as the incident electric field becomes aligned with the tip axis (see Section 13.2). The previously cited near-field investigations lead to preliminary 30 nm resolution nanopatterning based on TFE (see Figure 14.4 as an illustration).

All of these experiments stimulated interesting discussions on the nature of the optical response of the molecule. Especially, it was shown that while lateral field components tend to make molecules escape from light along the polarization, longitudinal (L) components lift the matter vertically as a consequence of free space requirement from the molecule. In particular, this point of view was confirmed by investigation of surface deformations in azo-polymers using tightly focused higher-order laser beams [13] and surface plasmon interference [14] as vectorial sources.

Considering that the field involved in tip-enhanced SPOL is mainly L, contrasts observed in Figures 14.2, 14.3, 14.4 can be explained by the described polarization sensitivity.

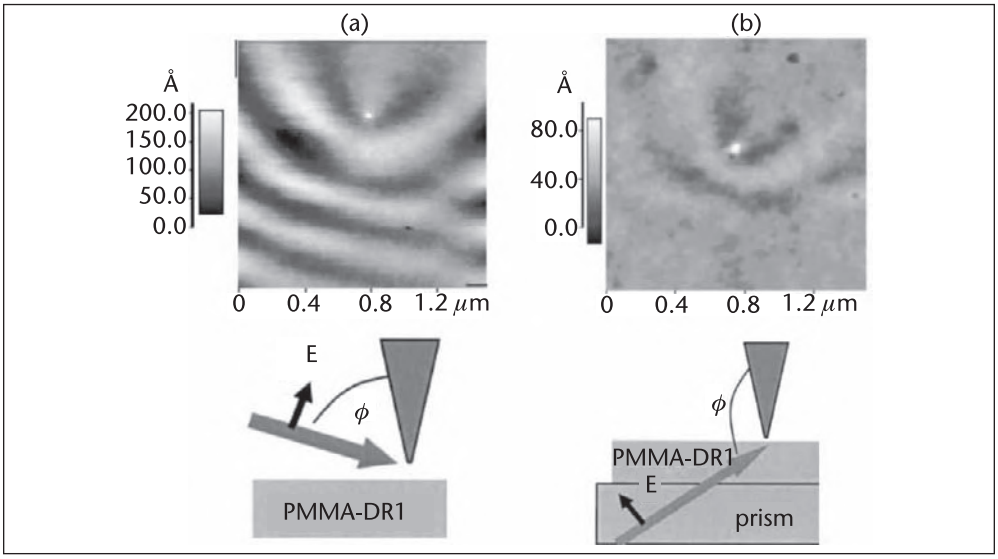

Figure 14.2 Tip-enhanced lithography on PMMA-DR1 films under p-polarization. Influence of the illumination geometry. (a) Tapping mode AFM image obtained after the reflection mode illumination ($\phi = 80°$, see configuration below). (b)Tapping mode AFM images obtained using TIR ($\phi = 130°$, see configuration below). From Bachelot et al. [12].

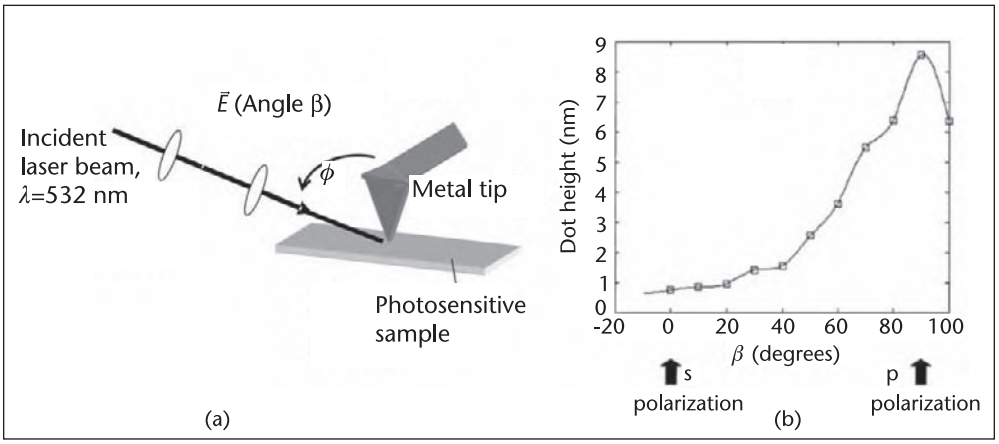

Figure 14.3 Tip-enhanced lithography on PMMA-DR1 films. Influence of the incident polarization. (a) Schematic diagram of the experimental configuration. $\phi = 80°$. (b) Obtained dot height as a function of polarization angle β.

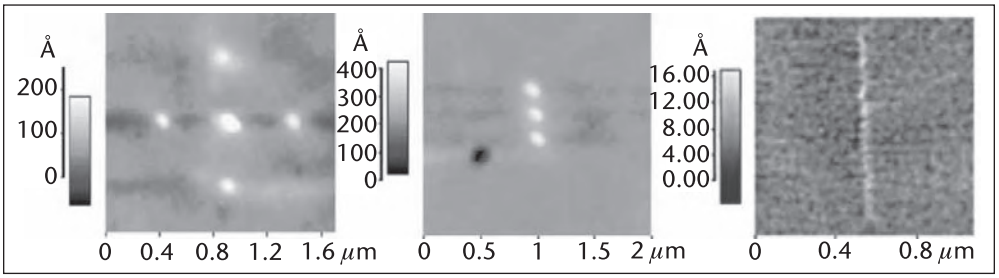

Figure 14.4 Tip-enhanced lithography on PMMA-DR1 films under p-polarized TIR mode illumination. Examples of dotted/continuous produced nanostructures with $\lambda = 532$ nm (AFM images).

14.3 Mask-Based SPOL on Azobenezene-Containing Polymers

As discussed in Section 14.2, the use of metal tips allowed for modification of nanometer scale matter. However, from an industrial point of view, these approaches are limited by low speed and tip lifetime. That is why, with the purpose to compete with UV, X-ray, and nanoimprints mask lithographies, mask-based SPOL was recently introduced [15].

Here we report an original mask approach based on the exposure of lithographically designed metallic nanostructures coated with the azo-dye polymer described in Section 14.2, where each chromophore acts as a probe of the intensity of the electric field [16]. In addition to optical nanostructuring, this approach allows for description of near-field effects without scanning optical probes.

The technique for photochemical optical near-field imaging consists of three steps. First, 50 nm high silver nanostructures are fabricated by electron beam lithography, typically through the lift-off method. The second step is the deposition of the PMMA-DR1. In our case, the thickness of the polymer film is equal to 80 nm, which is sufficient to cover the structures completely and thin enough to be sensitive to the optical near field of the particles. No drying was performed after spin coating. The third step consists of illuminating the sample, in this case, at normal incidence. To overlap the 400–600 nm absorption band of the DR1 molecule [Figure 14.1(a)], we

used the 514 nm or 532 nm lines of an argon ion laser or a frequency doubled, diode-pumped Nd:YAG laser, respectively. The polarization and irradiation intensity were carefully controlled and correlated with the detected topographic features. Following the illumination process (step 3), the "imaging" of the optically induced topography is performed through AFM. Theoretical modeling is used to support the experimental observations. We rigorously calculate the NFO intensities using the FDTD method [17, 18] and show that the negative image of the computed near-field intensities can be correlated with the observed photoinduced topographies. This negative image illustrates the fact that the matter escapes from high-intensity regions to low-intensity regions and that the involved field is mainly lateral. The FDTD calculations were fully three-dimensional with appropriate periodic and absorbing boundary conditions. The metals were described by Drude models with parameters fitting the experimental dielectric constant data for the wavelengths of interest, as described in [18]. The glass substrate and PMMA-DR1 also were included in the calculations, with dielectric constants of 2.25 and 2.89, respectively. Fourier transformations of the time-domain fields on the wavelengths of interest then yield steady-state fields and thus field intensities. As a first example of the near-field imaging capability of this method, Figure 14.5 shows the results obtained with an array of silver nanoparticles having a diameter of 75 nm, a height of 50 nm, and a periodicity of 500 nm. The extinction spectra of the arrays performed after spin coating shows a maximum near 540 nm. A 532 nm irradiation wavelength was used to overlap this resonance. In the case of linear incident polarization, after irradiation, two holes can be observed [top of Figure 14.5(a)] in the polymer that are close to the particles and are oriented with the incident light polarization. The depressions correlate remarkably well with the expected dipolar near-field spatial profile. Numerical calculations of the electric field intensity distribution around silver nanoparticles covered with PMMA-DR1 and irradiated with a linearly polarized laser beam show that intensity maxima are located at the same position as the holes observed in the topographic image. The bottom of Figure 14.5(a) shows the theoretical negative of the electric field intensity; it agrees qualitatively with its experimental counterpart. From these observations, we can argue that topographic modifications observed after irradiation are due to a mass transport phenomenon photoinduced by the optical near field of the metallic silver particles produced by dipolar plasmon resonance. Figure 14.5(b) shows an example of the ability of this method to spatially resolve complex fields. It shows the result obtained with silver nanoparticles covered with PMMA-DR1 but now irradiated with a circularly polarized laser beam. The silver particles are 50 nm in height, are 100 nm in diameter, and have a periodicity of 1 μm. In this case, large topographic modifications are again observed at the polymer film surface. The AFM image at the top of Figure 14.5(b) shows that an inner array of lobes around each particle can be distinguished, as well as an outer array of lobes, whose periodicity is equal to the lattice spacing. These outer lobes probably result from interferences of diffraction orders. Quite encouragingly, the negative computed field intensity [bottom of Figure 14.5(b)] also shows inner and outer high relief features around the particles, although they are not as structured as the experimental result. This probably originates from the fact that theoretical calculations do not take into account the diffusion of azodye molecules and thus cannot perfectly reproduce their behavior under illumination with very intense localized near fields.

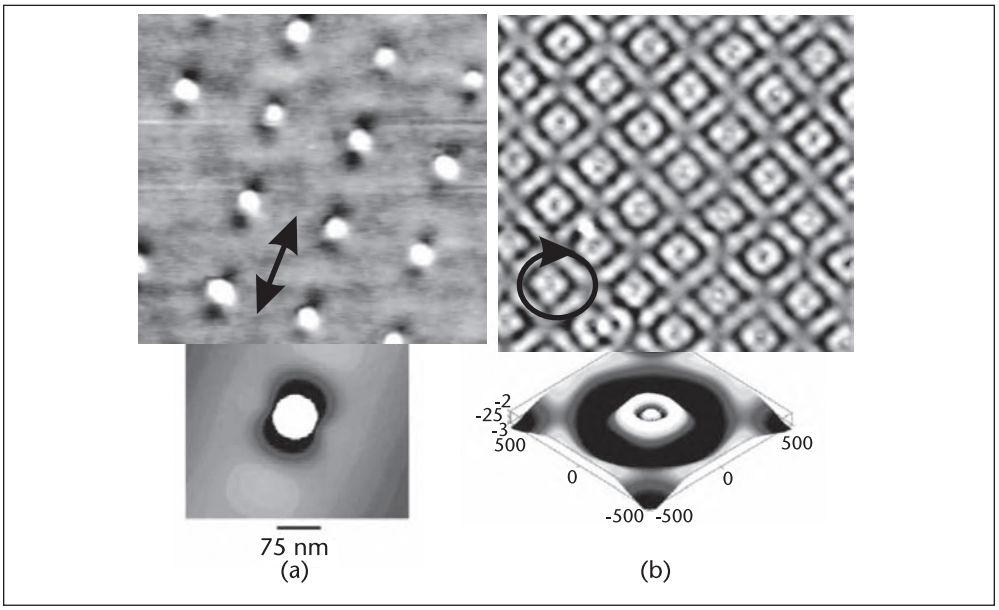

Figure 14.5 Mask-based SPOL on PMMA-DR1 films. AFM images taken after exposure (top) and theoretical calculations (bottom) of circular silver nanoparticles illuminated with linear polarization (a) or circular polarization (b). Irradiation wavelength, time, and intensity were equal to 532 nm, 30 min, and 100 mW/cm^2, respectively. Theoretical images represent the negative of the intensity. The black arrows depict the incident polarization. Period of the particles array is 500 nm in (a) and 1000 nm in (b).

Our approach has numerous advantages over other nano-optical characterization methods of noble MNSs based on the use of a scanning probe. First, topographic modifications of the polymer film surface are recorded directly with an AFM after exposure and without any chemical treatment. Second, removal of the spin-coated film with the polymer solvent enables the same sample to be characterized with this method several times without any degradation of the metallic structures. Finally, in addition to avoiding sample-probe electromagnetic interactions, this method avoids the problem of low signal-to-noise that can plague SNOM measurements. However, our method is not expected to compete with SNOM, whose efficiency has been demonstrated over the past 20 years [4]. On the contrary, our method should be viewed as a complementary tool to observe near-field features of nanostructures.

Figure 14.6 confirms the high potential of the method. It shows different examples of NFO imaging of silver nanostructures illuminated by a linearly polarized green light. In each figure, the white bar represents the light wavelength (532 nm) while the black arrows represent the direction of the incident polarization. Figure 14.6(a) shows optical near field around gold ellipsoidal particles under light polarization perpendicular to the long axis of the ellipsoids. The ellipsoids are 50 nm in height, with long and short axis lengths of 1 μm and 60 nm, respectively. Particle-to-particle distances are 800 nm in the long axis direction. Extinction spectra performed after spin coating of the azo-polymer layer indicate that for polarization parallel to the long axis, the 514 nm irradiation wavelength used is outside the resonance plasmon band. On the other hand, in the case of a polarization direction perpendicular to the long axis, the 514 nm irradiation wavelength is resonant with the plasmon band. This agrees

well with the experimental observation. In Figure 14.6(a), dips can be observed along the long axis of the particles. These dips are located at the same position as the optical near-field intensity maxima (not shown here) around ellipsoids for such a polarization. This is confirmed when looking at the corresponding calculated negative image of the field intensity around the particles for this illumination condition. Hence, Figure 14.6(a) is an observation of the resonant charge density excitation at the edges of the nanorods. For polarization parallel to the rod, an off-resonant electromagnetic singularity is excited and dips are observed at the extremities of the rods [16]. Partial interpretation of Figures 14.6(b)–(d) can be found in [19]. It includes the polarization sensitivity described in Section 14.2. These images are believed to give insight into interesting effects and behaviors of MNSs: excitation of quadripolar plasmon modes in elongated gold particles [Figure 14.6(b)], near-field diagram of bow-tie optical antenna [Fig. 14.6(c)], and near-field coupling between two close different nanostructures [Figure 14.6(d)].

The plasmonic effects are very sensitive to the illumination condition (polarization and direction of the incident wave vector). This sensitivity, illustrated in the preceding figures, can be exploited in new, powerful approaches of SPOL. For example, Figure 14.7 illustrates a concept of programmable SPOL proposed recently by Koenderink and colleagues [20]. In a controlled way, this method addresses selected sets of particles by adjusting illumination conditions (wavelength,

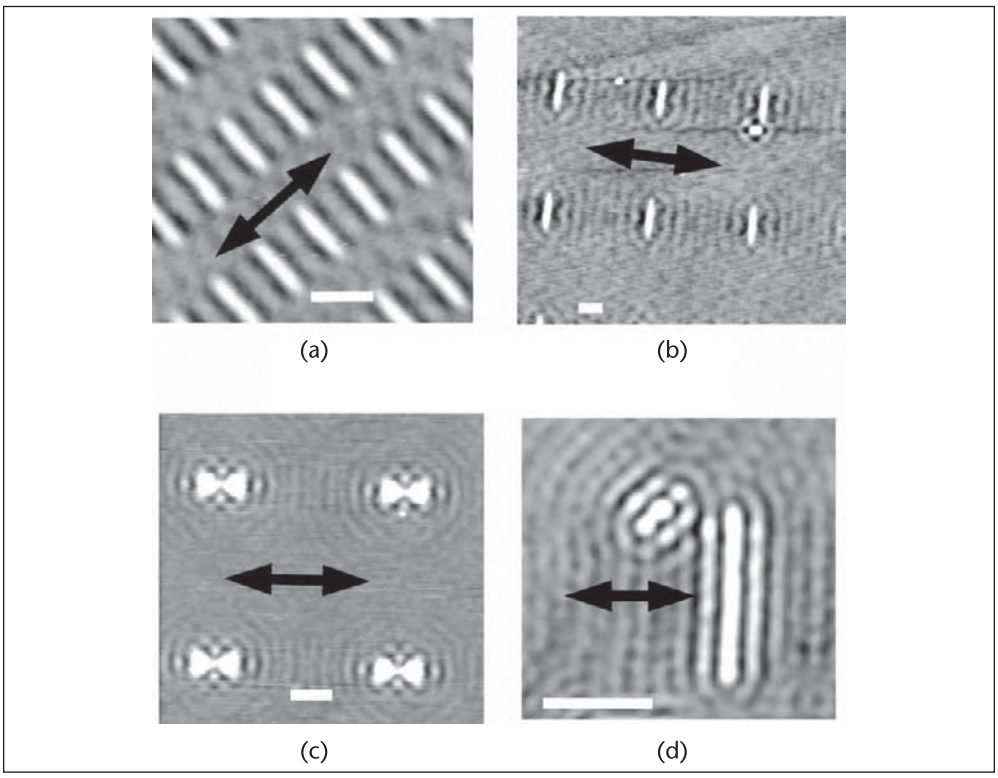

Figure 14.6 Mask-based SPOL on PMMA-DR1 films. AFM images of different silver nanostructures taken after linearly polarized exposure (normal incidence). The black arrows depict the incident polarization. The white bars represent 532 nm, which is equal to the value of the used wavelength. (a) ellipses, (b) longer ellipses, (c) bow-tie antenna, and (d) coupled rod and circular particles.

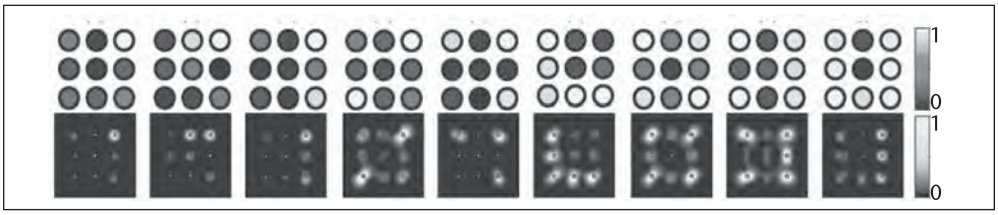

Figure 14.7 Concept of programmable mask-based plasmonic lithography. Each letter represents a specific set of incident wavevector and polarization. Top row: addressed silver particles. Bottom row: corresponding calculated intensity distribution. From Koenderink and colleagues [20].

polarization, and incident angle). This approach relies on the control of constructive interferences that give rise to hot spots on some particles and destructive interferences that keep other particles dark. The example of numerical calculation in Figure 14.7 shows that a single square array of silver particles enables numerous near-field combinations addressed by a specific illumination condition. This method could ultimately enable writing, by sequential exposures, of complex structures on a photopolymer placed in the vicinity of the array.

14.4 Near-Field Photopolymerization Based on Localized Surface Plasmons: Toward New Hybrid Particles for Nanophotonics

Photochemistry based on LSPs can enable controlling and studying the optical properties of resonant MNSs. This double interest is demonstrated remarkably through the approach described in this section. This recently introduced approach is based on controlled nanoscale photopolymerization triggered by local enhanced electromagnetic fields of MNSs [21]. Its principle is depicted in Figure 14.8. A drop of liquid photopolymerizable formulation, described in detail elsewhere [22], is deposited on MNSs made by electron beam lithography. A free-radical photopolymerizable formulation was used in this work. It is a mixture of three components: a xanthenic dye sensitizer (Eosin Y), a coinitiator (methyldiethanolamine, 8 wt%), and a triacrylic monomer base (pentaerythritol triacrylate, PETA). Such a system is sensitive between 450 and 550 nm and gets converted through a free-radical cross-linking polymerization under green light irradiation. After the absorption of actinic light by eosin, the triplet state of the dye reacts with the amine to form radicals. Radicals initiate the polymerization of the monomer. Free-radical polymerization is known to be very sensitive to oxygen quenching. In addition, the PETA contains 300 ppm of thermal polymerization inhibitors added to stabilize the monomer (e.g., to avoid unlike thermal polymerization). The effect of these compounds is to inhibit the polymerization process as long as the absorbed light dose remains lower than a threshold value. Consequently, the sensitivity of the system is characterized by a curve that shows the degree of cross-linking as a function of the received energy E_r. This curve, presented in the inset of Figure 14.8, corresponds to the typical behavior of a formulation that can be polymerized following a radical process. One can note that polymerization starts only when the absorbed energy is greater than a threshold value E_{th}. Thus, the formulation is characterized by a nonlinear threshold behavior allowing for high resolution patterning under evanescent illumination [23]. In a first approximation, we

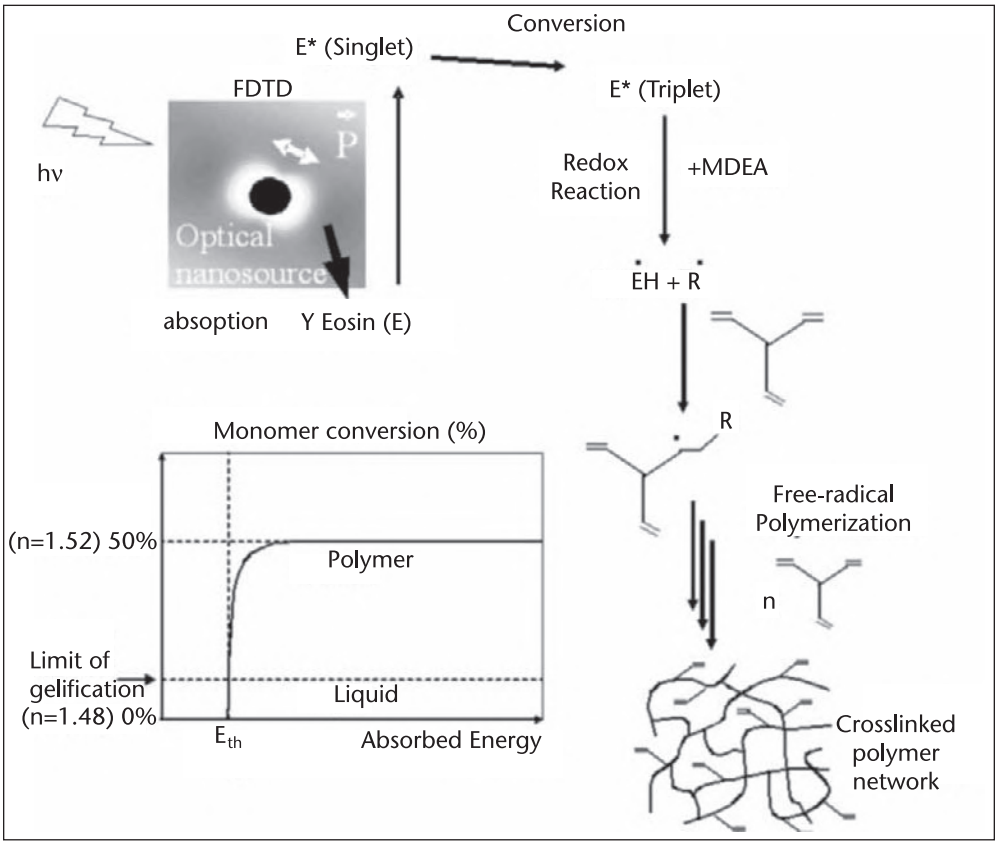

Figure 14.8 Principle of nanoscale near-field free-radical photopolymerization. The first step of the process is the local absorption of light by eosin. The inset shows the typical reticulation rate and associated refraction index as a function of absorbed energy density. E_{th} is the threshold energy.

simplified the photonic response of the photopolymerizable resin to a binary function: Polymerization is supposed to be completely ineffective under E_{th} and complete after E_{th}. After formulation deposition, the sample is illuminated ($\lambda = 514$ nm) in normal incidence by a linearly polarized plane wave. The incident energy is below the threshold so that polymerization occurs only around MNSs where local near fields are enhanced by surface plasmon resonance. Silver is chosen as a particle material to achieve mutual spectral overlapping between photopolymer absorption and surface plasmon resonance of metal particles embedded in liquid polymer. After exposure, the sample is washed with ethanol to remove any unpolymerized material, dried with nitrogen, and UV postirradiated to complete and stabilize the polymerization—and finally characterized by AFM and polarized extinction spectroscopy.

Knowledge of the threshold value ensures control of the procedure and is therefore of prime importance. This threshold was determined to be 10 mJ/cm^2 by using a two-beam interference pattern as a reference intensity distribution [21].

The characterized formulation was used for near-field photochemical interaction with the MNSs. The MNSs covered by the formulation were illuminated with an incident energy density *four times* weaker than the threshold of polymerization. Figures 14.9(a) and 14.9(b) show the result of the experiment as imaged by AFM. Two symmetric polymer lobes built up close to the particles can be observed,

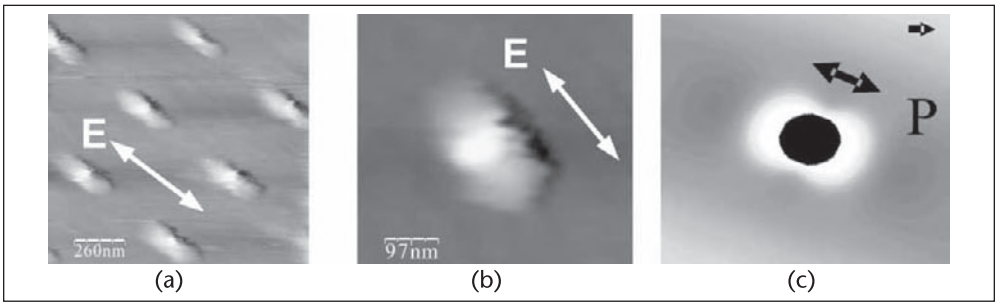

Figure 14.9 Near-field nanoscale photopolymerization in the vicinity of silver nanostructures. (a) and (b) are AFM images recorded after irradiation and development of the silver nanoparticles arrays covered with the photopolymerizable formulation. (c) Intensity distribution in the vicinity of a Ag particle embedded in the formulation as calculated by FDTD method $\lambda = 514$ nm. The white arrows represent the incident polarization used for exposure.

resulting in metal/polymer hybrid particles. The two lobes originate from the excitation of MNSs' dipolar SPR, as numerically illustrated in Figure 14.9(c) obtained through a FDTD calculation. The field distribution associated with the resonance is enhanced in a two-lobe region oriented with the incident polarization. The localized nanoscale photopolymerization is the result of the inhomogeneous field distribution showed in Figure 14.9(c). The two lobes can be viewed as a 3-D polymer molding of the locally enhanced optical fields. Figures 14.9(a) and 14.9(b) show that is possible to control nanoscale photopolymerization in the visible region of the spectrum by using the near field of resonant metal nanoparticles. This control was made possible through precise knowledge of the polymerization threshold and results from the abilities of the confined optical near field of MNS to quickly consume dissolved oxygen at the nanometer scale. (Oxygen acts as an inhibitor of polymerization [22].) Figure 14.9 also shows that the intrinsic resolution of the material is very high. This property is one intrinsic characteristic of the negative tone resin that was used to hybridize the metal nanoparticles: The elementary building blocks are of molecular size; in addition, a fast transition from liquid to gel under light excitation allows a well-defined border to be obtained between reacted and unreacted parts of the photopolymerizable material. On the other hand, our approach constitutes a unique way of quantifying experimentally the field enhancement associated with LSP resonance. This approach relies on the precise knowledge of a value characteristic of the photosensitive material: the threshold energy. In the present case, we learn that the intensity enhancement factor is greater than 4 because the polymerization threshold was exceeded locally. This result is in agreement with the calculated enhancement factor of 12 (not shown). We performed the same exposure using gold particles instead of silver particles. No local polymerization was observed. This is due to the fact that resonance enhancement factor is not superior to 4. This point was confirmed by a FDTD calculation that predicted an intensity enhancement factor of about 3.5 for embedded gold particles at $\lambda = 514$ nm. Further studies based on multiple exposures will allow us to quantify precisely the enhancement factors involved in SPR in a near future.

Figure 14.9 clearly shows that polymerization was not isotropic due to the inhomogeneous nature of the actinic field. This suggests that the modification of the Ag particle's plasmon resonance due to local change of the medium is not isotropic.

This is confirmed by Figure 14.10. The top of Figure 14.10 shows extinction spectra of the array taken under different conditions. Spectrum (a) is the initial spectrum of the particles deposited on glass exposed in air. Spectrum (b) shows a 50 nm red shift in the liquid polymer (just before exposure). For spectra (a) and (b), the SPR shows an isotropic response to the polarization, within the sample plane, due to the circular symmetry of the particles. Spectra of the hybrid particles were measured for two extreme polarization angles. Spectrum (d) was measured for a polarization parallel to the major axis of the hybrid particle. Compared to spectrum (a), it shows a 28 nm red shift in the resonance. Spectrum (c) was obtained for a polarization perpendicular to the minor axis of the hybrid particle, and compared to spectrum (a), a 8 nm red shift is measured. The anisotropy of the medium surrounding the particle is the consequence of these two different red shifts and are the indicators of a spectral degeneracy breaking. Before local photopolymerization, metallic nanoparticles are characterized by a $C\infty v$ symmetry corresponding to the rotation Cv axis [23]. After polymerization, the two polymerized lobes induce a new lower symmetry: $C2v$, for which any pattern is reproduced by π in-plane rotation. This new symmetry induces the breakdown of the SPR spectral degeneracy. The bottom of Figure 14.10 is a polar diagram of SPR peaks obtained by measuring 50 spectra of the hybrid particles for different angles of in-plane linear polarization. The two polymerized lobes clearly induced a quasi-continuously tunable SPR in the 508–522 nm range. The local polymerization leads to two plasmon eigenmodes centered at 508 and 522 nm. For any polarization angle, a linear combination of the two eigenmodes is excited, with respective weights depending on the polarization direction. We conclude that the apparent continuous plasmon tuning is the result of a shift in position of the barycentre of the spectral linear combination. This was confirmed by analysis of the FWHM of the spectra acquired. The FWHM was found to be maximal for a polarization at 45° relative to the axis of the hybrid particle, where both eigenmodes are equally excited. These results confirm the importance of symmetry in a nanoparticle in nanophotonics [21].

The data of Figure 14.10 can be discussed in terms of nanoscale effective index distribution n_{eff} that expresses the effect of the respective weights of the eigenmodes. n_{eff} is equal to $n_m + \Delta n_m$, where n_m is the initial refraction index of an external medium taken as a reference and Δn_m is the polymerization-induced shift in the refractive index. n_m was chosen to be 1.48 [22] (silver particles embedded in photopolymer formulation before exposure). By differentiating the denominator of the particle polarizability [24], Δn_m was deduced from Equation 14.1, as follows:

$$\Delta\lambda = -4n_m\Delta n_m(d\varepsilon/d\lambda)^{-1} \tag{14.1}$$

where ε is the dielectric constant of silver whose dispersion is known from [25] and $\Delta\lambda$ is the measured shift of SPR peak relative to the reference spectrum (see the top of Figure 14.10). The derivation was performed for spherical particles, which is a good approximation for in-plane measurements. For Ag particles in air deposited on a glass substrate, n_{eff} is found to be 1.06 as a result of the glass/air interface modifying the SPR. For the hybrid particles, an effective index of 1.15 was found for an excitation along the minor axis (suggesting the presence of a thin

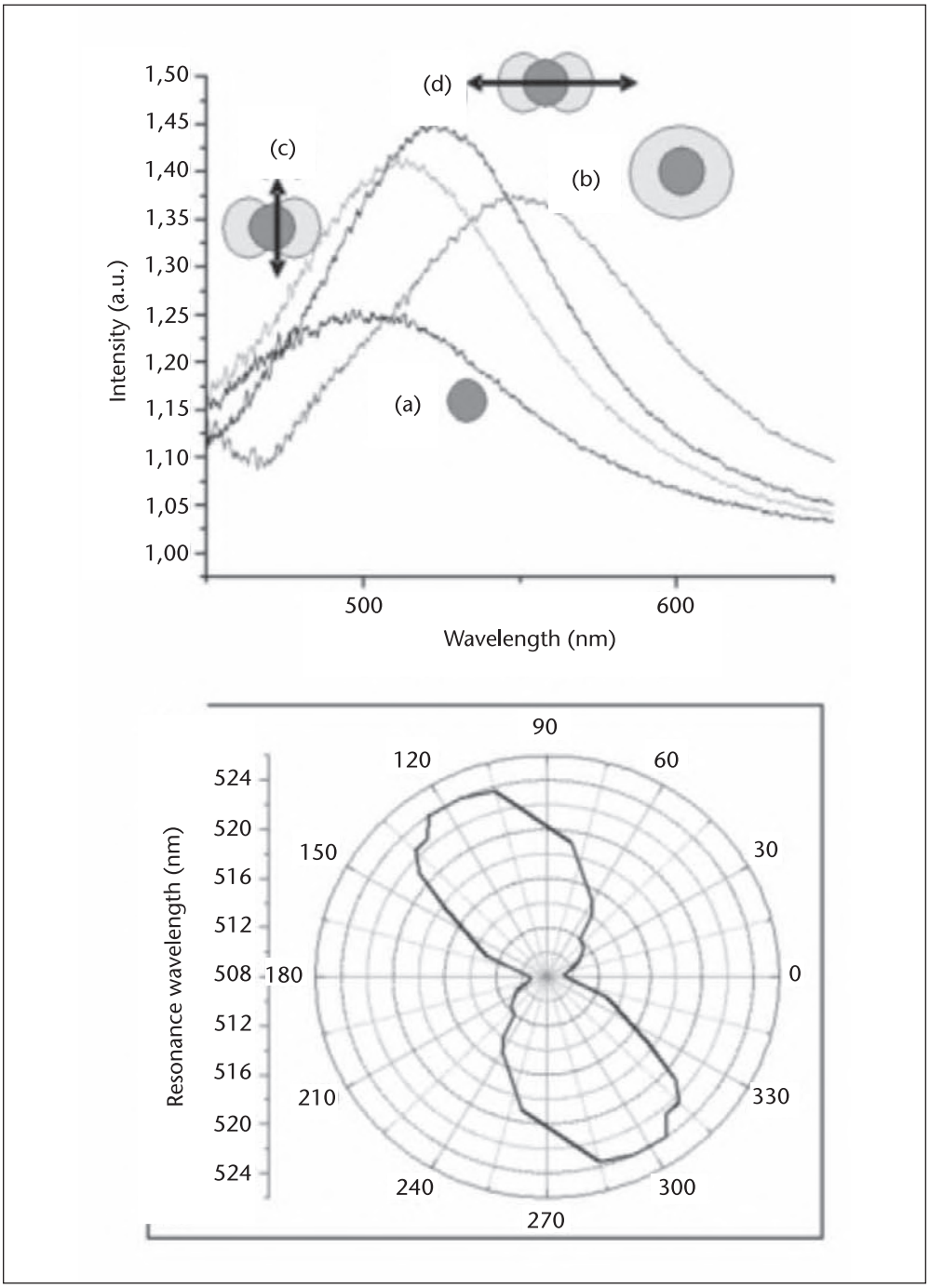

Figure 14.10 Spectral properties of the hybrid metal/polymer obtained through near-field photopolymerization. Top: The extinction spectra from a silver nanoparticle array. (a) Array in air on a glass substrate. (b) Array in initial liquid polymer (before exposure). (c) On hybrid particles excited along the minor axis; (d) on hybrid particles excited along the major axis. Bottom: Polar diagram showing the particle plasmon resonance peak as a function of the polarization angle around the hybrid nanoparticles. 120° and 30° correspond to the particle major axis and minor axis, respectively.

polymer layer along this axis), while the major axis was associated with a 1.3 index as a consequence of a thicker polymer region along this axis. Note that the bulk polymer index is 1.52 [22]. The difference between the effective index associated with the long axis and the bulk value can be attributed to the spatial extent of polymerization, which is limited by the threshold value. The field surrounding the hybrid particle extends beyond the area defined by the two polymerized lobes, resulting in a lower effective index. Between the two extreme values, a continuous variation of n_{eff} was deduced [21]. Thus, the method allowed the controlled production of a dielectric encapsulant that can be viewed as an artificial nanometric refractive-index ellipsoid.

Based on control of the geometry of the metal particles, the approach presented in this section has unique and numerous advantages compared to the standard approaches. In particular, several properties and processes involved in polymer science [26] can be coupled to (or assisted by) MNSs at the nanoscale. They include nonlinear/electro-optical properties, possible doping with luminescent (non)organic materials, and chemical control of the refractive index. Furthermore, different degrees of symmetry may be achieved by using high-order plasmon modes selected by proper incident polarization or wavelength.

14.5 Conclusions and Future Routes

This chapter presented the recent exploration of optical interaction between MNSs and photosensitive organic materials. Three selected examples have shown the ability of MNSs to induce physical and chemical processes at the molecular scale. These experiments not only allow production of nanostructures using visible light but also have opened the door to nanophotochemistry based on MNSs. Moreover, they lead to progress in nanometals, in both experimental and theoretical points of view. Taking into account associated economical and scientific challenges, the future of optical lithography based on MNSs is likely to be successful. Regarding the tip-enhanced SPOL, it is now possible to control the array of tips working simultaneously [34], the concept of high-density multiprobes optical data storage making a priori relevant. Regarding the mask-based SPOL approach, the control of the mask-photosensitive material distance turns out to be the key parameter. This issue will certainly take advantage of the superlens concept that enables the access of near-field information through negative refraction [27, 28].

SPOL is not intended to compete with the objectives defined by the International Technology Roadmap for Semiconductors (ITRS) [29] that relies on the decrease of the wavelength. Rather, SPOL should be viewed as a complementary approach appreciated because of its low cost and easy procedures. In particular, the use of visible light and the possibility of taking advantage of the polarization state of the light represent clear assets. Furthermore, the domain of application of SPOL is far beyond that of nanolithography for microelectronics since it can involve, for example, high data storage and molecular manipulation. SPOL also can be used as one step of a more complex procedure of nanolithography. For example, the mold used in nanoimprint [1] can be fabricated by SPOL.

Finally, this technology shall take advantage of the large variety of powerful physical effects in nanometals that have been investigated recently, such as second harmonic generation [30], photoluminescence [31], strong near-field coupling [32], and multipole excitation [33]. All of these effects will permit higher resolution and better control of intensity and wavelength of the actinic light with regard to photosensitive materials.

References

[1] "Fabrication of Sub-45 nm Structures for the Next Generation of Devices," *MRS Bulletin*, Vol. 30, No. 12, December 2006.

[2] Sheats, J. R., and B. W. Smith (eds.), *Microlithography Science and Technology*, New York: Marcel Decker, 1998

[3] Lin, B. J., "The Ending of Optical Lithography and the Prospects of Its Successors," *Microelectron. Eng.*, Vol. 83, 2006, pp. 604–613.

[4] Novotny, L. and B. Hecht, *Principles in Nano-Optics*, Cambridge: Cambridge University Press, 2006.

[5] Royer, P. et al., "Near-Field Optical Patterning and Structuring Based on Local-Field Enhancement at the Extremity of a Metal Tip," *Philos. Trans. R. Soc. Lond., Ser. A*, Vol. 362, 2004, pp. 821–842.

[6] Tseng, A., "Recent Developments in Nanofabrication Using Scanning Near Field Optical Microscope Lithography," *Optics and Laser Technology*, Vol. 39, 2007, pp. 514–526.

[7] Bachelot, R., "Near-Field Optical Structuring and Manipulation Based on Local Field Enhancement in the Vicinity of Metal Nanostructures," in *Advances in Nano-Optics and Nanophotonics—Tip Enhancement* (S. Kawata and V. M. Shalaev, eds.), The Netherlands, Elsevier, 2006, pp. 205–234.

[8] Jersch J., and K. Dickman, "Nanostructures Fabrication Using Laser Field Enhancement in the Near-Field of a Scanning Tunneling Microscope Tip," *Appl. Phys. Lett.*, Vol. 68, 1996, pp. 868–870.

[9] Lu, Y. F. et al., "Laser-Induced Nano-Oxidation on Hydrogen-Passivated Ge (100) Surfaces under a Scanning Tunneling Microscope Tip," *Appl. Phys. Lett.*, Vol. 75, 1999, pp. 2359–2361.

[10] Tarun A. et al., "Apertureless Optical Near-Field Fabrication Using an Atomic Force Microscope on Photoresist," *Appl. Phys. Lett.,* Vol. 80, 2002, pp. 3400–3402.

[11] Natansohn A., and P. Rochon, "Photoinduced Motions in Azo-Containing Polymers," *Chem. Rev.*, Vol. 102, 2002, pp. 4139–4175.

[12] Bachelot, R. et al., "Apertureless Near-Field Optical Microscopy: A Study of the Local Tip Field Enhancement Using Photosensitive Azobenzene-Containing Films," *J. Appl. Phys.*, Vol. 94, 2003, pp. 2060–2072.

[13] Gilbert, Y. et al., "Longitudinal Anisotropy of the Photoinduced Molecular Migration in Azobenzene Polymer Films," *Opt. Lett.*, Vol. 31, 2006, pp. 613–615.

[14] Derouard, M. et al., "Polarization-Sensitive Printing of Surface Plasmon Interferences," *Opt. Expr.*, Vol. 15, 2007, pp. 4238–4246.

[15] Srituravanich, W. et al., "Plasmonic Nanolithography," *Nano Lett.*, Vol. 4, 2004, pp. 1085–1088.

[16] Hubert, C. et al., "Near-Field Photochemical Imaging of Noble Metal Nanostructures," *Nano Letters*, Vol. 5, 2005, pp. 615–619.

[17] Taflove, A., and S. C. Hagness, *Computational Electrodynamics: The Finite-Difference Time-Domain Method*, 2nd edition, Boston: Artech House, 2000.

[18] Gray, S. K., and T. Kupka, "Propagation of Light in Metallic Nanowire Arrays: Finite-Difference Time Domain of Silver Cylinders," *Phys. Rev. B*, Vol. 68, 2003, Art. No. 045415.

[19] Hubert, C. et al., "Near-Field Polarization Effects in Molecular-Motion-Induced Photochemical Imaging," *Journal of Physical Chemistry C*, Vol. 112, 2008, pp. 4111–4116.
[20] Koenderink, A. F. et al., "Programmable Nanolithography with Plasmon Nanoparticles," *Nano Letters*, Vol. 7, 2007, pp. 745–749.
[21] Ibn El Ahrach, H. et al., "Spectral Degeneracy Breaking of the Plasmon Resonance of Single Metal Nanoparticles by Nanoscale Near-Field Photopolymerization," *Phys. Rev. Lett.*, Vol. 98, 2007, Art. No. 107402.
[22] Espanet, A. et al., "Photopolymerization by Evanescent Waves: Characterization of Photopolymerizable Formulation for Photolithography with Nanometric Resolution," *Appl. Surf. Sci.*, Vol. 87, 1999, pp. 138–139.
[23] Tinkham, H. *Group Theory and Quantum Mechanics,* New York: McGraw-Hill, 1964.
[24] Bohren C. F., and D. R. Hoffmann, *Absorption and Scattering of Light by Small Particles,* New York: John Wiley, 1983.
[25] Palik, E. D., *Handbook of Optical Constants of Solids,* Orlando, FL: Academic Press, 1985.
[26] Mark, J. E., ed., *Physical Properties of Polymers Handbook*, New York: Springer Verlag, 2001.
[27] Pendry, J. B., "Negative Refraction Makes a Perfect Lens," *Phys. Rev. Lett.*, Vol. 85, 2000, pp. 3966–3969.
[28] Fang, N. et al., "Sub-Diffraction-Limited Optical Imaging with a Silver Superlens," *Science,* Vol. 308, 2005, pp. 534–537.
[29] c.f. www.itrs.net
[30] Hubert, C. et al., "Role of Surface Plasmon in Second Harmonic Generation from Gold Nanorods," *Appl. Phys. Lett.*, Vol. 90, 2007, Art. No. 181105.
[31] Bouhelier, A. et al., "Surface Plasmon Characteristics of Tunable Photoluminescence in Single Gold Nanorods," *Phys. Rev. Lett.*, Vol. 95, 2005, pp. 1–4.
[32] Atay, T., J.-H. Song, and A. V. Nurmikko, "Strongly Interacting Plasmon Nanoparticle Pairs: From Dipole-Dipole Interaction to Conductively Coupled Regime," *Nano Lett.*, Vol. 4, 2004, pp. 1627–1631.
[33] Krenn, J. R. et al., "Design of Multipolar Plasmon Excitations in Silver Nanoparticles," *Appl. Phys. Lett.*, Vol. 77, 2000, pp. 3379–3381.
[34] Despont, M., "Millipede Probe-Based Storage," *SPIE Advanced Lithography*, 2007.

CHAPTER 15

Fluorescence Resonance Energy Transfer Scanning Near-Field Optical Microscopy

S. K. Sekatskii

15.1 Fluorescence Resonance Energy Transfer

FRET, also known as Förster resonance energy transfer, involves the nonradiative energy transfer from an excited "donor" fluorophore (*D*) to a proximal "acceptor" fluorophore (A). It has numerous applications in a range of disciplines including optics, chemical, and biological physics and materials science. Many excellent reviews in the field exist (see, for example [1–4]), so this chapter will concentrate on those aspects of this phenomenon that are especially important for application in NFO.

An electric dipole $\boldsymbol{d}_D$ oscillating at a frequency $\omega = 2\pi\nu$ is a source of an electric field at the same frequency, and the spatial distribution of this field at the distance $\boldsymbol{r}$ from the dipole can be written as follows [5]:

$$E_D = -\frac{k^2}{r^3}[\vec{r} \times (\vec{r} \times \vec{d}_D)] - \frac{ik}{r^4}[3\vec{r}(\vec{r} \cdot \vec{d}_D) - \vec{d}_D r] + \frac{1}{r^5}[3\vec{r}(\vec{r} \cdot \vec{d}_D) - \vec{d}_D r^2] \tag{15.1}$$

Here $k = 2\pi n/\lambda$ is a wave vector, where n is the refractive index of the surrounding medium and λ is the emission wavelength of the dipole cgs system units are used throughout this chapter.

Only the first term, inversely proportional to the distance r from the dipole, is responsible for the dipole radiation appearing in the far field [5]. Alternatively, for the FRET phenomenon, which is effective only at distances of a few nanometers from the donor dipole $\boldsymbol{d}_D$ (see below), only the third near-field term in Equation 15.1 is important; so we can write

$$E_D = \frac{1}{r^5}[3\vec{r}(\vec{r} \cdot \vec{d}_D) - \vec{d}_D r^2] \tag{15.2}$$

Acceptor dipole $\boldsymbol{d}_A$, if it is able to absorb the radiation at the same frequency, interacts with the electromagnetic field of a donor via the usual Hamiltonian $H = -\boldsymbol{d}_A \boldsymbol{E}_D$. The quantum transition rate W_{FRET} (FRET rate: Excitation energy is

transferred from donor to acceptor) can be found by applying the Fermi golden rule:

$$W_{FRET} = \frac{2\pi}{\hbar} < DA^*|H|D^*A >^2 \rho(\omega) \tag{15.3}$$

Here the matrix element is taken between the initial $|D^*A>$ state (the donor is excited while the acceptor is not; the asterisk designates the location of an excitation energy) and the final $< DA^*|$ state of the system. $p(\omega)$ is a density of final states; indeed, finding this is technically the most challenging step for the derivation of the FRET rate (see [6] for details). The FRET rate should compete with the radiation decay rate of a donor W_{RAD}, which is known to be [7]:

$$W_{RAD} = \frac{4\omega^3}{3\hbar c^3} d_D^2 \tag{15.4}$$

Assuming that the frequency ω is a constant, from Equations 15.2 and 15.3, it follows that $W_{FRET} \propto d_D^2 E_D^2 \propto d_D^2 / r^6$. Because from Equation 15.4 $d_D^2 \propto W_{RAD}$, we can immediately write the FRET rate as a function of the donor-acceptor distance r and W_{RAD}:

$$W_{FRET} = W_{RAD}(R_0/r)^6$$

Here R_0 is the characteristic FRET radius (also referred to as the Förster radius) defined to be the donor-acceptor distance such that $W_{FRET} = W_{RAD}$. For its precise calculation, one needs to average Equations 15.3 and 15.4 over the whole frequency range of the donor emission and acceptor absorption. This is more convenient to do using not the dipole moments, but the closely related optical emission (absorption) cross sections σ_D and σ_A ($d_{A,D}^2 \propto \int \sigma_{A,D}(\nu) d\nu$). Such an averaging gives the following result:

$$R_0 = \left(\kappa^2 q \frac{9c^4}{128 n^4 \pi^5} \int \frac{\sigma_A(\nu)}{\nu^4} f_D(\nu) d\nu \right)^{1/6}$$

Here q is the fluorescence quantum yield of the donor (which usually but not always is included in the definition of R_0) and f_D is directly proportional to the donor fluorescence cross section ($f_D \propto \sigma_D$) but unity-normalized ($\int f_D(\nu) d\nu = 1$). κ is the orientation dependence of the FRET probability, which readily follows from Equation 15.2 and the angular dependence of the vector dot product $\boldsymbol{d}_A \boldsymbol{E}_D$. Introducing angles ϑ_1, ϑ_2 between the vectors $\boldsymbol{d}_D$ and $\boldsymbol{r}$, $\boldsymbol{d}_A$ and $\boldsymbol{r}$, respectively, and an angle θ between the planes ($\boldsymbol{d}_D$, $\boldsymbol{r}$) and ($\boldsymbol{d}_A$, $\boldsymbol{r}$), one obtains:

$$\kappa = 2\cos\vartheta_1 \cos\vartheta_2 - \sin\vartheta_1 \sin\vartheta_2 \cos\theta$$

For the best case (the most "efficient" donor-acceptor orientation), κ can attain the value of 2, while for the worst case, it is equal to zero. Averaging over all angles gives $<\kappa^2> = 2/3$. See the reviews of FRET cited previously for a more detailed discussion. Numerically, the value of R_0 ranges from 2 to 7 nanometers for good FRET

donor-acceptor pairs. To give some examples, let us cite a few references from Molecular Probes, Oregon, USA (www.probes.com). All data are given for water solution: fluorescein-fluorescein is characterized by $R_0 = 4.4$ nm; fluorescein-tetramethylrodamine is characterized by $R_0 = 5.5$ nm; for the EDANS-DABCYL dye pair, $R_0 = 3.3$ nm; and so on.

From those considerations, the distinctive features of FRET may be clearly identified. First, such a process is very effective when $r \leq R_0$ and becomes ineffective once r becomes larger than R_0. This so-called "pseudo-contact" character of FRET makes it an excellent instrument for measuring intermolecular and, in some cases, intramolecular distances (a "molecular ruler"). Second, the ratio of W_{FRET} to W_{RAD} (and, hence, the value of R_0) do not depend on the absolute value of $\boldsymbol{d_D}$ and σ_{D}. This means that "weak" donors (such as so-called forced electrical dipole transitions in the rare earth ions, which are characterized by micro- and even millisecond radiation decay times [8]) can be successfully used for FRET. Indeed, its usage, especially for the case of europium and terbium chelates, which can be effectively excited by UV light, is becoming more popular. (For example, see [9] for a review.) At the same time, the value of R_0 depends on the acceptor's absorption cross section. This dependence is not strong ($R_0 \propto \sigma_A^{1/6}$), which explains why, on one hand, numerous molecules whose absorption cross sections differ by orders of magnitude can still be used for FRET as acceptors, while on the other hand, very inefficient absorbers (e.g., magnetic dipoles) cannot be used for FRET as acceptors.

In a similar fashion to the preceding discussion, one also can consider FRET involving electromagnetic transitions of a different nature than the electric dipoles. Magnetic dipoles $\boldsymbol{m}$, also can be effectively used as donors (but not as acceptors) for FRET. This is due to the fact that FRET is a competition between two processes: the energy transfer from donor to acceptor and of a radiation decay of a donor. For a magnetic dipole, the rates of both of these processes are proportional to the $\boldsymbol{m}^2$ value, like the case of an electric dipole for which both rates are proportional to $\boldsymbol{d}^2$. For the magnetic dipole case, the dependence of the electric field on r and n is different from that for the electric dipole, which should be taken into account [see [10] for a detailed discussion]. Electric quadrupoles Q also, in some cases, can be rather effective acceptors for FRET [6]. This is due to the fact that the excitation of an electric quadrupole is sensitive to the gradient of an electric field, which, as follows from Equation 15.2, is large for small distances $\boldsymbol{r}$ from a $\boldsymbol{d_D}$: $grad E_D \cong 3d_D/r^4$. To describe the $\boldsymbol{d} - Q$ interaction, the Hamiltonian H should be replaced with $H_1 = -\sum_{i,j} (\partial E_D^i/\partial x^j) Q_A^{ij}$ [7]; here Q_A^{ij} is the quadrupole moment tensor. Using the characteristic value of the field gradient given previously, we see that the ratio of the FRET rate for a $\boldsymbol{d} - Q$ interaction to that of a $\boldsymbol{d} - \boldsymbol{d}$ interaction is of the order of $9Q_A^2/r^2 d_D^2$. Since Q can be estimated to be da, where a is the characteristic size of a molecule, we know that a quadrupole acceptor will be as effective as an electrical dipole acceptor when $r \cong 3a$, which is still a reasonable distance.

We have outlined a quantum mechanical description of FRET. Nevertheless, the Planck constant h does not appear in the final formulae, which means that this effect is indeed of a "classical" nature and that a complete classical derivation can be given. This is indeed the case, and the reader is encouraged to see the FRET reviews cited previously. Here we would like to mention the illuminative work of Kuhn [11], in which he closely follows the "quantum mechanical derivation" lines

given previously. Kuhn recalls that FRET and light absorption by an acceptor in the far-field are *one and the same* physical process. Both are due to the dipole interaction of a molecule (atom) with an electric field E at frequency ω. This electric field can be that of a donor (Equation 15.2) or that of incident light. In the latter case, one needs to use the known relation $E = (8\pi I/cn)^{1/2}$ to calculate the value of an electric field starting from the light intensity I. Traditionally, all experimental parameters (e.g., light absorption cross section) are measured and calculated with the use of a light intensity I in mind, rather than the physically relevant electric field E. For this reason, instead of recalculating all experimental data from I to E, Kuhn proposed quite the opposite: To describe FRET formally, introducing a light intensity I_D corresponding to the near-field electric field of a donor (from Equation 15.2), it immediately follows that $I_D = \frac{cn}{8\pi} \frac{1}{r^{10}} [3\vec{r}(\vec{r} \cdot \vec{d}_D) - \vec{d}_D r^2]^2$.

This enabled him to use for the discussion of FRET all "far-field" experimental data without any modification.

To conclude this section, it is worthwhile to emphasize the following. During the last few years, there has been a significant increase in applications of FRET as a result of progress in the field of single-molecule detection. The whole field of single-pair FRET [12] has emerged, which has resulted in the fulfillment of a number of excellent and important experiments. To cite only a few examples, we could mention a study of individual protein molecules folding and unfolding [13–15], foreign molecule-induced protein conformations [16], and dynamic polymorphism of single actin molecules [17].

15.2 The Idea of FRET-Based Scanning Near-Field Optical Microscopy

SNOM has already been discussed extensively in this book, making it unnecessary to describe SNOM in detail here [18–20]. It is only important to emphasize again the well-known limitation in NFO of the rapid decrease of the intensity of light I passing through a subwavelength aperture with decreasing aperture diameter. In practice, this limits the spatial resolution of the more usual apertured SNOM at the limit of 50–100 nm. One cannot increase the intensity of light at the entrance of a SNOM probe for it not to be damaged. For very small apertures, the number of photons "seeping" through such a probe becomes too small for real measurements.

This motivated Sekatskii and Letokhov to propose the FRET-SNOM approach [22]. One needs to introduce onto the SNOM tip apex an "artificial" fluorescence center (this can be a dye molecule, semiconductor nanocrystal, dopant ion, or luminescent color center in an appropriate matrix; see below), excite it by laser light, and scan close to the sample surface (see Figures 15.1 and 15.2). If the distance between this center (which can be a donor or an acceptor) and the corresponding fluorescence center of the sample is smaller than the characteristic Förster radius, R_0, for this pair, the excitation energy will be transferred to the acceptor instead of being emitted by the donor. Fluorescence of an acceptor can then be monitored in the usual fashion (e.g., collecting light through a high NA micro-objective) using monochromators, appropriate filters, and/or dichroic mirrors to discriminate between donor and acceptor fluorescence. Obviously, the spatial resolution for such an approach is governed not by the aperture size, but by the value of R_0 and thus can

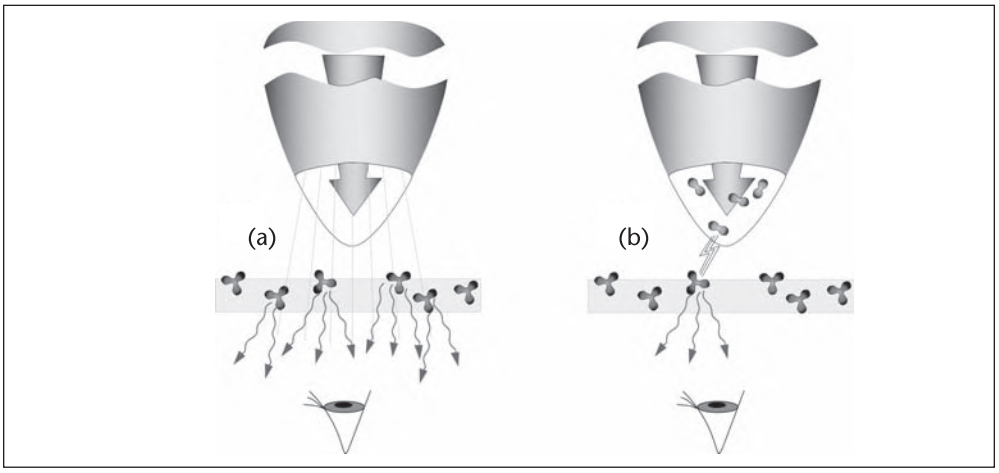

Figure 15.1 Illustrating the idea of FRET SNOM (b) in comparison with usual apertured SNOM (a).

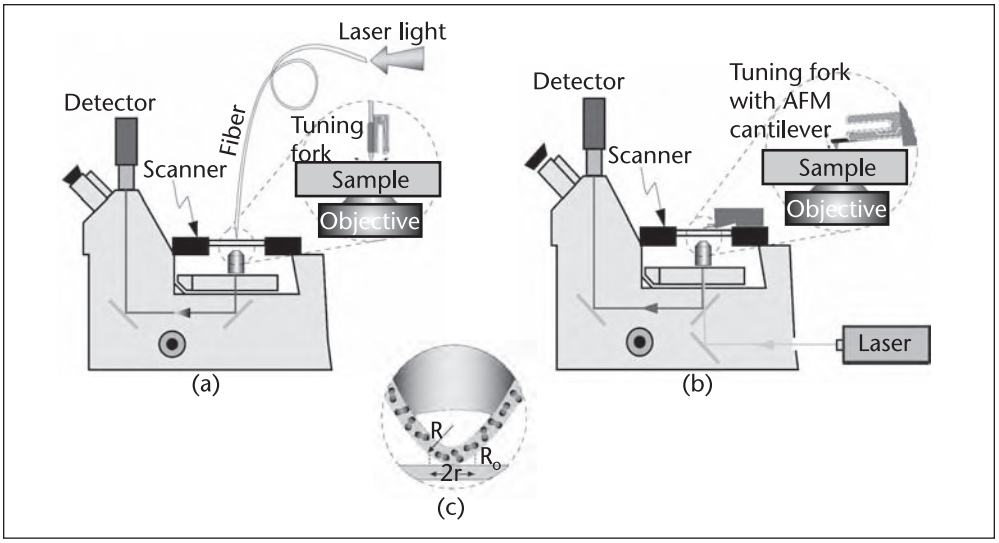

Figure 15.2 Schematic of the FRET-SNOM experimental equipment for an (a) apertured SNOM or for (b) AFM geometry, shown for the case of tuning fork-based feedback and in combination with an inverted fluorescence optical microscope. (c) The apex of the tip is coated with a FRET-active layer.

be two orders of magnitude larger. Note that it is not necessary to use the smallest achievable aperture: Apertures in the range of 300–500 nm (and, even apertures a few microns in size) will work analogously well provided that only one color center exists sufficiently close to the apex in the "FRET-active" area. Similarly, FRET SNOM can be realized in an "apertureless" version. For example, as a combination with AFM, donor (acceptor) molecules are deposited onto the sharp tip that is illuminated in epifluorescent conditions {see Figure 15.2(b) and [23]}.

Note that the sensitivity also can be higher than that of apertured SNOM: When the distance between donor and acceptor is smaller than R_0, even a rather weak acceptor will be excited at the excitation rate of the donor—that is, at the rate of $W_{ex,D} = I\sigma_D/h\nu$ rather than at the excitation rate of the acceptor, $W_{ex,A} = I\sigma_A/h\nu$.

For the case when $\sigma_A \ll \sigma_D$, FRET-induced excitation of an acceptor essentially will be more effective than it would in the case of its direct excitation by the light "seeping" from an apertured SNOM probe.

Later it was recognized that, similarly to the possibility of visualizing single dipoles using the FRET-SNOM approach, the same method can be used to visualize single quadrupoles [24]. This is due to the fact that in many cases, electric quadrupoles can be as efficient as acceptors as they can as electric dipoles (see Section 15.1).

Let us now consider the situation when many donors located in the tip apex can contribute to the FRET signal. It is easy to show that an improved spatial resolution over that of the aperture size can be achieved. Qualitatively, this can be understood from the fact that only donor (acceptor) molecules contained in a spherical segment of thickness R_0 can contribute efficiently to the FRET signal. [See Figure 15.2(c).] Here we assume a sphere of the radius R as a SNOM tip model and a simple contact between this sphere and a flat sample surface (without any deformation) as a tip-sample interaction model. For the usual case of $R \gg R_0$, the radius r of this segment is equal to

$$r = (2R_0R)^{1/2} \tag{15.5}$$

and its volume to

$$V = \pi R_0 r^2 = 2\pi R_0^2 R \tag{15.6}$$

Evidently, for such a case, the spatial resolution ($\sim r$) is smaller than R. (Spatial resolution of the standard apertured SNOM is determined by the size of the aperture, which in typical cases is of the order of R.)

More quantitatively, the spatial resolution achievable with a FRET-active tip of an arbitrary shape containing many donors (acceptors) can be analyzed by calculating the dependence of the FRET signal on the (properly defined) imaged molecule-tip distance. Such numerical calculations have been fulfilled for a number of tips (unpublished), including the interesting case of a spherical segment of thickness h and radius of curvature R filled with the FRET-active molecules with a concentration n. Their results confirmed the formula (Equation 15.5): for all "smooth" tips, the spatial resolution could be estimated as a $\gamma(R_0R)^{1/2}$, where $\gamma \sim 1$ is an appropriate numerical coefficient and R is the characteristic size of the FRET-active tip. Formally, the spatial resolution can be much improved if one considers a kind of a "supertip"; that is, relatively long ($\gg R_0$)and very sharp ($\sim R_0$) needles on the top of a smooth tip (see [25]). However, there is no reliable technology to produce such structures, and we will not discuss the case here.

Finally, when working with a FRET-active layers rather than with single fluorescence centers, one should pay attention to the fact that the FRET probability is larger than the probability of an acceptor being excited by photons reemitted by donors. For this, the condition $q\sigma_D hn \ll 1$ should be fulfilled. Inserting the typical values $q \approx 1$, $\sigma_D \approx 10^{-16}$ cm^2, $n \approx 10^{19}$ cm^{-3}, and $h \approx 100$ nm, one can see that this is valid for thin layers: $q\sigma_D hn \cong 10^{-2}$.

15.3 Experimental Realizations of FRET SNOM

15.3.1 FRET-SNOM Imaging with Many FRET Pairs: Subtip Resolution

The first experimentally obtained FRET-SNOM images were presented by Vickery and Dunn [23, 26]. The original and interesting method of deposition of dye molecules onto the tip, elaborated by Vickery and Dunn, contributed greatly to the success of their work. Our earlier attempts to realize FRET SNOM by exploiting a simple dipping of fiber tips into dye solutions with the subsequent drying of the solvent failed because the donor (acceptor) layers were very rapidly removed from the tip while scanning. To prepare the FRET-active tips, a Langmuir-Blodgett technique was used. First, L-α-dipalmitoylphosphatidylcholine (DPPC) monolayers containing 0.5 mol% of octadecyl rhodamine B chloride (acceptor) were prepared; then such a monolayer was transferred onto an uncoated SNOM tip at a pressure of 6 mN/m. It was demonstrated that at such conditions, the tip apex is coated homogeneously and that the coating exists mainly in a fluorescence-active liquid-expanded phase [26]. The stability of the coating was sufficient to survive during the shear force-based scanning.

In Figure 15.3, we reproduce one of the FRET-SNOM images obtained by Vickery and Dunn. The sample is a multilayer film composed of two monolayers of DPPC containing 0.5 mol% of fluorescein (donor) separated by three layers of arachidic acid containing no dye molecules. (A Langmuir-Blodgett technique similar to that used for the preparation of the FRET-active tips was used to prepare the sample.) Comparison of Figures 15.3(a) and 15.3(b) (images of donor and acceptor fluorescence, respectively) enables the identification of those domains located on the upper side of a sample (i.e., those closer to the FRET-active tip, which gain intensity when the acceptor fluorescence is recorded) and those domains on the sample's lower side.

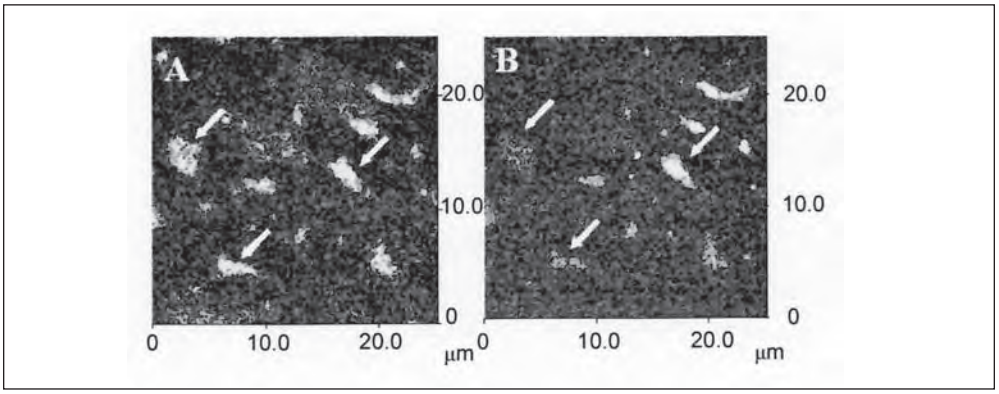

Figure 15.3 Fluorescence images of a multilayer film in which the upper and lower monolayers containing the donor dye are separated by three spacer layers. Images are obtained using a FRET-active SNOM tip coated with a monolayer of DPPC containing the acceptor dye. (a) donor fluorescence is recorded; (b) acceptor fluorescence is recorded. Domains indicated by arrows lose intensity, indicating that they are located on the bottom layer of the film, or gain intensity, indicating that they are located in the upper layer of the film. Reproduced with permission from [23]. Copyright 2001 The Royal Microscopical Society.

Vickery and Dunn also reported the first FRET images recorded, using the deposition of acceptor dye molecules onto a standard silicon nitride AFM tip (employing a contact scanning method) [23]. Chemical fixation of dye molecules on the tip surface, borrowed from single-molecule force spectroscopy AFM research, was employed for the preparation of FRET-active tips.

Shubeita and coworkers (2002) also have succeeded in recording FRET-SNOM images by exploring other FRET-active local fluorescent probes [27]. These probes are thin dye-stained polymer layers deposited onto the standard apertured fiber probe; they are prepared by dipping the tip into a 3×10^{-5} mol/L chloroform solution of the dye containing 1–2 vol.% of dissolved PMMA or PS. According to data obtained by depositing similar polymer solutions by controllable withdrawal [28], 30–100 nm thick layers of the PMMA stained with the dye (in our case, with a concentration of $n = 1.9 \times 10^{18}$ cm^{-3}) are formed on the tip surface after the solvent dries; existence of such layers also has been confirmed by SEM studies of the tips. This concentration provides sufficient acceptor molecules to contribute to the FRET signal. In addition to the better photostability and immobilization of the molecules embedded in the polymer matrices, a "self-sharpening" behavior may be realized for such a probe. Apical layers of the FRET-active tip coating are mechanically worn out during scanning; hence, an active apex containing fresh acceptor molecules is continuously exposed to imaging. Note that the probe contains acceptor rather than donor molecules. The former do not absorb the laser excitation light, which continuously illuminates them through the fiber. Hence, only those molecules lying within a few nanometers of the apex that participate in FRET are subject to eventual photobleaching. These molecules are those refreshed by the "self-sharpening" mechanism.

In Figure 15.4, fluorescence data and an example of the optical approach curve obtained with such local fluorescence probes are presented [29]. The pair of dyes DCM (Spectra Physics, Germany; donor) and OM57 (Alpha Akonis Comp., Moscow; acceptor) has been selected as one of the best pairs for the FRET investigations due to the high fluorescence yield of the donor and acceptor, the large Stokes shift, and a very inefficient direct excitation of acceptor by the laser radiation used (488 nm line of argon ion laser). This is well demonstrated on the left

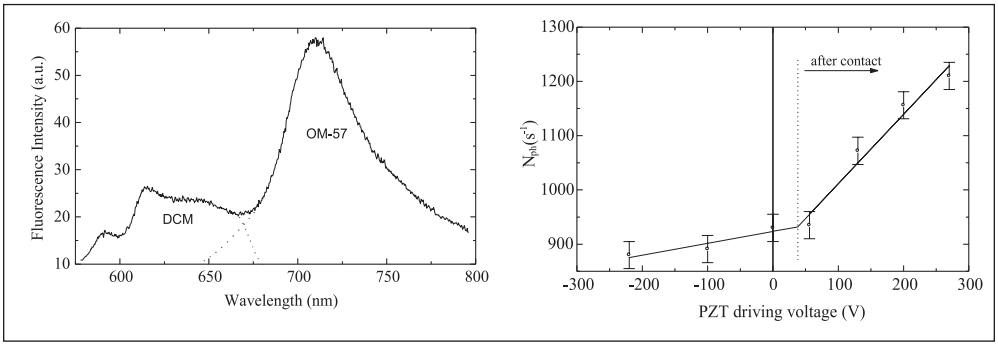

Figure 15.4 Fluorescence spectra of monolayers of donor (DCM) and acceptor (OM57) dye molecules codeposited onto the glass slide surface (left) and the dependence of the acceptor fluorescence signal on the tip-sample force recorded during one approach of the SNOM tip (right). The tip is coated with the PMMA layer containing OM57 acceptor molecules, and the sample is a glass slide coated with a monolayer of DCM dye donor molecules.

side of Figure 15.4, where a fluorescence spectrum from two monolayers of these dyes codeposited onto the glass slide surface is shown. It is clearly seen that in these conditions, the acceptor (OM57) fluorescence intensity exceeds that of the donor (DCM); recorded at the same conditions, fluorescence of the monolayer of acceptor molecules deposited without donor molecules was indiscernible from the noise level. A glass plate coated with a monolayer of DCM acceptor dye molecules was used as a sample in the recording of approach curves, shown on the right side of Figure 15.4. It is clearly seen that the acceptor fluorescence starts to increase rapidly after the tip-glass slide surface contact is established. This can be explained as an increase in the number of FRET pairs contributing to the signal due to the deformation of the SNOM tip upon an increase of applied force.

A FRET-SNOM image of DCM molecules nonhomogeneously deposited onto a glass slide surface (small droplets, $10-20\ \mu$L, of DCM dye solution dropped onto the glass slide surface and then air-dried; the nominal surface concentration of the DCM molecules is 5×10^{14} molecules/cm^2) is presented in Figure 15.5. The shear force topography signal, recorded simultaneously with the optical signal, reveals that the bright spots are "hills" formed where DCM molecules have "condensed" in some places of the sample, where the local dye concentration essentially exceeds the average for the whole image.

The value of FRET-active pairs contributing to the signal N_{ac} is defined by the number of acceptor molecules contained in a FRET-active spherical segment (see Section 15.2). Applying Equation 15.6 for the Förster radius $R_0 = 3$ nm and the radius of curvature of the tip $R = 250$ nm, we have $N_{ac} = 2\pi R_0^2 Rn \sim 15$. This estimate is consistent with the magnitude of the optical signal recorded. Hence, we have a case when many molecules contribute to the FRET signal. So we can estimate the spatial resolution as outlined in Section 15.2. Applying Equation 15.5, we

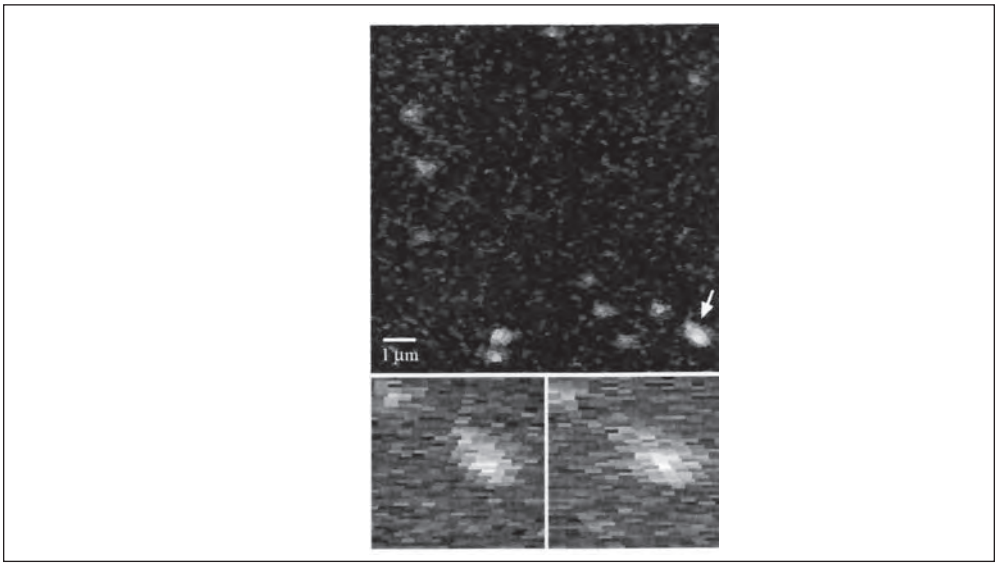

Figure 15.5 FRET-SNOM image of donor dye "clusters" on a glass slide surface recorded using a SNOM tip coated with a PMMA layer that contains acceptor molecules. In the insert, we show details of the raw images of one of the clusters (indicated by an arrow) recorded for the left-to-right and right-to-left movements of the tip.

obtain the value $r \approx 80$ nm. This value corresponds to the experimental data; a good reproducibility of small details of the light intensity distribution within the DCM "clusters" (the bottom two panels in Figure 15.5) can be considered as an indication of a spatial resolution of the order of $\sim 60-80$ nm.

Similar FRET-SNOM images also were obtained for analogous local fluorescent probes but stained with CdSe/ZnS nanocrystals [30]. Lately, CdSe/ZnS, InAs, and CdTe nanocrystals were used for the FRET-SNOM imaging by Ebenstein and colleagues [31, 32] and Müller and coworkers [33]. A single latex bead of 450 nm in diameter coated with CdTe nanocrystals and fixed on the sharpened SNOM tip was used by Müller and coworkers [33]. Silicon AFM tips whose surface was modified to chemically bind semiconductor nanocrystals and used in an apertureless SNOM scheme were exploited by Ebenstein and colleagues [31, 32]. FRET-SNOM imaging based on the fluorescent F-aggregated color centers in LiF crystals was attempted by Sekatskii and his colleagues [34].

15.3.2 Single-Molecule FRET-SNOM Imaging

In all cases of FRET-SNOM imaging discussed in the previous section, many tens or hundreds of FRET-active centers are involved in the imaging process. This enables one to attain subtip resolution, and such an approach may be useful for understanding the nature of the imaged chromophores. However, the full realization of all advantages of the method can be achieved only with true single-molecule FRET imaging. Such a situation, with only one donor (or acceptor) molecule embedded in the SNOM tip used to image the acceptor (or, correspondingly, donor) centers of the samples, was not attained until very recently. The reason is because of the limited photostability of the fluorescence centers: For a typical optical absorption cross section of a single fluorescent center $\sigma \cong 10^{-16}\text{cm}^2$, photon energy $h\nu \cong 3 \cdot 10^{-19} J$, and near-field illumination intensity $I \cong 10^3 W/\text{cm}^2$, a (good) photostability of around $N = 10^7$ cycles determines the lifetime of a center to be equal to $t = Nh\nu/I\sigma \cong 30$ seconds. Hence, very rapid scanning is required to achieve the desirable single-center imaging. The whole SNOM image (or preferably a number of images) should be taken over a period of only 30 seconds or so; otherwise, the single center used for FRET-SNOM imaging photodestructs before any useful information is gained. This requires the use of a SNOM instrument capable of such a fast scanning rate. Recently, we constructed such a microscope [35], which enabled the first observation of true single-molecule FRET-SNOM images [36] briefly discussed next. Rapid scanning with this microscope was achieved primarily because of the large quality factor of the near-field probe due to the original double-resonant montage of a sharpened fiber on a tuning fork. The use of specially designed proprietary electronics capable of fast measurements of the resonant frequency and Q-factor of the probe interacting with the sample also contributed to fast scanning (see [35] for further details).

A FRET-SNOM image of a single CdSe nanocrystal (donor, fluorescence maximum at 590 nm, synthesized in Mainz University in the group of Prof. Th. Basché; see, for example, [37]), which is obtained by detecting FRET photons emitted by Alexa Fluor 594 (Molecular Probes, Oregon) dye molecules (acceptors), is

presented in Figure 15.6. The dye molecules are embedded in a ~ 50-nm-thick PMMA layer, which is deposited onto the apex of an apertured fiber (Nanonics, Israel, nominal aperture size 100 nm). Nanocrystals were deposited onto the glass slide surface by spin coating from toluene solution in such a concentration that, on average, one nanocrystal over a few square microns can been seen. The whole scan presented in Figure 15.6 was recorded in only ca. 12 seconds. All necessary adjustments were done without the laser light entering into the fiber probe; laser light was introduced into it immediately before the start of the scanning.

The same "self-sharpening" FRET-active probes and the same method to excite and record the fluorescence as discussed in [27, 30] were used, but the concentration of acceptor molecules in the probe was reduced to ca. $4 \times 10^{16}\text{cm}^{-3}$. This means that in a "FRET-active" area of the fiber with a volume $V = \pi R_0^2 R_c$ (a Förster radius for the donor-acceptor FRET pair is 5 nm, and $R_c \approx 100 - 200$ nm), about one acceptor molecule is capable of contributing to the optical signal. Such a "one FRET-active pair" character of the image also is consistent with the maximal fluorescence signal recorded in these experiments. At best, four to five photocounts per pixel (for the photon collection time $\tau_0 = 0.7$ ms) were detected, while $N = I\sigma\eta\tau_0/(h\nu) \cong 10$ photocounts could be anticipated for the typical single-molecule optical parameters given and an overall detection efficiency η of around 0.05.

Note that for a photon collection time of $\tau_0 = 0.7$ ms and the noise level of the detector (Perkin Elmer single photon avalanche diode) of around $500\,s^{-1}$ (ca. $100 - 150\,s^{-1}$ dark noise and residual excitation light background, with the rest unavoidable stray light contamination), we have essentially a "zero background image" (on average 0.3–0.4 counts/point; hence, usually zero), which helps facilitate the detection of single nanocrystals. The FWHM of images of a single nanocrystal, such as the one in Figure 15.6, is around 12 nm, which attests that the spatial resolution of the order of the FRET Förster radius has been attained with FRET SNOM. Note that apart from the estimated Förster radius of 5 nm, the size of the nanocrystal (CdSe core diameter equal to 4.8–4.9 nm and protective ZnS layer with a thickness of ~ 1−2 nm) also contributes to the size of the image spot of a single nanocrystal.

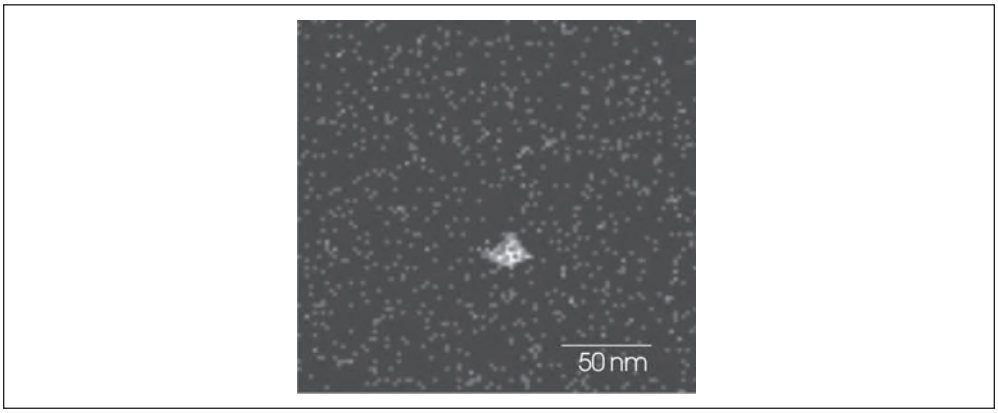

Figure 15.6 FRET-SNOM image of single CdSe nanocrystal (donor) on a glass slide surface. Scan size is 220 × 220 nm. The simultaneously taken shear force topographical image (not shown) is completely flat and structureless.

15.4 Concluding Remarks

Among different existing approaches to SNOM, scanning near-field exciton microscopy, proposed and explored by Kopelman and colleagues [25, 38, 39] (also see [40] for a detailed theoretical exposition of the method), should be considered as the closest analogue to FRET SNOM. Its main idea can be understood from Figure 15.1(b). However, isolated fluorescence centers should not be used inside a transparent matrix, but small molecular crystals capable of effective exciton energy transfer (e.g., anthracene or perylene) should be placed at the tip apex. These structures were implemented by Kopelman and coauthors using different methods of crystal growth (growth from solution, from melt, from vapor, from chemical reactions) inside glass micropipettes. Excitation transport inside a molecular crystal is affected not via a light propagation, but via an exciton propagation. It was argued that by this manner, the excitation energy can be efficiently transferred into the very apex of a tip ("supertip" according to [25]) and then be transferred to the sample via a kind of a FRET process (which in this case also can be named "exciton tunneling").

For such an approach, one can attain the spatial resolution characteristic for FRET-active tips containing many donor (acceptor) molecules in the apex area (Section 15.2); of course, a resolution of the order of R_0 characteristic for a single FRET-active fluorescence center cannot be achieved. The resolution can be improved and made just the order of R_0 if, in addition to the molecular crystal supporting an effective exciton propagation, an appropriate fluorescent center is added to the very apex of this tip. This center should work as an exciton trap ("supertrap") that collects an excitation from the molecular crystallite of the size up to 50–100 nm, working in this case as an antenna (c.f. photosynthetic antenna). Molecular engineering methods are potentially capable of designing a "funnel" consisting of host crystal molecules perturbed by impurity molecules. The closer the host molecule is to the trap, the lower its excitation energy. Thus, molecules in the funnel catch the excitation from the host nanocrystallite and pass it deeper and deeper up to the supertrap [38]. Lately, it has been argued that specific dendrimer supermolecules can be used as corresponding supertraps [41].

The potential of such a scanning exciton microscopy (when equipped with a single-molecule "supertrap") can be considered to be more or less the same as that of the FRET-SNOM approach described previously. A possible advantage is more effective light collection. But, as discussed, for FRET SNOM, we are not limited to the smallest attainable apertures, so this advantage does not seem to be an important one. This possible advantage is not gained for free; molecular engineering methods capable of producing a supertip suitable for exciton microscopy are rather complicated, and molecular nanocrystals do not seem to be very stable. To the best of our knowledge, we believe this explains why no SNOM image obtained using the scanning exciton microscopy approach has been demonstrated so far.

While discussing connections of FRET SNOM with other SNOM approaches, it makes sense to look at this technique in the context of the local electromagnetic field enhancement. It is well known that such an enhancement is vital for the

success of an apertureless SNOM, especially when plasmon resonances are involved. Let us estimate the magnitude of a resonant electric field E in the vicinity of a donor center. For the characteristic value of a dipole moment $d_D \sim 1$ Debye and a donor-acceptor distance r of 3 nm, one has $E \cong d_D/r^3 \approx 10$ kV/cm. At the same time, using a value for the light intensity $I = 1$ kW/cm^2, which is characteristic for an apertured SNOM probe (for CW laser excitation, this value cannot be higher because of tip fragility), we obtain $E \sim 1$ kV/cm as an estimate for the corresponding field magnitude for the case of a standard apertured SNOM. This simple example demonstrates that the physics appearing in FRET SNOM can be viewed to some extent in a similar fashion to the lightning rod effect in apertureless SNOM: Artificial fluorescence centers introduced into the SNOM tip work as field concentrators (remembering that an increase of the field E by one order of magnitude is equivalent to an increase of the light intensity I by two orders of magnitude).

Thus, the first ten years of the development of FRET SNOM has brought the experimental realization of the method, including the observation of true single-molecule FRET-SNOM images. The problem of photostability remains the main obstacle hindering further progress and widespread use of the method; the exploration of semiconductor nanocrystals has been an important step in this direction but has not solved all of the problems. (Exploration of F-aggregated color centers in LiF [34] was rather disappointing in this sense.) Perhaps photostability of fluorescent color centers in diamond, which are currently considered as prospective fluorescent media [42, 43] (and were proposed for the FRET-SNOM imaging from the beginning [22]) will be large enough to bring new, exciting possibilities to the field.

Finally, we recently proposed the application of FRET SNOM for quantum computing [44] and started the first experiments in this direction [45]. Usually, FRET is an irreversible and incoherent process, as can be seen from the discussion in Section 15.1. But the situation can be different at low (liquid helium) temperatures. For example, for a number of rare-earth ions in different crystalline matrices, decoherence times lying in the region of micro- and even milliseconds have been demonstrated [8]. For such a case, the FRET interaction between two neighboring ions has a reversible and coherent character. Such large optical dephasing times imply very narrow spectral lines, but there are many possibilities for adjusting the spectra of the donor and the acceptor using local (e.g., SNOM or AFM tip-induced) external electric or magnetic fields [44]. Dividing a donor-acceptor pair between a SNOM tip and a sample and performing controllable motion of the tip offers the potential of manipulating the donor-acceptor quantum system in a desirable way to enable, for example, the preparation of multiparticle entangled states or to perform quantum logic operations on the qubits.

Acknowledgments

The author acknowledges very important contributions to this work from numerous colleagues and collaborators; the list is too long to be presented here. Many years of financial support from Swiss National Science Foundation is also greatly appreciated.

References

[1] Agranovich, V. M., and M. D. Galanin, *Electron Excitation Energy Transfer in Condensed Matter,* Amsterdam: North Holland, 1982.

[2] Clegg, R. M., "Fluorescence Resonance Energy Transfer," in *Fluorescence Imaging Spectroscopy and Microscopy* (X. F. Wang and B. Herman, eds.), New York: John Wiley, 1996, pp. 179–253.

[3] Jares-Erijman, E. A., and T. M. Jovin, "FRET Imaging," *Nature Biotechnol.*, Vol. 21, 2003, pp. 1387–1395.

[4] Clapp, A. R., I. L. Medintz, and H. Mattoussi, "Förster Resonance Energy Transfer Investigations Using Quantum-Dot Fluorophores," *Chem. Phys. Chem.*, Vol. 7, 2006, pp. 47–57.

[5] Stratton, J. A., *Electromagnetic Theory*, New York: McGraw-Hill, 1941.

[6] Dexter, D. L., "A Theory of Sensitized Luminescence in Solids," *J. Chem. Phys.*, Vol. 21, 1953, pp. 836–850.

[7] Berestetskii, V. B., E. M. Lifshitz, and L. P. Pitaevskii, *Relativistic Quantum Theory*, New York: Pergamon Press, 1971.

[8] Macfarlane, R. M., and R. M. Shelby, *Spectroscopy of Solids Containing Rare Earth Ions*, Amsterdam: North Holland, 1987.

[9] Bunzli, J. C. G., "Lanthanide-containing luminescent molecular edifices," *J. Alloys Compounds*, Vol. 408, 2006, pp. 934–944.

[10] Sekatskii, S. K., and G. Dietler, "Using Magnetic Dipole Transitions for Fluorescence Resonance Energy Transfer," *Anal. Biochem.*, Vol. 299, 2001, pp. 263–266.

[11] Kuhn, H., "Classical Aspects of Energy Transfer in Molecular Systems," *J. Chem. Phys.*, Vol. 53, 1970, pp. 101–108.

[12] Weiss, S., "Fluorescence Spectroscopy of Single Molecules," *Science*, Vol. 283, 1999, pp. 1676–1683.

[13] Deniz, A. A. et al., "Single-Molecule Protein Folding: Diffusion Fluorescence Resonance Energy Transfer Studies of the Denaturation of Chymotrypsin Inhibitor 2," *Proc. Nat. Acad. Sci. USA.*, Vol. 97, 2000, pp. 5179–5184.

[14] Rhoades, E., E. Gussakovsky, and G. Haran, "Watching Proteins Fold One Molecule at a Time," *Proc. Natl. Acad. Sci. USA.*, Vol. 100, 2003, pp. 3197–3202.

[15] Kuzmenkina, E. V., C. D. Heyes, and G. U. Niehaus, "Single-Molecule FRET Study of Denaturant Induced Unfolding of RNase H," *J. Mol. Biol.*, Vol. 357, 2006, pp. 313–324.

[16] Majumdar, D. C. et al., "Single-Molecule FRET Reveals Sugar-Induced Conformational Dynamics in LacY," *Proc. Nat. Acad. Sci. USA.*, Vol. 104, 2007, 12640–12645.

[17] Kozuka, J. et al., "Dynamic Polymorphism of Single Actin Molecules in the Actin Filament," *Nature Chem. Biol.*, Vol. 2, 2006, pp. 83–86.

[18] Ohtsu, M., *Near-Field Nano/Atom Optics and Technology*, Tokyo: Springer, 1998.

[19] Dunn, R. C., "Near-Field Scanning Optical Microscopy," *Chem. Rev.*, Vol. 99, 1999, pp. 2891–2927.

[20] Novotny, L., and B. Hecht, *Principles of Nano-optics*, Cambridge: Cambridge University Press, 2006.

[21] Bethe, H. A., "Theory of Diffraction by Small Holes," *Phys. Rev.*, Vol. 66, 1944, pp. 163–182.

[22] Sekatskii, S. K., and V. S. Letokhov, "Single Fluorescence Centers on the Tips of Crystal Needles: First Observation and Prospects for Application in Scanning One-Atom Fluorescence Microscopy," *Appl. Phys. B*, Vol. 63, 1996, pp. 525–530.

[23] Vickery, S. A., and R. C. Dunn, "Combining AFM and FRET for High Resolution Fluorescence Microscopy," *J. Microsc.*, Vol. 202, 2001, pp. 408–412.

[24] Sekatskii, S. K., G. T. Shubeita, and G. Dietler, "On the Possibility of Observation of Single Quadrupoles by Fluorescence Resonance Energy Transfer Scanning Near-Field Optical Microscopy," *Opt. Commun.*, Vol. 188, 2001, pp. 41–45.

[25] Kopelman, R., and W. H. Tan, "Near-Field Optical Microscopy, Spectroscopy, and Chemical Sensors," *Appl. Specrosc.*, Rev. Vol. 29, 1994, pp. 39–66.

[26] Vickery, S. A., and R. C. Dunn, "Scanning Near-Field Resonance Energy Transfer Microscopy," *Biophys. J.*, Vol. 76, 1999, pp. 1812–1818.

[27] Shubeita, G. T. et al., "Local Fluorescence Probes for the Fluorescence Resonance Energy Transfer Scanning Near-Field Optical Microscopy," *Appl. Phys. Lett.*, Vol. 80, 2002, pp. 2625–2627.

[28] Yang, C. C., J. Y. Josefowicz, and L. Alexandru, "Deposition of Ultrathin Films by a Withdrawal Method," *Thin Solid Films*, Vol. 74, 1980, pp. 117–127.

[29] Shubeita, G. T. et al., "Investigation of Nanolocal Fluorescence Resonance Energy Transfer for Scanning Probe Microscopy," *Appl. Phys. Lett.*, Vol. 74, 1999, pp. 3453–3455.

[30] Shubeita, G. T. et al., "Scanning Near-Field Optical Microscopy Using Semiconductor Nanocrystals as a Local Fluorescence and Fluorescence Resonance Energy Transfer Source," *J. Microsc.*, Vol. 210, 2003, pp. 274–278.

[31] Ebenstein, Y., T. Mokari, and U. Banin, "Quantum-Dot-Functionalized Scanning Probes for Fluorescence-Energy-Transfer-Based Microscopy," *J. Phys. Chem. B*, Vol. 108, 2004, pp. 93–99.

[32] Ebenstein, Y. et al., "Interaction of Scanning Probes with Semiconductor Nanocrystals; Physical Mechanism and Basis for Near-Field Optical Imaging," *J. Phys. Chem. A*, Vol. 110, 2006, pp. 8297–8303.

[33] Müller, F., et al. "Investigation of Energy Transfer between CdTe Nanocrystals on Polystyrene Beads and Dye Molecules for FRET-SNOM Applications," *J. Phys. Chem. B*, Vol. 108, 2004, pp. 14527–14534.

[34] Sekatskii, S. K. et al., "Subwavelength-Size Local Fluorescent Sources Based on Color Centers in LiF for Scanning Near-Field Optical Microscopy," *J. Lum.*, Vol. 122–123, 2007, pp. 362–364.

[35] Cherkun, A. P. et al., "Double Resonance Probe for Scanning Optical Near-Field Microscopy," *Rev. Sci. Instr.*, Vol. 77, 2006, Art. No. 033703.

[36] Sekatskii, S. K., V. S. Letokhov, and G. Dietler, "Single Molecule Fluorescence Resonance Energy Transfer Scanning Near-Field Optical Microscopy," *Chem. Phys. Lett.*, Vol. 452, 2008, pp. 220–224.

[37] Potapova, I. et al., "Semiconductor Nanocrystals with Multifunctional Polymer Ligands," *JACS*, Vol. 125, 2003, pp. 320–321.

[38] Kopelman, R., A. Lewis, and K. Liberman, "Nanometer Light-Source and Molecular Exciton Microscopy," *J. Lum.*, Vol. 45, 1990, pp. 298–299.

[39] Kopelman, R., W. H. Tan, and D. Birnbaum, "Subwavelength Spectroscopy, Exciton Supertips and Mesoscopic Light-Matter Interactions," *J. Lum.*, Vol. 58, 1994, pp. 380–387.

[40] Paule, E., and P. Reineker, "Scanning Near-Field Exciton Microscopy: Detection of Single Molecules on an Organic Surface," *J. Phys. Chem. B*, Vol. 105, 2001, pp. 4293–4304.

[41] Swallen, S. F. et al., "Exciton Localization Hierarchy and Directed Energy Transfer in Conjugated Linear Aromatic Chains and Dendrimeric Supermolecules," *J. Lum.*, Vols. 76–77, 1998, pp. 193–196.

[42] Yu, S.-J. et al., "Bright Fluorescence of Nanodiamonds: No Photobleaching and Low Cytotoxicity," *JACS*, Vol. 127, 2005, pp. 17604–17605.

[43] Dutt, M. V. G. et al., "Quantum Register Based on Individual Electronic and Nuclear Spin Qubits in Diamond," *Science*, Vol. 316, 2007, pp. 1312–1316.

[44] Sekatskii, S. K., M. Chergui, and G. Dietler, "Coherent Fluorescence Resonance Energy Transfer: Construction of Nonlocal Multiparticle Entangled States and Quantum Computing," *Europhys. Lett.*, Vol. 63, 2003, pp. 21–27.

[45] Sekatskii, S. K. et al., "Experimental Preparation of Entangled Bell's Vacuum—Single Exciton and Vacuum—Biexciton States for Pair Centers of Neodymium Ions in a Crystal," *Opt. Communicat.*, Vol. 259, 2006, pp. 298–303.

CHAPTER 16

Recent Developments in Near-Field Optics

Ferhat Culfaz and David Richards

16.1 Tip-Enhanced Spectroscopy

In the preceding chapters, some of the exciting new possibilities for high-resolution optical imaging and spectroscopy promised by ASNOM were considered. We will provide a brief overview in this chapter of other recent advances in the development of new optical nanoprobes that offer the promise of optical microscopy with true nanometer spatial resolution and optical spectroscopy of single molecules.

16.1.1 Tip-Enhanced Raman Scattering

The ability of Raman spectroscopy to measure the frequencies of molecular and crystal vibrations, with the high degree of chemical specificity that this provides, has led to a burgeoning interest in recent years in tip-enhanced Raman scattering (TERS). As discussed in Chapter 13, by placing a molecule close to a metallic tip, local fields are resonantly excited in the tip under optimal conditions, producing a strong, highly localized electric field enhancement such that an enhancement of Raman scattering intensity of the order of 10^7 can be expected on the sample surface beneath the tip over an area of diameter ~ 10 nm [1]. In particular, this high spatial resolution avoids the surface generality of SERS and allows Raman imaging of single molecules.

In addition to the application of TERS to the study of SWNTs by Hartschuh, Novotny, and coworkers, discussed in Chapter 13, TERS has now been applied successfully to a range of systems. TERS measurements (by Pettinger and coworkers) of monolayers of absorbates on gold or platinum surfaces [2, 3] have demonstrated tip enhancement of the Raman signal by up to 10^6, with evidence of Raman scattering from single dye molecules [4]. Kawata's group has shown how the strain induced through the application of mechanical pressure by the ASNOM tip to adenine nanocrystals [5], C_{60} [6], and SWNTs [7] can be observed from shifts in near-field Raman spectra obtained from TERS measurements and have employed TERS to study nanoscale strain in silicon surfaces [8, 9]. Biological applications of TERS have been demonstrated by Deckert and coworkers who have measured Raman signals of DNA bases [10] and at the surface of bacteria [11].

However, caution needs to be exercised in the interpretation of tip-enhanced Raman spectra, as tip contamination [12, 13] or sample contamination [14, 15] can ruin spectra for single-molecule sensitivity; the same problems also hold true for SERS measurements. It also is crucial to obtain TERS tips with very high

enhancement, given the small area probed, and the quality and form of the metal tip and the polarization and wavelength of the incident light are all critically important for this.

16.1.2 Tip-Enhanced Fluorescence

The tip also can be used to enhance fluorescence emission from molecules or quantum dots. As Gerton described in Chapter 12, near-field fluorescent images of quantum dots [16], single molecules, and DNA [17] have all been observed. However, as was discussed by Hecht in Chapter 3, placing an etched gold tip in the vicinity of a fluorophore also leads to significant modifications to the radiative and nonradiative decay rates, as well as an enhancement in local incident field and, hence, excitation rate. The enhanced local field and radiative decay rate tend to increase the fluorescence intensity, while the increased nonradiative decay rate, which results from energy transfer from the fluorophore to metal, will diminish the fluorescence intensity dramatically. The net enhancement of fluorescence results from a competition between this enhancement and quenching, and whether enhanced or diminished fluorescence intensity is observed depends strongly on the particular experimental conditions [18]. For example, a tip-enhanced fluorescence image of an isolated cluster of CdSe quantum dot nanoparticles is presented in Figure 16.1 [19]. Confocal fluorescence imaging leads to the observation of a resolution of 200 nm, consistent with the size of the diffraction-limited focus. When a sharp gold tip is brought within a few nanometers of the sample surface, the resulting enhancement in quantum dot fluorescence in the vicinity of the tip leads to a resolution of about 60 nm. The observed fourfold enhancement of the fluorescence is consistent with the value expected from the competition between fluorescence quenching and electromagnetic field enhancement.

16.1.3 Fluorescence Enhancement by Single Metal Nanoparticles

The optical properties of metallic nanoparticles and their plasmon resonances are well known. So to provide a more precise probe of the effect of a MNS on single-molecule fluorescence, recent work has employed as a tip a metal nanoparticle glued to the end of a glass tip. A schematic of an experimental arrangement for this kind of measurement is shown in Figure 16.2; a gold nanoparticle is picked up by a glass tip and then subsequently brought into close proximity with a single dye molecule deposited on a surface to provide near-field imaging and to enable an interrogation of the dependence of the fluorescence emission on the separation of the nanoparticle and molecule.

Using this approach, the influence on the fluorescence emission of a single terrylene molecule by a 100 nm spherical gold nanoparticle has been investigated by the Sandoghdar group [20] with the observation of more than 20 times fluorescence enhancement of the molecule with a simultaneous 20-fold shortening of the excited state lifetime. They also have demonstrated the importance of bringing the excitation wavelength into resonance with the gold nanoparticle. The molecule's excitation rate is directly proportional to its fluorescence rate if the nanoparticle does not affect the molecule's quantum yield. However, on resonance, the nanoparticle does affect the quantum yield, introducing radiative and nonradiative decay

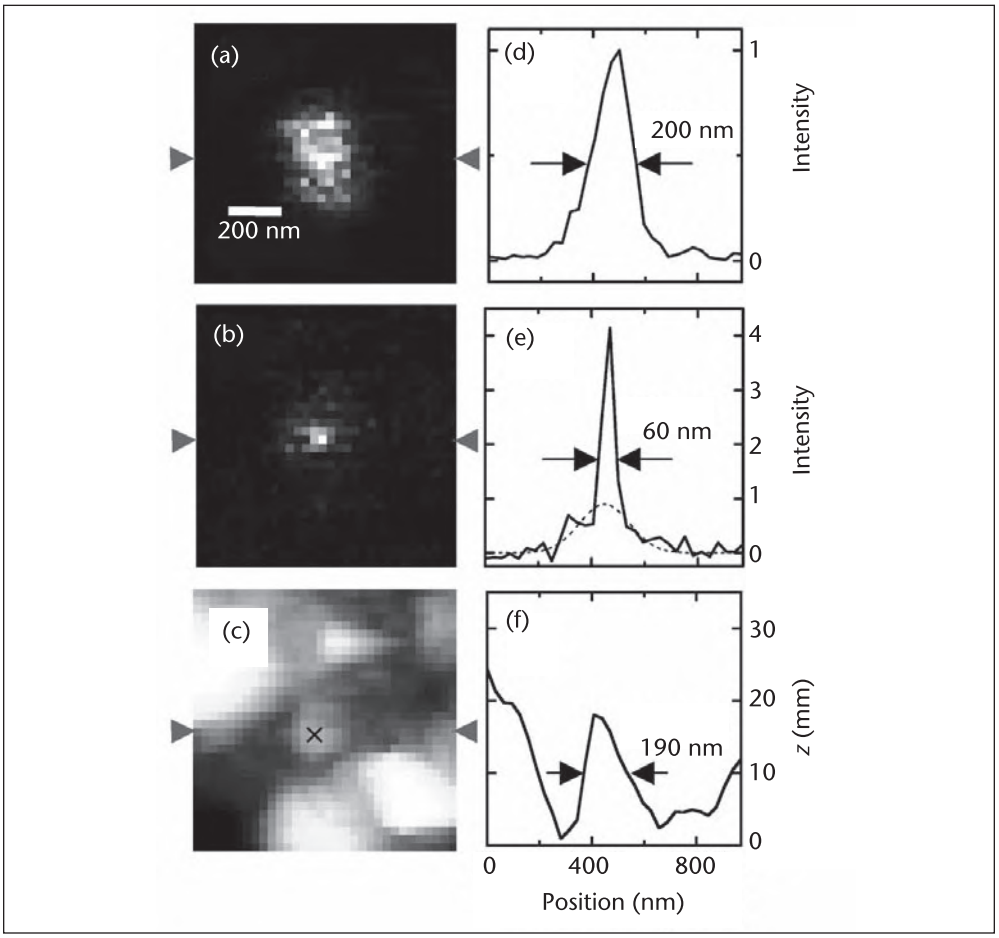

Figure 16.1 $1\mu m \times 1\mu m$ (a) fluorescence confocal (no tip) image (the fluctuations result from intermittent "blinking" of the quantum dot fluorescence), (b) fluorescence apertureless SNOM image, and (c) topographic image of a small quantum dot cluster. (b) and (c) obtained simultaneously with a sharp gold tip close to the center of the laser focus. The cross in (c) indicates the nanoparticle cluster. (d) Fluorescence confocal, (e) fluorescence ASNOM, and (f) topographic line profiles along the scan lines indicated by the arrows in (a), (b), and (c), respectively. The fluorescence signals in (d) and (e) are normalized to the diffraction-limited signal in both scans; a fit to the diffraction-limited signal is indicated by the dashed line in (e). ©AIP [19].

channels. If the distance between the nanoparticle and the molecule is small, the nonradiative energy transfer is stronger, thus quenching the fluorescence.

In a similar series of experiments employing 80 nm gold and silver nanoparticles, Novotny and coworkers have measured the single-molecule fluorescence of Nile blue dye molecules as a function of nanoparticle-sample distance [21]. A near-field image of Nile blue was obtained, and the fluorescence was observed to be enhanced as the nanoparticle was approached to the molecule. At small separations, quenching was again found to occur as a result of nonradiative decay from the molecule to the particle; with decreasing separation, the onset of quenching occurred at 4 nm for a silver nanoparticle and 1 nm for a gold nanoparticle (Figure 16.3), with a maximum fluorescence emission intensity when using a silver nanoparticle almost double that when compared to a gold nanoparticle.

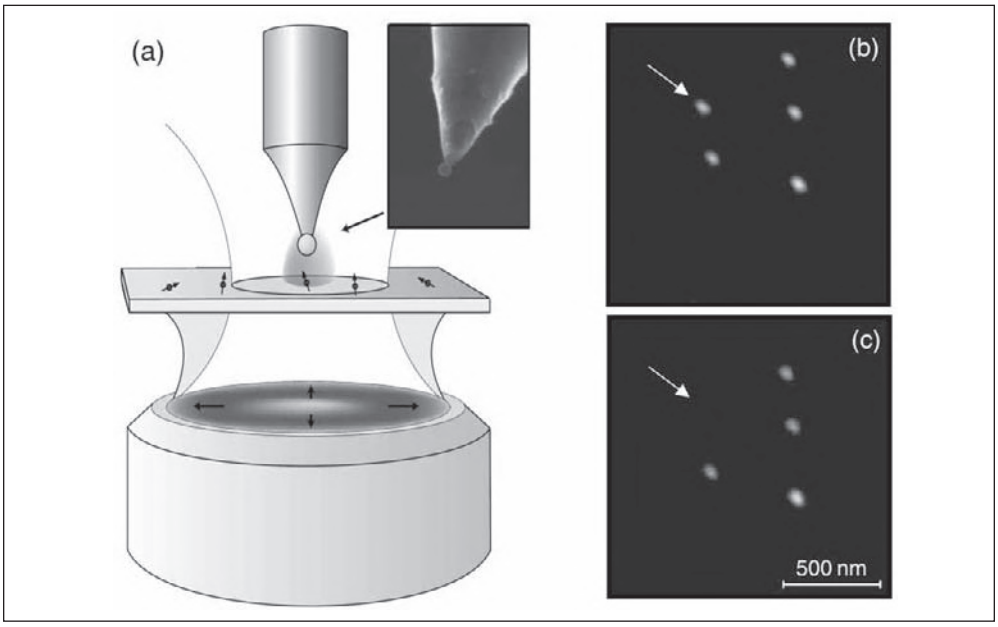

Figure 16.2 (a) Schematic diagram of the experimental setup for a gold or silver nanoparticle on a glass tip (SEM image shown in inset). (b) Topography image of isolated gold nanoparticles before and (c) after picking up with the glass tip. Bharadwaj et al. ©IOP Publishing Ltd [21].

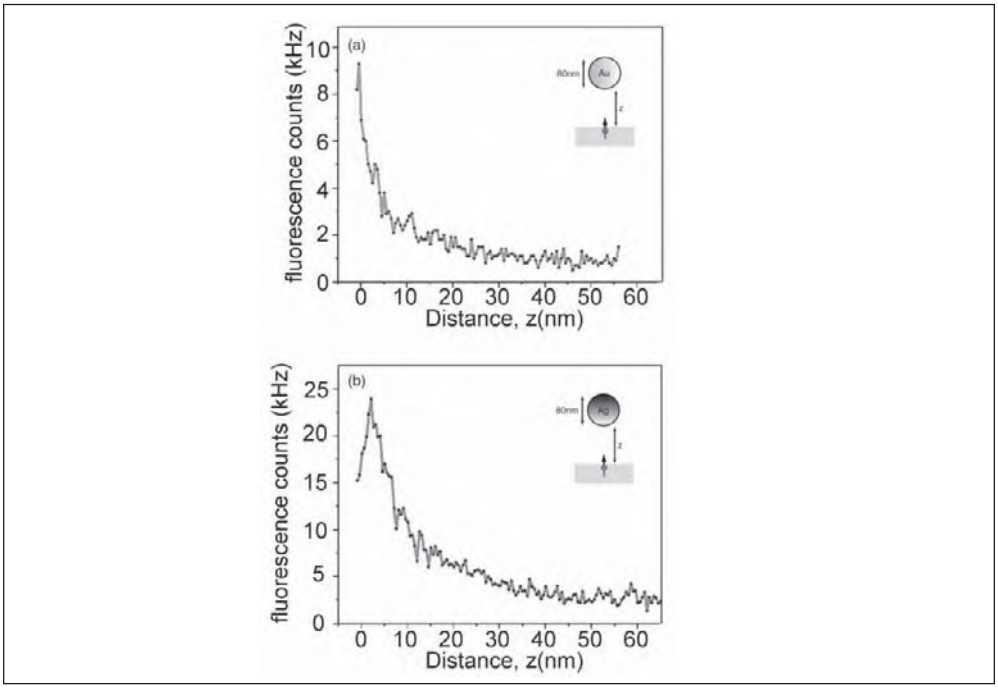

Figure 16.3 Fluorescence rate from a single molecule as a function of particle-sample distance for an 80 nm (a) gold and (b) silver particle. Due to the dominance of nonradiative decay at short distances, the fluorescence is quenched. Bharadwaj et al. ©IOP Publishing Ltd [21].

16.2 Optical Antennas

The sharp gold tips and the single noble metal nanoparticle probes considered previously may be regarded as acting as optical nano-antennas. In this case, the tip or nanoparticle is coupled in the near-field to the fluorophore through the resonant excitation of LSP modes, resulting in enhanced local fields in the optical near-field of the tip or nanoparticle. However, resonant excitation of local optical fields also may be achieved through geometric effects by the realization of optical antennas in which the dimensions of a MNS are matched to an odd integer multiple of half the wavelength of the incident radiation, similar to the radio frequency equivalent. The main objective of the antenna is to couple between the far-field and near-field by impedance matching of the optical waves with the right antenna size. The optical antenna then allows efficient subwavelength confinement of the electromagnetic radiation. Optical antennas using a bow-tie shape were first demonstrated by Grober, Schoelkopf, and Prober [22] at microwave frequencies and recently in the midinfrared [23], near-infrared [24, 25], and visible frequencies [26–28]. Apart from applications in high-resolution microscopy/spectroscopy and optical sensors, the antenna concept also has been used in photovoltaics [29] and solid state lighting [30, 31]. For implementation as the near-field probe of a scanning near-field optical microscope, two approaches have been adopted—the creation of a nanotip on an aperture SNOM probe and a bow-tie antenna on an AFM tip.

In the tip-on-aperture (TOA) method, a metal tip is fabricated at the edge of an aperture in the metal coating at the apex of an optical fiber tip, normally used in aperture SNOM. Light from the aperture couples efficiently to the tip, with a resultant field localization at the tip apex. In particular, this approach can overcome the problem of the far-field background from standard tips in ASNOM, leading to higher signal-to-background ratios, as well as providing a resolution determined by the dimension of the tip rather than the aperture. Guckenberger and coworkers have used this TOA technique to obtain 10 nm resolution of Cy-3 molecules [32]; more recently, the van Hulst group has imaged isolated DiI molecules [33]. In particular, Taminiau and colleagues tuned the length of the tips employed (fabricated using FIB milling) so that they acted as grounded optical antennas with resonant enhancement of local field intensity at the tip apex.

Resonant optical antennas composed of a pair of strongly coupled metallic nanorods have been shown to lead to a large intensity enhancement localized in the gap between the rods [25]. Hecht and coworkers have obtained near-field images of single quantum dots using such bow-tie optical nano-antennas fabricated using FIB at the apex of metal-coated AFM tips (Figure 16.4) [34]. By positioning the antenna probe inside the laser focus at the sample surface and raster-scanning the sample in contact-mode AFM, Farahani and coworkers did not find any significant quenching of the PL due to the proximity of the metal, but did observe a threefold reduction in the fluorescence lifetime.

Following a similar theme, Wang and Lu improved the throughput of a regular aperture SNOM probe by FIB drilling a bowtie [35], with the observation of a sevenfold improvement in the optical transmission when compared to the regular

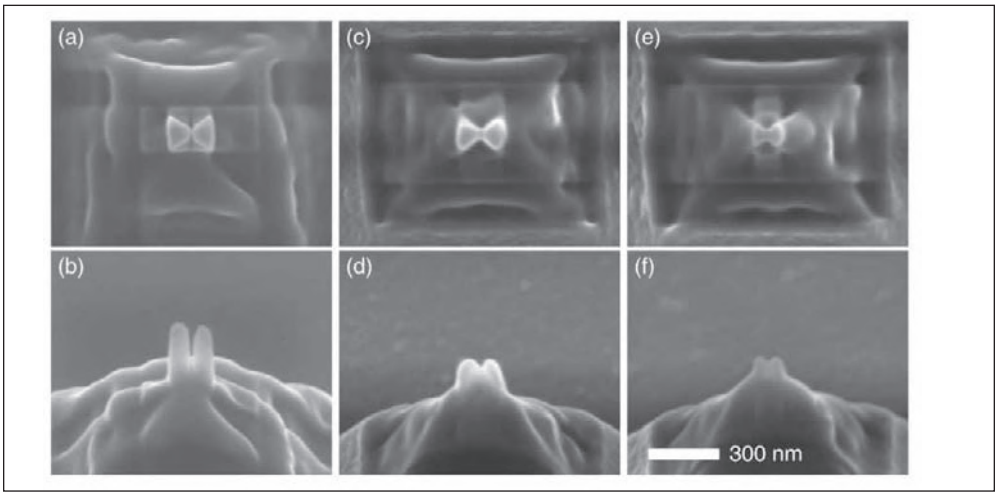

Figure 16.4 SEM images of different bow-tie antenna lengths: (a, b) 170 nm; (c, d) 120 nm; (e, f) 120 nm. The antenna feed gap varies between 25–50 nm. Farahani et al. ©IOP Publishing Ltd [34].

aperture probe and one and a half times lateral resolution enhancement (66 nm). Other applications of bow-tie antennas include, for example, the demonstration by Cubukcu and colleagues of lasing by integrating two nanorods on the facet of a laser diode [36].

16.3 Far-Field Optical Nanoscopy

As identified in Chapter 12, in the context of biological imaging, in parallel with developments in near-field microscopy, there have been significant advances in the development of far-field techniques for the achievement of nanoscale optical imaging. To put the work on SNOM described in this book in context, we will conclude with a brief review of such far-field nanoscopy.

16.3.1 Stimulated Emission Depletion (STED) and 4π Microscopy

Hell and coworkers have made significant advances in recent years with the development of "point spread function engineering," in which the point spread function in the focal plane of the illumination or detection is modified by interference effects and nonlinear optical interactions such that the effective point spread function has a smaller volume. For example, in 4π confocal microscopy, the use of coherent counter-propagating beams has enabled a significant improvement in the axial resolution of a confocal microscope [37]. On the other hand, lateral high spatial resolution in the far-field regime may be achieved with stimulated emission depletion (STED) microscopy [38]. This technique involves the use of two pulsed lasers: (1) A short excitation pulse is employed to induce one-photon excitation of dye molecules present in the focal volume, and (2) a longer and red-shifted depletion pulse at a much higher power produces stimulated emission from the excited to the ground state of the fluorescent molecules. The depletion beam is shaped so that it has zero intensity at the geometrical focus, while the excitation beam has the usual

focus. This ensures that the second STED beam depopulates the excited states everywhere apart from the small region around the zero-intensity point. Using a combination of 4π and STED microscopy, the highest resolution achieved so far has been 33 nm in images of membranes of bacteria [39].

A problem with STED is that the high excitation powers required can cause sample damage, so the technique can only be used with specific types of fluorophores. It also requires complicated optics to align the stimulated emission beam intensity null with the focus of the second beam. The molecules to be imaged should have a fluorescence emission profile well removed from the excitation profile to make sure that the STED beam does not cause absorption and excitation of the molecule. However, this far-field imaging technique is advantageous for imaging soft biological systems that cannot be done in SNOM (e.g., imaging subsurface structures at distances greater than 100 nm). A review by Hell [40] provides a more detailed overview of STED and 4π microscopy.

16.3.2 STORM, PALM, and SSIM

There are alternative imaging techniques that use localization to determine the position of single particles with 20 nm resolution by reconstituting full images from multiple image cycles: STORM, which uses high-accuracy localization of photoswitchable fluorophores [41, 42], and PALM, in which fluorescent molecules are activated, localized, and then bleached [43]. The big disadvantage with both of these methods is that it can take many hours to collect the image.

Saturated structured illumination microscopy (SSIM) is an alternative method for the achievement of 50 nm resolution [44]. This works by introducing additional nonlinear frequencies into a structured illumination pattern by exciting the fluorophores above threshold intensity. The advantage of this method is that no beam scanning is required because the image can be acquired in wide-field form; however, the method suffers from limited photostability and signal-to-noise problems.

16.4 Conclusion

Since its first demonstration, the research field of scanning near-field microscopy has moved through periods of promise followed by disappointment, often because of the huge technical challenges that these techniques present. Yet the need for optical microscopy with nanometer spatial resolution is strong in order to address new challenges in the life sciences and nanotechnology. Near-field optical microscopy has been demonstrated to have great potential for the study of nanostructured semiconductor, ferromagnetic, photonic, biological, liquid crystal, and single molecular systems, and this powerful family of techniques has great potential for application in chemistry, physics, materials, and the life sciences. We now stand at the dawn of an exciting new era in optical microscopy with the development of new probes with great optical and chemical specificity and the achievement of true single-molecule sensitivity and resolution an attainable goal.

Aperture-based SNOM is now reaching maturity and is, in particular, finding niche applications: as a complementary optical technique to AFM and STM (see, for example, Chapter 5); for studies in which submicron optical resolution is

required with surface sensitivity, such as imaging of proteins in membranes of intact biological cells [45]; and as the only tool able to probe directly localized and evanescent optical fields in photonic and plasmonic nanostructures (see Parts II and III). For the dream of optical microscopy with true nanometer resolution, we must turn to apertureless techniques, introduced in Part IV. The chemical specificity of fluorescence and Raman spectroscopy with the high spatial resolution afforded by tip-enhanced techniques will enable the isolation and differentiation of single molecules through their Raman "fingerprint" or fluorescence spectrum and lifetime and will provide important information about molecular, biological, and nanostructured systems on nanometer length scales. Recent advances in the fabrication of custom-designed nanoantennas, as discussed in this chapter, offer much promise for the implementation of techniques for nanoscale imaging of materials and in biological applications. Although significant advances have been achieved in probe structures, many important experimental challenges must be overcome if near-field optical microscopy is to be a reliable and robust technique. There is still the problem of obtaining reliable and robust tips that work for near-field imaging on a more consistent basis. Also, important challenges lie ahead in truly understanding the physical nature of the optical near-field and the factors that dictate it.

Many other optical techniques are outside the scope of this book and are being developed continuously, each with its unique characteristic feature. The development of these techniques as well as SNOM should open up new avenues of research in the future, resolving new phenomena.

References

[1] Festy, F., A. Demming, and D. Richards, "Resonant Excitation of Tip Plasmons for Tip-Enhanced Raman SNOM," *Ultramicroscopy*, Volume 100, 2004, pp. 437–441.

[2] Pettinger, B. et al., "Surface-Enhanced and STM Tip-Enhanced Raman Spectroscopy of CN^- Ions at Gold Surfaces," *Journal of Electroanalytical Chemistry*, Vols. 554–555, 2003, pp. 293–299.

[3] Pettinger, B. et al., "Nanoscale Probing of Adsorbed Species by Tip-Enhanced Raman Spectroscopy," *Physical Review Letters*, Vol. 92, 2004, Art. No. 096101.

[4] Domke, K., D. Zhang, and B. Pettinger, "Toward Raman Fingerprints of Single Dye Molecules at Atomically Smooth Au(111)," *Journal of the American Chemical Society*, Vol. 128, 2006, p. 14721.

[5] Watanabe, H. et al., "Tip-Enhanced Near-Field Raman Analysis of Tip-Pressurized Adenine Molecule," *Physical Review B*, Vol. 69, 2004, Art. No. 155418.

[6] Verma, P. et al., "Near-Field Raman Scattering Investigation of Tip Effects on C-60 Molecules," *Physical Review B*, Vol. 73, 2006, Art. No. 045416.

[7] Yano, T., Y. Inouye, and S. Kawata, "Nanoscale Uniaxial Pressure Effect of a Carbon Nanotube Bundle on Tip-Enhanced Near-Field Raman Spectra," *Nano Letters*, Vol. 6, 2006, pp. 1269–1273.

[8] Saito, Y. et al., "Nanoscale Characterization of Strained Silicon by Tip-Enhanced Raman Spectroscope in Reflection Mode," *Applied Physics Letters*, Vol. 88, 2006, Art. No. 143109.

[9] Hayazawa, N. et al., "Visualization of Localized Strain of a Crystalline Thin Layer at the Nanoscale by Tip-Enhanced Raman Spectroscopy and Microscopy," *Journal of Raman Spectroscopy*, Vol. 38, 2007, pp. 684–696.

[10] Rasmussen, A., and V. Deckert, "Surface- and Tip-Enhanced Raman Scattering of DNA Components," *Journal of Raman Spectroscopy*, Vol. 37, 2006, pp. 311–317.

[11] Neugebauer, U. et al., "On the Way to Nanometer-Sized Information of the Bacterial Surface by Tip-Enhanced Raman Spectroscopy," *Chem. Phys. Chem.*, Vol. 7, 2006, pp. 1428–1430.

[12] Domke, K., D. Zhang, and B. Pettinger, "Enhanced Raman Spectroscopy: Single Molecules or Carbon?" *Journal of Physical Chemistry C*, Vol. 11, 2007, pp. 8611–8616.
[13] Richards, D. et al., "Tip-Enhanced Raman Microscopy: Practicalities and Limitations," *Journal of Raman Spectroscopy*, Vol. 34, 2003, pp. 663–667.
[14] Taylor, C., S. Garvey, and J.E. Pemberton, "Carbon Contamination at Silver Surfaces: Surface Preparation Procedures Evaluated by Raman Spectroscopy and X-ray Photoelectron Spectroscopy," *Analytical Chemistry*, Vol. 68, 1996, pp. 2401–2408.
[15] Schoenfisch, M., A. Ross, and J.E. Pemberton, "Electrochemical Cleaning of Surface-Confined Carbon Contamination in Self-Assembled Monolayers on Polycrystalline Ag and Au," *Langmuir*, Vol. 16, 2000, pp. 2907–2914.
[16] Xie, C. A. et al., "Tip-Enhanced Fluorescence Microscopy of High-Density Samples," *Applied Physics Letters*, Vol. 89, 2006, Art. No. 143117.
[17] Ma, Z. Y. et al., "Fluorescence Near-Field Microscopy of DNA at Sub-10 nm Resolution," *Physical Review Letters*, Vol. 97, 2006, Art. No. 260801.
[18] Huang, F., and D. Richards, "Fluorescence Enhancement and Energy Transfer in Apertureless Scanning Near-Field Optical Microscopy," *J. Opt. A: Pure Appl. Opt.*, Vol. 8, 2006, pp. S234–S238.
[19] Huang, F. M., F. Festy, and D. Richards, "Tip-Enhanced Fluorescence Imaging of Quantum Dots," *Applied Physics Letters*, Vol. 87, 2005, Art. No. 183101.
[20] Kühn, S. et al., "Enhancement of Single-Molecule Fluorescence Using a Gold Nanoparticle as an Optical Nanoantenna," *Physical Review Letters*, Vol. 97, 2006, Art. No. 017402.
[21] Bharadwaj, P., P. Anger, and L. Novotny, "Nanoplasmonic Enhancement of Single-Molecule Fluorescence," *Nanotechnology*, Vol. 18, 2007, Art. No. 044017.
[22] Grober, R. D., R. J. Schoelkopf, and D. E. Prober, "Optical Antenna: Towards a Unity Efficiency Near-Field Optical Probe," *Applied Physics Letters*, Vol. 70, 1997, pp. 1354–1356.
[23] Crozier, K. et al., "Optical Antennas: Resonators for Local Field Enhancement," *Journal of Applied Physics*, Vol. 94, 2003, pp. 4632–4642.
[24] Schuck, P. et al., "Improving the Mismatch Between Light and Nanoscale Objects with Gold Bowtie Nanoantennas," *Physical Review Letters*, Vol. 94, 2005, Art. No. 017402.
[25] Muhlschlegel, P. et al., "Resonant Optical Antennas," *Science*, Vol. 308, 2005, pp. 1607–1609.
[26] Farahani, J. N. et al., "Single Quantum Dot Coupled to a Scanning Optical Antenna: A Tunable Superemitter," *Physical Review Letters*, Vol. 95, 2005, Art. No. 017402.
[27] Fromm, D. et al., "Gap-Dependent Optical Coupling of Single 'bowtie' Nanoantennas Resonant in the Visible," *Nano Letters*, Vol. 4, 2004, pp. 957–961.
[28] Fumeaux, C., J. Alda, and G. Boreman, "Lithographic Antennas at Visible Frequencies," *Optics Letters*, Vol. 24, 1999, pp. 1629–1631.
[29] Derkacs, D. et al., "Improved Performance of Amorphous Silicon Solar Cells via Scattering from Surface Plasmon Polaritons in Nearby Metallic Nanoparticles," *Applied Physics Letters*, Vol. 89, 2006, Art. No. 093103.
[30] Choulis, S., M. Mathai, and V. Choong, "Influence of Metallic Nanoparticles on the Performance of Organic Electrophosphorescence Devices," *Applied Physics Letters*, Vol. 88, 2006, Art. No. 213503.
[31] Okamoto, K. et al., "Surface-Plasmon-Enhanced Light Emitters Based on InGaN Quantum Wells," *Nature Materials*, Vol. 3, 2004, pp. 601–605.
[32] Frey, H.G. et al., "High-Resolution Imaging of Single Fluorescent Molecules with the Optical Near-Field of a Metal Tip, *Physical Review Letters*, Vol. 93, 2004, Art. No. 200801.
[33] Taminiau, T.H. et al., "Lambda/4 Resonance of an Optical Monopole Antenna Probed by Single Molecule Fluorescence," *Nano Letters*, Vol. 7, 2007, pp. 28–33.
[34] Farahani, J. et al., "Bow-Tie Optical Antenna Probes for Single-Emitter Scanning Near-Field Optical Microscopy," *Nanotechnology*, Vol. 18, 2007, Art. No. 125506.

[35] Wang, L., and X. Lu, "High Transmission Nanoscale Bowtie-Shaped Aperture Probe for Near-Field Optical Imaging," Applied Physics Letters, Vol. 90, 2007, Art. No. 261105.
[36] Cubukcu, E. et al., "Plasmonic Laser Antenna," *Applied Physics Letters*, Vol. 89, 2006, Art. No. 093120.
[37] Hell, S., and H. K. Stelzer, "Properties of a 4pi Confocal Fluorescence Microscope," *Journal of the Optical Society of America A*, Vol. 9, 1992, pp. 2159–2166.
[38] Hell, S., and J. Wichmann, "Breaking the Diffraction Resolution Limit by Stimulated Emission: Stimulated Emission Depletion Microscopy," *Optics Letters*, Vol. 19, 1994, p. 780.
[39] Dyba, M., and S. Hell, "Focal Spots of Size $\lambda/23$ Open Up Far-Field Fluorescence Microscopy at 33nm Axial Resolution," *Physical Review Letters*, Vol. 88, 2002, Art. No. 163901.
[40] Hell, S. W., "Toward Fluorescence Nanoscopy," *Nature Biotechnology*, Vol. 21, 2003, pp. 1347–1355.
[41] Rust, M., M. Bates, and X. Zhuang, "Sub-Diffraction-Limit Imaging by Stochastic Optical Reconstruction Microscopy," *Nature Methods*, Vol. 3, 2006, pp. 793–796.
[42] Bates, M. et al., "Multicolor Super-Resolution Imaging with Photo-Switchable Fluorescent Probes," *Science*, Vol. 317, 2007, pp. 1749–1753.
[43] Betzig, E. et al., "Imaging Intracellular Fluorescent Proteins at Nanometer Resolution," *Science*, Vol. 313, 2006, pp. 1642–1645.
[44] Gustafsson, M., "Nonlinear Structured-Illumination Microscopy: Wide-Field Fluorescence Imaging with Theoretically Unlimited Resolution," *Proceedings of the National Academy of Sciences*, Vol. 102, 2005, pp. 13081–13086.
[45] Koopman, M. et al., "Near-Field Scanning Optical Microscopy in Liquid for High Resolution Single Molecule Detection on Dendritic Cells," *FEBS Letters*, Vol. 573, 2004, pp. 6–10.

List of Acronyms and Abbreviations

AAO	Anodic aluminum oxide
AFM	Atomic Force Microscope
ANR	Au Nano Rods
AOM	Acousto-Optic Modulator
APD	Avalanche Photodiode
ASNOM	Apertureless Scanning Near-Field Optical Microscopy
CCD	Charge Coupled Device
CGM	Constant Gap Mode
CHM	Constant Height Mode
CIM	Constant Signal Intensity Mode
COM	Classical Optical Microscope
CW	Continuous Wave
EOT	Enhanced Optical Transmission
EUV	Extreme UV
FDTD	Finite-Difference Time-Domain
FIB	Focused Ion Beam
FRET	Förster Resonance Energy Transfer
FTIR	Fourier Transform Infrared
FWHM	Full-Width at Half-Maximum
GSD	Ground-State Depletion
GVP	Group Velocity Dispersion
HG	Hermite Gaussian
HOMO	Highest Occupied Molecular Orbital
IMJ	Intramolecular Junction
LED	Light Emitting Diode
LIA	Lock-In Amplifier
LSP	Localized Surface Plasmon
LUMO	Lowest Unoccupied Molecular Orbital
MNS	Metal Nano Structures
NA	Numerical Aperture
NFO	Near-Field Optics
NFOL	Near-Field Optical Lithography
OLED	Organic Light Emitting Diode
PALM	Photoactivatable Localization Microscopy
PBG	Photonic Band Gap
PEEL	Phase Shifting Lithography, Etching, Electron Beam Deposition, and Lift-off

PhC	Photonic Crystals
PhCW	Photonic Crystal Waveguide
PL	Photoluminescence
PSTM	Photon Scanning Tunneling Microscope
RBM	Radial Breathing Mode
RESOLFT	Reversible Saturable Optically Linear Fluorescent Transitions
RIE	Reactive Ion Etching
RPG	Radial Polarization Generator
SEM	Scanning Electron Microscope
SERS	Surface Enhanced Raman Scattering
SH	Second Harmonic
SHG	Second Harmonic Generation
SNOM	Scanning Near-Field Optical Microscopy
SNR	Signal-to-Noise Ratio
SOI	Silicon-on-Insulator
SP	Surface Plasmon
SPEM	Saturated Pattern Excitation Microscopy
SPM	Scanning Probe Microscopy
SPOL	Surface Plasmon Optical Lithography
SPP	Surface Plasmon Polariton
SPP-BW	Surface Plasmon Polariton – Bloch Waves
SPR	Surface Plasmon Resonance
SSIM	Saturated Structured Illumination Microscopy
STED	Stimulated Emission Depletion
STM	Scanning Tunneling Microscopy
STORM	Stochastic Optical Reconstruction Microscopy
SWNT	Single-Walled Carbon Nanotubes
TCSPC	Time Correlated Single Photon Counting
TEFM	Tip-Enhanced Fluorescence Microscopy
TEM	Transmission Electron Microscopy
TERS	Tip-Enhanced Raman Scattering
TFE	Tip-Field Enhancement
TIR	Total Internal Reflection
TIRF	Total Internal Reflection Fluorescence
TOA	Tip-on-Aperture
TOD	Third-Order Dispersion
UV	Ultraviolet

About the Editors

Anatoly Zayats is a professor of physics at Queen's University in Belfast, United Kingdom. In 1999 he founded and currently leads the Nano-optics and Near-field Spectroscopy Group at the Centre for Nanostructured Media. He also is a visiting professor at Sogang University in Seoul, South Korea. He holds a M.Sc. and a Ph.D. in physics, both from the Moscow Institute of Physics and Technology. Professor Zayats' research interests are in the areas of near-field optics, scanning probe microscopy, nanophotonics, nonlinear optics and spectroscopy, surface plasmons and polaritons, and optical properties of surfaces, thin films, semiconductors, and low-dimensional structures. His recent research had wide-ranging positive coverage in general and professional press including *Physical Review Focus*, *Physics Today*, *New Scientist*, *Electronic Engineering Times*, and *Photonics Spectra*. He has been a principal investigator on a number of grants funded by the EPSRC (UK), the European Commission, the Royal Society, and industry. Professor Zayats sits on panels of various national and international funding bodies and serves on the program committees of major nanophotonics-related conferences. He is a fellow of the Institute of Physics and the Optical Society of America.

David Richards is a professor of physics and the head of the physics department at King's College London. He holds an M.A. and a Ph.D. in physics from the University of Cambridge and is a fellow of the Institute of Physics. Before moving to King's College London in 2000, he held a research fellowship at the Cavendish Laboratory, Cambridge, a Lloyd's of London Foundation fellowship at St. John's College Cambridge, and a Royal Society University research fellowship. His past research has been concerned with two main themes, electronic excitations in low-dimensional semiconductors, and nano- and bio-photonics, the latter now forming the main focus of his work. Present research interests include the development of scanning near-field optical microscopy techniques, surface enhanced Raman and fluorescence spectroscopy, and biological cell imaging.

List of Contributors

N. Anderson
University of Rochester
The Institute of Optics
Rochester
New York 14627
USA

R. Bachelot
Laboratoire de Nanotechnologie et d'Instrumentation Optique
ICD CNRS FRE2848
Université de Technologie de Troyes 12 rue Marie Curie
BP2060, 10010 Troyes cedex
France

S. I. Bozhevolnyi
Department of Physics and Nanotechnology
Aalborg University
Skjernvej 4A
DK-9220 Aalborg Øst
Denmark

F. Cacialli
Department of Physics and Astronomy University College London
Gower Street
London
WC1E 6BT
UK

P.C. Chaumet
Institut Fresnel (UMR 6133)
Université d'Aix-Marseille I & III
Avenue Escadrille Normandie-Niemen
F-13397 Marseille Cedex 20
France

F. Culfaz
Department of Physics
King's College London
Strand
London WC2R 2LS
UK

R. J. P. Engelen
FOM Institute for Atomic and Molecular Physics (AMOLF)
Kruislaan 407
1098SJ Amsterdam
The Netherlands

E. Fort
UMR 7162 CNRS and University Paris Diderot
Laboratoire Matériaux et Phénomènes Quantiques
Bâtiment Condorcet
case courier 7021
10 rue Alice Domon et Leonie Duquet
75205 Paris CEDEX 13
France

H. Gao
Northwestern University
Department of Materials Science and Engineering
2145 Sheridan Road
Evanston, IL
60208
USA

C. Georgi
Department Chemie und Biochemie and CeNS
Ludwig-Maximilians-Universität München
81377 München
Germany

J. Gerton
Department of Physics
University of Utah
115 S. 1400 E. Room 201
Salt Lake City,UT
84112
USA

S. K. Gray
Chemical Sciences and Engineering Division
Argonne National Laboratory
9700 South Cass Avenue
Argonne, IL
60439
USA

S. Grésillon
Centre d'Imageries Plasmoniques Appliquées
Laboratoire Photons et Matière
CNRS UPR A5 and Paris Universitas
Laboratoire d'Optique Physique,
ESPCI
10 rue Vauquelin
75231 Paris Cedex 5
France

A. Hartschuh
Department Chemie und Biochemie
and CeNS
Ludwig-Maximilians-Universität München
81377 München
Germany

R. Hillenbrand
Nano-Photonics Group
Max-Planck-Institut für Biochemie
82152 Martinsried (München)
Germany

C. Hubert
Laboratoire Hubert Curien
UMR CNRS 5516
18 rue du Professeur Benoît Lauras
42000 St-Etienne
France

G. H. Ibn El Ahrach
Center for Nanoscale Materials
Argonne National Laboratory
9700 South Cass Avenue
Argonne, IL
60439
USA

F. Keilmann
Max-Planck Institut fur Quantenoptik and Center for Nanoscience,
85741 Garching, Germany

L. Kuipers
FOM Institute for Atomic and Molecular Physics (AMOLF)
Kruislaan 407
1098SJ Amsterdam
The Netherlands

J. Lérondel
Laboratoire de Nanotechnologie et d'Instrumentation Optique
ICD CNRS FRE2848
Université de Technologie de Troyes
12 rue Marie Curie
BP2060, 10010 Troyes cedex
France

S. Leveque-Fort
Centre de Photonique Biomédical Université Paris Sud
Bâtiment 106
91405 Orsay Cedex
France

D. Lidzey
Department of Physics and Astronomy University of Sheffield
Hicks Building
Hounsfield Road
Sheffield
S3 7RH
UK

Z. Ma
Department of Bioengineering
Stanford University
318 Campus Drive
Clark Center Room S170
Stanford, CA
94305
USA

B. D. Mangum
Department of Physics
University of Utah
115 S. 1400 E. Room 201
Salt Lake City, UT
84112
USA

C. Mu
Department of Physics
University of Utah
115 S. 1400 E. Room 201
Salt Lake City, UT
84112
USA

M. Nieto-Vesperinas
Department of Condensed Matter Theory Instituto de Ciencia de Materiales de Madrid
Consejo Superior de Investigaciones Cientificas
Universidad Autonoma de Madrid
Campus de Cantoblanco
Madrid
28049
Spain

L. Novotny
University of Rochester
The Institute of Optics
Rochester
New York 14627
USA

T. W. Odom
Northwestern University
Department of Materials Science and Engineering and Department of Chemistry
2145 Sheridan Road
Evanston, IL
60208
USA

J. Plain
Laboratoire de Nanotechnologie et d'Instrumentation Optique
ICD CNRS FRE2848
Université de Technologie de Troyes
12 rue Marie Curie
BP2060, 10010 Troyes cedex
France

D.W. Pohl
Institute of Physics
University of Basel
Klingelbergstr 82
CH-4056 Basel
Switzerland

H. Qian
Department Chemie und Biochemie and CeNS
Ludwig-Maximilians-Universität München
81377 München
Germany

A. Rahmani
Department of Mathematical Sciences and CUDOS
University of Technology
Sydney NSW 2007
Australia

D. Richards
Department of Physics
King's College London
Strand
London
WC2R 2LS
UK

P. Royer
Laboratoire de Nanotechnologie et d'Instrumentation Optique
ICD CNRS FRE2848
Université de Technologie de Troyes
12 rue Marie Curie
BP2060 10010 Troyes cedex
France

S. K. Sekatskii
Laboratoire de Physique de la Matière Vivante
IPMC
Ecole Polytechnique Fédérale de Lausanne
CH-1015 Lausanne
Switzerland

I.I. Smolyaninov
Electrical and Computer Engineering Department
University of Maryland
College Park
MD 20742
USA

O. Soppera
Département de Photochimie Générale
CNRS UMR 7525
Ecole Nationale Supérieure de Chimie de Mulhouse
3 rue A. Werner
68093 Mulhouse Cedex
France

A. Vial
Laboratoire de Nanotechnologie et d'Instrumentation Optique
ICD CNRS FRE2848
Université de Technologie de Troyes
12 rue Marie Curie
BP2060, 10010 Troyes cedex
France

V. S. Volkov
Department of Physics and Nanotechnology
Aalborg University
Skjernvej 4A
DK-9220 Aalborg Øst
Denmark

G. P. Wiederrecht
Center for Nanoscale Materials
Argonne National Laboratory
Argonne, IL
60439
USA

G. A. Wurtz
Department of Chemistry and Physics University of North Florida
Jacksonville, FL
32224
USA

A. V. Zayats
Centre for Nanostructured Media, IRCEP
The Queen's University of Belfast
Belfast BT7 1NN
United Kingdom

Index

Related Titles from Artech House

Introduction to DNA Self-Assembled Computer Design, Christopher Dwyer and Alvin Lebeck

Design and Test of Digital Circuits by Quantum-Dot Cellular Automata, Fabrizio Lombardi and Jing Huang

Nanoelectronics Principles and Design, Mircea Dragoman and Daniela Dragoman

Nanotechnology Applications and Markets, Lawrence D. Gasman

Nanotechnology Regulation and Policy Worldwide, Jeffrey H. Matsuura

Organic and Inorganic Nanostructures, Alexei Nabok

Optics of Quantum Dots and Wires, Garnett W. Bryant and Glenn S. Solomon, editors

Semiconductor Nanostructures for Optoelectronic Applications, Todd Steiner, editor

New Photonics Technologies for the Information Age: The Dream of Ubiquitous Services, Shoichi Sudo and Katsunari Okamoto, editors

Bionanoreactor Technologies for Life Sciences and Medicine, Agnes Ostafin, Katharina Landfester, Lakshmi Sridar, and Alexander Moukasian

Micro- and Nanoengineering of the Cell Microenvironment: Technologies and Applications, Ali Khademhosseini, Jeffrey Borenstein, Mehmet Toner, Shuichi Takayama, editors

Micro and Nano Manipulations for Biomedical Applications, Tachung C. Yih and Ilie Talpasanu

For further information on these and other Artech House titles, including previously considered out-of-print books now available through our In-Print-Forever® (IPF®) program, contact:

Artech House
685 Canton Street
Norwood, MA 02062
Phone: 781-769-9750
Fax: 781-769-6334
e-mail: artech@artechhouse.com

Artech House
46 Gillingham Street
London SW1V 1AH UK
Phone: +44 (0)20 7596-8750
Fax: +44 (0)20 7630-0166
e-mail: artech-uk@artechhouse.com

Find us on the World Wide Web at: www.artechhouse.com